Zeitschrift: Helvetica Physica Acta

Band: 59 (1986)

Heft: 6-7

Vereinsnachrichten: Bericht über die Frühjahrstagung der Schweizerischen Physikalischen Gesellschaft am Physikinstitut von Neuenburg vom 9.-11. April 1986

Autor: [s.n.]

BERICHT UEBER DIE FRUEHJAHRSTAGUNG DER SCHWEIZERISCHEN PHYSIKALISCHEN GESELLSCHAFT AM PHYSIKINSTITUT VON NEUENBURG VOM 9. - 11. April 1986

I. Administrativer Teil

Vorstand der SPG:

Prof. P.	Minkowski	Präsident
Prof. S.	Steinemann	Vizepräsident
Prof. P.	Grieder	Sekretär
Dr. H.	Hänni	Kassier
Dr. J.P.	Egger	Teilchen-, Astro- + Kernphysik
Prof. P.	Martinoli	Kondensierte Materie
Dr. M.	Siegrist	Angewandte Physik
Dr. D.	Ryter	Theoretische Physik
Prof. R.	Dändliker	Wissenschaftspolitik
Prof. H.J.	Gerber	Helvetica Physica Acta
Prof. I.	Zschokke	I.U.P.A.P.

Rechnungsrevisoren:

Prof. W. Czaja
Prof. L. Schellenberg

Stellenvermittlung der SPG

Prof.Dr. Fritz K. Kneubühl
Labor f.Quantenelektronik
ETH Hönggerberg
CH-8093 Zürich
Tel. 01/377 23 40

Helvetica Physica Acta

Prof. Ph.A. Martin, Rédacteur
Institut de Physique Théorique
EPFL/PHB
CH-1015 Lausanne
Tel. 021/47 34 13

Sekretariat:

Schweizerische Physikalische Gesellschaft
Institut für Theoretische Physik der Universität Bern
Sidlerstrasse 5
CH-3012 Bern Tel. 031/65 86 24 / 65 44 17

Neue Mitglieder (seit dem 20. August 1985)

ARIOSA Daniel, BACH Pierre, BAVAUD François, BAY Aurelio, BRUGGMANN Guido, CERRI Alberto, CLAIR Jean-Jacques, GAILLE François, GUENTHER Christoph, HONGLER Max-Olivier, HUBER Erich, HUG Carl, JECKELMANN Beat, JURCZEK Edmond, KUEHNE René, MARCLAY Etienne, MARTI Othmar, MUELLER Ueli, PATTHEY François, REINHART Franz-Karl, RENTSCH René, RETTENMUND Ulrich, RICKA Jaroslav, ROMERO José, RUCHTI Christoph, SANJINES Rosendo, SBAI Ali, SEILER Kurt, SORMANI Philippe, STAMPFLI Peter, TURNBULL Alan, ZYSSET Beat.

Die Adressen können beim Sekretariat verlangt werden.

Damit zählt unsere Gesellschaft zurzeit 1240 Einzelmitglieder, 8 Gesellschaften und 14 Bibliotheken als Kollektivmitglieder.

Die Generalversammlung fand am 10. April 1986 in Neuenburg statt.

Protokoll

Anwesend: 40 Personen

1. Protokoll der Generalversammlung vom 3. Oktober 1985 in Biel
Das Protokoll wird ohne Einwände genehmigt.

3. Mitteilungen des Vorstandes

- Ankündigung von Tagungen
Herbsttagung: 9. - 10. Oktober 1986 in Bern
Frühjahrstagung: 3 Tage vom 18. - 20. März 1987 an der Universität Zürich
Gemeinsame Tagung mit der Oesterreichischen Physikalischen Gesellschaft und der Sektion Elementarteilchenphysik der Deutschen Physikalischen Gesellschaft.

- Anschaffung eines Personal-Computers (PC) für das Sekretariat
Der Vorstand hat sich zum Kauf eines PC für das Sekretariat entschlossen, um die Abwicklung der Sekretariatsarbeiten zu vereinfachen und zu verbessern. (Höhe der vorgesehen Auslage ca. Fr. 15'000.- bis 20'000.--).

- Mitgliederausweis
Auf vielseitigen Wunsch wird ein Mitgliederausweis in handlicher Form geschaffen, der es erlaubt, sich an Kongressen und andern wissenschaftlichen Anlässen auszuweisen.

- "Zukunft der Physik an den Eidg. Technischen Hochschulen"
Die Ausführungsbestimmungen des Schulrats der ETH wurden von verschiedenen Seiten verlangt, u.a. Holland, Ciba-Geigy. Sie wurden mit dem Hinweis abgegeben, dass sie vertraulich zu behandeln sind.

- Aktion zur Unterstützung von Orlov und Shcharansky
Die Befreiung von Prof. A. Shcharansky ist inzwischen erfolgt; mit derjenigen von Prof. Y. Orlov darf laut Bericht des Internationalen Komitees im Laufe des Monats Juni gerechnet werden.

3. Jahresrechnung 1985 - Rapport der Rechnungsrevisoren

Der Kassier präsentiert die Jahresrechnung 1985. Sie schliesst mit einem Ausgabenüberschuss von ungefähr Fr. 11'000.- ab, verursacht im wesentlichen durch zwei Posten: Erstens wurde im Jahre 1984 bei der HPA das

"Camera-ready"-Verfahren eingeführt, weshalb in jenem Jahr drei statt wie üblich nur zwei Autorenbeiträge à ca. Fr. 5'500.- einkassiert werden konnten. Infolgedessen blieb aber für das Jahr 1985 nur ein Beitrag übrig. Zweitens wurde der von der SPG gesprochene einmalige Beitrag von Fr. 15'000.- an das Startkapital der neuen europäischen Zeitschrift Europhysics- Letters (EPL) schon im Jahr 1985 fällig, statt wie vorgesehen erst 1986. An diesen Beitrag zahlte die SNG Fr. 10'000.-. Den Rest von Fr. 5'000.- musste die SPG aufbringen.
Die Jahresrechnung 1985 wird auf Antrag der Revisoren von der Generalversammlung einstimmig genehmigt.

4. Budget 1986 - Erhöhung der Beiträge
Das Budget für das Jahr 1986 sieht ebenfalls einen Ausgabenüberschuss von gut Fr. 7'000.- vor. Hauptverursacher ist in diesem Fall die Frühjahrstagung 86 in Neuenburg, die gemeinsam mit einigen Sektionen der SFP durchgeführt wurde, was einen beträchtlichen Mehraufwand an Tagungs- und Publikationskosten verursacht. In diesem Zusammenhang präsentiert der Kassier eine Kostenanalyse, die zeigt, dass der SPG pro zahlendes Mitglied und Jahr nur ca. Fr. 2.60, d.h. total nur etwa Fr. 2'500.- im Jahr für andere als mitgliedergebundene Aufwendungen zur Verfügung steht, und deshalb das Eingehen anderweitiger Verpflichtungen, wie z.B. das Durchführen gemeinsamer Tagungen mit den Schwestergesellschaften DPG, OePG und SFP sofort zu finanziellen Engpässen führt. Andererseits sollen solche gemeinsamen Anlässe in Zukunft vermehrt durchgeführt werden, da sie sich als sehr fruchtbar für unsere Gesellschaft erwiesen haben. Um diesbezüglich und auch hinsichtlich einer intensiveren Nachwuchsförderung und Oeffentlichkeitsarbeit etwas mehr Handlungsspielraum zu erhalten, beantragt der Kassier der Generalversammlung im Einvernehmen mit dem Vorstand eine Erhöhung der Mitglieder-Jahresbeiträge von Fr. 35.- auf Fr. 50.- für Einzelmitglieder und von Fr. 200.- auf Fr. 285.- für Kollektivmitglieder. (Die Beiträge der Bibliotheken von Fr. 25.- bleiben unverändert). Studenten, definiert als Mitglieder unter dreissig Jahren, bezahlen den bisherigen Beitrag von Fr. 35.-, Studenten über dreissig Jahre nur auf jährlich zu erneuernden Antrag. Wer die Mitgliedschaft auf Lebenszeit erlangen möchte, bezahlt neu Fr. 1'000.- minus 50% der bereits bezahlten Jahresbeiträge. Mitglieder über 65 Jahre in bescheidenen Verhältnissen können auf einmaligen Antrag vom Entrichten der Jahresbeiträge befreit werden. Der Kassier erwähnt zudem, dass sich für 1986 eine ausserordentliche Auslage von Fr. 15'000.- bis 20'000.-, bedingt durch die vom Vorstand beschlossene Beschaffung eines eigenen PC ergeben wird. Die erwähnte Erhöhung der Mitgliederbeiträge wird von der Generalversammlung mit einer Gegenstimme und drei Enthaltungen genehmigt.

5./6. Mitteilungen der Fachgruppenvertreter und der Kommissionspräsidenten

Festkörperphysik: Prof. Martinoli wird sich mit Herrn Prof. Schwarzenbach, Präsident der Schweiz. Gesellschaft für Kristallographie betreffend gemeinsames Symposium in Verbindung setzen.
Gleichzeitig teilt er mit, dass er auf nächsten Herbst sein Amt als Fachvertreter niederlegen und einen Nachfolger vorschlagen wird.
Der Präsident benützt die Gelegenheit um Prof. P. Martinoli im Namen der Gesellschaft für die hervorragende Arbeit, die er und seine Mitarbeiter zur Organisation des Kongresses geleistet haben, zu danken.

Angewandte Physik: Für die Tagung in Bern erwarten Dr. R.W. Meier (BBC Forschungszentrum) und Dr. M.R. Siegrist (CRPP-EPFL) Vorschläge von unseren Mitgliedern betreffend Durchführung eines Symposiums zum Thema Photovoltaik als Schwerpunktsthema unserer Herbsttagung.

Wissenschaftspolitische Kommission: Die Arbeiten für den Katalog 1985 "Forschung der Physik in der Schweiz" sind gut vorangeschritten, die Herausgabe des Werkes ist für den Monat Juni vorgesehen.

Helvetica Physica Acta: Prof.H.P. Gerber teilt mit, dass der Birkhäuserverlag vom Springerverlag in Heidelberg übernommen wurde, wie dies aus den Zeitungen ersehen werden konnte. Der HPA-Verlagsvertrag wird in der bestehenden Form vorläufig weitergeführt.
Prof. Ph. Martin wie auch Prof. H.P. Gerber fordern die Mitglieder der Gesellschaft erneut eindringlich auf, ihre guten Arbeiten in der HPA zu veröffentlichen.
Vol. 59 für das Jahr 1986 wird in 8 anstelle von 6 Nummern herausgegeben werden. Der Abonnementspreis ist entsprechend erhöht worden. Die Konferenzbeiträge "Stückelberg Memorial Lectures" und die Proceedings des "Gwatt Workshops on Broken Symmetry" werden publiziert.

7. Astrophysik : Eine engere Zusammenarbeit mit der Schweiz. Gesellschaft für Astrophysik wird gewünscht. Die Erweiterung der Sektion Kern- und Teilchenphysik wird vorgeschlagen wobei die Astrophysik aus der Sektion ANDO in die Sektion KETE verlegt wird. Ein neuer Name TASK (Teilchen-, Astro- und Kernphysik) wird vorgeschlagen. Diese Aenderungsvorschläge wurden genehmigt.

8. Europhysics-Letters: Die Herausgabe des ersten Journals ist erfolgt. Es ist noch zu früh für eine erste Stellungnahme.

9. Wahlen

- Anstelle des zurücktretenden Dr. J.P. Egger wird Prof. Lukas A. Schaller, Universität Freiburg als Fachpräsident der Sektion TASK (früher KETE) gewählt.

- Rechnungsrevisoren: Beide Rechnungsrevisoren, Prof. W. Czaja und Prof. W. Schellenberg sind am Ende ihres Mandates angelangt. Der Präsident dankt den beiden Herren für ihre wertvolle Mitarbeit. Als Nachfolger wurden in der Zwischenzeit die Herren Dr. Jürg Gasser und Dr. Jürg Schacher, Universität Bern verpflichtet.

- HPA: Der neue Vorstand der HPA Redaktion stellt sich wie folgt zusammen:

Redaktor:	Prof. Ph. Martin, EPF Lausanne
Präsident:	Dr. Th. Schucan, EIR Würenlingen
Mitglieder:	Prof. W. Amrein, Universität Genf (neu)
	Prof. H. Hofer, ETH Zürich (neu)
	Prof. T.M. Rice, ETH Zürich (neu)
	Prof. H. Rudin, Universität Basel
	Dr. M. Brüllmann, Meteor A.G., Rüschlikon

Der zurücktretende Präsident, Prof. H.P. Gerber, dankt dem Redaktor für seine Mitarbeit, und Prof. Minkowski richtet seinerseits seinen Dank für die gute Zusammenarbeit an den scheidenden Präsidenten.

10. Verschiedenes

- Mitgliederwerbung: Ein Zirkularbrief wird in diesem Jahr an alle Institute versandt, um unsere Gesellschaft vor allem bei jungen Physikern vermehrt bekannt zu machen.

- Werbung nach aussen: Die Firma Philips Eindhoven hat an dieser Tagung ausgestellt und die Kosten für einen Versand ihres Prospektes an alle Mitglieder übernommen. Prof. Grieder dankt dem anwesenden Vertreter der Firma Philips für sein Interesse.

- Zukunft des SIN: Eine generelle Diskussion zum Thema "Zukunft des SIN" wurde durch vier Kurzvorträge mit den folgenden Titeln eröffnet:

Zukunftsperspektive der Schweizer Hochenergiephysik . . .	(Dr. J. Schacher)
High and Ultra High Energy Non-Accelerator Physics	(Prof. P. Grieder)
Zukunftsperspektiven des SIN . .	(Prof. J.P. Blaser)
Zusammenfassung	(Prof. P. Minkowski)

Die Diskussion wird an der Herbsttagung 1986 im Rahmen einer "Panel Discussion", Zukunft der Physik, fortgesetzt.

SCIENTIFIC PART

Besides the contributed papers of the joint SPS/SFP parallel sessions, covering the sections

Applied Physics	(50 titles)
Condensed Matter	(51 titles)
Particle-, Astro- and Nuclear Physics	(17 titles)
Theoretical Physics	(17 titles)

Two special symposia had been organized:

1. Low Temperature Physics by
   Prof. D. Thoulouze and Prof. P. Martinoli (22 titles)

2. Astrophysics, "From Clouds to Stars" by
   Prof. Nicole Bel and Prof. J.-P. J. Lafon (16 titles)

The proceedings will be divided into two parts.

Part 1: Contributed papers and extended abstracts

Part 2: Invited lectures

Bern, 15.05.1986

Der Präsident:	Der Sekretär:	Der Kassier:
P. Minkowski	P. Grieder	H. Hänni

Symposium spécial

Physique des Basses Températures

organisé par les Professeurs

D. Thoulouze, CRTBT, Grenoble, France

et

P. Martinoli, Institut de Physique, Université Neuchâtel

PHYSIQUE DES BASSES TEMPERATURES

PBT I : Fermions lourds

ELECTRONIC STRUCTURE OF UPt_3 AS DETERMINED BY FAR-INFRARED OPTICAL SPECTROSCOPY

F. Marabelli, G. Travaglini and P. Wachter
Laboratorium für Festkörperphysik, ETH-Hönggerberg, 8093 Zürich, Switzerland

Abstract : The optical reflectivity of UPt_3 single crystals has been measured between 5 and 300 K for photon energies between 0.5 eV and 1 meV. The analysis of the low temperature data reveals heavy quasiparticles at E_F with an effective mass of 250 m. The lowest energy interband transition is at 4 meV.

INTRODUCTION

The ground state properties of heavy fermions have created a lot of interest in recent years. γ-values[1] of the specific heat indicate an enormously large density of states at E_F. This is common when f states coexist with d states at E_F because their hybridization will lead to narrow f bands. For such narrow bands Fermi liquid theory introduces an effective mass which becomes very much enhanced. At high temperatures thermal excitations will destroy the many body correlations and "normal" behavior will prevail. We have performed optical reflectivity measurements on UPt_3 at room temperature and at 5 K.

EXPERIMENTAL RESULTS

To perform optical reflectivity measurements on UPt_3 we used as surface the basal plane of the hexagonal crystals in order to avoid polarization dependances. In the infrared and far-infrared part of the spectrum (0.5 eV - 1 meV) we have employed a Fourier spectrometer with a liquid helium cooled germanium bolometer from 100 to 8 cm^{-1}. For photon energies larger than 30 meV our data could be linked with the reflectivity measurements up to 12 eV of Schoenes and Franse[2]. The reflectivity has been extrapolated for photon energies larger than 12 eV the same way as in ref.(2), whereas towards zero frequency the spectrum has been extended by means of the Hagens-Rubens relation. The complete spectrum was analyzed in terms of optical constants by means of the Kramers-Kronig transformation.

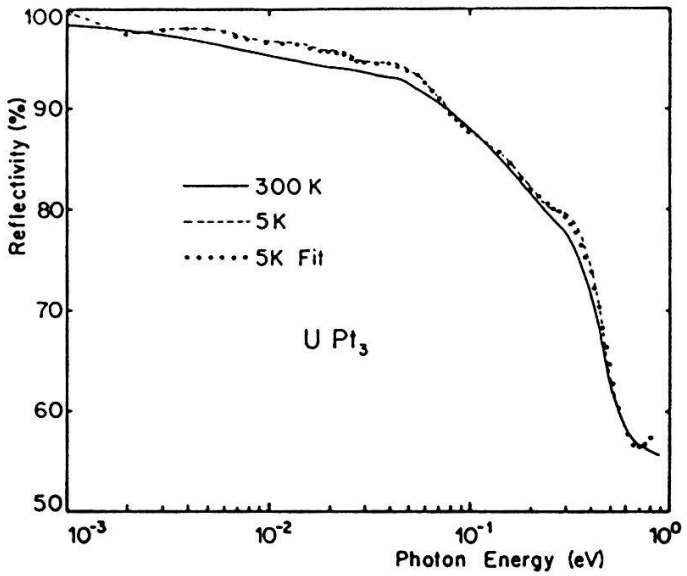

Fig. 1 : Near normal incidence reflectivity of UPt_3 at 5 K and at 300 K. Dots correspond to the fit with Lorentz oscillators.

DISCUSSION

Regarding the conductivity spectrum at room temperature we discern above a basic contribution due to free carriers one peak around 30 meV and another very broad structure at 0.3 eV, followed by a conductivity minimum at 0.5 eV. The main features which we observe at low temperature are a free carrier behavior for the lowest energies, then a gap followed by a series of peaks. The first transition is at 4 meV. These structures are indipendent from the extrapolation we adopt in order to reach a reflectivity of 1 for zero energy. We tried to find the plasma frequency and the effective mass of the heavy quasiparticles. For this goal we made a fit of the conductivity in such a way as to have consi-

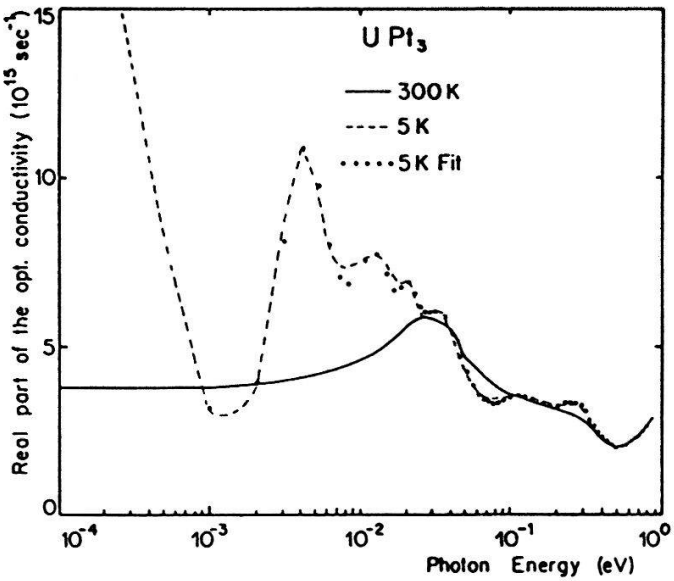

Fig. 2 : Real part of the optical conductivity of UPt_3 at 5 K and at 300 K. Dots correspond to the fit with Lorentz oscillators.

TABLE 1 : Parameters of the Lorentz oscillator fit of the low temperature peaks

energy (eV)	oscillator strenght (1 el/mol)	band width (eV)
0.004	0.018	0.0042
0.012	0.024	0.010
0.020	0.0065	0.008
0.034	0.072	0.037
0.114	0.153	0.145
0.27	0.256	0.285

stency between fit, extrapolation and experimental reflectivity values. We found convergence to the value of the plasma frequency ω_p = 280 meV. Fermi liquid theory and theoretical arguments[3] permit to determine both the effective mass m* and the Fermi vector k_F from the measured values of ω_p and γ.[1] Our analysis yiel ds m*= 250 m and k_F= 0.75 A^{-1} which correspond to closely 1 electron per uranium. Between 4 and 500 meV we can identify six structures in the spectrum of the optical conductivity at low temperatures. A fit performed on these structures gives the values reported in Table 1. Regarding the oscillator strength, the lowest energy transitions correspond in principle to f-f transitions which, however , have a strong d admixture. A d-f hybridization model according to Brandow [4] always yields a gap in the density of states. Also when the Fermi level is in the f band we expect f-f transitions from a lower occupied f band to empty states above E_F and, of course, a Drude behavior of the heavy quasiparticles.

REFERENCES

(1) G.R. Stewart, Rev. Mod. Phy. 56, 755 (1984)

(2) J. Schoenes and J.J.M. Franse, Physica 130 B, 69 (1985)

(3) T.M. Rice, private communication

(4) B.H. Brandow, Phys. Rev. B (1986) in press

Propriétés de transport du $CeCu_6$ monocristallin

A. Amato, D. Jaccard, E. Walker et J. Sierro
DPMC - Genève
et J. Flouquet, CRTBT - Grenoble

Le composé à fermions lourds, de structure orthorombique, $CeCu_6$ présente selon la direction [100] une résistivité quadratique en température: $\rho = \rho_o + AT^2$ pour $T < 0{,}1$ K, reflétant une interaction électron-électron. Le coefficient A ($\simeq$ 120 $\mu\Omega cm/K^2$) diminue sous l'action d'un champ magnétique. En dessous de 200 mK, notre échantillon suit la loi de Wiedemann-Franz, ainsi la conduction thermique montre une contribution liée à la variation en T^2 de la résistivité. A plus haute température, une contribution linéaire est observée.

Caractérisation du système à fermions lourds $CeCu_6$ par spectroscopie d'électrons

F. Patthey, B. Delley, W.-D. Schneider, Y. Baer
Institut de Physique, Rue Breguet 1, 2000 Neuchâtel

Nous avons tenté de caractériser le composé $CeCu_6$ faisant partie des systèmes à fermions lourds, à l'aide du modèle à une impureté qui a déjà été testé avec succès pour d'autres composés du cérium. Les spectres de coeur (XPS) et de valence (UPS et BIS) sont présentés et analysés. Nous montrons qu'il est possible de fixer une limite supérieure à la largeur de la structure très étroite située au niveau de Fermi, prédite par la théorie et qui devrait être responsable des propriétés exceptionnelles des systèmes à fermions lourds.

μ^+SR study of the magnetic heavy-electron systems U_2Zn_{17} and UCu_5.

S. Barth[a)], F.N. Gygax[b)], H.-R. Ott[a)], T.M. Rice[c)], A. Schenck[b)], A.J. v.d.Wal
a) Lab. of Solid State Physics, ETHZ, ETH-Hönggerberg, CH-8093 Zürich
b) Inst. for Intermediate Energy Physics, ETHZ, CH-5234 Villigen
c) Inst. for Theoretical Physics, ETHZ, ETH-Hönggerberg, CH-8093 Zürich

We have investigated polycristalline samples of the magnetic heavy-electron systems U_2Zn_{17} and UCu_5 by muon-spin-rotation spectroscopy between 1.5 and 300 K. While in UCu_5 the antiferromagnetic phase transition is accompanied by a critical behaviour in the relaxation rate, no such behaviour was found in U_2Zn_{17}. Most striking in U_2Zn_{17} is the field dependence of the relaxation rate suggesting a more complicated magnetic structure than the simple antiferromagnetic one predicted by neutron measurements. Detailed results of both μ^+ Knightshift and spin relaxation rate for both systems will be compared with each other and discussed in terms of the present understanding of magnetic heavy electron materials.

TRANSITION METAMAGNETIQUE DANS LES FERMIONS LOURDS : $CeRu_2Si_2$

P. Haen°, J. Flouquet°, F. Lapierre°, J.M. Mignot°, A. Ponchet°, G. Remenyi+
° CRTBT/CNRS, BP 166 X, 38042 Grenoble-Cédex, France
+ Max-Planck-Institut, CNRS, BP 166 X, 38042 Grenoble-Cédex, France

Le composé $CeRu_2Si_2$ présente une transition de type métamagnétique pour un champ H $\sim$ 75 kOe. Nous présentons des mesures de transport (effet Hall et magnétorésistance) sur une large gamme de champ et de température (0<H<20 T et 40 mK < T < 300 K. Nous discutons le lien entre polarisation et propriétés électroniques. L'interprétation en terme de liquide de Fermi très localisé est discutée.

TRANSITION MAGNETIQUE-NON MAGNETIQUE

J. Flouquet°, Y. Lassailly°, J.M. Mignot°, P. Morin+ et C. Vettier×
° CRTBT/CNRS, BP 166 X, 38042 Grenoble-Cédex, France
+ Laboratoire Louis Néel, CNRS, BP 166 X, 38042 Grenoble-Cédex, France
× Laboratoire de Magnétisme

On décrit les résultats des expériences de diffraction neutronique sur les composés de cérium. On discute la nature de l'état fondamental en fonction du caractère local de l'électron 4f, de son couplage avec la mer de Fermi et de la symétrie du réseau. On met l'accent sur le fait qu'une forte anisotropie, en augmentant les corrélations électroniques, décroît les couplages magnétiques. Pour les composés de cérium "trivalent", l'ordre magnétique semble toujours présent en symétrie cubique. Par contre, une forte anisotropie semble être une condition pour stabiliser une phase non magnétique de fermions lourds.

PBT II : Liquides quantiques - Supraconductivité

SUPRACONDUCTIVITE DE PAROIS DANS LES FERROMAGNETIQUES A SUPRACONDUCTIVITE REENTRANTE ET SUPRACONDUCTIVITE INDUITE PAR LE CHAMP DANS $HoMo_6S_8$

J.L. GENICON, M. GIROUX, J.P. MODONDANON, R. TOURNIER,
Centre de Recherches sur les Très Basses Températures, CNRS, BP 166 X,
38042 GRENOBLE Cédex, FRANCE

et

O. PENA, R. HORYN, M. SERGENT,
Laboratoire de Chimie Minérale B, Université de Rennes I,
35042 RENNES Cédex, FRANCE.

Une supraconductivité résiduelle est présente dans les phases ferromagnétiques de $ErRh_4B_4$, $HoMo_6S_8$ et $(Er_{1-x}Sn_x)Er_4Rh_6Sn_{18}$. On peut l'attribuer à une supraconductivité associée aux parois de Bloch car les chemins supraconducteurs sont orientés dans la direction de facile aimantation.

Dans $HoMo_6S_8$, un état métastable de résistance nulle est induit par le champ magnétique lorsqu'il est appliqué en sens inverse de l'aimantation rémanente. En champ nul et à partir d'une situation monodomaine, obtenue après saturation de l'aimantation d'un monocristal en champ intense, l'état de résistance nulle est brutalement induit par activation thermique. Cette supraconductivité, induite par le champ ou par activation thermique, disparaît à 180 mK sous l'effet du temps.

On discutera s'il s'agit d'une supraconductivité de volume ou d'une supraconductivité due à une structure feuilletée en domaines alternativement normaux et supraconducteurs.

ETUDE SIMULTANEE DES PROPRIETES DE TRANSPORT ET DE LA STRUCTURE MAGNETIQUE PAR DIFFRACTION DES NEUTRONS DE $HoMo_6S_8$

P. Burlet, A. Dinia, W.A.C. Erkelens, S. Quezel, J. Rossat-Mignod
CEN Grenoble, DRF/SPh-MDN, BP 85 X, 38041 Grenoble-Cédex, France

J.L. Genicon, R. Tournier
CRTBT-CNRS, BP 166 X, 38042 Grenoble-Cédex, France

O. Pena, R. Horyn, M. Sergent
Laboratoire de Chimie Minérale B, Univ. Rennes I, 35042 Rennes-Cédex, France

Une étude par diffraction neutronique des propriétés magnétiques de $HoMo_6S_8$ a été réalisée sur un monocristal de $HoMo_6S_8$ en même temps que la mesure de la résistance de cet échantillon. Pour toutes les phases magnétiques observées à basse température, l'échantillon présente, soit une résistance nulle (phase modulée en champ nul, phase modulée en champ intermédiaire (300, 700 Oe), phase ferromagnétique en microdomaines au voisinage de T_{M2}), soit une résistance réduite par rapport à la valeur normale R_N (phase ferromicrodomaine à basse température ($R = R_N/2$) phase modulée trempée ($R = R_N/3$)). L'ordre des moments des ions Ho est décrit pour chacune de ces phases.
En outre, une phase supraconductrice, observée quand l'échantillon est réchauffé depuis un état ferromagnétique saturé, est décrite. L'aimantation observée par diffraction neutronique correspond à environ la moitié du volume du cristal. Dans l'autre moitié, les moments 4f de l'holmium ne sont pas ordonnés et la supraconductivité peut s'établir.

Second sound intensity and wave number doubling in surface waves

J.L. Olsen and P. Caminada
Laboratorium für Festkörperphysik, ETH-Hönggerberg, 8093 Zürich

The slope of second sound induced standing surface waves on superfluid helium is connected by a cubic relationship with the intensity. The low intensity solution breaks down for a critical surface slope. For intensities larger than the critical the surface wave number doubles, and the wave pattern appears chaotic. An experimental test of the theoretical dependence of the critical intensity on frequency is described.

Supraconductivité induite par champ magnétique dans $EuMo_6S_{8-y}Se_y$ sous pression

J. Cors, M.G. Karkut, Ø. Fischer
Université de Genève, DPMC, 1211 Genève 4

U. Welp, G. Bruls
Max-Planck-Institut, Hochfeld Magnetlabor, Grenoble, France

Déjà mise en évidence dans $Eu_xSn_{1-x}Mo_6S_8$, la supraconductivité induite par un champ magnétique (MFIS) a été observé dans $EuMo_6S_{8-y}Se_y$, rendu supraconducteur par pression. T_c, paramètre critique pour l'observation de MFIS, a été ajusté par dopage au sélénium. Des mesures de la résistance jusqu'à 26 Tesla ont montré des champs critiques réentrants pour $T \leqslant 7$ K, et une forte chute de R(H) (80 %) au-delà du premier H_{c2} Si T_c avoisine cette valeur. A 1.49 K, le minimum se trouve à 21 Tesla. La concentration accrue d'europium étend donc MFIS à des champs et températures plus élevés, comme prévu par le mécanisme de Jaccarino et Peter.

PBT III : Effets quantiques - Supraconductivité

Topological excitations in two-dimensional SNS-arrays exposed to a transverse magnetic field

Ph. Lerch, R. Theron, Ch. Leemann and P. Martinoli
Institut de Physique, Université de Neuchâtel, CH-2000 Neuchâtel, Switzerland

Measurements of the ac dynamic conductance as a function of temperature and driving frequency of two-dimensional arrays of proximity-effect Josephson junctions exposed to a perpendicular magnetic field allow a study of the dynamics of various topological excitations (vortices, domain walls, dislocations) and thereby a characterization of the superconducting transition. For fields corresponding to an integer number of flux quanta per unit cell of the array, we observe a Kosterlitz-Thouless (KT) transition triggered by the unbinding of vortex-antivortex pairs. For half-integer occupancy, a detailed analysis of the ac response shows that it does not follow the predictions of the KT-theory. The possibility of an Ising-like transition triggered by domain-wall excitations is discussed.

Estimation théorique du courant de destruction de la couche mixte à deux dimensions (M)

E. Holguin, J. Casas et L. Rinderer
Institut de Physique Expérimentale, Université de Lausanne
1015 Lausanne-Dorigny

Les expériences montrent que lorsqu'on détruit la supraconductivité dans un fil creux supraconducteur de type-I au moyen d'un courant $I_o \geq I_c$, une couche de l'état M se forme à la surface interne de l'échantillon. Cette couche peut se déplacer à l'intérieur de l'échantillon en introduisant un courant axial I_b (i.e. circulant dans le trou) et son mouvement montre qu'elle est stable. Nous présentons quelques résultats expérimentaux de cet effet et donnons également une estimation théorique de son courant de destruction I_m. Quelques problèmes concernant la difficulté à le mesurer sont soulevés.

Vitesse longitudinale de destruction de la supraconductivité autour de $T\lambda$ pour des fils d'étain impur.

J. Casas, E. Holguin et L. Rinderer
Institut de Physique Expérimentale, Université de Lausanne
1015 Lausanne - Dorigny

La destruction longitudinale de la supraconductivité le long d'un fil en dessous du courant critique est produite par la création d'une zone normale qui par la suite se propage de proche en proche par dégagement Joule. Les mesures pour des températures plus basses que $T\lambda$ sont en bon accord qualitatif avec les prédictions théoriques tandis que pour des températures plus élevées la théorie ne prévoit pas un tel comportement.

PBT IV : Réseaux et quantification du flux - Supraconductivité

ETAT MIXTE D'UN RESEAU SUPRACONDUCTEUR

Y.Y. Wang, R. Rammal et B. Pannetier
CNRS/CRTBT, BP 166X, 38042 GRENOBLE Cedex, France.

Résumé : Quelques propriétés des réseaux supraconducteurs en champ magnétique transverse sont étudiés en utilisant le formalisme d'Alexander et en tenant compte du terme non linéaire des équations de Ginzburg-Landau. On détermine ainsi la configuration spatiale du paramètre d'ordre et donc l'état mixte du réseau au-dessous de la température critique. Ce modèle permet en particulier de prédire le comportement de l'aimantation d'un réseau supraconducteur pour les valeurs simples du flux magnétique réduit (0, 1, 1/2, 1/3... quantum de flux par cellule).

Au voisinage de la température critique, l'état d'équilibre d'un supraconducteur de seconde espèce est un état mixte dans lequel le flux magnétique est réparti aux nœuds d'un réseau triangulaire de Vortex. Les propriétés de cet état mixte ont d'abord été établies par Abrikosov (1) dans le cas d'un matériau homogène. Nous présentons ici les résultats préliminaires d'une etude de l'état mixte dans un réseau de filaments supraconducteurs (Fig. 1) periodique.

De façon générale, les propriétés d'équilibre sont décrites par les équations de Ginzburg-Landau. La configuration d'équilibre du paramètre d'ordre complexe $\psi(r)$ correspond à l'état propre de plus basse énergie de l'opérateur de Schrodinger (2) :

$$(i\nabla + \frac{2eA}{\hbar c})^2 \psi(r) = E\,(H)\,\psi(r)$$

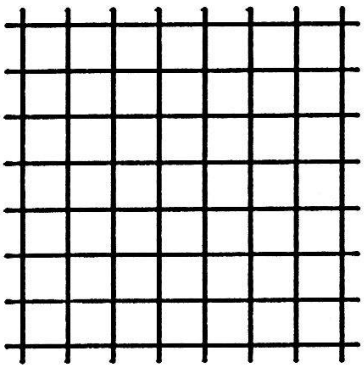

Fig. 1 : Réseau périodique de filaments supraconducteurs unidimensionnels. Dans un réseau idéal, le diamètre des fils est inférieur à la longueur de cohérence (~ 0.3 µm). Le pas du réseau est typiquement a ~ 3 µm (3,5).

L'énergie libre correspondant à cet état est donné par :

$$F = F_o + < \frac{h^2}{2m} [E(H) - \frac{1}{\xi^2}] \psi^2 + \frac{1}{2} b \psi^4 + \frac{h^2}{8\pi} >$$

Dans cette expression $\xi = \xi(0)/\sqrt{1-T/T_c}$ est la longueur de cohérence, b un paramètre dépendant de la température et h = rot A est l'induction magnétique. La moyenne est prise sur le volume supraconducteur. Pour un réseau bidimensionnel régulier, E(H) est une fonction périodique du flux magnétique réduit $\phi/\phi_o = 2e\ Ha^2/hc$ (par cellule élémentaire a x a) qui contient toute l'information sur la ligne de transition (2) :

$$E(H) = \frac{1}{\xi^2} = \frac{1}{\xi^2(0)} \frac{T_c(H) - T_o}{T_o}$$

Les propriétés spectaculaires de cette ligne ont été vérifiées avec précision par l'expérience (3).

L'approche utilisée pour calculer $\psi(r)$ sur un réseau (4) généralise l'approche originale d'Abrikosov (1). A une valeur donnée du flux réduit $\phi/\phi_o = p/q$ correspond un ensemble d'états de même énergie, états qui représentent les divers modes d'une supercellule de q x q cellules élémentaires (Fig. 3). La configuration d'équilibre est une combinaison particulière de ces modes qui minimise le terme d'ordre 4 de l'énergie libre. Elle est obtenue en minimisant le paramètre d'Abrikosov

$$\beta_A(H) = \frac{<\psi^4>}{(<\psi^2>)^2}$$

Ce paramètre ≥ 1 caractérise l'uniformité de la fonction $\psi(r)$ et augmente avec l'énergie du système.

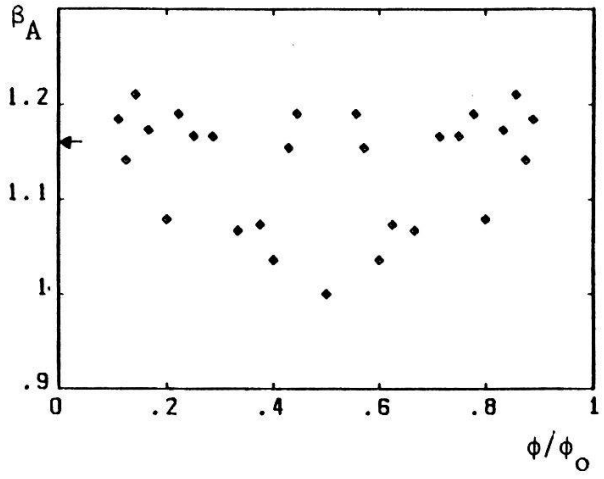

Fig. 2 : Paramètre d'Abrikosov $\beta_A(H)$ pour un réseau carré. La valeur $\beta_A = 1.16$ correspondant au réseau triangulaire idéal est indiquée par une flèche (limite du continuum).

A la différence du cas du supraconducteur homogène (1), β_A est ici une fonction de H (Fig. 2) qui doit être calculée numériquement pour chaque configuration.

L'état d'équilibre ainsi obtenu est illustré sur la Fig. 3 pour le cas $\phi/\phi = 1/5$. On n'observe plus l'arrangement triangulaire mais une configuration plus complexe résultant de la compétition entre les deux périodes spatiales propres du système : la période a du réseau supraconducteur d'une part et la période magnétique $\ell_H = \sqrt{\Phi_o/H}$ d'autre part. Lorsque ces deux périodes sont commensurables (i.e. $\phi/\phi_o = p/q$) l'état d'équilibre est un arrangement periodique dont le motif de base est une supercellule q x q qui représente la période spatiale commune q x q. On peut observer que les lignes de courant se referment autour des cellules correspondant au paramètre d'ordre minimum. En aucun point le paramètre d'ordre ne s'annule : aux vortexs du supraconducteur homogène correspondent ici des "vortex sans cœur" qui représentent les défauts élémentaires de la phase ordonnée (ψ uniforme).

Dans l'approximation de ce modèle, le paramètre d'ordre et donc l'ensemble des grandeurs thermodynamiques peuvent être calculées explicitement en fonction de β_A. En particulier, l'énergie libre et l'aimantation sont données par :

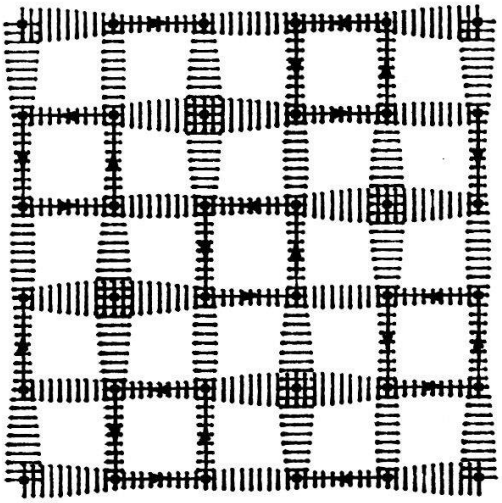

Fig. 3 : Configuration de l'état d'équilibre pour $\phi/\phi_o = 1/5$. L'amplitude de ψ est représentée par la largeur des lignes. Les flèches indiquent la circulation des supracourants. Cette supercellule 5 x 5 contient cinq quanta de flux.

$$F = F_o - \frac{1}{4\pi\beta_A} \frac{\kappa^2 (\frac{\phi_o}{2\pi})^2}{[2\kappa^2 - (\frac{\phi_o}{2\pi}\frac{dE}{dH})^2]^{\frac{1}{2}}} (\frac{T_c - T}{\xi^2(o)T_o})^2$$

$$M = \frac{1}{4\pi\beta_A} \frac{(\frac{\phi_o}{2\pi})^2 \frac{dE}{dH}}{2\kappa^2 - (\frac{\phi_o}{2\pi}\frac{dE}{dH})^2} \frac{T_c - T}{\xi^2(o)T_o}$$

où κ est le paramètre de Ginzburg-Landau.

Comme la température critique, l'aimantation est périodique en ϕ/ϕ_o et dépend de façon simple du spectre E(H). Cependant, alors que T_c est donnée par E(H), l'aimantation est reliée à la dérivée première de E(H), fonction discontinue pour tout nombre rationnel. Cette propriété vient de recevoir une première confirmation expérimentale (4).

References

(1) A.A. Abrikosov, Soviet Phys. JETP 5, 1174 (1957)
et P.G. de Gennes, Superconductivity of metals and alloys (Benjamin INC New York 1966)

(2) S. Alexander, Phys. Rev. B 27, 1541 (1983) ; R. Rammal, T.C. Lubensky and G. Toulouse, Phys. Rev. B 27, 2820 (1983)

(3) B. Pannetier, J. Chaussy, R. Rammal and J.C. Villegier, Phys. Rev. Lett. 53, 1845 (1984)

(4) P. Gandit et al, ce volume.

DERIVEES EXPERIMENTALES DE L'AIMANTATION D'UN RESEAU SUPRACONDUCTEUR

P. Gandit, J. Chaussy, B. Pannetier, R. Rammal, CNRS/CRTBT, BP 166 X, 38042 GRENOBLE Cédex, FRANCE
A. Vareille, A. Tissier, CNET, chemin du Vieux Chêne, BP 98, 38243 MEYLAN Cédex, FRANCE

Résumé : Nous proposons une nouvelle technique expérimentale qui permet de mesurer directement la dérivée de l'aimantation par rapport à la température $dM/dT|_H$ et d'accéder également à la dérivée dM/dH.

A l'aide de cette technique nous avons étudié un réseau supraconducteur d'indium.dM/dH nous renseigne sur la transition supraconductrice. Nous avons mis en évidence des oscillations de températures critiques comme dans le cas de l'étude de la magnétorésistance. dM/dT décrit la phase supraconductrice et nous permet d'accéder à l'aimantation du réseau.

1. Technique expérimentale

L'échantillon à étudier, à la température T et dans un champ magnétique H, est placé au centre d'une bobine de détection [fig. 1] . Nous faisons alors osciller sinusoïdalement sa température d'une amplitude ΔT. Si l'aimantation de l'échantillon varie, il apparaît une tension aux bornes de la bobine de détection proportionnelle à ΔM. En mesurant les deux quantités ΔM et ΔT nous avons accès directement à $\frac{dM}{dT}|_H$.

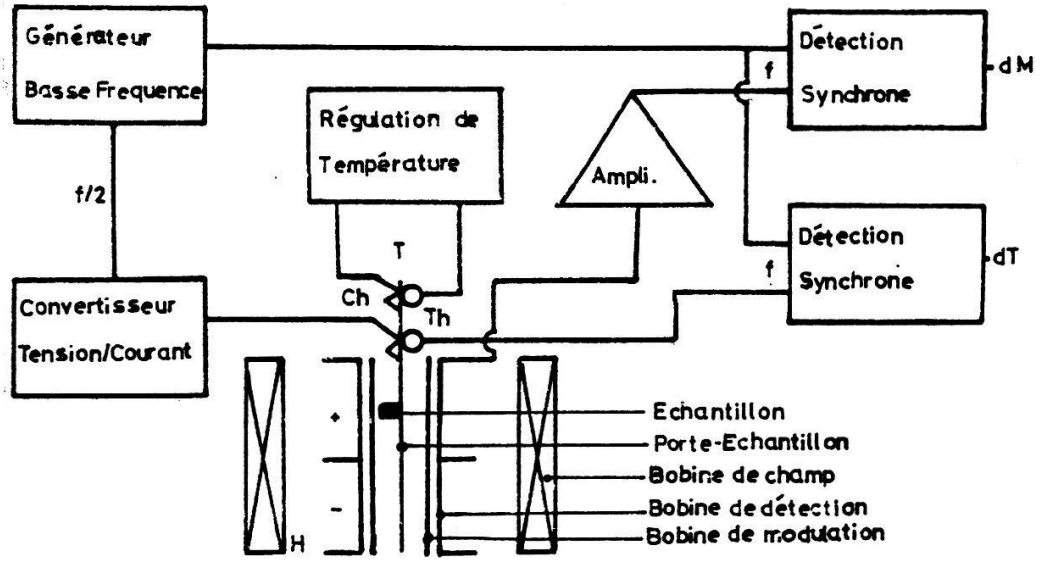

Figure 1 : Schéma de principe

Si maintenant l'échantillon est maintenu à la température T et que nous superposons au champ magnétique statique H un champ magnétique alternatif ΔH, nous mesurons dM/dH.

2. Echantillon

L'échantillon est réalisé sur une plaquette de silicium de 6 mm de côté, C'est un réseau carré d'indium d'épaisseur 1000 Å et comportant $4 \cdot 10^6$ boucles. La maille du réseau est de 3,2 µm et la largeur des traits est de 0,4 µm. Le masque "lift-off" a été obtenu par lithographie électronique.

Pour obtenir un quantum de flux ($\phi_o = 2 \cdot 10^{-7}$ G.cm^2) par boucle il faut théoriquement appliquer un champ magnétique de 2,02 G. Le champ mesuré est de 1,98 G.

3. Dérivée de l'aimantation par rapport au champ magnétique

L'échantillon étudié présente une transition assez large (40 mK) au voisinage de 3,05 K. La courbe représentée sur la figure 2a montre les oscillations de dM/dH en fonction du champ magnétique pour une température prise dans la transition. Elle illustre également la grande sensibilité de l'appareillage.

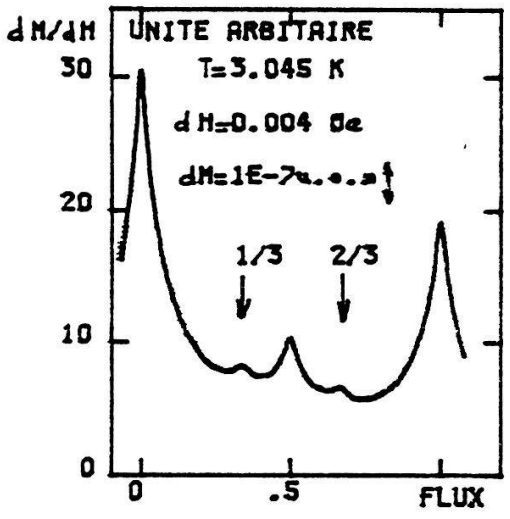

Figure 2a : Oscillations de dM/dH en fonction du champ magnétique appliqué normalisé au quantum de flux par boucle.

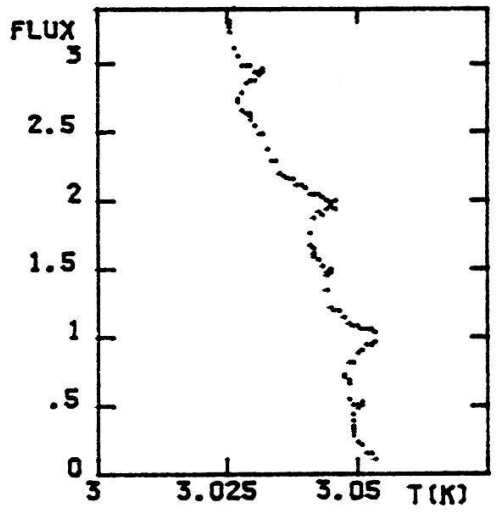

Figure 2b : Ligne de transition supraconductrice.

Les pics correspondent à une quantification du flux magnétique pour chaque rationnel p/q il y a p quanta de flux répartis sur q boucles du réseau. Cette mesure qui est en fait une mesure de la température critique nous permet de tracer le diagramme de phase de la figure 2b. La ligne de transition obtenue est tout à fait semblable à celle obtenue par magnétorésistance [1,2].

4. Dérivée de l'aimantation par rapport à la température

Nous pensons que ces mesures nous renseignent sur l'aimantation à l'équilibre de la phase supraconductrice. Sur la figure 3a est représenté le comportement de l'échantillon dans un cycle où le champ magnétique est appliqué à basse température. Il prend alors naissance des courants dans la périphérie de l'échantillon qui empêchent les vortex de pénétrer. Puis la température critique étant dépassée nous refroidissons ; le système pour conserver une énergie minimale laisse pénétrer des vortex qui sont piégés dans les boucles du réseau.

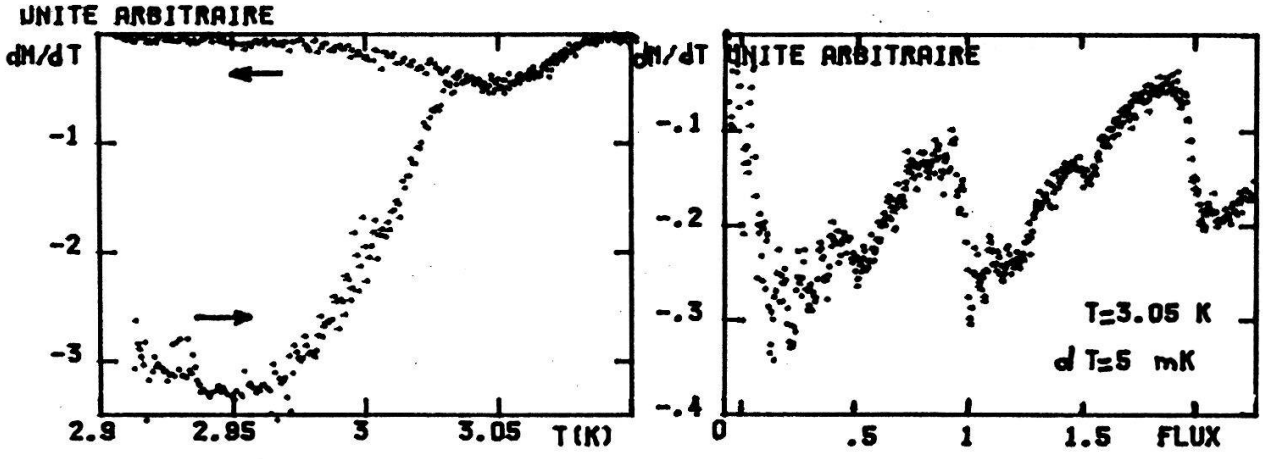

Figure 3a

Figure 3b

Dérivée de l'aimantation par rapport à la température en fonction de la température et du champ magnétique appliqué.

La figure 3.b représente la quantité dM/dT en fonction du champ magnétique : La dépendance en champ magnétique de dM/dT confirme les prédictions théoriques [3] pour l'aimantation : période ϕ_o, sous-harmoniques aux valeurs rationnelles de ϕ/ϕ_o (ici les pics à 1/2, 1, 3/2 et 2 se distinguent nettement du bruit), proportionnalité à dT_c/dH.

Ces nouvelles mesures permettront, à l'avenir, de mieux comprendre les phénomènes de quantification qui prennent naissance dans les réseaux supraconducteurs.

5. Références

[1] B. Pannetier, J. Chaussy, R. Rammal, J. Physique-Lettres 44, L853 (1983).

[2] B. Pannetier, J. Chaussy, R. Rammal, J.C. Villégier, Phys. Rev. Lett. 53, 1845 (1984).

[3] Y.Y. Wang, R. Rammal et B. Pannetier, ce volume.

Weak localization and oscillatory magnetoresistance in cylindrical Ag films

C. Cavalloni[1] and W. Joss[2]
[1]Laboratorium für Festkörperphysik, ETH-Hönggerberg, 8093 Zürich;
[2]Max-Planck Institut für Festkörperphysik, Hochfeld-Magnetlabor, C.N.R.S., 38042 Grenoble Cedex

The magnetoresistance of thin cylindrical Ag films ($\varnothing \sim 1$ μm) in the weakly localized regime has been investigated between 1.3 K and 4.2 K and in a longitudinal magnetic field up to 0.3 T. The measurements were carefully analyzed in terms of the recent theories of weak localization. The observed magnetoresistance oscillations are periodic in the magnetic flux quantum h/2e and in excellent agreement with the Altshuler-Aronov-Spivak theory. The values of the inelastic scattering time and the spin-orbit interaction time are comparable to those observed in plane films.

Soliton dynamics in the incommensurate phase of a vortex lattice pinned by a periodic potential

G.A. Racine, B. Jeanneret, H. Beck and P. Martinoli
Institut de Physique, Université de Neuchâtel, CH-2000 Neuchâtel, Switzerland

By changing the magnetic field, the vortex lattice in periodically modulated superconducting films can be driven through a sequence of commensurate (C) and incommensurate (I) phases. The CI-transition is triggered by soliton excitations which form a one-dimensional superlattice in the I-phase. We have studied the linear dynamic response of the soliton lattice using a drive-receive coil technique. We find that, at low temperatures, the driving ac field couples only to the optical modes of the soliton lattice. At higher temperatures, two-dimensional fluctuations destroy the long-range order in the vortex lattice, thereby allowing also the excitation of the acoustic mode of the soliton superlattice. This is demonstrated by the appearance of additional structures in the ac response measured at high temperatures.

The effects of addition of the third elements on T_c on multifilamentary Nb-Al wires

D. Abukay and L. Rinderer
Université de Lausanne, Inst. de Physique Expérimentale 1015 LS

The multifilamentary Nb-Al, Nb-(Al, Si) and Nb-(Al, Ge) wires have been fabricated by powder metallurgy processing. Their critical temperature T_c have been resistively measured after electrically heating them to elevated temperatures in He-gas for short time and followed by Low-temperature annealings. T_c values ranging over 18.8 - 20k for Nb_3Al and 19.26-20.3k for Nb_3(Al, Si) and Nb_3(Al,Ge) were measured.

PBT V: Superréseaux - Effets de proximité

CARACTÉRISATION STRUCTURALE DE SUPERRÉSEAUX MÉTALLIQUES SUPRACONDUCTEURS Mo/V PAR DIFFRACTION DE RAYONS X.

D.Ariosa,J.M.Triscone,M.G.Karkut,and Ø.Fischer
Université de Genève,DPMC,1211 Genève 4,Suisse.

Les profils de composition de superréseaux à une dimension de Mo et V ont été reconstruits d'après les données de diffraction X à bas angle. Les profils de composition sont utilisés pour le fit des diffractogrammes à haut angle, dans le cadre d'un modèle élastique couplant la diffusion à la distorsion aux interfaces. La distance d'interdiffusion Di,la deformation τ et la distance moyenne ξ entre dislocations aux interfaces sont ainsi obtenues en fonction de la période de modulation Λ. Les résultats sont discutés en comparaison avec l'évolution du rapport de résistivité résiduel (RRR) et de la température de transition supraconductrice T_c des échantillons.

Superconductivity of Quasiperiodic Metallic Superlattices

M.G.Karkut,J.-M.Triscone,D.Ariosa,and Ø.Fischer
Université de Genève, DPMC, 1211 Genève 4, Suisse

We have sputtered Mo/V superlattices with quasiperiodicity in the growth direction. We have analysed the structure by x-ray θ-2θ diffractometry and have measured residual resistivity ratios RRR, superconducting transition temperature Tc, and upper critical fields Hc2(T,θ). The RRR's are approximately independent of wavelength Λ, while Tc and the critical field anisotropy slowly increase with Λ. We will also present results for the corresponding series of periodic samples.

GROWTH AND SUPERCONDUCTIVITY OF BCC/FCC METALLIC SUPERLATTICES: V/Pt AND Nb/Pt.

J.-M.Triscone,M.G.Karkut,D.Ariosa,and Ø. Fischer
Université de Genève,DPMC,1211 Genève 4, Switzerland

We have grown,by magnetron sputtering, multilayers of bcc V/fcc Pt and bcc Nb/fcc Pt on substrates of $(11\bar{2}0)$ Al_2O_3 heated to about 600°C. The full widths at half maximum of the satellite peaks of the θ-2θ x-ray diffractograms imply coherence lengths in the growth direction of ~250 Å for V/Pt but only ~150 Å for Nb/Pt . We also find that layering is strongly dependent on the base pressure and for the best results P_{base} was $\sim 5 \cdot 10^{-9}$ Torr. We have been unable to grow either of these combinations on (001) MgO. We will also present measurements of low angle x-rays and superconducting properties.

Magnetic properties of proximity induced superconductors

A.C. Mota, D. Marek and P. Visani
Laboratorium für Festkörperphysik, ETH-Hönggerberg, 8093 Zürich

At millikelvin temperatures, thick proximity induced superconductors behave like bulk, inhomogeneous type I superconductors with Ginzburg-Landau parameters as low as 10^{-3}. The magnetic properties of such superconductors, in low and high magnetic fields, in the temperature range 5×10^{-4} $T_{CNS} < T < T_{CNS}$, will be discussed. Here T_{CNS} is the transition temperature of the NS proximity system.

PHYSIQUE DE LA MATIERE CONDENSEE

KOND I : Surfaces et interfaces

GROWTH OF $NiSi_2$ LAYERS ON Si(111) BY MOLECULAR BEAM EPITAXY (MBE)

H. von Känel, T. Graf, J. Henz and P. Wachter, Laboratorium für Festkörperphysik, ETH Zürich, CH-8093 Zürich, Switzerland

Abstract : Thin epitaxial layers of $NiSi_2$ have been grown on Si(111) by MBE. Instead of evaporating on the clean Si surface directly, an ultrathin continuous silicide film was formed first by depositing 4 A of Ni at room temperature and annealing to 300 ^{o}C. Surprisingly, the epitaxial layers grown by MBE at substrate temperatures between 550 ^{o}C and 750 ^{o}C were no longer continuous for thicknesses below 300 A. From the analysis of the Kikuchi pattern observed by RHEED the orientation was determined to be type B, i.e. rotated by 180^{o} with respect to the Si lattice.

1. Introduction

Epitaxial silicides have aroused great interest in the past few years, since they belong to the most perfect metal/semiconductor interfaces which have ever been made. In particular, the formation of the Schottky barrier at the Ni-silicide/Si(111) interface has been investigated in great detail (1,2).
This work is of a somewhat different nature, aiming at the fabrication of thin single crystalline metal films, e.g. as a first step towards metal/semiconductor superlattices. We have chosen $NiSi_2$ due to its simple CaF_2 structure and the small mismatch to the Si lattice (0.4 %).

2. Experimental results and discussion

3" (111)-oriented Si wafers were introduced into the growth chamber of a VG V80 MBE machine, as received by Wacker Chemitronic (no further cleaning). After removal of the surface oxide by heating to 800 ^{o}C at a base pressure of $3 \cdot 10^{-11}$ mbar, a sharp 7x7 RHEED pattern was usually observed. Small traces of carbon contamination were, however, just barely discernible by XPS. In order to start out with a perfectly clean substrate, an epitaxial buffer layer of 2500 A of Si was then grown at 700 ^{o}C. This resulted in a perfect 7x7 RHEED pattern, indicating a flat, smooth surface. The latter was corroborated by optical interference microscopy and SEM.

In a next step a layer of 4 A of Ni was evaporated near room temperature (below 100 °C). According to ref. (3), annealing of such templates in the temperature range of 450 - 550 °C leads to the formation of a continuous, epitaxial $NiSi_2$ layer. Our XPS measurements indicated, that heating to much lower temperatures, i.e. typically to 300 °C, is already sufficient to cause the complete transformation of such thin Ni layers to $NiSi_2$. This can be seen in curve b) of fig. 1, showing the valence band region of the XPS spectrum, taken after the sample had been annealed to 290 °C. The spectrum is identical to the UPS spectrum ($h\nu$ = 120 eV) obtained by other authors on bulk $NiSi_2$ (4). The 1x1 RHEED pattern displayed by the annealed sample indicated that the $NiSi_2$ layer was epitaxial and perfectly smooth. Its thickness could be increased by evaporating another layer of 10 A of Ni at room temperature. Annealing to 185 °C resulted in the formation of NiSi, as can be seen (4) from the change of the XPS spectrum characteristic for Ni to that one of NiSi (curve c) and d) in fig. 1). Further annealing to 320 °C again produced $NiSi_2$ (curve e) in fig. 1).
The various surface reconstructions observed by RHEED during the annealing process will be discussed in a separate publication.
In order to increase the silicide thickness to several 100 A, we used MBE after the first step described above (deposition of 4 A of Ni at R.T. and subsequent annealing). Ni and Si were coevaporated at substrate temperatures between 550 and 750 °C at rates of 0.5 and 1.7 A/sec (stoichiometric ratio), respectively. Surprisingly, $NiSi_2$ of 300 A thickness turned out to be no longer continuous, especially at substrate temperatures above 650 °C. Nomarski interference contrast microscopy showed that films grown at a substrate temperature of 600 °C almost covered the whole surface. The surface roughness exhibited by thicker $NiSi_2$ films grown by MBE on Si directly, has been noted before (6). From the analysis of the Kikuchi pattern observed by RHEED, the orientation of the $NiSi_2$ layers was determined to be type B, i.e. rotated by 180° with respect to the underlying Si lattice.
Since our ultrathin $NiSi_2$ layers grown below 320 °C before the MBE step were known to be continuous and flat, we initiated a careful examination of the thermal stability of these templates. By combining RHEED and XPS measurements with SEM and optical interference contrast microscopy it could be shown conclusively, that templates of several tens of Angstroms are unstable for temperatures sig-

nificantly in excess of 400 °C. Whereas films annealed at 320 °C were continuous, heating to 400 °C resulted in the formation of pinholes. Above ~450 °C the silicide layers started to contract into small triangular islands, distributed over the whole surface. This is consistent with the findings of Liehr et. al. (2) in their investigation of the Schottky barrier at the $NiSi_2$/Si interface. Thus, we have to conclude that MBE at substrate temperatures above 500 °C is necessarily prone to result in rough surfaces. We do have indications, however, that MBE still might be possible at temperatures below 400 °C for sufficiently small growth rates.

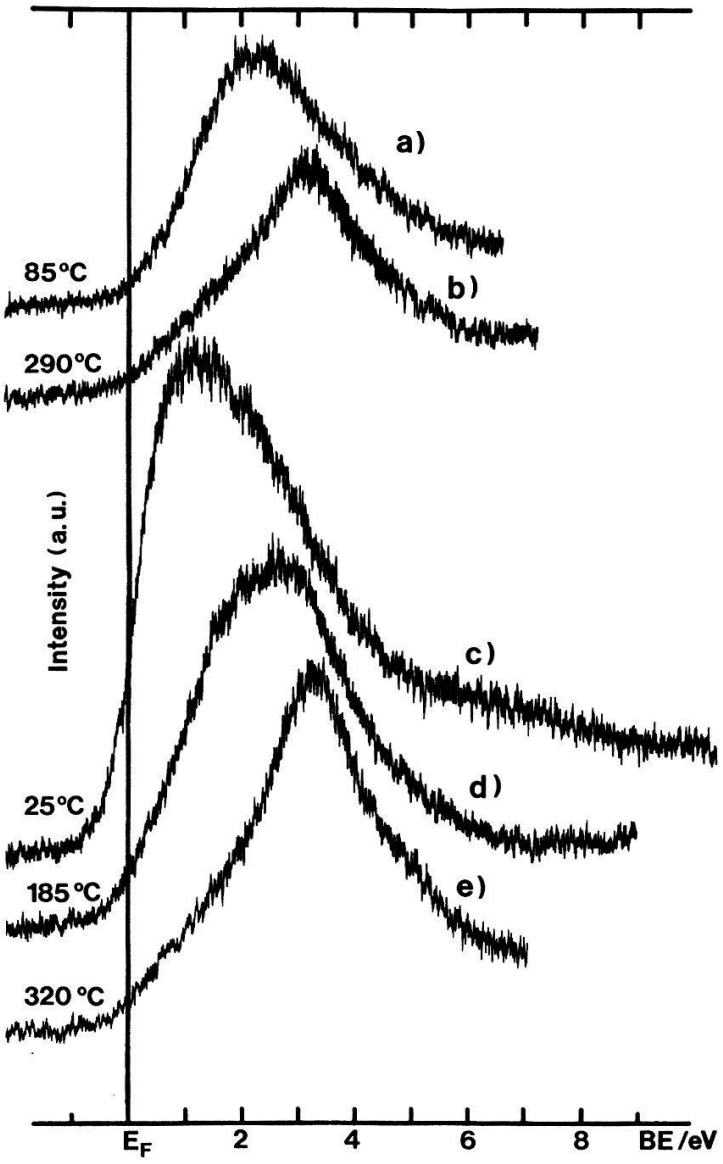

Fig. 1 :
XPS valence band spectra (Mg K_α) of various Ni-silicide phases on Si(111).
a) after the evaporation of 4 A of Ni at 85 °C, showing reaction to a NiSi-like phase.
b) after annealing to 290 °C, indicating complete reaction to $NiSi_2$.
c) after evaporation of an additional 10 A thick layer of Ni at 25 °C.
e) after annealing at 320 °C for 15 min, again showing complete reaction to $NiSi_2$.

3. Acknowledgements

The authors wish to express their deep gratitude to Mr. H. J. Gübeli for his competent technical support and to Mr. P. Wägli for the SEM investigations. Financial support by the Swiss National Science Foundation (NP 19) is also greatfully acknowledged.

4. References

(1) R. T. Tung, Phys. Rev. Lett. 52, 461 (1984)

(2) M. Liehr, P. E. Schmid, F. K. LeGoues, P. S. Ho, Phys. Rev. Lett. 54, 2139 (1985)

(3) R. T. Tung, J. M. Gibson, J. M. Poate, Phys. Rev. Lett. 50, 429 (1983)

(4) A. Franciosi, J. H. Weaver, F. A. Schmidt, Phys. Rev. B 26, 546 (1982)

(5) Xu Jian-hua, Xu Yong-nian, Solid State Commun. 55, 891 (1985)

(6) J. C. Bean, J. M. Poate, Appl. Phys. Lett. 37, 643 (1980)

UNTERSUCHUNG DER SPALTUNG VON H_2O AUF METALLOBERFLAECHEN

T. Greber, T. Riesterer und L. Schlapbach
Laboratorium für Festkörperphysik, ETHZ, 8093 Zürich

An der Oberfläche von Metallen der Seltenen Erden kann sich bei der Begasung mit H_2O-Dampf unter geeigneten Bedingungen (T,p) ein Metallhydrid und Oxyd anstelle eines Hydroxyds bilden. Wir haben diesen Wasserspaltprozess mit Photoelektronenspektroskopie und mit einem H-Detektor auf der Basis einer Pd-MOS-Struktur untersucht. Der Pd-MOS Detektor misst Aenderungen der Austrittsarbeit von Pd in Abhängigkeit des H-Gehaltes. Der Detektor und einige an Ce-Schichten gemessene Resultate werden vogestellt.

LEGIERUNGSBILDUNG AN DER GRENZFLAECHE Ce-Pd

M. Lerchmüller, L. Schlapbach und T. Riesterer
Laboratorium für Festkörperphysik, ETHZ, 8093 Zürich

In Ce und in Ce-Legierungen kann als Funktion der Temperatur oder der Zusammensetzung ein elektronischer Phasenübergang von magnetischem γ-Ce ($n_{4f} \approx 1$) zu nichtmagnetischem α-Ce ($n_{4f} \approx 0.8$, 4f mit 5d hybridisiert) beobachtet werden.

Wir berichten über Messungen der Photoemission aus Ce-3d-Rumpfniveaus aufgedampfter dünner Ce-Schichten auf Pd. Aus der Intensität des $4f^0$-Satelliten wird der Anteil α-Ce ermittelt und die Legierungsbildung an der Grenzfläche verfolgt. Einfluss von Schichtdicke, Temperatur und Wasserstoffgehalt des Substrates werden diskutiert.

CO Chemisorption auf amorphen und polykristallinen Uebergangsmetall-Si Legierungen

R. Hauert, P. Oelhafen und H.-J. Güntherodt
Institut für Physik, Universität Basel, Klingelbergstr.82, CH-4056 Basel

UPS Untersuchungen der CO Chemisorption als Funktion der Temperatur auf Ni-Si, Pd-Si und Ir-Si Legierungen zeigen eine Si-induzierte Schwächung der Substrat-CO-Bindung. Im Gegensatz dazu zeigte die Zr Zulegierung eine Schwächung der C-O Bindung (1). Aus den gemessenen Substrat- und Adsorbat-Zustandsdichten und der Kenntnis der Symmetrie der zugehörigen Elektronen-Orbitale lässt sich das CO Chemisorptionsverhalten, beziehungsweise die Wirkung der zulegierten Elemente auf die C-O und die Substrat-CO Bindung, qualitativ erklären. Untersuchungen an amorphen ternären Pd-Si-Zr Legierungen bieten die Möglichkeit, gleichzeitig die Substrat-CO und die C-O Bindung zu beeinflussen.

(1) R.Hauert, P.Oelhafen, R.Schlögl and H.-J. Güntherodt, Solid State Commun. 55 (1985) 583

Electron spectroscopy on in situ prepared hydrogenated amorphous carbon films (a-C:H)

P. Oelhafen, Institut für Physik, Universität Basel, Klingelbergstr.82, CH-4056 Basel

a-C:H films on different substrates (Si(100), Au and amorphous $Fe_{86}B_{14}$) have been prepared by the ion beam deposition technique in situ for UPS, XPS and AES. The UPS valence band data are in good agreement with earlier published measurements (1) performed on not in situ prepared samples. The interface properties are of particular interest in this work because of their relevance for adhesion and valence band/conduction band discontinuities. Compound formation with the substrate at the interface has been observed at room temperature in the case of the Si substrate (SiC formation) with a distinct valence band discontinuity.

(1) P. Oelhafen, J.L. Freeouf, J.M.E. Harper and J.J. Cuomo, Thin Solid Films 120 (1984) 231

Photoemission an Filmen organischer Moleküle

R. Zehringer, R. Schlögl*, P. Oelhafen, H.-J. Güntherodt, E. Rolli**, R. Houriet**, Institut für Physik, Universität Basel, Klingelbergstr. 82 CH-4056 Basel; *Hoffmann - La Roche & Cie AG, Basel; ** Institut de chimie physique, EPFL-Ecublens, CH-1015 Lausanne

Um Photoemission (XPS,UPS) zur Untersuchung chemischer Eigenschaften und Reaktionen organischer und anorganischer Moleküle anwenden zu können, ist man auf eine spezielle Technik zur Herstellung und Charakterisierung solcher Filme angewiesen. Wir haben ein Verfahren entwickelt, das uns erlaubt, dünne Schichten auf verschiedenen Substraten reproduzierbar aufzubringen. Als Anwendung stellen wir ein Experiment mit verschiedenen Indolen (stickstoffhaltigen Heterozyklen) vor, bei welchen die N1s-Bindungsenergien gemessen wurden. Es zeigt sich, dass zwischen den N1s-Bindungsenergien und der Protonenaffinität der Moleküle in der Gasphase ein Zusammenhang besteht.

The combination of scanning tunneling microscopy (STM) and X-ray photoelectron spectroscopy (XPS) applied on a thin film of Pd_2Si on a Si substrate.

A.J. Brunner, M. Ringger, L. Rosenthaler, A. Stemmer, R. Wiesendanger, P. Oelhafen, und H.-J. Güntherodt
Institut für Physik, Universität Basel, Klingelbergstr. 82, CH-4056 Basel

The local topography and the chemical composition of the surface of a Pd_2Si film on a Si substrate have been investigated by combining scanning tunneling microscopy (STM) and X-ray photoelectron spectroscopy (XPS). Measurement of the tunneling barrier height which is correlated with the work function yields some information on the local chemical composition. Various topographical features, among them islands, have been observed for several different sample treatments such as air exposure before and after ion etching.

Charakterisierung innerer Grenzflächen mit Hilfe von XPS, AES und UPS: Vorstellung einer Bruchapparatur und erste Ergebnisse

P. Brüesch, W. Foditsch
BBC Forschungszentrum, CH-5405 Baden-Dättwil

Die Segregation von Verunreinigungen oder zudotierten Materialien an die inneren Korngrenzen polykristaliner Materialien (Legierungen, Halbleiter, Keramiken, Kunststoffe) kann deren mechanischen oder elektrischen Eigenschaften entscheidend beeinflussen. Das Ziel unserer Untersuchungen besteht darin, die Bulk-Eigenschaften technisch interessanter Materialien mit der Chemie und Struktur der Korngrenzen zu korrelieren. Zu diesem Zweck haben wir eine Bruchapparatur konstruiert, mit welcher die Korngrenzen im UHV des Photoelektronenspektrometers freigelegt werden können. Beide Teile der gebrochenen Probe können zusammen oder separat gemessen werden. Mit Hilfe eines Kollimators werden nur die Photoelektronen der Bruchfläche, nicht aber jene der Kerbfläche detektiert. Erste XPS-Messungen an einer AlMgSiPb-Legierung mit ca. 1% Pb und von mit Bi dotiertem ZnO zeigen eine starke Segregation von Pb bzw. Bi an die Korngrenzen.

KOND II : Surfaces et interfaces II - Semiconducteurs

ETUDE DES PAROIS DE DOMAINES FERROELECTRIQUES DANS LE TITANATE DE PLOMB PAR MICROSCOPIE ELECTRONIQUE A HAUTE RESOLUTION

P.A. Buffat, B. Quenet, R. Spycher, P. Stadelmann, Ecole Polytechnique Fédérale de Lausanne, Microscopie Electronique I2M, CH-1015 Lausanne, Suisse
D. Rytz, Hughes Research Laboratories, Malibu, California 90265, USA

Abstract : The factors affecting the mobility or the pinning of the ferroelectric domain walls are not yet well established in ABO_3 perovskites. In the course of their study, high resolution electron microscopy (HREM) has been used to provide a better knowledge of the walls themselves in $PbTiO_3$. The transition between two domains with their polarisation vectors at right angles appear to be abrupt down to the atomic scale along the {101} twin planes. This implies that the Maxwell equations could be satisfied by a highly localized space charge rather than a lattice distorsion.

1. Introduction

Un certain nombre de perovskites de type ABO_3 présentent une transition de phase paraélectrique - ferroélectrique. C'est le cas notamment dans les composés $BaTiO_3$, $PbTiO_3$, $KTa_{1-x}Nb_xO_3$ ($0.05<x\leq 1$) où cette transition correspond au passage d'une structure cubique à une structure tétragonale. Le vecteur polarisation électrique est parallèle à l'axe c et deux types de parois entre domaines ferroélectriques adjacents sont observés [1]. Les unes, séparant des domaines de polarisations antiparallèles, adoptent des formes très variées (parois à 180°). Les autres, essentiellement planes et parallèles aux plans de macle {101}, délimitent des domaines de polarisations orthogonales (parois à 90°).

L'équation de Maxwell $\mathrm{div}\,\vec{D} = \rho$ (où $\vec{D}$ est le déplacement électrique) implique soit une forte densité de charge ρ dans les parois, soit une interface relativement épaisse où la polarisation tournerait progressivement d'un domaine à l'autre [2,6]. Des valeurs très différentes, allant de quelques centaines de nanomètres à quelques nanomètres, ont été avancées pour l'épaisseur des parois dans $BaTiO_3$ notamment [3,4]. Cette note présente les premiers résultats obtenus par microscopie à haute résolution sur des cristaux de $PbTiO_3$ qui ont

l'avantage d'un rapport des axes tétragonaux élevé (c/a = 1.064).

2. Conditions expérimentales

Les cristaux de $PbTiO_3$ utilisés sont préparés par refroidissement lent d'une solution $3PbO + TiO_2$ [5] et se présentent sous la forme de parallélipipèdes limités par des faces {100}, de quelques millimètres de côté et d'un millimètre d'épaisseur environ. Amenés à une épaisseur de 30 microns par polissage mécanique, ils sont ensuite amincis jusqu'à transparence aux électrons par bombardement ionique (20 $\mu A/mm^2$ d'ions Ar^+ de 4 keV et sous incidence de 15^o) ou par attaque chimique dans H_3PO_4 à 200^oC.

Les observations sont réalisées sur un microscope Philips EM 430 avec pièces polaires SuperTwin offrant un pouvoir de résolution ponctuelle de 0.20 nm à 300 kV. Sa bande passante permet de faire interférer les 13 faisceaux (000), {100}, {110} et {200} pour former les images haute résolution le long de l'axe de zone [010].

3. Calcul des images haute résolution

Le calcul des images haute résolution se fait par la méthode "multislice" à l'aide du jeu de programmes MASTER développé à l'Institut et implémentés sur un miniordinateur PDP 11/34 avec processeur vectoriel Analogic AP-500. Les parois à 90^o, parallèles au faisceau d'électrons, sont introduites en considérant le cristal comme la répétition périodique d'une supercellule (fig. 1) contenant 33 mailles élémentaires de part et d'autre de l'interface et décrite par 1024 x 64 pixels.

Deux modèles ont été considérés : l'un plaçant l'interface sur les plans {101} contenant les atomes métalliques, l'autre sur les plans ne contenant que des atomes d'oxygène.

4. Observations

Les parois de domaines à 90^o, parallèles au faisceau, apparaissent comme un brusque changement d'orientation des plans atomiques (fig.), bien visible lorsque l'on regarde les clichés sous incidence rasante. Elles sont planes, parallèles aux plans 101 et présentent parfois des marches d'une hauteur $1/2\sqrt{a^2+c^2}$. La rotation des plans (100) et (001) se fait sur une distance

de l'ordre du paramètre de maille du cristal (0.4 nm). L'absence d'une composante de translation le long de l'interface permet d'affirmer que le plan de macle passe par les atomes métalliques.

La préparation des échantillons pas bombardement ionique entraîne la présence de dégâts d'irradiation et d'une couche superficielle amorphe. Ces défauts rendent délicate la comparaison entre images expérimentales et images simulées. Les échantillons préparés par attaque chimique sont en ce sens de meilleure qualité malgré une contamination superficielle et un effet d'attaque sélective de l'interface observé parfois.

5. Conclusions

Les premières observations des domaines ferroélectriques dans le titanate de plomb par microscopie électronique à haute résolution permet d'affirmer que l'épaisseur des parois à 90^{o} n'excède pas une fraction de nanomètre. Le mécanisme de rotation progressive de la polarisation sur quelques 18 mailles proposé par Yakunin [2] pour $BaTiO_3$ semble difficilement applicable ici. Une comparaison entre images simulées et images expérimentales devrait permettre de décider de l'existence ou de l'absence d'une distorsion de la structure le long de l'interface, et par conséquent de la nature intrinsèque ou extrinsèque de la charge électrique nécessaire pour satisfaire aux équations de Maxwell.

6. Références

[1] M. Tanaka, T. Yatsuhashi and G. Honjo, J. Phys. Soc. Japan 28, suppl., 386, (1970).

[2] S.I. Yakunin, V.V. Shakmanov, G.V. Spivak and N.V. Vasil'eva, Sov. Phys. Sol. State 14, 2, 310, (1972).

[3] M.E. Lines and A.M. Glass, in Principles and Applications of Ferroelectrics and Related Materials, Clarendon Press, (1977).

[4] M.D. Dennis and R.C. Bradt, J. Appl. Phys. 45, 5, 1931-1933, (1974).

[5] J.P. Remeika and A.M. Glass, Mater. Res. Bull 5, 37, (1970).

[6] T. Malis and H. Gleiter, J. Appl. Phys. 47, 12, (1976).

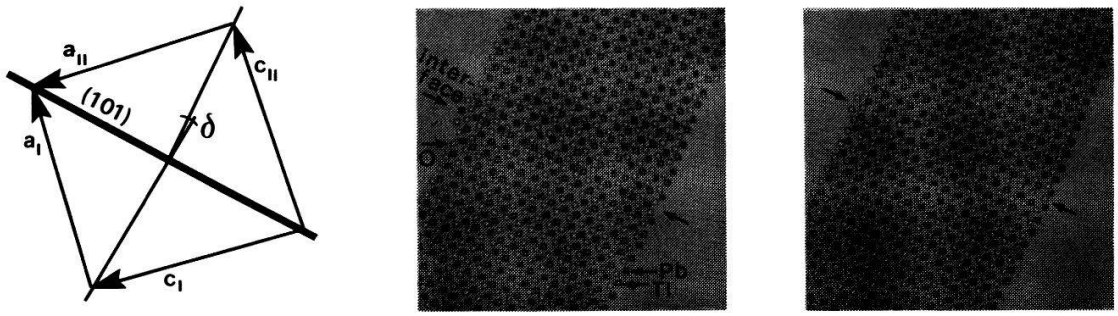

a) b) c)

Fig. 1 : Vue partielle des supercellules utilisées pour la simulation des parois à 90° . a) macle (101), b) paroi Pb-Ti-O, c) paroi O-O.

Fig. 2 : Images de parois à 90° simulées pour une lame de 15 nm d'épaisseur et une défocalisation de 40 nm. a) paroi Pb-Ti-O, b) paroi O-O.

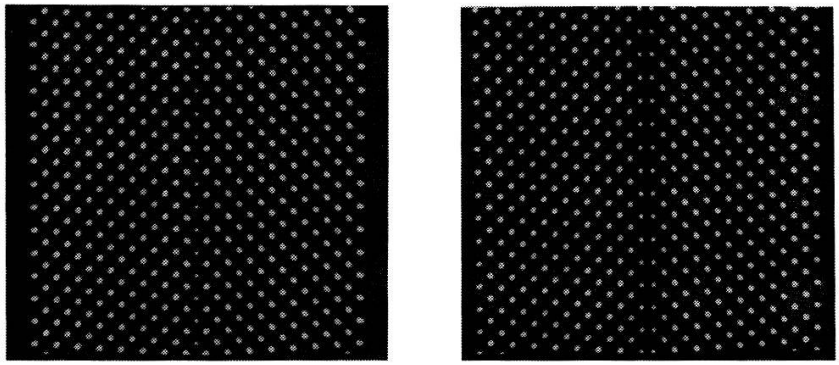

a) b)

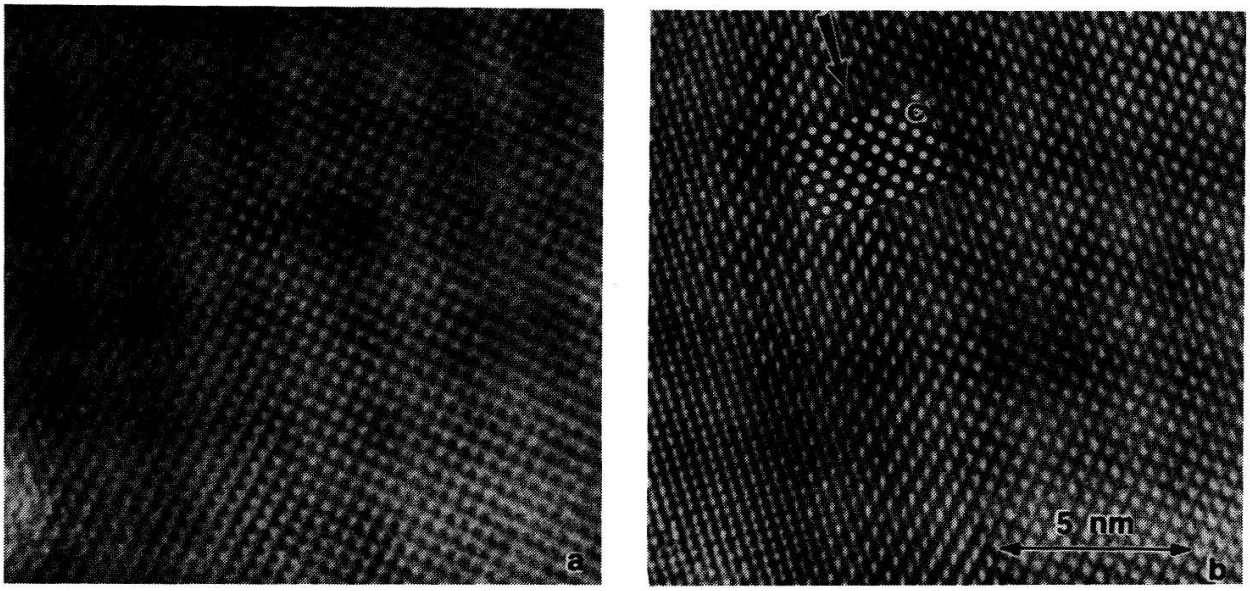

Fig. 3 : Paroi à 90° dans $PbTiO_3$ aminci chimiquement. Epaisseur de la lame : 7.8 nm, défocalisation : a) 100 nm, b) 80 nm, c) image simulée pour b) où les colonnes de Pb apparaissent noires et celles de Ti-O blanches.

OBSERVATION OF DENDRITIC CRYSTAL GROWTH IN NARROW GAPS BY MICROSEGREGATION OF LUMINESCENT TRACERS

Ch. Fattinger, F. Honegger and W. Lukosz, Swiss Federal Institute of Technology, Professur für Optik, ETH, 8093 Zürich, Switzerland

Abstract : We observed impurity controlled dendritic crystal growth of dimethylsulfoxide (DMSO, melting point $T_M \simeq 18.5^oC$) containing water, using dye molecules (DCM) as luminescent tracers. The dye molecules are enriched in the liquid phase during solidification. Therefore dendritic crystal growth in narrow gaps can be observed by the following methods : 1.) fluorescence microscopy, and 2.) intensity measurements of the evanescent-wave-induced luminescence of dye molecules close to one of the walls (a high refractive index glass prism). This method permits to distinguish the solid phase from the liquid phase within the penetration depth ($\simeq$ 100 nm) of the evanescent wave. After the dendritic crystal growth, recrystallization phenomena occurred, which we found to be different for gaps of widths $d_o > 2\,\mu m$ and for very narrow gaps ($d_o \lesssim 1\,\mu m$).

1. Introduction

Recently the mechanisms of dendritic crystal growth have been investigated intensively, see, e.g., the review paper [1] . Dendritic crystallization has been investigated in bulk, in capillaries and in narrow gaps [2,3] .

We investigated the dendritic solidification of dimethylsuloxide (DMSO) in narrow gaps of widths between $d_o \simeq 0.5\,\mu m$ and $d_o \simeq 10\,\mu m$ at an undercooling $\Delta T \simeq 15^oC$. The thermal diffusivity ($D_{th} \simeq 10^{-3} cm^2/s$) is two orders of magnitude higher than the typical diffusivity of impurities ($D \simeq 10^{-5}\ cm^2/s$). Therefore the dendritic solidification was impurity controlled; the water content of DMSO was varied between 0.1 and 1 vol%. We added a (laser) dye DCM to the DMSO in very small concentrations of 5×10^{-4} mole/liter. The dye molecules serve as luminescent tracers for the liquid phase. They are enriched in this phase during the solidification process. In this way the dendritic structure becomes visible.

2. Experimental Methods

In our experiments we sealed a thin film of DMSO in a narrow gap between a high refractive index glass prism and a glass slide(see Fig.1). Considerable care was taken to clean the glass surfaces before each experiment. The width d_o of the gap was defined by SiO_2 spacers (evaporated onto the glass slide). The

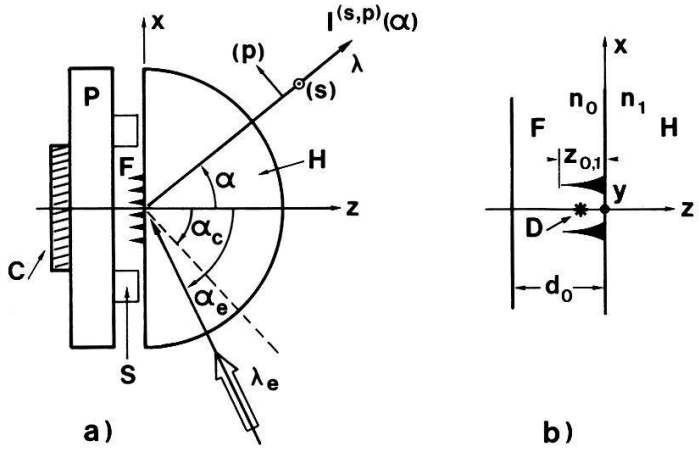

Fig. 1. a) Schematic of experimental set-up: H, hemicylindrical high index prism (n_1=1.89); F, solidifying film of refractive index n_0 (DMSO doped with DCM laser dye); P, glass plate; C, Peltier cooler; S, spacers (d_0 = 0.6, 1.2, 3.5, and 10 μm); α_e, angle of incidence of exciting laser beam of wavelength λ_e; $\alpha_c = \arcsin(n_0/n_1)$; α, angle of emission of luminescent light of wavelength λ; (s), (p), polarizations;
b) D, luminescent molecule in film F; $z_{0,1}$, penetration depth of evanescent wave.

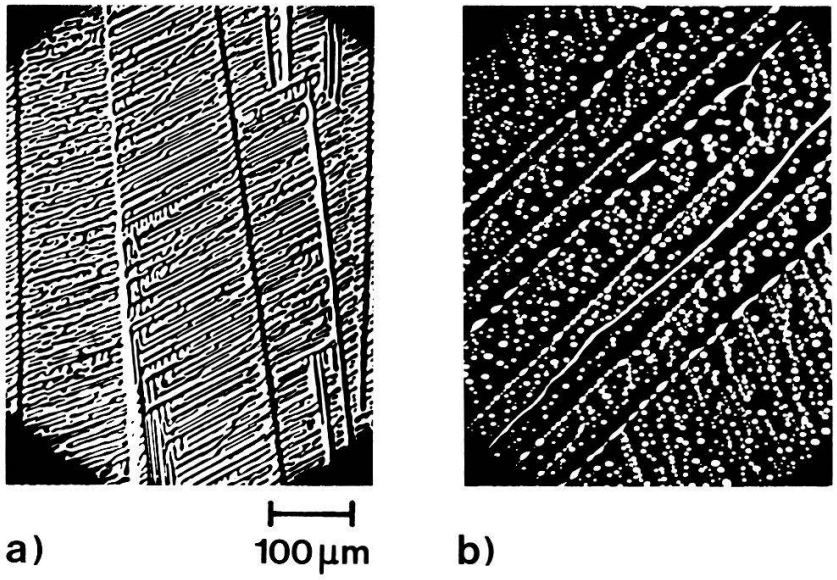

Fig. 2. Micrographs of DCM doped DMSO films after solidification for gap widths a) $d_0 \approx 10$ μm and b) $d_0 \lesssim 1$ μm; dark areas solid phase, bright areas liquid phase.

DMSO (spectroscopic grade) supplied by MERCK contained about 0.1 vol% water ($\hat{=}$ 5 x 10^{-2} mole/liter). In our experiments we used also higher water concentrations between 0.1 to 1 vol%. Compared to the water concentrations the dye concentration (5 x 10^{-4} mole/liter) is so low that the dye can be regarded as a negligible impurity which does not influence the crystallization; it only serves as a tracer for the liquid phase.

The film was cooled below its melting point T_M = 18.5°C with a Peltier cooler. At an undercooling of about 15°C (inhomogenous) nucleation takes place and a planar dendritic pattern grows out from a single seed. The dendritic crystallization was observed visually by fluorescence microscopy. The growth velocity (tip velocity) of the dendrites is v ≃ 1 cm/s. After the dendritic solidification recrystallization phenomena were observed. Typical structures which begin to appear a few seconds after solidification are shown in Figs.2a,b for a thick (d_o ≃ 10 μm) and a thin ($d_o \lesssim 1$ μm) film of DMSO sealed between two microscope slides.

The use of evanescent waves permits selective excitation of those dye molecules in the gap which are in the immediate vicinity of the high refractive index glass prism. By total internal reflection of a laser beam at the boundary between the high index prism (n_1 = 1.89) and the DMSO in the gap (n_0 ≃ 1.48) an evanescent wave is produced (see Fig.1). Its penetration depth is $z_{0,1}$ = 80 nm at angle of incidence α_e = 70° (for λ_e = 488 nm). We measured the luminescence intensity of the evanescent-wave-excited dye molecules as a function of time during the solidification and the recrystallization processes. This intensity is proportional to the number of dye molecules in the penetration depth layer. From these measurements we obtained information about the depth (z coordinate) dependance of the structure of the solidified film. This information is complementary to that obtained from fluorescence microscopic observations about the crystallization patterns in the x-y plane of the film.

3. Results and Discussion

Figure 3 shows the variation of intensity of the evanescent-wave-induced luminescence as a function of time for different values of gap width d_o and water content. The most striking effect is the increase (of up to one order of magnitude) of the luminescence intensity within a fraction of a second. The intensity increase (at t=0) coincides with the formation of the dendritic pattern inside the spot (of diamter ≃ 2 mm) illuminated by the laser beam. From visual observations we estimated the velocity of the advancing solidification front to

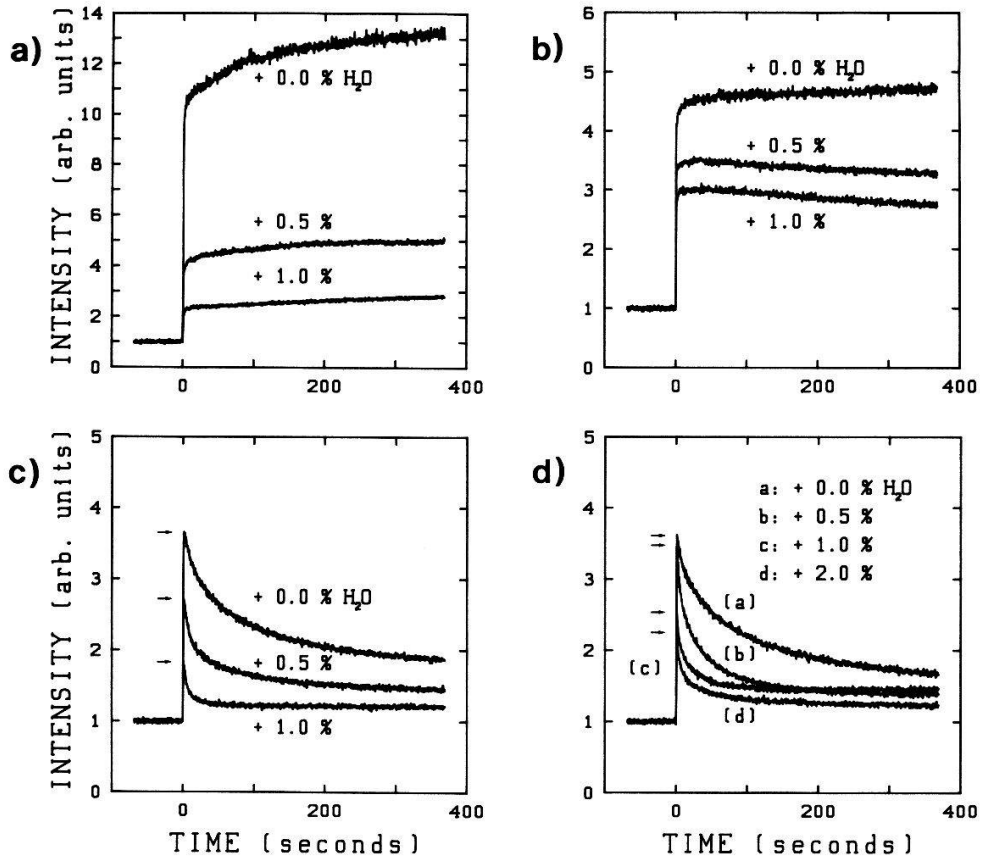

Fig. 3. Evanescent-wave-induced luminescence intensity versus time during solidification of DCM dye doped DMSO film for different film thicknesses a) d_0 = 10 μm, b) d_0 = 3.5 μm, c) d_0 = 1.2 μm, and d) d_0 = 0.6 μm. Parameter is the water content of the DMSO.

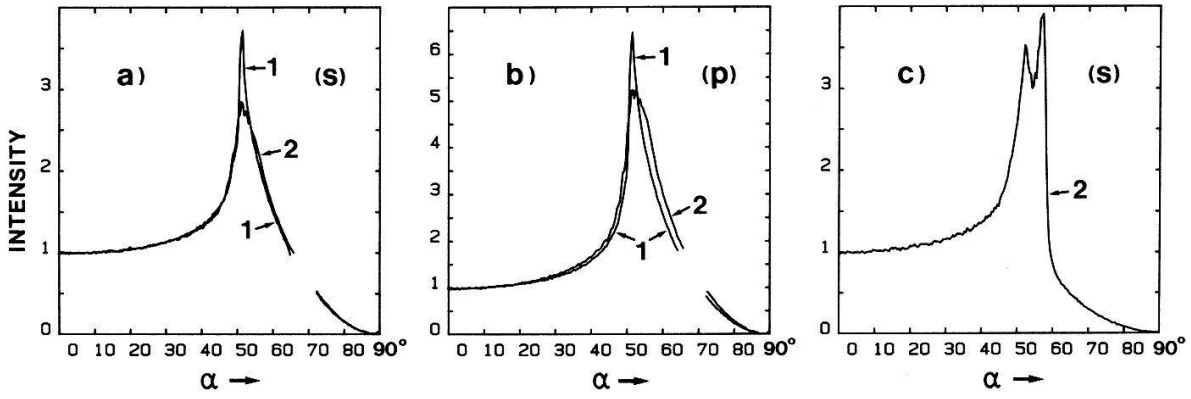

Fig. 4. (Normalized) angular distribution of evanescent-wave-induced luminescence $I^{(s,p)}(\alpha)$ vs angle α of liquid film (1), after solidification (2), for gap thickness a) and b) d_0 = 3.5 μm and c) d_0 = 1.2 μm. Normalization: $I^{(s,p)}(\alpha=0) = 1$.

be $v \simeq 1$ cm/s. The intensity increase at $t \simeq 0$ indicates that the following process occurs: The dendritic crystal pattern forms in a median plane of the thin DMSO film rejecting the impurities water (and dye molecules) towards the walls. During the growth of the solid phase in the middle of the gap, the water concentration C in the remaining liquid phase near the walls rises accordingly. The solidification stops as soon as the freezing point depression is equal to the undercooling ΔT, i.e., $K \cdot C_{eq} = \Delta T$, where $K = 3.8^{o}C$ liter $mole^{-1}$ is the molecular freezing point depression of DMSO and C_{eq} is the water concentration in the liquid phase in equilibrium with the solid phase.

If we assume the dye concentration in the solid phase to be negligibly small, the dye concentration in the liquid phase C(DCM) is inversely proportional to the relative volume of the liquid phase. The latter is proportional to the initial water concentration. The sharp increase of the luminescence at $t \simeq 0$ is caused by the increase of the dye concentration of the liquid phase near the walls. For gap thicknesses $d_o > 2$ µm this intensity remains practically constant, while for $d_o \lesssim 1.2$ µm the intensity decreases with time (see Fig.3). The reason is that the solid phase comes into contact with the walls. The liquid phase (which had covered the dendrites and which had wetted the walls) contracts into droplets; the relative volume of the liquid phase remaining constant. The droplets are visible in the fluorescence microscope (see Fig.2b). These results are confirmed by the measurements of the angular intensity distribution $I^{(s,p)}(\alpha)$ of the luminescence excited by an evanescent wave (cf.Fig.4). The peak of $I^{(s,p)}(\alpha)$ occurs at the critical angle $\alpha_c = \arcsin(n_0/n_1)$ where $n_1 = 1.89$ is the refractive index of the prism and n_0 is the refractive index of the adjacent medium. For a thin film ($d_o \lesssim 1$ µm), where both liquid and solid phase are in contact with the prism surface (for $t > 0$), a second peak is found, corresponding to the refractive index $n_0 \simeq 1.57$ of the solid phase. The latter results can be expressed using the concept of 'complete' and 'partial' wetting which recently has attracted renewed interest [4]. The 'complete wetting' of the glass surface by the (water rich) liquid phase in equilibrium with the solid phase is stable only for gap thicknesses $d_o > 2$ µm, while for $d_o < 2$ µm partial wetting occurs.

4. References

[1] J.S. Langer, Rev. Mod. Phys. 52, 1 (1980).

[2] H. Honjo and Y. Sawada, J. Cryst. Growth 58, 297 (1982).

[3] H. Honja, S. Ohta, and Y. Sawada, Phys. Rev. Lett. 55, 841 (1985).

[4] M. Wortis, Physics Today, January 1985, p.22.

Spektroskopische Untersuchungen an Trimethylaluminium

G. Josten, W. Lüthy
Inst. für angew. Physik, Universität Bern, Sidlerstr. 5, 3012 Bern

Es ist möglich, ausgehend von Trimethylaluminium durch pyrolytische Abscheidung mit dem Laser Mikrostrukturen von Aluminium zu erzeugen. Um eine Erwärmung des Substrates über Zimmertemperatur zu vermeiden und um nahe der optischen Auflösungsgrenze zu arbeiten, wäre jedoch photolytische Abscheidung wünschenswert. Eine Untersuchung der Absorptionsspektren sowohl im Gas als auch in der Adsorptionsschicht die sich aus den Gasmolekülen auf dem verwendeten Substrat bildet, erlaubt die Auswahl der für die Photolyse geeigneten Laserwellenlänge. Vergleiche mit Experimenten zur Aluminiumabscheidung bei 257 nm und 193 nm bestätigen die Annahme, dass die bei der Deponie wichtigen photolytischen Prozesse im Falle von Trimethylaluminium in der Adsorptionsschicht stattfinden.

Effet tunnel à travers des barrières semiconductrices de très grande épaisseur

P.Guéret, E. Marclay*, A. Baratoff
IBM Zurich Research Laboratory, CH-8803 Rüschlikon
*Adresse permanente: Institute de Microélectronique, EPFL, CH-1015 Lausanne

Une étude de l'effet tunnel dans un cas particulier et nouveau, utilisant des barrières de potentiel épaisses mais basses dans des structures semiconductrices a été entreprise dans le but d'accroître nos connaissances sur cet effet complexe et technologiquement important. Le système étudié est du type $GaAs(n^+)/Al_xGa_{1-x}As$ (non-dopé)/$GaAs(n^+)$ où l'$Al_xGa_{1-x}As$ joue le rôle de la barrière. Les échantillons sont fabriqués par épitaxie à jets moléculaires (MBE). Des mesures électriques ont permis de mettre en évidence la conduction par effet tunnel dans un régime de basse tension et très basse température, pour des épaisseurs de 300 à 600 Å et des hauteurs de barrière de 80 à 20 meV. Des résultats sont également présentés pour le cas où un champ magnétique est appliqué perpendiculairement au courant. Ce champ a pour effet de diminuer le courant tunnel et nous interprétons ce résultat en termes de "temps" de tunneling.

SELF-CONSISTENT HARTREE-FOCK AND SCREENED EXCHANGE CALCULATIONS OF THE EXCITATION ENERGIES OF SEMICONDUCTORS

F. Gygi (a) and A.Baldereschi (a,b)
(a) Institut de Physique Appliquée, EPFL, 1015 Lausanne
(b) Istituto di Fisica Teorica & GNSM-CNR, U. of Trieste, Italy

A simple technique to perform Hartree-Fock calculations in solids using extended basis functions is proposed and applied to Silicon. Adding correlation through the self-consistent Coulomb Hole plus Screened Exchange approximation, the lowest excitation energies are predicted with an accuracy of about 15 percent (we obtain 1.32 eV and 3.87 eV for the lowest indirect and direct gaps respectively). Energies and wavefunctions are critically compared with those obtained in the local density approximation.

GROUND STATE OF DOUBLE ACCEPTORS IN GE

N. Binggeli and A. Baldereschi
Institut de physique Appliquée, EPFL, 1015 Lausanne

The binding energy of double acceptors in Ge is calculated within the effective-mass approximation using the spherical model. We find, due to the coulomb hole-hole coupling, that the ground state splits into a (Γ_1) singlet and a ($\Gamma_3+\Gamma_5$) quintuplet, the latter being more bound in agreement with Hund's rule. The calculated value of the splitting agrees with the result of recent measurements [1] for the isocoric system Ge : Zn.

[1] M.L.W. Thewalt, B.P. Clayman, and D. Labrie
Phys. Rev. B 32, 2663 (1985)

KOND III : Métaux liquides et amorphes - Propriétés de transport

STUDY OF THE TEMPERATURE COEFFICIENT OF THE RESISTIVITY OF LIQUID AND AMORPHOUS METALS : CLUSTERS CALCULATIONS.

R. Frésard and H. Beck, Institut de Physique, Université de Neuchâtel, Rue A.-L. Breguet 1, CH-2000 Neuchâtel.

Abstract: Using a multiple scattering approach, we have studied the influence of increasing structural disorder on the resistivity of small clusters of s-scatterers. We find a transition from Ziman behaviour (weak scattering regime) to Mooij behaviour (strong scattering regime).

1. Introduction: The temperature coefficient of the resistivity ρ of many amorphous and liquid metals is negative particularly when ρ is higher than a critical value of about 150 $\mu\Omega\cdot$cm. This is Mooij's rule, which has not yet found a generally accepted explanation.

This paper is based on an expression for ρ in terms of the total scattering matrix $T(\mathbf{k}, \mathbf{k}')$ of the metal giving the scattering amplitude for an elastic electron-ion collision from momentum $\hbar\mathbf{k}$ to $\hbar\mathbf{k}'$. At T=0 it has the form:

$$\rho = \frac{3\hbar}{2^7 \pi \Omega e^2 k_F^4} \int d\Omega_k \int d\Omega_{k'} \left| T(\vec{k}, \vec{k}', E_F) \right|^2 (\vec{k} - \vec{k}')^2 \qquad (1)$$

Ω being the volume of the system and the integration running over the directions of $\mathbf{k}$ and $\mathbf{k}'$, with $(\hbar k)^2 = (\hbar k')^2 = (\hbar k_F)^2 = 2mE_F$. As stated by [1], this result can be obtained by a Bolzmann equation approach [2] where the transition probability in the collision integral is given by $|T(\mathbf{k}, \mathbf{k}')|^2$. We have calculated the exact T-matrix, describing rigorously the scattering effects of all ions on an incoming free electron, for some clusters. The resistivity of a piece of metal, connected to a perfect conductor, is then taken to be the incoherent sum of cluster contributions, calculated according to (1). This allows us to discuss multiple scattering contributions to ρ for a given arrangement of ions, and to study the influence of a change in this arrangement on ρ. For more details see [3].

2. Theoretical framework: We consider the one-electron Hamiltonian:

$$H = \frac{p^2}{2m} + \sum_{n=1}^{N} V_n(\vec{r} - \vec{R}_n) \qquad (2)$$

where V_n is a muffin-tin potential at site R_n. For such a Hamiltonian it is possible, [4], to calculate the T-matrix and the generalized phase-shift [5], [6]. The latter are the eigenvalues of the matrix τ_{nm}, describing all scattering processes beginning at site n and ending at site m. In order to exhibit multiple scattering effects, it will be useful to compare the results with the single site approximation ρ_{ss} given by the usual Ziman T-matrix formula [7]:

$$\rho_{ss} = \frac{3\hbar\pi^3}{e^2 k_F^6 \Omega} \int_0^{2k_F} dq\, q^3\, S(q)\, |T(q, k_F)|^2 \qquad (3)$$

where:

$$q^2 = 2k_F^2 (1 - \cos\theta) \qquad (4)$$

and:

$$T(q, k_F) = -\frac{1}{k_F} \sum_{l \geq 0} (2l+1)\, e^{i\delta_l(k_F)} \sin\delta_l(k_F)\, P_l(\cos\theta) \qquad (5)$$

θ being the scattering angle between $\mathbf{k}$ and $\mathbf{k}'$. We have done our calculations for various clusters of N identical s-scatterers. The neglect of all single-site phase-shifts δ_l for $l>1$ considerably simplifies the computational scheme and should be adequate in order to discuss simple metals. The muffin-tin potential was modelled by the square well of depth V_0 and radius a. Where we use V_0 values for which the phase-shifts δ_l, $l>1$ would be non-negligible, our restriction to s-phase shifts has of course only model character.

We have studied the following types of clusters:

i) Ordered clusters of fcc symmetry comprising the first and second shell of neighbors, i.e N=13 and N=19. The distance d between nearest neighbors was chosen to be 2.2 a. The fcc structure has the advantage to represent a close packed neighbor structure typical of a disordered metal with a high coordination number. Even though it has the point symmetry of a perfect crystal, the electronic properties of such a cluster are typical of a disordered metal, since by summing the contributions of many clusters incoherently we discard any long range order.

ii) In order to study the influence of the cluster structure, more particularly of its degree of order or disorder, on its electronic properties, we have deformed the two ordered fcc-like clusters by random displacements of the atomic sites, respecting the condition that two potential wells do not overlap.

Two clusters with the same number of particles but with different degree of disorder can be used to simulate the effect of thermal vibrations of the ions on the electronic properties. In the regime of sufficiently high temperatures an electron moving through the cluster sees the instantaneous ionic configuration. Thus the disordered cluster will represent a high temperature system and the ordered cluster models the same system at low T. We will use the notation (13.0) and (13.D) for ordered and disordered N=13 clusters, respectively.

3. Results: Let us introduce the quantity

$$\gamma = \frac{\rho_{DIS}}{\rho_{ORD}} - 1$$

in an obvious notation.

γ can be thought of as the "temperature coefficient of the resistivity" in particular $\gamma < 0$ when increasing disorder lowers the resistivity which is "unusual" for a "normal" metal. Figure 1 shows γ, the structure factor and the resistivity as functions of k_F. The single site result γ_{SS} has the same behaviour for all values of the potential: it is negative when 2 k_F is located near a peak of S(q). This is the well-known Ziman behaviour [8], [9]. The γ_{MS} curves for weak potentials differ little from γ_{SS}, and therefore follow Ziman's behaviour too. For strong potentials, γ_{MS} oscillate little and lies somewhat below 0 up to a value of k_F corresponding to a critical value ρ_c of ρ. Having chosen an interatomic distance typical of simple metals, ρ_c is around 120 $\mu\Omega \cdot$ cm. It is interesting to notice that ρ_c is augmented by decreasing the disorder. Here γ_{MS} obeys Mooij's rule: when, in a disordered metal ρ is larger than a critical value, (of the order of 150 $\mu\Omega \cdot$ cm in real systems), the temperature coefficient is negative, otherwise it is positive.

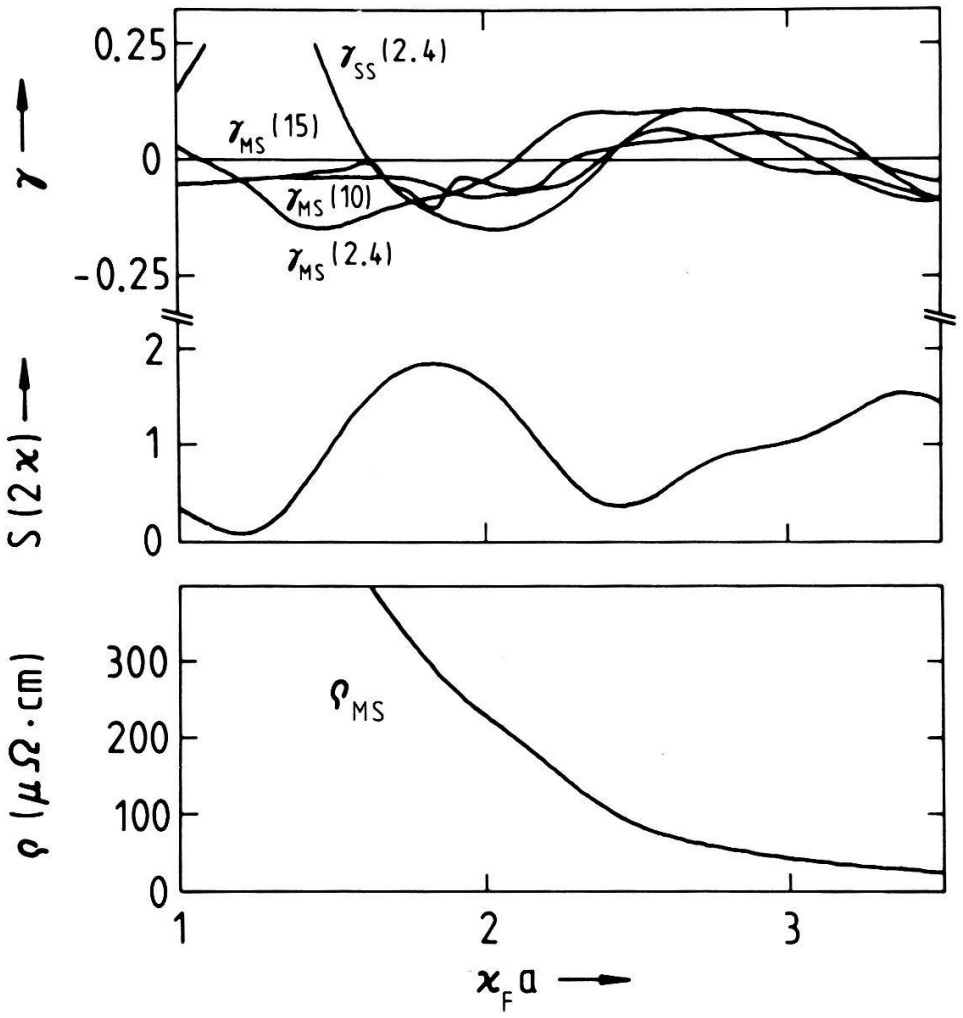

fig. 1

Figure 2 shows the cluster phase-shifts as functions of the Fermi wave number k_F for the potential strength $V_0\ a^2 = 10$. This is a strong potential which has a bound state. Due to the symmetry, the cluster (13.0) has only 6 distinct phase-shifts, the degeneracies of which are removed by the disorder. Let us discuss the influence of increasing disorder on the scattering power of the cluster in terms of the total cross-section given by [5]:

$$\sigma = \frac{4\pi}{k_F^2} \sum_{\lambda} \sin^2 \eta_\lambda(k_F) \qquad (6)$$

For the cluster (13.0) a three-fold degenerated phase-shift η_λ yields the contribution $\sigma_\lambda^{(0)} = (4\pi/k^2)3\ \sin^2\eta_\lambda$ to σ. In the cluster

(13.D) the corresponding branch is split into three $\eta_\lambda^1, \eta_\lambda^2, \eta_\lambda^3$, which yields $\sigma_\lambda^{(D)} = 4\pi/k^2 \sum_i \sin^2\eta_{\lambda i}$. For strong scattering systems many branches η_λ are close to $\pi/2$ for typical values of k_F for simple metals (this case is shown in Fig. 2). For such a branch, σ_λ is large ($\sin \eta_\lambda \simeq 1$) and a simple estimate yields $\sigma_\lambda^{(D)} < \sigma_\lambda^{(0)}$.

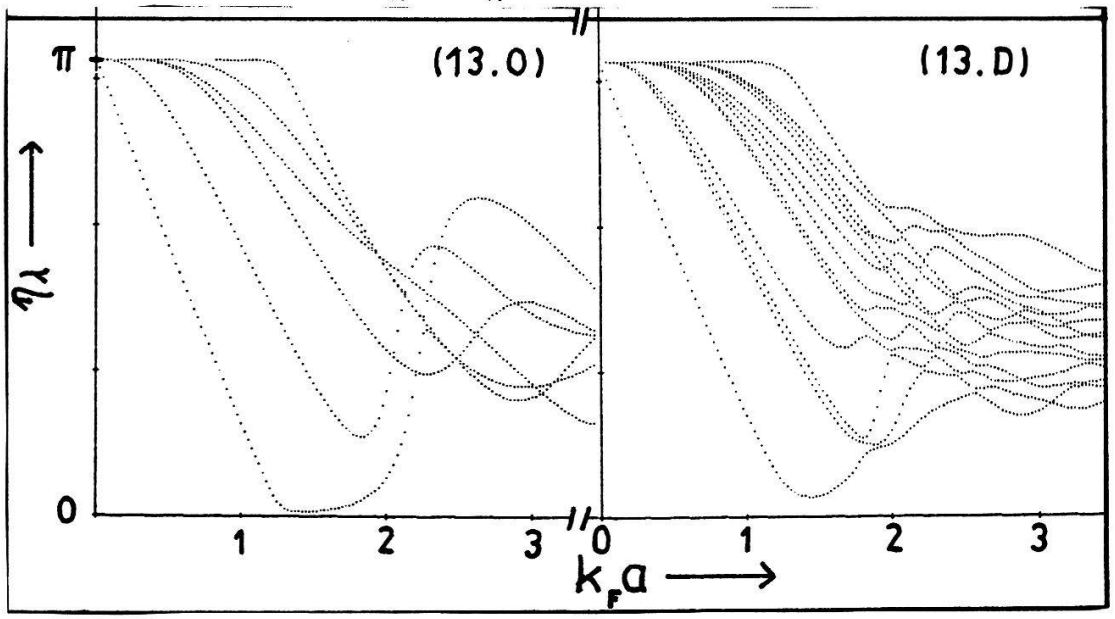

fig. 2

Contrary to this, for weak potentials the relevant phase-shifts are small. Then σ_λ is small and $\sigma^{(D)} > \sigma^{(0)}$. Therefore Mooij's rule for the total cross-section, $\sigma^{(D)} < \sigma^{(0)}$ if σ is larger than a critical value finds a simple explanation in terms of the splitting of local degeneracies of the cluster phase-shifts by an increasing disorder.

4. Conclusion: Our cluster calculations exhibit both Ziman and Mooij behaviour, depending on the potential strength which suggests that the T-dependance of the resistivity of liquid and amorphous materials can be explained in the framework of potential scattering. Obviously such cluster calculations will not yield reliable numerical values for the resistivity of real systems but they can be used as a test for an analytical calculation. Work in this direction is in progress. This work has been supported by the Swiss National Foundation.

References

[1] H. N. Dunleavy, W. Jones, J. Phys. F: Metal Phys. 8, (1978), 1477
[2] J. Ziman, "Electrons and Phonons", Oxford, Clarendon Press (1960)
[3] H. Beck, R. Frésard, to be published in Physica B
[4] H. Ehrenreich, L. M. Schwarz, Solid State Physics 31,(1976), 149-286
[5] Yu. N. Demkov, V. S. Rudakov, JETP 32, (1971), 1103
[6] W. John, P. Ziesche, Phys. Stat. Sol. (b)47, (1971) 555-564
[7] O. Dreirach, R. Evans, H.-J. Güntherodt, H. U. Künzi, J. Phys. F:Metal Phys. 2, (1972),709
[8] Shimoji, 1977 "Liquid Metals", London, Academic Press
[9] B. Delley, H. Beck, D. Trautmann, F. Rösel, 1979 J. Phys. F: Metal Phys. 9, (1979), 505

Elektrischer Widerstand und Hall-Effekt von amorphen und quasikristallinen Legierungen

T. Zingg, A. Tschumi, H.-J. Güntherodt
Institut für Physik, Universität Basel, Klingelbergstr.82, CH-4056 Basel

$Pd_{60}U_{20}Si_{20}$ besitzt im glasartigen und im quasikristallinen Zustand ähnliche Transporteigenschaften. In beiden wird ein sehr hoher spezifischer Widerstand gemessen, der mit steigender Temperatur abnimmt. Der Hall-Koeffizient ist für beide positiv und nimmt mit einem Curie-Weiss-Gesetz ab. Der Uebergang vom Glas zum Quasikristall zeigt eine Abnahme des Widerstands und eine Zunahme des Hall-Koeffizienten.
Die starke Erhöhung des Widerstands von glasartigem PdSi durch die Zulegierung von U ist auffallend, ebenso der Vorzeichenwechsel des Hall-Effekts. Reines flüssiges U besitzt einen positiven, temperaturunabhängigen Hall-Koeffizienten. Die quasikristalline Pd U Si-Legierung verhält sich ähnlich wie die (partiell) quasikristallinen Aℓ-Mn-Legierungen.

Electron Spectroscopy on Liquid Metals: New Results

G. Indlekofer, P. Oelhafen and H.-J. Güntherodt
Institut für Physik, Universität Basel, Klingelbergstr.82, CH-4056 Basel

The investigation of the electronic structure of liquid metals has only reached a modest level compared with the solid state. Most of the experimental data published so far originate from UPS studies for $h\nu \leqslant 21.2$ eV. In the new experiments, involving a novel efficient and reliable mechanical surface preparation, UPS ($11.8\ \text{eV} \leqslant h\nu \leqslant 48.4\ \text{eV}$) valence band spectra have been recorded in combination with XPS for contamination control and core level spectroscopy, AES and EELS. The variation of the UV-excitation energy over a wider range demonstrates the importance of the ionization cross sections. A nearly free electron like behaviour has been found in liquid Ga in contrast to published data, whereas Sn showed pronounced tendency to valence band splitting in the liquid state. Highly resolved UV d-core level spectra yield additional information on the electronic interaction in cases like In and Bi.

Band Structure Investigation of Liquid Alloys by Electron Spectroscopy

G. Indlekofer, P. Oelhafen and H.-J. Güntherodt
Institut für Physik, Universität Basel, Klingelbergstr.82, CH-4056 Basel

The relationship between the liquid and the metastable amorphous state of condensed matter is of fundamental interest. Liquid alloys offer the possibility to study alloying effects on the electronic structure without the complications of phase mixtures and k-conserving transitions in photoemission. A comparison of photoemission results of liquid and solid amorphous systems yields distinct differences in the case of Cu-Sn where the Cu 3d-resonance shows lower binding energy and higher symmetry in the liquid state indicating some structural relaxation which occurs in the quench condensed films. Differences in surface segregation can be understood in terms of surface tension and mobility of the alloy constituents. A minimum near E_F in the density of occupied states has been found in the case of liquid $Au_{81}Si_{19}$.

Observation of a negative temperature derivative of the surface resistivity in pure cadmium: the effect of surface reflectivity

J. van der Maas and R. Huguenin.
Institut de Physique Expérimentale de l'Université de Lausanne
1015-Lausanne, Switzerland

Measurements of the resistivity of cadmium [RRR(bulk)=$2x10^4$] show, that under size-effect conditions (l~d) the temperature derivative of the surface resistivity, $\Delta(\varrho-\varrho(bulk))/\Delta T$, can be changed from negative to positive by polishing the surface, and from positive to negative by subsequent etching. While this is in qualitative agreement with models for surface scattering which include an angle dependence of the specularity parameter, the range of thicknesses over which this is observed is unexpectedly large.

Influence de la fréquence sur les taux de diffusions électroniques déterminés par effet de taille en radio fréquences.

R. Stubi, P.-A. Probst et R. Huguenin
Institut de Physique Expérimentale, 1015 Lausanne

La contribution électrons-électrons au taux de diffusion est en général masquée par un terme électrons-phonons qui varie fortement avec la température. On peut réduire ce dernier terme en diminuant la fréquence d'excitation. Nos mesures entre 5 MHz et 80 kHz mettent directement en évidence, et dans le même échantillon, l'inefficacité des collisions des électrons avec les phonons de petits vecteurs d'ondes. En utilisant cet effet on obtient dans le cuivre une valeur du terme électrons-électrons qui est en bon accord avec les mesures de résistivité électrique.

Eddy Current Size Effect in Thin Wires

J. Romero and G. Brändli *)
Institut de Physique Expérimentale de l'Université de Lausanne
1015 Lausanne, Switzerland
*) Schanzmättelistr. 27, 5000-Aarau, Switzerland

A theory of the eddy current size effect in thin wires is presented. A comparison with the theory of eddy currents in thin plates is established. The theory is based on a spherical Fermi surface and isotropical mean free path l of the electrons. The partially specular scattering of the electrons at the sample surface is taken into account by the specularity parameter, p, which can be angularly dependent. Results are given for the relaxation times and the amplitudes of the electrical and magnetic fields as function of r/l, r being the radius of the wire.

KOND IV : Propriétés optiques - structure électronique

HYBRIDISIERUNG DER 4f- ELEKTRONEN IN SmSe UNTER HOCHDRUCK

M.W. Elmiger und P. Wachter, Laboratorium für Festkörperphysik,
ETH Hönggerberg, 8093 Zürich

Zusammenfassung: Das Verhalten des ersten angeregten Zustandes J=1 im tiefstliegenden Multiplett ^7F_J der Sm $4f^6$-Konfiguration wurde in einer Diamantstempelzelle untersucht. Der Zustand verschwindet fast schlagartig bei 31±2 kbar. Dieses Resultat steht im Widerspruch zu den Ergebnissen in verdünnten Systemen.

1. Einleitung

Die Samariumchalkogenide SmSe, SmSe und SmTe machen unter Hochdruck einen Phasenübergang vom halbleitenden zum zwischenvalenten Zustand. Er wird durch Hybridisierung des Leitungsbandes mit den 4f- Elektronen, deren Spin-Bahn aufgespaltenes ^7F_J- Multiplett ganz oder teilweise in der Bandlücke liegt, bewirkt. Dieses Grundzustandsmultiplett wird genau nach der Hund'schen Regel gebildet wie im freien Sm^{2+}-Ion; es stellt sich also die Frage, wie die Hybridisierung diesen hochkorrelierten Zustand ändert. Man kann versuchen, die Hybridisierung durch "internen Druck", d.h. durch Zulegieren eines Ions mit kleinerem Ionenradius zu simulieren. Mit dieser Methode wurde in $Sm_{1-x}Y_xSe$ mit zunehmender Konzentration von Yttrium eine Renormalisierung und Verbreiterung des J=1 Zustandes festgestellt [1]. Allerdings liefert das dreiwertige Yttrium eine erhebliche Anzahl zusätzlicher Ladungsträger, die neben Gitterverzerrungen und Störstellenniveaus das System stark stören.

Elektronische Raman-Streuung ist als Zweiphotonen-Prozess in der Lage, Uebergänge zwischen Zuständen gleicher Parität, in diesem Falle also innerhalb des Grundzustand-Multipletts, zu messen. Um Aufschluss über das Verhalten zu bekommen, haben wir den Uebergang J=0 ---> J=1 von SmSe in einer Hochdruck-Diamantstempelzelle untersucht.

2. Experiment

Da die Probe im üblicherweise verwendeten Methanol-Aethanol-Gemisch photokorrodierte, wurde Pentan-Isopentan als Druckübertragungsmedium ver-

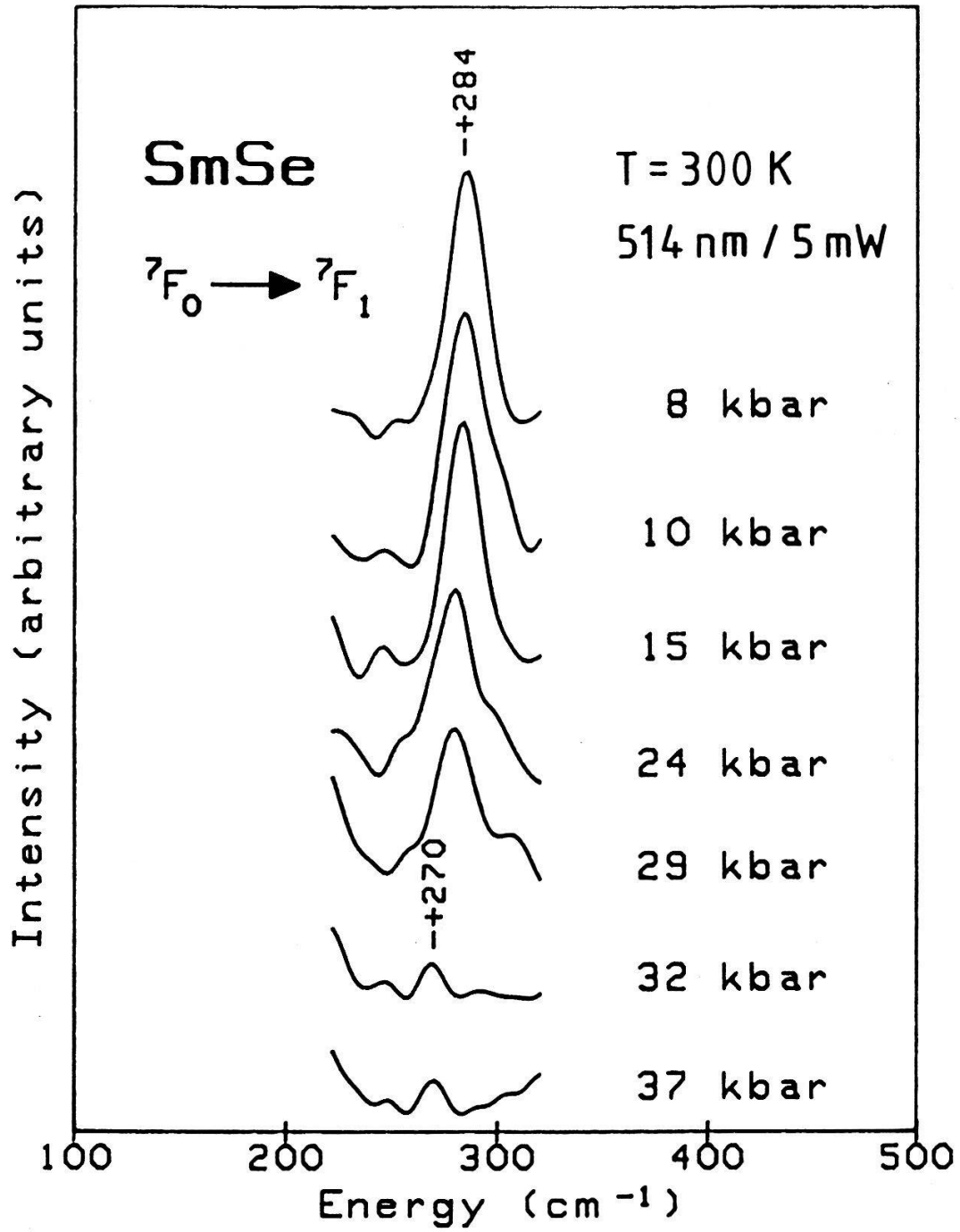

Fig. 1: Ramanspektrum des ^7F_J- Zustandes in SmSe unter Hochdruck. Die kleinen Strukturen auf beiden Seiten und der Peak bei 270 cm^{-1} stammen vom Druckübertragungsmedium

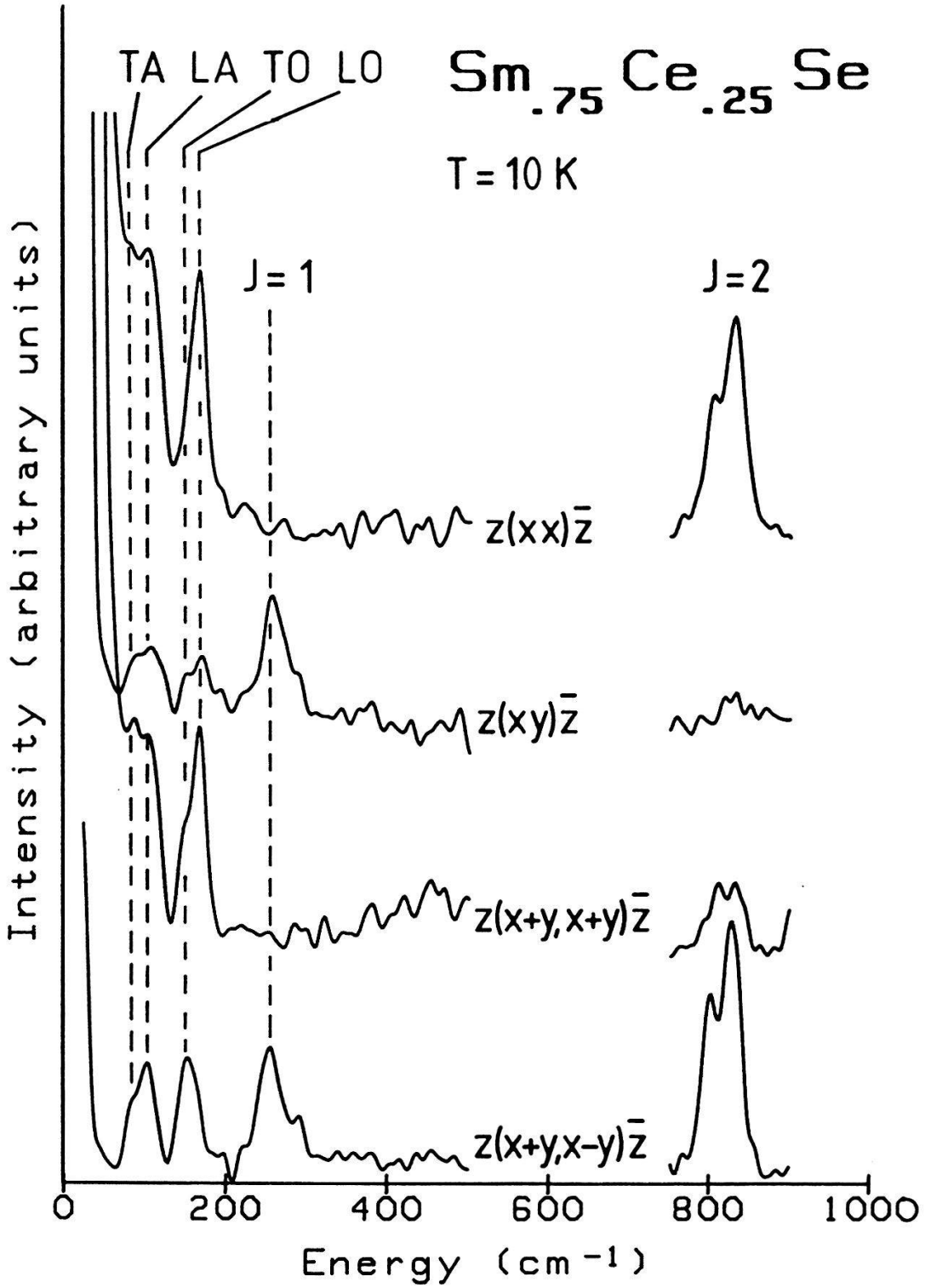

Fig. 2: Polarisierte Ramanspektren von $Sm_{.75}Ce_{.25}Se$

wendet und die Laserleistung auf 5 mW reduziert. Um den sehr starken Fluoreszenz-Untergrund von den Diamanten zu vermindern, wurde der optische Teil der Zelle so modifiziert, dass grössere Einfallswinkel möglich wurden. Die Probe wurde an einer Ecke auf die untere Stirnfläche des oberen Diamanten geklebt, um Vignettierung der Probe und Mehrfachreflexionen an den Probenraumwänden zu vermeiden.

3. Resultate / Diskussion

Es war möglich, den Uebergang von 0 bis 37 kbar zu verfolgen (Fig. 1). Es tritt im Gegensatz zu $Sm_{1-x}Y_xSe$ weder eine Renormalisierung noch eine Verbreiterung auf; der Peak verschwindet aber nach einer geringen Intensitätsverminderung fast schlagartig bei 31±2 kbar.

Um die Ursache des "Softenings" abzuklären, haben wir $Sm_{.75}Ce_{.25}Se$ untersucht. Ce^{3+} hat fast denselben Ionenradius wie Sm^{2+}, sodass kein "interner Gitterdruck" ausgeübt wird (Gitterkonstante SmSe : 6.1975 Å; $Sm_{.75}Ce_{.25}Se$: 6.131 Å). Hingegen injiziert es zusätzliche Elektronen genau wie Yttrium in $Sm_{1-x}Y_xSe$. Das Spektrum (Fig. 2) ist fast identisch mit demjenigen von $Sm_{1-x}Y_xSe$ [1]; insbesondere findet man dieselbe Renormalisierung und Verbreiterung des J=1 - Niveaus.

4. Schlussfolgerungen

Das "Softening" in substituierten Systemen wird durch die zusätzlichen Elektronen bewirkt und ist kein Effekt der Hybridisierung. Das Experiment mit dem Legierungssystem ist somit nicht gleichbedeutend mit einem echten Hochdruckexperiment.

5. Referenz

[1] G. Güntherodt, A. Jayaraman, E. Anastassakis, E. Bucher, H. Bach: Phys. Rev. Lett. 46, 855 (1981)

ELEKTRONENSTRUKTUR UND H_2-ABSORPTION VON Zr-Pd-VERBINDUNGEN

S. Büchler, T. Riesterer, S. Hüfner und L. Schlapbach
Laboratorium für Festkörperphysik, ETHZ, 8093 Zürich

Zr und Pd und die intermetallische Verbindung Zr_2Pd bilden mit Wasserstoff stabile Metallhydride; im Gegensatz dazu absorbiert $ZrPd_2$ unter "normalen" Laborbedingungen keinen Wasserstoff.

Wir berichten über Messungen des Valenzbandes und der Rumpfniveaus von Zr, Pd, $ZrPd_2$ und Zr_2Pd mittels Photoelektronenspektroskopie. In $ZrPd_2$ ist das Pd d-Band voll und vom Ferminiveau weggeschoben. Entsprechend ist die d-Zustandsdichte an E_F klein. Das Wasserstoffelektron erfordert damit eine grössere Verschiebung von E_F, was einen stark endothermen Beitrag zu Bildungsenthalpie liefert.

Optische Reflektivität von metallischen Gläsern

R. Lapka und H.-J. Güntherodt
Institut für Physik, Universität Basel, Klingelbergstr.82, CH-4056 Basel

In Abweichung zur üblichen Interpretation von optischen Reflektivitätsspektren im Rahmen einer Kramers-Kronig-Analyse wird in der vorliegenden Arbeit ein anderer Weg beschritten. Während bei Kristallen die optische Reflektivität stark durch die Bandstruktur und die direkten optischen Uebergänge bestimmt wird, ist bei nichtkristalliner Materie, wie den metallischen Gläsern, die $\vec{k}$-Erhaltung als Auswahlregel nicht anwendbar. Die die optischen Eigenschaften bestimmende Grösse ist dann anstelle der Bandstruktur die elektronische Zustandsdichte. Ausgehend von einer typischen Zustandsdichte einer binären Legierung aus zwei Uebergangsmetallen soll die Berechnung der optischen Reflektivität gezeigt und das Resultat mit gemessenen Daten verglichen werden.

Etude théorique de la liaison chimique des dimers Cs_2 et Cs_2^+

I. Moullet et W. Andreoni, Institut de Physique Expérimentale, EPFL, 1015 Lausanne

Nous présentons des calculs des propriétés d'équilibre des dimers Cs_2 et Cs_2^+ dans l'approximation locale (local spin density). Nous étudions la formation de la liaison et une comparaison avec d'autres dimers alcalins est effectuée. En particulier, le rôle des effets relativistes et de l'hybridation s-d des orbitales atomiques ainsi que celui de la polarisation des coeurs des atomes est mis en évidence. Nous comparons nos résultats à ceux provenant d'un calcul d'interaction de configurations.

SPINPOLARISIERTE AUGER- UND SEKUNDAERELEKTRONENEMISSION AUS DUENNEN FERROMAGNETISCHEN FILMEN.

F. Lärmer, M. Taborelli, R. Allenspach und M. Landolt
Laboratorium für Festkörperphysik, ETH Hönggerberg, 8093 Zürich

Spinpolarisierte Sekundärelektronenemission erlaubt die oberflächennahe Messung der mittleren Magnetisierung, und die Polarisation der Augerelektronen enthält elementspezifische Information über das magnetische Verhalten der Einzelkomponenten. An amorphen $Co_{80}Ni_{20}$-Filmen auf Silizium haben wir beobachtet, dass die magnetischen Momente von Co und Ni parallel koppeln. Mit abnehmender Filmdicke (bis 10 Å) steigt die Koerzitivkraft stark an, und gleichzeitig dreht die leichte Magnetisierungsrichtung in die Filmebene. Solche Messungen sind ein wichtiger Schritt zur gezielten Erzeugung sputter-induzierter magnetischer Anisotropien, die bei der Entwicklung neuer magnetischer Speichermaterialien bedeutend sind.

On the three-spin exchange interaction in magnetic systems

U. Falk and A. Furrer, Lab.f.Neutronenstreuung ETHZ, 5303 Würenlingen, H.U. Güdel, Inst. f. anorg. Chemie, Universität, Bern

There are indications for important effects of many-body forces in various fields, e.g. effects on the correlations in disordered binary alloys, on the spin coupling of polynuclear transition metal complexes, on the spin structure of solid ^3He, on the stability of nuclear matter, etc. In all these cases the importance of many-body forces was made plausible by theoretical arguments alone. The present work provides the first direct experimental proof of the existence of three-body forces in an interacting system, specifically the existence of a three-spin interaction in the magnetic solid solution $CsMn_{0.28}Mg_{0.72}Br_3$ with use of the inelastic neutron scattering technique.

Zeroenergy spin-waves and quadratic dispersion in fcc type I antiferromagnets

B. Hälg, Labor für Neutronenstreuung ETHZ, CH-5303 Würenlingen

It is a general statement in solid-state physics lecture books that the spin waves in Heisenberg ferromagnets follow a quadratic dispersion law, whereas, in antiferromagnets they show a linear dispersion. However, there is the great class of simple fcc type I antiferromagnets (AF/I) which breaks this rule. Similar to the ferromagnets in the AF/I magnets the Heisenberg Hamiltonian is invariant under special rotations in spin space, but the ordered state has broken this symmetry by choosing $\langle\vec{S}\rangle$ to be along some direction. The choise of direction is arbitrary which means that the spins can rotate compatible with the AF/I ordering without a restoring force leading to zero-energy spin-waves and quadratic dispersion at the X-points in the Brillouin zone. Above behavior has been observed in the AF/I magnet CeAs by neutron scattering (B. Hälg et al., Phys. Rev. Lett. 50, 1085 (1983)).

Kristallfeld-Bestimmung in $PrBr_3$ mittels Neutronenstreuung

B. Schmid[+], B. Hälg[+], A. Furrer[+], W. Urland[*] und R. Kremer[*]
+ Labor für Neutronenstreuung, ETH, 5303 Würenlingen
* MPI für Festkörperforschung, 7000 Stuttgart, BRD

Es wurden unelastische Neutronenstreuexperimente an einem Einkristall des hexagonalen $PrBr_3$ bei Temperaturen zwischen 1.5 und 300 K für verschiedene Streuvektoren durchgeführt. Die Identifikation von vier Kristallfeldübergängen und deren Polarisation im aufgespaltenen $^3H_4$ J-Multiplett der Pr^{3+} Ionen erlaubt eine eindeutige Bestimmung der vier Parameter des Kristallfeldoperators für hexagonale Punktsymmetrie. Der Kristallfeldgrundzustand charakterisiert $PrBr_3$ als nahezu ideales effektives S=½ Ising System.

KOND V : Métallurgie - spectroscopie par positrons

POSITRON CAPTURE IN THALLIUM AND Tl_xPb_{1-x} ALLOYS

K. Ghazi Wakili, E. Cartier and F. Heinrich, Laboratorium für Festkörperphysik ETH, CH-8093 Zürich, Switzerland

1. Introduction

Investigations of vacancies in metals by positron annihilation methods have given promising results in recent years [1]. However, in some cases such as Tl, the values of different observables (S-parameter [2], lifetime [3] or peakrate [4]) make the interpretation rather difficult because the effects observed are very small: an increment of 10 psec of the lifetime due to trapping [3] or a weak increase $\Delta S/S = 0.9$ % of the S-parameter [2]. For this reason we decided to get direct evidence of trapping from the localization length [5] of trapped positrons. For this purpose we used the 2γ-correlation-method as follows. The experimental angular correlation function

$$N(\Theta) = \int_{-\infty}^{+\infty} \left[P(\Theta')+G(\Theta')\right] \cdot g(\Theta-\Theta')d\Theta'; \quad \Theta = p_z/mc$$

has been analyzed by the following procedure. $P(\Theta) = P_o(1-\Theta^2/\Theta_F^2)$ represents the free electron contribution, with $\Theta_F = p_F/mc$ being the Fermi angle. $G(\Theta) = G_o \exp(-\Theta^2/\Theta_G^2)$ is the core contribution. The resolution function $g(\Theta-\Theta')$ is a Gaussian given by

$$g(\Theta) = (1/\sqrt{\pi}\,\sigma_{tot})\cdot\exp(-\Theta^2/\sigma_{tot}^2) \quad \text{with} \quad \sigma_{tot} = (\sigma_{op}^2+\sigma_{th}^2+\sigma_v^2)^{1/2} \qquad (1)$$

σ_{op} is the optical resolution of the 2γ-spectrometer and $\sigma_{th}^2 = 2m^*kT/m^2c^2$ ($m^* = 1.23m$ [1]) the width of the thermal momentum distribution of the e^+. The contribution σ_v is due to the localization of positrons trapped in vacancies. σ_v is correlated to the localization length r_o by $\sigma_v(T)$. $r_o = \lambda_c \varphi_v(T)$ where $\varphi_v(T)$ is the fraction of positrons trapped in vacancies. This quantity has been determined by peakrate measurements [4] using a simple 2-state-trapping model. If the same model is applied to describe the temperature variation of σ_{tot}, we obtain

$$\sigma_{tot} = (1-\varphi_v)\cdot(\sigma_{op}^2+\sigma_{th}^2)^{1/2} + \varphi_v\cdot(\sigma_{op}^2+\sigma_{th}^2+\sigma_{vs}^2)^{1/2} \qquad (2)$$

with σ_{vs} being the saturation value of σ_v: $\sigma_v(T) = \sigma_{vs} \cdot \varphi_v(T)$. In the following a comparison of experimental results obtained with Aℓ, Tℓ and Pb will show the applicability of (2) to detect poor e^+-trapping in metals such as Tℓ. Furthermore, analogous experiments made with Tl_xPb_{1-x} alloys are presented to study the dependence of r_o on the Tℓ-concentration x.

2. Experimental

Tl_xPb_{1-x} alloys as well as samples of pure Tℓ and Pb have been prepared from high purity degassed components. They have been molten into an iron sample holder and finally annealed during 12 hours at a temperature close to the melting point. 900 mCi of ^{64}Cu have been used as e^+ source. All measurements with the Tl_xPb_{1-x} alloys have been made at $T = T_m - 20^o$ (T_m = melting point). At this temperature the capture probability is very close to the saturation value $\varphi_v \simeq 1$. Thus, it was reasonable to assume a constant value $\varphi_v = 0.91$ for the whole range of x.

3. Results and discussion

Fig. 1 shows the T-dependence of σ_{tot} for Aℓ, Tℓ and Pb. For $T \leq 250^oC$ vacancy formation in Aℓ is known to be negligible, whereas pronounced e^+-trapping occurs in Pb. The data obtained with Tℓ have been found between these two extreme cases clearly indicating e^+-trapping in Tℓ. The dotted curve has been

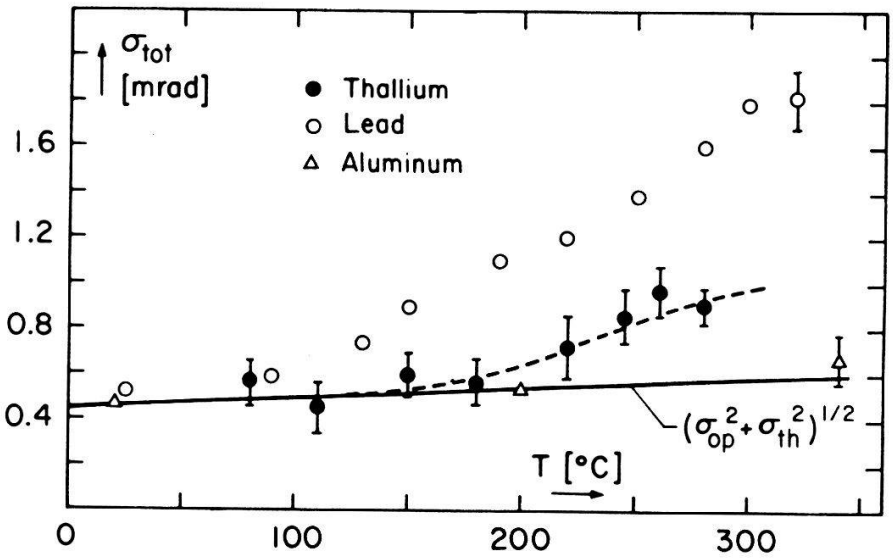

Fig. 1 Temperature dependence of σ_{tot} for Aℓ, Tℓ and Pb. Dotted curve calculated from (2).

calculated from (2) using data for $\varphi_v(T)$ obtained from peakrate measurements similar to those described in [4].

In Fig. 2 the variation of the localization length r_o with the Tℓ-concentration x is shown for nine Tl_xPb_{1-x} alloys and the components Tℓ and Pb. As suggested earlier [6], the e^+-localization becomes weaker with increasing number of Tℓ-atoms as nearest neighbours of a vacancy. This is reflected by the linear increase of r_o for $x < 0.7$. Near $x = 0.7$ r_o jumps to higher values. A similar discontinuity at the same concentration has been observed in peakrate measurements [4]. This might be due to the formation of ordered phases as Tl_3Pb and Tl_7Pb [7] where only two kinds of vacancies with Tℓ-rich surroundings exist. A more detailed discussion of these considerations will be published later.

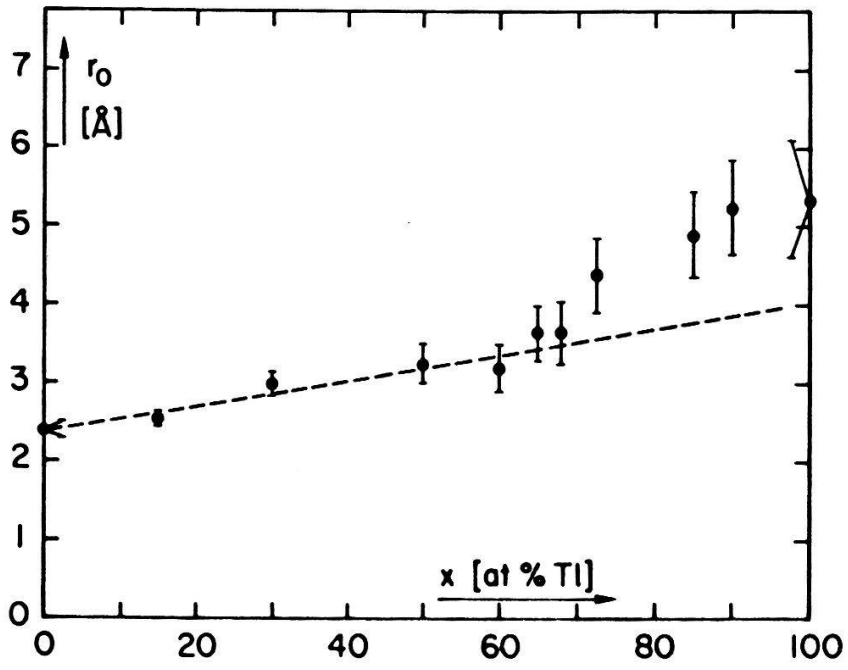

Fig. 2 Localization length r_o versus Tℓ-concentration x in Tl_xPb_{1-x}.

We gratefully acknowledge helpful discussions with Dr. J. Brunner and Dr. U. Zimmermann and the technical assistance of Mr. O. Knecht.
This work has been supported by the Swiss National Science Foundation.

4. References

[1] Positrons in solids, edited by P. Hautojärvi, Topics in current physics, Springer Verlag 1979

[2] I.K. MacKenzie and J. Fabian, Can. J. Phys. 58, 1635 (1985)

[3] W. Puff and P. Mascher, Phys. Lett. 112A, 90 (1985)

[4] F. Heinrich and U. Zimmermann, Helv. Phys. Acta 52, 200 (1979)

[5] M.A. Shulman and S. Berko, Abst. of 4th Int.Conf.Positron Annihilation, Helsingør, E 31 (1976)

[6] F. Heinrich and U. Zimmermann, Helv. phys. Acta 52, 349 (1979)

[7] Y.C. Tang and L. Pauling, Acta Cryst. 5, 39 (1952)

Spectre de frottement intérieur du WC-Co

J.-J. Ammann, R. Schaller, Institut de Génie Atomique, EPFL, 1015 Lausanne

Le composite carbure de tungstène-cobalt est caractérisé par une relativement bonne ténacité (résistance à la propagation de fissures) pour un matériau d'une dureté comparable à celle des céramiques. Dans le but de mieux comprendre les causes microscopiques de ces propriétés mécaniques remarquables, des mesures de frottement intérieur ont été réalisées sur divers composites WC-Co, de la température ambiante à 1300 K. Les résultats montrent une augmentation exponentielle du frottement intérieur en fonction de la température à laquelle se superpose un pic situé à $\sim$ 900 K. Ce pic est un pic de relaxation activé thermiquement ($E_R \simeq 2.7$ eV). L'origine de la relaxation pourrait être la phase Co car la hauteur du pic augmente avec la concentration de Co. De plus, ce pic peut être associé à l'augmentation de ténacité observée dans le même domaine de température par H. Si Mohand* et interprétée par une augmentation de ductilité de la phase métallique Co. (*H. Si Mohand, Thèse INSA-Lyon, 83).

Wechselwirkung zwischen dem Risswiderstand und den Mikromechanismen von WC-Co Hartmetallen

H.G. Schmid, W. Benoit, C. Bonjour*
Institut de Génie Atomique, EPFL, 1015 Lausanne, *Stellram SA, Nyon

Der Risswiderstand (Risszähigkeit) ist gegeben durch die äussere Arbeit und die elastisch gespeicherte Energie die sich während des Rissfortschritts in nicht elastische Energieen umwandeln. Hauptsächlich kommen dafür in Frage:
1. Oberflächenenergien
2. Wärme die während plastischer Verformung entsteht
3. Gibb's freie Energie durch Phasentransformation

Es wird mit Hilfe verschiedener Modelle gezeigt, dass alle diese Energieformen den Risswiderstand von WC-Co Hartmetallen in Abhängigkeit von der Temperatur beeinflussen können.

Résistance à la rupture de fontes grises à fort amortissement

D. Krähenbühl, H.G. Schmid, R. Schaller
Institut de Génie Atomique, EPFL, 1015 Lausanne

Les fontes grises sont des composites formés de précipités de graphite (lamellaires ou nodulaires) dispersés dans une matrice d'acier. La capacité d'amortissement de ces matériaux est due à des mécanismes dissipatifs dans la phase graphite, qui sont favorisés par la structure lamellaire. La dimension des lamelles doit cependant être optimalisée pour que l'augmentation d'amortissement ne conduise pas à une chute des propriétés mécaniques. Nous avons évalué la résistance à la rupture de diverses nuances de fonte grise lamellaire par la méthode de l'"intégrale J", car les essais mécaniques ont montré que le comportement des fontes grises est non-linéaire et non-élastique. Finalement, nos résultats montrent clairement que bonne résistance à la rupture n'est pas contradictoire avec forte capacité d'amortissement.

Transition hc $\rightleftarrows$ cfc du cobalt étudiée par méthodes acoustiques

J.-E. Bidaux, R. Schaller, Institut de Génie Atomique, EPFL, 1015 Lausanne

Des mesures d'impédance acoustique sont effectuées dans du cobalt de pureté nominale 5N au voisinage de la température de transition hc $\rightleftarrows$ cfc ($\sim$417°C). Aux basses fréquences ($0{,}1 < f < 10$ Hz), un pic de frottement intérieur important (Q^{-1}) apparaît à la température de transition, dont la hauteur augmente avec la vitesse de chauffage $\dot{T}$ et diminue avec la fréquence de mesure ω ($Q^{-1} \sim \dot{T}/\omega$). Ce pic pourrait être dû au mouvement des interfaces hc-cfc. Le frottement intérieur étant lié à la quantité de matière transformée au cours d'un cycle de vibration. Aux moyennes fréquences ($\sim$ 5 kHz), cette quantité est négligeable. Néanmoins, il apparaît une chute de module associée à un maximum de frottement intérieur. Les mesures effectuées par ondes ultrasonores tendent à montrer que ces effets sont liés à un affaiblissement de la constante élastique de cisaillement C_{44}.

KOND VI : Diélectriques - transitions de phases

"GROUND STATE OF SMALL TWO-DIMENSIONAL AGGREGATES"

R. Rentsch, Ph. Choquard, B. Piller

Institut de Physique Théorique-EPFL, CH-1015 Lausanne, Switzerland

1. Introduction

In order to understand some consequences of pure Coulomb forces in two-dimensional systems, we consider an assembly of N polarizable "classical atoms". Each "atom" is made up of a point nucleus (n) surrounded by a neutralizing cloud (c) spread uniformly over a disk of radius σ.

Our first purpose will be to study the ground state of such a system.

The model implies three interaction potentials ($V^{nn'}$, V^{nc}, $V^{cc'}$), conveniently normalized to zero at a distance $r = 2\sigma$.

Let's denote by $\pm q, \underline{r}_n$ and $\underline{r}_c$, the charges, the positions of the nucleus and of the center of the neutralizing cloud respectively. We can write :

$$V^{nn'}\left(\frac{|\underline{r}_n-\underline{r}_{n'}|}{2\sigma}\right) = V^{nn'}\left(\frac{r}{2\sigma}\right) = q^2 \ln\left(\frac{2\sigma}{r}\right) \tag{1}$$

$$V^{nc}\left(\frac{|\underline{r}_n-\underline{r}_c|}{2\sigma}\right) = -\frac{q^2}{\pi\sigma^2}\int_{|\underline{y}|\le\sigma} d^2y \ln\frac{2\sigma}{|\underline{r}_n-\underline{r}_c-\underline{y}|} = q^2\begin{cases}\left(-\frac{1}{2}-\ln 2+\frac{r^2}{2\sigma^2}\right); & r=|\underline{r}_n-\underline{r}_c|\le\sigma\\ \ln\frac{r}{2\sigma}\ ; & r\ge\sigma\end{cases} \tag{2}$$

$$V^{cc'}\left(\frac{|\underline{r}_c-\underline{r}_{c'}|}{2\sigma}\right) = \frac{q2}{(\pi\sigma^2)^2}\int_{|\underline{y}|\le\sigma} d^2y \int_{|\underline{z}|\le\sigma} d^2z \ln\left(\frac{2\sigma}{|\underline{r}_c-\underline{r}_{c'}-\underline{y}+\underline{z}|}\right) = q^2\begin{cases}\frac{1}{2\pi}\left\{\arccos\left(\frac{r}{2\sigma}\right)\left[1-8\left(\frac{r}{2\sigma}\right)^2\right]\right.\\ \quad+\left[5\left(\frac{r}{2\sigma}\right)+2\left(\frac{r}{2\sigma}\right)^3\right]\sqrt{1-\left(\frac{r}{2\sigma}\right)^2}\\ \quad\left.-4\int_1^{r/2\sigma}\frac{\arcsin t}{t}\,dt\right\}; \quad r=|\underline{r}_c-\underline{r}_{c'}|\le 2\sigma\\ -\ln\left(\frac{r}{2\sigma}\right); \quad r\ge 2\sigma\end{cases} \tag{3}$$

In particular, for two "atoms" without dipole moments, the interaction energy can be written :

$$\phi\left(\frac{r}{2\sigma}\right) = V^{nn'}\left(\frac{r}{2\sigma}\right) + 2V^{nc}\left(\frac{r}{2\sigma}\right) + V^{cc'}\left(\frac{r}{2\sigma}\right) \tag{4}$$

and is shown on figure 1.

2. Questions and results

With the model defined above the questions to be answered are the following ones : considering an aggregate of N "atoms" each having a dipole moment :

(i) Is there a critical distance between these "atoms" such that the interaction with dipoles is smaller than that without dipoles, and if so, what is the geometrical configuration of these dipoles ?

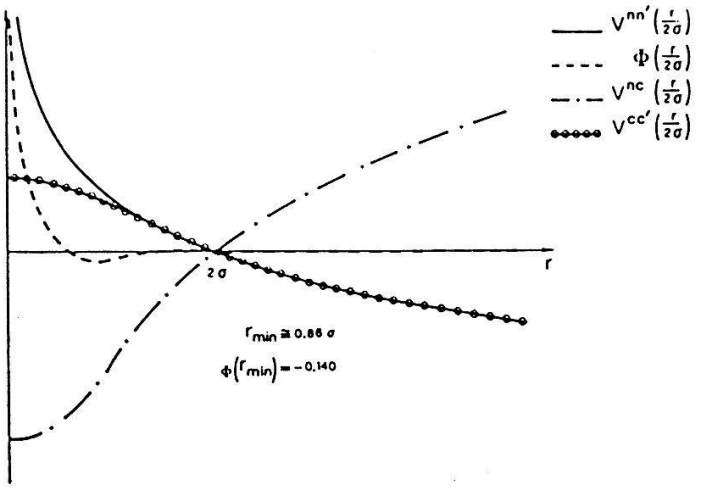

Fig. 1.

(ii) For which configuration does the interaction energy reaches its absolute minimum ?

Two cases which can be solved analytically are considered : aggregates made up of two, respectively three "atoms". The study of aggregates containing a larger number of "atoms" requires numerical simulations.

The results are :

(i) The interaction energy of the system with two and three dipoles can be lower than that without dipoles if they take some well defined geometrical configuration (see sections 3 and 4). The same feature is observed in computer simulations of the ground state of larger clusters.

(ii) The interaction energy reaches its absolute minimum in the limit of the "unified molecule model", i.e. when the disks are completely overlapping. The system collapses and becomes a droplet of jellium. This collapse can be prevented if additional repulsive forces between the overlapping clouds come into play. Exchange forces are natural candidates for this task.

3. Two-dipole interaction

Let us consider a system made up of two "atoms", each having a dipole moment denoted by $\underline{b}$ and $\underline{b}'$. They are supposed to be of equal lengths and making an angle θ_b, respectively $\theta_{b'}$, with the vector $\underline{r}$ joigning the centres of the spread charges.

The interaction energy is written in that case :

$$\Phi_{dip} = V^{nn'}(|\underline{r}+\underline{b}'-\underline{b}|) + V^{nc}(|\underline{r}+\underline{b}'|) + V^{nc}(|\underline{r}-\underline{b}|)$$
$$+ 2\,(V^{nc}(|\underline{b}|) - V^{nc}(o)) + V^{cc'}(|\underline{r}|) \qquad (5)$$

One shows that in the approximation $|\underline{b}| = |\underline{b}'| = b \ll |\underline{r}| = r$ (allowing a limited development of $V^{nn'}$, V^{nc} and $V^{cc'}$), the equation (5) becomes for $r \geq \sigma$:

$$\Phi_{dip} = \Phi(r) + b^2 \left(\frac{1}{\sigma^2} - \frac{1}{r^2} \cos(\Theta_b - \Theta_{b'})\right) \qquad (6)$$

where $\Phi(r)$ is the interaction potential between two "atoms" without dipole moment.

Equation (6) is minimized for $\Theta_b = \Theta_{b'} = \alpha$. We get then :

$$\Phi_{dip} \begin{cases} = \Phi(r); \; r = \sigma \\ > \Phi(r); \; r > \sigma \end{cases} \qquad (7)$$

For $\Theta_b = \Theta_{b'}$ and still with the above mentionned approximation, eq. (5) can be written for $r \leq \sigma$:

$$\Phi_{dip} = \Phi(r) + \frac{2b^2}{\sigma^2} + \frac{b^2}{r^2} (\cos 2\alpha - 1) \qquad (8)$$

Since this function is continuous at $r = \sigma$, we get $\alpha = \Pi/2$ and hence :

$$\Phi_{dip} \begin{cases} = \Phi(r); \; r = \sigma \\ < \Phi(r); \; r < \sigma \end{cases} \qquad (9)$$

One shows finally that Φ_{dip} reaches its absolute minimum for $r = 0$, $b = \sigma/2$ and $\Theta = \Theta_{b'} = \Pi/2$. The above situation is summarized in the figure 2.

4. Three-dipole interaction

Let us consider three "atoms" (each having a dipole moment denoted by $\underline{b}_1$, $\underline{b}_2$, $\underline{b}_3$ of equal lengths and making the angles Θ_1, Θ_2, Θ_3 respectively with the x-axis) initially placed so that the centers of the spread charges are the vertices of an equilateral triangle of side $|\underline{r}_i| = r$, $i = 1,2,3$

Let's denote by $\underline{d}ij$ the vector joigning dipole i to dipole j. The interaction energy of this system becomes :

$$\begin{aligned} \Phi_{dip} = {} & V^{nn'}(|\underline{d}_{21}|) + V^{nn'}(|\underline{d}_{13}|) + V^{nn'}(|\underline{d}_{32}|) + V^{nc}(|\underline{b}_1 - \underline{r}_1|) \\ & + V^{nc}(|-\underline{r}_3 - \underline{b}_1|) + V^{nc}(|\underline{r}_1 + \underline{b}_2|) + V^{nc}(|\underline{r}_2 - \underline{b}_2|) + V^{nc}(|\underline{b}_3 - \underline{r}_3|) \\ & + V^{nc}(|-\underline{r}_2 - \underline{b}_3|) + \sum_{i=1}^{3} V^{nc}(|\underline{b}_i|) + \sum_{i=1}^{3} V^{cc'}(|\underline{r}_i|) - 3\, V^{nc}(o) \end{aligned} \qquad (10)$$

One shows that in the approximation $|\underline{b}_i| = b \ll |\underline{r}_i| = r$, $i = 1,2,3$; eq. (10) becomes for $r \geq \sigma$:

$$\Phi_{dip} = \Phi(r) + \frac{3b^2}{2\sigma^2} - \frac{b^2}{r^2}\{\cos(\Theta_1-\Theta_2-\frac{\Pi}{3}) + \cos(\Theta_1-\Theta_3) + \cos(\Theta_2+\Theta_3-\frac{\Pi}{3})\} \quad (11)$$

where $\Phi(r)$ is the interaction potential of three "atoms" without dipole moments.

We can see that :

(i) Φ_{dip} is minimized for $\Theta_1 = \Theta_3 = \Pi/3$ and $\Theta_2 = 0$ (i.e. when the system is so arranged as the dipoles make an angle of 120° with each other).

(ii) For $\Theta_1 = \Theta_3 = \Pi/3$ and $\Theta_2 = 0$

$$\Phi_{dip} \begin{cases} > \Phi(r); & r > \sigma\sqrt{2} \\ = \Phi(r); & r = \sigma\sqrt{2} \\ < \Phi(r); & \sigma \leq r < \sigma\sqrt{2} \end{cases} \quad (12)$$

One shows finally that Φ_{dip} reaches its absolute minimum for $r = 0$ and then $b = \frac{\sigma}{\sqrt{3}}$.

The situation is summarized in the figure 3.

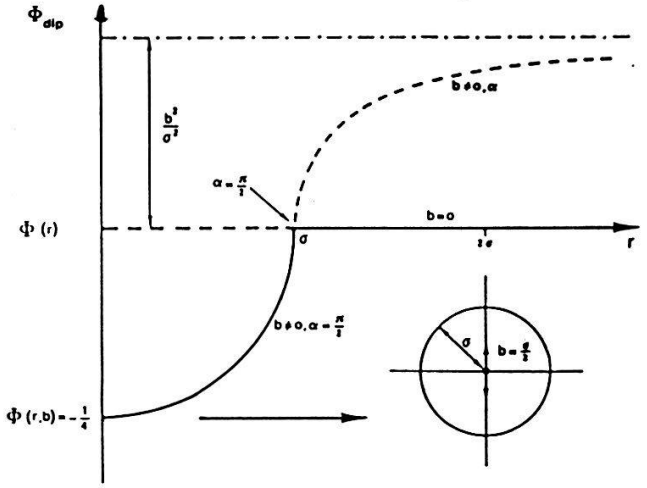

Fig. 2

TWO - DIPOLE INTERACTION

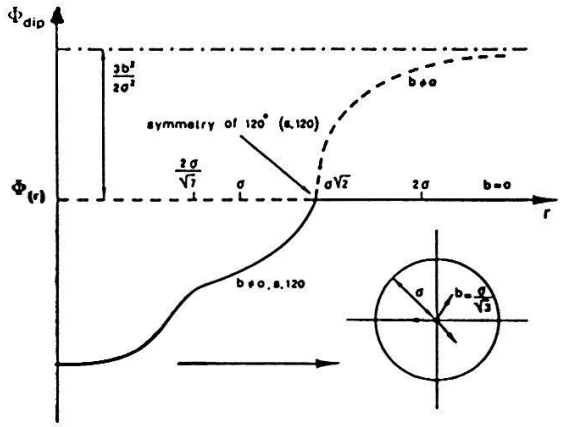

Fig. 3

THREE - DIPOLE INTERACTION

Untersuchungen von heissen Elektronen und von Haftstellen in organischen Dielektrika mittels elektronenspektroskopischer Methoden

E. Cartier, P. Pfluger, Brown Boveri Forschungszentrum, CH-5405 Baden-Dättwil

Die Energieverteilung und die Relaxation heisser (E>>kT) Ladungsträger sind für das Verhalten von Dielektrika in hohen Feldern entscheidend. Die Leitungselektron-Phonon Wechselwirkungen (Streulängen) konnten für Ladungsträger im Energiebereich 0.1-18eV mit elektronenspektroskopischen Methoden quantitativ untersucht werden. Oberhalb einer Schwellenergie von 3.5eV tragen zusätzlich strahlenchemische Effekte zur Relaxation bei. Dabei entstehen Haftstellen, die durch langsamere Elektronen besetzt und abgetastet werden können. Mittels Exoelektronen- und induzierter optischer Emission aus den Störstellen sowie nachfolgender elektronenspektroskopischer Analyse konnten in Kohlenwasserstoffen Haftstellen bis in den Konzentrationsbereich unter 10^{-10} cm^{-3} untersucht werden. Temperaturabhängige Messungen zeigen, dass die Störstellen nur gerade den Transport der langsamsten Leitungsbandelektronen beeinflussen, während Ladungsträger mit E>0.5eV unbeeinflusst bleiben.

High mobility charge carriers in polymeric dielectrics

Th. Baumann, E. Cartier, T. Hibma*, P. Pfluger, H.R. Zeller
Brown Boveri Research Center, CH-5405 Baden, Switzerland, * University of Groningen, NL-9747 Groningen, The Netherlands

According to a recent model for the understanding of dielectric ageing, charge carriers of high, band type mobility may be locally present in otherwise insulating dielectrics[1]. A necessary condition to keep these "hot" carriers in the high mobility state is an electric field of the order of the breakdown field, which exists locally at points of strong field enhancements, e.g. needle tips or defects. Model calculations show that the hot carriers can form homogeneous space charge regions around the tips. In experiments using samples of different commercial polymers, the development of space charge clouds of the expected size and voltage dependence could be confirmed as well as the high mobility character of charge carriers.

[1]) H.R. Zeller and W.R. Schneider, J. Appl. Phys. 56, p.455 (1984).

Frequency-dependent susceptibility of KCl:OH dipole glass

Michel St. Paul, Laboratoire de très basses temperatures, CNRS, Grenoble, France
Mario Maglione, Ecole Polytechnique Fédérale, 1016 Lausanne, Switzerland
U.T. Höchli, IBM Zurich Research Laboratory, 8803 Rüschlikon, Switzerland

Dielectric susceptibilities are reported for KCl:OH in the MHz-frequency range. The results are explained in terms of broad distributions of relaxation times similar to those found in other glass-like systems.

STRUKTURELLE PHASENUMWANDLUNGEN UND SOFT-MODE IN BROMELPASOLITEN

W. Bührer, Labor für Neutronenstreuung ETHZ, Würenlingen und H.U. Güdel, Institut für anorganische Chemie, Universität Bern

Die Brom-Elpasolite $Cs_2NaSEBr_6$ (SE=seltene Erde) durchlaufen bei tiefen Temperaturen eine strukturelle Phasenumwandlung mit Symmetrie Erniedrigung (kubisch-tetragonal). Unelastische Neutronenstreu-Experimente in der kubischen Phase zeigen, dass die Umwandlung durch einen Soft-mode getrieben wird. Die weitere strukturelle Evolution in der Tieftemperaturphase kann durch die Beobachtung elastischer Reflexe verfolgt werden.

Die Charakteristik des Phasenüberganges wird im Zusammenhang mit den strukturell verwandten Perovskiten diskutiert.

PHASES AND PHASE TRANSITIONS IN $(TMA)_2ZnCl_{4-x}Br_x$ SOLID SOLUTIONS

E. Colla, V. Gramlich*, W. Petter*, H. Arend
Lab.of sol. st. phy. ETH Zürich *Inst.of Crystallog. ETH Zürich

We analyzed the phases and phase transitions in the known (x,T)-phase diagram of $(TMA)_2ZnCl_{4-x}Br_x$ by means of different techniques. The structures of the high temperature phase and of an interesting commensurable low temperature phase with $k_x=1/2a^*$ were determined by successive use of direct method and least square calculations on measurements performed with a four-circle X-ray diffractometer. Strain application by small pincers mounted on the diffractometer removed twins present in these ferroic crystals.
First results of optical measurements on second harmonic generation and phase matching effects and of neutron scattering experiments under pressure up to 60 MPa are presented.

NMR study of the martensite transformation in a Cu-Zn-Al alloy

E. Handschin, C. Dimitropoulos, R. Gotthardt*, Institut de Physique Expérimentale et *Institut de Génie Atomique, EPFL, 1015 Lausanne

The NMR spectra of $^{63,65}Cu$ and ^{27}Al nuclei have been investigated in a Cu (73.6 % wt) - Al (6.9 % wt) - Zn (19.5 % wt) alloy in the temperature range 350 K $\geqslant$ T $\geqslant$ 250 K. The first order quadrupole splitting in the line shape of both nuclei suggest that the local symmetry around Cu and Al atoms is not cubic, even in the austenite phase. Near the critical region, ($M_S \simeq 265$ K), a significant variation of the line width (Δf) quadrupole splitting (ν_Q) and spin-lattice relaxation rate (T_1^{-1}) has been observed. These results can be understood with the assumption that at least certain atoms of the austenitic lattice start to oscillate strongly around their equilibrium position in a temperature interval up to 30°C above M_S.

Propriétés locales et ordre longue-distance dans $KTa_{1-x}Nb_xO_3$

S. Rod, J.J. van der Klink, A. Châtelain
Institut de Physique Expérimentale, EPFL, CH-1015 Lausanne

Nous présentons un ensemble de mesures NMR sur les atomes ^{39}K, ^{93}Nb et ^{181}Ta de cristaux perovskite $KTa_{1-x}Nb_xO_3$ faiblement dopés Nb. Ces mesures sont compatibles avec une transition displace se déroulant à basse température. Cependant les mesures sur ^{181}Ta montrent que la distorsion sur le réseau $KTaO_3$ n'est pas uniforme. En accord avec les propriétés globales de ces cristaux, ceci peut être expliqué par une transition collective dans le système Nb, engendrée par le mode mou du réseau hôte.

KOND VII : Structures cristallines - divers

MESURE DE LA RESOLUTION PONCTUELLE DU MICROSCOPE PHILIPS EM 430 ST PAR COMPARAISON D'IMAGES EXPERIMENTALES ET SIMULEES DE $Ti_2Nb_{10}O_{29}$

P. Stadelmann, Ph. Buffat, Ecole Polytechnique Fédérale de Lausanne, Microscopie Electronique I2M, CH-1015 Lausanne, Suisse

Résumé : La comparaison d'images simulées et expérimentales de $Ti_2Nb_{10}O_{29}$ permet d'évaluer la résolution ponctuelle des microscopes électroniques à haute résolution dans les conditions expérimentales et pour des objets habituellement rencontrés. Cette méthode d'évaluation, appliquée au cas du microscope Philips EM 430 équipé d'une lentille SuperTwin, a montré que le coefficient d'aberration de sphéricité de sa lentille objectif est proche de 1.1 mm. La résolution ponctuelle de ce microscope est ainsi meilleure que 0.2 nm.

1. Introduction

En optique conventionnelle la résolution d'un système optique est définie par le critère de Rayleigh en illumination incohérente ou par la fonction de transfert du système en illumination cohérente. En microscopie électronique à haute résolution l'illumination est partiellement cohérente et les coefficients de Fourier I(h) de l'image observée sont reliés à la fonction d'onde 0 produite par l'interaction des électrons et de l'objet par l'intermédiaire des coefficients croisés de transmission [1,2] :

$$I(h) = \sum_g T(h,h+g)\ O(h)\ O^*(h+g) \qquad (1)$$

Le système optique n'a pas un comportement linéaire et la définition de la résolution dépend de l'objet choisi. Un critère de résolution est cependant nécessaire pour l'interprétation des images expérimentales. Les films minces de carbone qui ont un comportement d'objet de phase faible du fait de leur faible interaction avec les électrons sont souvent choisis pour mesurer la résolution ponctuelle. Pour un objet de phase faible la relation (1) se simplifie car il n'est plus nécessaire de tenir compte de l'interaction mutuelle des ondes diffractées et une fonction de transfert dite fonction de transfert du contraste peut être définie. Cette fonction est le produit de la fonction de transfert en illumination cohérente C(h) et de 2 fonctions décrivant l'at-

ténuation due à la cohérence partielle spatiale et temporelle [3,4] . Elle est représentée sur la figure 1. La résolution ponctuelle est définie par h^{-1} tel que f(h) = 0. Les paramètres expérimentaux intervenant dans le calcul de f(h) sont le coefficient d'aberration de sphéricité C_s qui dépend de la position de l'objet dans la lentille objectif, la défocalisation Z, la divergence du faisceau incident (cohérence spatiale) et la distribution en énergie des électrons de la source (cohérence temporelle). Ces 2 dernières grandeurs sont mesurées de manière indépendante sur les figures de diffraction et par spectrométrie de perte d'énergie (EELS). Pour un objet d'amplitude et de phase (tous les cristaux non infiniment minces) la méthode d'évaluation consiste à comparer des images expérimentales et calculées de manière à en déduire C_s et Z et à définir la résolution en traçant la fonction de transfert du contraste. L'objet idéal doit être de structure connue et présenter des paramètres de maille dans le plan perpendiculaire à la direction d'observation de quelques nanomètres [5]. Le titanate de Niobium $Ti_2Nb_{10}O_{29}$ (a=0.38, b=2.85, c=2.05 nm, groupe d'espace Cmcm) satisfait à ces conditions et est généralement choisi comme objet de référence [6] .

2. Application

L'image 2 montre une image expérimentale de $Ti_2Nb_{10}O_{29}$ obtenue avec le microscope Philips EM 430 ST. La direction d'observation est [100] et des colonnes d'ions Nb/Ti distantes de 0.2 nm sont indiscutablement imagées comme 2 points séparés. Cependant cette séparation ne permet pas d'affirmer que la résolution ponctuelle, au sens défini plus haut, est meilleure que 0.2 nm puisque le critère de Rayleigh est inapplicable.

3. Simulation

La simulation des images de $Ti_2Nb_{10}O_{29}$ se fait en 2 étapes successives :

1) Calcul de la fonction d'onde complexe O(h) à la sortie du cristal, et
2) Calcul des coefficients de Fourier de l'image.

Le calcul de O(h) est effectué par la méthode "multislice" utilisant un algorithme FFT (Fast Fourier Transform). Le potentiel projeté d'une maille de titanate de Niobium est échantillonné suivant une grille de 256x256 points, l'épaisseur d'une couche de cristal est de a/2 (0.19 nm). Après 20 mailles

(7.6 nm) l'atténuation intrinsèque de la méthode "multislice" est inférieure à 0.9%. Les programmes utilisés font appel à un calculateur vectoriel AP 500 d'Analogic, couplé au PDP 11/34 de l'Institut. Une itération multislice qui comprend 4 FFT et 4 multiplications de matrices complexes à 256x256 éléments s'effectue en 4 secondes.

Les images simulées ont permis de déterminer l'épaisseur la plus probable du cristal de l'image 2 (entre 1.5 et 2.8 nm) et la valeur de la défocalisation affichée par le microscope (40 nm) a pu être vérifiée. L'image 3 calculée avec un C_s de 1.2 mm montre que l'image est stable pour des défocalisations comprises entre 30 nm (minimum du contraste) et 50 nm (défocalisation de Scherzer). Cette propriété du titanate de Niobium est très importante car il est difficile expérimentalement d'obtenir une défocalisation avec une précision meilleure que 7 nm. D'autre part, la stabilité des images en fonction de l'épaisseur du cristal est nécessaire à la comparaison images simulées - images expérimentales. Cette condition est ici également réalisée et observable sur l'image expérimentale (image 2). L'image 4 montre une série de simulations pour des valeurs de C_s comprises entre 1.05 et 1.20 mm, la valeur de la défocalisation est de 50 nm. On constate que l'augmentation de C_s s'accompagne d'une diminution de la résolution des images. Pour une valeur de C_s de 1.2 mm il n'est plus possible d'affirmer que les colonnes atomiques de Ti/Nb sont séparées. La valeur la plus probable de C_s déduite de la comparaison est proche de 1.1 mm, ce qui induit une résolution ponctuelle inférieure à 0.2 nm (point 3, figure 1).

4. Conclusion

La méthode proposée d'évaluation de la résolution ponctuelle du microscope Philips EM 430 ST permet d'affirmer que celle-ci est inférieure à 0.2 nm. Cette méthode utilise un objet de référence comparable aux cristaux étudiés et dans des conditions expérimentales équivalentes. Elle nécessite cependant le recours systématique à la simulation d'images.

5. Références

[1] M. Born, E. Wolf, Principles of Optics, Pergamon Press N.Y., (1959).

[2] K. Ishizuka, Ultramicroscopy 5, 55, (1980).

[3] J. Frank, Optik 43, 25, (1974.

[4] J. Frank, Optik 44, 379, (1976).

[5] J.C.H. Spence, Experimental High-resolution Electron Microscopy, Clarendon Press Oxford, (1980).

[6] D.J. Smith, Ultramicroscopy 11, 263, (1983).

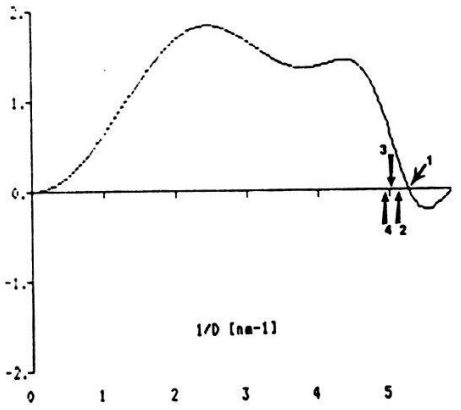

Fig. 1 : Fonction de transfert C_s=1.1mm (1), 1.15 (2), 1.2 (3), 1.3 (4); tension 300 kV

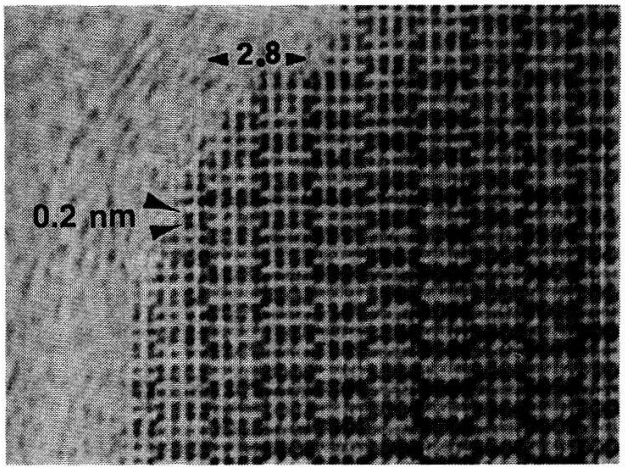

Image 2 : Image expérimentale de $Ti_2Nb_{10}O_{29}$, direction [100], tension 300 kV

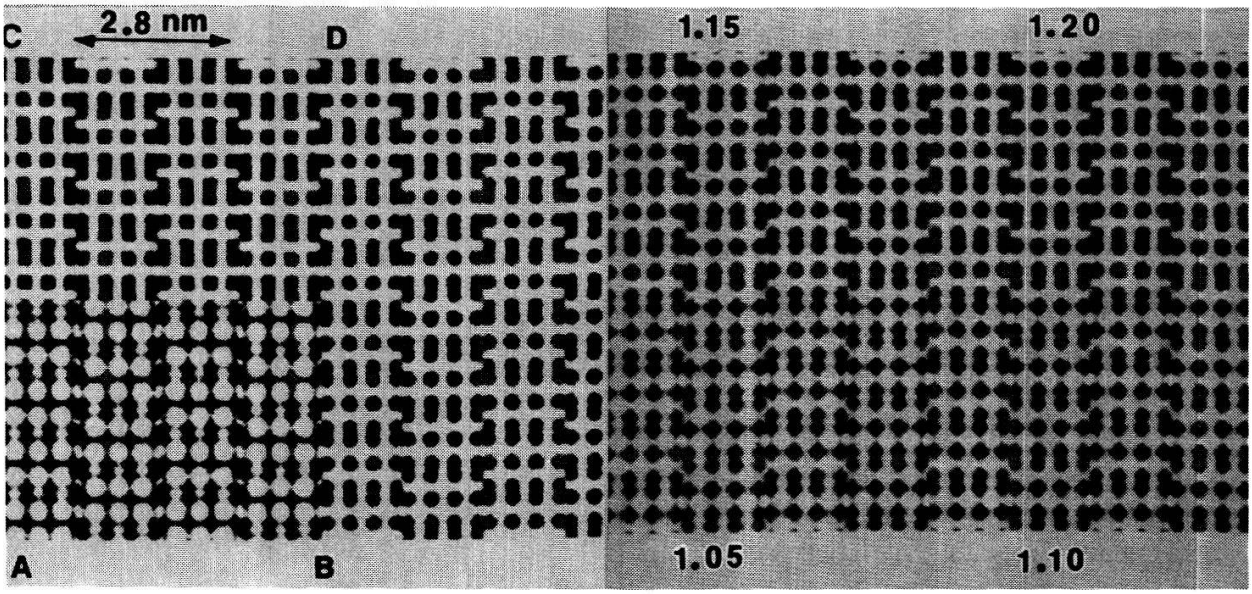

Image 3 : Image simulée de $Ti_2Nb_{10}O_{29}$, défocalisation A:60 nm, B:50, C:40, D:30.

Image 4 : Image simulée de $Ti_2Nb_{10}O_{29}$, défocalisation 50 nm, C_s=1.05mm, 1.10, 1.15, 1.20.

Spezifische Wärme von ikosaedrischem $Al_{0.8}Mn_{0.2}$ bei tiefen Temperaturen

H. Rudigier und H.R. Ott
Laboratorium für Festkörperphysik, ETH-Hönggerberg, 8093 Zürich

Wir berichten über den Versuch, die spezifische Wärme von ikosaedrischem $Al_{0.8}Mn_{0.2}$ bei tiefen Temperaturen (0.7-8.5 K) zu messen. Die Proben bestehen aus dünnen Folien (25 μm) geringer Masse (6 mg), welche zu 90% aus kristalloidem Material bestehen. Der Rest ist gemäss elektronenmikroskopischer Untersuchungen kristallines Al. Wir diskutieren zuerst die Probleme, welche sich bei Experimenten dieser Art und deren Auswertung ergeben. Die Resultate zeigen, dass im untersuchten Temperaturbereich die für Metalle übliche Temperaturabhängigkeit der spezifischen Wärme $c_p = \gamma T + \beta T^3$ mit temperaturunabhängigen Parametern γ(elektronischer Beitrag) und β(Gitterbeitrag) nicht erfüllt ist. Bei Temperaturen unterhalb 5 K steigt das Verhältnis c_p/T mit sinkender Temperatur an. Mögliche Ursachen dieses Verhaltens werden diskutiert.

Etude de la microstructure des craquelures par la diffusion des rayons X aux petits angles

A. Sbaï, M. Dettenmaier, H.H. Kausch
EPFL, Laboratoire de polymères, 32, chemin de Bellerive, 1007 Lausanne

La structure fibrillaire des craquelures se prête à la technique de la diffusion des rayons X aux petits angles (SAXS) généralement utilisée pour un sytème à deux phases.
La simulation de cette diffusion, selon un modèle de "cylindres durs" a permis une bonne estimation du diamètre des fibrilles par la loi de Bragg.
Le rôle d'autres paramètres comme la fraction volumique et la distribution de taille des fibrilles a été élucidé.

Porenabschluss beim isothermen Sintern

B. Stauffer und J. Schwander, Physik. Institut der Universität Bern, Sidlerstrasse 5, 3012 Bern

In sehr kalten Gebieten entsteht Eis durch isothermes Sintern von trockenem Schnee und Firn. Der Sinterprozess erfolgt sehr langsam, in gewissen Gebieten dauert es über tausend Jahre, bis Sinterstadium 3 (geschlossene Poren) erreicht wird. Wir haben die Entwicklung des Porenvolumens in der Uebergangszone Firn zu Eis untersucht und vergleichen die Resultate mit einem einfachen statistischen Modell.

POSTERS

CARACTERISTIQUES ELECTRIQUES ET LOIS D'ECHELLE DANS DES ENSEMBLES TRIDIMENSIONNELS DE JONCTIONS JOSEPHSON

C. Lebeau, P. Peyral, A. Raboutou, J. Rosenblatt.
I.N.S.A.,Laboratoire de Physique des Solides, UA 786 - F 35043 RENNES CEDEX

Abstract : Un ensemble de jonctions josephson constitué par des grains supraconducteurs liés par des contacts ponctuels présente une transition vers la cohérence de phase à une température T_c inférieure à la température de transition supraconductrice T_{cG} des grains. La mesure des caractéristiques $V(I_S)$ (tension-supercourant) dans la région paracohérente ($T_c < T < T_{cG}$) montre que $V \sim I_S^{a(T)}$ avec $a(T_c) = 2.1 \pm 0.2$. En tenant compte des lois d'échelle et d'hyperéchelle satisfaites par les exposants critiques décrivant la transition vers la cohérence et du caractère de paramètre pertinent du supercourant, nous montrons que $a = 4/2+\eta$. Cette relation conduit à la valeur -0.1 ± 0.2 pour l'exposant η de la fonction de corrélation.

1. Echantillons

Les échantillons étudiés sont des systèmes tridimensionnels comportant environ 10^8 jonctions josephson par cm^3. Ils sont constitués par des grains de tantale légèrement oxydés de diamètre compris entre 10 µm et 50 µm et noyés dans une résine époxy. L'ensemble grains-résine est comprimé dans des moules cylindriques jusqu'à obtention d'une résistivité de l'ordre de 0.1 à 1Ω.cm [1]. Après polymérisation de la résine et démoulage,des contacts électriques sont effectués pour faire des mesures à 4 points.

2. Méthode de mesure

Les échantillons sont caractérisés par leur transition résistive. Le tracé de la résistance dynamique $R_D(T)$ en fonction de la température permet la détermination de la température de transition T_c à la cohérence des échantillons [2]. Les caractéristiques V(I) (tension aux bornes de l'échantillon-courant à travers celui-ci) sont tracées à différentes températures. A partir de V(I) nous obtenons les courbes $V(I_S)$ où $I_S = I - V/R_N - I_c$, I_c étant le courant critique des échantillons, R_N la résistance des échantillons à $T > T_{cG}$ (T_{cG} : température de transition supraconductrice des grains). Un exemple de ces courbes est indiqué figure 1. Pour les valeurs suffisamment faibles de V,

les points se placent sur une droite. Pour $T < T_c$, le courant I_c est choisi de façon à accroître la linéarité aux faibles valeurs de V. La valeur de I_c ainsi obtenue concorde avec celle déduite directement de la caractéristique V(I). Ces résultats montrent que les courbes $V(I_S)$ sont décrites par une loi $V \sim I_S^{a(T)}$.

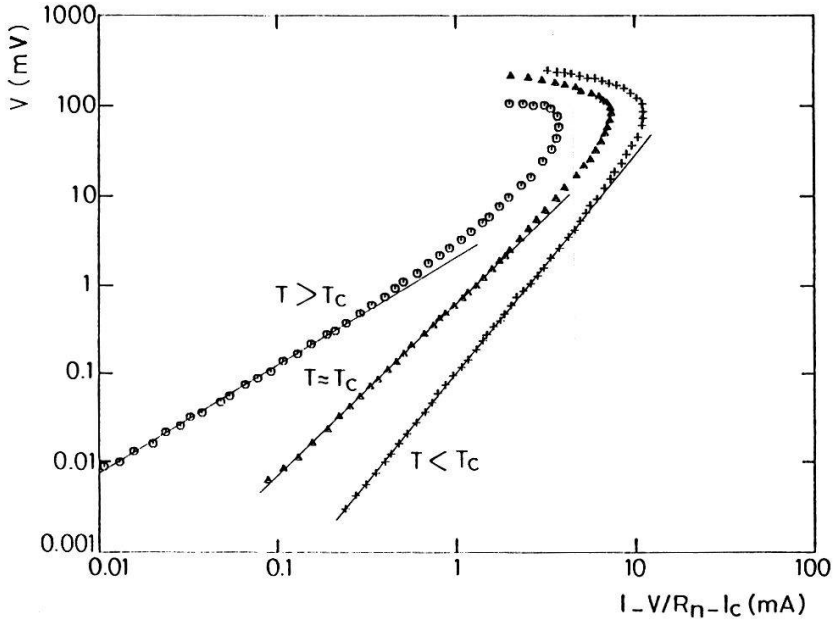

Figure 1 : Caractéristiques expérimentales $V(I_S)$ aux températures 3.072 K, 2.713 K et 2.233 K d'un échantillon de tantale (R_N = 5.05 Ω, T_c = 2.69 K). Les valeurs de a(T) sont 1.22, 1.94 et 2.5.

3. Interprétation

Il a déjà été montré [1] que l'hamiltonien décrivant le couplage entre grains supraconducteurs de taille supérieure à la longueur de corrélation supraconductrice est semblable à celui du modèle X-Y du ferromagnétisme [3] $H = -\sum_{<ij>} J_{ij} S_i^+ S_j^- - 2\mu_o \sum_i S_{3i}$ où $J_{ij} = (R_o/R_{ij})\Delta(T) \tanh(\Delta(T)/2k_BT)$ est l'énergie de couplage entre les grains i et j ayant une résistance de jonction R_{ij} et $R_o = \pi\hbar/4e^2 = 3250\ \Omega$; S_{3i} est l'opérateur nombre de paires, S_i^+ et S_j^- sont les opérateurs annihilation et création, μ_o le potentiel chimique. Cette similitude avec le modèle X-Y a permis de montrer que la conductivité supplémentaire σ_S dans la région paracohérente $T > T_c$ se comporte comme la susceptibilité d'un ferromagnétique caractérisée par l'exposant critique γ :

$$\sigma_S \sim \chi \sim \tau^{-\gamma} \quad \text{avec} \quad \tau = |T - T_c| / T_c \text{ [4].}$$

L'existence expérimentale d'un courant critique laisse supposer que le courant est un paramètre pertinent de la transition de second ordre. Dans ces conditions, la conductivité supplémentaire due au supercourant I_S satisfait une loi d'homogénéité [5] :

$$\sigma_S = \tau^{-\gamma} f \pm (I_S/\tau^{\phi})$$

où f+ et f- se rapportent à $T > T_c$ et $T < T_c$. Ces deux fonctions peuvent différer avec T, avec les échantillons, mais l'exposant γ et l'exposant ϕ de cross-over doivent être universels. On peut en déduire [6] que la tension V est reliée au spercourant I_S à T_c par la relation $V \simeq I_S^a = I_S^{(\gamma+\phi)/\phi}$. En utilisant les lois d'échelle l'exposant a de I_S s'écrit $a = (d + 1)/ (d - 1 + \eta)$. Dans les transitions de phase de second ordre et dans un système 3D l'exposant associé à la fonction de corrélation du paramètre d'ordre est petit. Il en résulte que $a = a(T_c) \simeq 2$.

Nous avons déterminer l'exposant a à différentes températures (figure 2) et pour différents échantillons dont les caractéristiques sont donnéesdans le tableau I.

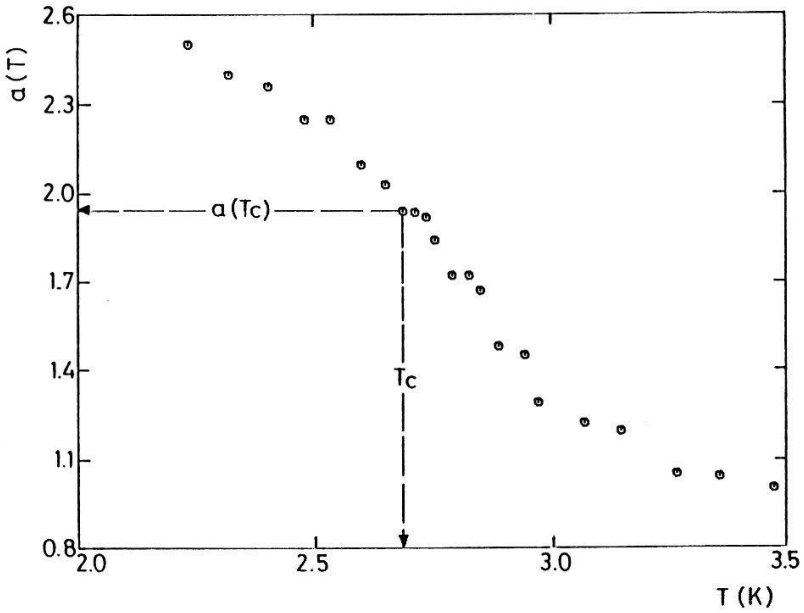

Figure 2 : Variation de l'exposant a(T) avec la température pour l'échantillon décrit figure 1.

R_N (Ω)	T_c (K)	a (T_c)
3.7	2.85	2
5.05	2.69	1.95
10.5	2.46	2.2

Tableau 1 : Valeurs expérimentales de l'exposant a(T_c) pour différents échantillons de tantale.

La température critique T_c est obtenue en cherchant l'exposant qui décrit σ_s en l'absence de courant [4]. L'ensemble des valeurs a(T_c) obtenues conduit à une valeur moyenne a(T_c) $\simeq$ 2.1 $\pm$ 0.2. En tenant compte de la relation liant a et η on en déduit η = - 0.1 $\pm$ 0.2.

4. Références

[1] J. Rosenblatt, A. Raboutou et P. Pellan, Proceedings of LT14, édité par M. Krusius et M. Vuorio, Vol. 2 (North Holland, Amsterdam, 1975) p. 361.

[2] P. Pellan, G. Dousselin, H. Cortès et J. Rosenblatt, Solid State Commun., 11, 427 (1972).

[3] D.D. Betts : Phase Transitions and Critical Phenomena, édité par C. Domb et M.S. Green (Academic Press, New York, 1974).

[4] J.Rosenblatt, P. Peyral et A. Raboutou, Phys. Lett., 98, 463 (1983).

[5] G.Toulouse et P. Pfeuty : Introduction au groupe de renormalisation et à ses applications (Presses Universitaires de Grenoble, 1975).

[6] J. Rosenblatt, C. Lebeau, P. Peyral et A. Raboutou. Institute for Scientific interchange workshop on the josephson effects-achievements and trends. Turin, Sept. 85.

PHENOMENES DE LOCALISATION FAIBLE DANS DES COUCHES MINCES DE NITRURE DE NIOBIUM

G. Dousselin, J.P. Durand, J. Pinel et J. Rosenblatt,
Laboratoire de Physique des Solides, UA 786, F-35043 RENNES CEDEX

Résumé : Des films minces de NbN, qui présentent des températures de transition supraconductrices T_c entre 16 K et 5 K, suivent, sur un large intervalle de température ($\gtrsim T_c - 100$ K), une loi caractéristique d'un régime de localisation faible à 3 dimensions.

1. INTRODUCTION

Le NbN, particulièrement en couche mince, a fait l'objet de nombreuses études (cf par exemple : [1]), du au fait, notamment, qu'il possède dans sa phase δ une température de transition supraconductrice T_c élevée ($\simeq$ 17 K). Par pulvérisation magnétron rf dans une atmosphère Ar-N_2, nous avons fabriqué une série de films, en faisant varier le taux d'azote dans la chambre de pulvérisation. Des films qui présentent des valeurs de T_c différentes, sur une large étendue, ont ainsi pu être réalisés. Les films dont les épaisseurs sont comprises entre 160 nm et 560 nm, sont déposés sur substrats de verre chauffés à 400° C. Nous nous sommes intéressés au mécanisme de conduction en mesurant la résistivité électrique entre 100 K et T_c.

2. RESULTATS

Les spectres de diffraction X ont mis en évidence les deux pics (111) et (200), caractéristiques de la phase cubique : δ - NbN. La taille d des grains cristallisés diminue, de 50 nm à 6 nm, corrélativement avec une dilatation du paramètre de maille a (fig. 1). En outre, l'orientation, qui est très nettement du type (111) pour les films à gros grains ($d > 20$ nm) se répartit de façon plus équilibrée entre (111) et (200) pour les films à petits grains ($d < 10$ nm). Ces comportements correspondent à une augmentation probable du nombre de défauts dans les films aux plus fortes valeurs de a.

Les T_c sont obtenues à partir du point milieu des transitions résistives, dont les largeurs sont comprises entre 0,1 K et 0,3 K. L'évolution de T_c avec le paramètre de maille a (figure 1) montre que la supraconductivité

est étroitement liée à la structure des grains δ - NbN. Dans le cas d'un système ordonné pour lequel la densité d'états électroniques et le spectre de phonons sont bien définis, la T_c dépend fortement de la constante de couplage électron-phonon λ ; les valeurs élevées de λ, et donc de T_c, se situant près de la stoéchiométrie [2]. La diminution observée de T_c lorsque a augmente correspond probablement à une diminution de λ liée aux modifications du spectre de phonons lorsque le degré de désordre augmente.

La résistivité à basse température ρ(20) est une indication du taux de défauts locaux. La figure 2 montre que ρ(20) augmente avec d^{-1}, entre environ 200 μΩcm et une valeur, $\hbar d/e^2$, qui représente une estimation de la résistivité métallique maximum [3], et où on s'attend à l'apparition des effets de localisation. Tous les films ont un coefficient de résistance en température négatif ; le rapport r = ρ(300)/ρ(20), des résistivités à températures ambiante et basse, varie de 0,96 à 0,22 lorsque la taille des grains diminue (figure 2). En outre, des films avec des tailles de grains comparables, présentent des valeurs de ρ(20) et de r nettement différentes ; les films ayant des valeurs plus élevées de ρ_{20}, ou plus basses de r, ont systématiquement des valeurs de T_c plus basses.

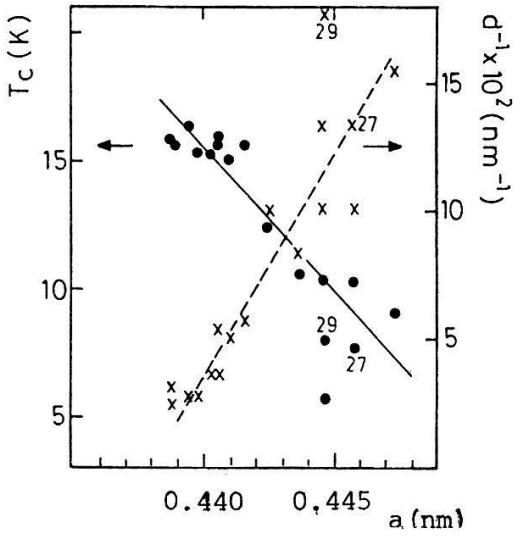

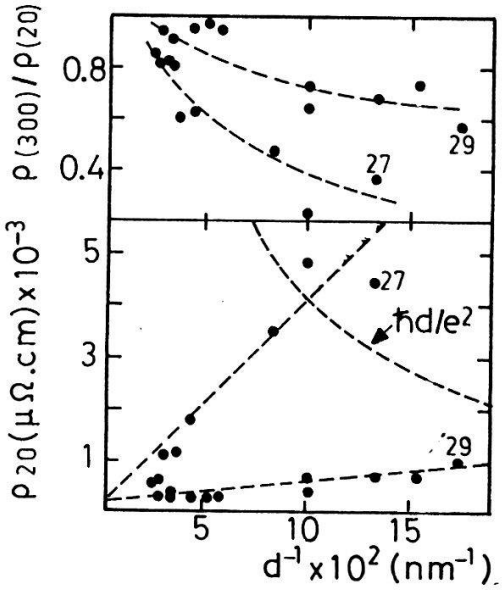

Fig. 1 : Variation de la température critique T_c et de l'inverse de la taille des grains d^{-1} en fonction du paramètre de maille a.

Fig. 2 : Variation du rapport de résistivité r = ρ(300)/ρ(20) et de la résistivité ρ(20) en fonction de l'inverse de la taille des grains.

Les valeurs des résistivités $\rho(T)$ mesurées entre 100 K et un peu au-dessus de T_c, ont été testées avec des lois du type : $\rho(T) \propto \exp(T_o/T)^n$ qui correspondent à une conduction : pour n = 1, par saut activé entre plus proches voisins [3] ; pour n = 1/2, par transfert activé de charges entre grains de capacité finie [4] ; pour n = 1/4, par saut à portée variable [5]. La figure 3, donnée pour un échantillon typique, montre que l'accord est mauvais ; il fournit en particulier, des valeurs non physiques pour T_o : par exemple pour n = 1/2, $T_o \simeq 10$ K, alors qu'il est attendu environ 10^3 K.

Par contre, l'expression : $\rho^{-1} - \rho_o^{-1} \propto T^q$, résultant d'un phénomène de localisation faible à 3 dimensions [6], donne un bon accord. Les échantillons représentatifs (figure 4) ont des valeurs de $\rho(20)$ très différentes, mais proches de $\hbar d/e^2$, et des T_c voisines. Le terme fini ρ_o, dont la valeur est voisine de $\rho(20)$, indique que les films de NbN sont proches de la transition isolant-métal, côté métallique. L'exposant q, lié aux collisions inélastiques, est dans la gamme des valeurs attendues.

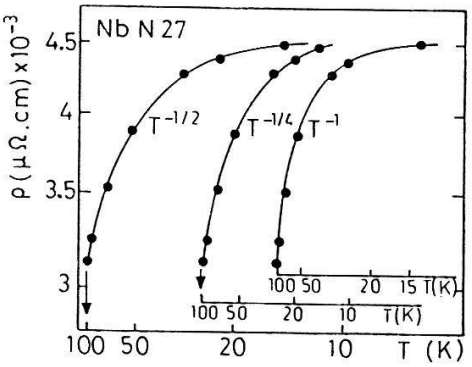

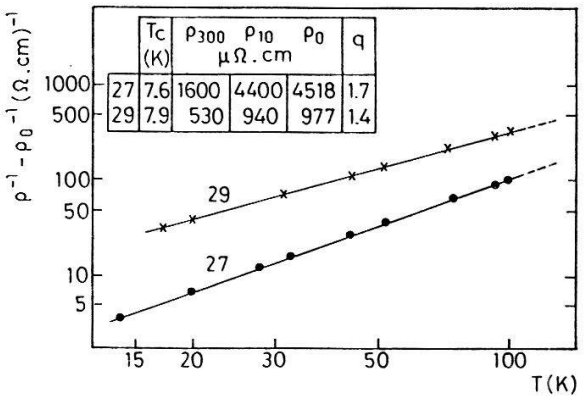

Fig.3 : Lois du type $\rho(T) \propto \exp(T_o/T)^n$ pour n = 1 ; n = 1/2 ; n = 1/4.

Fig.4 : Loi du type $\rho^{-1}(T) - \rho_o^{-1} \propto T^q$

3. REFERENCES

[1] J.C. VILLEGIER, L. VIEUX-ROCHAZ, M. GONICHE, P. RENARD and M. VABRE, I.E.E.E. Trans. Mag. 21 (1985).

[2] I.R. GOMERSALL and B.L. GYORFFLY, J. Phys. F : Metal Phys. 3, 138 (1973).

[3] N.F. MOTT and A. DAVIS in : Electronic Process in Non Crystalline Materials, Clarenton Press, Oxford (1979).

[4] B. ABELES, P. SHENG, M.D. COUTTS and Y. ARIES, Advances in Physics, 24, 407 (1975).

[5] N.F. MOTT, Rev. Mod Phys., 50, 203 (1978).

[6] Y. IMRY in : Percolation, Localization and Superconductivity Edited by A.M. GOLDMAN and S.A. WOLF, Nato ASI Series B, Vol. 109, 189 ; Plenum Press New-York and London (1984).

Pouvoir thermoélectrique et résistivité du cérium

Ch. Fierz, P. Donzé et J. Sierro

DPMC, Section de Physique, 24, Quai Ernest-Ansermet, 1211 Genève 4

Nous avons mesuré entre 1.5 K et 300 K le pouvoir thermoélectrique (PTE) et la résistivité du cérium-α sous pression hydrostatique ($0 \leq P \leq 16.5$ kbar) et du cérium-β sous pression normale.
Le PTE du cérium-β montre un comportement typique de composés de cérium presque trivalents, e.g. $CeAl_2$: un pic négatif de $-4.5\mu VK^{-1}$ à 10 K suivi d'un pic positif de $13\mu VK^{-1}$ à 80 K. Le PTE du cérium-α quant à lui est caractérisé par un pic positif à 50 K, indépendamment de la pression. Dans la phase α, la qualité de notre échantillon se reflète dans un rapport de résistivité résiduelle de plus de 200.

Optical Properties of Cr^{3+} in Elpasolite Lattices

R. Knochenmuss, C. Reber, H.U. Güdel
Institut für Anorg. und Physik. Chemie, Universität Bern, Freiestr. 3
3000 Bern 9

Cr^{3+} doped into the lattices Cs_2NaYCl_6, $Cs_2NaInCl_6$ and Cs_2NaYBr_6 exhibits broad-band luminescence in the near IR, corresponding to the $^4T_{2g} \rightarrow {}^4A_{2g}$ transition. Excited state geometries are derived from the rich fine structure. Lifetime data yield information about radiative and non-radiative deactivation mechanisms.

PHYSIQUE APPLIQUEE

ANDO I : Semiconducteurs, couches minces, microtechnique

LASER CHEMICAL VAPOUR DEPOSITION of Ga and GaAs

D. Braichotte and H. van den Bergh, Laboratoire de Chimie Technique, Ecole Polytechnique Fédérale de Lausanne, CH-1015 Lausanne, Switzerland

Laser chemical vapour deposition (LCVD) is a new technique to "write" microscopic patterns on semiconductor surfaces. Multiple applications in microelectronic include the writing of ohmic contacts about 1 micrometer wide [1]. These may be useful in circuit repair [1] ,in the contacting of gate arrays [1] ,or in the design of new circuits. Metal deposition also appears useful for the repair of lithographic masks [1] . LCVD can also be used for the deposition of composite materials (see below for instance),for localised surface reactions [2] and doping [1] . Furthermore laser induced microchemistry also includes surface etching. One of the main advantages of LCVD is that it is a one step process which contrasts it with the more classical multistep lithographic processes. Studies of metal deposition have revealed some aspects of the LCVD mechanism [3,4] . Deposition can be pyrolytic (the metal-organic (MO) vapour strikes the laser heated surface,decomposing to leave a metal film behind), photolytic (the MO vapour is phtolysed either in the gas phase or in the adlayer), or hybrid (photolysis is enhanced by some thermal effects [5]). In the present paper we describe several experiments on the pyrolytic and photolytic LCVD of Ga and GaAs, as well as hybrid deposition of the latter. The experimental setup has been described previously [2,4-6] .

I) Pyrolytic deposition of Ga

Figures 1a,b show the transmission electron micrographs which demonstrate how the Ga deposit changes in shape with the variation in laser power. This change in shape appears to be typical for low melting metal such as Ga and Sn and is not found in Pt LCVD at the applied conditions. This change in shape may have implications for the fast deposition of thin metallic conductors on semiconductor surfaces. At low laser power densities no deposit is observed at all. In Fig. 1a we observe a central spot with a diameter of about 7 micrometers. This spot is surrounded by a zone with no deposit. Further away from the center of the spot, small debris are observed. In

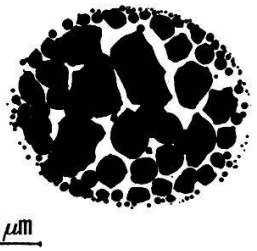

Fig. 1a: Transmission electron microscope (TEM) picture of pyrolytic deposited Ga. The pressure of trimethylgallium is 10 torr, the exposure time is 10 s, the power density is 3 kW cm^{-2}. The wavelenght is 514.5 nm.

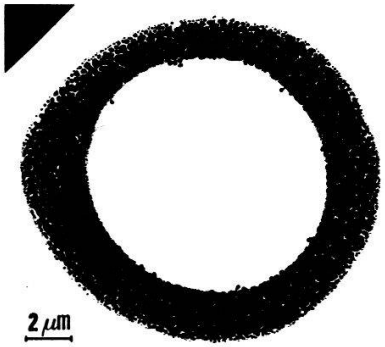

Fig. 1b: TEM picture of pyrolytic deposited Ga. The trimethylgallium pressure is again 10 torr and the exposure time 10 s. The power is higher than in Fig. 1a, it is now 7.5 kW cm^{-2}. The wavelenght is 514.5 nm. The high temperature in the central part of the deposit prevent the metal from sticking there.

Fig. 1b, at somewhat higher laser power density, we observe a metal deposit in the shape of an annulus of about 14 microns outside diameter. The higher laser power density implies a higher surface temperature. The absence of a metal deposit in the center is probably due to the fact that the temperature is so high that the deposited metal atoms don't stick to the surface. We have studied this change in shape of the Ga deposit with changing power density, keeping all parameters constant. Defining θ as the outside diameter of the annulus, and δ as its width (outer radius - inner radius), these results are shown in Fig. 2. Fig. 3 shows the scanning electron micrograph of such an annular Ga deposit on amorphous carbon by pyro-deposition. The deposit is that of Fig. 1b. As could already be seen from the TEM picture the deposit is quite irregular, and consists mainly of quite large particles. The electron diffraction pattern shows that these deposits are amorphous, however this absence of a diffraction pattern may be due to the heating of the Ga sample with the analysing electron beam above its freezing point of 301 ^{o}K.

The annulus we observe at intermediate power densities (at very high power densities no metal is deposited at all) is also found in the pyrodeposition of Sn, but not in the pyrodeposition of Pt. Platinum clusters are much more stable at high temperature than both Ga and Sn as is born out by boiling and melting points of these three metals.

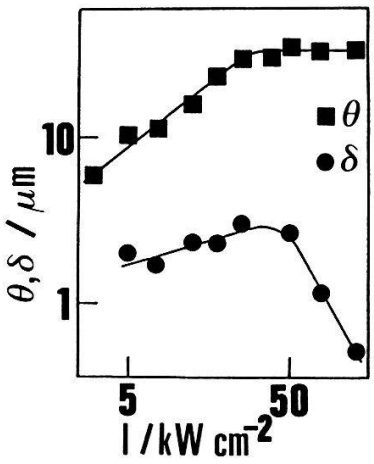

Fig. 2: Variation of the shape of the Ga deposit formed in pyrolytic LCVD with the power density of the laser beam at the focal point. At very low power densities and very high power densities no deposit is formed at all. With increasing power density the diameter (θ) of the deposit increases and its width (δ) and thickness decrease.

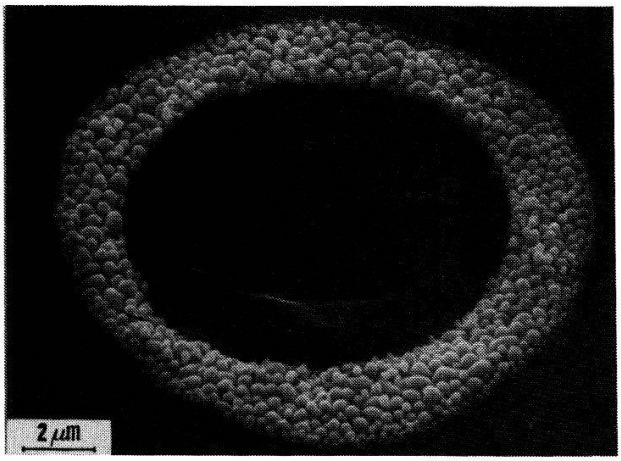

Fig. 3: Scanning electron microscope (SEM) picture of an annular Ga deposit formed in pyrolytic LCVD. The experimental conditions are the same as Fig.1b. The deposit is quite irregular and consists mainly of quite large and amorphous particles.

II) Photolytic deposition of Ga

Fig. 4a shows the deposited metal film obtained upon irradiation of trimethylgallium near the carbon surface with light at 257.2 nm. The metallic halo around the center of the deposit is again observed. This halo could be due to metal particles being formed in the gas phase and diffusing to the surface outside to the area struck by the laser light. The structure of the metal deposited in the center part of the pattern is shown in Fig. 4b to consist of small spheroids with a diameter between about 10 and 20 nm. Again the deposited metal appears amorphous, as was the case for the photolytic LCVD of Sn and Pt. The deposited structure appears more homogeneous overall than in the case of pyro-LCVD.

III) LCVD of GaAs

Both pyrolytic and photolytic LCVD of GaAs from a mixture of $Ga(CH_3)_3$ and $As(CH_3)_3$ was not successful. In pyrolytic LCVD at least part of the

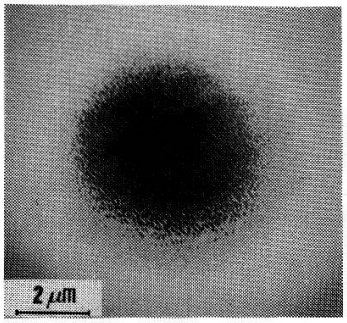

Fig. 4a: TEM picture of photodeposited Ga. The experimental conditions are: trimethylgallium pressure is 10 torr, the wavelength is 257.2 nm, exposure time is 60 s, the power density is 500 W cm^{-2}. This deposit is significantly more homogeneous than the pyrolytically deposited Ga of Fig. 1a.

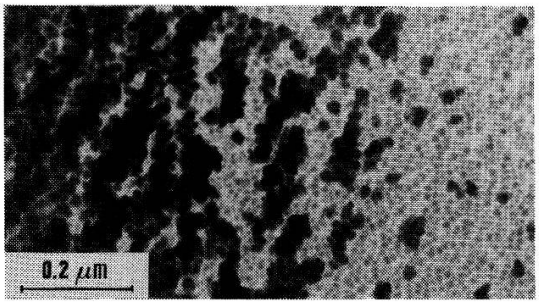

Fig. 4b: This TEM picture is an enlargement of a section at the fringe of Fig. 4a showing the microscopic structure of the deposited Ga. The particles are quite spherical, have a diameter between 10 and 20 nm and are amorphous.

deposit tended to evaporate quickly again from the surface. However LCVD using the small amont of green light (514.5 nm) coming through the Glan-Thompson prism together with the frequency doubled light (257 nm), a reasonable deposit of GaAs was obtained by the hybrid method. In future experiments we will try to start with the $Ga(CH_3)_3.As(CH_3)_3$ adduct, which may give better results.

Acknowledgment

The authors are grateful to the Swiss Fonds National for financial support.

References

1. Laser Processing and Diagnostics, D. Bäuerle Ed., Springer Series in Chem. Phys. 39 (Springer, Berlin 1984), and references therein.
2. D. Braichotte, K. Ernst, R. Monot, J.-M. Philippoz, M. Qiu and H. van den Bergh, Helv. Phys. Acta 58 (1985) 879.
3. R.M. Osgood, Ann. Rev. Phys. Chem. 34 (1983) 77.
4. D. Braichotte and H. van den Bergh, Integrated Optics, Springer Series in Optical Sciences 48, H.P. Nolting and R. Ulrich Eds., (Springer, Berlin 1985).
5. D. Braichotte and H, van den Bergh, SOQC Proc. Laser '85 in press.
6. M. Qiu, R. Monot and H. van den Bergh, Scientia Sinica A 27 (1984) 531.

DEVELOPMENT OF MOM-DIODES

I. Gienal, W. Herrmann and F.K. Kneubühl
Institute of Quantum Electronics, Physics Department, ETH
CH-8093 Zurich, Switzerland

In its simplest form a metal-oxide-metal diode consists of two conductive metal electrodes separated by a thin insulating oxide layer. There exist two groups of MOM-diodes, one includes point-contact arrangements, the other comprehends planar structures. MOM-diodes serve as radiation detectors or harmonic mixers from far-infrared to optical wavelengths.

Hitherto, most of the experimental work was performed on point-contact diodes because of their easy fabrication and good performance. One advantage of this configuration is the small contact area of $\approx 10^{-2}$ μm^2 with a low capacitance of $\approx 10^{-2}$ pF and a spreading resistance of only a few ohms. This allows to achieve RC-time constants of the order of 10^{-13} s [1]. The severe disadvantages are the poor mechanical stability of the arrangement and the impossibility to fabricate diodes with reproducible characteristics, e.g. oxide thickness or contact area.

These disadvantages have been overcome by a planar arrangement of the metal strips using standard photolithographic and evaporating techniques. These planar diodes have been realized by overlapping two metal strips which are separated by a specific deposited oxide layer [2,3,4]. In these devices the width of the metal strips has a lower limit of 1 μm which is imposed by the photolithographic technique. This restriction implies a contact area 100 times larger than that of the point-contact configuration. The consequences are larger capacitance and resistance. Various experiments with planar MOM-diodes [2,3,4,5] as well as theoretical considerations [6] demonstrate that the contact area has to be lowered to increase the performance of the planar diodes.

Smaller contact areas can be achieved by reducing the width of the metal strips. For this reason we have started a project to develop MOM-diodes with the aid of e-beam lithography which allows to fabricate submicron structures. Our first experiments make use of a chromium mask produced by e-beam lithography at the "Centre Suisse d'Electronique et de Microtechnique SA" (CSEM), Neuchâtel, and with minimum dimensions of 0.4 μm. With this mask we attempt to fabricate thin-film MOM-diodes with contact areas of the order of 0.2 μm^2. First, a 3000 Å Ti film is put on a silicon waver with a SiO_2 layer by vapor deposition. Subsequently, a positive photoresist is spin-coated on the metal film and illuminated through the mask produced by e-beam lithography. After development the photoresist is covered by a 2000 Å Al layer by vapor deposition. The unexposed part of the resist is now lifted off together with its Al layer by application of acetone. The remaining Al layer now represents a negative replica of the mask and serves for the plasma etching of the Ti. After optimization of various processing parameters we have succeeded in producing structures with a width between 0.4 and 0.5 μm. Fig. 1 shows pictures of a contact strip taken by a scanning electron microscope. Cleary visible is the Al layer on top which acted as etching mask.

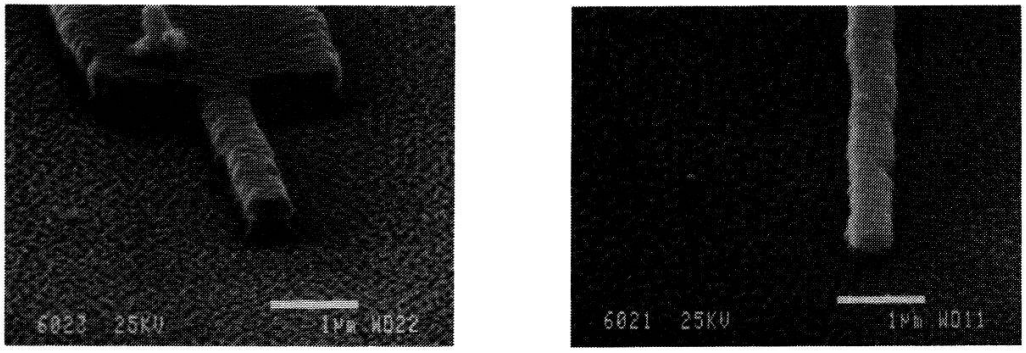

Fig. 1 SEM pictures of a contact strip. Its width is 0.5 μm.

Fig. 2 shows a schematic of the MOM-diode under development. The antenna consists of a long Al strip with a width of about 2.5 μm.

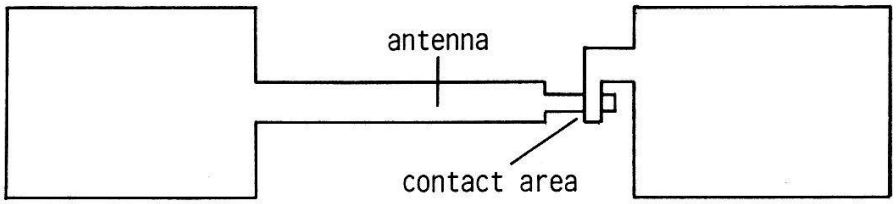

Fig. 2 Schematic of future planar MOM-diode (not scaled)

References

[1] M. Heiblum et al., IEEE J. Quantum Electron., QE-14, 159 (1978)
[2] J.G. Small et al., Appl. Phys. Lett. 24, 275 (1974)
[3] T.K. Gustafson et al., Appl. Phys. Lett. 24, 620 (1974)
[4] G.M. Elchinger et al., J. Appl. Phys. 47, 591 (1976)
[5] E. Wiesendanger and F. Kneubühl, Appl. Phys. 13, 343 (1976)
[6] S.I. Green, J. Appl. Phys. 42, 1166 (1971)

EPITAKTISCHES WACHSTUM VON CdTe AUF Si MITTELS IIa-FLUORID ZWISCHENSCHICHT

H. Zogg, H. Melchior, Fachgruppe für Mikro- und Optoelektronik und AFIF,
ETH Hönggerberg, 8093 Zürich

Zusammenfassung: CdTe wurde mit Aufdampftechniken (MBE) auf Si(111) abgeschieden. Epitaxie wurde trotz der grossen Gitterfehlpassung (19%) dank einer graduierten CaF_2-BaF_2 Zwischenschicht erreicht. Typische Substratemperaturen für erfolgreiches Wachstum mit spiegelnden Schichtoberflächen liegen um 300 ^{o}C. Es wird über strukturelle Eigenschaften dieser ersten Schichten berichtet.
- Mit CdTe auf Si Kombinationen können in integrierten Schaltungen die Vorteile von Silizium mit den optoelektronischen Anwendungsmöglichkeiten von CdTe monolithisch verknüpft werden, wobei auf dem CdTe für IR-Anwendungen im $\sim$1-20 µm Bereich HgCdTe mit variabler Bandlücke weiter aufgewachsen werden kann.

Das epitaktische Wachstum von CdTe auf Fremdsubstraten ist für die Mikro- und Optoelektronik von grossem Interesse, da hochqualitatives massives CdTe als Substratmaterial nur in unbefriedigender Qualität verfügbar und extrem teuer ist. Weiter dient CdTe üblicherweise als Pufferschicht zum Weiterwachsen von HgCdTe, welches als Schmalbandhalbleiter mit variabler Bandlücke für Infrarot-Sensoren Anwendung findet. Bereits wurden Saphir [1], InSb [2] sowie GaAs [3] als Fremdsubstrate für CdTe Epitaxie erfolgreich benützt und in darauf weiter aufgewachsenem HgCdTe IR-Sensoren fabriziert.

Könnte Si als Substrat verwendet werden, ergäbe sich nebst günstigeren Substratkosten auch die Möglichkeit, in monolithischen Bauteilen sowohl IR-Sensoren im HgCdTe als auch die Signalverarbeitung als integrierte Schaltung im Si zu realisieren. Insbesondere für grosse Sensorenarrays in Wärmebildkameras würden dadurch beträchtliche Vereinfachungen resultieren.

Für die Blei-Chalkogenid Schmalbandhalbleiter PbSe, PbSnSe und PbTe haben wir in vorhergehenden Arbeiten gezeigt [4-6], dass diese mittels einer CaF_2-BaF_2 Pufferschicht epitaktisch auf Si aufgewachsen werden können. Erste empfindliche IR-Sensoren mit Grenzwellenlängen bis oberhalb 9 µm wurden in solchen PbSnSe-$(Ba,Ca)F_2$-Si Heterostrukturen bereits realisiert [7].

In der vorliegenden Arbeit haben wir dieselben Fluoridschichten verwendet,

um epitaktisches CdTe auf Si abzuscheiden. Die grosse Gitterfehlpassung zwischen den beiden Materialien von fast 20% wird dabei zu etwa 3/4 von der graduierten $(Ca,Ba)F_2$ Zwischenschicht aufgenommen (Gitterkonstanten: Si 0.543 nm, CaF_2 0.546 nm, BaF_2 0.620nm, CdTe 0.648 nm).

Dazu wurden ca. 5 nm CaF_2 (bei 700°C Probentemperatur), gefolgt von ca. 200 nm BaF_2 mit Molekularstrahl-Epitaxie (MBE) auf Si(111) aufgewachsen [4,5]. Darauf wurde CdTe aus einer widerstandsgeheizten Quelle in situ bis ca. 1 µm Schichtdicke und bei ca. 300°C Substrattemperatur abgeschieden.

Fig. 1 zeigt die Oberfläche einer so gewachsenen CdTe Schicht in einer Rasterelektronenmikroskop (REM) Aufnahme. Abgesehen von gelegentlichen Fehlern werden glatte, strukturlose Oberflächen beobachtet. Das ebenfalls im Rasterelektronenmikroskop aufgenommene Channeling-Diagramm in Fig. 2 demonstriert die bereits erreichte strukturelle Qualität dieser ersten Schichten.

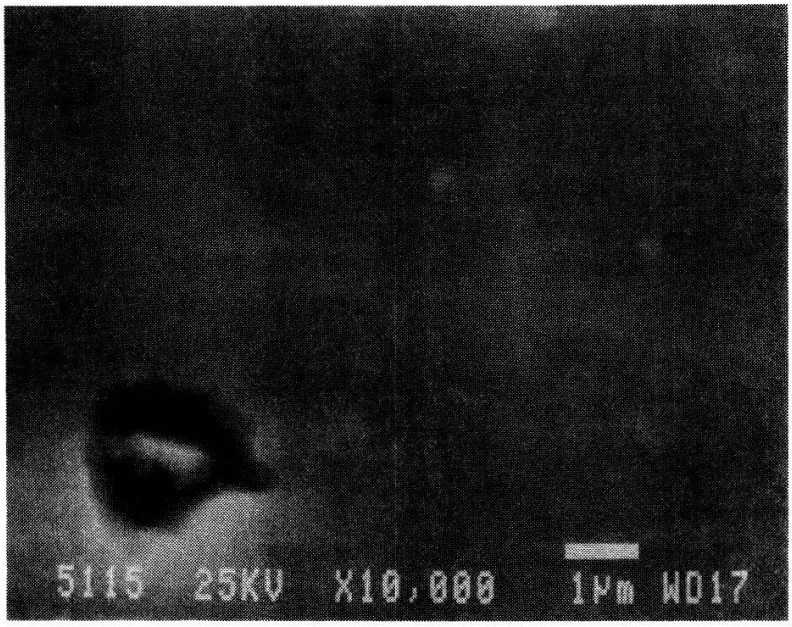

Fig. 1. REM-Aufnahme von epitaktischem CdTe auf $(Ba,Ca)F_2/Si(111)$.

Am Diffraktometer (Bragg-Brentano Geometrie) mit Cu-Strahlung aufgenommene Röntgenspektren zeigen nur die bei Epitaxie zu erwartenden (hhh)-Reflexe. Die daraus bestimmte Gitterkonstante des CdTe bei Raumtemperatur stimmt innerhalb der Messgenauigkeit von ca. 0.02% mit dem Gleichgewichtswert von massivem Material überein. Trotz den stark unterschiedlichen thermischen Ausdehnungskoeffizienten der verschiedenen aufeinander aufgewachsenen Materialien und der Gitterfehlpassung treten somit bei Raumtemperatur keine nennenswerten mechanischen Spannungen im CdTe auf. Beim Wachstum von $(Ba,Ca)F_2$ Schichten auf Si wurde ebenfalls gefunden, dass mechanische Spannungen beim Abkühlen auf

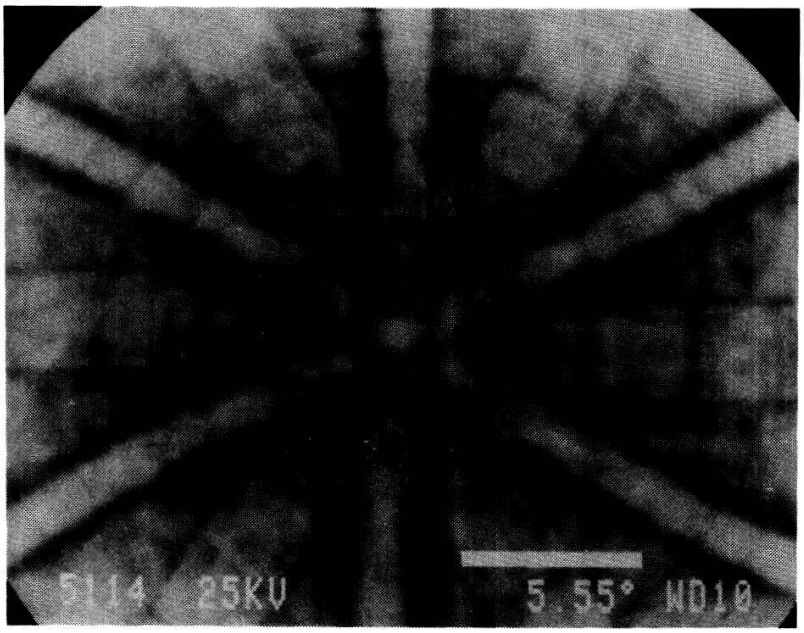

Fig. 2. REM-Channeling Diagramm von epitaktischem CdTe auf $(Ba,Ca)F_2/Si(111)$.

Raumtemperatur sofort relaxieren [6]. Es ist deshalb zu vermuten, dass die Fluorid-Zwischenschicht einen entscheidenden Einfluss auf die Spannungsrelaxation des CdTe ausübt.

Herrn P. Wägli, Lab. für Festkörperphysik ETH Zürich, sei für die Arbeiten am Rastermikroskop herzlich gedankt. Die Gruppe für Rüstungsdienste, Bern, hat die Arbeiten finanziell unterstützt.

Referenzen:

[1] R.A. Reidel, E.R. Gertner, D.D. Edwall, W.E. Tennant, Appl. Phys. Lett. 46, 64, 1985.

[2] W.E. Hoke, R. Traczewski, V.G. Kreismanis, R. Korenstein, P.J. Lemonias, Appl. Phys. Lett. 47, 276, 1985.

[3] E.R. Gertner, S.H. Shin, D.D. Edwall, L.O. Bubulac, D.S. Lo, W.E. Tennant, Appl. Phys. Lett. 46, 851, 1985.

[4] H. Zogg, M. Hüppi, Appl. Phys. Lett. 47, 133, 1985.

[5] H. Zogg, W. Vogt, H. Melchior, 2nd Int. Tech. Symp. Opt. and Electro Opt. Appl. Sci. and Eng., Cannes, Nov. 1985, Proc. SPIE 587, to be published.

[6] H. Zogg, P. Maier, P. Norton, Proc. Mat. Res. Soc. Meeting, Boston, Dec. 1985, Vol. 56.

[7] H. Zogg, P. Norton, Techn. Digest Int. Electron Devices Meeting IEDM, Washington D.C. Dec. 1985, p. 121.

Optimierung von integrierten Vertical-Hall-Sensoren mit Hilfe zweidimensionaler Computersimultion

A.Krause, H.U. Schwarzenbach
LGZ LANDIS & GYR ZUG AG, ZBT-Zentrallabor, 6301 Zug

Ausgehend von einem bestehenden Vertical-Hall wurden einfache Modelle zur Simulation der aktiven Zone (n-Silizium) und der pn-Uebergänge entworfen und die entsprechenden Gleichungen ins Finite-Element-Programm von IMSL eingegeben. Nachdem die Similationen die Messergebnisse ohne Parameteranpassung bestätigt hatten, ging man daran, die Sensoreigenschaften zu optimieren. Ziele: ein möglichst grosses Verhältnis Hallspannung/Spannungsabfall (bei B=1T) bei guter Symmetrie und Linearität gegenüber dem Sensorstrom. Das liess sich durch Variation des Layouts und der Dottierungsverteilung erreichen. Die Messung der gemäss den Simulationsdaten realisierten Sensoren bestätigte die Resultate mit grosser Genauigkeit.

Properties of r.f. magnetron sputtered thin TiN films

K. Solt
Central Research and Development, LGZ LANDIS & GYR ZUG CORP. 6301 Zug

TiN films were prepared by reactive sputtering of titanium in a gas mixture of argon and nitrogen using r.f. powered sputter gun. Auger Electron Spectroscopy, X ray diffractometry and electrical resistivity and optical reflectivity measurements were applied to investigate the dependence of film properties upon the deposition parameters.
Stochiometric TiN films with golden yellow colour and low resistivity were obtained with a sputtering gas mixture of 10% N_2 and 90% Ar, an r.f. input power of 1,75 KW and a substrate bias of about -100V.

Das Wachstum und die physikalischen Eigenschaften von Tantalsilizid/n^+ Polisilizium-Schichten für Leiterbahnen von hochintegrierten Silizium-Bauelementen

A.E. Widmer and R. Fehlmann, Laboratories RCA Ltd., Badenerstrasse 569, 8048 Zürich

Für hochintegrierte Silizium-Bauelemente wird die angestrebte Erhöhung der Schaltgeschwindigkeiten durch die Reduktion der kritischen Dimensionen in zunehmendem Masse beschränkt durch die entstehenden Schaltverzögerungen infolge hoher Schichtwiderstände der Polysilizium Gate- und Leiterbahnen. Wir berichten über die Ergebnisse der Abscheidung von Tantalsilizid/n^+ Polysilizium-Doppelschichten aus der Gasphase bei niedrigem Druck sowie über deren physikalischen Eigenschaften. Der gewählte Prozess erlaubt die Herstellung solcher Doppelschichten in sequentieller Reihenfolge ohne Prozessunterbrechung.

Dreidimensionale Strukturen in der Dünnschicht-Hybrid-Elektronik

R. Hug*, K.P. Ackermann* und G. Berner **
BBC Aktiengesellschaft BROWN, BOVERI & Cie.,* 'Methoden-Labor' (RLX) CH-5401 Baden, **'Hybridschaltungen' (EKH), CH-5600 Lenzburg

KleinereStrukturen der aktiven Elemente in der Halbleiterelektronik ermöglichen einen zunehmenden Integrationsgrad. Dies führt zwangsläufig zu einer erhöhten Dichte der elektrischen Interkonnektionen zwischen den einzelnen integrierten Bauteilen. Ebenso werden immer grössere Anforderungen an die Bauteileminiaturisierung bzw. Packungsdichte auf Printplatten gestellt. Dieser Tendenz unterliegt auch die Hybrid-Technologie. Ausgehend von den Problemlösungen in der Halbleiterelektronik bezüglich Packungsdichte, wird am Beispiel der Dünnfilm-Technik über äquivalente Methoden berichtet. Für solche dreidimensionale Strukturen mit dielektrischen Polyimidschichten werden die Applikationsprobleme hinsichtlich Strukturierung dieser Schichten und der Adhäsion von Metall-Polyimid-Verbunden beschrieben und geeignete Lösungsmöglichkeiten aufgezeigt.

Surface roughness and electrical conduction of oxide/polyoxide Interfaces

G. Harbeke and A.E. Widmer, Laboratories RCA Ltd, Badenerstr.569, 8048 Zurich, and
L. Faraone, RCA Laboratories, Princeton, NJ 08540, U.S.A.

Vertical structures of n^+ polysilicon/SiO_2/n^+ polysilicon have been prepared by LPCVD of silicon and thermal oxidation of the lower polysilicon film. The interface roughness has been measured by the roughness-induced optical excitation of surface plasmons in thin silver films deposited onto the bare interface. Destructive breakdown fields, Fowler-Nordheim currents and wear-out mechanisms of the oxide were studied by electrical measurements. The results reveal a close correlation between interface roughness and conductivity of the thermal oxide.

Lichtstreutopographie zur Charakterisierung von Silizium

E.F. Steigmeier and H. Auderset, Laboratories RCA Ltd., Badenerstrasse 569, 8048 Zürich

Die elastische Lichtstreuung wird in der Halbleitertechnologie erfolgreich benutzt zur Detektion von Staubpartikeln und Einzeldefekten. Darüberhinaus können wir zeigen, dass die Intensität der elektrischen Lichtstreuung - ausser von der Oberflächenbeschaffenheit - auch sehr empfindlich abhängt von der strukturellen Perfektion (d.h. Abweichung von der Idealkristallstruktur) im Materialinnern, innerhalb der Lichteindringtiefe. Unter Benutzung der Rastertechnik kann man damit Siliziumscheiben, epitaktische und polykristalline Schichten, oder andere Materialien lichtstreutopographisch abbilden und charakterisieren.

OPTIMIERUNG VON SILANDISSOZIATION IN DER GLIMMENTLADUNG

P. Kocian, D. Erni, G. Bugmann, EPFL, Dépt. de physique, IPA, 1015 Lausanne

Um den Abscheidungsprozess von a-Si Schichten in einer elektrischen Entladung höchstens zu ökonomisieren, d.h. den Dissoziationsgrad so hoch wie möglich tun, ist es nötig die Dissoziation von Silan in Abhängigkeit von verschiedenen Plasmaparametern zu untersuchen. Wir haben die Produkte der Dissoziation von Silan, d.h. Si, SiH, H und H_2 mittels der optischen Spektroskopie untersucht. Wir haben die Intensitäten der Linien Si(3905A), SiH(4145A), H(4101A) und H_2(4630A) in Abhängigkeit vom Elektrodenabstand, von der Gasdurchflussmenge usw. untersucht. Wir haben gefunden, dass diese Intensitäten nicht monotone Funktionen dieser Plasmaparameter sind.

Die Forschung ist vom NEFF finanziert.

Dielectric breakdown measurements in thin films of SiO_2 used for EEPROM*

P. Fazan, J. Manthey, M. Dutoit, IIME, EPFL, 1015 Lausanne
J.M. Moret, CSEM, 2000 Neuchâtel

The dielectric breakdown strength of thin oxides can be characterised by the total charge Q_{BD} that can cross them before destruction. This latter concept is particularly useful for predicting the endurance of EEPROM (Electrically Erasable and Programmable Memories). We evaluate an alternate method for measuring Q_{BD} that consists in injecting current pulses of alternate polarity into the oxide (1). It yields significantly higher values for Q_{BD} than constant current injection (Q_{BD} = 42 Cb/cm^2 versus 14 Cb/cm^2 for 12 nm thick oxides at J= 0.2 A/cm^2). This difference is ascribed to reduced electron trapping in the oxide. Results for different oxide thickness, current densities and pulse length will be shown. We believe that this method allows us to characterise tunneling oxides as used in EEPROM more accurately than previous methods.

*) Work sponsored by the Nat. Fund. for Scientific Research (PN 13)
(1) E. Harari, J. Appl. Phys. 49, 2478 (1978)

Formation of self-aligned $TiSi_2$ by rapid thermal processing for VLSI circuits

E. Stocker, Inst. interdép. de microélectronique, EPFL, 1015 Lausanne
P. Weiss, Centre suisse d'électronique et de microtechnique, 2000 Neuchâtel

Because of its very low electrical resistivity and its high temperature stability, $TiSi_2$ is attractive for gate electrodes, interconnections and contacts in very-large-scale-integrated (VLSI) circuits. $TiSi_2$ has been formed by sputtering 40 nm Ti onto (100) Si and rapid (1 min) sintering in a lamp-heated reactor. The silicidation as a function of parameters such as anneal temperature, metal film thickness, substrate doping, has been investigated by electrical resistance measurements, Auger electron spectroscopy, electron microscopy and diffraction. A two step annealing process at 600 and 800 °C, which is used in order to avoid lateral growth, provides a 50 nm thick polycrystalline (grain size $\sim$500 nm) layer of phase $TiSi_2$ with a resistivity of a few Ω/□ . The use of such layers in a VLSI CMOS technology will be discussed.
Ref.: C.Y. Ting et al., ECS Proc. VLSI Sci. and Technol. (Detroit,1982)

ANDO II : Recherche de l'espace, cosmologie, atmosphère

IN-SITU MEASUREMENTS OF GASEOUS AIR POLLUTANTS WITH A MOBILE CO_2 LASER-PHOTOACOUSTIC SYSTEM

P.L. Meyer, B. Suter and M.W. Sigrist, Institute of Quantum Electronics
Physics Department, ETH, CH-8093 Zurich, Switzerland

Abstract : A mobile CO_2 laser-photoacoustic system which is installed in a trailer for in-situ monitoring of gaseous air pollutants is presented. The first measurements have been performed close to a main road in Zurich with emphasis on the detection of ethylene (C_2H_4). A minimum detectable concentration of ca. 5 ppb in the real atmosphere is obtained for this pollutant. Daily extreme concentrations for C_2H_4 range from $\leq$ 10 ppb during the night to $\geq$ 50 ppb during the morning and evening rush hours.

1. Introduction

In recent years, laser-photoacoustic spectroscopy has been demonstrated to be sensitive enough for the detection of trace gases in ppb concentrations [1]. However, only few studies have been performed on real atmospheres. As pointed out earlier many important air pollutants absorb in the wavelength range of a CO_2 laser [2]. Our main emphasis is put on ethylene (C_2H_4) which represents a major car exhaust gas and which is known for its harmful effects on plants already at concentrations below 50 ppb [3]. The continuous monitoring of the C_2H_4 concentration is therefore of special interest. Gas chromatography is sensitive enough to detect ppb concentrations yet cannot be applied for continuous measurements. In this report we present a study on the photoacoustic monitoring of C_2H_4. Special attention is given to the problem of interfering gases.

2. Experimental Setup

Our experimental setup has been described previously [4]. The whole system with the sealed-off $^{12}C^{16}O_2$ laser and the photoacoustic cell is now installed in a special trailer. Our first outdoor measurements have been performed with the trailer parked on the sidewalk of a transit road in Zurich. The air is collected at a distance of 3 meters from the road and 1.5 meters above the ground. The air is pumped through the cell continuously at

a flow rate of ≈ 1 l/min. The special design of the cell with an acoustic resonance at 2660 Hz permits continuous measurements on flowing air even in a noisy environment. Photoacoustic spectra over the full spectral range of the CO_2 laser have been obtained by collecting air samples in situ and closing the cell during the measurements. In the course of these studies meteorological data which certainly influence the concentrations of pollutants have not yet been recorded simultaneously.

3. Results and Discussion

The photoacoustic system has been calibrated periodically yielding a spectrophone responsivity of 4.5 Vcm/W. The average background signal of < 500 nV/W is only slightly higher than that for the laboratory system [4]. The small increase is probably due to the traffic noise. However, it should be mentioned that our resonant cell is much better suited for this type of studies than a nonresonant cell operating at low frequencies.

Since the composition of polluted air is not known a priori, complete photoacoustic (PA) spectra of outside air samples have been taken first. Figs. 1a and 1b (solid lines) show the results for the 10.4 μm CO_2 laser branch for the times 8 am and 12 noon of December 26, 1985. Since this day is a holiday in Switzerland the traffic was in general slack yet busier at noon time than at 8 am. This is just opposite to a usual working day when traffic is heavier in the morning and late afternoon than at noon. The representation of the spectra in Figs. 1a and 1b is unusual because the phase of the PA signals has been taken into account. A 'negative' signal corresponds to a phase shift of 180^0 which is caused by the kinetic cooling effect of CO_2 present in the air [5]. A numerical analysis of the measured PA spectra has been performed on the basis of PA spectra of single pollutants including the signal phase. The analysis has been restricted to C_2H_4, H_2O vapor and CO_2 which are the main absorbing components in the spectral region considered. The calculated PA spectra are represented by open bars in Figs. 1a and 1b. A least square fit to the experimental data (solid lines) yields the individual concentrations with uncertainties for H_2O, CO_2 and C_2H_4 as listed in the Figure. The agreement between theory and experiment is remarkable and the concentrations deduced for CO_2 and H_2O agree with independent measurements performed with conventional equipment. The higher C_2H_4 and CO_2

concentrations at 12 noon (Fig. 1b) compared to 8 am (Fig. 1a) reflect the increase of traffic. Note the reversed phase of the PA signal at the 10P(14) laser transition which is dominated by C_2H_4 absorption [2].

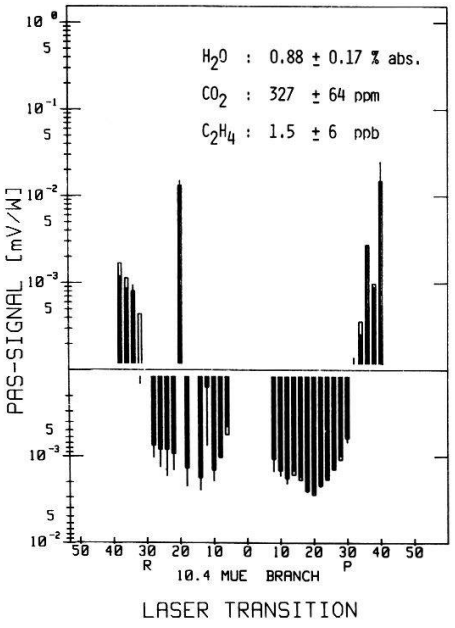

Fig. 1a

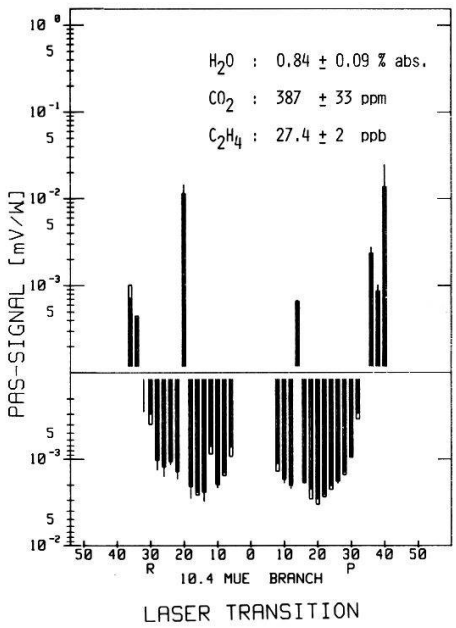

Fig. 1b

Measured (—) and calculated (⊐) PA spectra of urban air for Dec 26, 1985
a) Time: 8 am b) Time: 12 noon

In general, PA spectra measured on a busy working day show poorer agreement with calculated spectra due to the presence of many additional interfering pollutants with considerable concentrations. However, the absorption peak at the 10P(14) laser transition is still dominated by C_2H_4 absorption whereas the 10R(20) and 10P(20) transitions can be attributed to H_2O and CO_2 absorption respectively. Fig. 2 shows continuous measurements for a typical working day (February 4, 1986) between 6:00 am and 22:30 pm performed at the 10P(20), 10P(14) and 10R(20) laser transitions. The data at the 10P(20) and 10R(20) transitions which represent CO_2 and H_2O absorption have been taken at 15 min intervals. The signal variation during the day is in general within 10 %. A calculation with the averaged PA signals at these two laser transitions yields the scale for the C_2H_4 concentration as well as a mean value of 365 ppm for CO_2 and of 0.67 % absolute for H_2O vapor. A fluctuation of 10 % in CO_2 or H_2O concentration causes an uncertainty of only 2.5 ppb each in the calculated C_2H_4 concentration scale. The measured C_2H_4 profile as plotted in Fig. 2 represents data from continuous measurements

which have been averaged over 1 hour intervals. The daily variations are considerable. The characteristic concentration maxima of 50 to 60 ppb coincide with the morning and evening rush hours.

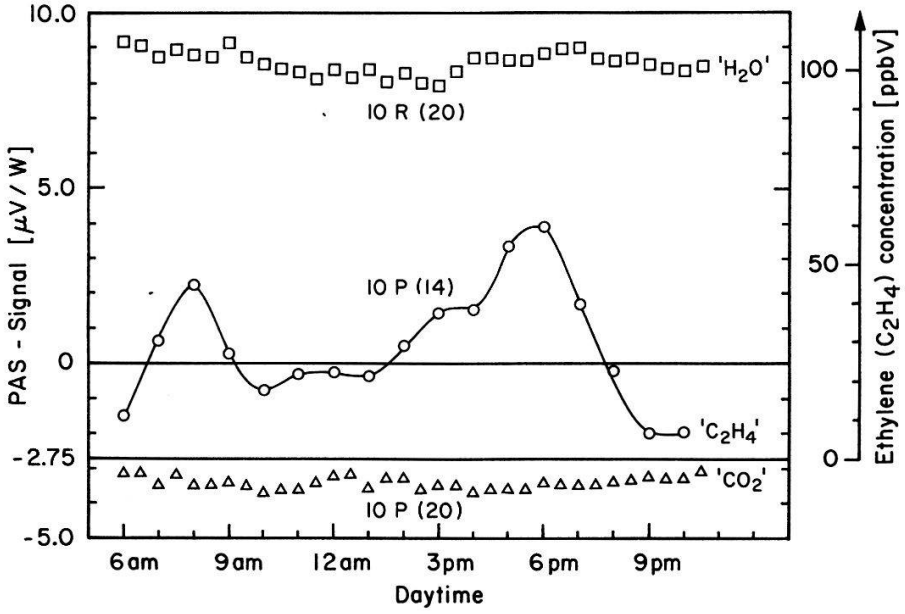

Fig. 2 PA signals for H_2O, C_2H_4 and CO_2 versus daytime. Date: Feb 4, 1986

Further measurements are in progress and a more detailed report will be published elsewhere.

Acknowledgment

This project is supported by the National Research Program NFP 14 of the Swiss National Science Foundation.

References

[1] G.A. West, Rev. Sci. Instrum. 54, 797 (1983)

[2] St. Bernegger, P.L. Meyer and M.W. Sigrist, Can. J. Phys., to be published in Vol. 64 (1986)

[3] F.B. Abeles and H.E. Heggestad, J. Air Poll. Contr. Assoc. 23, 517 (1973)

[4] P.L. Meyer, St. Bernegger and M.W. Sigrist, Helv. Phys. Acta 58, 833 (1985)

[5] A.D. Wood, M. Camac and E.T. Gerry, Appl. Optics 10, 1879 (1971)

CONTINUUM AND LINE ABSORPTION OF WATER VAPOR WITHIN THE 8 TO 14 μm ATMOSPHERIC WINDOW

J. Hinderling, M.W. Sigrist and F.K. Kneubühl
Institute of Quantum Electronics, Physics Department, ETH
CH-8093 Zurich, Switzerland

1. Introduction

The atmospheric window at wavelengths between 8 and 14 μm determines the global radiative energy balance and the performance of communication and remote-sensing systems. The relevant absorption process in this spectral window is the water-vapor continuum absorption. The continuum can be explained only partially by the monomer absorption of the water vapor. Equilibrium water dimers, larger water clusters and hydrated ions have been suggested as possible sources of the continuum absorption. On the other hand, new calculations for the pressure-broadened line shape of the water monomer absorption have been proposed as an alternative. Until recently, all line shape theories failed to predict the proper magnitude of the continuum absorption and the strong negative temperature dependence observed [1]. In addition to the continuum absorption water vapor exhibits a number of weak absorption lines within the 8 to 14 μm window. Over ten of these absorption lines are observed at selected $^{12}C^{16}O_2$-laser wavelengths. Hitherto, a proper identification of these absorption lines by comparison with accurate experimental results has not been reported.

2. Laboratory experiments with laser photoacoustics

Our laboratory measurements have been performed on the basis of laser-photoacoustic spectroscopy whose sensitivity permits reliable measurements even in small gas cells. A detailed description of our detection system has been presented previously [2]. The ultimate sensitivity limit of our spectrophone is equivalent to an absorption of less than $2.6 \cdot 10^{-8}$ cm^{-1}. Up to the present, sensitivity problems generally restricted the application of this technique to temperatures above $+20^0C$. However, our detector still shows an adequate sensitivity for measurements of the continuum absorption at temperatures as low as -20^0C.

3. Line absorption

We have peformed laboratory experiments on the temperature dependence of the narrow absorption lines at the CO_2-laser transitions 10P(40), 10R(20), 9P(38) and 9R(36) [3]. These measurements have been carried out at selected temperatures between 280 and 305 K on water-vapor samples buffered with nitrogen to 950 mbar. In contrast to the continuum all line absorptions exhibit a positive temperature dependence. On the basis of experimental and numerical studies we identified these absorption lines as weak pure rotational transitions of the H_2O molecules in the vibrational ground state. A detailed identification has been presented in ref. [3].

In order to verify our line identification we performed numerical calculations on the line strengths and line intensities of the pure rotational transitions of the H_2O molecule. The calculated intensities are compared to our measured absorption cross sections. We find good agreement.

A further test of our line identification has been obtained by a comparison of our absorption measurements on the temperature dependence with predictions based on the pure rotational line model. The energies of the lower rotational state have been derived from regression fits of the slope of the absorption cross section versus temperature. These experimentally derived energies agree within 5.3 % with the data calculated by Messer et al. [4]. Hence, we conclude that these weak absorption lines are due to pure rotational transitions of the water molecule.

4. Continuum absorption

Our measurements on the temperature dependence of the continuum absorption have been performed in order to test the dimer model which predicts a negative exponential temperature coefficient. The temperature range below 300 K is of special interest mainly for two reasons. Firstly, discrepancies between experiment and dimer predictions are expected at temperatures below 300 K. Secondly, most laboratory experiments have been performed at or above 23^0C because of inherent sensitivity limitations of the applied techniques of measurement.

Therefore, we performed measurements on the pressure dependence of the continuum absorption for the first time at the temperatures 5^0C, 0^0C, -6^0C, -10^0C, -15^0C and -20^0C. These absorptions were measured at the two laser transitions 10P(20) and 10P(24). With respect to collisional-broadening effects the total pressure of the water-vapor/nitrogen mixtures was always kept at 950 mbar.

The measured absorption coefficient taken at the 10P(24)-laser transition is plotted versus relative humidity s in Fig. 1. The so-called self-broadening coefficients C_S have been derived by regression fits of the quadratic pressure dependence (Fig. 1, solid lines). The results for the coefficients C_S are presented in Fig. 2 as a function of temperature for the 10P(24)-laser transition.

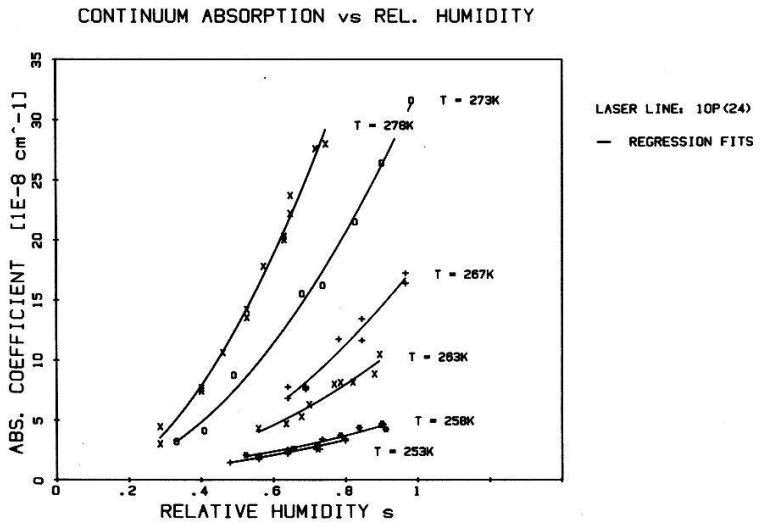

Fig. 1 Measured continuum absorption versus relative humidity at the 10P(24) CO_2-laser transition.

With respect to the dimer model the pressure quadratic coefficient C_S can be interpreted by terms of dimer absorption. The solid line shown in Fig. 2 represents the best fit on the basis of the dimer model by Suck et al. [5]. The fits result in an average value for the electronic binding energy of -6.05 kcal/mole which is in good agreement with ab-initio calculations. Recently, Reimers et al. [6] published calculations on electronic binding energies which range from -5.9 to -6.1 kcal/mole. Furthermore, we derived an absorption cross section of the dimer molecule of $\sigma = 3.1 \cdot 10^{-20}$

cm^2/molecule. For comparison, liquid water exhibits a cross section of $2.55 \cdot 10^{-20}$ cm^2/molecule at the laser wavelengths considered in this study.

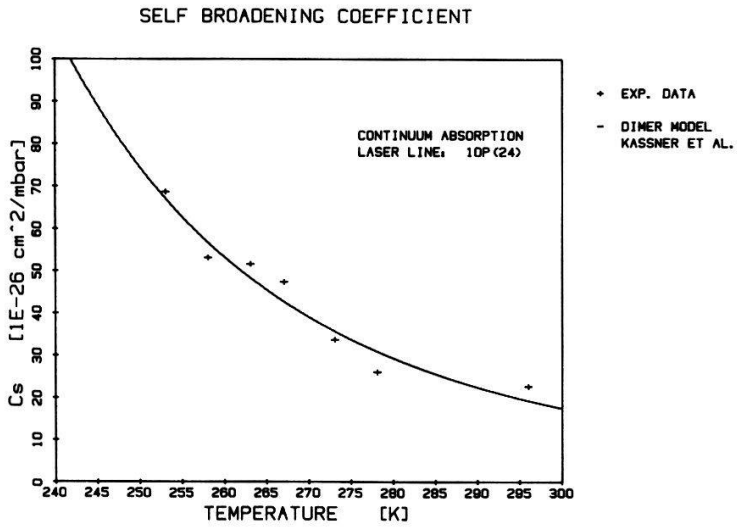

Fig. 2 Temperature dependence of the water-pressure quadratic component of the continuum absorption at the 10P(24) CO_2-laser transition. The solid line represents the best fit based on the dimer model.

5. Summary

Contributions of aggregates larger than the dimer have not been observed because they would cause an unequivocal stronger temperature dependence than measured. Yet, our results do not prove the dimer interpretation. However, the results on the negative temperature dependence indicate that at least two water molecules are involved in the absorption process of the continuum.

References

[1] M.E. Thomas and R.J. Nordstrom, Appl. Opt. 24, 3526 (1985)

[2] J. Hinderling, M.W. Sigrist and F.K. Kneubühl, Proc. Int. Conf. on Lasers'84, S.F., STS Press, McLean, VA, 634 (1985)

[3] J. Hinderling, M.W. Sigrist and F. Kneubühl, Infrared Phys. 25, 491 (1985)

[4] J.K. Messer, F.C. DeLucia and P. Helminger, Int. J. Infrared and mmWaves 4, 505 (1983)

[5] S.H. Suck et al., Appl. Opt. 21, 1610 (1982)

[6] J.R. Reimers and R.O. Watts, Chem. Phys. 85, 83 (1984)

BIPOLARE AUFLADUNG VON KLEINEN TEILCHEN

B. Eliasson, W. Egli and M. Hirth, Brown Boveri Forschungszentrum, CH-5405 Baden, Schweiz

Zusammenfassung: Wir betrachten die elektrische Aufladung kleiner kugelförmiger Teilchen (> 0.1 micron) durch gleichzeitig vorhandene positive und negative Ionen. Dabei wird der Ionentransport sowohl als Folge eines angelegten elektrischen Feldes als auch durch Diffusion berücksichtigt. Dies ist im Gegensatz zu allen uns bekannten Arbeiten, die entweder nur die Feldaufladung oder nur die Diffusionsaufladung getrennt behandeln. Wir bestimmen das zeitliche Anwachsen der Ladung auf dem Teilchen als Funktion des Radius, des angelegten Feldes und der vorhandenen Ionendichten. Das Problem wird hier in einer analytischen Näherung behandelt.

1. Einführung

Wir betrachteten eine eindimenionsale Entladungsstrecke (z.B. ein bipolares Elektrofilter), in die wir über die Elektroden Ionenströme einspeisen (Fig. 1). Die Ionenrekombination führt zu fast linear abnehmenden Ionenströmen. An der Stelle $z = z_0$ befindet sich ein kugelförmiges Teilchen mit dem Radius R. Das Teilchen sei ursprünglich ungeladen. Wir berechnen die auf dem Teilchen sich aufbauende Ladung als Funktion der Zeit. Insbesondere bestimmen wir die nach langer Zeit erreichte Grenzladung als Funktion des Radius, des Feldes und der Ionenströme.

2. Die Aufladungsmechanismen

Die positiven und negativen Ionen können auf zweierlei Arten auf das Teilchen gelangen, nämlich durch

a. Feldaufladung, d.h. die Ionen driften unter Einfluss des angelegten Feldes auf das Teilchen.

b. Diffusionsaufladung, d.h. durch die Brownsche Bewegung gelangen Ionen auch auf das Teilchen. Dieser Aufladungsmechanismus ist immer vorhanden, auch wenn kein Feld angelegt ist.

Bei unseren nachfolgenden Betrachtungen machen wir die folgenden Einschränkungen:

a. Wir betrachten nur solche Teilchen die wesentlich grösser sind als eine freie Ionenweglänge, d.h. für welche gilt: Knudsenzahl: $Kn = \lambda_i/R \leq 0.1$

b. Falls eine Ladung auf dem Teilchen auftritt, haftet sie und kann nicht mehr entfernt werden.

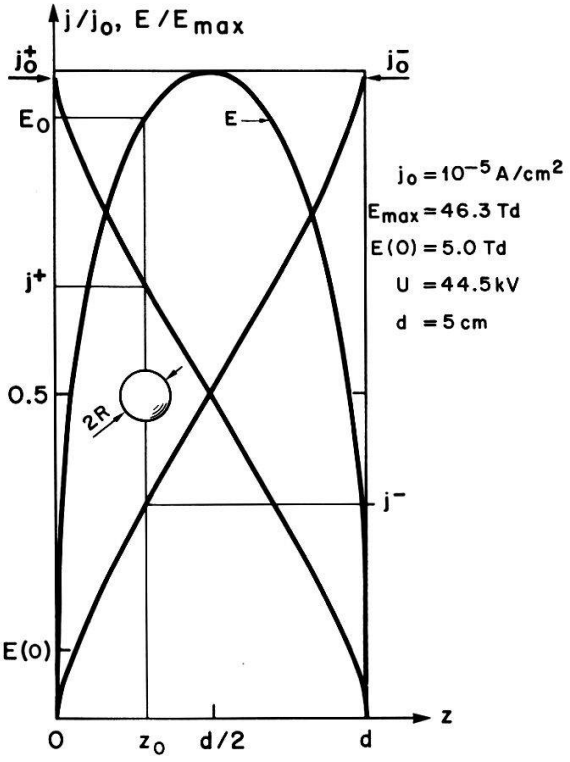

Fig. 1. Das elektrische Feld und die Ionenströme in einer eindimensionalen Entladungsstrecke. Das Teilchen mit dem Radius R befindet sich an der Stelle z_0.

Die erste Bedingung trennt den Kontinuumsbereich, wo wir mit der Kontinuitätsgleichung und der Poisson-Gleichung rechnen können, vom mikroskopischen Bereich, wo die Statistik der Ionen- und Teilchenbewegungen berücksichtigt werden muss (Fig. 2). Es wird sich zeigen, dass für Teilchen, die wesentlich grösser sind als die freie Wegelänge, die Feldaufladung gegenüber der Diffusionsaufladung dominiert. Umgekehrt, falls die Knudsenzahl wesentlich grösser als 0.1 ist, dominiert die Diffusionsaufladung. Wir können somit drei Aufladungsbereiche unterscheiden, nämlich

Bereich I:	$Kn \lesssim 10^{-2}$	Feldaufladung
Bereich II:	$10^{-2} \lesssim Kn \lesssim 1$	Übergangsbereich. Feld- und Diffusionsaufladung
Bereich III:	$Kn \gtrsim 1$	Diffusionsaufladung

Die obigen Grenzen sind natürlich etwas willkürlich gewählt. Tabelle I enthält die wichtigsten Parameter für positive und negative Ionen in Luft. Die Werte wurden der Referenz [1] entnommen.

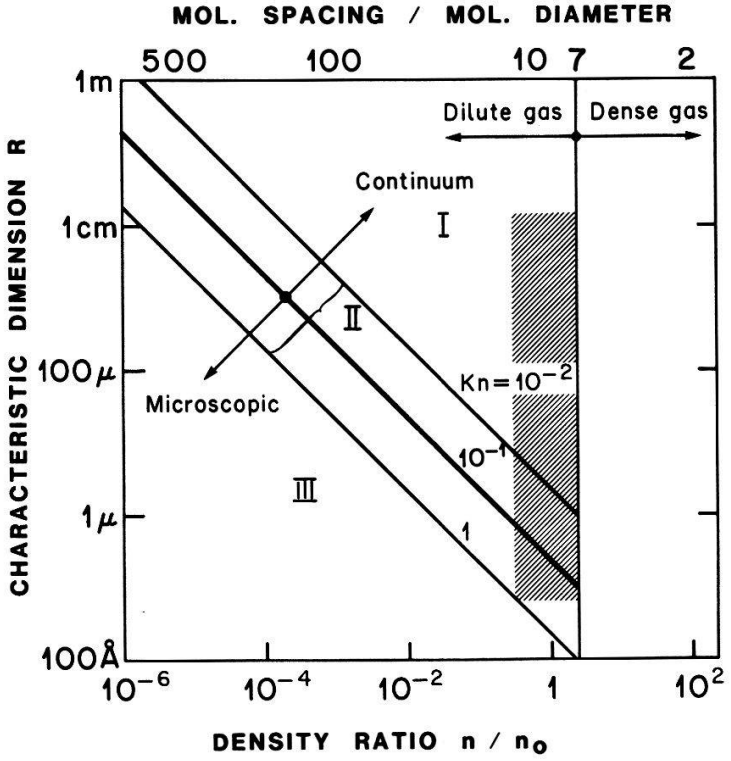

Fig. 2. Die drei Aufladungsbereiche. $n_o = 2.410^{19}$ cm^{-3}.

Tabelle I

		Positive Ionen	Negative Ionen
Beweglichkeit μ	[cm^2/Vsec]	1.4	1.9
Molekülmasse M	[g/mol]	109.	50.
Diffusionskonstante D	[cm^2/sec]	0.0335	0.0490
Mittlere Geschwindigkeit $\bar{v}$	[cm/sec]	$2.38\ 10^4$	$3.52\ 10^4$
Mittlere freie Weglänge λ_i	[cm]	$1.44\ 10^{-6}$	$1.79\ 10^{-6}$

Im Folgenden werden wir uns nur mit der Aufladung in den Bereichen I und II befassen.

3. Die Feldaufladung (Bereich I)

Falls das Teilchen einen Radius $R \gtrsim 2\ \mu$ hat, befinden wir uns im Bereich I der Feldaufladung.

Wir betrachten den Fall einer zunächst ungeladenen Kugel im homogenen Feld E_o. Die Feldstruktur um die Kugel herum wird in Ref. [2], S. 205 angegeben. Falls wir weiter annehmen dass die Dichten der positiven und negativen Ionen so niedrig sind, dass sie dieses elektrostatische Feld nicht verändern, dann sind die von [2] gerechneten Feldlinien zugleich die Stromlinien für die Aufladung des Teilchens. Aus der in [2] angegebenen Lösung ist ersichtlich, dass sobald sich eine Ladung q auf der Kugel befindet, die Kugeloberfläche in zwei Zonen aufgespalten wird, nämlich die normierte Fläche A, innerhalb welcher die Feldlinien des radialen Feldes in das Teilchen hineinzeigen und die Fläche B innerhalb welcher die Feldlinien aus dem Teilchen herausschauen (Fig. 3). Der kritische Winkel θ_o, der die beiden Flächenteile trennt ist gegeben durch

$$\cos\theta_o = -\, q/q_{so}; \quad A = 2\pi\,(1+\cos\theta_o); \quad B = 2\pi\,(1-\cos\theta_o) \tag{1}$$

wobei $q_{so} = p\cdot 4\pi\varepsilon_o R^2\cdot E_o$, $p = 3\varepsilon_r/(\varepsilon_r+2)$ und ε_r die relative Dielektrizitätskonstante des Teilchens ist. Wir nehmen an, dass sich die Ladungen gleichmässig auf das Teilchen verteilen. Die Zunahme der auf dem Teilchen befindlichen Ladung q ist gleich dem gesamten auf das Teilchen fliessenden Strom, nämlich

$$\frac{dq}{dt} = p\cdot\pi R^2\,[j^+\,(1+\cos\theta_o)^2 - j^-\,(1-\cos\theta_o)^2] \tag{2}$$

Mit der Substitution $u = q/q_{so}$ kann Gl. (2) umgeschrieben werden als

$$\frac{du}{dt} = \frac{(u-\gamma)(u-1/\gamma)}{\bar{\tau}} \tag{3}$$

mit

$$\gamma = \frac{\sqrt{j^+/j^-} - 1}{\sqrt{j^+/j^-} + 1} \tag{4}$$

und

$$\frac{1}{\bar{\tau}} = \frac{1}{\tau^+} - \frac{1}{\tau^-}; \quad \frac{1}{\tau^\pm} = \frac{j^\pm}{4\varepsilon_o\cdot E_o} \tag{5}$$

Die Integration von Gl. (3) liefert

$$q(t) = \gamma \cdot q_{so} \cdot \frac{1 - \exp(-t/\tau)}{1 - \gamma^2 \exp(-t/\tau)} \tag{6}$$

mit

$$\tau = \frac{1}{2} \frac{1 + \gamma^2}{1 - \gamma^2} \tau_o \; ; \quad \tau_o = \frac{4\varepsilon_o E_o}{(j^+ + j^-)} \tag{7}$$

Die Grenzladung ist

$$q_s = \gamma \cdot q_{so} \tag{8}$$

d.h. das Teilchen in der Figur 1 hat in der linken Hälfte der Entladungsstrecke eine positive Ladung, rechts eine negative Ladung und in der Mitte wird es gar nicht aufgeladen (γ=0). Das Resultat in Gl. (8) wurde zum ersten Mal und gleichzeitig in den Refs. 3 und 4 publiziert.

4. Feld- und Diffusionsaufladung (Bereich II)

Im Bereich II ($0.02 \lesssim R \lesssim 2\ \mu$) muss man sowohl Diffusions- als auch Feldaufladung berücksichtigen. Zu den oben aufgeführten Gliedern in Gl. (2) kommen noch die Diffusionsglieder dazu. Um diese abzuleiten, machen wir Gebrauch von Resultaten, die in der Ref. [5] bestimmt wurden. In dieser Arbeit werden Ionendichten um ein geladenes kugelförmiges Teilchen herum berechnet. Dabei werden Ionen beider Polaritäten berücksichtigt. Diese stehen aber nur unter Einfluss des Eigenfeldes des Teilchens (kein angelegtes Feld). Die für unsere Berechnungen zugrunde liegenden Kontinuitäts- und Poisson-Gleichungen gelten bis an eine um das Teilchen herumgelegte gedachte Hilfskugel mit dem Radius $\delta = R+\rho$ wobei ρ von der Grössenordnung einer freien Weglänge ist (Fig. 3). Basierend auf diesen Überlegungen und den in der Ref. [5] abgeleiteten Resultaten kann man den folgenden allgemeinen Aufladungsmechanismus für das Teilchen postulieren:

1. Im Gebiet A werden:
   - die positiven Ionen nur durch den Feldstrom j^+ auf das Teilchen gebracht
   - die negativen Ionen nur durch Diffusion mit einer Ionendichte $n^-(\delta)$
2. Im Gebiet B werden:
   - die negativen Ionen nur durch den Feldstrom j^- auf das Teilchen gebracht
   - die positiven Ionen nur durch Diffusion mit der Teilchendichte $n^+(\delta)$

Durch ein Flächenelement dA diffundieren $\frac{1}{4}\, n\bar{v}\cdot dA$ Teilchen pro Sekunde mit der mittleren thermischen Geschwindigkeit $\bar{v}$. Somit erhalten wir die neue, er-

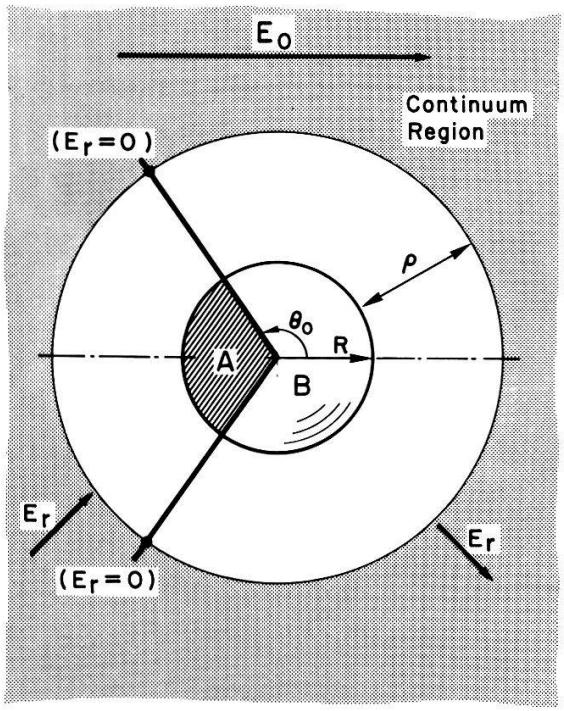

Fig. 3. Die Randzone um das aufgeladene Teilchen herum.

weiterte, Aufladungsformel als:

$$\frac{dq}{dt} = \pi R^2 p \left[j^+ (1+\cos\theta_o)^2 - j^- (1-\cos\theta_o)^2\right] + \frac{1}{4} f \left[\bar{v}^+ \int_B n^+(\delta)dB - \bar{v}^- \int_A n^-(\delta)dA\right] \qquad (9)$$

mit $\bar{v}^{\pm}=(8\ kT_i/\pi M_i^{\pm})^{1/2}$, T_i=Ionentemperatur, $M_i^{\pm}$=Ionenmasse, $f=1-\sqrt{1-(R/\delta)^2}$. Mit dem Faktor f wird berücksichtigt, dass nicht alle Ionen, die von der Hilfskugeloberfläche wegfliessen, auf dem Partikel auftreffen.

Eine ähnliche Konfiguration für den Aufladememechanismus wurde von [6] vorgeschlagen. Dort wurden aber die Dichten der diffundierenden Ionen falsch berechnet.

Die Ionendichten $n^-(\delta)$ und $n^+(\delta)$ in den Zonen A und B auf der Hilfskugel lassen sich mit dem in der Ref. [5] bestimmten Ausdruck für die Ionendichten angeben:

$$n^{\pm}(\delta) = \frac{n_o^{\pm} \exp\left(-\phi(\delta)/kT_i\right)}{1 - \frac{\bar{v}^{\pm}\delta^2}{4\,D^{\pm}} \exp\left(-\phi(\delta)/kT_i\right) \psi} \qquad (10)$$

mit $D^{\pm}$ = Diffusionskonstante und $\psi = \int_{\infty}^{\delta} \frac{1}{r^2} \exp(\phi(r)/kT_i)dr$.

Falls wir nur das von der Ladung q herrührende Potential $\phi(r) = \frac{eq}{4\pi\varepsilon_o r}$ berücksichtigen kann man das Integral ψ lösen und wir erhalten:

$$n^{\pm}(\delta) = \frac{n_o^{\pm} \exp(-\phi(\delta)/kT_i)}{1 + K^{\pm}(kT_i/\phi(\delta))\,(1-\exp(-\phi(\delta)/kT_i))} \qquad (11)$$

mit $K^{\pm} = \bar{v}^{\pm} \cdot \delta/4D^{\pm}$ und n_o ist die Ionendichte weit weg vom Teilchen. In der Auswertung der Gl. (9) unter Berücksichtigung der Gl. (11) setzen wir jetzt das resultierende, aus der Ref. [2] erhaltene Potential ein.

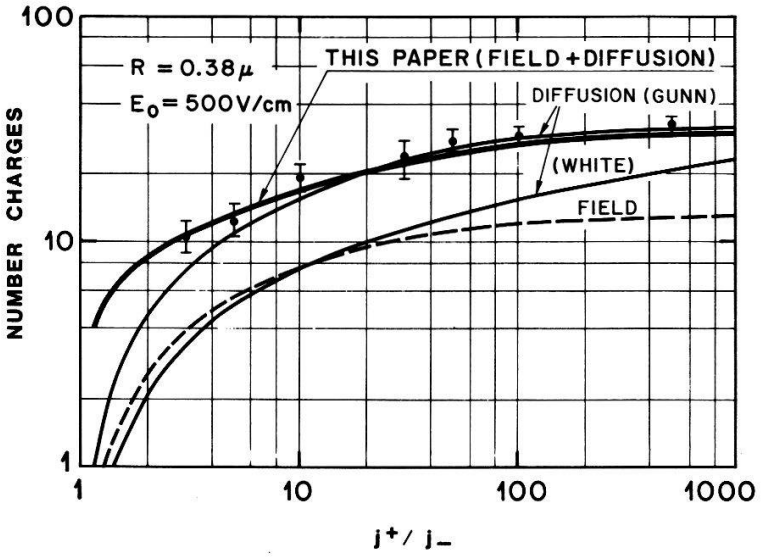

Fig. 4. Vergleich verschiedener Theorien mit gemessener Ladung auf einem Latex-Teilchen mit Radius = 0,38 μ als Funktion des Verhältnisses j^+/j^-. Die Aufladezeit betrug t = 0.2 s und $n_o = 6 \cdot 10^7$ cm^{-3}.

Falls kein oder nur ein kleines angelegtes Feld vorhanden ist und die positiven Ionen überwiegen, resultiert ein Gleichgewicht zwischen den diffundierenden positiven Ionen und den durch das Eigenfeld angezogenen negativen Ionen. In diesem Falle ($\theta_o = \pi$) erhält man die Sättigungsladung q_s in erster Näherung als

$$q_s = 4\pi\varepsilon_o\, \delta\, kT_i\, \Gamma/e \qquad (12)$$

wobei Γ eine Lösung der Gleichung

$$\exp(\Gamma)(\Gamma+K^+) = K^+\left(1+f\,\frac{D^+}{D^-}\,\frac{n_o^+}{n_o^-}\right) \qquad (13)$$

ist. Falls mehr negative als positive Ionen vorhanden sind, müssen in Gl. (13) in den Indizes die Vorzeichen vertauscht werden.

In der Fig. 4 werden Berechnungen basierend auf der Aufladeformel (9) vergleichen mit Messungen und Theorien aus der Ref. [7].

Die hier abgeleitete Aufladeformel (9) hat den Vorteil, dass sie sowohl die Feldaufladung als auch die Diffusionsaufladung in einem einzigen Ausdruck vereinigt. Der Vergleich in Fig. 4 zeigt auch, dass die hier berechneten Werte von allen theoretischen Werten am besten mit den Messergebnissen übereinstimmen.

Referenzen

[1] M. Adachi, Y. Kousaka und K. Okuyama, "Unipolar and Bipolar Diffusion Charging of Ultrafine Aerosol Particles", J. Aerosol Sci., 16 (2), 109-123, (1985).

[2] J.A. Stratton, Electromagnetic Theory, McGraw-Hill, New York 1941, pp. 205.

[3] R. Reffay, "Lois de charge des particules sphériques isolantes en champ électrique mono-ionisé et bi-ionisé", Proceedings La Physique des Forces Electrostatiques, Grenoble 27.9.-1.10.1960, Editions CNRS, Paris 1961, 255-262.

[4] M. Pauthenier, "Lois de charge des particules sphérique conductrices dans un champ électrique bi-ionisé", Proceedings La Physique des Forces Electrostatiques, Grenoble 27.9.-1.10.1960, Editions CNRS, Paris 1961, 279-287.

[5] N.A. Fuchs, "On the Stationary Charge Distribution on Aerosol Particles in a Bipolar Ionic Atmosphere", Geophysical Pure Appl. 56, 1963, 185-193.

[6] R.J. Heinsohn, S.H. Levine, R.J. Fjeld, and G.W. Malamud, "Radiation Charging: A Novel Way to Charge Fine Particles Electrically", J. Air Poll. Control Assoc., 25 (2), February 1975, 179-184.

[7] R.J. Fjeld, R.O. Gauntt, G.J. Laughlin, and A.R. McFarland, "Measurement of the Charge on Submicrometer Aerosol Exposed to Bipolar Ions", The Industry Application Society Annual Meeting, 28.9.-3.10.1980, Cincinnati, Ohio, IEEE, N.Y., 1063-1067.

NEUN-NIVEAUS-MULTIPOLE UND URKRISTALLINE GITTER. BEISPIELE: ELEMENTARTEILCHEN, QUARKMASSEN, UNIVERSALE SCHALENSTRUKTUR

J.T. Muheim, Lab. für Festkörperphysik ETHZ, Hönggerberg, 8093 Zürich

Auszug: Neben den s-r-Strukturen tritt der Neun-Niveaus-Multipol als neue fundamentale Quantenstruktur hervor. Bisher lassen sich zwei Typen unterscheiden. Mit den s-r-Strukturen scheint er unerschöpflich viele Varianten einzugehen. Diese wiederum sind stets in eines der beiden bisher unterscheidbaren urkristallinen Gitter eingebettet: das Ma(teriale Han)tel-Gitter und das Lich(tmässige Han)tel-Gitter. Da es unendlich viele Atomzellgrössen gibt, gibt es auch unendlich viele Matel- und Lichtelkristalle. Es resultieren Lyman-s-r-Atome mit Atmosphären- und Kernteil. Beispiel: Proton, Elektron. Aus dem displazierten f'-WW-MP folgen sofort Elementarteilchen- und Quarkmassen, Wechselwirkungen und Superformmassen etc.. Nukleonenzahl und universale Schalenstruktur sind direkt aus dem Multipol ableitbar.

Einführung

Wegen der gewaltigen Komplexität des universalen Aufbaus können im folgenden nur die wichtigsten Aspekte skizziert werden. Alles Begriffliche aus früheren Arbeiten [1a-e] wird als bekannt vorausgesetzt. Für die raumzeitliche Strukturierung des Universums gewinnt neben der s-r-Struktur der Neun-Niveaus-Multipol (9N-MP) immer grössere Bedeutung. In der Regel treten beide Strukturen gemeinsam und in beliebig vielen Varianten auf. Da ein g-Radius einerseits über $r_C=\hbar/mc$ an die formale Wechselwirkung (WW) $\alpha_{fo}=(m/m_o)^2$ koppelt gemäss $R=\alpha_{fo}(r_C)R_{g,v\to c}$, und anderseits via λ gemäss $R=f_g\lambda$ mit der Rezessionsstrahlung verknüpft ist, lassen sich ein r_C-Typ- und ein λ-Typ-9N-MP unterscheiden. Als Folge der endlichen (aktualen) Nukleonenzahl N_u ist die Zahl der Niveaus auf 9 beschränkt. Den Niveaus kommt primär Längen-, sekundär Massenbedeutung zu. Beim r_C-Typ folgen sich Comptonradien, beim λ-Typ λ-proportionale universale Längen in bestimmter geometrischer Progression. Beim idealen, "nicht-abgeregten" MP beträgt der Progressionsschritt 2, beim "abgeregten" MP im Mittel $\zeta_f=\sqrt{\pi}$, entsprechend einer Gesamtabregung für den 9N-MP mit 8 Teilschritten: $(2/\zeta_f)^8=2.628\cong e$. In der nichtsingulären Urkugel vom Ra-

dius R_o ist die gesamte materiale Masse $M_u=N_u m_p$ in Form von Planckmassen-Hanteln auf ein Gitter mit $N_u/2\zeta_g$ Gitterpunkten aufgeteilt. Die Atomzelle je Gitterpunkt ist dann gerade eine Lichtzelle vom Radius R_{LZ} und enthält als "Kern" eine Materiale Planck-Hantel (Matel) vom Radius R_{Pl}. Als Folge von S_γ scheint es zur Matel ein lichtmässiges Analogon zu geben, die Lichtmässige Hantel (Lichtel), bei der entsprechend ζ_g Photonen der Rezessionsstrahlung zu einer Lichtel-Partnermasse aggregieren. Das Lichtelgitter hat demzufolge $N_u S_\gamma/2\zeta_g$ Gitterpunkte mit je einer Lichtel je Gitterpunkt. Die beiden Gitter scheinen für den späteren Aufbau des Universums von extremer Bedeutung zu sein, und gemeinsam mit MP- und s-r-Strukturen aufzutreten. Da es oo viele Atomzellradien x zu adaptieren gilt, gibt es oo viele Matelkristalle(x) und Lichtelkristalle(x), wobei bei konkretem Zellradius x_i der Radius des Lichtelkristalls(x_i) $\sqrt[3]{S_\gamma}=991.46$ mal so gross ist wie jener des Matelkristalls(x_i). Beide Typen haben generell auch die Struktur eines Lyman-s-r-Atoms mit s_{21} als Kern-Radius und $r_{21}=5.6186\ s_{21}$ als Atmosphären-Radius (r_{21} steht abgekürzt für: $r_{i,21}$ in i-ter WW).

Universale Schalenstruktur

Die dem expandierenden Universum zugrundeliegende Quantenstruktur hat beliebig viele Aspekte. Einer davon ist die Schalenstruktur. Der g-Hubble-Radius $R_{g,v\to c}$ markiert lediglich die Grenze des lichtmässig zugänglichen Universums ($z<\infty$). Die Schalenstruktur wird zum Hubble-Rand hin durch die Niveaus von "abgeregten" λ-9N-MP in o- und f-WW bestimmt. So ist $R_{g,v\to c}$ festgelegt durch das Produkt aus der "potentiellen" Nukleonenzahl N_u, und einer elementaren gravitativen Erkennungslänge. Die Erkennungslänge ist dabei ein Schwarzschildradius (SS-Rad.). Da der SS-Radius prinzipiell eine Kommunikationsbarrière darstellt, so fungiert er als Erkennungslänge. Da nun der SS-Radius proportional einer Masse ist, so nimmt beim λ-Typ das Niveau mit der grössten Masse -das Monopolniveau!- auf die maximale Erkennungslänge einerseits, und das Niveau mit der grössten Polzahl - das 256-Pol-Niveau!- auf N_u, anderseits Einfluss. Beim λ-Typ ist wegen $\alpha_{fo}=(m/m_o)^2=R/R_{g,v\to c}$, $m\sim\sqrt{R}$. Da im abgeregten Fall die mittlere Längenprogression ζ_f ist, so ist die Massenprogression $\sqrt{\zeta_f}=s^2=\sqrt[4]{\pi}$. Generell ist dem Dipolniveau für i-WW die ladungsäquivalente Masse $m_i\hat{=}e_i\sim\sqrt{\alpha_i}$ zugeordnet, dem Monopolniveau also $s^2 m_i$. Die Erkennungslänge

ist dann $R_{g,SS}(s^2m_i)=2Gs^2m_i/c^2$. Da alle Längen kohärent oder phasengerecht ausgemessen werden, so wird die grösste Weite des MP durch das Entscheidungsproblem bestimmt, das sich aus dem Niveau mit grösster Polzahl ergibt. Für die phasengerechte Plazierung der 256-Pol-Welle aber sind unabhängig für jeden Pol 2^{256}, also insgesamt $N_u'=256x2^{256}$ Entscheidungen "richtig-falsch" zu treffen. Dies garantiert für Ur-WW (i=o) die Kohärenz auf $R_{g,v\to c}=N_u'R_{g,SS}(s^2m_o)$ als o-WW-monopolare Weite (=Nebenfixstelle). Das Dipolniveau bestimmt mit $R_{g,v\to c}/\zeta_f=R_{gr}$ die Hauptfixstelle, das Quadrupolniveau mit $R_{g,v\to c}/\zeta_f^2=D_{g,SS}(M_u)$ den SS-Durchmesser der Gesamtnukleonenmasse M_u, das Oktupolniveau mit $R_{g,v\to c}/\zeta_f^3=s_{g,21}=R_{g,SS}(M_u)$ etc.. Da $m_f=m_p=m_o/\zeta_f$ ist, kommen die starken oder f-WW-MP-Niveaus von R_{gr} an mit jenen des o-WW-MP zur Deckung. Dies beleuchtet die hohe Auszeichnung von $R_{gr}=Z_o=s_{g,ool}=r_{g,ool}$ als Hauptfixstelle. Fazit: Die ersten 4 Niveaus des abgeregten o-WW-MP bzw. 3 des f-WW-MP koinzidieren sehr angenähert mit Niveaus des Lyman-s-r-Atoms in g-WW (Quasar-Galaxie-Assoziationen!). Anderseits ist die g-Bohrzelle $a_g=\lambda\!\!\!^{-}_e/\alpha_g=R_{g,v\to c}/e$ in N_u Längen ausgemessen. Damit ergibt sich für die aktuale Nukleonenzahl $N_u=2^{264}/e=1.090x10^{79}$, in guter Uebereinstimmung mit dem genaueren Wert des Parametermodells, $N_u=1.1082x10^{79}$. Damit lassen sich im Prinzip alle dimensionslosen Grössen des PM-Modells als reine Zahlenausdrücke darstellen.

Elementarteilchen, Quark- und Superformmassen

Im Gegensatz zur universalen Schalenstruktur folgen die wichtigsten Mikromassen einem r_C-9N-MP. Der monopolaren Comptonlänge gehört jetzt wegen $r_C=\hbar/mc$ die kleinste Masse an, und die Massenprogression ist ζ_f. Mit wachsender Polzahl bzw. kürzerer Niveaulänge, wächst die Masse. m_i bleibt dem Dipolniveau zugeordnet. Proton-Nukleon und Elektron stehen in direkter Beziehung zum Urzustand. Das Proton-Nukleon ist ein Matelkristall(R_{Pl}), das Elektron näherungsweise ein Lichtelkristall($\zeta_f R_{Pl}$). Beide haben Lyman-s-r-Struktur. Rein bildlich gesprochen entsteht das Proton-Nukleon dadurch, dass die Urkugel R_o die Lichtzelle R_{LZ} am Gitterpunkt auf den Raum einer Matel R_{Pl} schrumpfen lässt, und das "Elektron-Atom", indem das Volumen des Gitterpunkts auf den Sphärenradius $\zeta_f R_{Pl}$ schrumpft. Durch diese ideelle Form der Nachbildung des Urzustands wird im Fall der Elementarmassen in der Reihenfolge Müon, Pion, u,d-Q, s-Q, p, c-Q etc. die Comptonzelle des Matelkristalls "2π-topologisch"

auf Dimensionen $\{R_{Pl}$ ausgedehnt und solchermassen fiktiv die Grenze maximaler Elementarteilchenmasse M_{Pl} überwunden. Der Uebergang liegt bei $\sqrt{2}R_{Pl}$, da für $M_{Pl}/\sqrt{2}$ g-SS- und Comptonradius übereinstimmen. $\sqrt{2}R_{Pl}=1.414R_{Pl}$ liegt zwischen R_{Pl} und $\zeta_f R_{Pl}$, d.h. zwischen den zu R_{Pl} und $\zeta_f R_{Pl}$ proportionalen Dipol- und Monopollängen eines m_p-regierten f-WW-r_C-9N-MP, und entspricht dem 1-dimensionalen Heim-Metron $\sqrt{\tau}=\sqrt{3\pi/4}\ R_{Pl}=1.534R_{Pl}$ [2]. Dies kreiert zusätzlich zum f-WW-MP einen um ζ_f displazierten f'-WW-MP mit $m(s\text{-}Q)=m_p/\zeta_f$ als f'-WW-Aequivalentmasse. Die intrinsische f'-WW ist dann $\alpha_{f'}=((m_p/\zeta_f)/m_o)^2=\alpha_f/\pi=\pi^{-2}=0.101$ $(=g/\hbar c)$, und die displazierte WW $\alpha_{f''}=\alpha_f/\zeta_f=\zeta_f^{-3}=\pi^{-3/2}=0.1795$ $(=\alpha_{QCD}$ [3]). In diesem Licht werden viele Teilcheneigenschaften verstehbar. Sowohl Proton wie Elektron haben eine sehr komplexe Struktur. In der Urgitternäherung betragen m_p- und m_e-Masse: $m_p=(\hbar/c)(r_{21}/s_{21})/(\sqrt[3]{N_u/2\zeta_g}\ R_{Pl})=1.625\text{x}10^{-27}$kg, und $m_e=m_p/(\sqrt[3]{S_\gamma}\zeta_f)=0.924\text{x}10^{-30}$kg. Tab. 1 zeigt $m_p\zeta_f^i$ (1.Ng.) und 3-QS-Hybridisierung (2.Ng.) im Fall von u,d-,s- und c-Quarks im Vergleich zur Beobachtung oder PM-Wert für den f'-MP und i=-2,-1,0,..6. i=-3 gehört nicht zum MP und stellt mit $r_C(m_\pi)$ die Nukleonatmosphäre zum s-r-Atom mit dem Kern $r_C(m_p)=\hbar/m_p c$ und i=0. $r_C(m_p)$ wiederum ist Atmosphäre zu $r_C(b\text{-}Q)$ mit i=3; $r_C(b\text{-}Q)$ selbst ist Atmosphäre zum s-r-Atom mit dem Kern $r_C(t\text{-}Q)$ und i=6. i=-2 liefert mit $r_C(u,d\text{-}Q)$ die Atmosphäre zum Atom mit dem Kern $r_C(c\text{-}Q)$ und i=1. In Multibedingung gibt es Koinzidenzen mit andern Elementarteilchen und Fleck-Superformmassen $m_{F,\Delta i}$.

Tabelle 1

i	$\zeta_f^i m_p$(kg) 1.Ng.	2.Ng.	Beob.od.PM(kg)		Bedeutung
6	5.18x(-26)		ca. 5.5 x(-26)	m(t-Q)	top-Quark [4]
5	2.92x(-26)				
4	1.65x(-26)		1.685x(-26)	m(Y)	Y($b\bar{b}$)-Masse
3	9.31x(-27)		ca. 8.91 x(-26)	m(b-Q)	bottom-Quark
2	5.25x(-27)		5.524x(-27)	$m_{F,\Delta o}$	F-o-WW-Superformmasse
1	2.96x(-27)	2.655x(-27)	2.673x(-27)	m(c-Q)	charm-Quark, $m_{F,\Delta f,\Omega}$
0	1.67x(-27)		1.672x(-27)	m_p	Protonmasse
-1	9.43x(-28)	9.012x(-28)	9.002x(-28)	m(s-Q)	strange-Quark, $Z_o(m_{F,\Delta o})$
-2	5.32x(-28)	5.571x(-28)	5.526x(-28)	m(u,d-Q)	up,down-Quark, $m_{F,\Delta s}$
-3	3.00x(-28)		2.488x(-28)	m_π	Pionmasse

Literatur

[1a-e] J.T. Muheim, Helv. Phys. Acta a) 57, 781 (1984); b) 57, 787 (1984); c) 58, 902 (1985); d) 59, 173 (1986); e) 59, 177 (1986)

[2] B. Heim, Elementarstrukturen Bd.1 (Resch, Innsbruck 1980) p. 61

[3] Chris Quigg, Spektrum der Wissenschaft, Juni 1985, p. 110

[4] H. Spitzer und B. Kröger, Phys. Bl. 37, 73 (1981) Nr. 3

ZUR UNIVERSALITAET DES SONNENSYSTEMS: GROSSE HALBACHSEN DER BAHNELLIPSEN

J.T. Muheim, Lab. für Festkörperphysik ETHZ, Hönggerberg, 8093 Zürich

Auszug: Die dem Sonnensystem zugrundeliegende Quantenstruktur (Standard-Sonnensystem) ist universell und gehorcht einem λ-Typ-Neun-Niveaus-Multipol. Aus der Hybridisierung des Multipols mit einer adaptierten s-r-Struktur lassen sich die grossen Halbachsen der Ellipsenbahnen mit guter Genauigkeit bestimmen. Zahlreiche Eigenschaften wie Planetenmassen, -dichten, Rotation, Anzahl Satelliten etc. lassen sich anhand der s-r-Quantenstruktur verstehen, und scheinen einem universellen Muster zu folgen.

Einführung

Dem Sonnensystem, bestehend aus der Sonne als Zentralgestirn und 9 in annähernd geometrischer Progression plazierten Planeten (ohne Neptun, und die Planetoiden schwerpunktsmässig vertreten durch Ceres!), liegt ein Quantensystem zugrunde, das selber universell ist und somit allen gleichartigen stabilen Systemen des Universums als Gerüst dient. Die grossen Halbachsen der Planetenbahnen lassen sich daher wechselwirkungskosmologisch bestimmen. Die Ableitung ist im Prinzip einfach, setzt jedoch umfassende Modellkenntnis voraus. Aus Platzgründen muss alles Begriffliche aus früheren Arbeiten übernommen werden. Die Struktur des Sonnensystems (Bahnen, Dichten, Massen, Rotation, Satelliten, Asteroidenverteilung etc.) gilt als ein ungelöstes Problem. Für die Bahnradien sind zwei empirische Formeln bekannt: a)das Titius-Bode-Gesetz $r_i=0.4+0.3x2^n$ (AE), mit n=-oo,0,1,2...7 für i=Merkur, Venus,...Pluto, und b) $r_i=r(\text{Erde})xk^n$, mit r(Erde)=1AE (Astronomische Einheit=$1.495x10^{11}$m), n=-2,-1, 0,1,...6 und $k\cong 1.85$. a) ist unphysikalisch, beschreibt aber die Radien erstaunlich genau; b) ist physikalisch, dafür aber weniger genau. In Wirklichkeit liegt dem Sonnensystem ein λ-Typ-9-Niveaus-Multipol (λ-9N-MP) zugrunde. Wäre der MP ideal, d.h. quantenphysikalisch "nicht-abgeregt", so hätten benachbarte Niveaus die Längenprogression 2, gemäss 2^n-Term in a); wäre er "homogen abgeregt", so wäre die mittlere Progression (gleich Basis der geometrischen Folge) gerade gleich der "starken large number" $\zeta_f=1/\sqrt{\alpha_f}=\sqrt{\pi}=1.772$. entsprechend b). In Wirklichkeit sind beide Aspekte realisiert. Der Grund da-

für ist, dass in dieser Näherung 2 fundamentale Quantenstrukturen bahnbestimmend sind: der MP und die s-r-Struktur. Dies führt zu einem "deformierten abgeregten" MP. Die Deformation ist eine Folge der Hybridisierung des MP mit dem adaptierten s-r-System. Das Ergebnis ist folgendes: der MP ist zwar als ganzer "abgeregt", entsprechend einem Grundzustand; jene Bahnen, denen Koinzidenzen von MP-Niveaus mit s-r-Niveaus zugrundeliegen, zeigen annähernd formale Idealprogression 2. Dies ist für Pluto, Uranus, Saturn und Merkur der Fall. Die Globalabregung, entsprechend einer Kontraktion des Quantensystems um ca. e, muss sich daher auf die übrigen Bahnen verteilen. Durch einen einfachen Ansatz gelingt die Lösung fast exakt. Die WW-kosmologischen Eigenschaften der s-r-Struktur machen auch die übrigen Eigenschaften des Sonnensystems plausibel.

Grösse des Sonnensystems

WW-kosmologisch gehen alle Quantenstrukturen des Universums aus dem Urzustand hervor, charakterisiert durch den nichtsingulären Urradius R_o. Als Folge der Phasenraumsymmetrie existieren zu R_o zwei nichtunendliche Endradien R_e und $R_{e'}$, je nachdem ob die Abbildung im Phasenraum über die Hauptfixstelle R_{gr} oder die Nebenfixstelle $R_{g,v\to c}$ erfolgt. Der durch die Hauptachse des fernsten Planeten Pluto charakterisierte Quantenraum des Systems steht in direkter Verknüpfung zu R_o und $(R_e+R_{e'})/2$:

(i) Der Systemraum ist gleich der KKW-Synchronwelt zur Ursphäre $R_o=2.746\mu$. Wenn nach dem Urknall die Lichtfront formal nach $t_o=R_o/c$ den nichtsingulären Rand R_o erreicht, hat die dazu synchrone "Kleine Kohärenzwelle" KKW mit der Supergeschwindigkeit $v_{KKW}=(a_b/a_w)c=(\alpha_{GW}/\alpha_g)c=2.114\text{x}10^{18}c=6.337\text{x}10^{26}ms^{-1}$ den Systemrand r(Pluto) erreicht. v_{KKW} fungiert wahrscheinlich als Bewusstseinsgeschwindigkeit, und aus α_{GW} leiten sich die elektromagnetischen EEG-Wellen des Gehirns ab (Elektroenzephalogramm). $r(\text{Pluto})=v_{KKW}t_o=5.804\text{x}10^{12}m=38.82$ AE.

(ii) Der Systemraum ist gleich der Strahlungskavität zum universalen Endradius $(R_e+R_{e'})/2=1.003\text{x}10^{42}m=1.061\text{x}10^{26}Lj$. Die mit der g-Rezession des Universums einhergehende Planckstrahlung erreicht durch Rotverschiebung am nichtunendlichen Endrand für die typische Wellenlänge den Wert $\lambda_e=(R_e+R_{e'})/2f_g=5.785\text{x}10^{12}m=38.69$ AE. λ_e entspricht dem Radius der Strahlungskavität und koinzidiert mit dem Systemradius. Es gilt dabei: $R_e=\sqrt{R_{gr}^3/R_o}=5.956\text{x}10^{41}m$, $R_{e'}=$

$$\sqrt{R^3_{g,v\to c}/R_o} = 1.412\text{x}10^{42}\text{m}$$

Halbachsen für mittlere (äquiprogressive) und hybridisierte "abgeregte" Progression

Nach der WW-mässigen Form des Hubble-Gesetzes sind beim λ-MP die den Niveaus zugeordneten Längen proportional einer Masse im Quadrat. Da beim λ-Typ die Massenprogression $s^2=\sqrt{\zeta_f}=\sqrt[4]{\pi}$ beträgt, so folgt in der Tat für die Längenprogression ζ_f. Dem entspricht beim "abgeregten" MP mit 9 Niveaus und 8 Progressionsschritten im Vergleich zum idealen MP die Abregung $(2/\zeta_f)^8=2.628\cong e=2.718$. Dazu gehören die "äquiprogressiven" Halbachsen (1.Näherung!): $r_i=r(\text{Pluto})\text{x}\zeta_f^{-i}$ mit i=0,1,2,...8 für Pluto, Uranus,...Merkur. Für i=8 folgt $r_8=r(\text{Merkur})=r(\text{Pluto})\text{x}\zeta_f^{-8}$ = 0.398 AE. Die deformierende s-r-Struktur ist an den λ-9N-MP adaptiert gemäss der Funktion

$$f(r_i) = 1 + (\frac{r_{21}}{s_{21}} - 1)(\frac{r_i - r(\text{Merkur})}{r(\text{Pluto}) - r(\text{Merkur})})$$

Dabei gilt für eine diskrete aber sonst beliebige WW für die s-r-Verhältnisse der Lyman-Serie $r_{m1}/s_{21}=(4/3)^4/(1-m^{-2})^2$ und $s_{m1}/s_{21}=\{(4/3)(1-m^{-2})\}^4$. Tab. 1 zeigt, dass in der äquiprogressiven 1. Näherung $f(r_i)$ und r/s bzw. s/s für Pluto, Uranus, Saturn und Merkur fast ideal übereinstimmen. Diese Niveaus hybridisieren paarweise zu 100%. Hybridisierung bedeutet "Anregung", deshalb haben sie formal Idealprogression 2. Formal deshalb, weil die Progression als Längenverhältnis an sich auf das Intervall zugeschnitten ist. Daraus folgt, dass die Globalabregung e sich auf die 6 Intervalle zwischen Saturn und Merkur aufteilen muss.

Tabelle 1

Planet	i	r_i(AE)	1.Ng.	$f(r_i)$	s-r-Zustand
Pluto	0	38.82		5.618	$r_{21}/s_{21}=5.618$
Uranus	1	21.90		3.584	$r_{41}/s_{21}=3.596$
Saturn	2	12.35		2.436	$s_{41}/s_{21}=2.441$
Jupiter	3	6.97		1.790	$s_{31}/s_{21}=1.973$
(Ceres)	4	3.93		1.424	
Mars	5	2.21		1.217	
Erde	6	1.25		1.102	
Venus	7	0.70		1.037	
Merkur	8	0.39		1.000	$s_{21}/s_{21}=1.000$

Es ist naheliegend, für den Abfall von den beiden Randniveaus ins Intervallinnere einen linearen Ansatz zu machen. Die mittlere Progression für 6 Schritte

ist nun $2/\sqrt[6]{2.628}=1.702$. Da auf der Saturnseite die Hybridisierung von der grossen Zustandsdichte s_{31} und den oo vielen Niveaus bis s_{ool} bzw. r_{21} profitiert, erfolgt der Abfall langsamer als auf der Merkurseite, wo nur das Niveau s_{21} mit überdies kleiner Zustandsdichte (wegen Z_f!) wirkt. Der das Minimum markierende Geradenschnittpunkt liegt im Fall einer 1/5-Teilung bei Venus, im Fall einer 2/4-Teilung bei der Erde. Die Rechnung ist elementar und das Ergebnis der Progression $a_{i,i+1}$ für die Fälle 1/5 und 2/4 zusammen mit der Beobachtung in Tabelle 2 widergegeben.

Tabelle 2

Planet	i	$a_{i,i+1}(1/5)$	$a_{i,i+1}(2/4)$	Beobachtung
Pluto	0	2	2	2.05
Uranus	1	2	2	2.01
Saturn	2	1.9405	1.9251	1.83
Jupiter	3	1.8215	1.7768	1.87
(Ceres)	4	1.7025	1.6282	1.82
Mars	5	1.5835	1.4794	1.52
Erde	6	1.4645	1.5534	1.38
Venus	7	1.7025	1.8510	1.84
Merkur	8			

In Tabelle 3 sind für den Fall 1/5 die Werte der grossen Bahn-Halbachsen in der 2. Näherung des deformierten λ-9N-MP zusammen mit der Beobachtung widergegeben. Die Uebereinstimmung liegt bei einigen %. $r_i=r(\text{Pluto})/\prod_{\nu=0}^{i} a_{\nu-1,\nu}$ mit $a_{-1,0}=1$ und $r_0=r(\text{Pluto})=38.82$ AE. 2^i ist gleich der Polzahl des Niveaus, also Monopol für Pluto, Dipol für Uranus..., 256-Pol für Merkur.

Tabelle 3

Planet	r_i(AE) 2.Ng.	r_i(Beobachtung)	Abweichung (%)
Pluto	38.82	39.52	(-1.7)
Uranus	19.41	19.20	(1.1)
Saturn	9.705	9.54	(1.7)
Jupiter	5.001	5.20	(-3.8)
(Ceres)	2.745	2.77	(-0.9)
Mars	1.612	1.52	(6.0)
Erde	1.018	1.00	(1.8)
Venus	0.695	0.72	(-3.4)
Merkur	0.408	0.39	(4.6)

Typisch biomentale Modellgrössen sind: $a_w=\lambda\!\!\!^{-}_e/\alpha_w=\lambda\!\!\!^{-}_{C,b}=7.695\text{x}10^{-2}$m, schwacher Bohrradius (=Comptonradius Gehirnsphäre); $a_b=\lambda\!\!\!^{-}_e/\alpha_b=\lambda\!\!\!^{-}_{C,b'}=1.627\text{x}10^{17}$m=17.2 Lj, superschwacher Bohrradius (=Radius kosmische Gesellschaftszelle). $\alpha_{GW}=1.250\text{x}10^{-20}$, WW elektromagnetischer Gehirnwellen (EEG: β=20.2Hz, α=10.24, θ=5.05, δ_2=2.69)

Hochempfindliche photoakustische Zelle zur Detektion von Luftschadstoffen

St. Bernegger, P.L. Meyer und M.W. Sigrist
Physik-Departement, ETH, Hönggerberg, CH-8093 Zürich

Um einen möglichst empfindlichen photoakustischen Detektor zu konstruieren, wurden mit einem Computerprogramm akustische Spektren von verschiedenen Zellkonfigurationen berechnet. Das neue Modell verwendet kontinuierliche akustische Impedanzen und liefert akustische Spektren in sehr guter Uebereinstimmung mit experimentellen Daten. So konnte eine sehr empfindliche Zelle entworfen werden, mit welcher ein minimaler Absorptionskoeffizient von ca. 10^{-9} cm^{-1} pro Watt Laserleistung nachweisbar ist. In Kombination mit einem CO Laser wird die Zelle zur selektiven Messung von Luftschadstoffen in kleinen Konzentrationen eingesetzt.

Anstieg der atmosphärischen Methankonzentration

G. Fischer und B. Stauffer, Physik. Institut der Universität Bern, Sidlerstrasse 5, 3012 Bern

Luft in den Blasen sehr kalten Eises hat annähernd die gleiche Zusammensetzung wie die atmosphärische Luft zur Zeit der Eisbildung. Wir haben die Luft aus Eisproben von Siple Station (Westantarktis) extrahiert und deren Methankonzentration gemessen. Die Ergebnisse erlauben es, den Anstieg der atmosphärischen Methankonzentration während den letzten 200 Jahren zu rekonstruieren. Der Anstieg der Methankonzentration ist durch ein Anwachsen der Quellen, möglicherweise aber auch durch eine Verlangsamung des Abbaus bedingt. Eine höhere Methankonzentration hat wegen des Treibhauseffekts eine globale Temperaturerhöhung zur Folge.

The Cold Arctic Mesopause Project (CAMP) 1982

E. Kopp, F. Bertin, L.G. Björn, P.H.G. Dickinson, C.R. Philbrick and G. Witt
Physikalisches Institut, Sidlerstr. 5, 3012 Bern

The mesopause at high latitudes in summer is known to possess the highest clouds of the earth atmosphere, named noctilucent clouds (NLC). The formation of NLC in the summer arctic mesosphere is associated with a region having the coldest atmospheric temperatures. Results from several rocket measurements to study the physics and chemistry of NLCs in summer 1982 above Kiruna will be presented. The rocket measurements were supported by ground based, airplane and satellite remote sensing experiments.

$^{13}C/^{12}C$-Verhältnis von in altem Polareis eingeschlossenem Luft-CO_2

H. Friedli, H.P. Lötscher, U. Siegenthaler, Physik. Institut der Universität Bern, Sidlerstr. 5, 3012 Bern

Infolge der Produktion von Kohlendioxid durch fossile Brennstoffe und Waldrodungen nimmt das $^{13}C/^{12}C$-Verhältnis in der Atmosphäre ständig ab. Messungen an Luftblasen in Eisbohrkernen von Siple-Station (Antarktis) erlauben es nun, den Verlauf der CO_2-Konzentration und des $^{13}C/^{12}C$-Verhältnisses der Atmosphärenluft zwischen 1750 und 1950 detailliert zu rekonstruieren. Die Resultate zeigen, dass bereits im 19. Jahrhundert grössere Mengen an CO_2 (durch Rodungen) in die Atmosphäre gelangten.

Cosmic-ray effects in a meteorite from the Moon and their interpretation

O. Eugster[1], J. Geiss[1], U. Krähenbühl[2] and S. Niedermann[1]
[1]Physikalisches Institut, Universität Bern, Sidlerstr. 5, 3012 Bern
[2]Anorg. chem. Institut, Universität Bern, Freiestr. 3, 3012 Bern

A small meteorite (Allan Hills A81005), collected on the Antarctic ice in 1982, has been recognized to be a lunar rock. Our study of the cosmic-ray produced noble gas isotopes within this meteorite leads to the conclusion that the A81005 material resided during 580 million years at a shallow depth below the lunar surface. After ejection from the Moon as a result of a large meteorite impact, A81005 travelled in free space for less than a few million years. From the concentration of the cosmic-ray produced radioisotope ^{81}Kr we calculate the capture by the Earth to have occurred more than 140'000 years ago.

Xenon isotopes in old lunar rocks: A clue for the origin of the Moon?

O. Eugster
Physikalisches Institut, Universität Bern, Sidlerstrasse 5, 3012 Bern

Lunar rock 60018 collected during the Apollo 16 mission contains Xe with an isotopic composition very similar to terrestrial Xe. This is a unique situation for extraterrestrial matter as meteoritic Xe and modern solar wind Xe are isotopically different from Xe in the terrestrial atmosphere and rocks. This lunar Xe may have been acquired during lunar formation or it may be old solar wind Xe. The similarity of lunar trapped Xe with terrestrial atmospheric Xe would be of considerable importance elucidating the formation of the Earth-Moon system.

ANDO III : Laser, électronique quantique

GRAZING-INCIDENCE FIR GAS LASER WITH PHASE MATCHING

D. Wildmann, S. Gnepf and F.K. Kneubühl
Institute of Quantum Electronics, Physics Department, ETH
CH-8093 Zurich, Switzerland

In recent years the optically pumped 496 μm CH_3F laser [1] proved to be a valuable tool for the development of new types of gas lasers, i.e. the linear distributed feedback (DFB) gas laser [2], the helical feedback (HFB) laser [3] and the grazing-incidence gas laser [4]. In this paper we report on a grazing-incidence and DFB gas laser with phase matching by a variable gap in the periodic waveguide.

The experimental arrangement is similar to that described in [4]. Fig. 1 shows a schematic view of our rectangular waveguide with periodic corrugations and a variable gap D for phase matching.

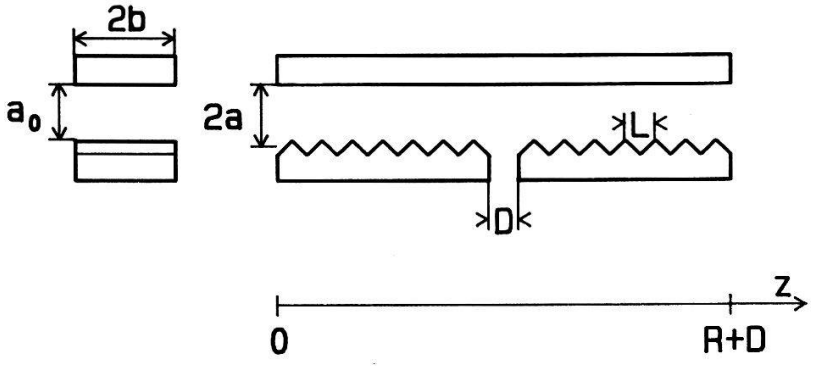

Fig. 1 Schematic of waveguide

We apply the perturbation theory of corrugated waveguides [5] to the special case of a two-mode coupling which combines a forward (+) with a backward (-) mode. We restrict our considerations to $TM_{m_+n_+}$-$TM_{m_-n_-}$ coupling since in our experiment only these two modes couple efficiently [2,5]. The index $m_\pm$ indicates the transverse mode number with respect to the width 2b (Fig. 1) of the rectangular waveguide while $n_\pm$ is the transverse mode number with respect to the height a_0. The symmetry of the waveguide requires that m_+ equals m_-.

For the limit of high threshold gain we have derived a resonance condition which is similar to that found by Kogelnik and Shank [6]. We have demonstrated experimentally the validity of this approximation with the aid of uniform gratings for first- and for second-order DFB [4].

In order to achieve laser oscillation near the Bragg frequency and to take advantage of DFB performance in the stopband [7] we have introduced a variable gap D in the center of the corrugation. On the basis of the perturbation theory [5] we have derived a resonance equation for resonances inside the stopband:

$$(\beta_+ - \beta_-)\, D = 2\ \mathrm{arctg}\left(\frac{\gamma}{\Delta}\ \frac{(1 + \exp(-\gamma R))}{(1 - \exp(-\gamma R))}\right) \qquad (1)$$

$\beta_\pm$ are the propagation constants of the forward or the backward mode, Δ is the detuning factor and is given by

$$\Delta = (\beta_+ - \beta_- - 2\pi/L)/2 \qquad (2)$$

and γ is defined as

$$\gamma = (\kappa^2 - \Delta^2)^{1/2} \qquad (3)$$

κ is the coupling constant given by the perturbation theory [5]. In Fig. 2 the theoretical resonance condition is plotted as a function of the gap D for different mode couplings. For a wavelength λ_{guide} = 0.5 mm, a gap

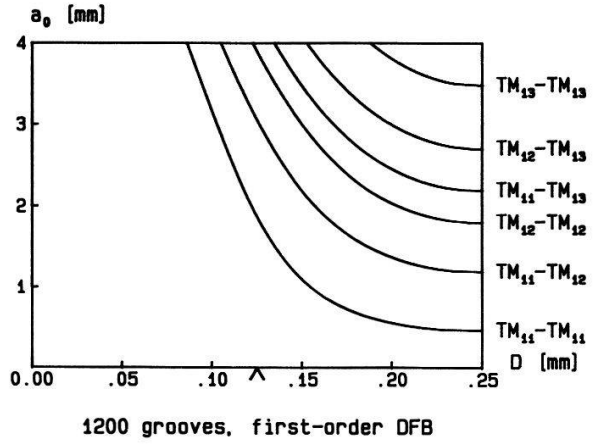

Fig. 2 Resonance condition

D = 0.125 mm corresponds to a phase shift $\phi = \pi$ per roundtrip. Therefore, this gap implies a laser oscillation exactly at the Bragg frequency ($\Delta = 0$), i.e. in the center of the stopband.

In Fig. 3 we present an example of a mode coupling inside the stopband. At a gap D = 0, which corresponds to a grating without discontinuity, no emission is observed. A resonance occurs first at a gap D_1 = 0.17 mm which is near the stopband center of D = 0.125 mm. The same resonance is reproduced at a gap D_2 = 0.42 mm. As expected, the difference of D_1 and D_2 corresponds to half the guide wavelength. According to Fig. 2 this resonance corresponds approximately to the TM_{11} - TM_{13} coupling.

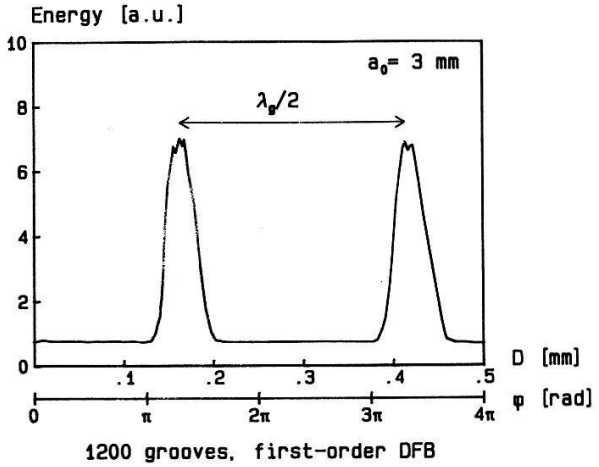

Fig. 3 Gap scanning

In conclusion we have demonstrated first operation of a grazing-incidence gas laser inside the stopband by the introduction of a variable phase shift in the center of the DFB structure. The higher feedback inside the stopband improves the DFB performance, e.g. a low threshold gain.

References

[1] T.Y. Chang, T.J. Bridges, Opt. Comm. 1, 423 (1970); Proc. Symp. on Submillimeter Waves, Polytechnic Press, N.Y., 93 (1970)

[2] E. Affolter and F.K. Kneubühl, IEEE J. Quantum Electron., QE-17, 1115 (1981)

[3] H.P. Preiswerk, M. Lubanski, S. Gnepf and F.K. Kneubühl, IEEE J. Quantum Electron., QE-19, 1452 (1983)

[4] D. Wildmann, X. Zheng, H.P. Preiswerk and F.K. Kneubühl, Int. J. Infrared and mmWaves, 5, 537 (1984)

[5] N.F. Kovalev et al., Sov. Phys.: Radio Phys. and Quant. El. 11, 449 (1968)

[6] H. Kogelnik, C.V. Shank, J. Appl. Phys. 43, 2327 (1972)

[7] S.H. Kim, C.G. Fonstad, IEEE J. Quantum Electron., QE-15, 1405 (1979)

RF-EXCITED DISCHARGES FOR A 10 μm DFB CO_2 LASER

W. Leuthard and F.K. Kneubühl,
Institute of Quantum Electronics, Physics Department, ETH
CH-8093 Zurich, Switzerland

1. Introduction

Distributed Feedback (DFB) was first introduced by Kogelnik and Shank [1] in a dye laser in 1971. Later, Affolter and Kneubühl [2] also realized DFB in a gas laser with the 496 μm emission of CH_3F. The advantage of DFB over standard external mirrors is longitudinal mode selection, especially for the broad gain profiles caused by high laser-gas pressures, e.g. in CO_2 lasers.

Hitherto, many attempts have been made to operate a 10 μm DFB CO_2 laser [3]. Sufficient feedback in periodic waveguides of DFB gas lasers is achieved only for waveguide heights less than 10 λ [2,3] which implies severe problems concerning excitation of the laser gas. After experiments with transverse and longitudinal excitation we have succeeded to produce homogeneous and stable discharges with RF excitation for DFB waveguides with heights of less than 100 μm.

2. Apparatus

The walls of the open waveguide are used as the electrodes of the RF-discharge. One wall consists of a titanium structure covered with a thin evaporated gold layer. The structure includes a grating of 40 mm x 30 mm, a periodicty of 4.8 μm and a corrugation depth of 2.4 μm. A 3 mm broad gold stripe evaporated on a quartz glas is used as the opposite wall of the waveguide. Perpendicular to this stripe there is a 3 mm broad and 20 mm long electrical connection. Therefore, the discharge covers a total area of 180 mm^2. The waveguide is adjusted during operation the differential micrometers through the wall of the gas chamber. The laser is tuned by variation of the waveguide height and, consequently the guide wavelength.

The discharge circuit consists of the capacity of the waveguide and a coil. A π-network matches the circuit to a 50 Ohm cable. The circuit is driven by a "hp 3200 B VHF" oscillator followed by a 30 W 110 MHz "Amplifier Research" amplifier. The power consumed by the discharge circuit is determined with two standing-wave-ratio meters.

3. RF-Discharges

We have operated RF-discharges in gaps of 40 μm to 100 μm at excitation frequencies between 85 MHz and 90 MHz. The circuit had to be tuned by frequency variation. As gas we have used CO_2:N_2:He mixtures of 6:18:76, 20:20:60, 17:33:50, etc. at pressures between 150 and 400 mbar. At higher pressures the discharge becomes instable. For lower pressure the discharge burns outside the gap because of the geometrical arrangement and Paschen's law.

Since we do not dispose of an HF probe suited for the measurement of the voltage over the electrodes during the discharge, we could determine only the breakdown voltage as a function of the gas pressure. For an electrode separation of 60 μm we observe a minimum breakdown-voltage amplitude of 380 V at a pressure near 210 mbar. The corresponding breakdown RMS voltage of 270 V is slightly more than the breakdown DC voltage of the same gas mixture. For a waveguide height of 40 μm the conditions are even more critical.

From our voltage and pressure measurements we find a characteristic ratio $E/N = 5 \cdot 10^{-15}$ Vcm^2 which is high compared to $E/N = 3 \cdot 10^{-16}$ Vcm^2 typical for standard CO_2 laser plasmas. The high E/N ratio is due to the high amplitudes of the electron oscillation [4] in the discharge which causes high wall losses. Thus, this E/N ratio should be lowered by an increase of the excitation frequency by a factor of 10.

4. Conclusion

In contrary to DC-discharges, homogeneous and stable RF-discharges can be maintained over a relative large area even at small electrode separations of the order of magnitude of 50 μm.

5. References

[1] H. Kogelnik and C.V. Shank:
Appl. Phys. Lett. 18, 152 (1971)

[2] E. Affolter and F.K. Kneubühl:
Phys. Lett. 74A, 407 (1979);
IEEE J. Quantum Electron. QE-17, 1115 (1981)

[3] R.O. Miles and R.W. Grow:
IEEE J. Quantum Electron. QE-14, 275 (1978); QE-15, 1396 (1979);
QE-17, 1071 (1981)

[4] D. Hey, C.J. Baker and D.R. Hall:
J. Appl. Phys. 55, 4120 (1984)

Neue Laserlinien in $YAlO_3$:Er bei 1.7 µm

M. Dätwyler, W. Lüthy und H.P. Weber
Inst. für angew. Physik, Universität Bern, Sidlerstr. 5, 3012 Bern

Erbium dotierte YAG oder $YAlO_3$ Kristalle emittieren bei Zimmertemperatur Laserlinien bei 0.8 µm, 1.7 µm und 3 µm. Insbesondere die Wellenlänge bei 1.7 µm ist wegen ihrer Augensicherheit, der guten Detektierbarkeit und der guten Transmission durch feuchte Luft zur Entfernungsmessung geeignet. Es ist uns gelungen in $YAlO_3$:Er neben der bekannten Laserlinie bei 1.663 µm drei neue Linien bei 1.678 µm, 1.708 µm und 1.729 µm zur Lasertätigkeit anzuregen. Die Linien lassen sich mit einem Etalon im Resonator einzeln abgleichen. Es sind Uebergängen zwischen den Stark-aufgespaltenen zwei Linien des $^4S_{3/2}$ Niveaus und fünf Linien des $^4I_{9/2}$ Niveaus. Die Reihenfolge der Laserschwellen der vier Linien ist in guter Uebereinsstimmung mit theoretischen Vorausagen. Das Laserlicht ist polarisiert, wobei die Polarisation der Linie bei 1.663 µm senkrecht zu den drei anderen Linien ist. Die Laserparameter werden diskutiert.

Laser-induzierte reversible Absorption in planaren SiO_2-TiO_2 Wellenleitern

R. Jenny und W. Lukosz
Professur für Optik, ETH, 8093 Zürich

Bei Bestrahlung mit Excimer-(λ=308 nm) und Farbstoff-Laser-Pulsen wurde in — mit einem Tauch-Beschichtungs-Verfahren (Sol-Gel Prozess) hergestellten — SiO_2-TiO_2 Wellenleitern eine starke laser-induzierte Absorption (Bildung von Farbzentren) beobachtet, welche zur Belichtung proportional ist. Gemessen wurde die Dämpfung geführter TE_o und TM_o Moden; die Absorption nimmt als Funktion der Wellenlänge vom blauen zum roten Spektralbereich ab. Die induzierte Absorption ist reversibel, die Abklingzeiten liegen bei Raumtemperatur im Minuten-, bei Temperaturen um 100°C im Sekundenbereich.

ANDO IV : Application de lasers

FIELD CALCULATIONS ON A NEW LASER PARTICLE ACCELERATOR

S. Gnepf+, J. Arnesson+, F.K. Kneubühl+,
D. Billeter*, M. Nessi*, W. Neumann*, W. Wölfli*
+ Institute of Quantum Electronics, ETH, CH-8093 Zurich, Switzerland
* Institute of Medium Energy Physics, ETH, CH-8093 Zurich, Switzerland

Abstract : We present results of field calculations for a new infrared-laser accelerator scheme [1] which makes use of hollow oversized linear periodic and helical waveguide structures orginally designed for distributed feedback (DFB) and helical feedback (HFB) lasers.

1. Introduction

The present performance of high-power IR, VIS and UV lasers suggests that in particle accelerators [2] the microwave sources could be replaced by powerful lasers [3-5]. Their short wavelengths would increase field gradients and, therefore, either reduce the size or increase the particle energy of the accelerators. Here we report on field calculations for a new particle-accelerator scheme [1] based on oversized periodic [6] or helical [7] waveguides and driven by 10 μm CO_2 or submillimeter-wave free-electron lasers.

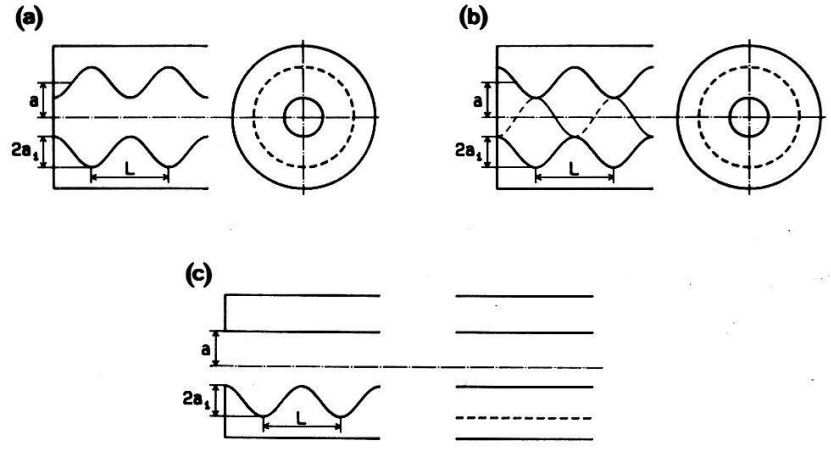

Fig. 1 Three types of corrugated waveguides

Mode-coupling in a corrugated waveguide

In Fig. 1 we show three types of harmonically corrugated structures: linear periodic cylindrical (a) and helical (b), as well as linear periodic parallel-plate (c) waveguide. For a_1 considerably smaller than a and the wavelength λ, the effect of the corrugation can be described by perturbation theory [8]: A forward running mode is scattered into a backward running mode. The corrugation acts as a slow-wave structure: Although in the unperturbed waveguide the phase velocities of the modes are always greater than the speed of light, phase velocities equal to or smaller than the speed of light can be achieved in the corrugated structure. This is illustrated by the dispersion relation $\beta(\omega)$ in Fig. 2. A typical feature shown is the stopband at $Re\beta = \pi/L$. The width of this stopband depends on corrugation depth and types of coupled modes [8].

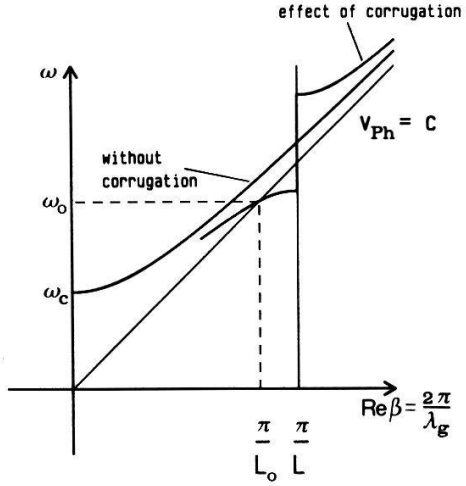

Fig. 2 Dispersion relation of a corrugated waveguide

For particle acceleration, the coupling between a TM_{01} forward and a TM_{01} backward mode has been found to be the most advantageous combination [1]. This is due to the fact, that the longitudinal field displays a single maximum on the waveguide axis, where both, the transverse electric and the transverse magnetic fields vanish. An example is provided in Fig. 3 for the linear periodic cylindrical and parallel-plate waveguide. For helical corrugations, all possible mode combinations exhibit off-axis field maxima.

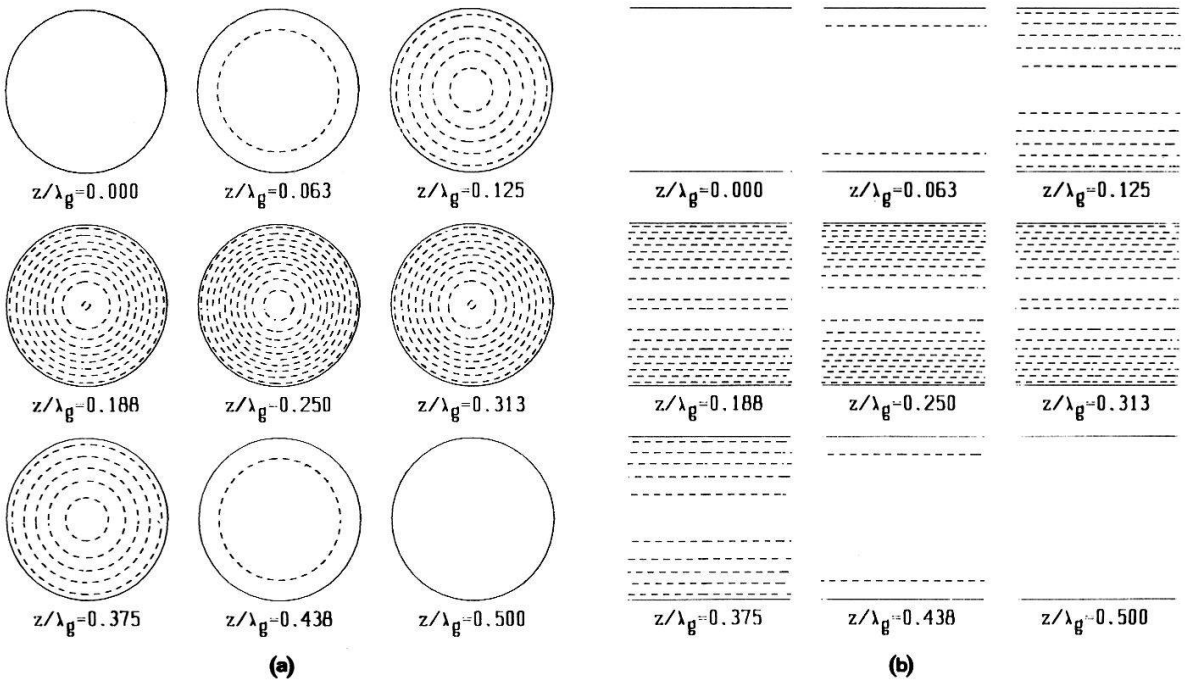

Fig. 3 Contours of the longitudinal electric field for an eigenmode of the TM_{01}/TM_{01} coupling at the lower stopbandedge. For a particle with velocity equal to the phase velocity of the eigenmode.
a) cylindrical
b) parallel-plate waveguide with linear periodic corrugations

Conclusion

Oversized hollow metallic waveguide structures with periodic corrugations appear to be feasible for laser acceleration of particles. More details will be published elsewhere. Future studies will include waveguide losses, material breakdown and parasitic modes.

References

[1] J. Arnesson, S. Gnepf, M. Nessi, W. Wölfli and F.K. Kneubühl, Proc. 1st Int. Laser Science Conf., Dallas, TX, Nov 1985

[2] P.M. Lapostolle, A.L. Septier, eds.: Linear Accelerators; North Holland Publ. Comp.; Amsterdam (1970)

[3] K. Shimoda, Appl. Opt. 1, 33 (1962)

[4] P.J. Channell, ed.: Laser Acceleration of Particles; Am. Inst. of Physics Conf. Proc. No 91, NY (1982)

[5] J. Arnesson, F.K. Kneubühl, Infrared Phys., 25, 121 (1985)

[6] E. Affolter and F.K. Kneubühl, IEEE J. of Quantum Electron., QE-17, 1115 (1982)

[7] H.P. Preiswerk, M. Lubanski, F.K. Kneubühl, Appl. Phys., 33, 115 (1984)

[8] V.L. Bratman, G.G. Denisov, N.S. Ginzburg, M.I. Petelin, IEEE J. of Quantum Electron., QE-19, 282 (1983)

ELECTRON TRAJECTORY CALCULATIONS ON A NEW LASER PARTICLE ACCELERATOR

D. Billeter[+], M. Nessi[+], W. Neumann[+], W. Wölfli[+]
S. Gnepf[++], J. Arnesson[++], F.K. Kneubühl[++]
[+] Institut für Mittelenergiephysik, ETH Zürich, CH-8093 Zürich
[++]Institut für Quantenelektronik, ETH Zürich, CH-8093 Zürich

Abstract: We present the results of electron trajectory and energy gain calculations for a new infrared-laser accelerator scheme, which makes use of hollow oversized linear periodic and helical waveguide structures.

Recently, a new laser accelerator[1] scheme has been proposed that makes use of oversized linear periodic and helical waveguides driven by a 10.6 μm CO_2-laser or by a submillimeterwave free-electron laser[2,3]. The accelerating longitudinal electrical field has maximum values along the waveguide axis so that problems of beam calibration and material breakdown are less severe than in near-field accelerators[1,3].

In order to study the feasibility of this new scheme, we have performed calculations of electron trajectories and energy gain for several cavity configurations. These computations are based on the field calculations by Gnepf et al.[4], and apply numerical integration of the relativistic equation of motion by the Runge-Kutta method.

If not stated otherwise, the following conditions are chosen: The corrugated waveguide of length 2 cm and diameter 0.1 mm selects modes near the stopband, most advantageous mode coupling is assumed. Waveguide losses are not taken into account. The CO_2 laser beam with a power of 5 MW propagates along the cavity axis. The electrons start with an energy $E = 6$ MeV and optimum phase matching to the wave.

Variation of the electron starting parameters, i.e. distance from the axis, azimuth angle, inclination angle towards the axis, exhibits maximum energy gain along the axis and slight focussing by the cavity as shown in fig. 1.

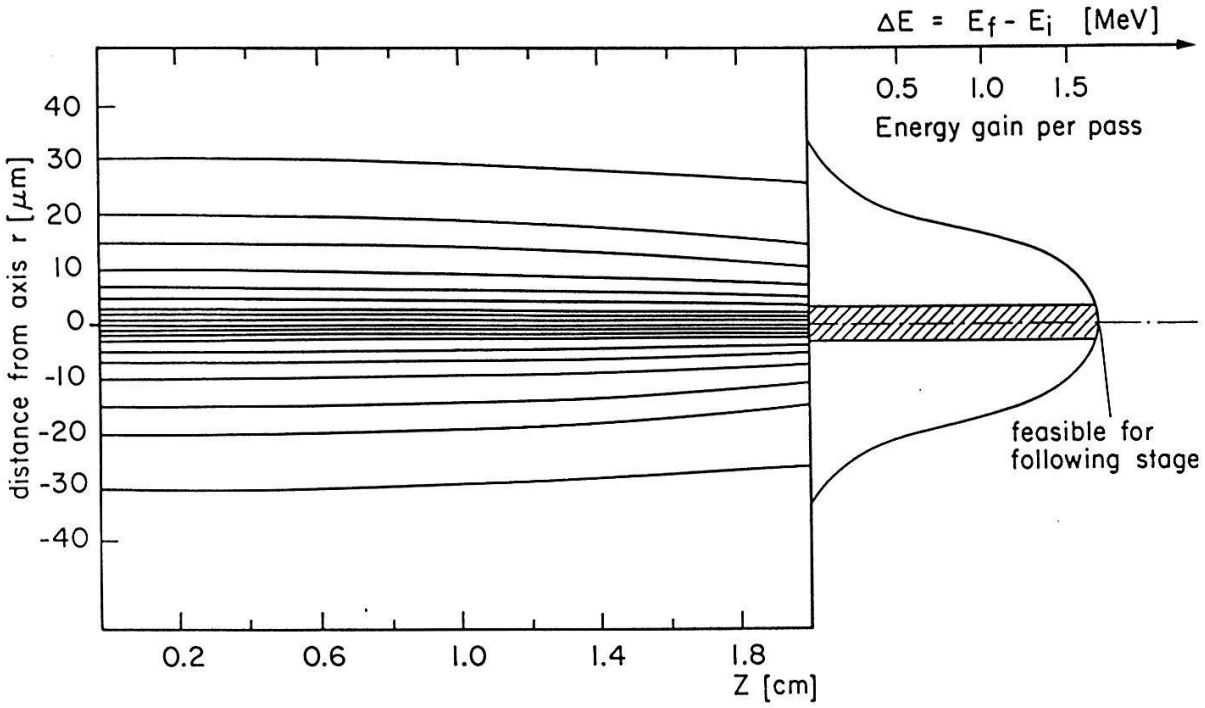

Fig. 1 Electron trajectories and energy gain in a linear periodic cylindric waveguide for axially injected electrons.

In the following, we always assume that the electrons start along the axis without divergence . Table 1 presents the energy gain of the three different structures studies so far.

Table 1: Energy gain of different structures.

WAVEGUIDE	maximum energy gain	mode coupling
periodic linear planar	0.8 MeV	TM_{01}-TM_{01}
periodic linear cylindric	1.6 MeV	TM_{01}-TM_{01}
helical	1.6 MeV	TM_{01}-TM_{11}

The energy gain of a planar cavity is only half of that of the cylindric structures. However, the electron acceptance is considerably larger in the first case. Subsequently, we will focus on linear periodic planar waveguides, as these structures can be manufactured by means of

known techniques. The proper corrugation period length will be L = 5 μm, and the pertinent corrugation depth a_1 = 2.2 μm.

In order to obtain maximum energy gain per pass, optimum phase and velocity matching between electron and wave must be achieved. The actual energy gain is affected by

- the initial energy spread $\Delta E/E$
- the initial phase mismatch $\Delta T/T$,
  where T denotes the waveguide period
- variation of the corrugation depth $\Delta a_1/a_1$
- variation of the corrugation period length $\Delta L/L$,
  e.g. by thermal effects.

Moreover, as the electron velocity increases during acceleration, a phase mismatch occurs. Its magnitude increases with decreasing initial energy E_i, with increasing laser power and cavity length R. We have investigated these effects, and derived limitations on $\Delta X/X$ (X = E, T, a_1, L) assuming that the energy gain is more than 90% of the maximum gain. First results of these computations are summarized in table 2.

Table 2: Computed limitations on $\Delta X/X$ for energy gain per pass >90% of the maximum value for different combinations of initial energies and cavity lengths.

E_i = 6 MeV R = 2 cm	
$\Delta E/E$	$\leq$ 1 %
$\Delta T/T$	$\leq$ 4 %
$\Delta a_1/a_1$	$\leq$ 0.7 %
$\Delta L/L$	$\leq$ 0.1 %[+]

R = 2 cm	
E_i	$\Delta a_1/a_1$
4 MeV	$\leq$ 0.1 %
6 MeV	$\leq$ 0.7 %
10 MeV	$\leq$ 1.3 %

E_i = 4 MeV		
R	maximum gain	$\Delta E/E$
1.0 cm	0.41 MeV	$\leq$ 1.0 %
1.5 cm	0.52 MeV	$\leq$ 0.5 %
2.0 cm	0.62 MeV	$\leq$ 0.2 %

[+] $\Delta L/L$ = 0.1% corresponds to a thermal expansion caused by a temperature variation of 60°C in copper.

In a further step, waveguide losses and material breakdown limits will be studied.

References

1) Channell, P.J. (ed.), Laser Acceleration of Particles, AIP Conf. Proc. No. 91, N.Y. 1982

2) J. Arnesson, S. Gnepf, M. Nessi, W. Wölfli, and F.K. Kneubühl, Proc. 1st Int. Laser Science Conf., Dallas, TX, Nov. 1985

3) J. Arnesson and F.K. Kneubühl, Infrared Physics 25, 121-131, 1985

4) S. Gnepf, J. Arnesson, F.K. Kneubühl, M. Nessi, W. Wölfli, these Conference Proceedings.

Photobleaching Velocimetrie

J. Ricka
Institut für angewandte Physik, Sidlerstr. 5, 3012 Bern

Eine mit einem ausbleichbaren fluoreszierenden Tracer versetzte strömende Flüssigkeit wird von einem Laserstrahl mit einem steilen Intensitätsprofil beleuchtet. Ist nun die Beleuchtung so stark, dass alle Farbstoffmoleküle bei der Durchquerung des Strahles ausgebleicht werden, so ist die Fluoreszenzintensität zu der Rate des Farbstofftransportes über die Strahlgrenze proportional.
Dieses Prinzip ermöglicht es, komplexe Geschwindigkeitsfelder, wie sie z.B. bei der Bénard-Instabilität auftreten, in Bruchteilen von Sekunden und mit mikroskopischer Ortsauflösung auszumessen.

Analyse von Oberflächenfilmen auf Flüssigkeiten mittels gepulster IR photoakustischer Spektroskopie

M.W. Sigrist und Z.H. Chen*
Physik-Departement, ETH, Hönggerberg, CH-8093 Zürich
*Akademischer Gast, Chinese Academy of Sciences, Beijing

Die thermooptische Erzeugung von akustischen Signalen in Flüssigkeiten mit CO_2 Laserimpulsen wird diskutiert. Erstmals wurde beobachtet, dass eine dünne Schicht einer zweiten Flüssigkeit, welche auf der ersten aufliegt, das akustische Signal in Abhängigkeit von der Schichtdicke d und den optischen Eigenschaften dieser Flüssigkeitsschicht verstärkt. Erste spektroskopische Messungen an organischen Flüssigkeitsfilmen auf Wasser zeigen, dass diese Methode zur Charakterisierung von Flüssigkeitsfilmen mit $d \gtrsim 1$ µm geeignet ist.

ANDO V : Physique des plasmas

APPLICATION OF ALGORITHMS FOR THE CALCULATION OF THE DIMENSION OF CHAOTIC DYNAMICAL SYSTEMS

M.L. Sawley, W. Simm, F. Skiff and A. Pochelon
Centre de Recherches en Physique des Plasmas, Association Euratom - Confédération Suisse, Ecole Polytechnique Fédérale de Lausanne, 21, Av. des Bains, CH-1007 Lausanne / Switzerland

Abstract : Many dynamical systems exhibit chaotic behaviour associated with phase space trajectories of low dimension. Recently developed algorithms for the calculation of dimension have been studied on known mathematical attractors, as well as on numerical and experimental data from a simple model system. Their application to data from a more complex system, a tokamak plasma, has also been investigated.

1. Introduction

In a dissipative dynamical system, a trajectory with given initial conditions may tend asymptotically with time (after the decay of transients) to some subset of the phase space, called the attractor. Such attractors are said to be "strange" if they exhibit chaotic behaviour associated with a non-integer value of dimension [1,2].

Several quantities have been used to characterize chaotic, but deterministic, nonlinear systems. The Lyapunov exponents λ_i measure the exponential separation of adjacent orbits and give, using the Kaplan-Yorke conjecture, an estimate of the attractor's dimension. Unfortunately, the application of the proposed algorithms to calculate these exponents from experimental data [3,4] is not straightforward. Among the various other definitions of dimension, the correlation dimension ν [5] has been applied in many fields of research. It is possible, using the time series of a single measurable quantity, to calculate ν from experimental data. We have tested our application of this algorithm by using time series from mathematical systems with known attractors (Logistic, Hénon and Kaplan-Yorke maps), and have obtained the already tabulated values for the correlation dimension.

2. The bipolar motor : mathematical solutions

The equation of motion for a dipole magnet in a linearly polarized magnetic field oscillating at frequency ω is

$$\ddot{\theta} + \gamma\dot{\theta} = F \sin\theta \cos\omega t$$

where γ is the damping coefficient. For certain values of the strength parameter F, the system exhibits chaotic motion as well as the expected "stretching" and "folding" of phase space associated with a strange attractor. A plot of the spectrum of the Lyapunov exponents versus the strength parameter (Fig. 1) illustrates the behaviour of the system: bands of chaos (i.e., where $\lambda_1 > 0$), separated by regions of periodic solutions. A detailed examination of the onset of chaos near F = 1.8 reveals a period doubling route to chaos. The calculated values of the correlation dimension compare favourably with the dimension obtained from the Lyapunov exponents (e.g., $\nu \simeq 2.7$ for F = 3).

3. The bipolar motor : experimental data

An experimental model of the motor has also been studied. For ω = 2 Hz and various values of F, 8192 samples of cos θ, measured using a Hall probe, have been recorded at a sampling frequency of 100 Hz, with 8 bit resolution. Qualitative features similar to those of the mathematical solutions appear: bands of chaotic behaviour separated by periodic motion bands, as well as single period and period doubled motion. Figure 2 shows an example of the power spectrum obtained during chaotic motion.

Figure 3 shows how the correlation dimension is obtained. The slopes of the curves saturate with increasing imbedding dimension m, yielding for this example $\nu \simeq 2.6 \pm .2$. This non-integer value reflects the chaotic behaviour of the system.

4. Tokamak experimental data

Are the fluctuations observed in the TCA tokamak [6] associated with a chaotic dynamical system of low dimension? To address this question, we have recorded, for many tokamak discharges, 8192 samples at 2 MHz from magnetic probes placed in the scrape-off layer. Figure 4 shows that a broadband spectrum is observed above the frequency of the coherent Mirnov oscillations ($f \simeq 15$ kHz), indicating well-developed turbulence associated with a strongly

nonlinear system. (Note the similarity between Fig. 2 and Fig. 4.)

Even though a linear dependence is evident in the plots of the correlation function shown in Fig. 5 (log C(r) versus log r), no saturation can be observed for filtered signals (f > 40 kHz). This indicates, with the present resolution, a high dimension for the broadband fluctuations, $\nu > 8$. Similar results have been obtained from filtered (f > 40 kHz) signals both from Langmuir probes in the scrape-off layer and from a CO_2 laser phase contrast diagnostic that measures chord-integrated density fluctuations.

The analysis of signals that contain a large low frequency component have proved to be less conclusive : since log C(r) does not exhibit a linear relation with log r over a significant range of r, an estimate of the correlation dimension could not be obtained in these cases.

5. Conclusions

The application of algorithms for the calculation of dimension has been studied on both mathematical systems and experimental data. This has been found to be relatively straightforward for a simple model system, the bipolar motor, and yields the expected low values. Despite spectral similarities with the motor signals, the broadband tokamak fluctuations exhibit a higher correlation dimension, indicating an intrinsically complex nature that may not be correctly modelled mathematically by a low order set of coupled differential equations.

Acknowledgements : The authors would like to thank Dr. Ch. Hollenstein and H. Weisen for providing some of the tokamak data. This work was partly supported by the Swiss National Science Foundation.

References :

[1] J.P. Eckmann, D. Ruelle, Rev. Mod. Phys. 57, 617 (1985).

[2] H.G. Schuster, Deterministic chaos, New York, Plenum (1984).

[3] A. Wolf, J. Swift in: Statistical physics and chaos in fusion plasmas, W. Horton and I.E. Reichle Eds New York, Wiley (1984).

[4] M. Sano, Y. Sawada, Phys. Rev. Lett. 55, 1082 (1985).

[5] P. Grassberger, I. Procaccia, Phys. Rev. Lett. 50, 346 (1983).

[6] Ch. Hollenstein et al., Proc. 13th Europ. Conf. Contr. Fusion and Plasma Phys., Schliersee (1986).

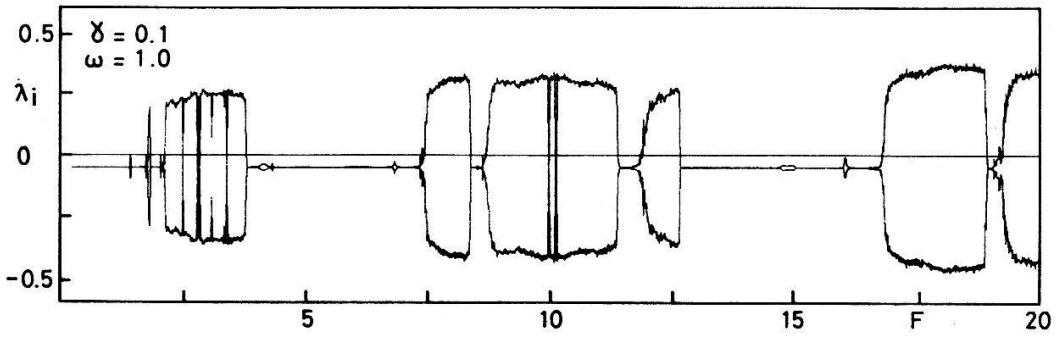

Fig. 1

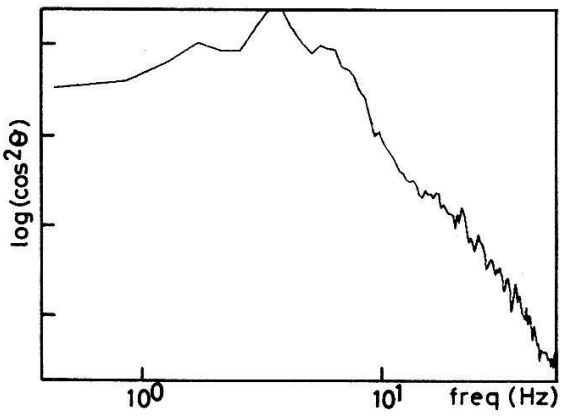

Fig. 2

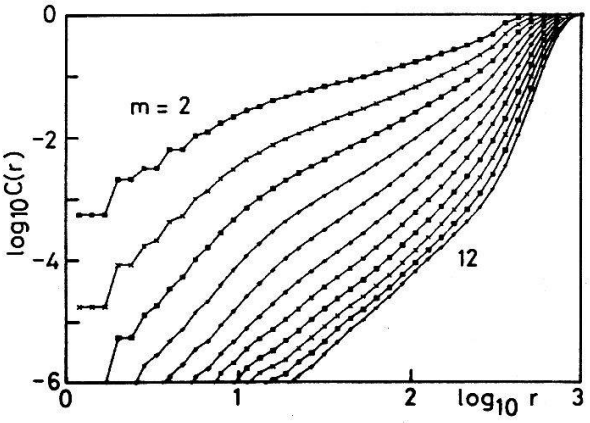

Fig. 3

Fig. 4

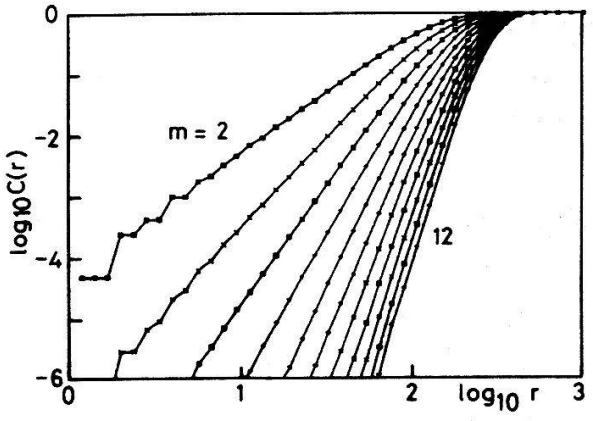

Fig. 5

INVESTIGATIONS OF NOZZLE MATERIALS IN SF_6 CIRCUIT BREAKERS

R. Meier, H.J. Schötzau* and F.K. Kneubühl
Institute of Quantum Electronics, ETH, CH-8093 Zurich, Switzerland
*Sprecher + Schuh Ltd., CH-5001 Aarau, Switzerland

Abstract : PTFE is a common nozzle material in high-voltage circuit breakers (CB). During current interruption the teflon is thermally degraded and changes the plasma composition. In order to study the exhausted gas contaminated with ablated material a model SF_6 breaker has been attached to a time-of-flight mass spectrometer. Thus, we have demonstrated that during the current phase the degraded teflon consists mainly of CF_2, while CF_4, which is the main decomposition product, is formed only after the current pulse. The nozzle ablation is mainly determined by the geometry of the arcing device, yet it depends only weakly on the quality of the PTFE.

1. Introduction

Sulfurhexafluoride (SF_6) is used as an insulating and arc-quenching medium in gas-blast circuit breakers (CB). During current interruption the gas is dissociated into ions and neutral atoms. In addition, the arc energy induces ablation of material from the electrodes and the walls. Decomposed SF_6 together with this material gives rise to the formation of new products. These are of primary concern for the reliability and the lifetime of the CB. The short-lived products can influence the interrupting capabilities, while the long-lived products, mostly aggressive gases, give rise to corrosion in the CB.

For these reasons we have studied the chemical composition of arced SF_6 gas during and after current interruption with the aid of a small modell CB attached to a time-of-flight mass spectrometer. The experimental setup has already been described by Rüegsegger et al. [1].

2. Long-lived Products

The main stable decomposition products of arced SF_6 with a PTFE nozzle are

CF_4, SF_4, CS_2, SOF_2, S_2F_2, WF_6, CuF_2, HF

Most of the ablated nozzle material reacts to CF_4. Therefore, the CF_4 concentration is a direct measure for the evaporated PTFE mass. Fig. 1a shows the CF_4 concentration for different PTFE qualities as a function of the number of arced discharges, i.e. the cummulated arc energy. From this plot it can be concluded that the ablated PTFE is a linear function of the arc energy and does not vary strongly for different PTFE qualities. The formation rate of CF_4 has been determined to 1.3 Vol %/kJ/l SF_6.

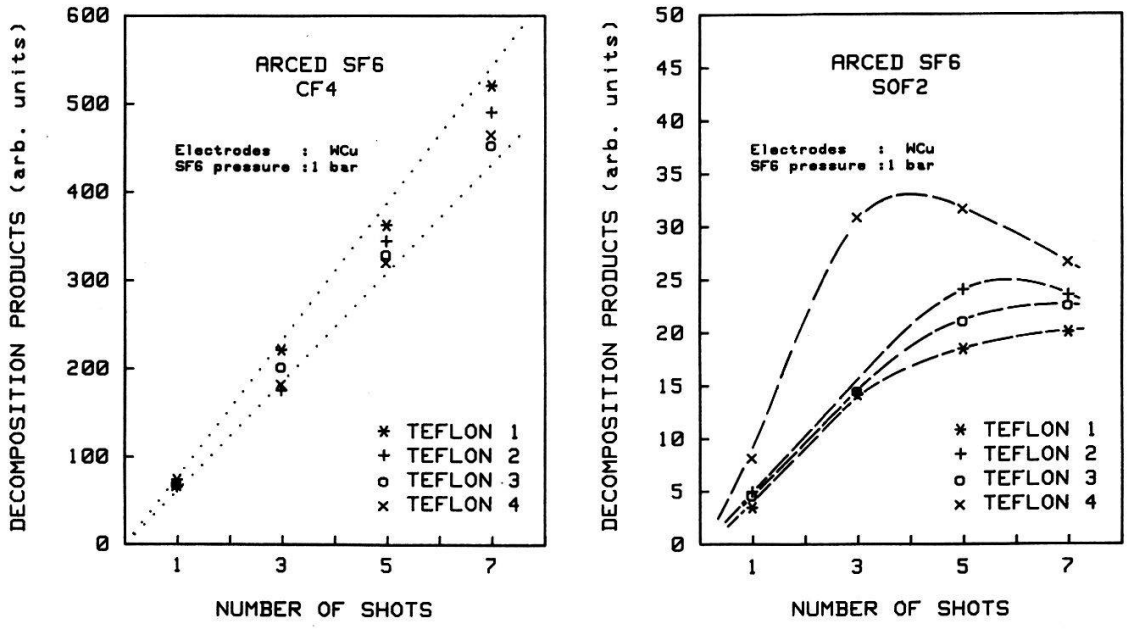

Fig. 1 Concentration of CF_4 and SOF_2 as a function of the cumulated arc energy which is proportional to the number of shots

On the other hand, decomposition products containing oxygen or hydrogen differ for the various applied materials (Fig. 1b). The SOF_2 molecule is formed according to the reaction [2].

$$SF_4 + H_2O \rightarrow SOF_2 + 2HF$$

The formation of SOF_2 is caused by water impurities in the SF_6 gas, the nozzle material or in the electrodes. This explains the observed scatter and saturation in the formation of SOF_2.

3. Short-lived Products

During the transient phase of arc interruption the dynamic behaviour of material ablation has been studied with the aid of the free jet sampler described in [1]. The main short-lived decomposition products found are

$CF_2(CF^+)$, $C_2F_4(C_2F_3^+)$, $C_2F_6(C_2F_5^+)$

where the ions in parantheses represent these products in the mass spectrum.

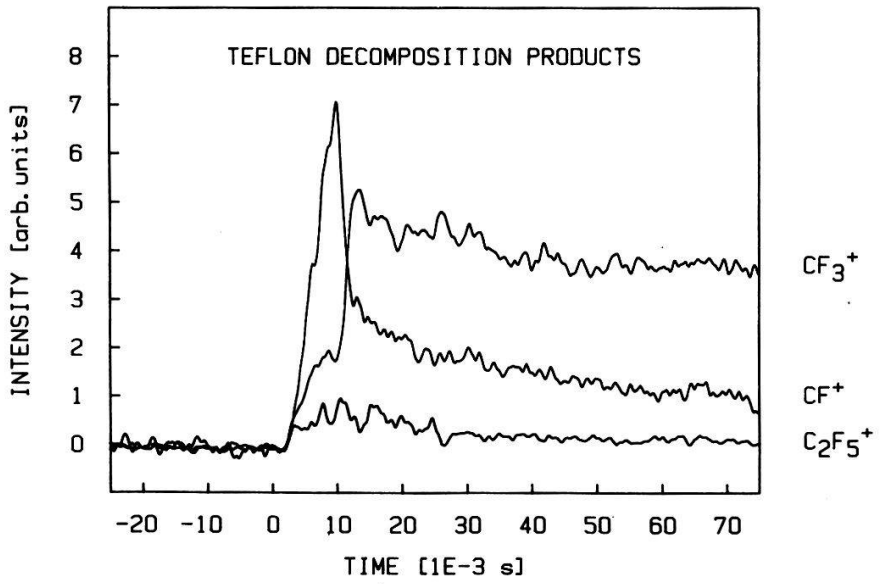

Fig. 2 Temporal evolution of CF molecules during and after current pulse. The current pulse is about 700 A from 0 to 12 ms.

Fig. 2 shows the temporal evolution of the intensity of these CF-molecules. While CF_2 is present already during the current phase, CF_4 appears only after the main current pulse. In the hot gas the ablated PTFE consists mainly of CF_2, and the formation of CF_4 starts only with the continuous temperature decrease.

For the various PTFE-qualities, however, the dynamic behaviour of the concentration of the CF-compounds varies only slightly. Nevertheless, we have observed that the ablated PTFE depends strongly on the geometrical arrangement. This is demonstrated in Fig. 3, where the transient CF_4 intensities are given for two different geometrical arrangements of the nozzle.

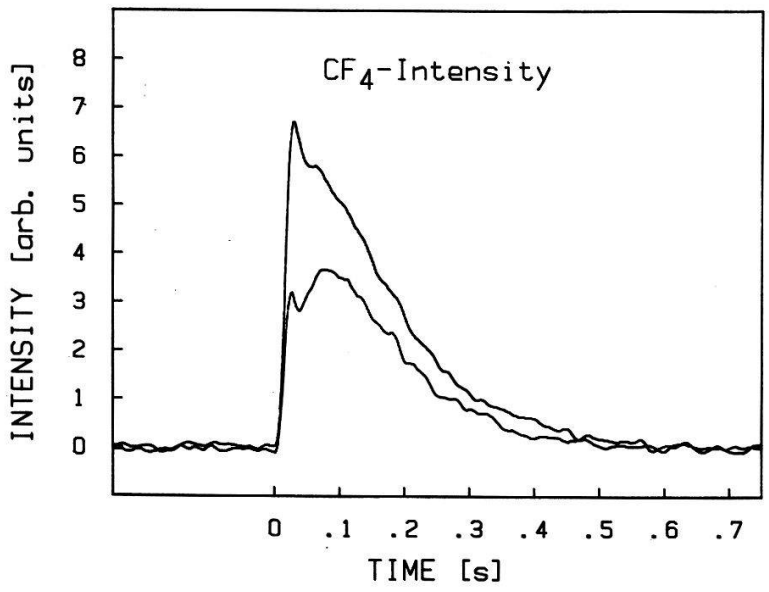

Fig. 3 Temporal evolution of the CF_4 concentration for two different geometrical arrangements of the PTFE nozzle.

The pressure rise caused by the ablation has a positive influence on the interrupting capabilities. On the other hand, the change of the plasma composition may also be important because the excitation, dissociation and recombination processes largely affect the arc quenching performance. For these reasons it is of importance to know the temporal evolution of the plasma composition after current zero.

Acknowledgement

This study is supported by the Kommission zur Förderung der wissenschaftlichen Forschung, Berne, ETH Zurich and Sprecher + Schuh Ltd., Aarau.

References

[1] W. Rüegsegger, R. Meier, F.K. Kneubühl and H.J. Schötzau, Appl. Phys. B., Vol. B37, p. 115, 1985

[2] I. Sauers, H.W. Ellis, L.C. Frees, L.G. Christophorou: Gaseous Dielectrics 3, Proc. 3rd Intern. Symp. Gaseous Dielectrics (Pergamon, New York 1982), p. 387

Das Strahlungsprofil des TCA-Tokamaks mit Ohm'scher Heizung

B. Joye, J.B. Lister, Ph. Marmillod, J.-M. Moret, S. Nowak[+]

Centre de Recherches en Physique des Plasmas, Association Euratom-Confédération Suisse, Ecole Polytechnique Fédérale de Lausanne, 21, Av. des Bains, CH-1007 Lausanne/Schweiz
[+]Physikinstitut der Universität Freiburg/Schweiz

Das Strahlungsprofil des TCA-Tokamakplasmas wurde während der Ohm'schen Heizphase mit einem Multikanal-Bolometersystem analysiert. Hierzu wurden die Parameter B_φ, I_p und n_e in einem grossen Bereich variert. Die Funktionsweise des neuen 16-Kanal-Bolometers wird erklärt. Messungen des Strahlungsverhaltens in Funktion der Plasmaparameter, insbesondere an der Dichtegrenze, werden präsentiert. Die Resultate dieser Analyse werden verglichen mit solchen, die mit Einschiessen von Verunreinigungen erhalten wurden.

Wave phenomena in the scrape-off layer of TCA during rf wave heating

Ch. Hollenstein and Y. Martin

Centre de Recherches en Physique des Plasmas, Association Euratom-Confédération Suisse, Ecole Polytechnique Fédérale de Lausanne, 21, av. des Bains - 1007 Lausanne / Switzerland

Extensive wave studies in the boundary layer of the TCA tokamak have been performed. In using movable Langmuir probes and correlation techniques it was found that the rf antenna excites waves at the driving rf frequency in the scrape-off layer. The low frequency turbulence observed in TCA during the ohmic phase is found to be strongly affected by the rf. During both ohmic and rf heating, the phases of the waves increase approximately proportionally to the frequency. However, the direction of wave propagation reverses during Alfvén wave heating.

Progress towards ion temperature measurement in TCA tokamak by collective Thomson scattering of far infrared laser radiation

S.A. Salito, R. Behn, I. Kjelberg, P.A. Krug and M.R. Siegrist

Centre de Recherches en Physique des Plasmas, Association Euratom-Confédération Suisse, Ecole Polytechnique Fédérale de Lausanne, 21, av. des Bains - 1007 Lausanne / Switzerland

Following the first observation of far infrared radiation scattered by collective thermal fluctuations in a tokamak at MIT and subsequently by the Lausanne group, an upgraded experiment is at present in progress to attempt to obtain a single-shot measurement of Ti in the TCA tokamak in Lausanne.
We will present results obtained with a feasibility experiment during 1985. In addition we will discuss the expected performance of the large scale system involving a ten-fold increase in D_2O FIR laser power.

ANDO VI : Optique, spectroscopie

EVANESCENT-WAVE-INDUCED LUMINESCENCE AS A PROBE FOR ADSORPTION OF DYE MOLECULES AT A LIQUID-SOLID INTERFACE

Ch. Fattinger, F. Honegger, and W. Lukosz, Swiss Federal Institute of Technology, Professur für Optik, ETH, 8093 Zürich, Switzerland

Abstract : We studied laser-induced luminescence of dye molecules in solution near a liquid-glass interface; the molecules were excited by an evanescent wave with a penetration depth of typically $z_{0,1}$ = 100 nm. Measurements of the angular distribution of the luminescent light permit: 1.) to distinguish between molecules which are adsorbed on the glass surface and those in solution close to the interface, and 2.) to obtain information about the orientation of the adsorbed molecules with respect to the interface. Luminescence lifetimes were measured by time-correlated single photon counting. We found the lifetimes of adsorbed molecules to be shorter by a factor of 2-3 compared with lifetimes for molecules in solution.

1. Introduction

The use of evanescent waves permits selective excitation of those dye molecules in a solution which are in the vicinity to the interface of a high refractive index glass prism. This method of excitation does not permit to distinguish between molecules in solution (within the penetration depth $z_{0,1}$ of the evanescent wave) and molecules actually adsorbed at the interface. This distinction becomes possible by comparison of measured and calculated radiation patterns $I^{(s,p)}(\alpha)$, i.e., of the angular distributions of the luminescent light. From this comparison we obtain the ratio of the numbers of molecules adsorbed at the interface and those in solution within the penetration depth $z_{0,1}$.

The time decay of the luminescence was measured with time correlated single photon counting. Differences in luminescence lifetimes between molecules in solution (bulk), in solution near the interface, and adsorbed at the interface were investigated.

2. Experimental Set-up

The cell with the dye solution was pressed against the plane face of a high refractive index hemicylindrical glass prism (see Fig.1). The thickness of the liquid film was typically $d_o \approx 10$ µm.

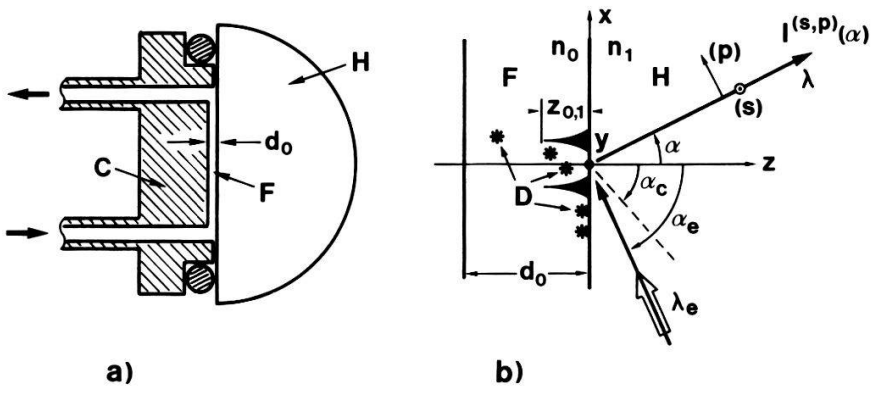

Fig. 1. a) Schematic of dye cell: H, hemicylindrical high index (n_1=1.89) glass prism (LASF15); C, cell; thickness of liquid film F typically $d_0 \simeq 10$ μm; b) α_e, angle of incidence of exciting laser beam of wavelength λ_e; $z_{0,1}$, penetration depth of evanescent wave; n_0, refractive index of dye solution; D, dye molecules; $\alpha_c = \arcsin(n_0/n_1)$; α, angle of emission of luminescent light of wavelength λ; $I^{(s,p)}(\alpha)$, angular intensity distribution of luminescent light; (s), (p), polarizations.

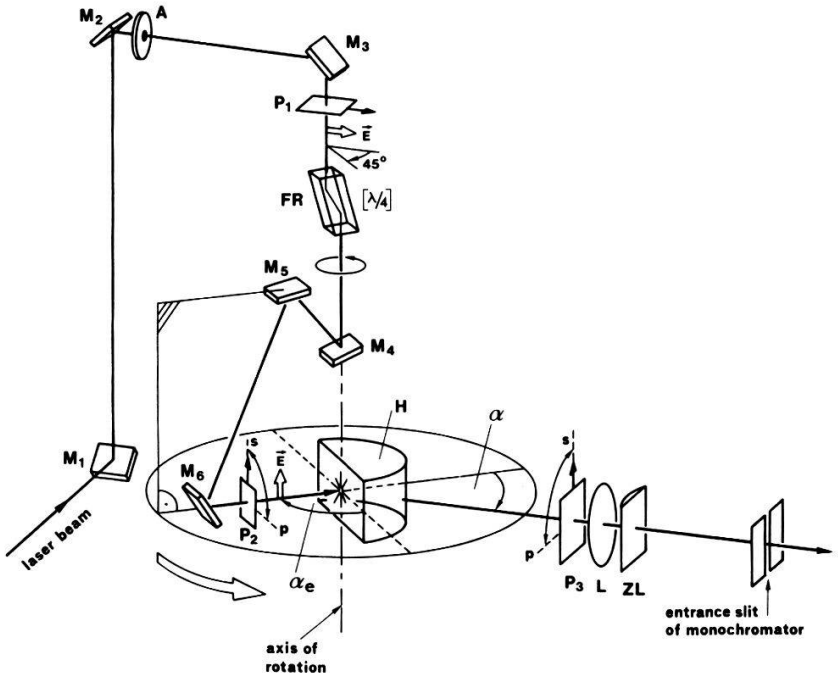

Fig. 2. Schematic of experimental set-up: H, hemicylindrical prism (cf.Fig.1a); M_j, mirrors; P_j, polarizers; FR, λ/4-Fresnel-rhombe; the optics (polarizer P_3, lens L, cylindrical lens ZL) before the monochromator defines the emission angle α and the polarization (s), (p).

We have built an apparatus (see Fig.2) to measure the angular distribution of the luminescent intensity $I^{(s,p)}(\alpha)$ versus angle of emission α. We mention only one important feature of the instrument: To change α, the glass prism is rotated, since monochromator and photodetector are stationary. During this scan the angle of incidence α_e of the excitation beam remains the same.

Excitation for measurements of the radiation patterns $I^{(s,p)}(\alpha)$ was by a c.w. Ar-Laser, for measurements of the luminescence lifetimes by a synchronously pumped cavity dumped dye laser. Both the radiation patterns $I^{(s,p)}(\alpha)$ vs α and the time decay of the luminescence were recorded on a multichannel analyzer (LeCroy system 3500 with multichannel scaling module 3521 A, and time-to-digital conversion module 4201, respectively).

3. Results and Discussion

The luminescence of a dye molecule located at z (cf. Fig.1b) is proportional to the intensity of the exciting evanescent wave at this location. The intensity of luminescent light emitted in direction α is

$$I^{(s,p)}(\alpha) = \left[A_{0,1}^{(s,p)}(\alpha_e)\right]^2 \int_{z=0}^{-\infty} C(z)\, P^{(s,p)}(z,\alpha)\, \exp(2z/z_{0,1})\, dz \qquad (1)$$

where $C(z)$ denotes the dye concentration as a function of the distance to the interface ($z=0$), $P^{(s,p)}(z,\alpha)$ the normalized radiation pattern of electric dipoles which depends on the location z of the dipoles, their orientation, the polarization of the exciting wave, and on the luminescence depolarization effects caused, e.g. by rotational diffusion. $A_{0,1}^{(s,p)}(\alpha_e)$ is the amplitude of the evanescent wave at the interface $z = 0$.

We measured radiation patterns $I^{(s,p)}(\alpha)$ for different dye concentrations C, e.g., for rhodamine 6G in ethanol at $C = 5 \times 10^{-6}$, 5×10^{-5}, and 5×10^{-4} mole/liter (see Fig.3a,b). The curves are normalized; $I^{(s,p)}(\alpha=0) = 0$. In Fig.3a both the exciting wave and the detected luminescence are s-polarized, in Fig.3b both are p-polarized. The peak in $I^{(s,p)}(\alpha)$ appears at the critical angle $\alpha_c = \arcsin(n_0/n_1)$.

From a comparison of the measured and the calculated radiation patterns $I^{(s,p)}(\alpha)$ shown in Figs. 4a,b we obtain the following information:
1) from $I^{(s)}(\alpha)$ in the interval $\alpha_c \leqq \alpha \leqq 90^o$ the ratio $C_0/(C\, z_{0,1})$ of the numbers of adsorbed molecules C_0 and those molecules in solution $(C\, z_{0,1})$ within a distance $z_{0,1}$ from the interface. The underlying physics is: Plane waves in the prism with angles $\alpha > \alpha_c$ correspond to evanescent waves in the dye solution.

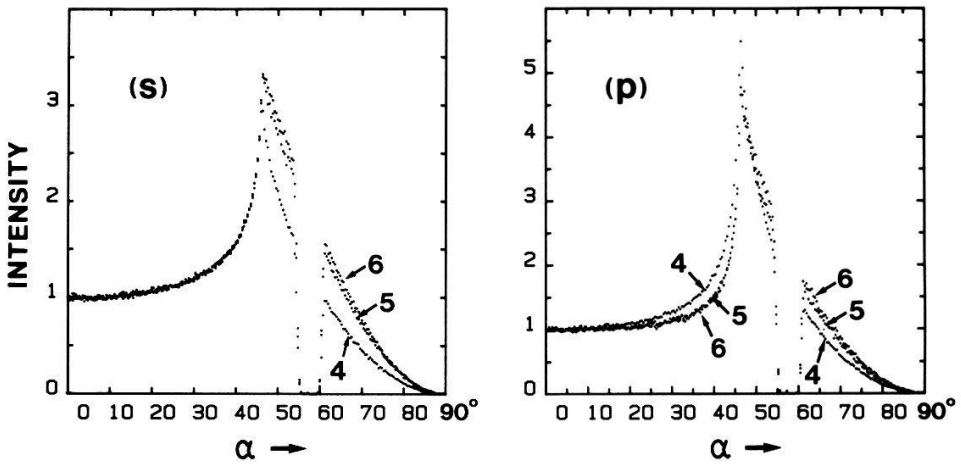

Fig. 3. Measured radiation patterns $I^{(s,p)}(\alpha)$ of rhodamine 6G in ethanol (n_0=1.36) at concentrations C = 5×10^{-6} mole/liter (6), 5×10^{-5} mole/liter(5) and 5×10^{-4} (4), respectively. $\alpha_e = 58^o$; penetration depth $z_{0,1}$ = 100 nm; excitation: Ar^+-laser λ_e = 514 nm; selected emission wavelength λ = 556 nm.

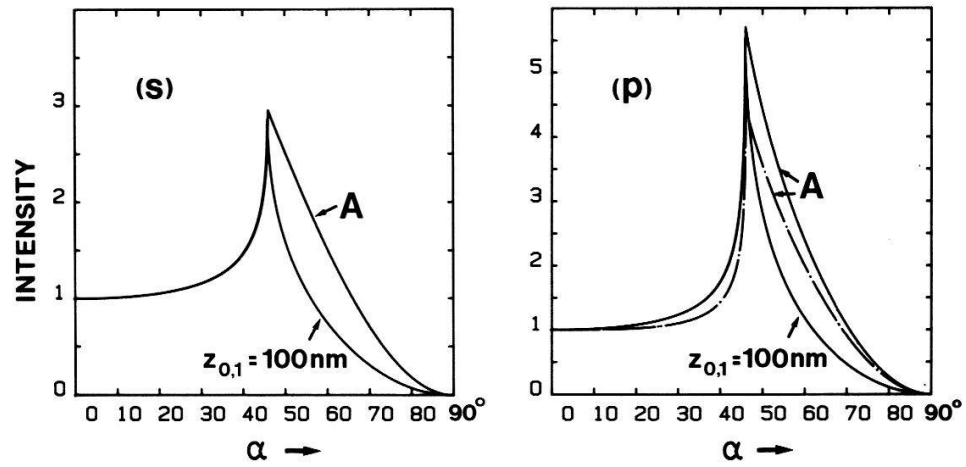

Fig. 4 a,b. Calculated radiation patterns $I^{(s,p)}(\alpha)$ versus α for ensemble of randomly oriented electric dipoles: (A) adsorbed on the interface 0/1; ($z_{0,1}$) located in the solution, excited with evanescent wave of penetration depth $z_{0,1}$ = 100 nm. n_0 = 1.36, n_1 = 1.89. (—·—·-) radiation pattern as (A) for non-isotropic dipole orientation (see text).

Evanescent waves in the near field of a luminescent molecule at location z are transmitted with a probability $\exp(2z/z_{0,1})$ into the prism as plane waves with $\alpha > \alpha_c$. Therefore, an enhancement of $I^{(s,p)}(\alpha)$ for angles $\alpha > \alpha_c$ indicates an increase in the ratio $C_0/(C\, z_{0,1})$. For the lowest concentrations of rhodamine

6G (5) and (6) in Fig.3 we found the ratio $C_0/(C\, z_{0,1})$ to be $>> 1$; with increasing concentration C the interface adsorption saturates.

2.) For $0 \leq \alpha \leq \alpha_c$, the shape of $I^{(s,p)}(\alpha)$ is independent of the concentration profile C(z). In this interval, $I^{(s)}(\alpha)$ is independent of the orientation of the emitting dipoles, while $I^{(p)}(\alpha)$ depends sensitively on their orientation. The emission dipole moments of molecules in solution within the distance $z_{0,1}$ from the interface were found to be randomly orientated; the weight factors are $g_\perp = 1/3$, $g_\parallel = 2/3$, respectively for perpendicular and parallel orientation to the interface. This holds independently of the polarization of the exciting wave which shows that the rotational diffusion time is much shorter than the luminescence life time.

Also for molecules adsorbed at the interface the measured radiation patterns $I^{(s,p)}(\alpha)$ were found to be practically independent of the polarization of the exciting wave. The orientational weight factors were determined to be $g_\perp = 0.28$ and $g_\parallel = 0.72$. This is an indication that the molecules (emission dipole moments) are slightly preferential oriented parallel to the interface.

In our experiments with different laser-dyes and solvents we found no adsorption on the glass interface for DCM in DMSO (dimethylsulfoxide), but adsorption for rhodamine 6G in ethanol, and an even stronger adsorption for sulforhodamine 101 in ethanol. The affinity of the sulforhodamine 101 to the glass appears to be smaller in methanol; an adsorbed layer is removed by purging the cell with methanol (see Fig.5).

We found the luminescence lifetimes for molecules in solution within the penetration depth layer near the interface slightly smaller than for molecules in bulk solution. These results were obtained with dyes which exhibit only small adsorption, as, e.g., suforhodamine 101 in ethyleneglycol or methanol. For sulforhodamine 101 in ethanol the measured time decay of the luminescence for molecules adsorbed at the interface and those in bulk solution are shown in Fig.6. For parallel (∥) polarization the excitation and emission were both s-polarized (or both p-polarized with practically the same time decay). For orthogonal (⊥) polarization the same time decay was observed when the exciting and emitted light were s- and p-polarized or p- and s-polarized, respectively. The most striking observation is that the decay times for adsorbed molecules (A) are shorter by a factor of about 3 than those for molecules in solution (L). To this effect the following mechanisms contribute:

i) luminescence quenching caused by energy transfer (Förster mechanism) from excited molecules (monomers) to traps (non-luminescent dimers),

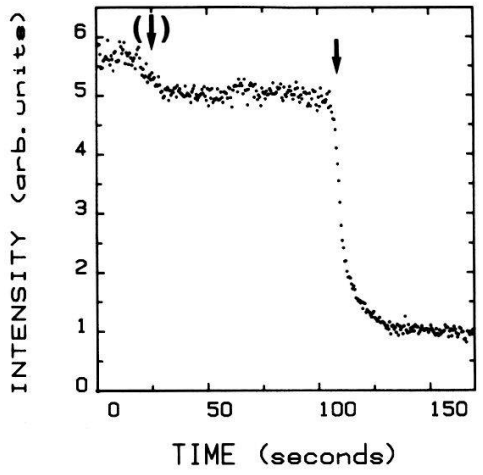

Fig. 5. Luminescence of sulforhodamine 101 adsorbed on glass surface vs time: purging of cell with methanol (↓) removes the adsorbed molecules completely, whereas purging with ethanol ((↓)) has a slight influence only.

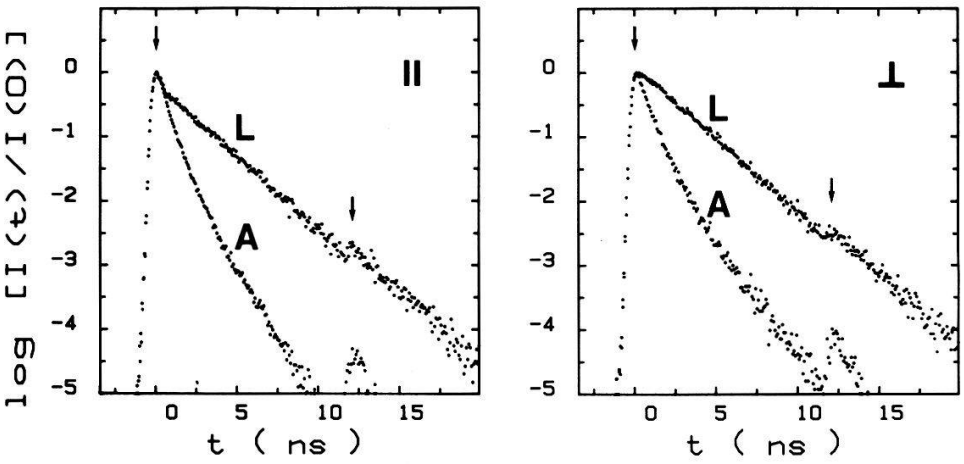

Fig. 6. Decay of luminescent intensity of sulforhodamine 101 versus time t (measured by time correlated single photon counting). Excitation λ_e = 565 nm, emission λ = 600 nm; polarizations in emission and excitation parallel (II), and orthogonal (⊥). Dye molecules in bulk solution (L), and adsorbed on glass surface (A). 1/e-decay-times: τ_L^{II} = 3.7 ns, $\tau_L^{\perp}$ = 4.9 ns, τ_A^{II} = 1.3 ns, and $\tau_A^{\perp}$ = 1.6 ns. Arrows indicate the positions of the main excitation pulse and of a weak second pulse.

ii) interaction of the adsorbed dye molecules with the glass interface, and iii) **electrodynamic effects:** Changes in the optical environment of the molecules - the adjacent glass has a high refractive index - induce a decrease of the radiative lifetimes which become dependant on the orientation of the dipole with respect to the interface.

4. Reference

[1.] R.E. Kunz and W. Lukosz, Phys. Rev. B 21, 4814 (1980)

BEOBACHTUNG DER REDUKTION VON METHYLVIOLOGEN AUF Ag- UND β-ZnP_2-ELEKTRODEN

I. Mörke, H. von Känel und P. Wachter, Laboratorium für Festkörperphysik, ETH-Zürich, 8093 Zürich, Switzerland

Wir haben die Reduktion von Methylviologen (MV = 1,1'-Dimethyl 4,4'-bipyridinium dichlorid), welches in wässeriger Lösung als MV^{2+} vorliegt, zu MV^{+} auf einer Ag- und auf einer Halbleiterelektrode (β-ZnP_2) mittels Ramanstreuung untersucht. Die Experimente wurden in einem standard 3-Elektrodenmessystem unter potentiostatischen Bedingungen durchgeführt. Die polykristalline Ag-Arbeitselektrode war von 99.98% Reinheit und war vor der mechanischen Bearbeitung (Schleifen, Polieren) 20 Stunden lang bei 750°C unter H_2 Durchfluss-Atmosphäre getempert worden. Die Halbleiterelektrode (p-typ, $N_A = 4.1 \cdot 10^{16} cm^{-3}$) war eine ringförmige Scheibe mit ohmschen Rückkontakt. Die Gegenelektrode bestand aus einem Platindraht, und als Referenz diente eine gesättigte Kalomel-Elektrode (SCE).

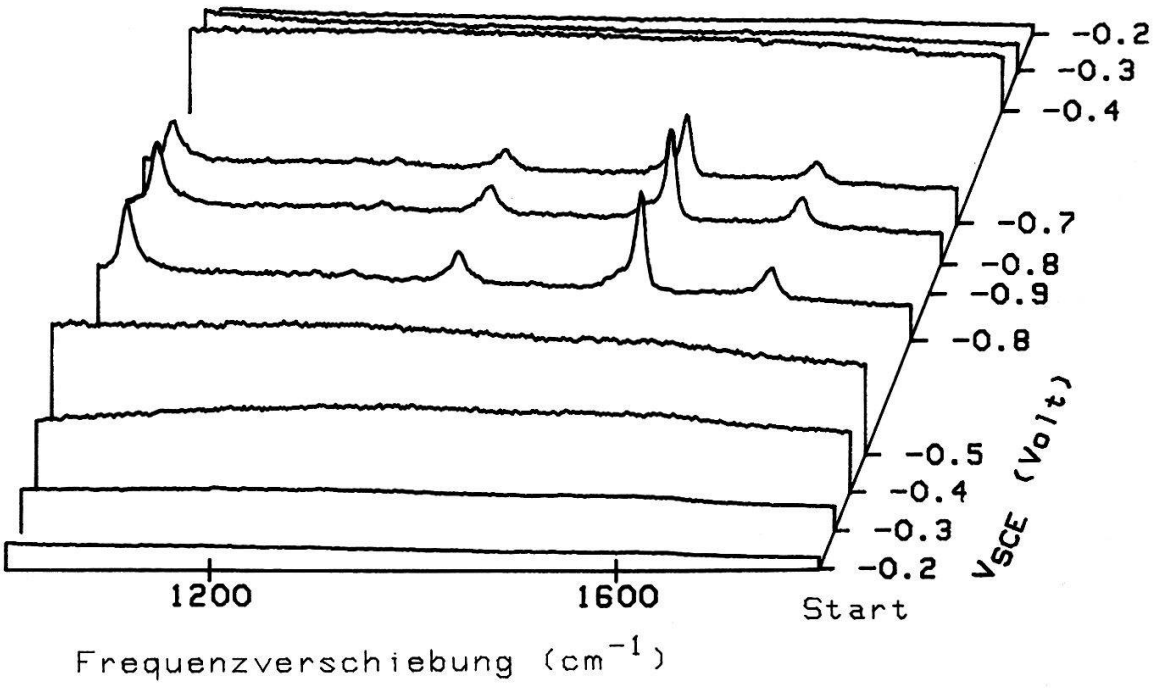

Fig. 1: Ramanspektren von MV^{+} auf einer "glatten" Silberoberfläche als Funktion des Elektrodenpotentials.

Der Elektrolyt hatte folgende Zusammensetzung: bidestilliertes Wasser mit 0.1M KCl (Merck suprapurum) sowie 10^{-3}M Methylviologen(Fluka purum), welches vor Verwendung zweimal umkristallisiert wurde.

MV^{2+} wird bei -0.69 V gegen SCE zu MV^{+} reduziert. In Figur 1 sind die Ramanspektren an einer "glatten" Ag-Elektrode gemessen als Funktion des Elektrodenpotentials dargestellt. "Glatt" heisst, dass die Ag-Elektrode auf Hochglanz poliert wurde und zwar mit einer wässerigen Al_2O_3 Suspension bis hinunter auf eine Korngrösse von 0.5µm. Zur Messung der Ramanspektren wurde das Potential zyklisch von -0.2 V_{SCE} bis -0.9 V_{SCE} und wieder zurück bis -0.2 V_{SCE} variiert. Beim jeweiligen Potential wurde gerade solange angehalten als zur Aufnahme des Ramanspektrums

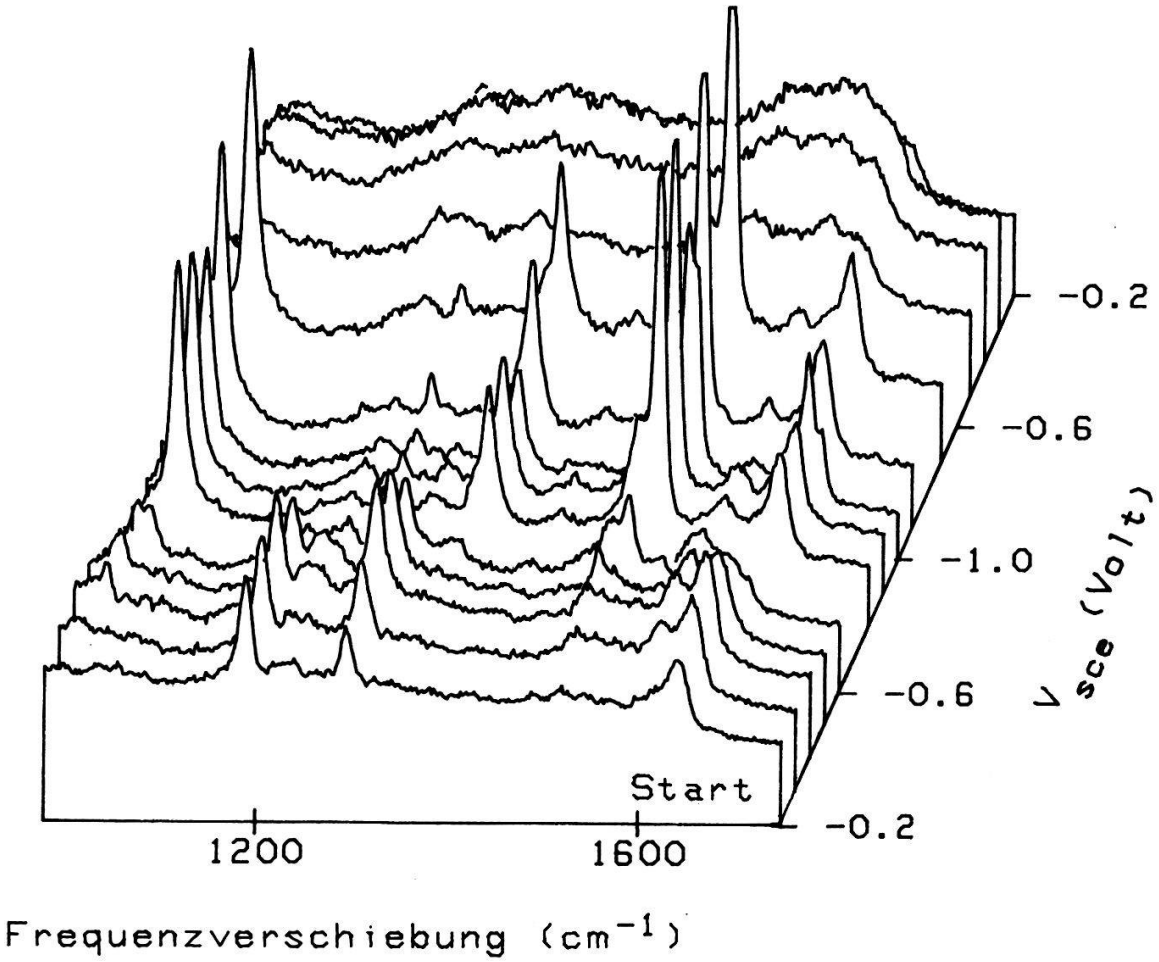

Fig. 2: Ramanspektren von MV^{2+}/MV^{+} auf einer aufgerauhten Silberelektrode als Funktion des Elektrodenpotentials.

nötig ist. Im Bereich $V > V_{SCE}$ werden die Spektren der reduzierten Komponente MV^+ nachgewiesen. Die dominanten Linien bei 1028, 1356, 1534 und 1662 cm^{-1} gehören zu Ringschwingungen des MV^+ Ions [1,2]. Es wird hier der resonante Ramaneffekt beobachtet, da die benutzte Laserwellenlänge von 514 nm auf der Flanke eines Absorptionsmaximums liegt [3].

Durch geeignetes Aufrauhen der Ag-Elektrode kann man mittels des oberflächenverstärkten Ramaneffekts (SERS) auch die Schwingungen der oxidierten Komponente sichtbar machen (Figur 2). Dabei ist es von Bedeutung, ob man die Silberoberfläche im Beisein von Methylviologen oder in einer separaten 0.1 M KCl Lösung aufrauht, da je nachdem andere Adsorptionskomplexe gebildet werden, was im Ramanspektrum und in den zyklischen Voltamogrammen sichtbar ist [4,5]. Bei den in Figur 2 gezeigten Spektren wurde die Oberfläche in einer separaten Zelle aufgerauht, und die Oberflächenrauhigkeit lag in der Grössenordnung von 1000 Å. Dies hatte sich

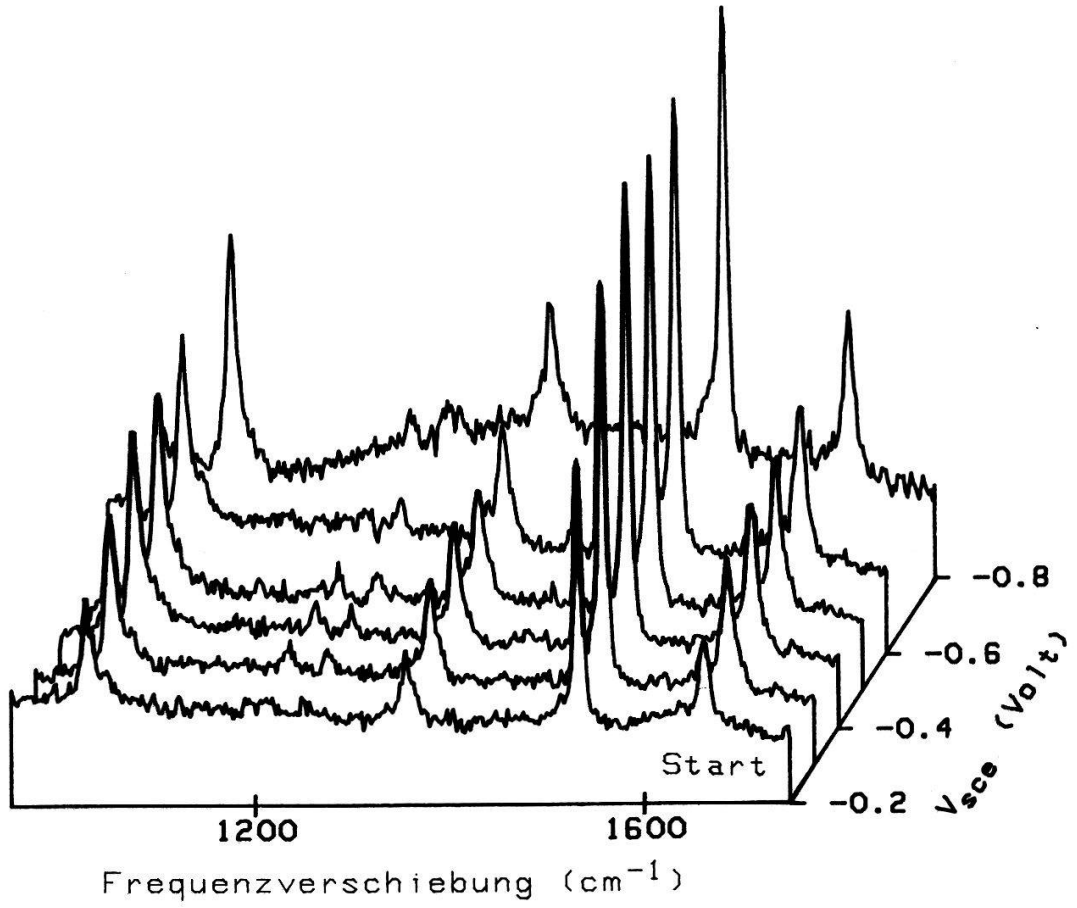

Fig. 3: Ramanspektren von MV^+ auf einer β-ZnP_2 Elektrode als Funktion des Elektrodenpotentials.

für das System Pyridin auf Silber als optimal erwiesen [6]. Die Linien im Spektrum bei 1190, 1242, 1296 und 1642 cm^{-1} gehören zu Schwingungen des MV^{+} Ions, die aber in ihrer Frequenzverschiebung von den Werten abweichen, welche für MV^{2+} in wässeriger Lösung von 0.2M gemessen wurden 2 . SERS an MV^{+} war schon von Regis und Corset [7] an in situ aufgerauhten Ag-Elektroden gemessen worden. Bei der vorliegenden Arbeit wird die Reaktion MV^{2+}/MV^{+} als Funktion des Elektrodenpotentials dargestellt. Im Bereich von -0.6 V_{SCE} ist der Uebergang von einem Spektum zum andern sehr deutlich zu beobachten. Leider erscheint das SERS-Spektrum nach der Oxidation der MV^{+} Ionen nicht wieder. Dies hängt wahrscheinlich damit zusammen, dass sich die Oberfläche doch während der langen Messzeit verändert, welche zur Aufnahme der vorhergehenden Spektren benötigt wird.

Auf der p-typ Halbleiterelektrode (β-ZnP_2) erzeugt der einfallende Laserstrahl einen Photostrom, welcher zur Reduktion der MV^{2+} Ionen am Halbleiter/Elektrolyt Kontakt führt. Diese Reduktion setzt nicht wie an der Ag-Elektrode bei -0.69 V_{SCE} ein, sondern schon bei viel niedrigeren Potentialen, d. h. mit dem Einsatz des Photostroms (Figur 3). Das Ramanspektrum ist identisch zu dem, welches an der "glatten" Ag-Oberfläche gefunden wurde (Figur 1). Die Intensitäten der Ramanlinien, welche mit breiten Monochromatorspalt (Auflösung 8 cm^{-1}) gleichzeitig mit dem Photostrom gemessen wurden, sind zu diesem proportional.

In dieser Arbeit wurde die Reduktion von Methylviologen auf einer Metall- oder Halbleiterelektrode sowohl qualitativ als auch quantitativ erfasst. Es hat sich gezeigt, dass Ramanstreuung eine leistungsfähige Methode ist um Oberflächenreaktionen in situ zu untersuchen.

Referenzen

[1] R.E.Hester,S.Suzuki, J. Phys. Chem. 86, 4626 (1982)

[2] P.C.Lee, K.Schmidt, S.Gordon, D.Meisel, Chem. Phys. Lett. 80, 242 (1981)

[3] M.Forster, R.B.Griling, R.E.Hester, J. Raman Spectr. 12, 36 (1982)

[4] C.A.Melendres, P.C.Lee, D.Meisel, J.Electrochem. Soc. 130, 1523 (1983)

[5] Auf diese Problematik wird in einer zukünftigen Arbeit eingegangen.

[6] Y.Mo, I.Mörke, P.Wachter, Surf. Science 133, L452 (1983)

[7] A.Regis, J.Corset, J. Chimie Phys. 78, 689 (1981)

PRODUCT STATE DISTRIBUTIONS IN THE PHOTODISSOCIATION OF IODINE - RARE GAS CLUSTERS

J.-M. Philippoz, R. Monot and H. van den Bergh, Laboratoire de Chimie-Technique and Institut de Physique Expérimentale, Ecole Polytechnique Fédérale de Lausanne, CH-1015 Lausanne, Switzerland

The quantum yield for the photodissociation of free molecular iodine ($I_2 \rightarrow 2I$) is unity for excitation just above the dissociation limit of the B state [1]. In van der Waals clusters I_2M the inert gas atom (or molecule) M may hinder the formation of free iodine atoms, and processes like

$$I_2M \xrightarrow{h\nu} I_2 (B^3\Pi_{o^+_u})_{v',J'} + M + \text{kinetic energy} \qquad (1)$$

can become significant. Pathways like (1) may play a role in the phenomenon called the solvent cage effect, which describes the reduction in photolysis quantum yields caused by "solvent interaction" in dense media [2,3]. Also, reaction (1) is a choice model system for photodissociation studies [4]. If, as is the case here, the I_2 product is formed in an electronically excited state, dispersion of its fluorescence allows for measurement of its rovibrational state distributions. This is providing the measurement is made under collision free conditions and sufficient spectroscopic data is available to convert fluorescence intensities to relative populations. Early reports on reaction (1) include a measurement of the unevaluated fluorescence intensities observed in the dissociation of I_2Ar at 488 nm [5], and more detailed measurements from which the actual product vibrational state distributions were obtained for the case of I_2He, I_2Ne and I_2Ar dissociated at 496.5, 488, and 476.5 nm [6].

In the present work we report on new and improved measurements of reaction (1) at several photodissociation wavelengths with M = He, Ne, Ar, Kr and Xe. The results are compared with trajectory calculations [7]. Measurements at higher dispersion giving rotationally resolved spectra are also presented.

For these experiments the apparatus [6] was modified by exciting the I_2M complexes in the free jet with the much higher power levels available from the argon ion laser <u>inside</u> the laser cavity. Power levels in excess of 20 Watts were thus available for instance at 488 nm in a laser which gives about 2 W on this line outside the cavity. The free jet is intersected by the laser beam 4 mm downstream from the nozzle. The fluorescence is collected at right

angles to both with a plexiglas bar of 20 mm diameter, the polished end of which is 15 mm from the intersection of jet and laser beam. The F = 1 monochromator is fitted with a grating with 2400 grooves/mm to give a maximum resolution of 70 mÅ. The photomultiplier is cooled to 250 K to give a dark current of 2 cps. Fig. 1A shows a vibrationally resolved fluorescence spectrum of I_2 formed in the photodissociation of I_2Xe at 488 nm. Fig. 1B shows the relative vibrational state populations extracted from such measurements at 3 wavelengths above the B state dissociation limit. The spectra are unchanged when

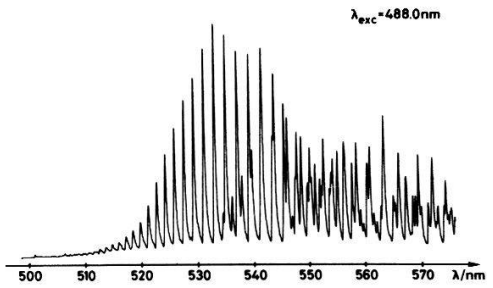

Fig. 1A : Fluorescence from free I_2 produced by the photodissociation of I_2Xe at 488 nm. $P_o = 0,5$ bar, $P(I_2) = 2$ mbar, T = 350 K. The fluorescence observed is from v'= 20-46 to v" =0-3.

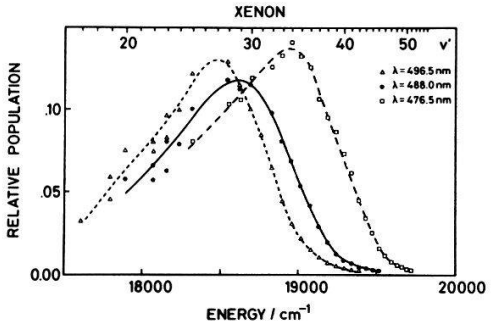

Fig. 1B : The relative vibrational populations of the B state of free I_2 after photodissociating I_2Xe at 496.5 nm (△), 488 nm (●), and 476.5 nm (□). Conditions as in 1A. Energy is relative to $X^1\Sigma^+$ (v" = J" = 0).

we irradiate farther downstream from the nozzle which rules out collisional perturbations and the possibility of fluorescence arising from atom recombination into excited states [8]. The measurements are made under conditions where the fluorescence yields are proportional to the square of the carrier gas pressure which indicates photodissociation of I_2M rather than of I_2M_n with n larger than 1. Fluorescence intensities are converted to vibrational state populations by

$$N_{v'} = C.(n_{v'v''}/FCF_{v'v''}) \cdot (\Gamma_{tot,v'}/\nu^3_{v'v''} \mid \mu_e \{\bar{R}_{v'v''}\}|^2) \qquad (2)$$

where C is a constant, $n_{v'v''}$ is the measured intensity which includes a correction factor for the frequency dependence of the apparatus detection efficiency, FCF is the known Franck-Condon factor [9], Γ_{tot} is the total decay rate from one vibrational level including predissociation [10], and the last term is the transition dipole moment [11]. Fig. 1B shows broad vibrational state distributions which shift to higher vibrational states as the energy of

the photon is increased. The energy lost to translational motion of the photodissociation fragments ($E_{h\nu} - E_{v'}$) slightly increases with the excitation energy which is in contradiction with the trajectory calculation predictions [7]. The mean energy lost to translation $\overline{(E_{h\nu} - E_{v'})}$ is shown in Fig. 2 for I_2He through I_2Xe. At 476.5 nm at high excess energy above the dissociation limit of the B state the energy lost to translation is rather independent of the inert gas atom, whereas at 496.5 nm a clear minimum of about 1200 cm^{-1} appears for Ar, 1600 cm^{-1} being lost for M = Xe and in excess of 1700 cm^{-1} for both He and Ne. Calculated energy losses [7] corresponding to 496.5 nm excitation are also shown, and found to be much smaller. It should also be noted how different these results are from those obtained by Levy and coworkers [12] upon excitation to a bound level of the B state, where small energy losses corresponding to an energy gap law were observed.

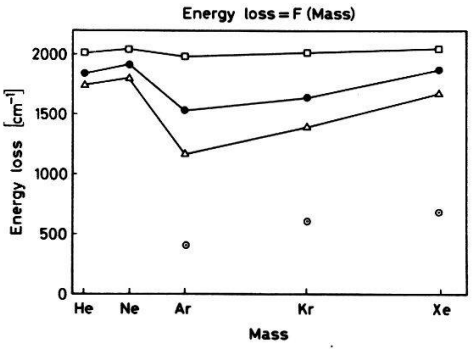

Fig. 2 : The mean energy lost by the cage effect in the photodissociation of I_2M for M = He, Ne, Ar, Kr, Xe at 496.5 nm (△), 488 nm (●), and 476.5 nm (□). (⊙) are results of trajectory calculations (ref. 7).

Fig. 3A shows the fluorescence from I_2 in the B state with v' = 29 to the ground state (X) with v'' = 0 with resolved rotational states. Fig. 3B shows a similar spectrum which has been computer simulated with a Boltzmann

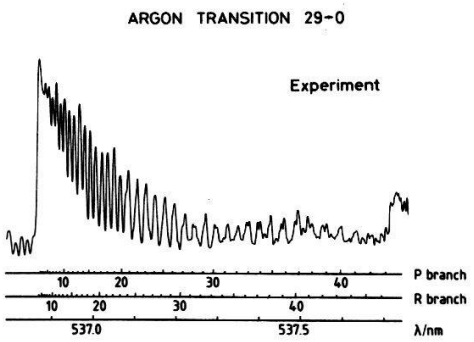

Fig. 3A : Rotationally resolved fluorescence spectrum following I_2Ar dissociation at 488 nm. Observation on the 29 - 0 vibrational transition.

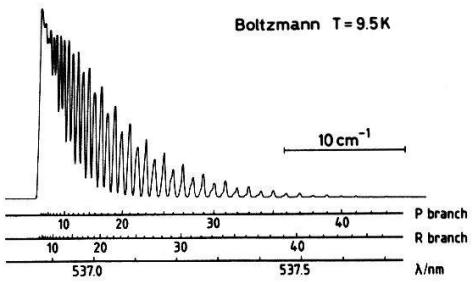

Fig. 3B : Computer simulation of 3A for I_2(B) rotational temperature of 9.5 K assuming Boltzmann distribution.

distribution of rotational states at T = 9.5 K. Whereas the "fit" for low rotational levels is reasonably good, clearly the photodissociation is producing a significant population of higher rotational levels which is strictly non-Boltzmann. The population of nuclear spin states appears to be statistical. A similar "non-Boltzmann" tail of high rotational states has also been measured in the case of I_2Xe. Fig. 3C shows the rotational envelope of $v = 0$ ground vibrational level of the free I_2 molecule in the beam measured using a tunable dye laser. If we assume (and this is not necessarily so) that the rotational "temperatures" for I_2 and I_2M in the beam are equal, the observed low temperature of I_2 would imply significant rotational excitation occuring in the photodissociation process.

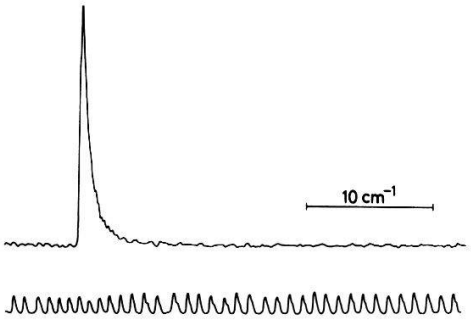

Fig. 3C : Measured rotational temperature of $I_2(X)$ in the free jet. $T_{rot} \simeq 3$ K.

Acknowledgments

The authors are grateful to B. Calpini for help with perliminary measurements and to the Fonds National Suisse for financial support.

References

1. D.H. Burde, R.A. McFarlane and J.R. Wiesenfeld, Phys. Rev. A10 (1974) 1917.
2. See for instance J.-C. Dutoit, J.-M. Zellweger and H. van den Bergh, J. Chem. Phys. 78 (1983) 1825, and references therein.
3. B. Otto, J. Schroeder and J. Troe, J. Chem. Phys. 81 (1984) 202.
4. R. Schinke and V. Engel, J. Chem. Phys. 83 (1985) 5068.
5. J.J. Valentini and J.B. Cross, J. Chem. Phys. 77 (1982) 572.
6. J.-M. Philippoz, B. Calpini, R. Monot and H. van den Bergh, Helv. Phys. Acta 58 (1985) 875.
7. I. Noorbatcha, L.M. Raff and D.L. Thompson, J. Chem. Phys. 81 (1984) 5658.
8. K.-H. Stephan-Rossbach and F.J. Comes, Chem. Phys. 80 (1983) 121.
9. J. Tellinghuisen, J. Quant. Spectrosc. Radiat. Transfer 19 (1978) 149.
10. J. Vigué, M. Broyer and J.C. Lehmann, J. Physique 42 (1981) 961.
11. J. Tellinghuisen, J. Chem. Phys. 76 (1982) 4736.
12. K.E. Johnson, W. Sharfin and D.H. Levy, J. Chem. Phys. 74 (1981) 163.

Absorptionsspektroskopie in $YAlO_3$:Er

S. Schnell, W. Lüthy
Inst. für angew. Physik, Universität Bern, Sidlerstr. 5, 3012 Bern

Die Absorptions- und Emissionsspektren von Erbium-dotierten YAG Kristallen sind gut bekannt. Bei Erbium dotierten $YAlO_3$ Kristallen, die vielversprechende Eigenschaften als Lasermedien aufweisen, kennt man bis heute vor allem das Absorptionsspektrum bei 4,2 K. Wir untersuchten das Absorptionsspektrum bei hoher Erbiumkonzentration, zum Teil in Abhängigkeit der Polarisationsrichtung. $YAlO_3$:Er ist ein orthorhombischer Kristall mit drei Achsen a, b und c. Da bei den von uns verwendeten Laserstäben die b Achse mit der Stabachse zusammenfällt, haben wir vor allem die Abhängigkeit der Absorption von der Polarisation des einfallenden Lichts parallel zur a und zur c Achse untersucht.

Spectroscopie de fluorescence de $YALO_3$:Er

P.-D. Henchoz, M. Dätwyler, S. Schnell et W. Lüthy

Inst. de Phys. Appl., Université de Berne, Sidlerstr. 5, 3012 Berne.

Des cristaux de $YALO_3$:Er ont été illuminés à l'aide de lasers dans l'ultraviolet, le visible et l'infrarouge. Les spectres de fluorescence ont été mesurés et une estimation des temps de vie et des rapports d'embranchement a pu être faite. Les mécanismes conduisants à la population du niveau $^4S_{3/2}$, niveau supérieur de différentes transitions laser à environ 1,7 µm, ont été mis en évidence.

ANDO VII : Capteurs, détecteurs

Physikalische Eigenschaften einer Metallteilchen Suspension

M.Stalder und W.Lüthy
Inst. für Angew. Physik, Universität Bern, Sidlerstr.5, 3012 Bern

Bei der Bestrahlung einer dünnen Flüssigkeitsschicht mit Licht oder Wärmestrahlung entstehen charakteristische Strömungen. Gibt man kleine Metallplättchen in die Flüssigkeit, werden diese Strömungen, vor allem an der Oberfläche sichtbar. Basierend auf diesem Mechanismus lässt sich mit einfachen Mitteln Infrarotstrahlung sichtbar machen. Es wurde ein Bildwandler gebaut, der eine Detektionsempfindlichkeit von etwa 3 mJ/cm^2 aufweist. Ein Objekt von 41° C konnte damit in einer Umgebung von 20° C noch abgebildet werden. Die suspendierten Metallplättchen lassen sich zudem in äusseren elektrischen oder magnetischen Feldern ausrichten. Dabei werden die optischen Eigenschaften der Suspension verändert. Eine Spannung von 9 V über einer Suspension von 1 mm Schichtdicke führt bereits zu einer sichtbaren Transmissionsänderung. Es werden Möglichkeiten demonstriert, diese Wechselwirkung für die Herstellung von Displays zu verwenden.

ANDO VIII : Recherche sur l'énergie, écologie

REGELUNG EINER STUECKHOLZFEUERUNG

D. Kerschbaumer, R. Tscharner, Institut de Microtechnique, Université, CH-2000 Neuchâtel, Suisse
P. Schweizer, TIBA AG, 4416 Bubendorf, Schweiz

Zusammenfassung: Messung und periodische Aufzeichnung der Rauchgaszusammensetzung und der Temperaturen von Flamme und Rauch sowie der Luftzufuhr an einer Stückholzfeuerung um einen kostengünstig zu messenden Parameter für die Regelung der Verbrennung zu erhalten.

1. Einleitung

Das Ziel des Projektes ist, bei einer Stückholzfeuerung eine möglichst gleichbleibende, gute Verbrennung zu sichern. Dies bedeutet eine vollständige Verbrennung des Holzes, eine Minimierung der Schadstoffe und ein guter Wirkungsgrad. Zur Kontrolle der Verbrennung wird der CO-Gehalt der Rauchgase gemessen. Kohlenmonoxid in den Rauchgasen bedeutet immer eine unvollständige Verbrennung. Repräsentierend für die Gruppe der Stickoxide, als Schadstoffe jeder Feuerung, wurde die NO-Konzentration im Rauch gemessen. Ein wichtiger Parameter für den Wirkungsgrad ist der CO_2-Gehalt der Rauchgase. Dieser definiert den Luftüberschuss als Quotienten der maximal möglichen CO_2-Konzentration, entsprechend einer minimal benötigten Luftmenge für eine stöchiometrische Verbrennung, dividiert durch die gemessene CO_2-Konzentration der Rauchgase. Für Holz ist der maximale CO_2-Gehalt gleich 20,4%.

2. Regel- und Messgrössen

Die kontinuierlich gemessene Menge der zugeführten Primär- und Sekundärluft steuert die Verbrennung. Die Primärluft dient der Glutbildung und Holzgasproduktion und bestimmt die Leistung der Feuerung. Die Sekundärluft dient der Verbrennung der entstandenen Holzgase und bestimmt die Verbrennungsqualität über den Luftüberschuss. Um die Verbrennungsqualität zu überwachen, wurden an Versuchsofen noch die Flammtemperatur, die Rauchgastemperatur und die Leistung am Wärmetauscher gemessen.

3. Versuchsofen

Fig. 1 Schema des untersuchten Versuchsofens

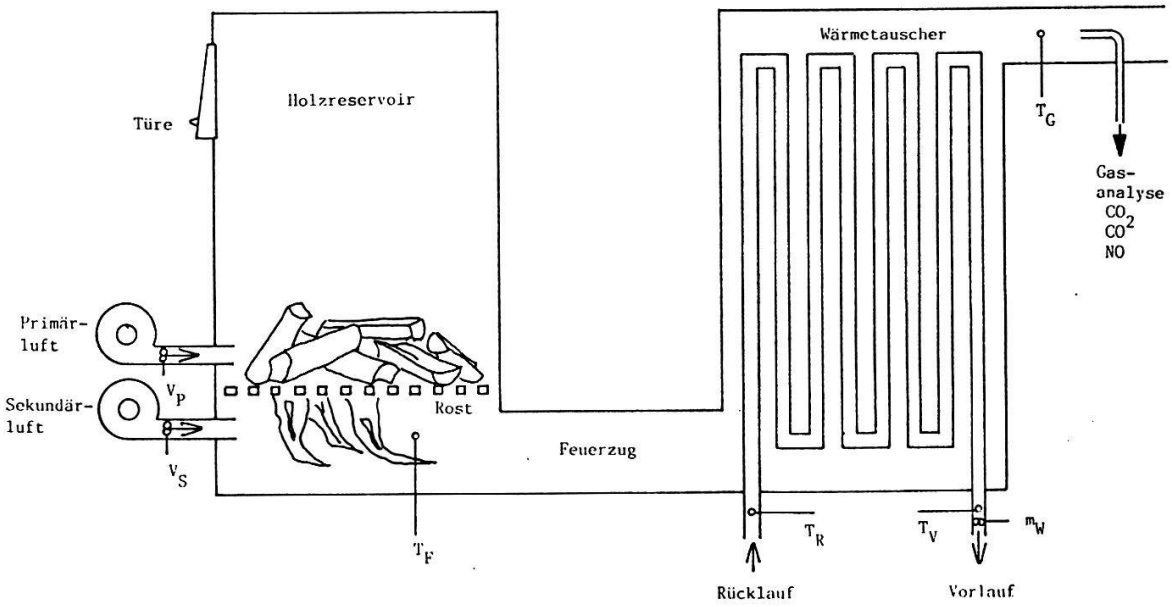

Charakteristisch für den neuen TIBA-Versuchsofen sind die getrennt regulierbare Primär- und Sekundärluftzufuhr sowie ein auf dem Kopf stehendes Feuer, was einen automatischen Holznachschub gewährleistet. Eine heikle, aber wichtige Voraussetzung zur Messung aller Parameter ist die Dichtigkeit des Ofens. Ein allfälliger unkontrollierter Luft- oder Rauchaustausch würde alle Messungen verfälschen.

4. Messresultate

Die Messungen am beschriebenen Ofen zeigen klar, dass bei einer guten Einstellung des Verhältnisses von Primär- zu Sekundärluft eine hervorragende Verbrennung möglich ist. Konzentrationen von weniger als 100 ppm CO sind bei unterschiedlichen Leistungen auch bei geringem Luftüberschuss zu erreichen. An Stickoxid wurden maximal 250 ppm gemessen, typisch sind ca. 100 ppm (siehe Fig. 2). Ein Zusammenhang zwischen Rauchgastemperatur und Verbrennungsqualität ist nicht offensichtlich; die starken Schwankungen des CO-Wertes haben keinen direkten Einfluss auf die Rauchtemperatur. Die Abkühlung im Wärmetauscher ist nicht linear. Hingegen verlaufen die Rauchtemperatur und die Leistung annähernd parallel, was theoretisch aus den Wärmeübergangsgleichungen der Strömungslehre hervorgeht. Die anfangs hohen CO-Werte sind eine Folge von brüsken Aenderungen der Luftzufuhr, die Verbrennung braucht eine gewisse Zeit um sich zu stabilisieren(siehe Fig. 3).

Fig. 2 Rauchgaskonzentrationen

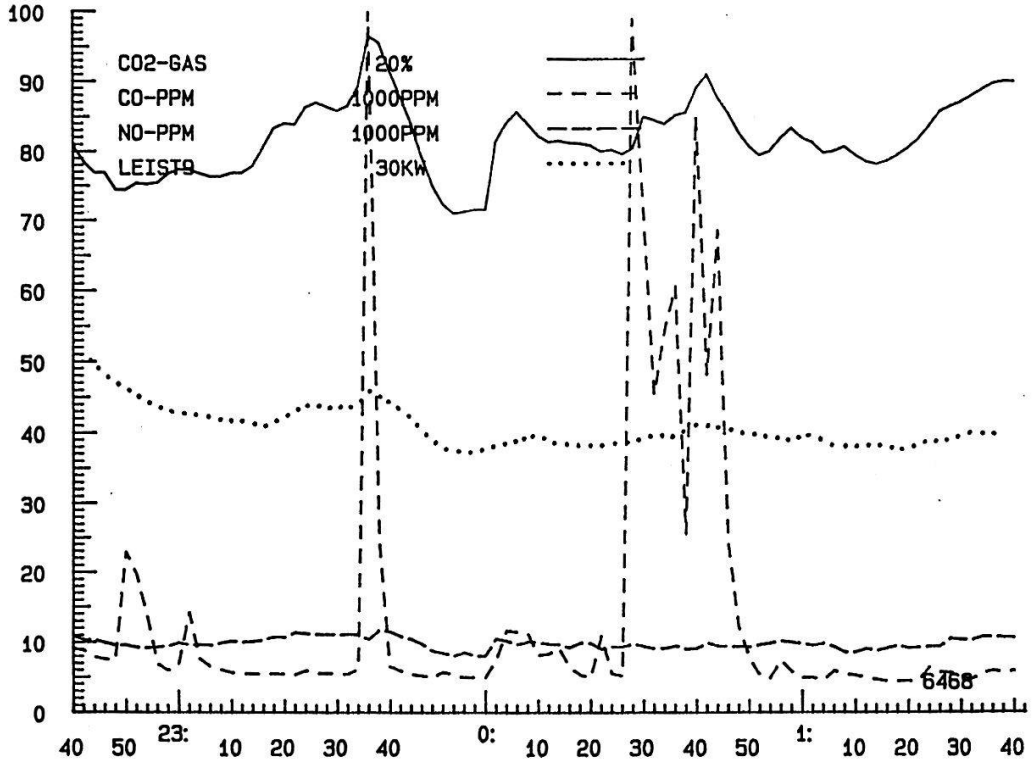

Fig. 3 Verbrennungsqualität - Rauchgastemperatur

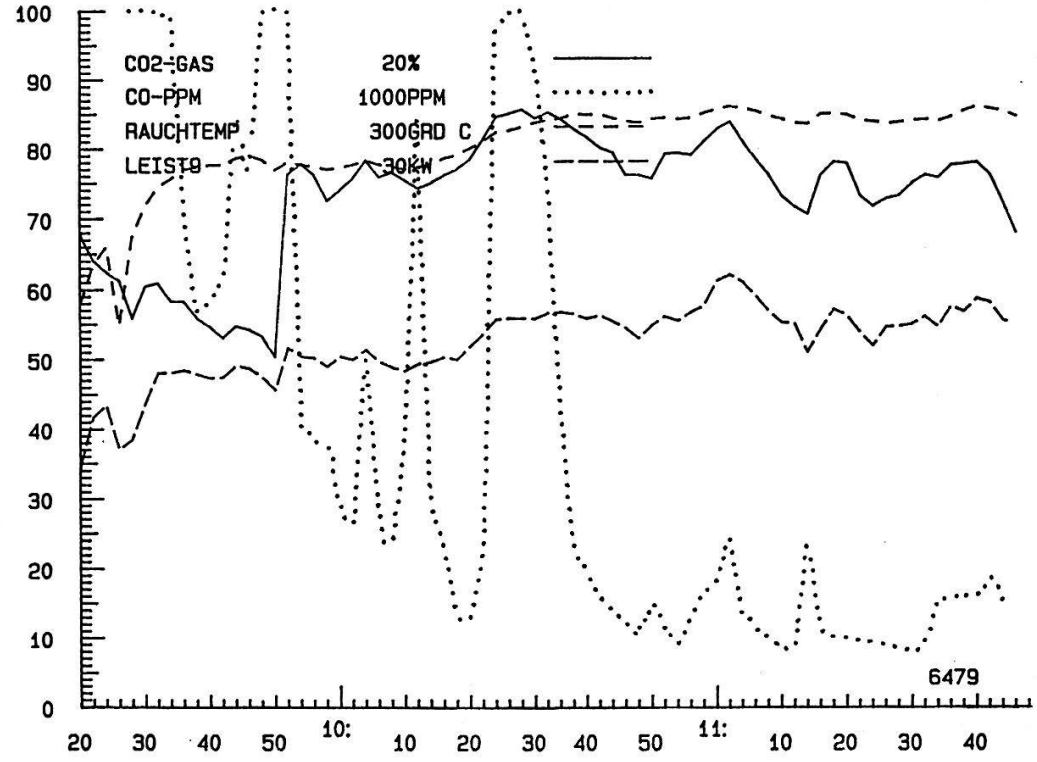

5. Steuerung

Bis jetzt wurde eine erste Version einer Ofensteuerung entwickelt, welche noch keine Regelung der Luftzufuhr durch eine rückgekoppelte Messgrösse enthält. Es handelt sich also lediglich um eine Programmsteuerung. Diese kennt zwei Leistungsstufen mit programmierbaren Ventilstellungen für die Luftzufuhr. Um dennoch eine akzeptable Verbrennung zu erreichen wird die Luftzufuhr möglichst selten verändert. Das Prinzip der Steuerung besteht im Aufladen eines kleinen Zwischenspeichers in Form eines Warmwasserreservoirs in Abhängigkeit von dessen Temperatur. Realisiert wurde die Steuerung mit einer kommerziellen "speicherprogrammierbaren Steuerung" sowie entsprechenden Interfaces für die Messung der Speichertemperatur sowie einer Flammtemperaturschwelle. Die Ausgänge steuern die Stellungen der Luftventile, die Ventilatoren und die Kontrolllampen. Das Programm enthält einen festen Startzyklus, welcher wiederholt wird, bis die eingestellte Flammtemperatur erreicht ist. Wird diese nach einigen Versuchen nicht erreicht, wird angenommen dass der Ofen leer sei. Sonst wechselt das Programm dann zwischen den zwei Leistungsstufen oder stellt die Luftzufuhr ganz ab, je nach der Speichertemperatur. Während des Betriebs wird die Flammtemperatur laufend überwacht und beim Unterschreiten einer Schwelle der Ofen neu gestartet, weil eine Flammtemperatur unter der Verbrennungstemperatur von Kohlenmonoxid, d.h. ca. 600 Grad, eine schlechte Verbrennung anzeigt. Der Ofen kann maximal sechs Stunden ausgeschaltet bleiben, ansonsten erfolgt ein Start um das bestehende Glutbett nicht erlöschen zu lassen.

6. Schlussfolgerungen

Die Messungen zeigen eine deutliche Verbesserung des Wirkungsgrades und geringere Kohlenmonoxidemissionen des Versuchsofens mit der gegenwärtigen Steuerung gegenüber konventionellen Feuerungen mit Verbrennungsluftzufuhr über den Kaminunterdruck und einer Luftregelung über Klappen, ohne die Trennung von Primär- und Sekundärluft. Eine weitere Verbesserung ist noch durch eine kontinuierliche Regelung der Luftzufuhr möglich.

ENERGY BALANCE OF WINDOWS

R. Furler, P. Williams and F.K. Kneubühl,
Institute of Quantum Electronics, Physics Department, ETH
CH-8093 Zurich, Switzerland

1. Introduction

The energy transfer through windows is significant in relation to the energy consumption of buildings. After a detailed study [1] on the influence of solar and thermal radiation on the energy consumption of buildings we have focussed our attention to the energy performance of conventional and advanced multiple-glazed windows with respect to the spectral properties of the glass panes, heat transfer, external air flow and convection. The multiple-glazed windows studied include glasses with selective coatings. The aim of our study is a detailed knowledge of the physical phenomena controlling the energy transfer through different types of windows. Thus, we intend to provide a basis for the measurement and the comparison of glazings with respect to solar and thermal radiation, heat conduction and convection as well as atest for the parameters which are used to characterize window glazings [2]. For this purpose we measure the spectral transmission and reflection of the glass panes from multiple-glazed windows in the wavelength range 0.2 to 45 μm. We also perform in-situ measurements on a test cabin, which are compared with a computer model [3] on radiation and heat transfer through windows. In the following we present some recent results of spectroscopic and in-situ measurements on multiple-glazed windows.

2. Spectral Properties of Windows

For the measurements of the spectral properties of the glazings we make use of two commercial spectrometers (Perkin Elmer 330 and 580). They cover the wavelength range 0.2 to 45 μm, which includes the whole spectrum of solar and thermal radiation. Both spectrometers enable us to determine the transmission of multiple glazings and the reflection of single glass panes. Therefore, we have to calculate the multiple-glazing reflection from the single-glass spectra. For additional measurements of the diffuse reflection from 0.2 to 2.5 μm we apply a Ulbricht-sphere.

Most of the glazings are sold as multiple glazings. These usually consist of a combination of "float" glasses or a combination of one spectrally selective glass with one or more "float" glasses. Selective glasses are normally formed by depositing a thin-film coating on "float" glass. Fig. 1 shows as an example the reflection and transmission spectra of a single "float" glass pane. In the solar range (0.3 to 0.8 μm) the transmission is high, approximately 86 %, where as for wavelengths greater than 4.5 μm the transmission is zero. The reflection for one air-to-glass interface is nearly constant for wavelengths between 0.3 μm and 4 μm.

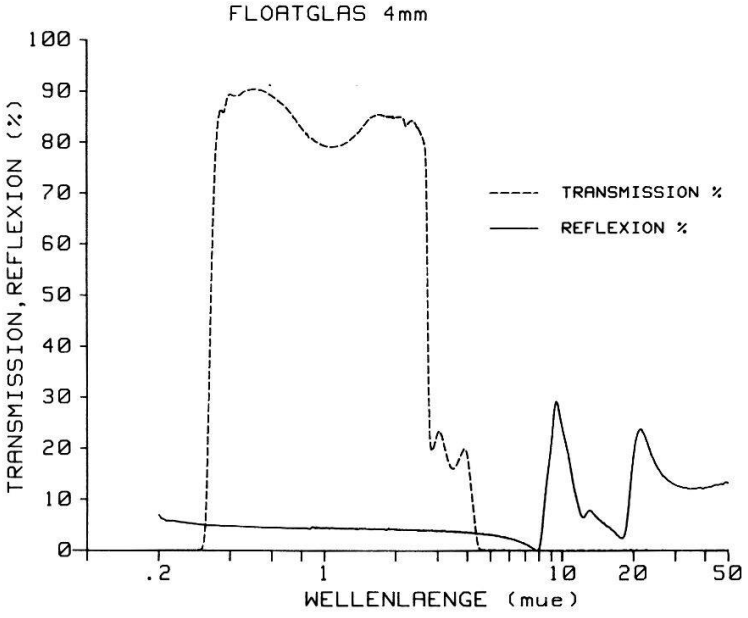

Fig. 1 Spectral transmission and reflection of "float" glass.

Hitherto, we have determined the spectral transmission and reflection of over 20 different types of window glasses.

3. In-situ Measurements

The energy transfer through glazings is determined by conduction, convection and solar and thermal background radiation. Additional relevant parameters describing the interior and exterior climate include ambient air temperature, cloud cover, wind speeds above the roof, wind direction and air stream velocity next to the glazings due to free and forced convection. In order to estimate the influence of these parameters on the energy balance of

windows we perform in-situ measurements on a test cabin at the EMPA in Dübendorf, Switzerland. This test cabin is equipped with two different windows, a double-glazed "Comfort" window and a triple-glazed "float" glass window. The "Comfort" window consists of a "float" glass pane and a selective glass pane with a SnO_2 doped coating on the inside of the indoor pane, which results in a low emissivity of about 0.1. This reduces the radiative energy exchange between the glazing layers. We determine the surface temperatures of the individual glass panes with the aid of thermoelements and infrared radiometers. This arrangement enables us to investigate two different glazings simultaneously, i.e. under identical environmental conditions. The indoor air temperature is regulated to 20^0C by heating. All measurments and the heating are controlled by a "HP 9836" computer. Data are stored every 5 minutes.

Fig. 2 shows the indoor surface temperatures of the "Comfort" window, measured by "Keller PH01" infrared radiometer and a thermoelement. The radiometer is equipped with a 8 to 14 µm transmission filter and a reference blackbody. The latter is required for the evaluation of the thermal infrared radiation reflected by the glass pane.

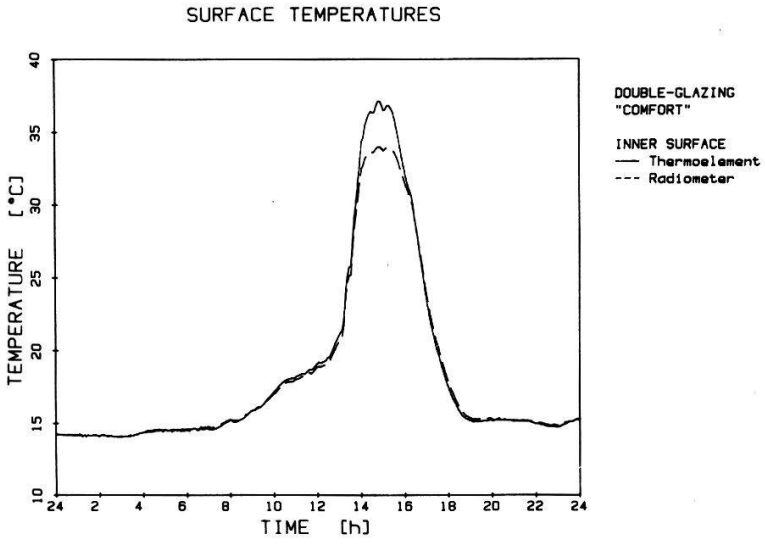

Fig. 2 Indoor surface temperature of a double-glazed "Comfort" window measured by a thermoelement and by a 8 to 14 µm radiometer on March 11, 1986

We calculate the emissivity of the glass panes from the measurements by thermoelements and by radiometer at night with the assumption that they agree. In Fig. 2 we observe a marked difference between thermoelement and radiometer measurements during the day. This difference is due to different solar heating of thermoelement and glass pane. For this reason the radiometer data are more reliable.

Our in-situ measurements will be compared to the theoretical model of Rubin [3] on the energy transfer through windows. This model assumes a stationary state, which is justified by the short response time of the glass temperatures due to the high heat capacity of glazings and the small thermal resistance of the glass panes as demonstrated in Fig. 3.

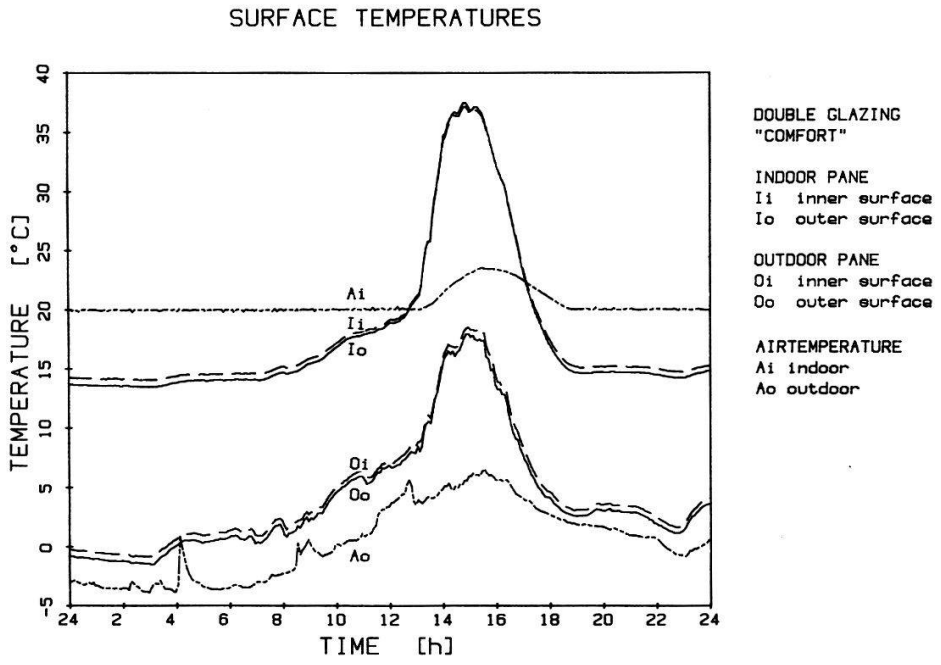

Fig. 3 In-situ measurements of indoor and outdoor air temperatures and surface temperatures of a double-glazed "Comfort" window measured thermoelements, recorded on March 11, 1986

In order to obtain more information on the convective heat transfer coefficient we are also performing experiments with a model of the test cabin in a water channel and in a wind channel [4]. These and further results of our study on the energy balance of windows will be published in detail.

Acknowledgements

This study is supported by NEFF; EMPA, Dübendorf; Heglas AG, St. Gallen; Schweizerisches Institut für Glas am Bau, Zurich; and ETH, Zurich.

References

[1] Ch. Zürcher, G. Finger, F.K. Kneubühl, F. Thiébaud, H. Vetsch, Infrared Physics 22, 277-291 (1982)

[2] F. Thiébaud and F.K. Kneubühl, Helv. Phys. Acta 57, 277-280 (1984), ibid. 57, 529-532 (1984)

[3] M. Rubin, Lawrence Berkeley Laboratory, Report Nr. 12486, May (1981)

[4] P. Williams, R. Furler, F.K. Kneubühl, Helv. Phys. Acta, in print

THE INFLUENCE OF THE AMBIENT WIND VELOCITY ON THE EXTERIOR CONVECTION HEAT TRANSFER COEFFICIENTS OF BUILDING ENVELOPES

P. Williams, R. Furler and F.K. Kneubühl
Institute of Quantum Electronics, Physics Department, ETH,
CH-8093 Zurich, Switzerland

1. Introduction

Heat transfer between the exterior surface of a building envelope and the environment occurs via radiation and combined conduction and convection. The influence of both thermal and solar radiation on the energy consumption of buildings has been examined by Zürcher et al. (1982). Both natural convection, due to the density changes of warm air, and forced convection, due to wind, occur at the exterior surfaces of buildings. The convective heat transfer coefficient due to natural convection has been measured, for laboratory situations, by both Saunders (1936) and Weiss (1935), whose results are summarised by McAdams (1954). In the work reported here consideration is given to the forced convective heat transfer coefficient occurring at the windows of a test cabin (Furler et al., 1986) used to assess the energy performance of windows.

In order to compare the energy performance of windows and calculate the energy requirements of buildings it is common to use a combined convective and radiative heat transfer coefficient, often quoted as the 'U-value'. This U-value is normally given for a fixed wind speed and independent of wind direction. However, Ito et al. (1972) have shown that the convective heat transfer coefficient of a six storey building is dependent on the wind speed, wind direction and surface location. Both Kimura (1977) and Lokmanhekim (1971) use the experimental results of Ito et al. (1972) to determine the convective heat transfer coefficient for two categories of wind direction: windward surfaces and leeward surfaces. In this study a closer examination is made of the relation between the wind direction and the convective heat transfer coefficient at the windows of a test cabin. A water channel is used to enable the influence of differing fluid directions on the flow around the cabin to be visualised. The convective heat transfer

coefficient is measured as a function of wind direction using a scale model of the cabin in a wind tunnel.

2. Experimental

A 1:80 scale model of the test cabin was constructed from perspex, including relevant features such as external instrument boxes and an nearby cabin. To achieve dynamic similarity between the real cabin and a model, immersed in a water channel, the corresponding Reynolds numbers must be equal (McAdams, 1954). The average recorded wind speed at the test cabin is 1 ms^{-1} giving a Reynolds number of $3 \cdot 10^5$, whereas the maximum reasonable Reynolds number of the model in the water channel was $2.7 \cdot 10^4$. Thus, if turbulence is observed with the model in the water channel, for a given direction, it will be observed in reality due to the much greater Reynolds number of the test cabin. The water flow around the model was observed by injecting dye, upstream of the model, to form visible flow lines.

The convective heat transfer coefficient, due to forced convection along a flat plate, is given by the following expression (Kimura, 1977) derived from dimensional analysis:

$$Nu = k\, Re^{\ell}\, Pr^{m}$$

$Nu = \alpha_c \cdot d/\lambda$ = Nusselt number

$Re = ud/\nu$ = Reynolds number

$Pr = \nu/a$ = Prandtl number

α_c = convective heat transfer coeffiecient

d = relevant dimension

λ = thermal conductivity of fluid

u = velocity

ν = kinematic viscosity

a = thermal diffusivity

k, ℓ, m = constants

If the Reynolds and Prandtl numbers are held constant then the Nusselt number is fixed (McAdams, 1954). For normal air temperatures and pressures the Prandtl number is constant and thus, providing the Reynolds number is kept constant, a scale model in a wind tunnel can be used to determine the convective heat transfer coefficient for the full scale situation.

In order to quantify the influence of the wind direction on the convective heat transfer coefficient at the windows of the test cabin a 1:20 scale model was built. The power supplied to an electrically heated copper plate, placed at the window location, was used to calculate the convective heat transfer coefficient. Energy losses to the cabin were minimized by using insulating materials for the model construction and estimating the energy losses by altering the conductivity of the copper plate. Copper was used for the windows due to its high conductivity and low infrared emissivity. Results reported here were measured using a laminar air flow, for a fixed speed of 20 ms^{-1}, whilst altering the flow direction.

3. Results and Discussion

Turbulence is created at the front surface if the fluid flow strikes the instrument boxes (Fig. 1) or passes a sharp edge (Fig. 2) before reaching the surface. In Fig. 1 the flow is turbulent over part of the front surface whilst being laminar over the rest. When the flow passes a corner (Fig. 2) the strongest turbulence was seen to occur near that corner. As the convective heat transfer coefficient is dependent on the rate of fluid exchange, it can thus be seen how the former can vary with surface location. For certain flow directions the flow is laminar across the whole of the cabin front.

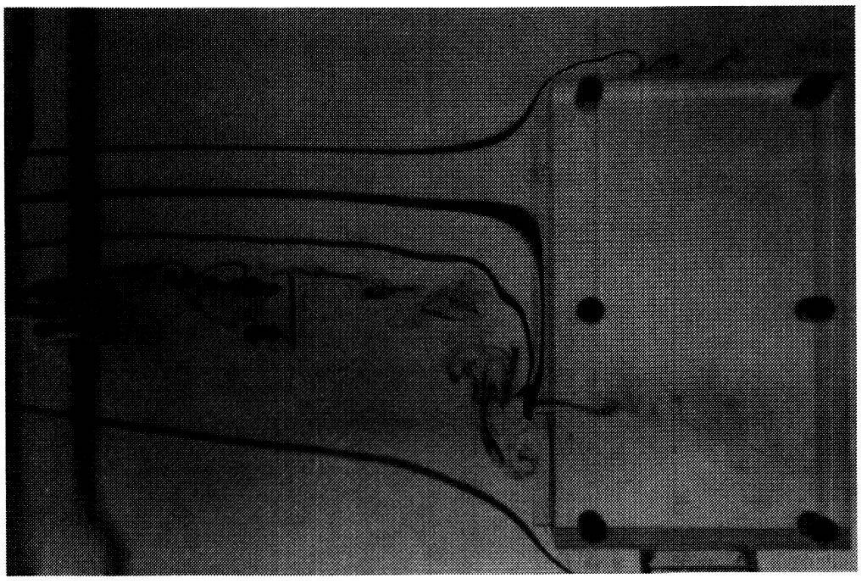

Fig. 1 Water flow of 0.12 m/s normal to window surface

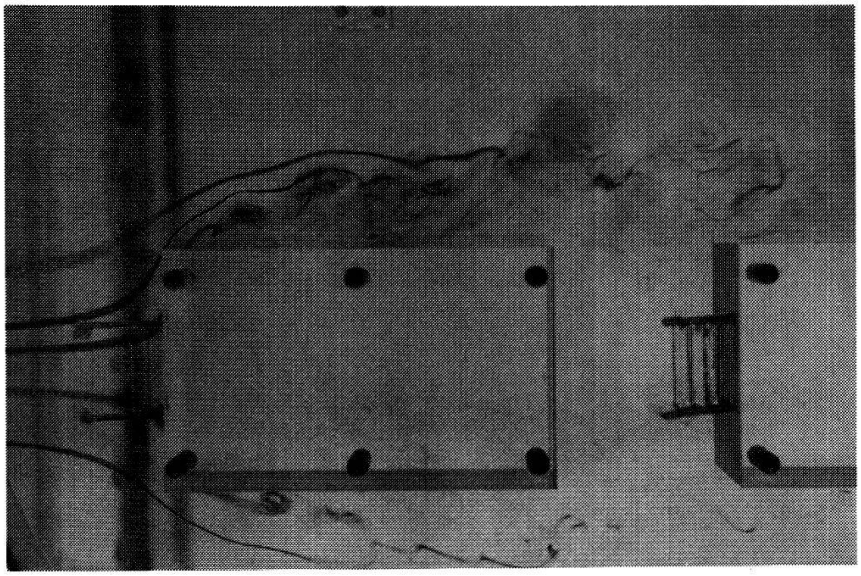

Fig. 2 Water flow of 0.12 m/s parallel to window surface

The wind channel air speed of 20 m/s corresponds to a windspeed of 1 m/s for the full scale test cabin. Convective heat transfer coefficients, adjusted for the full scale test cabin, are plotted as a function of direction in Fig. 3. The dominant peaks at 75^0 and 285^0 are due to the turbulence

created by the fluid passing the cabin corners, as seen in Fig. 2. The minimum convective heat transfer coefficient occurs at 15^0. This is due to the air flow being laminar at the copper plate, as seen over part of the cabin front in Fig. 1. Thus a much greater convective heat transfer coefficient occurs if the air flow is turbulent as opposed to laminar. Fig. 3 shows how the convective heat transfer coefficient is strongly dependent on the wind direction. The peak at 75^0 is significantly higher than that at 285^0, and the minimum at 135^0 is lower than that at 225^0. This non-symmetry of the graph is due to the window being located off-centre and shows that the convective heat transfer coefficient is dependent on the surface location.

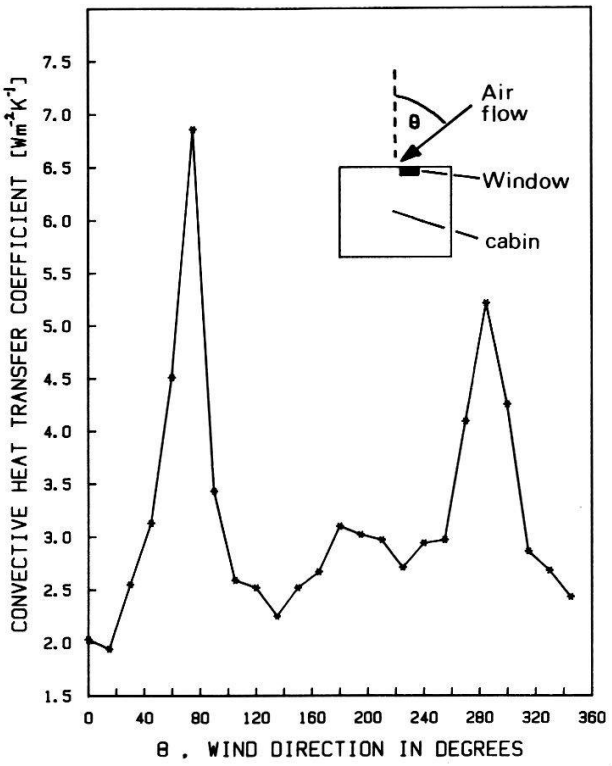

Fig. 3 Plot of convective heat transfer coefficient as a function of wind direction for real size cabin at 1 m/s

For a wind speed of 1 m/s the algorithm of Kimura (1977) gives a convective heat transfer coefficient of 6.3 W/m^2 K for a windward surface and 5.5 W/m^2 K for a leeward surface. These values correspond to the maximum convective heat transfer coefficients measured in this experiment, whilst the flow was turbulent at the window. Kimura's results are derived from experiments on a six storey building and probably include a much larger heat

loss due to natural convection, compared to this experiment. Projections on the building would also ensure the air flow is always turbulent in Kimura's experiment.

4. Conclusion

The convective heat transfer coefficient is dependent on the following:

a) For an incident laminar air flow, convective heat transfer is strongly dependent on direction.

b) For turbulent flows increased fluid exchange at the surface occurs, producing much greater heat exchange compared to laminar flows.

c) Heat transfer varies with surface location. The convective heat exchange is greater near to corners due to the strong turbulence created by the wind as it passes a sharp edge.

Acknowledgements

We wish to thank H.H. Thomann, Intitute of Aerodynamics, ETH Zurich, for advice and admission to the water tank facility.

This study is supported by NEFF and ETH Zurich

References

Furler, R., Williams, P. and Kneubühl, F.K., Helv. Phys. Acta, in print

Ito, N., Kimura, K. and Oka, J., 1972, ASHRAE Transactions, 78, pp 184-192

Kimura, K., 1977, Scientific Basis of Air Conditioning, Applied Science Publishers Ltd., London

Lokmanhekim, M., 1971, Procedure for Determining Heating and Cooling Loads for Computerized Energy Calculations: Algorithms for Building Heat Transfer Subroutines, ASHRAE, New York

McAdams, W.H., 1954, Heat Transmission, McGraw-Hill, New York, 3rd Ed.

Saunders, O.A., 1936, Proceedings of the Royal Society (London), A157, pp 279-291

Weise, R., 1935, Forschung Gebiete Ingenieurwesen, 6, pp 281-292

Zürcher, Ch., Finger, G., Kneubühl, F.K., Thiébaud, F., Vetsch H., Frank, Th. and Sagelsdorff, R., 1982, Infrared Phys., 22, pp. 277-291

ANDO IX : Chimie physique, médicine, biophysique

DIE BESTIMMUNG ZELLKINETISCHER MODELLPARAMETER AUS KLINISCH BEOBACHTBAREN STRAHLENREAKTIONEN

R.Mini, Abt.f.med.Strahlenphysik - Inselspital, CH-3010 Bern

Abstract : Um in der Strahlentherapie die Organreaktionen mittels Modellrechnungen vorhersagen zu können, müssen die modellabhängigen Gewebeparameter genügend genau bekannt sein. Wie gezeigt werden kann, lassen sich diese anhand von klinischen Beobachtungen an Therapiepatienten bestimmen.

1. Einleitung

Das Ziel einer optimalen Strahlentherapieplanung ist die Erarbeitung einer Bestrahlungsmodalität, welche ohne gravierende Beeinträchtigung der Funktionsfähigkeit des mitbestrahlten gesunden Gewebes zu einer grösstmöglichen Schädigung des Tumors führt. Eine Therapie tiefliegender Tumore besteht dabei in der Regel aus mehreren Bestrahlungssitzungen, bei welchen der Tumor je nach Bestrahlungstechnik aus verschiedenen Richtungen perkutan bestrahlt wird. Dank unterschiedlichster Reparatur-und Regenerationsprozesse können sich die betroffenen Gewebe zwischen den Bestrahlungssitzungen erholen, wobei durch eine zweckmässige Wahl der Bestrahlungsintervalle in manchen Fällen erreicht wird, dass sich das gesunde Gewebe im Vergleich zum Tumorgewebe besser regenerieren kann. Erst diese Tatsache erlaubt eine strahlentherapeutische Beherrschung vieler strahlenresistenter Tumore. Eine entsprechende Therapieplanung ist aber nur möglich, falls für jedes Bestrahlungsprozedere die resultierenden Gewebereaktionen mit genügender Genauigkeit vorhergesagt werden können. In der modernen Strahlentherapie wird deshalb in zunehmendem Masse versucht, die für eine bestimmte Tumortherapie optimalen Bestrahlungsvorschriften mittels Modellrechnungen zu bestimmen. Dies setzt allerdings voraus, dass das strahlenbiologische Verhalten der einzelnen Gewebe und Organe sich durch entsprechende Modellformalismen beschreiben lässt.

2. Die physikalisch-chemischen Primärwirkungen ionisierender Strahlen

Bekanntlich basiert die biologische Wirkung einer ionisierenden Strahlung immer auf den gleichen Primärvorgängen. Bei den in der Strahlentherapie

üblichen Strahlenarten, d.h. Photonen-und Elektronenstrahlen mit Energien unterhalb E = 50 MeV, ist der erste relevante Schritt der Wirkungskette stets die durch Wechselwirkung zwischen Strahlung und Materie verursachte Anregung und Ionisation von Atomen und Molekülen. Der Absorber übernimmt dabei einen Teil der Strahlenenergie, welche sich innert kurzer Zeit über mannigfaltige Zwischenstufen in andere Energieformen umwandelt. Der weitaus grösste Teil geht schliesslich in Schwingungs-, Translations-und Rotationsenergie, also in Wärme über. Vom biologischen Standpunkt aus tritt aber diese Energieumwandlung gegenüber den chemischen Sekundärreaktionen in den Hintergrund. Die angeregten Atome und Moleküle sind bekanntlich chemisch besonders aktiv. Sie reagieren schnell und gehen Reaktionen ein, die im Grundzustand bei gleicher Temperatur nicht möglich sind. Zudem können angeregte und ionisierte Moleküle unter Bildung von Ionen und Radikalen zerfallen. Die auf diese Moleküle übertragenen Energiebeträge reichen nämlich aus, um die Valenzbindungen organischer Moleküle zu sprengen. So beträgt beispielsweise die Bindungsenergie einer einfachen C-C-Bindung nur 2,55 eV und diejenige einer C=C-Doppelbindung 4,35 eV. Viele andere Kohlenstoffbindungen liegen dazwischen. Demgegenüber ist die Ablöseenergie für ein Elektron mindestens 10 eV. Auch ein Teil der durch elektronische Anregung übertragenen Energiequanten reicht noch aus um Valenzbindungen zu sprengen. Als Zwischenstufen der sekundären chemischen Strahlenwirkung werden somit veränderte Moleküle, im speziellen Ionen und freie Radikale gebildet. Diese können ihrerseits im wässerigen Milieu der Zellen Ursache chemischer Reaktionen sein, was zu zusätzlichen Molekülveränderungen führt.
Die physikalisch-chemischen Primärwirkungen lassen sich somit durch die strahleninduzierten Anregungen und Ionisationen von Atomen und Molekülen und durch die anschliessenden physikalisch-chemischen Reaktionen erklären. Als Endprodukte dieser Wirkungsphase resultieren stets chemisch veränderte Moleküle, welche den Ablauf der biologischen Prozesse stören können. Das Ausmass dieser Störung hängt im allgemeinen von der Anzahl veränderter Moleküle ab, welche weitgehend proportional zur ursprünglichen Anzahl Wechselwirkungen ist, wobei üblicherweise pro Bestrahlungssitzung zwischen 10^4 und 10^6 Ionenpaare pro Zelle erzeugt werden. Ein Mass hiefür ist die pro Masseeinheit deponierte Energie, d.h. die sog. Energiedosis.

3. Die Beschreibung klinisch beobachtbarer Strahlenreaktionen

Eine klinisch beobachtbare Strahlenreaktion ist stets als Antwort des lebenden Organismus auf die Veränderung biologisch relevanter Moleküle (Enzyme, DNS-Ketten usw) zu verstehen. Die auf allen Ebenen der langen Wirkungskette zwischen Molekülveränderung und biologischem Endeffekt eingreifenden Mikroprozesse, welche von der Reparatur, der Ausscheidung und der Substitution von Molekülen bis zu den komplizierten intrazellulären Erholungsvorgänge reichen, sind sehr komplex und werden von einer grossen Anzahl biochemischer und physiologischer Regelmechanismen des Gesamtorganismus beeinflusst. Eine umfassende Beschreibung dieser vitalen Mikroprozesse ist daher nicht möglich. Wie aber diesbezügliche Untersuchungen zeigen (1,2), lassen sich für die praktischen Bedürfnisse der Strahlentherapie die globalen Zusammenhänge zwischen den bestrahlungstechnischen Variablen und den klinischen Effekten trotzdem durch zellkinetisch-orientierte Modellformalismen ausdrücken. Die Gewebereaktionen werden hierbei summarisch, ohne auf die einzelnen Mikroprozesse einzugehen als Folge einer strahleninduzierten Primärschädigung, eines mittleren Regenerationsbeitrages der bestrahlten gesunden bzw. tumoralen Zellen und eines zusätzlichen Erholungsbeitrages der unbestrahlten Umgebung angesehen. Erst diese vereinfachte Betrachtungsweise erlaubt eine überschaubare Parametrisierung der einzelnen, der Beobachtung zugänglichen Vorgänge.

4. Die Bestimmung gewebeabhängiger Parameterwerte mittels Therapiedaten

Um mittels entsprechender Modellformalismen den unterschiedlichen Strahlensensibilitäten der einzelnen Gewebe Rechnung tragen zu können, enthalten diese gewebespezifische Parameter. Diese sind nicht von vornherein bekannt und lassen sich am Menschen auch nicht experimentell bestimmen. Da zudem die Uebernahme von an Tieren gemessenen Parameterwerten äusserst problematisch ist, empfiehlt der Schreibende deren Bestimmung aus den in den Krankengeschichten festgehaltenen Therapieangaben. Von jeder Patientenbestrahlung werden darin die Bestrahlungsdaten wie auch die beobachteten Strahlenreaktionen festgehalten.

Geht man einmal davon aus, dass jedes mathematische Wirkungsmodell für die Strahlentherapie zunächst nur ein Hilfsmittel darstellt, um durch Berechnung

eines Wirkungsindikators für jede Bestrahlungsmodalität eine Prognose der zu erwartenden Gewebereaktionen machen zu können, scheint es dem Verfasser naheliegend zu sein, die vorerst unbekannten Gewebeparameter durch Optimierung der Prognosewahrscheinlichkeit zu gewinnen. Für eine bestimmte Anzahl bekannter Strahlenbehandlungen werden hierzu anhand des interessierenden Modellformalismus und von beliebig vorgegebenen Werten für die Gewebeparameter die entsprechenden Wirkungsgrössen berechnet. Die hieraus resultierenden Reaktionsprognosen lassen sich mit den in den Krankengeschichten festgehaltenen Reaktionen vergleichen. Anhand einer einfachen Erfolgsstatistik kann dann eine Prognosewahrscheinlichkeit ermittelt und den Parameterwerten zugeordnet werden. Um die klinisch zweckmässigsten Parameterwerte feststellen zu können, ist diese Prozedur für viele verschiedene Wertvorgaben zu wiederholen, wonach schliesslich diejenigen Parameterwerte ausgesucht werden, für welche die grösste Prognosewahrscheinlichkeit resultiert. Diese Methode wurde mit Hilfe der Angaben von über 300 Strahlenbehandlungen an zwei Modellformalismen mit Erfolg getestet, wobei hierzu aus Platzgründen auf (3,4) verwiesen wird.

5. Schlussfolgerungen

Die klinische Anwendbarkeit entsprechender Modellformalismen ist nach wie vor umstritten. Diese hängt letztlich von der Genauigkeit ab, mit welcher die Gewebereaktionen anhand derartiger Formalismen vorhergesagt werden können, was entscheidend von der richtigen Wahl der gewebeabhängigen Parameterwerte abhängig ist. Das hier vorgeschlagene Evaluationsverfahren hat den Vorteil, dass es auf den praktischen Erfahrungen der Strahlentherapie beruht. Es ist frei von zusätzlichen biologischen oder statistischen Voraussetzungen und lässt sich leicht interpretieren. Allerdings lassen sich die auf diese Weise festgestellten Parameterwerte kaum mikrobiologisch erklären.

6. Referenzen

(1) L.Cohen, J.E.Moulder, Radiat.Res., 76, 250 (1978)
(2) R.Wideröe, Strahlentherapie, 156, 665 (1980)
(3) R.Mini,G.Poretti, Bullet.Schweiz.Ges.f.Str.Biol., 2, 107 (1979)
(4) R.Mini,G.Poretti, World Congress on Medical Physics and Biomedical Engineering, Hamburg, 26.12 (1982)

PHOTOTHERMAL DEFLECTION SPECTROSCOPY : SYSTEM DESIGN AND SOME MEASUREMENT RESULTS FOR α-Si:H.

G. Frosio, N. Wyrsch, H. Curtins*, A. Shah.
Institut de Microtechnique, Université, CH2000 Neuchâtel,Switzerland.

ABSTRACT

Design rules for photodeflection spectrocopy (PDS) apparatus are discussed; absorbtion curves obtained with such a system for α-Si:H films are presented.

1. INTRODUCTION

The density of states (DOS) is an important quality criterion for amorphous hydrogenated silicon α-Si:H. Currently, great efforts are underway to develop or refine techniques from which reliable information about the (joint) DOS can be obtained. Among the better known techniques, photodeflection spectroscopy (PDS) and photoconductive spectroscopy (PCS) deserve to be mentioned in particular because of their high sensibility and their simple practical realisation. Both PDS and PCS allow the determination of the extremely weak absorption values for photon energies below the (pseudo) band-gap, this in turn can lead to quantitative data for the DOS and related defects provided that adequate band-structure models are available [3].
In this paper we shall discuss some design aspects for a PDS apparatus; thereafter, we present results obtained for several α-Si:H films.

2. DIMENSIONNING OF PDS APPARATUS

The basic physical setup is schematically illustrated in Fig.1. A pump beam X incident on medium 0 (non absorbing, with large $\partial n/\partial T$, n=index of refraction,T=temperature) transverses the absorbing medium 1 (e.g. α-Si:H film) and subsequently propagates through medium 2 (nonabsorbing , e.g. glass substrate). The energy dissipated in region 1 will diffuse in all direction and consequently establish a certain temperature distribution T(x,y,z), which in turn gives rise to a variation of the index of refraction n(T). A laser beam Y (diameter of Y ≪ diameter of X) probes the gradient of index of refraction and will be deviated by an angle ϕ from its original path. Depen-

* To whom correspondence should be addressed.

dent on whether the probe beam passes through medium 0,1 and 2 or merely through region 0, one distinguishes between collinear PDS (beam Y_{col}) and transversal PDS (beam Y_{tr}), respectively.

	κ [W/cm°K]	k [cm^2/sec]
air	$2.5\ 10^{-4}$	20
CCl_4	$1.0\ 10^{-3}$	$7.5\ 10^{-4}$
glass 7059	0.1	$8.7\ 10^{-3}$
α-Si:H (≡X-tal)	1.7	1

Table I : Thermal parameters for different materials.

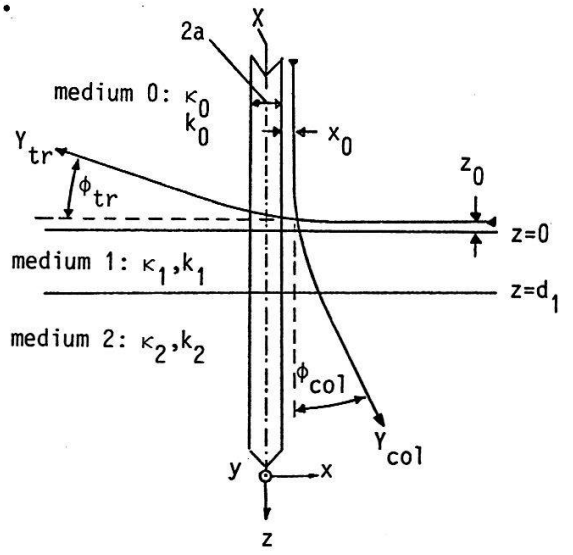

Fig.1 Geometry for coll. and transv. PDS

The deflection angle is a function of the following parameters : $P(\Delta\lambda)$= pump beam power, absorption coeff. α, ω =chopping (angular) frequency, material parameters κ_i,k_i, pump beam radius a, distances x_o and z_0 (see Fig 1), and interaction lentgh L. If we assume that the diffusitivity k_0,$k_2 \ll k_1$, i.e. that the heat diffusion into medium 0 and 2 can be neglected, one finds the dependence for ϕ according to Table II (for details the reader is referred to previous work [1-3], as well as to supplements given in a recent diploma thesis [4] at our Institute). Some values for κ and k for commonly used materials are summarised in Table I. Note that the diffusitivity k for air is quite large and consequently does not fulfill above condition. L is roughly d_1 for coll. PDS and $\simeq$ 2a (pump beam diameter) for trans. PDS. Fig.2. shows schematically the transversal PDS system realized by the authors; it is mounted on a vibration-free optical bench.

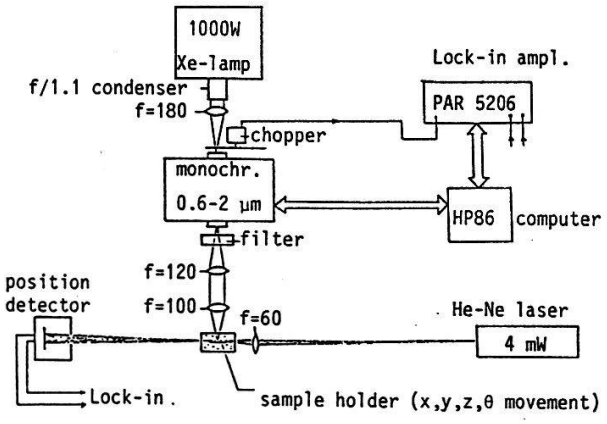

Fig.2 Setup for transversal PDS.

To increase the system's sensitivity (i.e. to increase ϕ) one should work with small values of the pump beam radius a and in particular, with minimal

	collinear PDS	transversal PDS
P , α	$\phi \propto P[1-\exp(-\alpha d_1)]$	
ω	$\phi \propto 1/\omega$ for $\ell_1=\sqrt{2k_1/\omega} \ll 2a$; high frequency $\phi \propto 1/\kappa_1$ for $\ell_1 \gg 2a$; low frequency	
L	$\phi \propto L \approx d_1$	$\phi \propto L \approx 2a$
x_0 , z_0	$\phi \propto x_0 \exp(-2x_0^2/a^2)$	$\phi \propto \exp(-z_0/\ell_0)$
a	$\phi \propto 1/a^4$	$\phi \propto 1/a^2$

Table II: Dependence of ϕ on different parameters.
(ℓ_i=diffusion length for medium i)

values of the geometrical offset z_0 (see Table II). Small values of the pump beam radius a are obtained by using good quality optical components (lenses) as well as small dimensions for the output slit of the monochromator. The latter values , however, also determine $P(\Delta\lambda)$ and the bandwidth $\Delta\lambda$. Typical practical values are $a \approx 0.5$-1mm and $\Delta\lambda \approx 10$-15nm. The minimum distance z_0^{min} that can be realized depends on the parameters of the He-Ne beam (assumed as Gaussian beam), on the focal length f and on the distance D_1 (see Fig. 3). Using geometrical optics, we have calculated $z_0^{min}(f,D_1)$ as follows [4]:

$$z_0^{min} = f w_{01} \sqrt{\left(\frac{S\lambda}{2\pi w_{01}^2 f^2}\right)^2 [(D_1-f)^2 + (\pi w_{01}^2/\lambda)^2] + \lambda^2/[\lambda^2(D_1-f)^2 + (\pi w_{01}^2)^2]} \quad (1)$$

Equation (1) is represented in Fig. 3. It can be seen that $z_0^{min} \geq \sqrt{\lambda S/\pi}$ and that this minimum value can only be realized if $f \geq f_c = w_{01}\sqrt{\pi S/2\lambda}$. A second interesting feature of the graph $z_0(f,D_1)$ is the increase of the angle $\sphericalangle f_i$ of the asymptotic straight lines for increasing focal length f and the appearance of weak "oscillations" in the curves. The amplitude of these "oscillations" increase for increasing f and is limited on the top by the envelope z_0^* and on the bottom by $z_0=\sqrt{\lambda S/\pi}$. This minimum value can be obtained at least for one value of D_1, if $f \geq f_c$. Example : f=50 mm , w_{01}=0.4mm, S=3mm. One obtains : $f_c \approx$ 35 mm (λ=632.8nm), taking D_1=80cm leads to a z_0^{min}=25μm. The distance D_3 (see Fig. 3) should be choosen such that the spot covers ~60-80 % of the active area of the position detector.

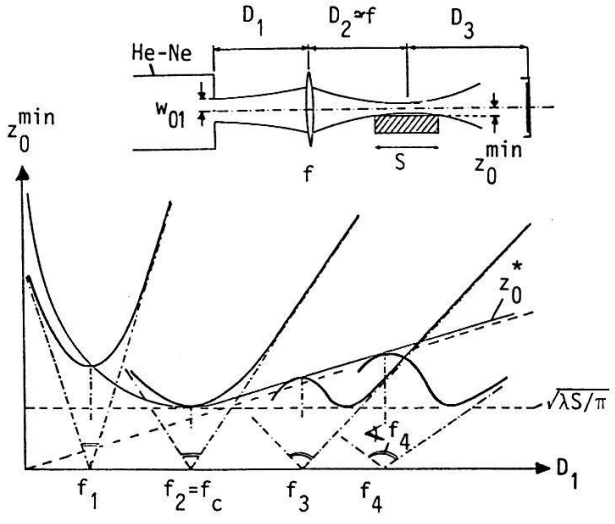

Fig.3 Minimum distance z_0^{min} as function of focal length f, distance D_1 and laser beam parameters.

3. MEASUREMENTS ON α-Si:H FILMS

We have measured the subband gap absorption for several α-Si:H films shown in Fig. 4 and listed in Table III. The absorption curve can roughly be divided into two parts : a) an exponential region (Urbach tail) $\alpha_0 \cdot \exp(\hbar\omega/E_0)$ for energies $1.5<\hbar\omega<1.7$ and b) the addition of a shoulder at lower energies, which is ascribed to defect densities N_s of the dangling bond type [2,5]. According to [2] N_s can be calculated as :

$$N_s = 7.9\ 10^{15} \int [\alpha - \alpha_0 \exp(\hbar\omega/E_0)]\, dE$$

All films were prepared in a capacitively coupled RF (81 MHz) glow discharge system on glass Dow Corming 7059 substrates.

The values $N_s \simeq 4x10^{16}$–10^{17} cm^{-3} can be considered as indicative of reasonably good quality films; they are, however, higher by about a factor of ~10 than the ones of the best reported α-Si:H films.

4. REFERENCES

[1] W.B. Jackson et al., Appl. Opt. 20, 1333 (1981).

[2] W.B. Jackson et al., Phys. Rev. B 25, 5559 (1982).

[3] G. Moddel et al., Phys. Rev. B 22, 1918 (1980).

[4] G. Frosio,Travail de diplôme,1986,Inst. de Microtechnique,Uni Neuchâtel.

[5] W.B. Jackson et al., Sol. Stat. Comm. 44, 477 (1982).

ACKNOWLEDGEMENTS

We would like to thank Dr. J. Magarino of Thomson CSF for his advice in planning the PDS apparatus. This work was supported by Swiss Federal Research grant OFEN (REN) 85/16.

	A180286/1	A200286/1	A210286/1	A210386/1
Dep. temp. [°C]	230	230	230	230
RF power [W]	15	15	15	20
Thickness [μm]	4.2	2.6	1.5	2.5
σ_{dark}(25°C) [1/Ωcm]	$1.1\ 10^{-10}$	$3.8\ 10^{-10}$	$8.7\ 10^{-11}$	$3.8\ 10^{-11}$
$\sigma_{AM1.5}$(25°C) [1/Ωcm]	$3.0\ 10^{-6}$	$1.2\ 10^{-5}$	$8.8\ 10^{-6}$	$5.4\ 10^{-6}$
Act. energy E_a [eV]	0.68	0.57	0.68	0.66
Opt. gap [eV]	1.69	1.70	1.72	1.68
Urbach's energy E_0 [eV]	0.067	0.076	0.072	0.075
Defect density N_s [1/cm^3]	$7.5\ 10^{16}$	$5.0\ 10^{16}$	$1.1\ 10^{17}$	$4.5\ 10^{16}$

Table III : Measured α-Si:H film parameters.

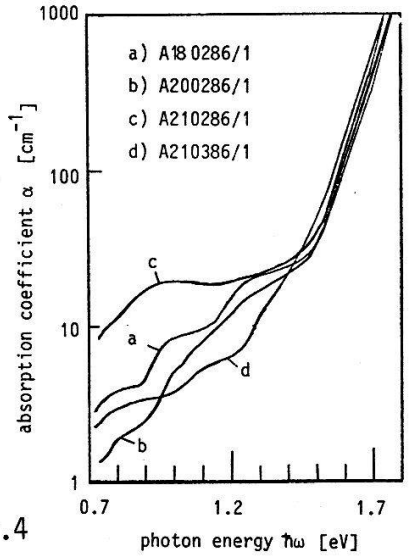

Fig.4

"Differential Skin Temperature (DST)" - Messung für die Ovulationsdetektion.

A.V.Shah und H.K.S.Rao
Institut de Microtechnique, rue Breguet 2, 2000 Neuchâtel

Die zuverlässige Bestimmung der Ovulationszeit innerhalb des Menstrualzyklus der Frau ist von Bedeutung für klinische Zwecke und Geburtenregelung. Eine erhöhte Durchblutung gewisser Körperregionen (Brüste, Vagina) wird durch Estradiol induziert und ist deshalb ein gutes Kriterium für die bevorstehende Ovulation. Die erhöhte Durchblutung führt u.a. zu Temperaturdifferenzen an der Brustoberfläche, die mittels der von uns eingeführten "DST"-Methode erfasst werden. Die Resultate klinischer Testreihen (mittels Infrarotthermographie) und erster ambulatorischer Messungen (mit einem "DST"-Kontaktthermometer) liegen vor.

On the origin of the pseudoresistance of electrolytic cells

Alois Marek, Brown Boveri Research Center, CH-5405 Baden

To separate the power losses in electrochemical cells into a physical and an electrochemical part, the cell series resistance Rs caused by physical dissipative processes is measured by means of varying cell current. We show that the resistance Rs* observed contains always a pseudoresistance term Rs**=Rs*-Rs being dependent nonlinearly both on electrochemical and on physical parameters of all basic components of the measurement set, including their mutual connections' geometry. Ways of keeping Rs** small even at cell currents in the 10..1000Å range are discussed and experimental results compared with data calculated by means of a nonlinear phenomenological cell model, supplying as a by-product also the D.C. Grahame's [1] pseudocapacitance.

[1] J. Phys. Chem. 57, 257 (1953).

POSTER

A "SMART" 35 cm Diameter Photomultiplier

G. van Aller, S-O Flyckt, W. Kühl and P. Linders
Philips Electronic Components and Materials Division
Eindhoven, The Netherlands

P.C. Bosetti
III. Physikalisches Institut der RWTH Aachen
Aachen, West Germany

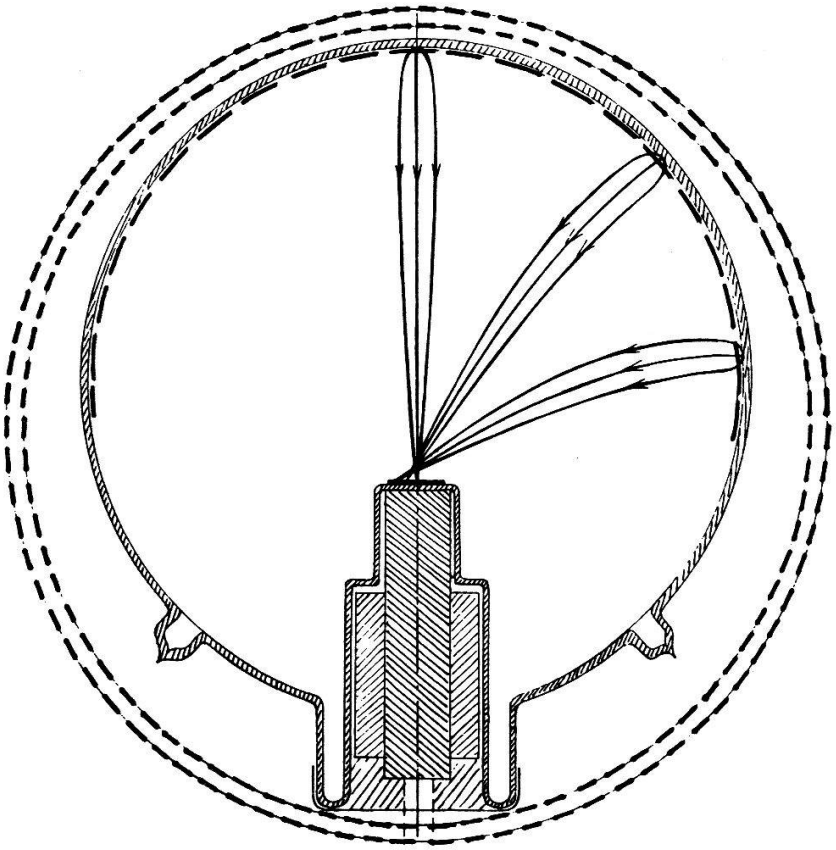

Abstract

Photoelectrons from a large hemispherical cathode with 3π sr viewing angle are accelerated by 25 kV to a fast high gain scintillator which is optically coupled to a conventional photomultiplier. First measurements show that it is possible to discriminate between one, two, three and several photoelectrons with high efficiency. The tube has a maximum transit time difference of around 5 ns and is able to efficiently detect a low level signal in a high single photoelectron background environment like deep underwater experiments, e.g. the DUMAND and Lake Baikal projects.

1. Introduction

1.1. Why a "smart" photomultiplier?

In large volume detectors in high energy physics and cosmic ray experiments the passage of relativistic particles through a medium results in light pulses that have to be discriminated from an abundance of background pulses. Sophisticated coincidence techniques are applied to select the true events from background effects that give rise to a high count rate of single photoelectrons in the photomultiplier. Therefore, good single electron resolution is essential. Secondly, very accurate timing is required to reconstruct the trajectory of a particle traversing the medium from the photomultiplier signals of the detector array. Furthermore, the area of the photocathode should be as large as possible for maximum response to faint Cerenkov light. The photomultiplier should have a uniform sensitivity over a large solid angle, up to at least 3π sr.
Today's large photomultipliers, essentially an extension of the technology used in smaller tubes, so far offer no possibility of combining these three important requirements. Hardly any single electron resolution can be found in commercially available tubes; moreover, the transit time difference between electrons released at the tube centre (0°) and at the edge (90°) is tens of nanoseconds [1].

1.2. The new principle

The single electron resolution in a photomultiplier is determined mainly by the statistics of secondary emission at the first dynode; to be more precise, it is the yield of secondary electrons for one primary photoelectron which is important. In small tubes, multiplication factors of 10-15 are obtained. In special tubes with III-V compounds values up to, say, 30 can be obtained, but this technology is impractical in large hemispherical tubes of traditional design.
Therefore a large smart tube should combine a high multiplication factor with small transit time difference. This goal is achieved by applying a high voltage in the input optics and transforming the high electron energy into may photons which are detected by a conventional photomultiplier [2]. In addition the high voltage will make the tube less sensitive to magnetic fields than traditional designs.

2. Description.

2.1. Design

We have built tubes according to the principle described above, see fig. 1. The large tube consists of a glass bulb of 35 cm diameter with a recess at the back and a hemispherical photocathode. Photoelectrons are accelerated by 25-30 kV towards a scintillator layer and the resulting light pulses are detected by a conventional fast photomultiplier like the XP2972 placed in the recess. In this way one photoelectron from the large cathode will give rise to 30 or more photoelectrons in the small photomultiplier. This "secondary emission factor" and the good statistics will enable pulses due to one, two, three and several photoelectrons to be clearly separated. The high voltage for the large "preamplifier" tube can be placed at the back of the tube. The present design has taken a 17" pressure vessel into account.

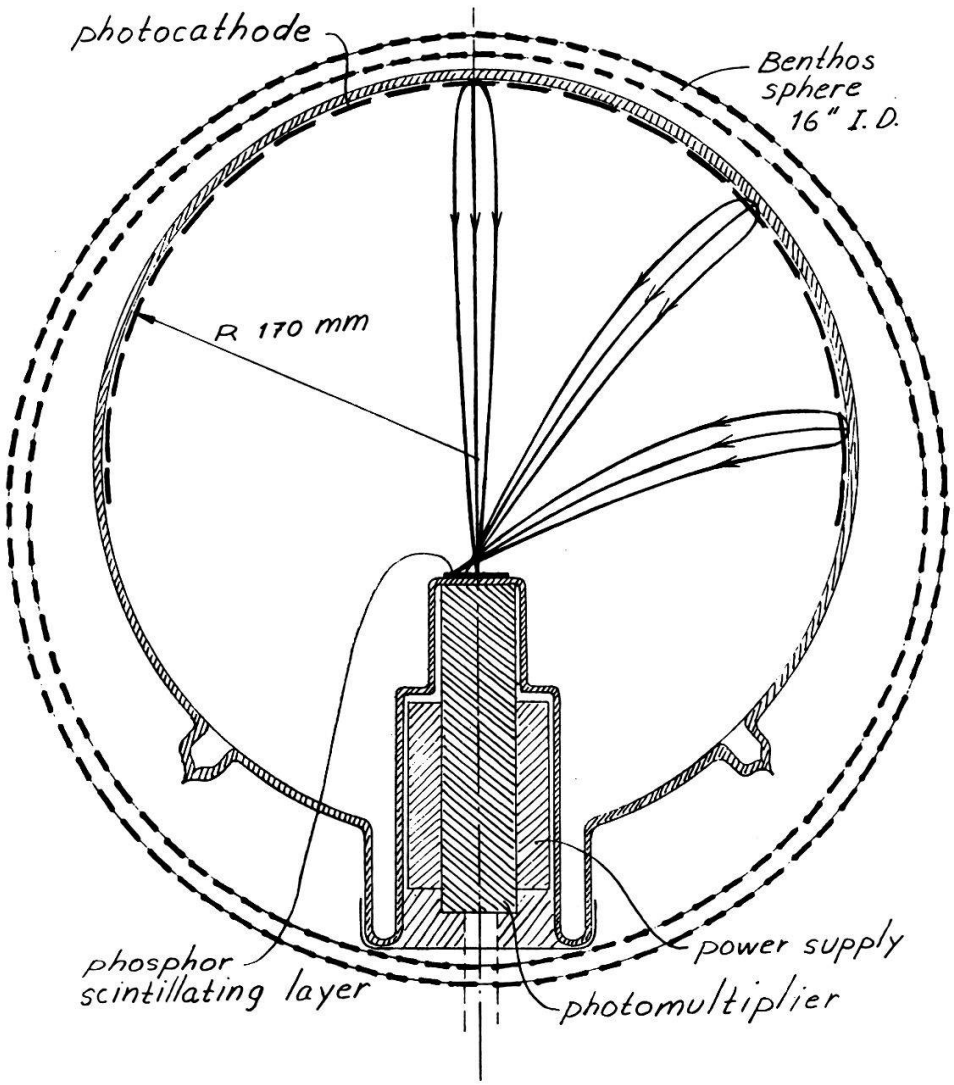

Figure 1.
Design, schematically.

2.2. Main properties

2.2.1. Photocathode and collection efficiency

The photocathode is of bialkaline type SbKCs because of its high spectral sensitivity for blue light and its low thermionic emission. The tube is sensitive over a solid angle of at least 3π sr because its back is transparent.
Fig. 2 shows that the collection efficiency of the electron-optics is effectively 100%.

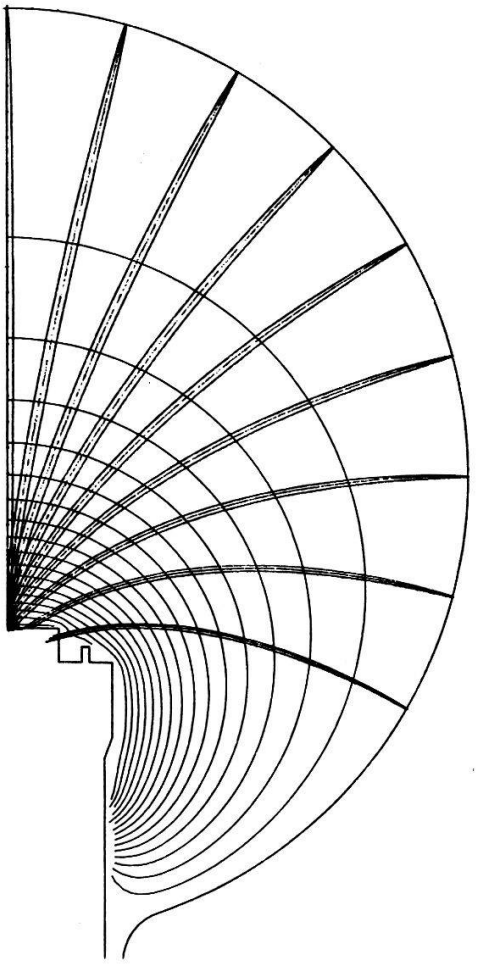

Figure 2.
Electron trajectories showing 100% collection efficiency up to 90° polar angle.

2.2.2. Single electron resolution

In ref. [3] it is shown that the uncertainty of separating single electron pulses from double electron pulses will decrease from 30% to 6% if the secondary emission coefficient, or conversion factor, is increased from 10 to 30. If the pulse height distribution is only determined by the statistical fluctuations of the number of secondary electrons per primary electron the FWHM resolution will depend on this number, the gain, as shown in fig. 8. In the preamplifier/photomultiplier combination presented here the gain can be 20-40, so in a first approximation the FWHM resolution of the single electron peak can be 50-35%. In practice, though, other effects will also contribute to the statistical fluctuations; nevertheless, with careful optimization a single electron resolution of less than 50% FWHM seems feasible.

2.2.3. Timing

The most interesting aspect of the new principle presented here is the possibility of accurate timing in large arrays of photomultipliers. Ideally the transit time of photoelectrons should not depend on their point of origin on the photocathode. Transit time differences have been minimized by the high accelerating voltage and an optimal design of the preamplifier tube. They are shown in fig. 3 for 35 kV. For 25 kV the data should be multiplied by $\sqrt{35/25}=1{,}18$.
In order to minimize pulse pile-up at high count rates, e.g. background, the scintillator should have a very short decay time. Yttrium silicate, cerium activated, is suitable because of its 1/e decay time constant of 35 ns, and its maximum emission at about 400 nm [4] matches well with the spectral sensitivity of the small photomultiplier.

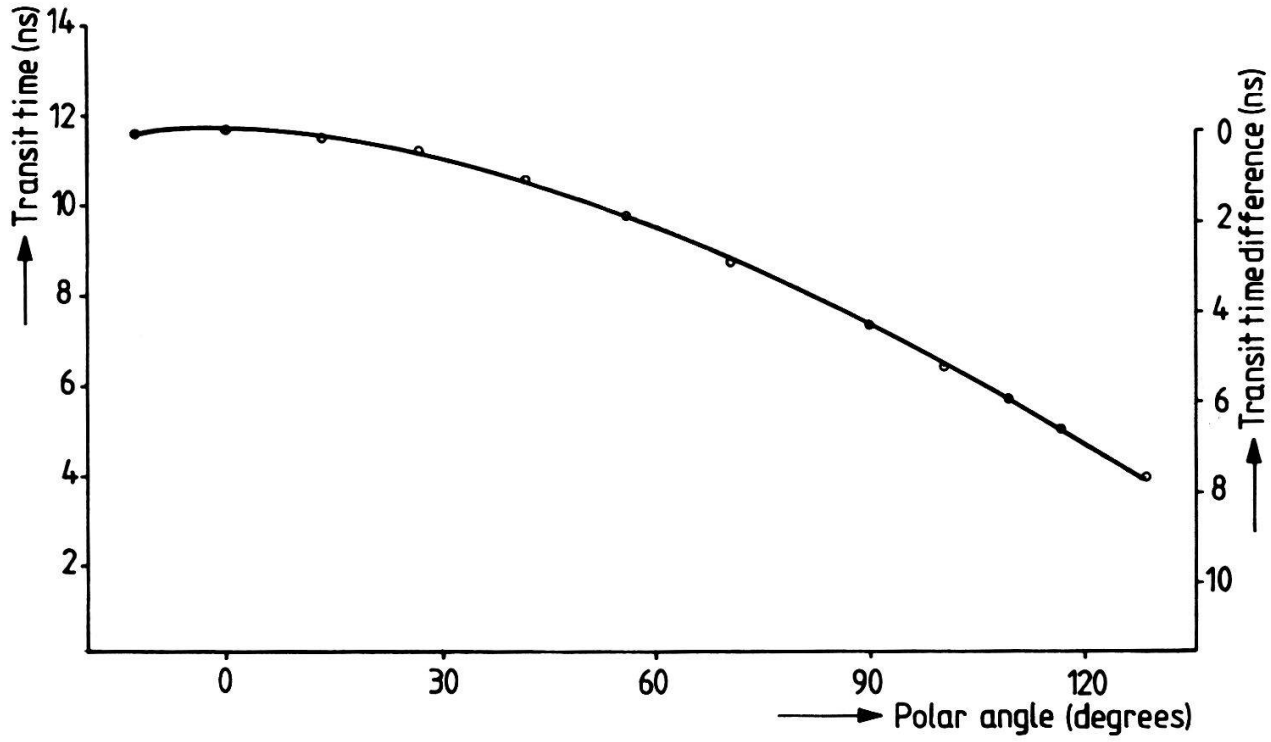

Figure 3.
Transit time and transit time difference as a function of polar angle at 35 kV.

3. Results

Several tubes have been made and some of the principal results are given below.

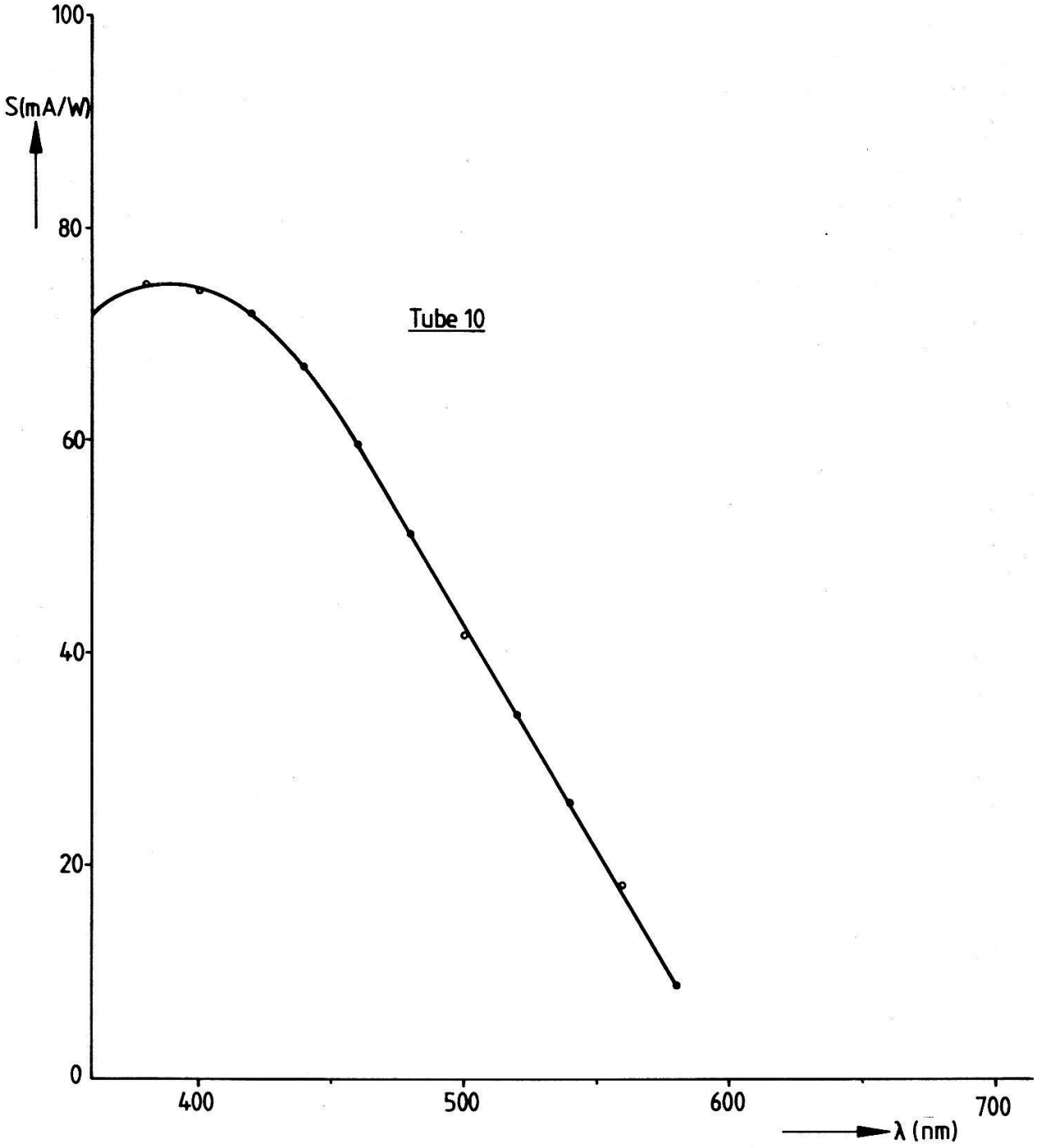

Figure 4.
Spectral sensitivity characteristic of the preamplifier tube.

3.1. Photocathode

Fig. 4 shows the spectral sensitivity characteristic of a typical tube, which is about 75 mA/W at 400 nm. More experience in producing the large preamplifier tube should lead to improved average cathode sensitivity. Fig. 5 shows the relative sensitivity as a function of the polar angle for two azimuthal angles. Up to about 120° the sensitivity is reasonably uniform in accordance with the 3π sr design goal.

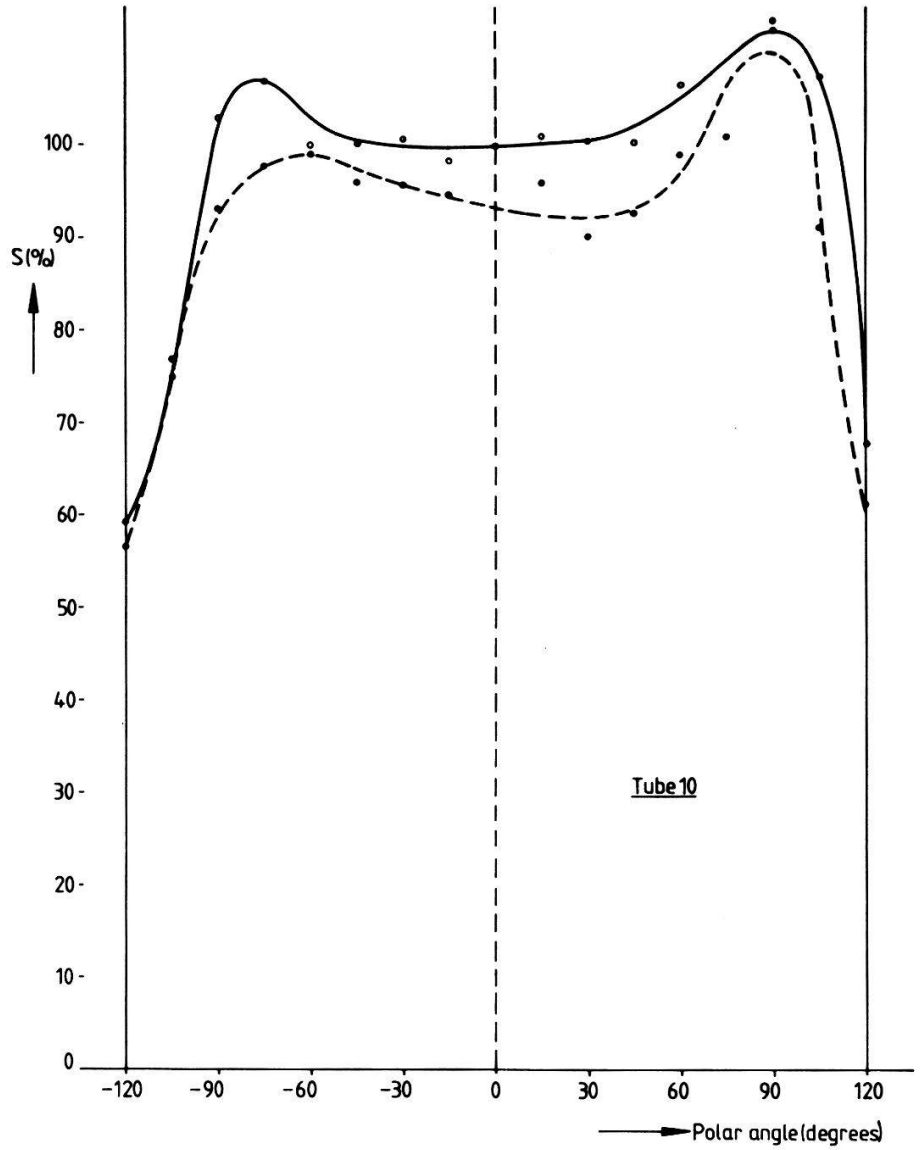

Figure 5.
Relative sensitivity as a function of polar angle, for two azimuthal angles.

3.2. Gain

The gain was measured by comparing the single electron pulse height distributions of the small photomultiplier itself and the preamplifier/photomultiplier combination. Fig. 6 shows a typical result confirming that the gain is a linear function of the high voltage, with a threshold voltage of about 5 kV due to the aluminium backing on the scintillator which prevents light feedback from the scintillator to the large photocathode.

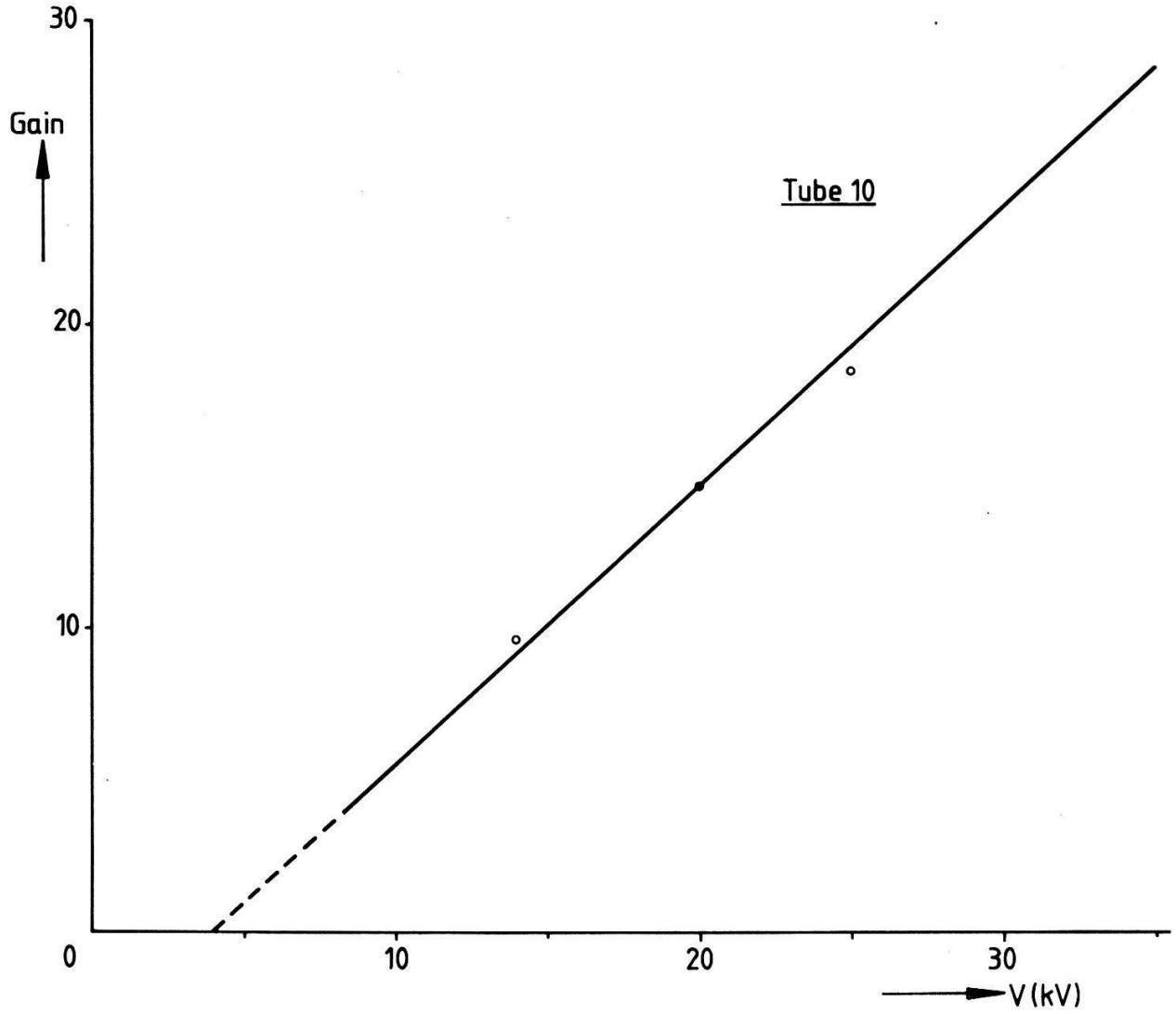

Figure 6.
Gain as a function of accelerating voltage.

TAG NO. = 3 SERIES 40 V- 2.4 10:53 12 FEB 1986
CH# 0 MEMORY = 1/4 VFS = 4K CH# 1023
CANBERRA

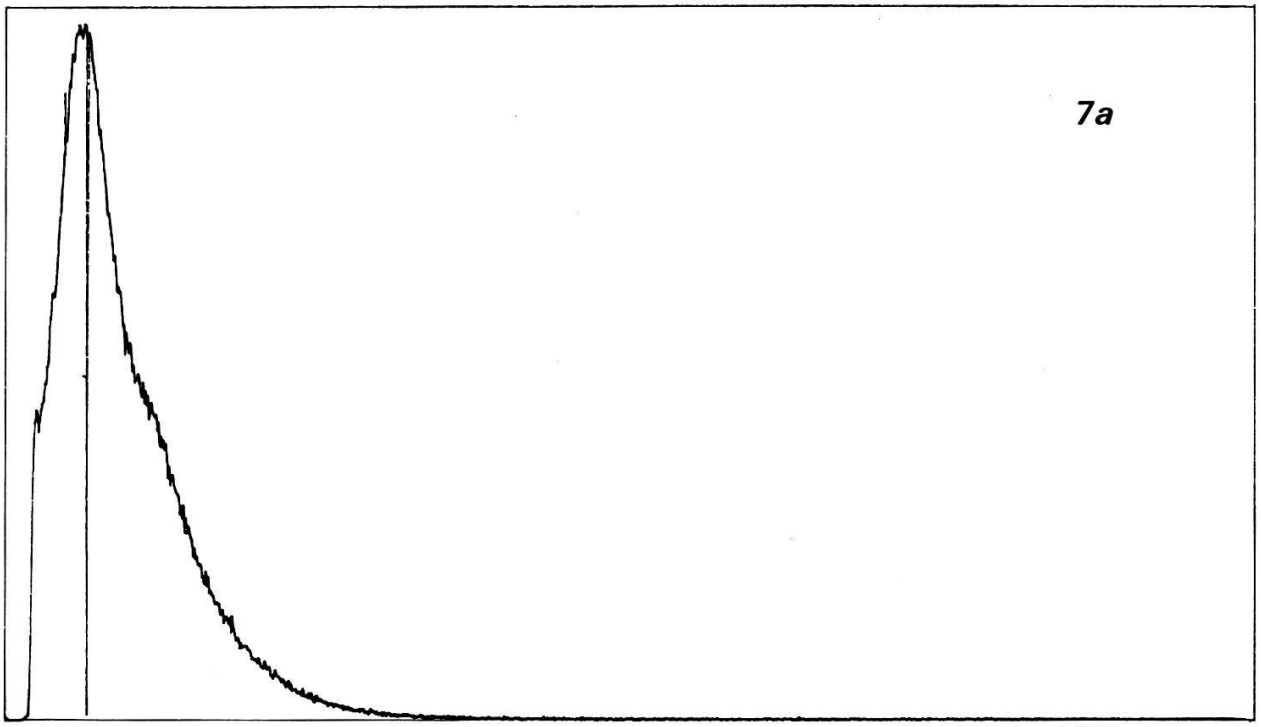

7a

CL= CH# 49 FROM CH# 0 TO CH# 1023 PSET(L) 100
COUNTS 3258 INT 375642 ELAP(L) 100

TAG NO. = 4 SERIES 40 V- 2.4 10:56 12 FEB 1986
CH# 0 MEMORY = 2/4 VFS = 4K CH# 1023
CANBERRA

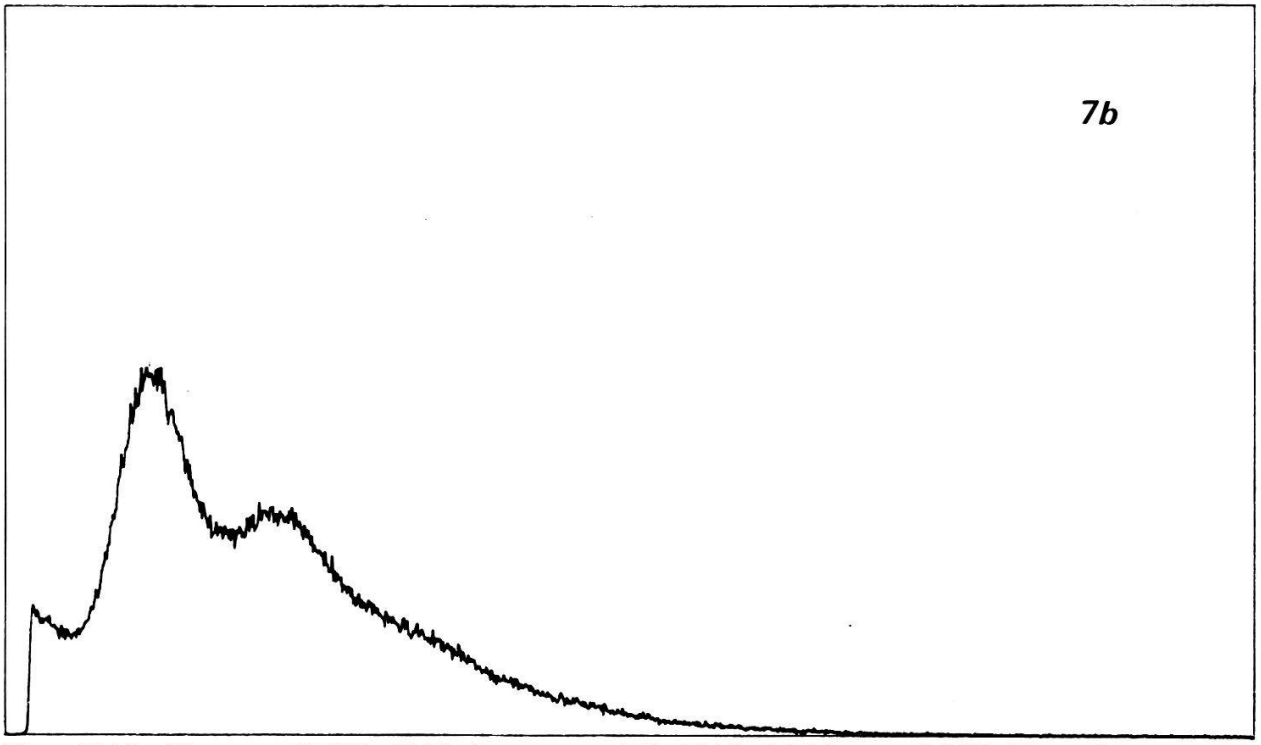

7b

CL= CH# 49 FROM CH# 0 TO CH# 1023 PSET(T) 100
COUNTS 554 INT 411682 ELAP(T) 100

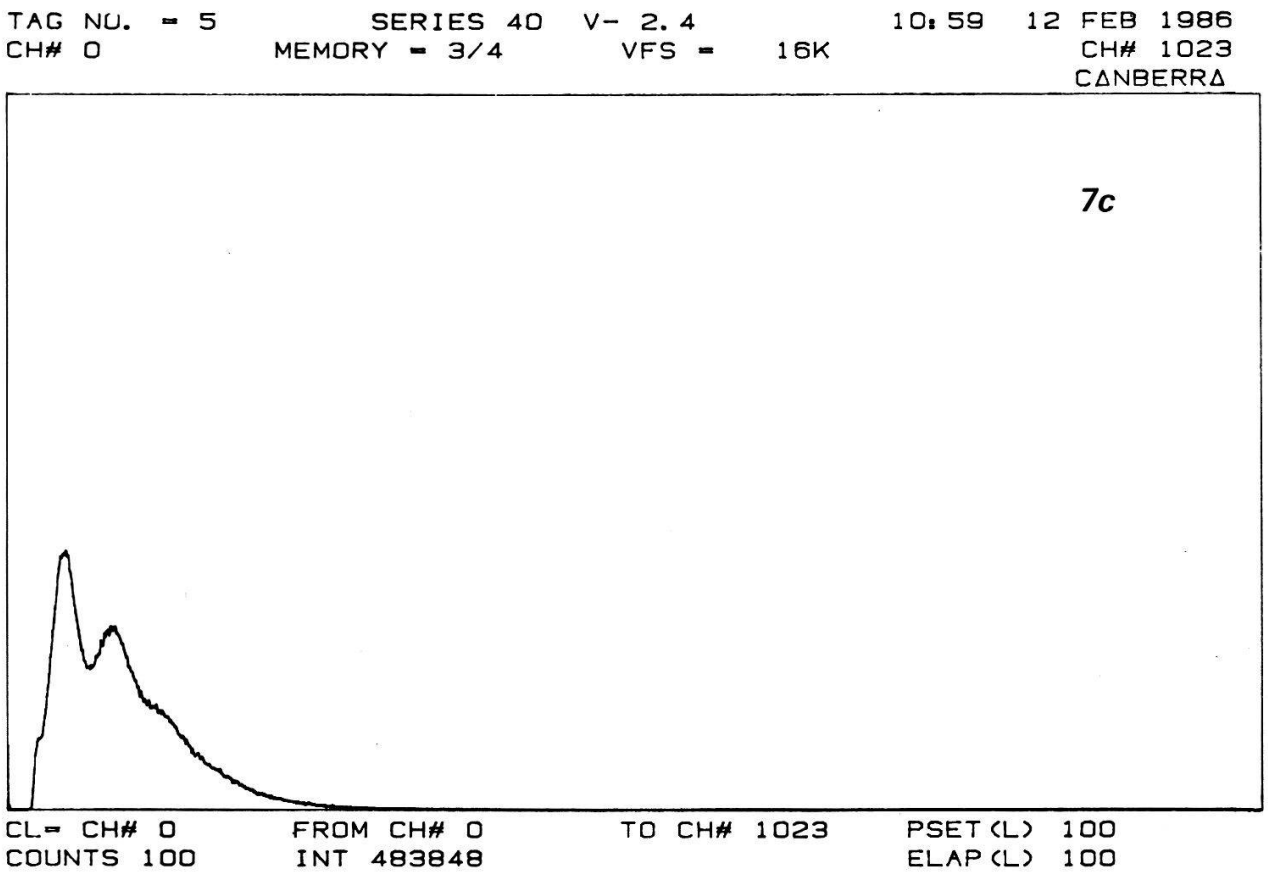

Figure 7.
Pulse height distributions for 15 kV (a), 25 kV (b) and 30 kV (c) with low light pulse intensity.

3.3. Pulse height distribution

Pulse height distributions were measured using a blue LED with a pulse rate of 5000 Hz; the sampling time was 100 s ($5 \cdot 10^5$ pulses). Fig. 7 shows the results for 15, 25 and 30 kV respectively. The LED pulse intensity has been chosen so that the single electron peak is very pronounced compared to the peaks for two and three electrons. It can clearly be seen that the single electron resolution improves with increasing voltage in the large tube. At 15 kV the two-electron peak is just about visible as a shoulder, at 25 and 30 kV the peaks are clearly separated. The resolution of the single electron peak is estimated to be around 100% FWHM at 15 kV and improves to 60% at 30 kV. This is higher than could ideally be expected, fig. 8.

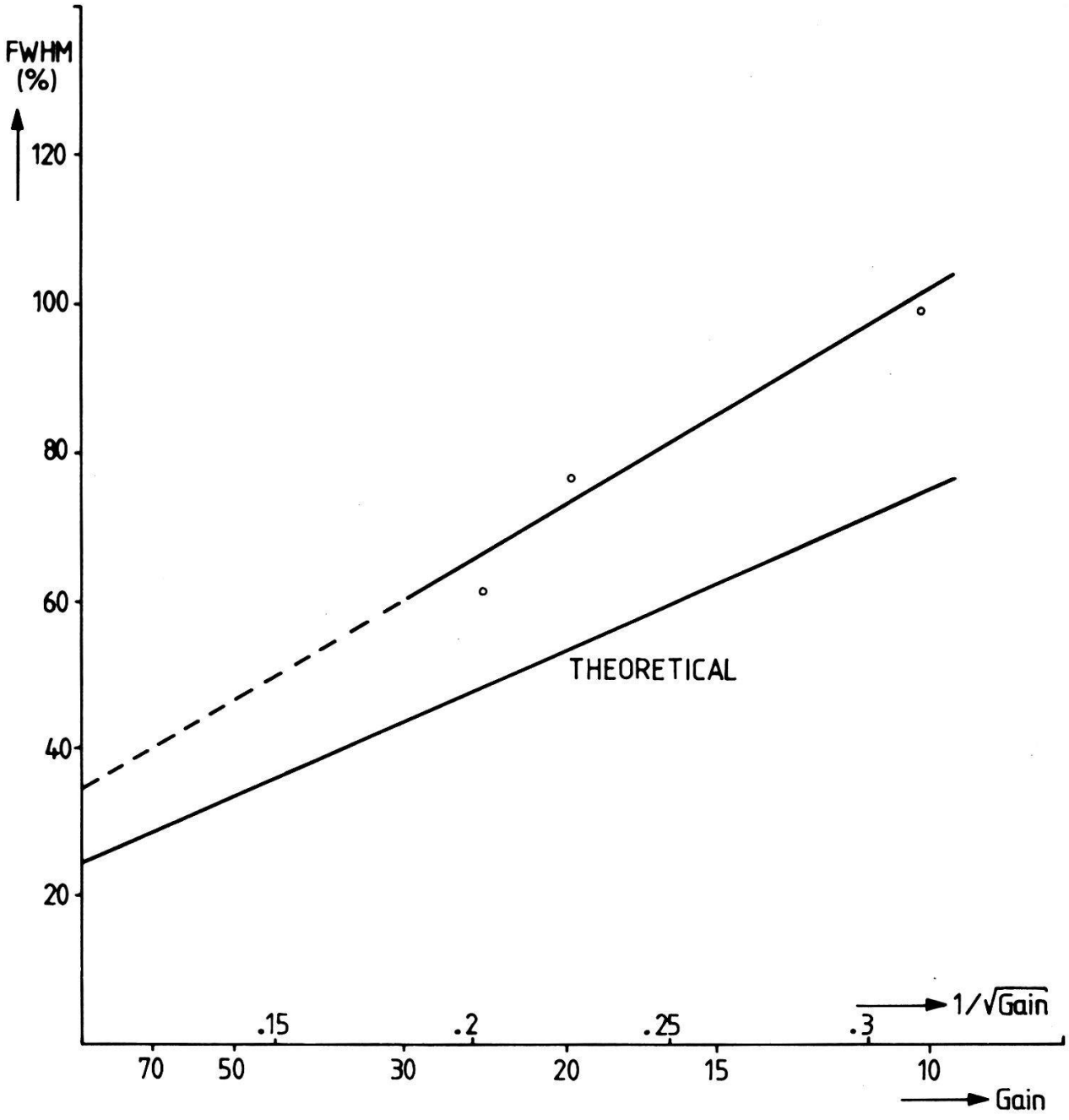

Figure 8.
FWHM resolution as a function of gain.
Theoretical curve and measurements.

By increasing the light intensity the ratio of the peak heights can be changed. This is demonstrated in fig. 9 where the single and double electron peaks have about the same height and the three-electron peak can be clearly recognized.

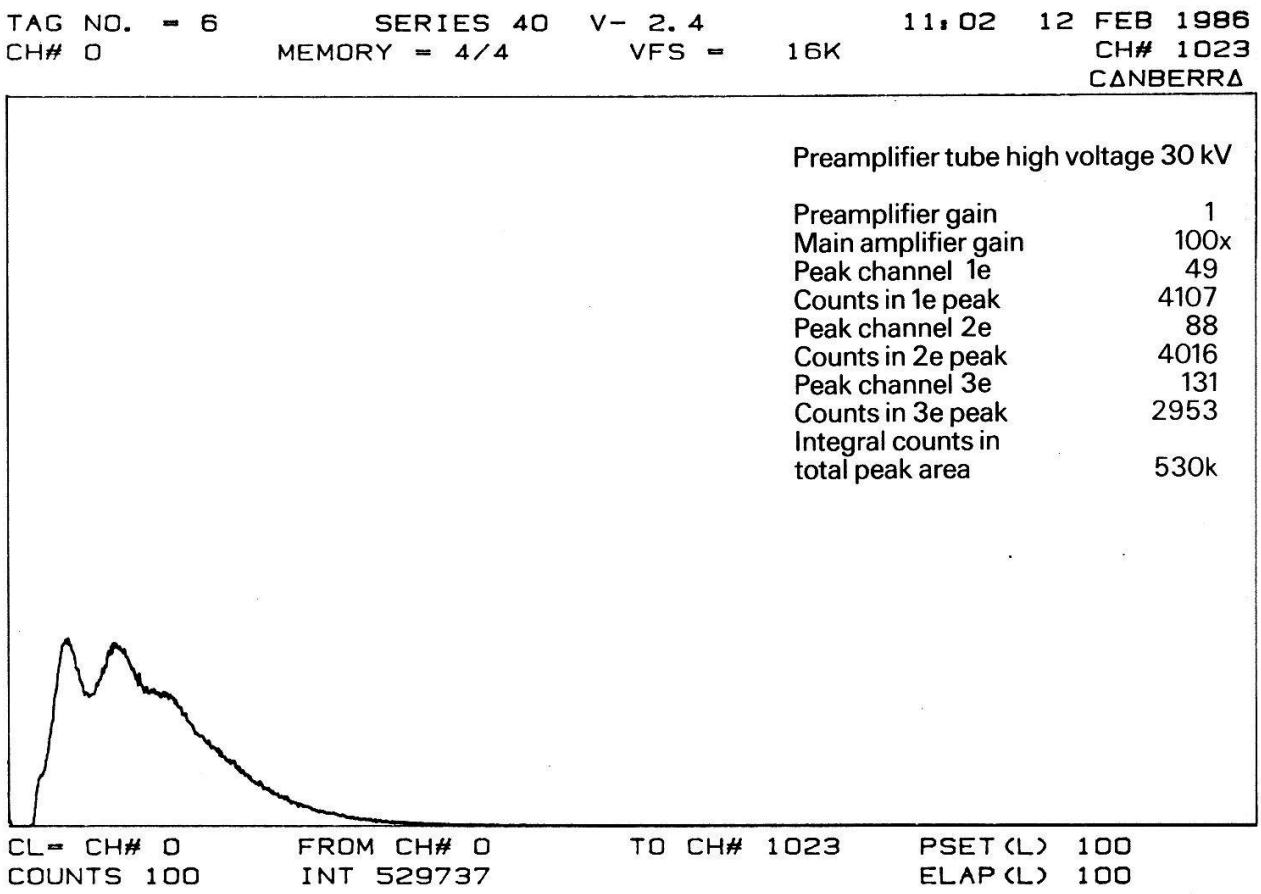

Figure 9.
Pulse height distribution for 30 kV, like 7c, but with increased light pulse intensity.

3.4. Dark current

The integral dark current as a function of the high voltage is shown in fig. 10. Up to about 30 kV it rises linearly with the high voltage. This means that it may be due to thermionic emission and/or background radioactivity. This has to be analysed further. First results indicate that the dark current is independent of the temperature and higher than would be expected from thermionic emission of a SbKCs photocathode.

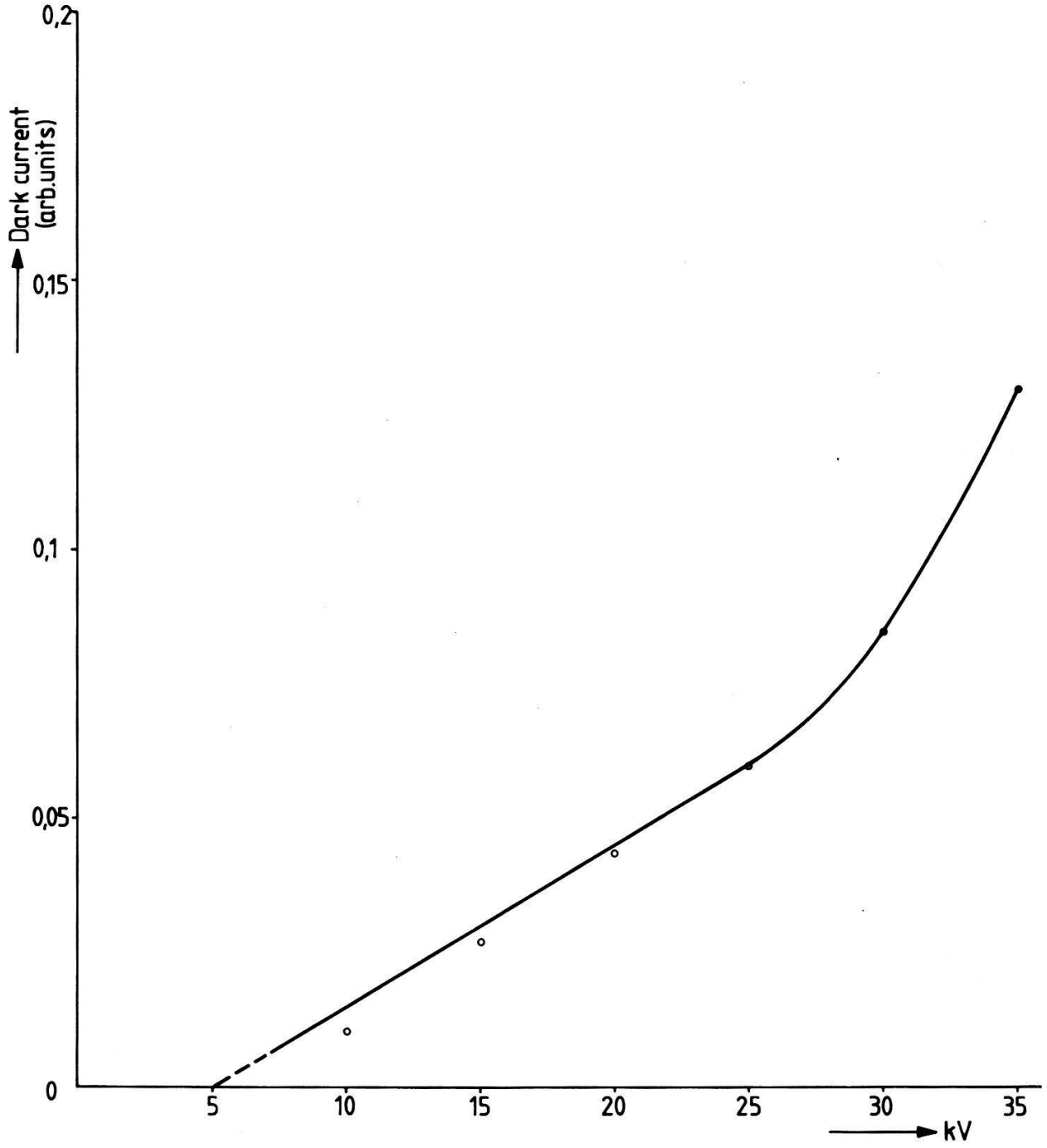

Figure 10.
Dark current as a function of the accelerating voltage.

4. Conclusions

We have demonstrated that large diameter "smart" phototubes combining good single electron resolution, excellent timing and uniform 3π sr response are now feasible.
This tube should open new possibilities for accurate detection and reconstruction of particle trajectories in high energy physics and cosmic ray experiments like DUMAND, the Lake Baikal monopole experiment, the Sudbury Neutrino Observatory and more sophisticated proton decay experiments. Further improvements are envisaged that will result in still better single electron resolution.

Acknowledgements

The authors wish to thank J. Nussli, RTC Brive, France and R. Kurz, KFA Jülich, West Germany for their measurement advice.

References

[1] H. Kume et. al., Nucl. Instrum. Meth. 205, 443 (1983).
[2] G. van Aller et., al, IEEE Trans. Nucl. Sci, NS-30, 469 (1983).
[3] T. Hayakawa, T. Hayashi, DUMAND 1, 83 (1980).
[4] TEPAC Publication no 116. Published by Electronic Industries Association, Washington (1980).

Symposium spécial

Astrophysique "From Clouds to Stars"

organisé par les Professeurs

Nicole Bel et J.-P. J. Lafon, Observatoire de Paris-Meudon

ASTROPHYSIQUE

ASTRO I : SIMULATION VON SOLAREN MIKROWELLENBURSTS

G. Bruggmann und A. Magun
Institut für Angewandte Physik, Sidlerstr. 5, 3012 BERN

Abstract

Mittels Modellrechnungen wird ein bei 11,8 GHz beobachteter Burst simuliert. Der zeitliche Verlauf der Intensität und des zirkularen Polarisationsgrades kann im Anstieg durch eine Zunahme der Elektronenzahl erklärt werden. In der Abfallsphase ist neben der sinkenden Elektronenzahl ein fallender Spektralindex erforderlich.

Einleitung

Bei Sonneneruptionen wird magnetische in kinetische Energie umgewandelt. Dabei werden unter anderem Elektronen auf mittelrelativistische Geschwindigkeiten beschleunigt. Der Beschleunigungsmechanismus ist im wesentlichen noch unbekannt und Gegenstand von indirekten Beobachtungen des Elektronenspektrums sowie theoretischer Untersuchungen. Infolge der Spiralbewegung der Elektronen im solaren Magnetfeld wird ein breitbandiges und zirkular polarisiertes Mikrowellenspektrum emittiert, das auf der Erde beobachtet wird. Sein zeitlicher Verlauf enthält wesentliche Information über die strahlende Elektronenverteilung und den Strahlungstransport in der Radioquelle.

Mikrowellenintensität und Polarisationsgrad vieler Eruptionen wurden im institutseigenen Radioobservatorium bei verschiedenen Frequenzen mit einer zeitlichen Auflösung von 100 ms gemessen. Mit Hilfe von Modellrechnungen wurde zum ersten Mal versucht, aus solchen Mikrowellendaten Rückschlüsse auf den zeitlichen Verlauf der physikalischen Parameter in der Radioquelle zu ziehen. Fig. 1 zeigt das Ereignis, das für diese Simulation ausgewählt wurde.

Das Modell

Das benutzte Modell fusst auf der Berechnung der Gyrosynchrotronstrahlung durch Ramaty (1). Vereinfachend wird angenommen, dass das Hintergrundsplasma kalt und stossfrei sei; die Plasmafrequenz betrage 500 MHz. Die örtlich auf ein Gebiet von 25 Quadratbogensekunden begrenzte Quelle ist von einem homogenen Magnetfeld von 400 Gauss durchzogen, was einer Gyrofrequenz von 1,12 GHz entspricht. Die Steigungswinkel der Spiralbahnen der schnellen Elektronen sind isotrop verteilt und die Elektronenenergien gehorchen einem Potenzgesetz (2):

$$N(E) = K \cdot E^{-\delta}$$

Die beiden Parameter δ und K der Elektronenverteilung sind die Variablen, mit denen der zeitliche Verlauf von I und ρ_C simuliert werden soll. Der Spektralindex δ beschreibt die Steilheit des Spektrums; in die Normierungskonstante K geht neben einer typischen unteren Grenzenergie von 25 keV vor allem die totale Anzahl strahlender Elektronen in Form der "column density" NL ein. K ist proportional zu NL, dem Produkt aus Elektronendichte N und geometrischer Dicke L der Quelle. Das Produkt aus column density und der konstanten Quellfläche ist gleich der Elektronenzahl.

Die Simulation

Fig. 2 zeigt das beste Resultat der Simulationsversuche. Der Intensitätsverlauf konnte bis auf eine mittlere Abweichung von 4 % der Beobachtung angepasst werden. Der berechnete Polarisationsgrad liegt im Mittel jedoch 38 % über den gemessenen Werten. Die mittlere Abweichung von einer um diese 38 % verschobenen Messkurve beträgt noch 14 %, was durchaus im Bereich der Messungsgenauigkeit liegt.

Als Erklärung für die generelle Ueberschätzung des Polarisationsgrades bietet sich "mode coupling" an: Teilweise Depolarisation kann auftreten, wenn die Strahlung zwischen Quelle und Beobachter ein transversales Magnetfeld mit grossen Gradienten durchläuft (3).

Folgerungen

Fig. 3 zeigt, wie der Verlauf von δ und NL gewählt werden musste, um eine optimale Simulation der Beobachtungen zu erreichen. Die Anstiegsphase des Intensitätsverlaufs lässt sich bei praktisch konstantem Spektralindex durch eine

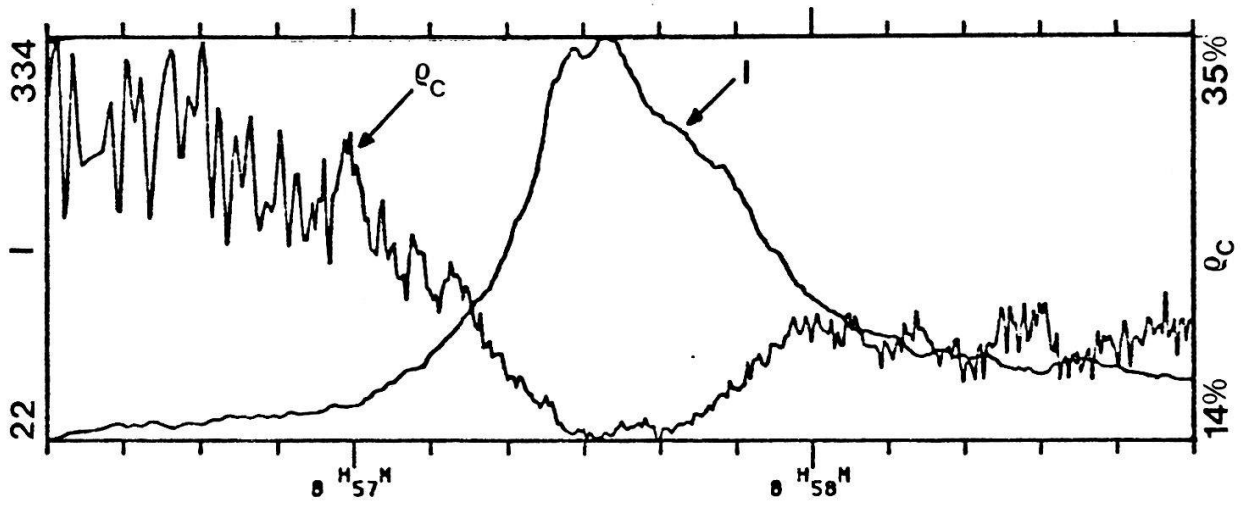

Fig. 1: 26. April 1984. Intensität I (10^{-22}Wm^{-2}Hz^{-1}) und Polarisationsgrad ρ_c bei 11,8 GHz

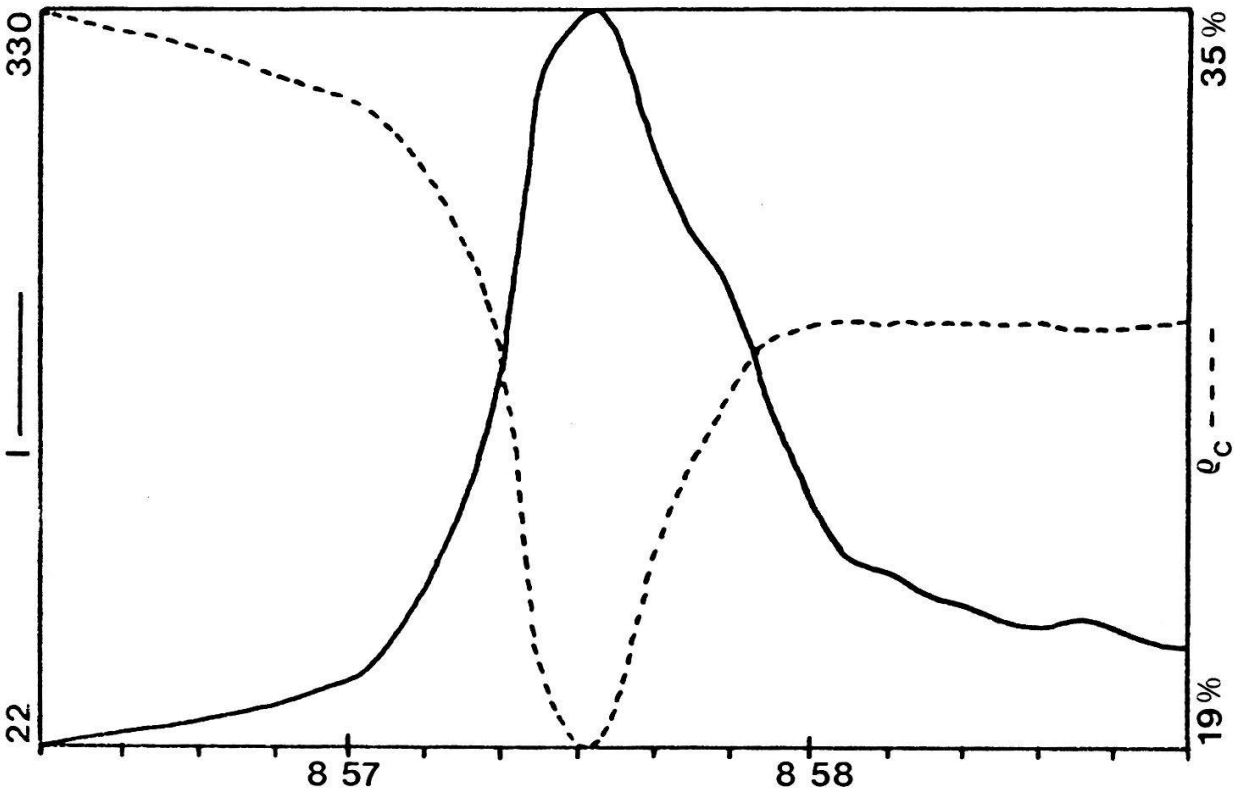

Fig. 2: Simulierter Zeitverlauf von Intesität I und Polarisationsgrad ρ_c des beobachteten Bursts (Fig. 1). Beobachtungswinkel: 75°

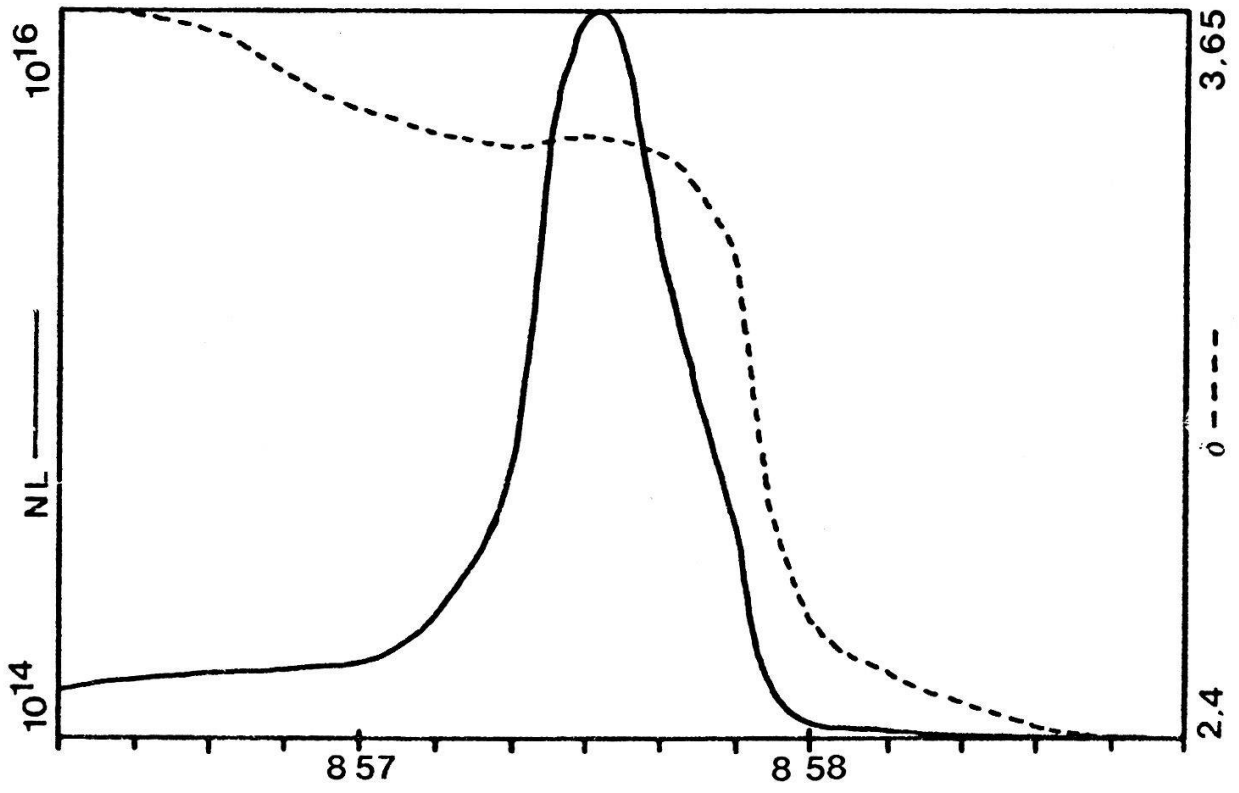

Fig. 3: Zeitlicher Verlauf von column density NL (cm^{-2}) und Spektralindex δ

Zunahme der column density simulieren, welche als Injektion beschleunigter Elektronen in die Mikrowellenquelle interpretiert werden kann. Das Minimum im Polarisationsgrad lässt sich damit auf eine erhöhte optische Dicke der Quelle zurückführen.

Um die Phase des Intensitätsabfalls zu simulieren, ist neben sinkendem NL auch ein fallendes δ erforderlich. Die Abnahme von NL kann einerseits durch Diffusion, andererseits durch Energieverlust der Elektronen erklärt werden. Der fallende Spetralindex wird für eine isotrope Steigungswinkelverteilung erwartet (2) und hängt mit der Tatsache zusammen, dass der Energieverlust durch Elektron-Elektron-Stösse bei niederenergetischen Teilchen am schnellsten erfolgt.

References

(1) RAMATY, R., Astrophys. J. 158, 753 (1969)

(2) VILMER, N.: Etude de l'accélération et du Piégeage des électrons lors des émissions de rayonnement X et radioélectriques, Paris (1985)

(3) McLEAN, D.J. und LABRUM, N.R.: Solar Radiophysics, Cambridge (1985)

CHEMICAL STRUCTURE AND EVOLUTION OF THE GALAXY

Ch. F. Trefzger, Astronomical Institute, University of Basel, Venusstr. 7, CH-4102 Binningen

Abstract: We review current ideas of the chemical structure and evolution of the Galaxy and discuss, in the light of the rapidly growing body of observational data, recent models of the enrichment processes of the chemical elements in the Galaxy.

1. Introduction

In the galactic system the two dominant components, the stars and the interstellar medium, are interacting in a complex way: stars are formed by gravitational contraction of dense interstellar gas clouds, whereas dying stars are returning a fraction of their mass to the interstellar medium together with freshly synthesized heavy elements. The resulting chemical evolution of the Galaxy is manifested by the steady increase of the heavy element abundance in the stellar and gaseous components; furthermore, the spatial variation of their chemical composition indicates that different evolutionary processes dominated in various parts of the Galaxy.

2. Methods of stellar abundance determination

The composition of cosmic matter is dominated by the elements H and He (mass fraction of 75 % and 23 %, respectively), the remaining few percents are in the form of all the heavier elements which are lumped together by astronomers under the term metals. The notion of stellar metallicity therefore indicates the amount of heavy elements observed relative to the solar value, usually expressed as $[\mathrm{Fe/H}] = \log(\mathrm{Fe/H})_{\mathrm{star}} - \log(\mathrm{Fe/H})_{\mathrm{sun}}$.

Detailed information on the chemical composition of stellar atmospheres can be obtained from aequivalent widths of absorption lines using high dispersion spectroscopy [1]. This method, which is based on model atmospheres yields accurate abundances for many elements; however, the sample of stars that can be studied in this way is limited due to the large observational and theoretical effort involved.

Photometric abundance determination is based on the fact that for stars cooler than 8000°K the energy distribution shortward of $\lambda = 5000$ Å is strongly affected by the presence of many absorption lines of Fe-peak elements (line blocking effect) [2]. Properly calibrated using stars with spectroscopic abundance determination, the gradient of the energy distribution in the blue spectral region can be used to estimate the metallicity of an extended sample of stars, thus making possible the investigation of the overall chemical structure of the Galaxy.

3. The chemical structure of the Galaxy

The solar system is the best studied region in the Galaxy whose elemental and nuclidic abundances are known in great detail and are often used as the standard distribution [3]. Important features are the following: (a) generally decreasing abundances with increasing mass numbers, (b) the light elements Li, Be and B are very rare, (c) pronounced peak around Fe and (d) smaller maxima at the magic neutron numbers 50, 82 and 126. This abundance distribution has been interpreted in terms of the nucleosynthesis of the elements in stars [4].

Analyses of stars in the solar neighborhood generally confirm the standard distribution; the metallicities of G-dwarfs show a mean of $[Fe/H] = -0.1$ with a dispersion between 0.08 and 0.18 [5]. A large scale metallicity gradient in the galactic disk seems well established (see [6] and references therein) in the sense that the metallicity of various objects (HII-regions, K-giants and open clusters) decreases with increasing galactocentric radius.

An investigation perpendicular to the galactic plane [7] shows that the

mean stellar metallicity drops to almost $[^{Fe}/_{H}] = -1$ at a height of 1 kpc above the plane. A first attempt to determine the iso-abundance contours at heights up to 6 kpc has been carried out on the basis of photographic three color photometry [8]; preliminary results indicate that they are flattened, corresponding fairly closely to the isodensity contours.

The globular cluster system extends much deeper into the halo, its chemical properties have recently been reviewed by Zinn [9]. The metallicity distribution shows two peaks at $[^{Fe}/_{H}] = -1.6$ and -0.5, corresponding to the socalled halo and disk clusters, respectively. The existence of a large scale metallicity gradient in the halo is still controversial because of the low space density far out in the halo and some uncertainties in the abundance scale of globular clusters.

In recent years an increasing number of halo stars have been studied spectroscopically [10]. Besides the well-known fact that heavy elements are deficient by one or two order of magnitudes in this oldest population of the Galaxy, deviations from the standard distribution are becoming evident. The most striking case is Oxygen which is systematically enhanced relative to Iron [10].

4. Models of galactic chemical evolution

An attempt has been made to describe the evolution of the solar neighborhood in the framework of the simple model, assuming a closed system starting initially with metal-free gas and a star formation with constant mass spectrum. The simple model predicts too many metal-poor stars, for a discussion we refer to [11]. One or more postulates must be dropped, e.g. if prompt initial enrichment of the gas is allowed by about 17% of its present metal content the observed metallicity distribution of stars is well represented. Such an initial enrichment may have occurred during an earlier phase of halo formation. Another way to solve the problem with the simple model is to allow infall of gas, either primordial or lost from halo stars, into the solar neighborhood during its evolution.

Hydrodynamical model calculations of a collapsing protogalaxy have been carried out by Larson [12] . The model galaxies show the basic structural features observed, e.g. the metal-rich disk and metal-poor halo populations and the metallicity gradients in the disk and halo.

5. References

[1] G. Cayrel de Strobel, C. Bentolila, Astron. Astrophys. 119, 1 (1983)

[2] R. Buser in: Obs. de Strasbourg, Comptes Rendus sur les Journées de Strasbourg, 7 ème Réunion (1985)

[3] A. G. W. Cameron in: Essays in Nuclear Astrophysics, C. Barnes, D. Clayton, D. Schramm Eds., Cambridge Univ. Press (1982)

[4] G. Burbidge, M. Burbidge, W. Fowler, F. Hoyle, Rev. Mod. Phys. 29, 547 (1957)

[5] B. Pagel, M. Edmunds, Ann. Rev. Astron. Astrophys. 19, 77 (1981)

[6] L. Cameron, Astron. Astrophys. 147, 47 (1985)

[7] Ch. Trefzger, J. W. Pel, A. Blaauw, ESO-Messenger 35, 32 (1984)

[8] Ch. Trefzger, Astron. Astrophys. 95, 184 (1981)

[9] R. Zinn, Astrophys. Journ. 293, 424 (1985)

[10] M. Spite, F. Spite, Ann. Rev. Astron. Astrophys. 23, 225 (1985)

[11] J. Audouze, B. Tinsley, Ann. Rev. Astron. Astrophys. 14, 43 (1976)

[12] R. Larson, Mon. Not. R. astr. Soc. 176, 31 (1976)

MISSING MASS AND STELLAR DYNAMICS IN FLAT GALAXIES

J.-P. J. Lafon, Observatoire de Paris-Meudon, 92195 Meudon Principal Cedex (France)

Abstract : Flat rotation curves do not imply the presence of (massive or not) invisible halos

In spite of the fact that mass is concentrated at various scales in the Universe and, strictly speaking, there cannot be any "missing" mass, this term (or "dark matter" or "unseen matter") is used to account for the discrepancy between what one finds (or expects to find) using various methods to determine the masses of individual galaxies, those of clusters of galaxies and that of the whole universe. A lot of papers have been devoted to the discussion of this discrepancy during the last decades, without clearly elucidating the problem.

This paper is devoted to the investigation of the dynamics of flat star systems through their rotation curve. The topology of this curve is often invoked infavour of the presence of fairly large amounts of matter that may surround the visible disc but cannot be seen. Other various arguments are invoked, depending on the object considered (see a list of them in the paper by Lafon, 1984). Of course a lot of candidates for invisible matter is envisaged : gas, dust, rocks, Jupiter-like bodies, low mass stars, heavy particles ...(references in the same paper)

Now the rotation curve of a flat disc of stars is that obtained by plotting the velocity of any body on a circular orbit in the equatorial plane, at the radial distance r from the center of the system (considered as roughly axisymmetric) v(r). This is another way to describe the gravitationnal potential V(r) since $dV/dr = v^2(r)/r$. Of course, V is related to the mass density by the Poisson equation.

The question is now :"what happens at large radial distances ?". At first glance, one can expect that the circular motion rapidly becomes Keplerian since most of the matter is concentrated

within a few kiloparsecs. However this is now not observed and the rotation curves that can be determined up to several tenths of kiloparsecs are <u>flat</u> : v(r) decreases very slowly, much less steeply than the $1/\sqrt{r}$-like behaviour characteristic of Keplerian systems. (Fig. 1, Rubin, 1983)

Fig.1
Rotation curves for

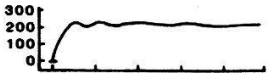

NGC 801

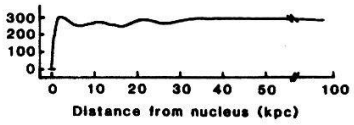

UGC 2885

A first effect due to the geometry (flatness) of the system can be observed comparing the rotation curve of an exponential disc (density decreasing exponentially with r) describing a highly concentrated system to that corresponding to the spherically symmetric distribution of matter with the same mass inside each sphere of radius r, which exhibits the keplerian behaviour in an equatorial plane (Fig. 2, Freeman, 1970). The curves can match only at extremely large distances, much larger than the physically meaningful dimensions of the system (that are scaled by the scale length of the exponential).

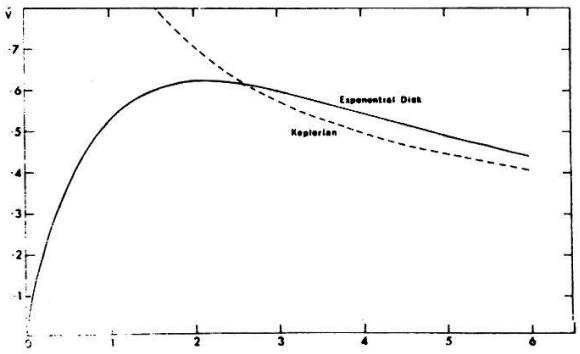

Fig. 2
The dotted curve is that of the Kepler rotation

Other arguments concerning the effects of flatness are analysed in the paper by Lafon, 1984

Nevertheless some authors assert that the existence of flat rotation curves can be explained only by the presence of a large amount of unobservable matter (at least of the same order as

the observable mass and often larger by orders of magnitude) and that the motion of the observable matter is in fact governed by the unseen matter: self gravitation would then be of minor importance. Though we do not exclude the presence of (massive or not) halos, we do not agree with this point of view and say that inobservable large amounts of mass are nor implied by flat rotation curves.

We have constructed 3 dimensionnal dynamically self consistent models of flat star systems (all stars moving in a plane) under the following fairly little restrictive conditions :

-the stars move in their own gravitational potential without close encounters, in steady state.

-the dynamics obey the coupled system of Poisson's and Vlasov's equations.

-the system is sufficiently well mixed by non-collisionnal relaxation to be described by a "coarse-grained" distribution function of mass proportional to one of the following functions:

1/ $e^{aE+b\xi}$ 2/ $(e^{a_1 E} - e^{a_2 E})e^{b\xi}$

where E,ξ respectively denote the energy and the angular momentum of a test star. The former describes a system more efficiently "thermalized" (by collective gravitational interactions, not by collisions) than the latter, in other words with a higher concentration of stars with highly elongated (non circular) orbits reaching the outer parts of it. The parameters $-1/a$ are like temperatures and b characterzes the total angular momentum of the system. Small $|a|$ and large b respectively describe "hot" and highly rotating systems.

The conclusions are (Lafon, 1976) (Fig. 3) :

-the temperature is the main parameter ; it governs the structure of the inner part of the system.

-the rotation and the extension of the system depend strongly on b.

-colder systems are more extended

-all rotation curves are flat at distances much larger than those for which most of the mass is concentrated.

- the rotation velocity in the outer parts is smaller for

systems with fewer elongated highly elliptic orbits reaching the outer parts.

The central part works as a non collisionnal "thermalizer" dominating the dynamics of the whole system through stars with elongated orbits whereas its structure appears fairly independent of the matter far from it. Note that this probably stabilizes the outer part otherwise dynamically very unstable.

Including a spherical halo would only globally increase the rotation velocity in the outer part of the system.

Thus, flat rotation curves do not imply the presence of invisible matter, though not excluding it.

Finally, in order to improve the answers to the questions it would be critically useful :

-to find systems for which several and not only one as usual arguments are in favour of the presence of unseen matter

-to analyse more clearly the problem of the ratio mass/ luminosity

References

Freeman K.C., Astrophys. J., 160, 1970, 811

Lafon J.-P. J., Astron. Astrophys., 46, 1976, 461

Lafon J.-P. J., Halos or no halos, in "19^{me} rencontre de Moriond / 4th Moriond workshop", " Massive neutrinos in particle and Astrophysics", Proceedings of a meeting held in La Plagne (France) in 1984, Ed. Frontières

Rubin V.C., Science, 220, 1983, 1339

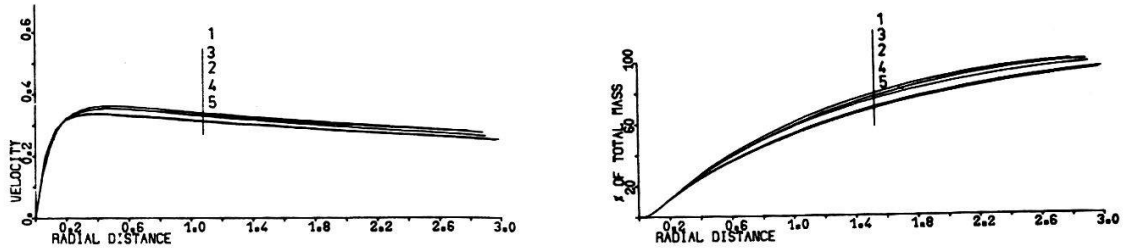

Curve	a_1	a_2	b	Radius	Total Mass
1	−4	−0.5	4.338	2.789	1
2	−4	−0.5	4.	3.220	1
3	−4	−1	4.703	2.884	1
4	−4	−1	4.127	3.704	1
5	−4	−1	4.	3.826	1

Fig 3. Rotation curve and % of total mass within radius r

Abundances of Solar Wind Minor Elements near Maximum of Solar Cycle 21

J. Schmid, P. Bochsler, A. Bürgi, J. Geiss and S. Kunz
Physikalisches Institut, Sidlerstrasse 5, 3012 Bern

We have determined abundances and ionisation states of solar wind oxygen, neon, carbon, and iron from four years of data provided by the Ion Composition Instrument on ISEE-3. Our results are compared with solar wind composition data obtained by other spacecraft and by the Apollo experiments, as well as with photospheric values and solar energetic particle composition data. The evidence is discussed in relation to recent models about fractionation mechanisms in the upper chromosphere and corona.

Sonneneruptionen - CCD-Kamera - Computer

Hans Marti Inst. für angew. Physik Sidlerstr. 5 3012 Bern

Sonneneruptionen entstehen in der Korona. Dabei werden in verschiedenen Höhen kurzzeitig Radiowellen und Strahlung im Lichte der H-alpha-Linie emittiert. Aus der zeitlichen Verzögerung dieser Strahlungskomponente kann auf die Natur des Energietransportes geschlossen werden. Zur Beobachtung der H-alpha-Intensität in Linienmitte verwenden wir eine CCD-Kamera, deren Daten direkt digital gespeichert und weiterverarbeitet werden. Diesem technischen Aspekt und ersten zeitlich hochaufgelösten Beobachtungen ist der Vortrag gewidmet.

ON THE CHEMICAL COMPOSITION OF THE PRIMARY COSMIC RADIATION BEYOND 10^5 GeV.

P.K.F. Grieder
Physikalisches Institut, Sidlerstrasse 5, 3012 Bern

We present data from a large set of Monte Carlo simulations of primary proton and iron nuclei initiated air showers, covering the primary energy range from 10^5 to 10^8 GeV, that are based on a very detailed hadron collision and particle production model which reproduces $\bar{p}p$ data correctly. Our predictions are compared with experimental hadron and muon spectra obtained with the large arrays at ground level. It is concluded that there cannot be a major change in the primary composition over the investigated primary energy range.

Suche nach Müonen aus der Richtung des Binärsystems Cyg X-3 mit Hilfe eines Drahtkammer-Szintillator Detektors im Tiefenlabor Gotthard

G. Czapek, B. Hahn, W. Krebs, J. Lauber und P. Schlatter

Laboratorium für Hochenergiephysik, Universität Bern

Cyg X-3 ist bekannt als eine sehr intensive Quelle elektromagnetischer Strahlung mit einer Periodizität von 4.8 h. Kürzlich wurden in drei Tiefenlabors (Soudan, Mt. Blanc und Fréjus) Anzeichen für einen überhöhten Müonfluss in Richtung Cyg X-3 gefunden, dessen Interpretation, falls wahr, mit bekannter Physik sehr schwierig ist. Es werden erste Ergebnisse vom Gotthard-Experiment mitgeteilt.

ASTRO II :

THE HIERARCHICAL STRUCTURE OF MOLECULAR CLOUDS

Jean-Pierre Chièze
Commissariat à l'Energie Atomique
Centre d'Etudes de Bruyères-le-Châtel
B.P. 12, F-91680 Bruyères-le-Châtel

A close parallel can be established between the scaling laws observed among molecular clouds and their fragments, namely $M \propto R^2$ and $\Delta v \propto R^{1/2}$, where Δv is the internal velocity dispersion of the structures (M, R) [1],[2],[3] and the properties of self-gravitating structures at the threshold of gravitational instability. Moreover, the optical extinction at the center of *any* cloud in this critical state is close to $Av = 1mag$. This means that interstellar clouds undergo gravitational contraction precisely when the gas turns from the mostly atomic phase to the molecular phase. This may be in favour of prompt fragmentation.

Properties of self-gravitating spheres at the onset of gravitational instability.

Interstellar clouds are in surface pressure equilibrium with the ambient hot phase of the intersrellar medium, in which the pressure (typically $\tilde{P}_0 = P_0/k = 3800 K cm^{-3}$) is regulated by supernovae explosions [4]. For definiteness we consider polytropic gas spheres in hydrostatic equilibrium. Their structure is described by the Lane-Emden equation of index n, where n is the polytropic exponent which characterizes the heat exchanges between the gas and it's surroundings (note that n may be negative for molecular gas). The three dimensionally independant quantities M, P_0, G, where G is the gravitational constant, form a natural dimensional basis for our study. In this basis, the radius of a cloud can be written as:

$$R = x\, M^{1/2} P_0^{-1/4} G^{1/4} \qquad (1)$$

The non-dimensional parameter x in Equ.(1), characterizes the physical state. The mass and the pressure are just scaling factors. One can show [5], that the first gravitationally ***unstable*** state in the sequence of equilibrium states is characterized by:

$$x_* = \left(\frac{1}{8\pi} \frac{n-3}{n+1} \right)^{1/4} \qquad (2)$$

According to Equ.(1) this means that clouds at the threshold of gravitational instability obey to the following mass-radius scaling law:

$$\frac{M}{1M_\odot} = 12.6\, x_*^{-2} \left(\frac{\tilde{P}_0}{3800 K cm^{-3}} \right)^{1/2} \left(\frac{R}{1pc} \right)^2 \tag{3}$$

For isothermal clouds (of different temperatures) and the reference interstellar pressure we have:

$$\frac{M}{1M_\odot} \approx 63 \left(\frac{R}{1pc} \right)^2 \tag{4}$$

We can express the internal velocity dispersion, using the virial theorem:

$$\frac{\Delta v}{1 kms^{-1}} = 0.59 \left(\frac{\tilde{P}_0}{3800 K cm^{-3}} \right)^{1/4} \left(\frac{R}{1pc} \right)^{1/2} = 0.21 \left(\frac{\tilde{P}_0}{3800 K cm^{-3}} \right)^{1/8} \left(\frac{M}{1M_\odot} \right)^{1/4} \tag{5}$$

Note the relatively weak dependance of these expressions upon the ambient pressure. These relations can be generalized to any polytropic equation of state provided that (i) equilibrium state do exist ($n \leq -1$ or $n > 0$), (ii) they can suffer gravitational instability ($n < 0$ or $n \geq 3$).

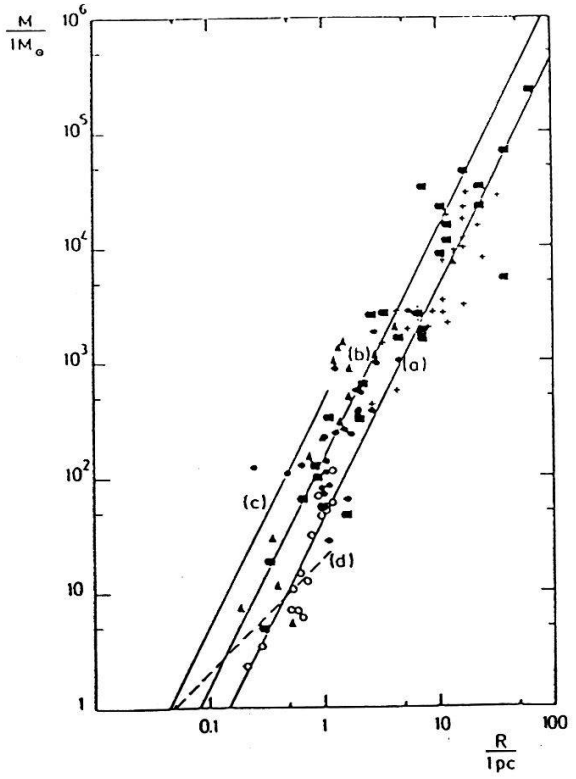

Fig.1: The mass-radius relation for molecular clouds.

Finally, the proton column density at the center of a critical cloud is:

$$\frac{N_H}{1cm^{-2}} = 4\ 10^{20} \left(\frac{\mu_H}{1amu}\right)^{-1} \left(\frac{\tilde{P}_0}{3800Kcm^{-3}}\right)^{1/2} \tag{6}$$

Adopting $N_H/Av = 1.5510^{21} cm^{-2} mag^{-1}$ [6] and $\mu_H = 1.3\ amu$, it turns out that:

$$Av_c^* = 1mag \tag{7}$$

Fragmentation

We suggest that the correlations observed among molecular clouds and their fragments reflect the properties of the state in which they actually formed. It is clear that Equ.(3) to (6) cannot directly describe the present physical state of molecular clouds. They have been derived without reference to turbulence. In other words, they hold for clouds supported by pure thermal pressure. Equ.(6) can be converted into:

$$\frac{T}{1K} = 5.3\ \mu \left(\frac{\tilde{P}_0}{3800Kcm^{-3}}\right)^{1/4} \left(\frac{M}{1M_\odot}\right)^{1/2} \tag{8}$$

from which one immediately see that irrelevant temperatures are derived for massive molecular clouds.

This apparent paradox can be resolved if efficient fragmentation does occur in a cloud at, or in the vicinity of gravitational instability. Fragmentation can be triggered by the transition from atomic gas to the molecular phase, since $Av \approx 1mag$ at the critical state. This transition has in effect to significantly lower the Jeans mass, since H_2 formation implies strong UV shielding -destabilizing the thermal balance. We show in the following paper in this conference that the Jeans mass in *molecular* gas is always lower than 100 $M_\odot$. Neglecting collisions, the fragmented structure settles down by dynamical phase mixing to a quasistatic equilibrium state. The relaxed configuration obey to the relations Equ.(4) and (5a,b) in which the normalizations must be replaced by 63 β_2, $0.16(2-\alpha)^{1/2}$ and $0.45\ [\beta(2-\alpha)]^{1/2}$ respectively. In these expressions Δv is now the velocity dispersion of the clumps contained in a region of linear scale R, P_0 is the ambient pressure when the parent cloud becomes unstable. α is the virial parameter of the clumpy system just before relaxation: $\alpha = 2T/|\Omega_*|$, and $\beta \sim 2-\alpha$ is the ratio of the initial to the final radius of the configuration. A conservative estimates for these values is $\alpha \sim 0.5$ and $\beta \sim 1.5$, so that we obtain:

$$\left(\frac{M}{1M_\odot}\right) = 142\left(\frac{R}{1pc}\right)^2 \tag{9}$$

$$\frac{\Delta v}{1kms^{-1}} = 0.2\left(\frac{M}{1M_\odot}\right)^{1/4} = 0.68\left(\frac{R}{1pc}\right)^{1/2} \tag{10}$$

These relations are compared to observations on fig.1, 2a,b.

Note that once they are formed, fragments themselves can suffer further cooling and subsequent fragmentation in the forementionned conditions. This leads to the formation of a hierarchy of embedded clumps obeying to the scalings Equ.(9) and (10), provided that the ambient pressure P_0 does not suffer too large variations during the fragmentation process (see [5] for a discussion of this point).

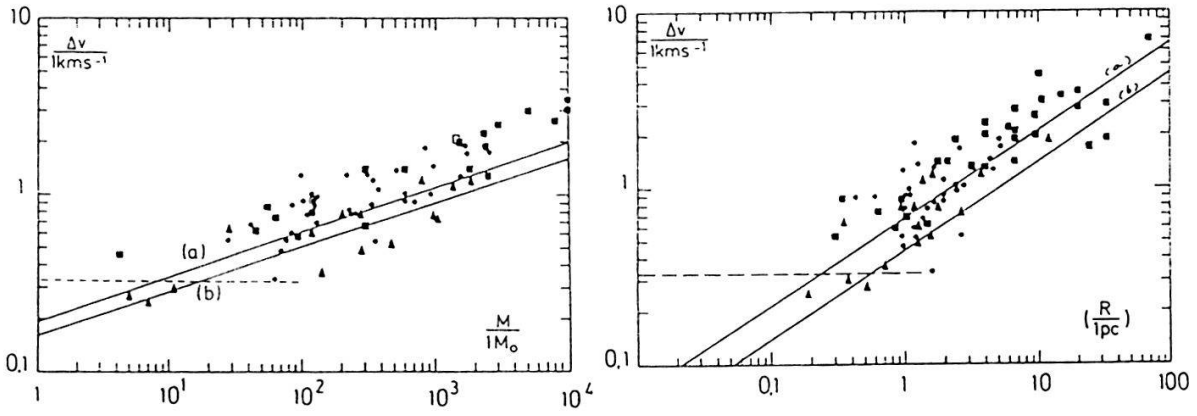

Fig.2: The internal velocity dispersion as a function of the mass and the radius of the clouds and their condensations.

In summary, we have shown that prompt fragmentation of clouds at the gravitational critical state - in a constant pressure environment - leads to the formation of a clustered structure governed by the definite scaling laws $M \propto R^2$ and $\Delta v \propto R^{1/2}$. The model is in favour of the formation of molecular clouds directly from hot cooling interstellar gas, rather than from HI clouds accretion processes.

References:

[1] Larson, R.B. : 1981, Monthly Notices Roy. Astron. Soc. **194**, 809.

[2] Myers, P.C. : 1983, Astrophys. J. **270**, 105.

[3] Pérault, M., Falgarone, E., Puget, J.L. : 1985, Astron. Astrophys. **152**, 371.

[4] Mc Kee, C.F., Ostriker, J.P. : 1977, Astrophys. J. **218**, 148.

[5] Chièze, J.P. : 1986, submitted to Astron. Astrophys.

[6] Bohlhin, R.C., Savage B.D., Drake J.F. : 1978, Astrophys. J. **224**, 132.

MEASUREMENTS OF MAGNETIC-FIELD STRENGTHS IN MOLECULAR CLOUDS

I.Kazès, Observatoire de Paris, Section de Meudon, 92195-MEUDON PRINCIPAL CEDEX, FRANCE

Abstract : The important physical conditions which govern the evolution of interstellar clouds and the process of star formation include the kinetic temperature, particle density, turbulent velocity and magnetic field. Detailed magnetohydrodynamic studies have shown the critical role that the magnetic field plays in the process. The 21-cm line of neutral hydrogen and the 18-cm mainlines of the hydroxyl radical have large Zeeman-splitting factors and lie at wavelengths where low-noise receivers are available. The large radio telescope located near Nançay, France, has been used to measure the Stokes-parameter I and V spectra of the 1665 and 1667 MHz lines of OH in emission and in absorption from extended (non-masing) molecular clouds. Comparison of magnetic fields in atomic and molecular regions along the same line-of-sight can provide an indication of how field strength scales with gas density.

1. Introduction

The existence of a galactic magnetic field was first proposed by Fermi in 1949 (1). Since then the available variety of data reveals an interesting picture of conditions governing interstellar space. It seems useful to review observational evidences where magnetic fields are involved.

-In dust clouds, elongated grains aligned by an ambient magnetic field scatter the starlight selectively in a direction perpendicular to the line of sight.

-The observed polarized emission from the non-thermal radio background is due to high-energy particles spiralling about magnetic fields.

-Thermal electrons contained in the interstellar medium permeated by magnetic fields are responsible for the observed rotation of the polarization plane of galactic continuum emission. Also, for long lines-of-sight, Faraday rotation of emission from polarized extragalactic radio sources provides information on the structure of the longitudinal magnetic field.

-Determination of pulsar dispersion and rotation measures yield the most reliable result concerning the local galactic magnetic field ($\sim 3.5\,\mu$G) since there appears to be no Faraday rotation intrinsic to pulsars.

It is generally believed that interstellar clouds form through a process by which interstellar gas increases in density flowing along local gravitational magnetic field lines which have suffered instabilities. As the cloud density increases in the background magnetic field, self-gravity becomes important and during the subsequent contraction phase of the cloud, the magnetic field increases since the field lines are drawn closer together. Theoretical studies (2),(3), have shown that the magnetic field is proportional to the cloud density on a logarithmic scale.

Experimental testing of these results was initiated by Verschuur (4) who in 1969 measured the first Zeeman splitting of the HI line in the direction of Cas A. Although other strong sources have been observed in diffuse atomic regions, it was not until 1983 that the first Zeeman splitting was observed in the dense molecular cloud of NGC 2024 (5).

2. Observations

The large collecting area of the Nançay radio telescope has been used for Zeeman observations of nine dense molecular clouds in the 18-cm mainlines of the OH molecule. The instrumental characteristics and configurations have already been described (5),(6). Here we shall only insist upon the instrumental effects which deteriorate the sensitivity of the system and make it necessary to take particular precautions, especially since the measured quantity is very small. In terms of velocity shift this quantity is of the order of 6.10^{-4} km $s^{-1}\mu G^{-1}$.

The purity of left and right circularly polarized lines must be checked prior to any Zeeman experiment. Therefore, for each circular polarization, observations of radiation from a transmitting helical antenna and of polarized OH masers were made. They showed a rejection in excess of 20 dB.

Misalignment of the feed horn and reflector axes of a radio telescope will produce beam displacement. Such displacement is determined by measuring the difference in time between left and right circularly polarized beam patterns of a strong continuum radio source. In the presence of a linear velocity gradient of 0.1 km s^{-1} $arcmin^{-1}$ in front of a molecular cloud, a beam displacement of 6 arcsec will correspond to a velocity difference of 0.01 km s^{-1} between the two polarized lines. For the 1667 MHz line the resulting false Zeeman splitting would correspond to a magnetic field of 28μG!

The measured beam displacement of the Nançay antenna was 23 arcsec in right ascension. This effect was corrected by position switching in right as-

cension by 23 arcsec, at the expense of 50 % efficiency for Zeeman observations. Recently this disadvantage has been minimized by installing a remotely controllable pivoting mechanical device for the feed horn. With this system the position of the horn has been optimized and the beam displacement is negligible; the resulting loss in gain is only 10 to 20 %.

The effects of instrumental circular polarization are very severe when 21-cm Zeeman observations are performed. HI lines are strong all over the sky and the distribution of their intensities affects the sidelobes of the antenna beam pattern. Polarized sidelobes can lead to spurious frequency-dependent polarization effects which limit the detectability of Zeeman splitting. These instrumental effects are negligible for OH since a very small fraction of the sky produces OH emission lines.

3. Results

Among the nine dense molecular clouds we have determined magnetic field strengths for NGC 2024, W 22 and W 3 with the respective values of +38, -18 and +73 μG. Toward the other six clouds observed, only upper limits to magnetic-field strengths were found: L 134 (32 μG), ρ Oph (71 μG), W 40 (20 μG), W 51 (24 μG), L 889 (32 μG) and TMC 1 (38 μG).

In the Zeeman analysis of the observed spectra, the quantity actually measured is the Stokes parameter V spectrum. The difference between the two slightly displaced circularly polarized profiles is a "sideways S" resulting from the first derivative of the power spectrum I and an amplitude proportional to the strength of the line-of-sight component of the magnetic field.

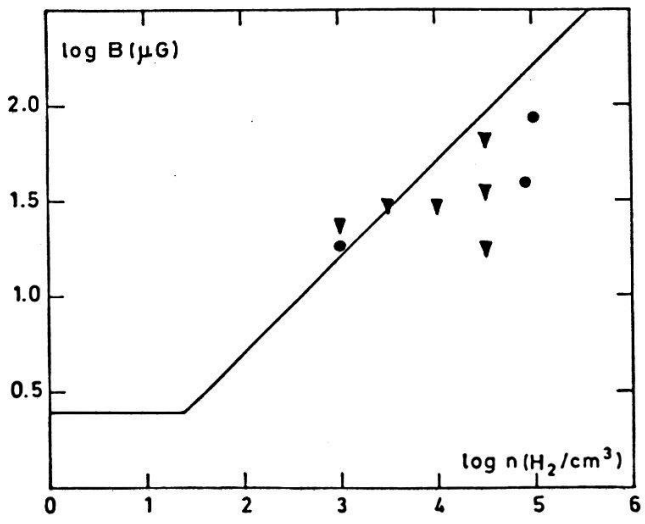

Fig. 1 The Nançay OH Zeeman results for the measured magnetic fields in molecular clouds plotted against the estimated gas densities of clouds. Filled circles correspond to detected fields and downward pointing triangles correspond to upper limits at the upper limit value. The line is a simplified version of the theoretical predictions (2).

In view of these results, it seemed that a useful step would be to compare them with existing theoretical studies associating magnetic field strength to gas density. Based on a review of the literature, we therefore attempted to estimate gas density for each cloud (Fig. 1). Ideally what is needed is a comprehensive study of the densities at which OH absorption and emission lines are formed. Unfortunately such a study is not yet available and therefore the best estimates of densities are marred by uncertainties of half an order of magnitude. Nevertheless, it is crucial to test the theoretical predictions stating that the magnetic field remains more or less constant until the cloud becomes self-gravitating at a proton density of approximately $n_p=137(B^3/M)^{1/2}$ cm^{-3} where B is the external magnetic field in microgauss and M is the cloud mass in solar masses (2). Taking for B the value of 5μG (7), the molecular cloud core 10^3 $M_\odot$, then $n(H_2)=25$ cm^{-3} if the cloud is entirely molecular. As the collapse proceeds, the magnetic field increases as $n^{1/2}$. This theoretical result is not contradicted by our experimental results associating measured magnetic field strengths to estimated cloud densities (Fig. 1).

4. Concluding remarks

We have mentioned both the difficulties and the usefulness of a test of the theoretical predictions concerning the scaling magnetic field strengths with gas density. Indeed one of the best ways to test the theoretical relation would be to perform aperture synthesis observations of strong radio sources like Cas A (8) and Orion A. Although these measured fields are stronger than those measured with single dish, there appears to be no obvious relation between magnetic field strength and HI fractional absorption toward Cas A.

5. References

(1) E. Fermi, Phys. Rev. 75, 1169 (1949).

(2) T.M. Mouschovias, in 'Solar and Stellar Magnetic Fields' (I.A.U. Symposium No. 102), J. Stenflo (ed.), p. 479 (1983).

(3) L. Mestel, R.B. Paris, Astr. Ap., 136, 98 (1984).

(4) G.L. Verschuur, Astrophys. J., 156, 861 (1969).

(5) R.M. Crutcher, I. Kazès, Astr. Ap., 125, L23 (1983).

(6) I. Kazès, R.M. Crutcher, Astr. Ap., in press (1986).

(7) T.H. Troland, C. Heiles, Astrophys. J., 301, 339 (1986).

(8) U.J. Schwarz, T.H. Troland, J.S. Albinson, J.D. Bregman, W.M. Goss, C. Heiles, Astrophys. J., 301, 320 (1986).

DISK AND FLOWS AROUND MASSIVE YOUNG STARS

S. Guilloteau, Groupe d'Astrophysique, Observatoire de Grenoble, CERMO
BP 68 F-38402 Saint Martin d'Hères Cedex France

Abstract : An almost perfect correlation exists between ultracompact HII regions and CO high velocity flows, indicating that dense disks may be confining the flows as claimed in recent star formation models. Direct observational data on disks is very scarce, and detailed comparison with theory is presently difficult.

1. Introduction

Recent models of "protostars" (i.e. young stars still embedded in their parent cloud) integrating magnetic forces and rotation present a coherent picture in which angular momentum is removed from a dense rotating "disk" or better "torus" by a magnetically driven wind originating at the inner boundary of the torus, which powers a neutral high velocity flow (1). I review here the current observational evidence for such disks and flows around massive young stars exciting the ultracompact HII regions.

2. Global properties

Ultracompact HII regions are obvious tracers of young massive stars, as their lifetimes are likely very small ($<10^4$ years). Most of the known regions have been mapped in the continuum at centimeter wavelengths with angular resolution about 0.1" (2,3), high enough to reveal the distribution of ionized gas on scales of 10^{16}cm. As summed up in Table I, more than half of the observed regions present an apparent shell structure. According to Turner and Matthews (2), this structure cannot be attributed to the ionization of the inner ridge of a dense spherically symmetric cocoon, as predicted by earlier theoretical models (4), or originally invoked for some sources (e.g. W3(OH) (3)). Preferred explanations include a stellar wind bubble model, or ionization of the inner side of a dense torus. The latter is strengthened by the frequent occurence of apparent shells with such a high contrast that it cannot be explained by any spherically symmetric density distribution. This implies torus like distributions, and in this

picture, flattened HII regions such as NGC7538 may be disks seen edge on.

Table I : Summary of disks and flows around ultracompact HII regions

(1)	(2)	(3)	(4)	(5)
W3(OH)	Shell	Yes	Yes	Yes
G10.6-0.4	Central	Yes,*	Yes	No
K3-50	Shell	?,*	Yes	?
ON 3	Shell	?	No	?
ON 1	Shell	?,*	Yes	?
G47.07+0.13	Shell	?	Yes	Yes
G19.6	?	?	Yes	Yes
NGC7538	Disk	Yes	Yes	?
W 75 N	Disk	Yes	Yes	?
ON 2	?	?	Yes	?
S 106	Bipolar	Yes	Yes	No

(1) Source name, (2) Aspect of HII region, (3) Existence of a molecular disk (stars indicate massive rotating cores of up to 4000 Mo), (4) Existence of a bipolar flow and (5) evidence for infall. Question marks indicate lack of observing data.

High velocity molecular flows are common in these regions. Due to the large distance of many objects, sensitivity is a major problem to detect these flows. Interferometers or the largest single dishes are required. In a recent search with the IRAM 30-m, five possibly six new flows out of seven sources searched for were detected, and the flow in K3-50 confirmed. Some of these flows are a hundred times more powerful than Orion. In addition, most OH masers found in these sources appear redshifted with respect to the recombination line velocities of the HII regions, thus suggesting infall (6). This conclusion may be invalid if significant asymmetric outflows exist in the ionized gas, as possibly in W3(OH), in which case the recombination line velocity may be biased.

3. Molecular observations of disks

The situation concerning molecular disks is less clear. The only well studied source is W3(OH), which has been mapped with the highest spatial resolution in NH_3 (0.25") (7), excited lines of OH (0.5") (8), 6 cm lines of H_2CO (0.5") (9), and J=1-0 line of HCN (1.5") (10). NH_3 and OH lines present strong evidence that a dense (10^7 cm^{-3}) warm (80 K) cloud covers only the western side of the HII region. The velocity field hardly show any evidence for rotation, but infall at velocities about 3 $km.s^{-1}$ (coherent with a central object of 30 Mo) seems present ; weak differences do exist between the two molecules, however. This cloud has been interpreted as the front side of a torus inclined 45° along the line of sight (7). Additional support for this model comes from the weak ionized extension detected along the axis of the presumed disk (8). H_2CO, on the opposite, also shows strong 6 cm absorption on the eastern side of the HII region (9). From the low average 2cm to 6cm ratio, this absorption must be due to lower density, colder material preferentially sampled at 6 cm. HCN confirms the existence of the warm dense condensation, and seems to suggest higher rotational velocities than OH and NH_3 ; this unfortunately may be partly an artefact of the low velocity resolution used (4.2 $km.s^{-1}$). The surprising result in HCN comes from the detection of a broad winged clump East of the HII region, close to the H_2O masers (10). This questions whether the high velocity flow detected in CO is due to the exciting star of W3(OH) or a nearby protostellar object, and may invalidate the previous conclusion about the correlation between ultracompact HII regions and high velocity flows.

4. Conclusions or prospects

Other objects in which disks have been unambiguously detected include S106 (11), which presents clear evidence for rotation, and Orion (12), in which expansion seems present. None of these objects are in the same evolutionnary stage as W3(OH). Clearly more observational data about disks around ultracompact HII regions is required. The case of W3(OH) shows that a single observed line is far from being sufficient to draw a coherent picture of an object, and the variety of behaviours, that a single object may be misleading. However, with the present data, although a correlation

between disks and flows seems present, the apparent densities of the detected disks, and their masses in consequence, are at least a factor ten lower than predicted by the models. Finally, these disks should not be confused with the more massive rotating cores detected in objects such as K3-50 or G10.6-0.4 which seem to surround the most compact HII regions (13).

5. References

1 Pudritz R.E. 1985, Astrophys. J. 293 216

2 Turner B.E. and Matthews H.E. 1984, Astrophys. J. 277 164

3 Dreher J.W. and Welch W.J. 1981, Astrophys. J. 245 857

4 Yorke H.W. and Krügel E. 1977, Astron. Astrophys. 54 183

5 Forveille T., Guilloteau S., Lucas R. and Winnberg A. 1986, in preparation

6 Garay G., Reid M.J. and Moran J.M. 1985, Astrophys. J. 289 681

7 Guilloteau S., Stier M.T. and Downes D. 1983, Astron. Astrophys. 126 10

8 Guilloteau S. Baudry A. and Walmsley C.M. 1985, Astron. Astrophys. 153 179

9 Dickel H.R., Lubenow A.F., Goss W.M. and Rots A.H. 1984, Astron. Astrophys. 135 107

10 Turner J.L. and Welch W.J. 1984, Astrophys. J. 287 L81

11 Bieging J.H. 1984, Astrophys. J. 286 591

12 Plambeck R.L., Wright M.C.H., Welch W.J., Bieging J.H., Baud B., Ho P.T.P. and Vogel S.N. 1982, Astrophys. J. 259 617

13 Vogel S.N. and Welch W.J. 1983, Astrophys. J. 269 568

MOLECULAR OUTFLOWS NEAR YOUNG STARS

F. Casoli, Ecole Normale Supérieure, 24 rue Lhomond, F-75005 Paris

Abstract : we present the general results of molecular observations of the bipolar flows around young stars, the physical parameters of the flows and their interpretation.

1. Introduction

Molecular flows have been discovered in the millimeter-wave rotation lines of the ^{12}CO molecule ; these lines have usually a width of 1 to 3 km/s ; but near young stellar objects, there is faint emission (from 0.1 to 5 K) at much higher velocities, that may be ten times the escape velocity from the central object (figure 1). If the velocity width at 0.1 K level is more than 10 km/s, one can suspect that a molecular flow is present. These flows are also detected in other molecules such as OH, HCO^+, NH_3. Outflow sources are found in star-forming regions, near infrared sources, H_2O masers, Herbig-Haro objects, and T Tauri stars (1)(2). Up to now, about one hundred of these objects have been recognized.

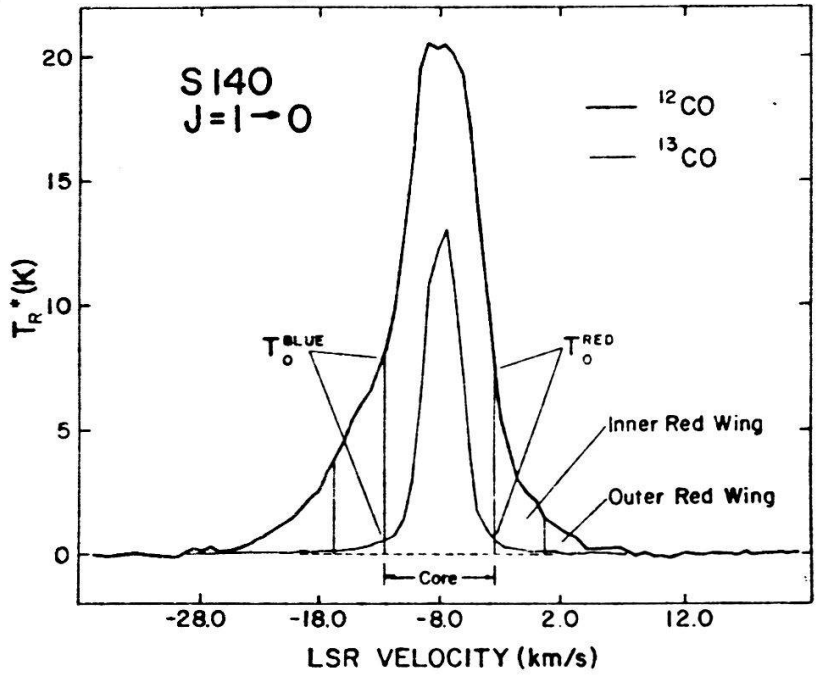

Figure 1 : example of a ^{12}CO spectrum with high-velocity wings (from (1))

2. Why outflows?

Because of the large velocities involved, rotation or collapse can be ruled out.

On the other hand, the proper motions of the H-H objects and of the H_2O masers, the presence of optical jets and the frequent bipolar morphology of the flows (figure 2), support strongly the idea of an outflow.

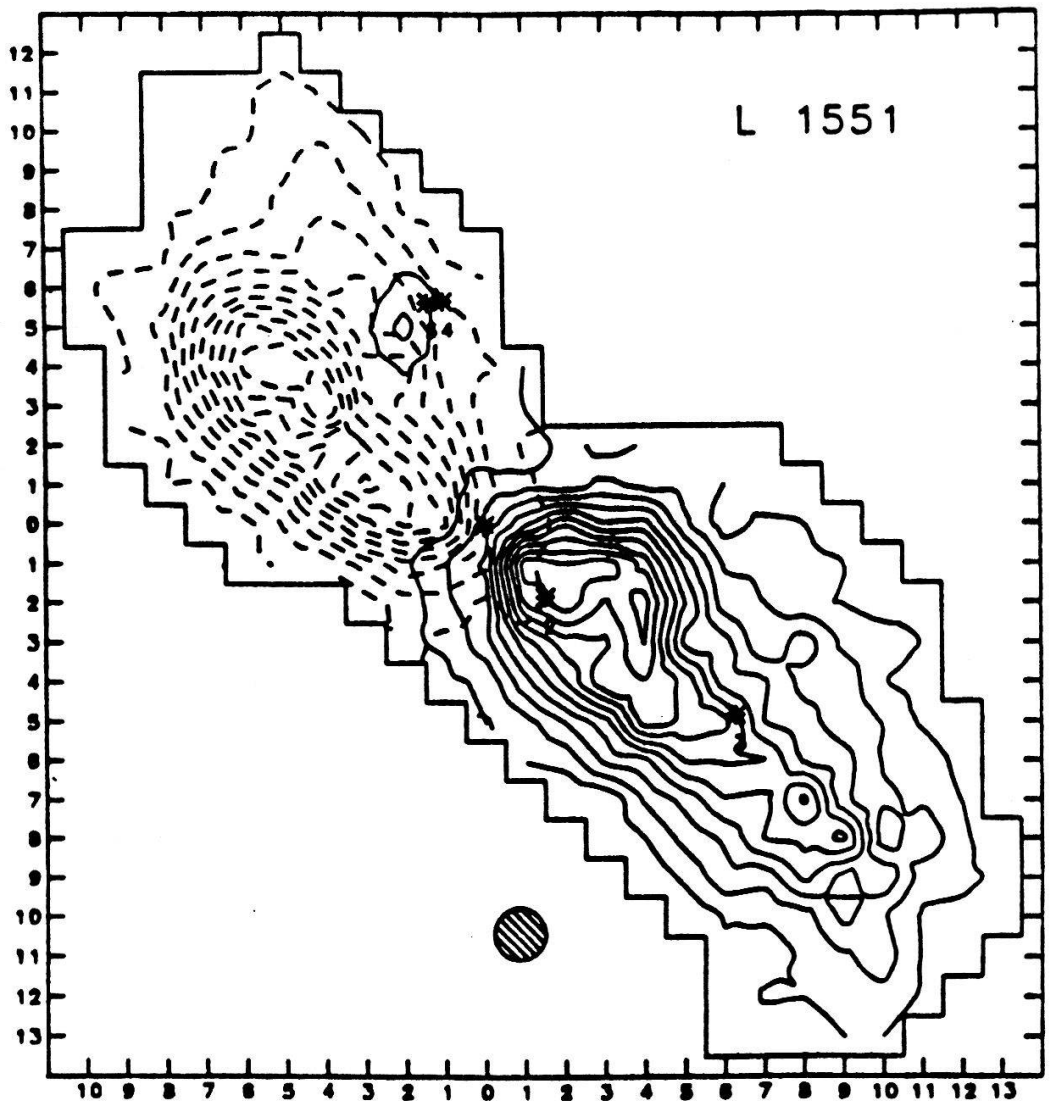

Figure 2 : bipolar morphology of the redshifted (broken lines) and the blueshifted (solid lines) molecular gas near L1551 (center of the map). From (2).

3. Physical parameters

Molecular mapping reveals that there is a wide variety among molecular outflows, especially for their morpholgies (figure 3), the luminosity of the central star (from 10 to 10^5 L_o), the collimation factor (from 1 to 6, but dilution may be dominant), their sizes...

From the ^{12}CO(1-0) maps, and, in the best cases, ^{13}CO(1-0) observations, one can deduce the physical characteristics of the flow. Some of them are given in Table

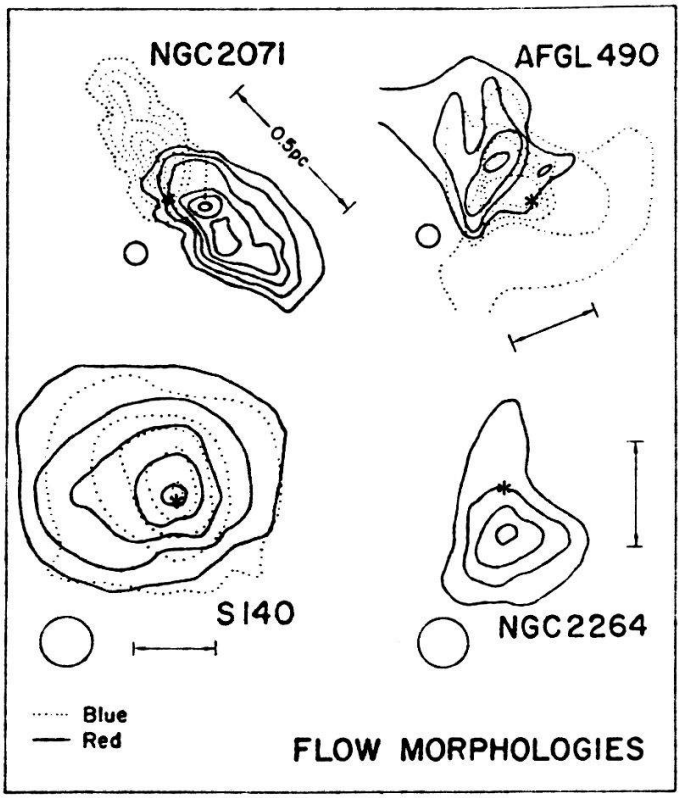

Figure 3 : flow morphologies : bipolar, multipolar, isotropic, unipolar. From (1).

1. Although the uncertainties are very large, the important point is that it is a very energetic phenomenon : the energies involved range from 10^{43} to 10^{47} ergs ; the H_2 masses may be large. It is then likely that these outflows play an important role in the dynamics of the parent molecular cloud (3).

Besides, there is a general correlation between the flow and the central star luminosities ; the energy in radiation is sufficient to drive the flow but the total momentum in photons is much lower than the flow momentum ($\dot{M}V \gg L_*/c$).

4. Interpretation

There are some important observational results that must be taken into account by the models : high-resolution maps show that the emitting molecular gas is located in a hollow shell of cold gas ($T_{ex} < 20$ K), with 2.2 μm emission of shocked H_2 at the outer edges ; besides, most central sources exhibit radio continuum emission, with a spectrum compatible with that of an ionized stellar wind. The

picture that emerges is then of a shell of swept molecular gas, filled with very hot gas due to the interaction of the stellar wind with the ambient medium. The collimation mechanism is still unclear : dense disks perpendicular to the outflow axis have been observed in CS and NH_3, of size 0.1 pc ; but there is some evidence of collimation at 100 a.u. distance of the central star, from optical and radio observations (4)(5).

A lot of models have been proposed, some purely hydrodynamical(6), some involving magnetic fields(7). Most of these models need a massive central object, and large accretion/outflow rates ; however, we know that objects like L1551-IRS5,with $L < 40\ L_\odot$ develop beautiful outflows.

5. Conclusion

Clearly, more observations are needed in order to obtain reliable statistics. One would like to know if every young star undergoes an outflow phase, its duration, and if stars below 1 $M_\odot$ also develop outflows ; in this case, outflows could be the dominant source of mechanical energy for molecular clouds. New outflow sources can be found among cold infrared sources ; during a ^{12}CO survey of 100 cold IRAS sources with a dust temperature below 50 K, we have found with the Bordeaux telescope that at least 15% showed outflows(8).

6. References

(1)Lada C.J., Ann. Rev. Astron. Astrophys. 23, 267 (1985)

(2)Levreault R.M., Ph. D. Thesis, The University of Texas at Austin (1985)

(3)Norman C., Silk J., Astrophys. J. 238, 158 (1980)

(4)Mundt R. in : Protostars and Planets II (1986)

(5)Bieging J., Cohen M., Schwartz P.R., Astrophys. J. 282, 699 (1984)

(6)Torbett M.V., Astrophys. J. 278, 378 (1984)

(7)Pudritz R.E., Norman C.A., Astrophys. J. 274, 677 (1983)

(8)Casoli F., Combes F., Dupraz Ch., Gerin M., Boulanger F., submitted to Astron. Astrophys. (1986).

Table 1 : range of the physical parameters of the observed outflows

Mass $M_\odot$	Velocity km/s	Size pc	Age yr	Luminosity $L_\odot$	Energy ergs	$\dot{M}V$ $M_\odot$ km/s/yr
.1-100	8-127	0.04-2	$3\,10^3$-10^5	1-10^5	10^{43}-10^{47}	$3\,10^{-5}$-0.5

Rapid time variations of interstellar maser features due to stimulated backscattering

Carlos Montes, GRECO-C.N.R.S. "Interaction Laser-Matière", Laboratoire de Physique de la Matière Condensée, Parc Valrose, 06054 NICE, and Observatoire de Nice, BP 139, 06003 NICE, France

Abstract : Compact interstellar sources of maser emission may show strong variability of flux intensity with time. We suggest that stimulated scattering, namely stimulated ion-Compton or Brillouin scattering, of the superradiant radiation through dense circumstellar plasma clouds could be a candidate mechanism for explaining rapid time dependent behaviours.

1. Introduction

H_2O vapor maser sources with wavelength $\lambda = 1.35cm$ ($\nu_0 = 22.235Ghz$), corresponding to the $6_{16} \rightarrow 5_{23}$ transition, seen in the vicinity of H II galactic regions are probably emitted in dense, hot (10^2 to $10^3 K$) shells or disks around massive stars in the later stages of their formation [1]. They present typical scales of intensity variations ranging from several months to few days [2]-[5]. Variation of the pumping mechanism due to variable radiative energy input or modification of the maser emission region may be responsible for the observed time dependent behaviour. We suggest an independent mechanism, namely stimulated ion-Compton or Brillouin backscattering, for explaining rapid time variations of H_2O maser features. In this case the evolution is determined by the propagation of the superradiant radiation through dense circumstellar plasma shells and is independent of the time variation of the maser sources itself. This follows a previous work where stimulated Compton scattering was proposed as a saturation mechanism for the maser emission giving rise to *photon soliton* production and time dependent relaxation oscillations [6]. For situations of moving expanding plasma shells at about the sound velocity, we also propose here a feed-back effect giving rise to multiple stimulated scattering and even to stochastic output flux intensities.

2. Counterstreaming stimulated Compton equations

A superradiant electromagnetic beam of very large photon occupation number $N(\nu\Omega, x, t)$, related to the spectral intensity $I(\nu\Omega, x, t)$ by

$$N(\nu\Omega, x, t)d\nu d\Omega = [c^2 I(\nu\Omega, x, t)/2h\nu^3]d\nu d\Omega \tag{1}$$

where Ω is the unit vector in the photon direction and $d\Omega$ the beam solid angle element, may stimulate a backscattered electromagnetic beam when interacting through a ionized medium (plasma). For electron plasma densities $n_e > 4 \times 10^6 cm^{-3}$ stimulated ion - Compton scattering dominates over electron one [6] [7]. The stimulated counterstreaming propagation is governed by two nonlinear integrodifferential equations [6] [8] [9] :

$$(\partial_t \pm c\partial_x)N_\pm(\nu, x, t) = N_\pm(\nu, x, t) \int d\nu' \quad W(\nu, \nu')N_\mp(\nu', x, t) \tag{2}$$

where the plus and minus signs stand respectively for the forward and backward radiation directions, and where the interaction kernel is given by

$$W(\nu,\nu') = W_0[(\nu'-\nu)/\Delta\nu_{D_i}] \quad exp\{-[(\nu-\nu')/\Delta\nu_{D_i}]^2\}, \tag{3}$$

the transition probability W_0 being proportional to the Thomson scattering cross section $\sigma_T = (8\pi/3)(e^2/m_ec^2)^2$ and function of the electron and ion susceptibilities $\chi_{e,i}$ by means of

$$W_0 = \frac{3n_e\hbar c\sigma_T}{(2\pi)^3 k_B T_i} \frac{|\chi_e|^2}{|1+\chi_e+\chi_i|^2}\Omega_0 \tag{4}$$

where n_e is the electron density, T_i is the ion temperature, and $\Delta\nu_{D_i}$ the ion - Doppler width associated with backscattering

$$\Delta\nu_{D_i} = 2(2k_BT_i/m_ic^2)^{1/2}\nu_0. \tag{5}$$

If we assume the spectrum composed of narrow lines

$$N_+(\nu) \propto \sum_{j=1}^{n}\delta(\nu-\nu_{2j-1}); \qquad N_-(\nu) \propto \sum_{j=1}^{n}\delta(\nu-\nu_{2j}) \tag{6-7}$$

separated each one from the other by $\Delta\nu_{D_i}/\sqrt{2}$, equations (2) lead to the following 2n Volterra equations

$$(\partial_t + c\partial_x)I_{2j-1}(x,t) = I_{2j-1}(x,t)\left[I_{2j-2}(x,t) - I_{2j}(x,t)\right] \tag{8}$$

$$(\partial_t - c\partial_x)I_{2j}(x,t) = I_{2j}(x,t)\left[I_{2j-1}(x,t) - I_{2j+1}(x,t)\right] \tag{9}$$

where $2j-1$ in the l.h.s. of Eq. (8) stands for the forward travelling lines and $2j$ in the l.h.s. of Eq. (9) stands for the backward scattered lines. Eqs. (8)-(9) have been normalized to the backscatter growth rate (gain)

$$\gamma = 10^{-7}n_e\lambda^3\beta_i[I_1/(1W/cm^2)]/[T_i/(1eV)] \tag{10}$$

where $\beta_i = |\chi_e|^2/|1+\chi_e+\chi_i|^2 \simeq (\nu_p/\Delta\nu_{D_e})[(T_i/T_e)^{1/2} + (T_e/T_i)^{1/2}]^{-1}$ for the low electron density case $[\nu_p = (n_ee^2/m_e\varepsilon_0)^{1/2} < \Delta\nu_{D_e}]$ we consider [7] [8].

3. Stimulated modulation of the maser radiation

For typical strong H_2O maser features, as e.g. in W49, we have high brightness temperatures $T_b \simeq 10^{15}K$ and line narrowness of $\delta\nu/\nu_0 \simeq 10^{-5}$. If the maser radiation is beamed into angular apertures $\Omega_0 \simeq 10^{-4}rad^2$ we obtain a flux intensity leaving the maser source of $I_1 \simeq 10^{-3}W/cm^2$. Dense plasma clouds of density $n_e = 4\times10^6cm^{-3}$ and H^+ temperature $T_i = 0.1eV$ yield a gain $\gamma \simeq 10^{-4}s^{-1}$ and thus an interaction length $l = c/\gamma = 20a.u.$. Plasma shells of depths $L < 100a.u.$ situated in the vicinity of the maser sources and standing between them and the Earth observer are sufficient for stimulate the backscatter of the emitted radiation in such a way to strongly deplete the flux intensity.

We shall consider a feed-back effect due to partially reflecting boundaries [8]. We can put small reflectivities at the boundaries of the plasma shell by considering their density gradients. The x-dependent density profile $n_e(x)$ leads to the x-dependent refractive index $n_r(x) = kc/\omega$ through the dispersion relation for the electromagnetic waves $\omega^2(x) = \omega_p^2(x) + k^2c^2$, where $\omega = 2\pi\nu$ and $\omega_p = (n_e e^2/m_e\varepsilon_0)^{1/2}$ is the plasma frequency. The differential reflectivity $r(x)$ is proportional to the density gradient [10]. Numerical integration of Eqs. (2) for an homogeneous plasma shell where small partial reflectivities $(r_{in}, r_{out}) < 1$ determine the boundary values and for an inhomogeneous plasma shell with the self-consistent reflectivity $r(x)$ leads to the same qualitative results [8], namely steady or relaxation oscillations for the flux intensities of period τ near the photon flight time through the dense medium, i.e. $\tau \simeq 2L/c$. For $L = 100a.u.$ it corresponds to $\tau \simeq 1$ day . Such rapid variability of maser features has been monitored by Little, White and Riley [4] [11] in NGC1333, W49, and W51S maser sources.

Two kind of boundary conditions (at $x = 0$) for forward $I_+(x,t)$ and (at $x = L$) for backward $I_-(x,t)$ flux intensities can be considered.

a) motionless shell: we can write the boundary conditions

$$I_+(0,t) = I_{input} + rI_+(0, t - L/c); \qquad I_-(L,t) = rI_-(L, t - L/c) \tag{11}$$

where $r = r_{in}r_{out}$. Eqs. (8)-(9) for $j = 1$ yield a two-mode intensity model which is completely integrable [12]. We have perform a linear stability analysis around the stationary solutions [8] and we obtain regimes of self-oscillations like those of I. Bar-Joseph et al. [13] depending on r and on $Q = \gamma L/c$; e.g. for $Q = 10$ we obtain steady oscillations for $r = 10^{-4}$ and relaxation oscillations for $r = 10^{-3}$ of period $\tau \simeq 2L/c$.

b) shell moving away from the maser source at a speed near the sound velocity: the boundary conditions couple forward- and backward-photon occupation numbers:

$$N_+(\nu,0,t) = N(\nu)_{input} + r_{in}N_-(\nu,0,t) \qquad N_-(\nu,L,t) = r_{out}N_+(\nu,L,t) \tag{12}$$

or, for the intensity approximation model governed by Eqs. (8)-(9):

$$I_1(0,t) = I_{input} + r_{in}I_2(0,t); \quad I_{2j}(L,t) = r_{out}I_{2j-1}(L,t); \quad I_{2j+1}(0,t) = r_{in}I_{2j+2}(0,t) \tag{13}$$

This feed-back effect leads to damped oscillations when the evolution concerns only two intensity modes [8], but undamped self-oscillations set in for multiple backscattering $(j > 1)$ or for the complete spectral problem governed by Eqs.(2) above some critical values of r_{in} and r_{out}. **Fig. 1** shows the time dependent reflection $\mathbf{R} = I_-(0,t)/I_+(0,t)$ and transmission $\mathbf{Tr} = I_+(L,t)/I_+(0,t)$ coefficients obtained by solving Eqs. (2) with boundary conditions (12). **Figs.2** (1-4) show the instantaneous spatial distributions of the flux intensities $I_\pm(x,t)$ for times shown in **Fig.1**, and **Figs.3** (1-4) show the instantaneous radiation spectra $N_\pm(\nu,x,t)$ for times shown in **Fig.1**. For the multiple backscattering model governed by Eqs. (8)-(9) for 10 lines $(j = 5)$ and $r_{in} = r_{out} = 0.2$, **Fig. 4** shows the time dependent **R** and **Tr**. We may observe that the excitation of several lines leads to a stochastic behaviour which could modelize the random rapid variations of the observed maser features.

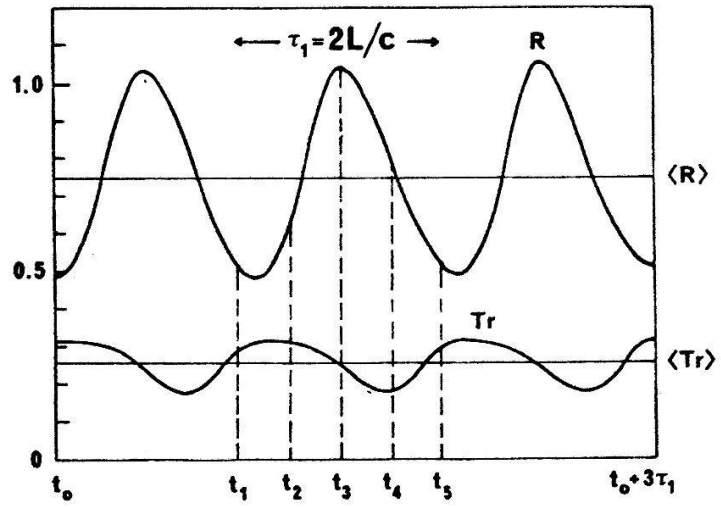

Fig. 1 *Steady self-oscillations of the reflection* **R** *and transmission* **Tr** *coefficients obtained from Eqs. (2) and boundary conditions (12) for* $r_{in} = r_{out} = 0.2$

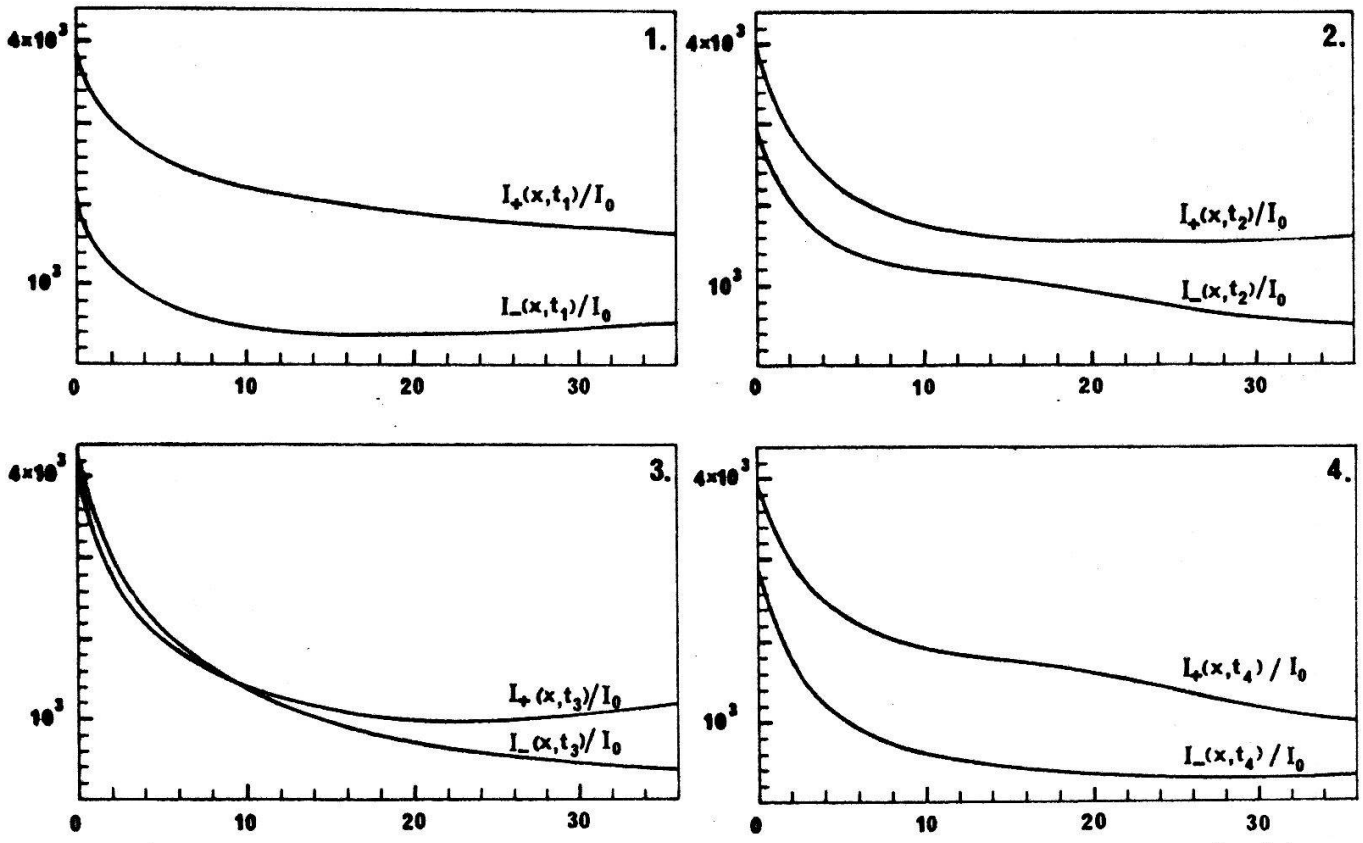

Fig. 2 *Instantaneous spatial distributions of the normalized flux intensities* $I_{\pm}(x,t)/I_0$ *for times shown in* **Fig.1**

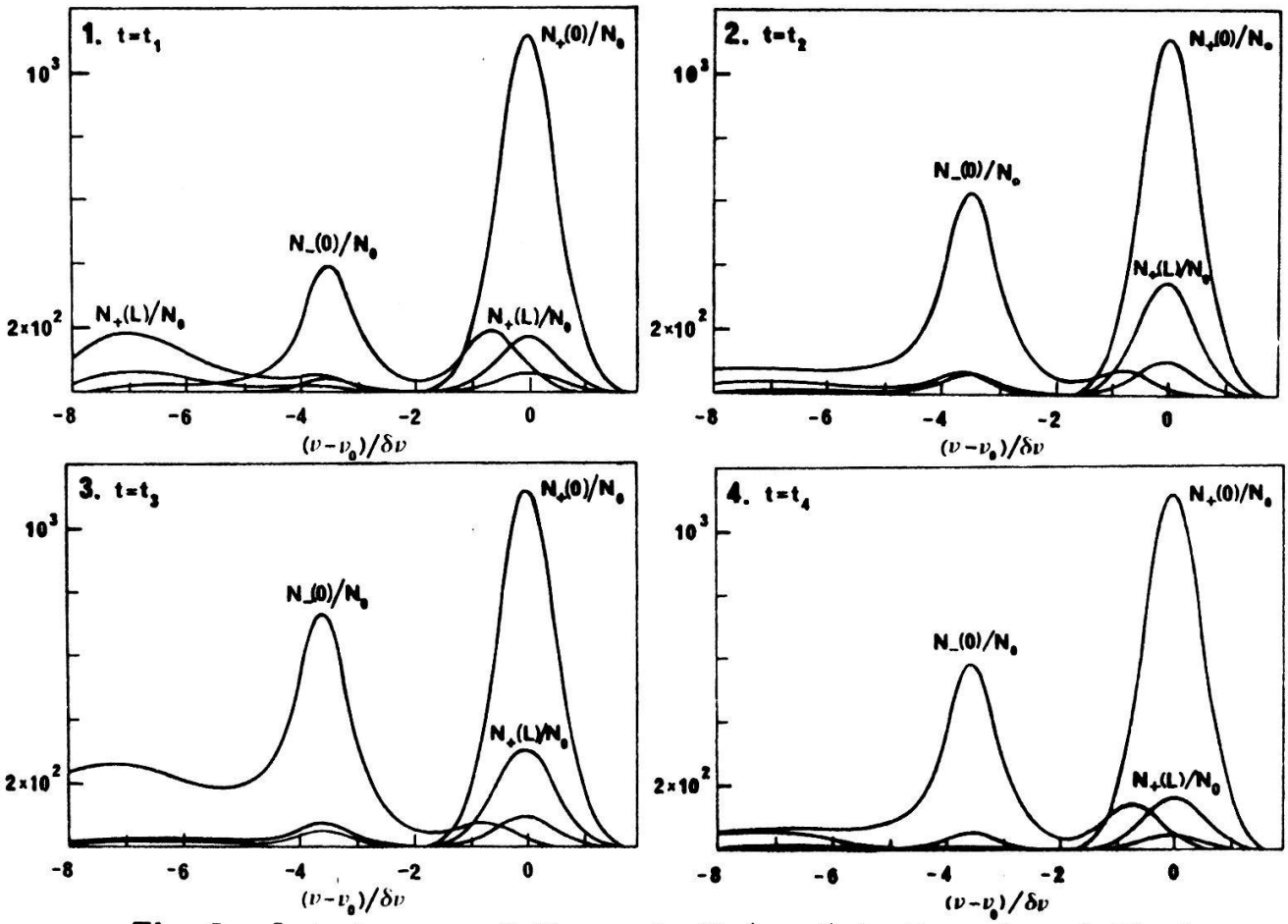

Fig. 3 *Instantaneous radiation spectra* $N_{\pm}(\nu, x, t)$ *for times shown in* **Fig.1**

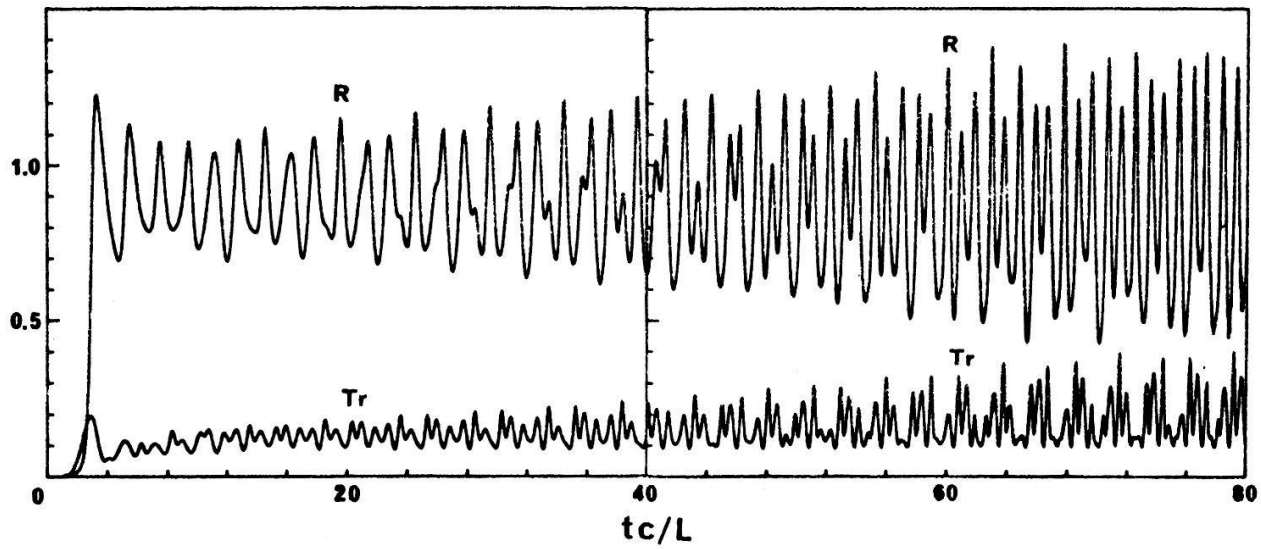

Fig. 4 *Time dependent* **R** *and* **Tr** *for the multiple backscattering model governed by Eqs. (8)-(9)*

4. References

[1] R. Genzel, D. Downes, Astron. Astrophys. Suppl. **30**, 145 (1977).
[2] W.T. Sullivan III, Astrophys. J. Suppl., **25**, 393 (1973).
[3] R.H. Gammon, Astron. Astrophys. **50**, 71 (1975).
[4] L.T. Little, G.J. White, P.W. Riley, Mon. Not. R. astr. Soc. **180**, 639 (1977).
[5] M.J. Reid, J.M. Moran, Ann. Rev. Astron. **19**, 231 (1981).
[6] C. Montes, Astrophys. J. **216**, 329 (1977).
[7] A.A. Galeev, R.A. Sunyaev, Soviet Phys. - JETP, **36**, 669 (1973).
[8] C. Montes, J. Peyraud, Proc. Soc. Photo-Opt. Instrum. Eng. **228**, 199 (1981).
[9] C. Montes, Phys. Rev. A, **31**, 2366 (1985).
[10] L. Landau, E.M. Lifshitz, *Electrodynamique des Milieux Continus*, Editions MIR, Moscou (1969), p. 356
[11] G.J. White, L.T. Little, Astrophys. Lett. **16**, 151, (1975).
[12] F. Chu, C. Karney, Phys. Fluids **20**, 1728 (1977).
[13] I. Bar-Joseph, A.A. Friesem, E. Lichtman, and R.G. Waarts, J. Opt. Soc. Am. B, **2**, 1606 (1985).

THE HIERARCHICAL STRUCTURE OF THE INTERSTELLAR MEDIUM

E. Falgarone: Observatoire de Paris-Meudon et Ecole Normale Supérieure.

La plus condensée des phases du milieu interstellaire est divisée en entités dites "nuages", tenues par leur propre champ de gravité. Certaines de leur propriétés (taille, fraction d'hydrogène sous forme moléculaire, abondance de molécules, dispersion de vitesses internes) sont remarquablement sensibles aux modifications de leur environnement. Ce sont les variations dans les paramètres de ces nuages qui dictent des conditions qui préludent au processes de formation d'étoiles, et jouent un rôle fondamental dans la distribution de masse des étoiles formées. Les observations dans le domaine millimétrique permettent aujourd'hui d'avoir accès à ces paramètres ainsi qu'à la structure du milieu interstellaire dans son ensemble. Sur plus de 4 décades en taille, les nuages forment une hiérarchie. Parmi les propriétés remarquables de cette structure citons: i) chaque échelle est en quasi équilibre du viriel et cependant à la limite de l'instabilité gravitationelle. ii) la matière est distribuée de façon à optimiser son irradiation en fonction du champ de rayonnement extérieur.

ASTRO III :

CURRENT IDEAS ON THE FORMATION OF MASSIVE STARS IN OUR GALAXY

D. Downes, Institut de Radioastronomie Millimétrique,
Domaine Universitaire, 38406 St. Martin d'Hères, France

According to current ideas, interstellar atomic hydrogen clouds contract to form molecular clouds. Further condensations form stable "cores", which contract to form protostars with flattened disks and outflows which eventually clear away enough material that the nuclear-burning object appears as a pre-main-sequence star. In this process, the critical hydrogen densities are:

10^2 cm^{-3}: Formation of molecular clouds from atomic gas; cloud contraction along galactic magnetic field lines.

10^4 cm^{-3}: Radiative coupling of gas and dust, leading to core-envelope structures and hydrostatic equilibrium in cores.

$>10^6$ cm^{-3}: Ion drift relative to neutrals, allowing further contraction

$>10^{11}$ cm^{-3}: Rapid loss of magnetic field, driving bi-polar outflows.

There are, roughly speaking, two types of clouds: warm, giant molecular clouds (GMC's), constituting the spiral arms of our Galaxy, and small, cold clouds, found throughout the galactic disk. The massive stars form in warm GMC's, while mainly low-mass stars form in small, cold clouds. The GMC's do not form by random coagulation of small clouds, but are presumably built up from the smaller clouds in the spiral density wave. The density-wave shocks do not compress the gas to form stars directly, but their pressure does induce the gas to form supercloud complexes. The formation rate of massive stars is thus higher in spiral arms than in the interarm region, probably in proportion to the amount of gas flowing through the spiral arms.

Once clouds have formed, further contraction is slowed by supersonic turbulence, rotation, winds, magnetic fields, and "gravito-turbulence". Of these mechanisms, it is generally agreed that unreplenished supersonic turbulence is ineffective in supporting clouds in the long term, as it decays on scales only a few times the gravitational free-fall time. Rotation is also unlikely as a support mechanism, as equilibrium rotation, balancing gravity, is not observed in most clouds. If stellar winds are to account for the internal kinetic energy of GMC's, that is, 1000 clouds x $(3\ \mathrm{km/s})^2$ x $10^5 M_\odot$ = 4 10^{50} erg, lasting 10^7 yr, the likely cloud lifetime, then conservation of momentum requires:

(no. of flows) x (Mv)/flow = (no. of clouds) x (M Δv)/cloud.

Hence for a star formation rate of 5 $M_\odot$/yr of stars of >1 $M_\odot$, and 5 10^7 flows over 10^7 yr in the Galaxy, one requires energies per flow of 10^{45} to 10^{46} erg, for flow velocities of 10 to 100 km/s, respectively. While the large molecular flows have up to 10^{47} erg, the average energy of the lower mass outflows is typically 10^{43} erg, so their winds may not be adequate for cloud support.

As for magnetic fields supporting cloud against collapse, current observations suggest constant magnetic field strengths of 10-20μGauss, for cloud densities 0.1 to 100 cm^{-3}, consistent with cloud contraction parallel to the local magnetic field lines for this density range. For the regime 10^2-10^4 cm^{-3}, the fields increase with density, although with large variations from cloud to cloud. Some low-density clouds with supersonic turbulence, and which are not gravitationally bound, appear to have high fields, while other, "dense" clouds have low fields. Calculations indicate that magnetic energy can dominate gravity for cloud masses $M > \sim 10^3\ M_\odot \frac{B}{30\mu G} (\frac{R}{2pc})^2$.

For B = 30μG and R = 20pc, the minimum cloud mass is 10^5 $M_\odot$.

The other possibility is that the clouds are supported by "gravito-turbulence": An ensemble of clouds with a gravitational correlation length, ℓ, can "emit" a gravity tide to a larger-scale ensemble with correlation length L. The smaller scale ensemble spins down, the larger-scale ensemble spins up. Simulation of three dimensional collapse shows development of long "tails", which transfer angular momentum outward. If the angular momentum transferred per unit time per unit volume is constant, then the internal velocity dispersion ΔV and mass M of the clouds are expected to scale as $\Delta V \sim L^{0.5}$ and $M(\text{cloud}) \sim \Delta V^4$. Observations of cloud condensations with no strong internal heat sources, agree with these predictions, and give:

$$\Delta V\ (km/s) = 0.8\ R_{pc}^{0.5} \text{ and } \Delta V\ (km/s) = 0.37\ (M/M_\odot)^{1/4}$$

Substituting the velocity of sound, v_s (km/s) = 0.2 (T/10 K)$^{1/2}$, one expects the minimum Jeans mass to be $M/M_\odot = 0.26\ (T/10\ K)^2$, leading to a minimum star mass of the order of 10^{-1} $M_\odot$ for typical cloud temperatures. This differs from the traditional view of opacity-limited fragmentation, which predicted a minimum Jeans mass of 0.01 $M_\odot$. The main change in viewpoint, due to modern data from molecular-line astronomy, is that the fundamental units in the hierarchy of collapse are recognised to be "cores" observed in molecular clouds. In a recent model by Falgarone and Puget, these condensations have a

core-halo structure, with the ambient far-IR field determining core temperature, and the external UV radiation determining halo extent and total mass. The critical density is 10^4 cm^{-3}, above which the gas and the dust are thermally coupled. The temperature of the core is 15-20 K, even if there is no internal heat source. The predicted core size is $\sim$ 0.05 to 0.1 pc, and the mass is a few solar masses.

One view of the formation of massive stars is that cores with subsonic internal motions collapse to form low-mass stars. Once low-mass star formation starts, more gas is attracted to the region, to form more massive cores. Under external influences (shocks induced by the accretion itself?, cloud-cloud collisions?), a massive core collapses to form the first massive star(s) in the region. These initial massive stars then produce further compressions by their outflows, HII regions, main-sequence winds, and supernovae. The process has runaway feedback, producing more and more massive stars.

An alternative view is that the spectrum of stellar masses simply follows the probability spectrum of cloud fragments. For a Miller-Scalo initial mass function, there are 500 stars of typical mass 0.6 $M_\odot$ for every OB star of typical mass 23 $M_\odot$. Hence by pure statistics, molecular clouds of 10^3 $M_\odot$ use up nearly all their mass in producing the low-mass part of the initial mass function. Only one such cloud in several hundred contains an O-type star, which are otherwise more likely found in giant molecular clouds. The classic observation by Herbig that massive stars form last in a cluster is then true only in a statistical sense, in that the probability of formation of low-mass stars is simply much higher than that of high-mass stars.

Regardless of these two approaches, either that additional physics is required to produce high-mass stars, after low-mass stars are formed, or that the result is purely statistical, most authors agree that once high-mass stars form, they heat their surroundings, and raise the minimum Jeans mass according to $M_J \sim T^{2+\delta}$, where $\delta>0$ and depends on grain properties. Formation of massive stars thus inhibits low-mass star formation. In the model of bi-modal star formation by Güsten and Mezger, the massive stars form mainly (but not exclusively) in the spiral arms of the Galaxy, where they inhibit formation of stars less massive than 3 $M_\odot$. Stars of all masses (0.1 to 60 $M_\odot$) form in the interarm regions.

The star formation rates are derived as follows. The observed production rate of Lyman continuum photons in a given region is proportional to the rate

of formation of massive stars in that region.

$$N_{Lyc} = K\ \psi_{OB} \qquad (1)$$

where N_{Lyc} is the Lyman continuum production rate, ψ_{OB} is the star formation rate for OB stars, and K is a constant: $K = \langle N/\tau\ M\rangle_{OB}$ where N, τ and M are the Lyman continuum rate, mean lifetime and mass for an average OB star, where the weighting is taken over an initial mass function (IMF). For the Miller-Scalo IMF, $K = 3.2\ 10^{53}$ (photons/sec) $(M_\odot/yr)^{-1}$. In the model by Güsten and Mezger, the star formation rate for massive stars is summed over interarm (ia) and spiral arm (sa) regions:

$$\psi_{OB} = \psi_{OB}^{ia} + \psi_{OB}^{sa} \qquad (2)$$

The star formation rate in spiral arms, at galactic radius R, is taken to be proportional to the amount of gas passing through the arms, namely $\psi^{sa}=\nu\psi^{ia}$, where ν is the difference between the rotational velocity Ω_R at galactic radius R and the spiral pattern speed, Ω_p, normalised to unity in the solar neighbourhood: $\nu = (\Omega_R-\Omega_p)/(\Omega_\odot-\Omega_p)$.

Hence,

$$\psi^{ia} = \frac{N_{Lyc}}{K}\ \frac{1}{1+\nu} \quad \text{and} \quad \psi_{OB}^{sa} = \frac{N_{Lyc}}{K}\ \frac{\nu}{1+\nu} \qquad (3)$$

Eq (3) yields star formation rates for massive stars (masses 10-60 $M_\odot$) from derived values of N_{Lyc}. Star formation rates for other stellar masses are obtained by scaling the values for OB stars by the corresponding areas under the initial mass function. There are three methods to derive star formation rates: discrete radio HII regions, the extended low-density thermal radio emission of the Galaxy and infrared radiation. In the third method, the infrared intensities from IRAS and from balloon observations are decomposed into contributions from various components. A component from 20 to 800μm comes from warm dust (30-40 K), heated by OB stars. The Lyman continuum rate is derived from the Far-IR flux of this component.

These three methods give consistent star formation rates. The results (Fig. 1) show that while most massive stars form in spiral arms, a significant number of them form in the interarm regions. For all stars, the interarm production rate dominates in the outer parts of the galaxy, but the interarm and spiral arm production rates are comparable for galactic radii <5 kpc. The total star formation rate over galactic radii 2 to 10 kpc, for all stars, spiral arm and interarm, is 5.3 $M_\odot$/yr.

Obviously the model of bi-modal star formation is only a global des-

cription of what is happening in the Galaxy, as the inital mass function may vary from star cluster to cluster, and with galactic age as well. It is nevertheless encouraging that a relatively simple model explains a number of results. For example, since oxygen is produced only by massive stars, its abundance in the Galaxy should vary with the relative proportions of the spiral arm and interarm production rates. In fact the model for bi-modal star formation is in good agreement with the observed gradients of $^{16}O/H$, He/H, $^{12}C/^{13}C$ and $^{18}O/^{17}O$ as a function of galactic radius. The model also removes the earlier inconsistency between derived star formation rates and the observed mass distribution in the galactic disk. The mass distribution of the Galaxy is determined by the component permanently locked up in stars (hence by the low-mass, interarm mode of star formation) and in remnants, while the recycling and enrichment of the interstellar matter is determined by the high-mass, spiral-arm mode of star formation. The model can also account for the unseen mass in the solar neighbourhood (as remnants of massive stars), age-metallicity relations, and the colours of the bluest galaxies, which are dominated by the high-mass mode. A further inference is that young spiral galaxies must have been much more luminous than present-day ones, producing almost exclusively massive stars.

Bibliography

Citations to original work may be found in an expanded version of this paper, in 1986 "Star Forming Regions", IAU Symp. 115, eds. M. Peimbert and J. Jugaku, Reidel, in press. Other general references on this topic are:

Appenzeller, I., 1982, Fund. Cosmic Phys. 7, 313

Güsten, R., Mezger, P.G., 1983, Vistas in Astron. 26, 159

Turner, B., 1984, Vistas in Astron. 27, 303

"Protostars and Planets II" (1985), eds. D. Black and M.S. Matthews, Tucson, Univ. Arizona Press

"Naissance et Enfance des Etoiles" (1985), eds. R. Lucas, A. Omont, R. Stora, North Holland, Amsterdam

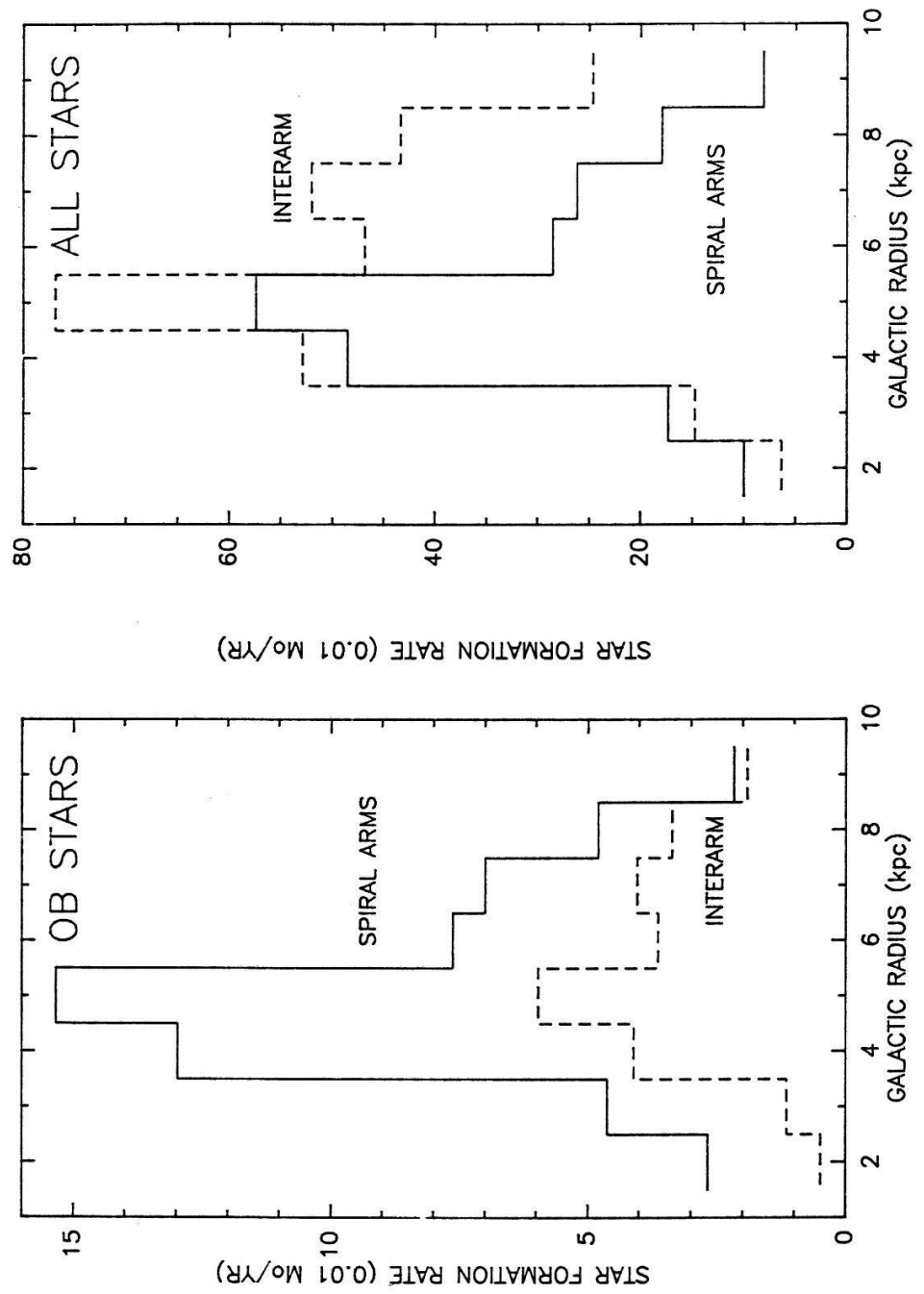

Fig. 1 Rate of star formation in an annulus $2\pi R\Delta R$, where ΔR = 1 kpc, vs. galactic radius. The rates have been calculated from the Lyman continuum rates, and the formulae of Güsten and Mezger (1983), for a Miller-Scalo IMF.
Left side: star formation rates of massive stars (10-60 $M_\odot$)
Right side: all stars (3-60 $M_\odot$ in spiral arms, 0.1 to 60 $M_\odot$ in interarm regions)

THE STABILITY OF DENSE MOLECULAR CONDENSATIONS

Jean-Pierre Chièze

Commissariat à l'Energie Atomique

Centre d'Etudes de Bruyères-le-Châtel

B.P. 12, F-91680 Bruyères-le-Châtel

We examine the gravitational stability of small dense condensations which are observed in molecular clouds. These dense cores are likely to be stellar birth places [1]. Their stability critically depends upon the *ambient* conditions, namely the interclump gas pressure and the local intensity of the UV field.

The equation of state.

The gas temperature is determined at each point of a cloud assuming thermal equilibrium. The major heating processes included in the model are:

(i) photoelectric effect on dust grains,

(ii) photoionization of the carbon,

(iii) photodissociation of H_2 molecules,

(iv) low energy cosmic ray heating.

The dominant cooling processes are:

(i) collisional excitation of the fine structure transitions within the ground terms of C^+, CI and OI,

(ii) excitation of rotational transitions of CO, H_2O, O_2, etc... .

In addition, we have included the heat exchanges between the gas and dust grains, assumed to be at a constant temperature $T \approx 15K$. These rates are mainly taken in [2] and[3]. They are expressed in terms of the total proton density, n_H and of the local visual extinction A_v. Assuming chemical equilibrium between species, the gas equation of state is of the form :

$$P = P(n_H, Av) \qquad (1)$$

(see figure 1).

Equilibrium configurations

The hydrostatic equation is solved in spherical geometry. According to Equ.(1), we have:

$$\frac{1}{r^2}\frac{d}{dr}\frac{r^2}{\rho}\left[\left(\frac{\partial P}{\partial \rho}\right)_{Av}\frac{d\rho}{dr}+\left(\frac{\partial P}{\partial Av}\right)_{\rho}\frac{dAv}{dr}\right]=-4\pi G\rho \tag{2}$$

$$Av(r)=const.\int_r^{R_s}\rho(r')dr' \;+\; Av_0 \tag{3}$$

where R_s is the radius of the clump and A_v the visual extinction in the ambient medium. The boundary conditions to be fullfilled are:

(i) at the center $(dP/dr)_{r=0}=0$

(ii) at the surface $P(r=R_s)=P_0,\ Av(r=R_s)=Av_0$.

For each set of ambient conditions (ii), their is an infinity of solutions depending, for example, upon the central density.

Clumps models

The central density range we have explored is $5\ 10^2 \leq n_H \leq 10^7 cm^{-3}$. The structures of clumps with the same central density, n_{Hc}, but different central extinctions, Av_c, are similar in particular in the central parts and for $n_{Hc} \geq 10^5 cm^{-3}$, since the equation of state weakly depends upon Av at high density. In the core-envelope transition region, the mass-radius relation is *approximatively*:

$$\frac{M}{1M_\odot}\sim 100\left(\frac{n_{Hc}}{10^5 cm^{-3}}\right)^{1/2}\left(\frac{R}{1pc}\right)^2 \tag{4}$$

In the envelopes the density profile is $\rho(r)\propto r^{-1/4}$.

On larger scales $(R\geq 0.3pc)$ the structure of the envelopes are independant of the core parameters. For massive clumps $(M\geq 5M_\odot)$, the mass-radius relation converges towards:

$$\frac{M}{1M_\odot}\sim 20\left(\frac{R}{1pc}\right)^{1.5} \tag{5}$$

An important feature of the models is that equilibrium structures have a maximum mass of about $500M_\odot$. This is mainly due to the rapid occurence of *thermal* instability in the envelopes, when the temperature reaches the critical value $T\approx 90-100K$. This maximum mass should be taken cautiously, since *large scale* structures may be mainly sustained by turbulence.

Gravitational stability

In order to examine the stability of the self-gravitating equilibrium structures, we have determined the normal modes of each models linearizing the hydrodynamical equations in discretized form. The normal modes are calculated as the eigenvectors of a real matrix. A mode is unstable if its associated eigenvalue has a positive real part.

We have reported on figure 1 the total mass and the surface pressure of different structures with central densities $n_{Hc} = 10^3,\ 10^4,\ 10^5,\ 10^6\ cm^{-3}$. Each vertical section corresponds to a given value of the ambient optical extinction. The dashed lines represent the gravitational instability threshold. They define a surface in the (M, P_0, Av_0) space which delimits the stability domain for spherical condensations. Representative points above this surface correspond to unstable configurations.

High mass protostellar condensations ($M \leq 100 M_\odot$) are found in low pressure and low extinction regions (i.e. periphery of molecular complexes). Deep inside a cloud, the maximum stable mass is $M_* \leq 1 M_\odot$. This is in favour of low mass star formation in dense cores [1].

This work has been made in collaboration with G. Pineau des Forêts, DAPHE, Observatoire de Paris, Meudon.

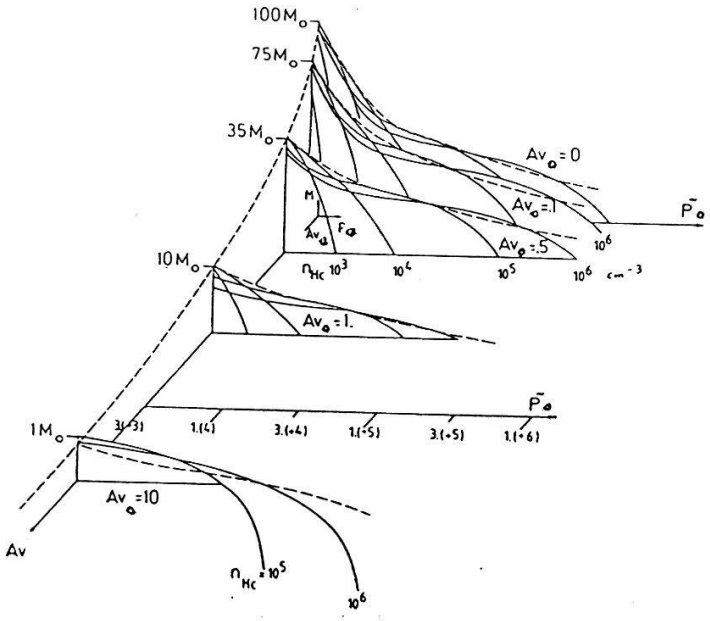

Figure 1. The stability domain of molecular cores in the (M, P_0, Av_0) space.

References

[1] Benson, P.J., Myers, P.C., Wright, E.L. : 1984, Astrophys. J. 279, L27.

[2] Falgarone, E., Puget, J.L. : 1985, Astron. Astrophys. 142, 157

[3] de Jong, T., Dalgarno, A., Boland, W. : 1980, Astron. Astrophys. 91, 68.

POSTER

COSMIC RAY PHYSICS AND NEUTRINO ASTROPHYSICS WITH DUMAND

P.K.F. Grieder
Physikalisches Institut, Sidlerstrasse 5, 3012 Bern

The scientific aims of the DUMAND (Deep Underwater Muon And Neutrino Detector) project are briefly reviewed. The principle of operation of the system is illustrated, relevant site, background and environmental aspects are pointed out, and a brief account of the current stage 1 activities is presented. These include besides the now completed construction of a short prototype string of detectors (SPS) with the necessary control, data link and handling equipment also deployment and operation of the SPS at the final DUMAND site and depth, to demonstrate the capabilities of the system and its technique. A brief account of the current project status is given.

PHYSIQUE NUCLEAIRE ET CORPUSCULAIRE
KETE I :

COMPLETE DETERMINATION OF THE MUON DECAY INTERACTION AND COMPARISON WITH THE STANDARD MODEL

W. Fetscher, H.-J. Gerber and K.F. Johnson
Institut für Mittelenergiephysik, ETH Zürich, CH-5234 Villigen, Switzerland

Muon decay, as a purely leptonic reaction, is especially well suited to determine the structure of the charged weak interaction. Until recently, however, only analyses including semileptonic data or with a restricted amount of parameters have been performed.

We present the complete analysis using only leptonic data based on a method described in more detail in ref. [1]. The standard model is taken as a basis, and we look for deviations from it. Although only eleven independent experiments have been performed, it will be shown that existing measurements determine completely all nineteen parameters of the interaction, and upper limits for all possible couplings different from V-A will be given.

The decay of the muon $\mu \to e\bar{\nu}_e\nu_\mu$ can be described by the most general, local, derivative-free lepton number conserving four-fermion interaction hamiltonian [2]. It contains ten complex coupling constants and therefore, neglecting an arbitrary common phase, 19 independent parameters. We will use the "helicity projection form" [3,4,5] (abbreviated HPF) to analyze the experimental results. This form uses fields of definite handedness. "V-A", the charged current interaction adopted by the standard model, is taken as a basis, from which deviations are looked for.

Our matrix element is given by

$$M \sim \sum_{\substack{\gamma = S,V,T \\ \varepsilon,\mu = L,R \\ (n,m)}} g^{\gamma}_{\varepsilon\mu} \langle \bar{e}_\varepsilon | \Gamma^\gamma | (\nu_e)_n \rangle \langle (\bar{\nu}_\mu)_m | \Gamma_\gamma | \mu_\mu \rangle \qquad (1)$$

γ labels the type of interaction: Γ^S, Γ^V, Γ^T (scalar-pseudoscalar, vector-axialvector, tensor). The indices ε and μ indicate the chiral projections (left-handed, right-handed) of the spinors of the experimentally observed particles, $\varepsilon \hat{=}$ electron, $\mu \hat{=}$ muon. n indicates the helicity of the electron antineutrino, m that of the muon neutrino. n and m are uniquely determined for given γ,ε,μ.

The decay rate determines the strength of the interaction. The $g^{\gamma}_{\varepsilon\mu}$ are normalized by setting

$$A \equiv 4(|g^S_{RR}|^2 + |g^S_{LR}|^2 + |g^S_{RL}|^2 + |g^S_{LL}|^2)$$
$$+ 16(|g^V_{RR}|^2 + |g^V_{LR}|^2 + |g^V_{RL}|^2 + |g^V_{LL}|^2)$$
$$+ 48(|g^T_{LR}|^2 + |g^T_{RL}|^2) = 16$$

"V-A" corresponds to $g^V_{LL} = 1$ and all other $g^\gamma_{\varepsilon\mu} = 0$. From the $g^\gamma_{\varepsilon\mu}$ we can define the four quantities $Q_{\varepsilon\mu}$:

$$Q_{RR} \equiv |g^S_{RR}|^2/4 + |g^V_{RR}|^2$$
$$Q_{LR} \equiv |g^S_{LR}|^2/4 + |g^V_{LR}|^2 + 3|g^T_{LR}|^2$$
$$Q_{RL} \equiv |g^S_{RL}|^2/4 + |g^V_{RL}|^2 + 3|g^T_{RL}|^2$$
$$Q_{LL} \equiv |g^S_{LL}|^2/4 + |g^V_{LL}|^2$$

We note: $0 \leq Q_{\varepsilon\mu} \leq 1$ and $\Sigma\, Q_{\varepsilon\mu} = 1$. A $Q_{\varepsilon\mu}$ is thus the probability for a transition from a muon of handedness μ to an electron of handedness ε.

Numerical values for the $Q_{\varepsilon\mu}$ can be derived from existing measurements on μ decay:

$$Q_{RR} = 2(b+b')/A,$$
$$Q_{LR} = \{(a-a') + 6(c-c')\}/(2A),$$
$$Q_{RL} = \{(a+a') + 6(c+c')\}/(2a),$$
$$Q_{LL} = 2(b-b')/A.$$

The values of the $Q_{\varepsilon\mu}$ were determined from normal muon decay as described in refs. [1,6], where also the references for the experimental data are given. We find upper limits for Q_{RR}, Q_{LR} and Q_{RL} and thereby upper limits for the absolute values of eight coupling constants $g^\gamma_{\varepsilon\mu}$, as given in Table 1. Since Q_{LL} is bounded by a lower limit, it is not possible to deduce an upper limit for $|g^S_{LL}|$. In fact, data from normal muon decay do not tell us, if

$$g^S_{LL} = 0, \quad g^V_{LL} = 1 \quad \text{(V-A)} \quad \text{or}$$
$$g^S_{LL} = 2, \quad g^V_{LL} = 0 \quad !$$

This ambiguity, however, is resolved by the data from inverse muon decay:

$$\nu_\mu + e^- \rightarrow \mu^- + \nu_e$$

The total rate S, normalized to the rate predicted by V-A, has been measured as

$$S = 0.98 \pm 0.12 \quad [7]$$

Table 1. Complete set of coupling constants $g^{\gamma}_{\varepsilon\mu}$ of the muon decay interaction determined from experiments without model assumptions. The "standard model" sets $g^{V}_{LL}=1$, all others to zero. An additional "V+A interaction" is represented by g^{V}_{RR}. The $Q_{\varepsilon\mu}$ are the relative rates. 68 (90%) C.L. is given.

Handedness of electron (ε) and muon (μ) $\varepsilon\mu$	Relative abundance $10^3 \times Q_{\varepsilon\mu}$	Type of interaction γ	Handedness of ν_μ(m) and $\bar{\nu}_e$(n) mn	Coupling constant $10^3 \lvert g^{\gamma}_{\varepsilon\mu} \rvert$	Main input
RR	<1.4(2.0)	S	LR	<74(91)	$\xi\delta/\rho$
		V	RL	<37(45)	
LR	<2.7(3.9)	S	LL	<116(137)	
		V	RR	<52(62)	$\xi\delta/\rho$, ρ, δ
		T	LL	<34(40)	
RL	< 36(45)	S	RR	<378(448)	
		V	LL	< 97(114)	$P_L(\xi')$
		T	RR	< 95(112)	
LL	>960(949)	S	RL	<743(961)	S, h_{ν_μ}
		V	LR	>928(877)	Q_{RR}, Q_{LR}, Q_{RL}

The influence of eight of the $g^{\gamma}_{\varepsilon/\mu}$ on S is found to be negligible. Thus

$$S \approx |g^{V}_{LL}|^2(1-\varepsilon) + (3/64)\ |g^{S}_{LL}|^2\varepsilon,$$

where $\varepsilon = h - (-1)$ is the deviation of the helicity of the muon neutrino from -1. The absolute value of ε is known very precisely: $|\varepsilon| < 4.1 \times 10^{-3}$ [8]; the sign of ε has been determined for ν_μ and $\bar{\nu}_\mu$ [9,10].

We finally obtain

$$|g^{V}_{LL}| \approx S \quad \text{and} \quad |g^{S}_{LL}|^2 \leq 4(1-S).$$

In summary, we have completely determined the weak interaction in muon decay from existing experiments. Present experimental errors, however, still allow substantial contributions from interactions other than V-A.

References

[1] W. Fetscher, H.-J. Gerber and K.F. Johnson, Phys. Lett. 173B (1986) Mai 29.
[2] L. Michel, Proc. Phys. Soc. A63 (1950) 514.
[3] F. Scheck, Leptons, Hadrons and Nuclei, North-Holland, Amsterdam (1983).
[4] K. Mursula and F. Scheck, Nucl. Phys. B253 (1985) 189.
[5] Review of Particle Properties, Rev. Mod. Phys. April 1986 (to be published).
[6] H. Burkard, F. Corriveau, J. Egger, W. Fetscher, H.-J. Gerber, K.F. Johnson, H. Kaspar, H.J. Mahler, M. Salzmann and F. Scheck, Phys. Lett. 160B (1985) 343.
[7] F. Bergsma et al., Phys. Lett. 122B (1983) 465.
[8] W. Fetscher, Phys. Lett. 140B (1984) 117.
[9] L.Ph. Roesch et al., Helv. Phys. Acta 55 (1982) 74.
[10] A.I. Alikhanov et al., JETP 11 (1960) 1380;
G. Backenstoss et al., Phys. Rev. Lett. 6 (1961) 415;
M. Bardon et al., Phys. Rev. Lett. 7 (1961) 23;
A. Possoz et al., Phys. Lett. 70B (1977) 265;
R. Abela et al., Nucl. Phys. A39 (1983) 413.

PRECISION MEASUREMENT OF THE MASS DIFFERENCE $m_{\pi^-} - m_{\pi^0}$

J.F. CRAWFORD*, M. DAUM*, R. FROSCH*, B. JOST*, P.-R. KETTLE*, R.M. MARSHALL**, B. WRIGHT**, and K.O.H. ZIOCK**

* SIN, CH-5234 Villigen, Switzerland.
**Physics Department, University of Virginia, Charlottesville, VA22901, USA.

Using the time-of-flight method to determine the velocity of the neutrons from the charge exchange reaction $\pi^- + p \longrightarrow \pi^0 + n$ of negatively charged pions stopped in liquid hydrogen, we have measured the mass difference $m_{\pi^-} - m_{\pi^0}$ to be (4.5930 ± 0.0013) MeV/c^2 . From a study of the measured neutron time-of-flight spread we also obtain a value for the mean kinetic energy $\bar{T}_{\pi p}$ of the pionic hydrogen atoms at the time of the charge exchange reaction, which will be reported at the conference.

Neue Präzisionsmessung der π^--Masse

B. Jeckelmann[1], W. Beer[2], G. de Chambrier[2], O. Elsenhans[2], K.L. Giovanetti[2], P.F.A. Goudsmit[2], H.J. Leisi[2], T. Nakada[1], O. Piller[3] und W. Schwitz[3]

1) Physikinstitut, Pérolles, 1700 Fribourg
2) Institut für Mittelenergiephysik der ETH-Z, c/o SIN, 5234 Villigen
3) Eidg. Amt für Messwesen, 3084 Wabern

Mit Hilfe des π-Kristallspektrometers am SIN haben wir die Wellenlänge des 4f-3d Röntgenüberganges in $\pi^-{}^{24}Mg$ gemessen und daraus das π^-/e^- Massenverhältnis mit einer Genauigkeit von 2.6 ppm bestimmt. Dank der extrem hohen Energieauflösung (0.75 eV bei 26 keV) war es erstmals möglich, - aus einer Analyse der Linienform - direkt die benötigte Information über die Besetzung der Elektronenzustände während des Pi-Ueberganges zu bekommen. Die Korrektur für die Elektronen-Abschirmung konnte so sehr genau vorgenommen werden.

Zur Modulation der solaren kosmischen Strahlung durch interplanetare Schocks

H. Neuenschwander, H. Debrunner und E. Flückiger
Physikalisches Institut, Sidlerstrasse 5, 3012 Bern

Die Ionenkomponente der bei starken Sonneneruptionen erzeugten solaren kosmischen Strahlung erfährt bei der Ausbreitung in den interplanetaren Raum in Gebieten starker örtlicher Aenderungen des interplanetaren Magnetfeldes Pitchwinkelstreuung. Bahnberechnungen für Protonen mit E_{kin} = 2.2 GeV in einem Modell-Magnetfeld interplanetarer Schocks zeigen, dass die Einfallsparameter in systematischer Weise bestimmen, ob die Partikel den Schock durchdringen oder reflektiert werden. Am Beispiel dieser ersten Analyse wird gezeigt, wie die Ergebnisse auf andere Parameter des Schocks und der Partikel übertragen werden können.

A micro-channel-plate detector with a 2 dimensional resistive anode encoder

A. Berdoz, F. Foroughi, Ch. Nussbaum
Université de Neuchâtel, Institut de Physique, rue A.-L. Breguet 1
CH - 2000 Neuchâtel

We present preliminary results obtained, using x rays and charge particles. Particular emphasis will be given to the choice of the type of anode.

Etude des niveaux de ^{242}Am par spectroscopie nucléaire

J.-L. Salicio, J. Kern, M. Gasser
Institut de Physique, Université de Fribourg
H.-G. Borner, G. Colvin, K. Schreckenbach
Institut Laue-Langevin, F-38042 Grenoble

L'étude des noyaux impairs-impairs est intéressante pour plusieurs raisons. Elle permet de déterminer l'influence des interactions entre les particules impaires sur les énergies des niveaux de faible énergie d'excitation. Nous avons observé les réactions ^{241}Am(n,γ)^{242}Am et ^{241}Am(n,e$^-$)^{242}Am à l'Ill/Grenoble et EIR/Würenlingen avec différents instruments. Nous présenterons les résultats et leur interprétation.

Test of QCD using a high intensity hadron facility

Y. Onel - DPNC, University of Geneva, Geneva, Switzerland
A. Penzo - INFN & University of Trieste, Trieste, Italy

The search for a new hadron spectroscopy associated with QCD, a necessary complement for its successful confrontation with experiments at very high energy, would strongly benefit by the impact of a flavour-rich high intensity machine at intermediate energy.
Tests of QCD (perturbative and non-perturbative effects) in this case might involve polarization studies of hadron spectrum and binary and quasi two-body reactions initiated by a variety of hadrons (polarized when possible) and in particular kaon beams on polarized targets.

KETE II :

Complete experimental reconstruction of the scattering amplitudes in the reaction pp → πd at 447, 515 and 580 MeV

P. Bach, G. Cantale, S. Degli-Agosti, Ph. Demierre, E. Heer, R. Hess, C. Lechanoine-LeLuc, W.R. Leo+, Ph. Sormani, Y. Onel, D. Rapin, P.Y. Rascher
DPNC, University of Geneva, 1211 Geneva 4, Switzerland

S. Jaccard
Schweizerisches Institut für Nuklearforschung, CH-5234 Villigen, Switzerland

+ present address: IGA, Dept. of Physics, EPFL, 1015 Lausanne, Switzerland

Abstract

Scattering amplitudes for the pp → π^+d reaction at 447, 515 and 580 MeV have, for the first time, been reconstructed from polarization measurements including vectorial and tensorial deuteron polarizations. This analysis also provided indicative values for the d-C effective analyzing power for 150 to 350 MeV kinetic energy deuteron. The reconstructed amplitudes are compared with those from theoretical calculations.

To achieve a complete understanding of the Nucleon-Nucleon reaction, it has long been recognized that the study of the pp → π^+d is of greatest interest. Within the last 10 years, a rather extensive study of this reaction has been stimulated mainly by it_{11} [1] and t_{20} [2] measurements in elastic πd scattering which show strong oscillatory behaviors. Significant progress in the reaction pp → π^+d was also achieved with the measurements of the spin correlation parameters A_{pq} [3][4], but this set of data is insufficient to enable the reconstruction of the 6 complex amplitudes describing the reaction [5]. This consideration lead us to perform extensive measurements of the vector and tensor polarization of the outgoing deuteron, using an experimental set-up and an approach similar to our work in pp elastic scattering [6].

A total of 10 different asymmetries ε have been measured between 52° and 147° cm scattering angle at three incident kinetic energies 447, 515 and 580 MeV, providing 520 new experimental data points. Those are presented in detail in the thesis of G. Cantale [7], together with the amplitude reconstruction.

At a given energy, the reaction pp $^+$d is completely described at each cm scattering angle by six complex

amplitudes, F_d^{bt}, such that (using the formalism of ref.8-see Fig.1)

$$F_d^{bt}(\theta) = + (-1)^{b-t+d} F_d^{tb}(\pi-\theta) \quad (1)$$

with b, t = ± 1/2 referring respectively to the beam and the target proton and d = 1, 0, -1 referring to the deuteron. We called these amplitudes A,B,C,D,E and F, defined as follows:

$$A=F_1^{\frac{1}{2}\frac{1}{2}} = -F_{-1}^{-\frac{1}{2}-\frac{1}{2}}, \quad B=F_0^{\frac{1}{2}\frac{1}{2}} = F_0^{-\frac{1}{2}-\frac{1}{2}}, \quad C=F_{-1}^{\frac{1}{2}\frac{1}{2}} = -F_1^{-\frac{1}{2}-\frac{1}{2}}, \quad (2)$$

$$D=F_0^{-\frac{1}{2}\frac{1}{2}} = -F_0^{\frac{1}{2}-\frac{1}{2}}, \quad E=F_1^{-\frac{1}{2}\frac{1}{2}} = F_{-1}^{\frac{1}{2}-\frac{1}{2}}, \quad F=F_1^{\frac{1}{2}-\frac{1}{2}} = F_{-1}^{-\frac{1}{2}\frac{1}{2}}.$$

All of the 144 possible observables (36 linearly independent) can be expressed as bilinear relations of these amplitudes, for example

$$I = 1/2\ (AA^* + BB^* + CC^* + DD^* + EE^* + FF^*) \quad (3)$$
$$I\ t_{22} = (\sqrt{3}/2)\ \mathrm{Re}(AC^* + EF^*)$$

However the amplitude reconstruction cannot yet been performed since the measured asymmetries ε are also dependant of the uncalibrated deuteron polarimeter, i.e. of the unknown values of the 4 analyzing powers of the carbon for a deuteron scattering, T^{11}, T^{22}, T^{21} and T^{20}. To solve the problem the $pp \to \pi^+ d$ reaction was globally studied, using the data at the three energies together, making use of partial waves energy independent analysis with $J < 5$, but including an a priori energy dependant parametrization of the analyzing powers. A total of 860 data points (520 from these asymmetry measurements) were used with 97 free parameters (3x25 for the partial wave analysis and 22 for the dC analyzing powers). After convergence two independent minima were found referred later as Sol.1 and Sol.2.

The direct reconstruction of these amplitudes at each energy and each angle was then performed, using as starting point the two partial waves solutions and based on 27 observables, i.e. the differential cross-section (1), the polarization parameter P (2x1), the spin correlation parameters A_{pq} (4) and the deuteron asymmetries (2x10), taking into account the symmetry of eq.1. The fit has 19 free parameters, i..e. 11 for the six complex amplitudes since one common phase is arbitrary and 2 x 4 for the analyzing powers T^{ij} of the carbon polarimeter. After convergence, only one solution is left, because either they both converge to the same or only the best one is kept. A preliminary study has shown that imposing $T^{20} = 0$ does not increase significantly the χ^2/d.f values. We are quite insensitive to this analyzing power. We therefore set T^{20} to zero, leaving us with 17 unknowns. The χ^2/d.f was 1.47, 1.51, 1.44 at 447, 515 and 580 MeV respectively. Fig.2 shows the results for the 6 amplitudes at 447 MeV. In order to do easy comparison with other people calculations, we represent at each angle the amplitudes in a polar representation, e.g.

$A = A \exp(i\phi_A)$ where the phases are taken relative to A with the overall phase fixed by the convention $\phi_A = 0$. The dashed lines are theoretical predictions by M. Locher [9], based on relativistic perturbation theory, which are in relatively good agreement. The full and dotted lines are results of our partial wave analysis referred to as Sol.1 and Sol.2 respectively.

The fact that the normes of amplitudes A and C are found to deviate from zero near 90° might be an indication of possible systematic errors in the data sets used. A comparison of Locher's predictions with our results might indicate that the triplet pp waves are underestimated: this reflects itself in two facts: first the symmetry relation between amplitude A and -C is broken as energy increases, and secondly the norm of F is larger than in Locher's calculation.

REFERENCES
1. G.R. Smith et al., Phys. Rev. C29 (1984)2206
2. W. Gruebler et al., Phys. Rev. Lett. 49 (1982) 444
3. E. Aprile et al., Nucl. Phys. A379 (1982) 369
4. E. Aprile et al., Nucl. Phys. A415 (1984) 365
5. M.P. Locher, J. de Phys., Colloque C2, Tome 46 (1985) p.c2-319
6. E. Aprile et al., Phys. Rev. Lett. 46 (1981) 1047 and E. Aprile et al., Phys. Rev. Lett. 47 (1981) 1360
7. G. Cantale, Ph.D. thesis, University of Geneva, No.2175(1986)
8. M. Simonius "Pol.Nucl.Phys.", Lect., Notes in Phys.30, Springer-Verlag (1974)
9. M.P. Locher, private communication.

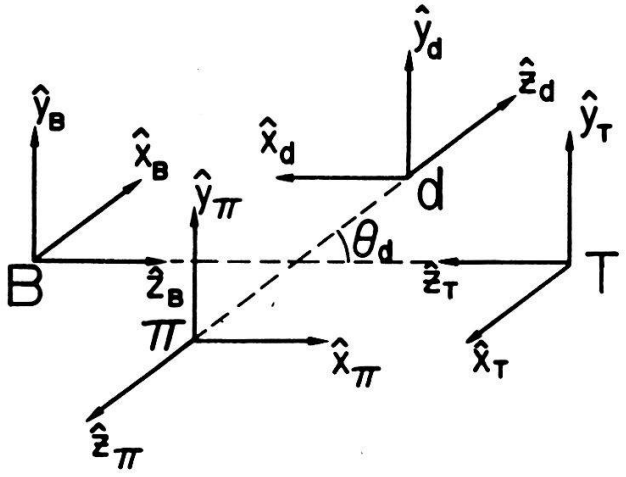

Fig.1: helicity reference frame used in this work.

We adopt the Madison convention, i.e. the polarization of a particle is such that the z-axis is along its momentum.

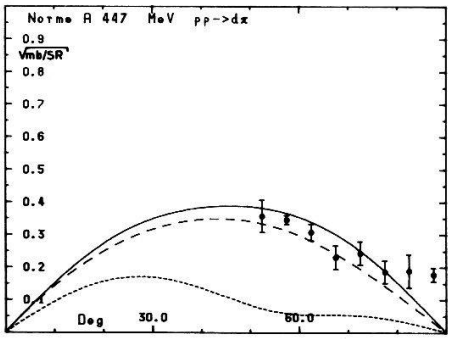

Figure 2

The scattering amplitudes A, B, C, D, E and F of the reaction pp - $d\pi^+$ at 447 MeV.
The norms are expressed in $\sqrt{mb/sr}$ and the phases are in rad.
The phase of A was choosen to be zero.
The full line (SOL1) and the dotted line (SOL2) result from a partial wave analysis. The points are the results of the direct experimental reconstruction.
The dashed line is the theoretical predictions of M. Locher [9].

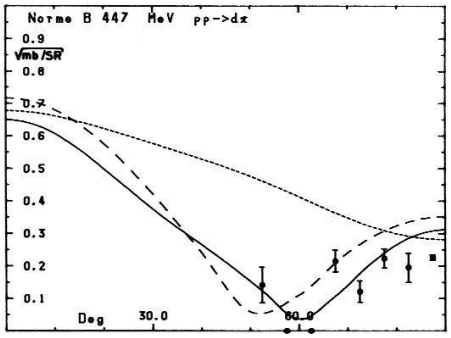

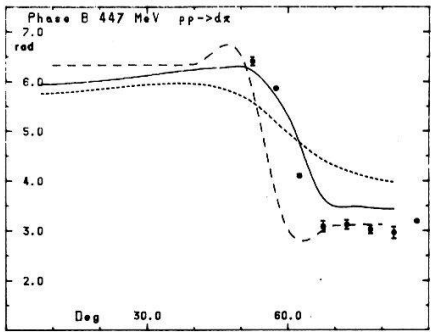

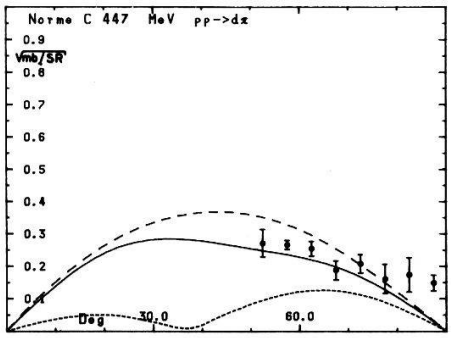

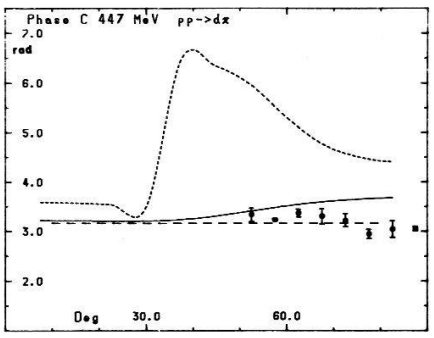

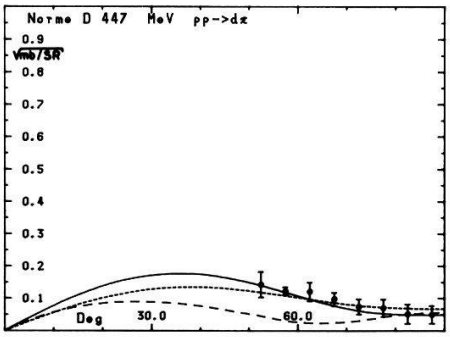

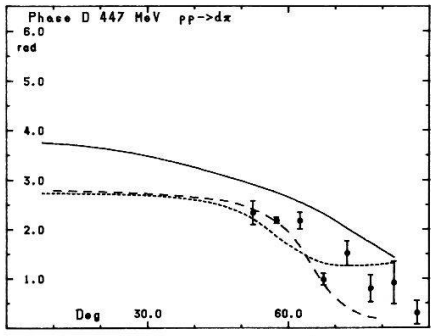

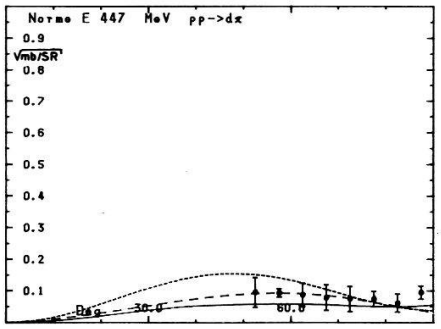

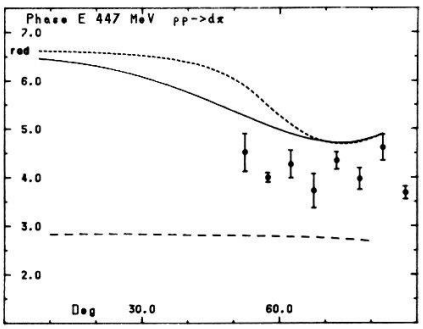

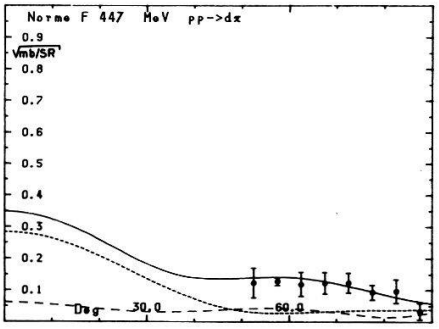

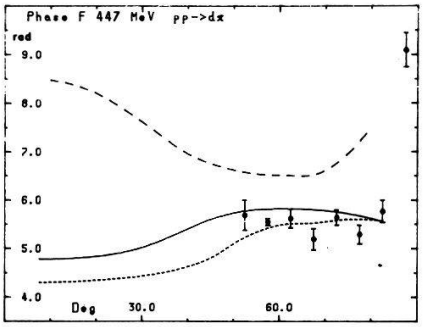

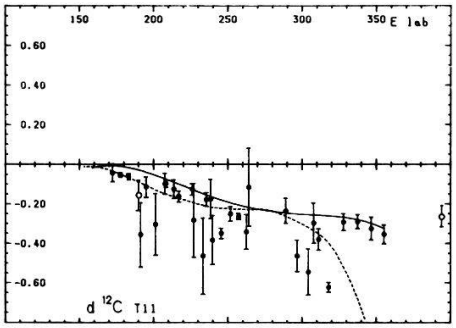

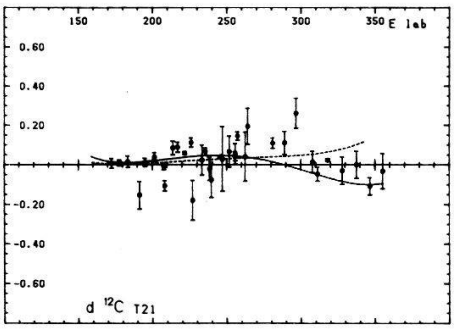

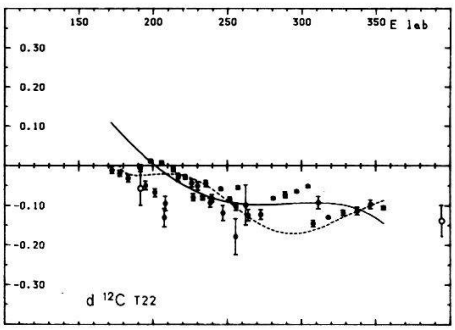

Figure 3

Carbon analyzing powers T^{11}, T^{21} and T^{22} for incident deuterons.

ρ^0 MESON PRODUCTION AT p_T > 1 GeV/c IN 300 GeV π^- INTERACTIONS -- EXPERIMENTAL EVIDENCE FOR HIGHER TWIST DIAGRAMS OF QCD

WA77 Collaboration: Athens[1]-Bari[2]-Birmingham[3]-CERN[4]-Paris(Coll. de France)[5]-Paris(LPNHE)[6]

A. Angelopoulos[1], A. Apostolakis[1], M. Baubillier[6], M. Benayoun[5], W. Beusch[4], I.J. Bloodworth[3], A.J. Burns[4], J.N. Carney[3], B.R. French[4], B. Ghidini[2], Y. Goldschmidt-Clermont[4], G. Ingelmann[4], A. Jacholkowski[6], J. Kahane[5], J.B. Kinson[3], K. Knudson[4], J.C. Lassalle[4], V. Lenti[2], Ph. Leruste[5], A. Malamant[5], W. Mitaroff[4], C. Néaume[6], F. Navach[4], A. Palano[2], M. Pimenta[4], R. Petronzio[4], I.C. Print[3], E. Quercigh[4], H. Rozaki[1], M. Sené[6], R. Sené[5], H.R. Shaylor[3], M. Stassinaki[2], Z. Strachman[6], M.T. Trainor[3], G. Vassiliadis[1], O. Villalobos Baillie[3], M.F. Votruba[3] G. Zito[2] and R. Zitoun[6]

This experiment, done with the Omega spectrometer at CERN, selected events with a transverse momentum of a $\pi^+\pi^-$ pair. p_T(pair) > 1 GeV/c recoiling against an opposite particle with p_T(opposite) > 1 GeV/c. The signal/(signal + background) ratio is about 40% higher for the sample of events with p_T(pair) > 2 p_T(opposite) than for the sample with more nearly equal transverse momenta. This dependence on p_T ratios can be explained with a QCD model if direct ρ production via higher twist diagrams is included.

An Upper Limit for the Mass of $\bar{\nu}_e$ from Tritium β-Decay

M. Fritschi, E. Holzschuh, W. Kündig, J.W. Petersen, R.E. Pixley, and H. Stüssi
Physics Institute, University of Zurich, SIN Villigen

The endpoint region of the tritium β-spectrum has been measured with 27 eV resolution, using a magnetic spectrometer. The tritium activity was implanted into a thin layer of carbon. The $\bar{\nu}_e$ mass determined is consistent with zero with an upper limit of 18 eV, which includes instrumental and statistical uncertainties as well as uncertainties due to the energy loss in the source and the final electronic states.

Measurement of Tritium Depth Profiles

H. Stüssi, R.E. Pixley
Physics Institute, University of Zurich

A knowledge of the tritium depth profile of the sources used in the Univ. Zurich-SIN $m_{\bar{\nu}e}$ experiment is essential for the analysis of the beta-spectrum data. It has been possible to measure the very shallow tritium distribution in graphite of these sources using the nuclear recoil method. The tritium recoils at 45° resulting from 400 keV ^{12}C bombardment were detected in a solid state detector. They were separated from the much more numerous ^{12}C ions scattered from the backing using an ExB filter. A depth resolution of ~50 A near the surface was obtained.

KETE III :

Untersuchung über BGO-Stäbe zur Verwendung in "preshower"-Detektoren

C. Hug und B. Hahn

Laboratorium für Hochenergiephysik, Universität Bern

Zur Bestimmung des Konversionspunktes von γ-Strahlen bei elektromagnetischen Kalorimetern werden sogenannte "preshower"-Detektoren verwendet. Bei γ-Energien kleiner einige GeV müssen diese aktiv sein, um den Enenergieverlust bestimmen zu können. Zu diesem Zweck eignen sich dünne BGO-Stäbe. Es werden Resultate über Lichtsammlung und Energieauflösung präsentiert.

Untersuchung von 3-jet Ereignissen und Produktion von einzelnen Photonen am CERN "$\bar{p}p$-collider"

UA2-Kollaboration (Bern, CERN, Heidelberg, Kopenhagen, Orsay, Pavia, Saclay)

Bern: K. Borer, B. Hahn, K. Hara, E. Hugentobler, R. Moning, J. Schacher und F. Stocker

Laboratorium für Hochenergiephysik, Universität Bern

Die Winkelverteilungen von 3-jet Ereignissen lassen auf die Existenz starker Bremsstrahlung schliessen, in guter Uebereinstimmung mit QCD. Die starke Kopplungskonstante α_s wird aus den Daten abgeleitet.
Inklusive Wirkungsquerschnitte der Produktion von einzelnen Photonen bei hohem Transversalimpuls wurden bestimmt und mit der QCD-Theorie verglichen. Das γ/π°-Verhältnis wird angegeben.

Polarisationstransfer in $(\vec{p},\vec{n})$- Reaktionen bei $\Theta = 0^\circ$

C. Gysin, S. Burzynski*, M. Hammans, R. Henneck, W. Lorenzon, M.A. Pickar, I. Sick

Institut für Physik, Universität Basel, 4056 Basel

Am Neutronenstrahl des SIN Injektorzyklotrons wurde der Polarisationstransfer in $(\vec{p},\vec{n})$-Reaktion an leichten Kernen bei $\Theta = 0^\circ$ gemessen. Für den longitudinalen Transfer ergaben sich für die Kerne ^{2}H, ^{6} ^{7}Li und ^{9}Be Werte <0.2. Der transversale Transfer, gemessen bei 55 und 72 MeV ist am grössten für ^{2}H. Damit steht am SIN ein quasi-monoenergetischer (~3 MeV FWHM) Neutronenstrahl hoher Intensität ($\sim 10^5 n/s \cdot cm^2 \cdot \mu A$) und Polarisation ($P_n \simeq 0.35$) zur Verfügung.

*Permanente Adresse: Institute for Nuclear Studies, Warszawa, Polen

Comparison of Complex Particle Emission in 72 MeV Proton and Stopped Pion Induced Reactions

R. Wagner and Z. Lewandowski*
Institut für Physik der Universität Basel, CH-4056 Basel
H.H. Müller, W. Reichart, P. Schober and S. Steiner
Physik-Institut der Universität Zürich, CH-8001 Zürich

Using a 72 MeV proton beam of the SIN injector cyclotron, the emission of ^{3}He- and α-particles has been studied in the continuum for the target nuclei ^{12}C, ^{59}Co and ^{197}Au. Angle-integrated spectra are compared to stopped-pion induced emission of complex particles. A striking similarity of the spectral shapes and nearly equal yields are observed.

*On leave from the Institute of Nuclear Physics, Cracow, Poland

Sur le coefficient de transfert K_{y}^{y} dans la réaction $D(\vec{p},\vec{n})pp$ à 0^{o}

A. Berdoz, F. Foroughi
Université de Neuchâtel, Institut de Physique, rue A.-L. Breguet 1
CH - 2000 Neuchâtel

Les analyses de la polarisation du faisceau de neutrons produit au SIN par la réaction $D(\vec{p},\vec{n})pp$ à 0^{o} entre 50 et 70 Mev ont montré un comportement inattendu du coefficient de transfert de spin K_{y}^{y} en fonction de l'énergie.

On tentera de reproduire cette variation par un modèle simple et l'on montrera les limites d'un tel modèle.

Fast deuteron production following pion absorption in ^{4}He

J.-F. Germond, Institut de Physique, CH - 2000 Neuchâtel, Switzerland
C. Wilkin, University College London, UK

The ^{4}He(π^{-},d)nn reaction is studied in a cluster model where the capture of the pion is assumed to take place on a ^{3}He constituent of the target. Good absolute agreement with stopped pion data is achieved for the high energy part of the deuteron spectrum where the n-n system is governed by the $^{1}S_{0}$ final state interaction. Using the d(p,π^{0})^{3}He data as input, the forward ^{4}He(π^{-},d)nn deuteron production cross section is predicted to decrease rapidly in function of the incoming pion energy. The relevance of these results for the study of the charge-symetry-breaking d(d,π^{0})^{4}He reaction as well as the role of the deuteron tensor polarization will be discussed.

Search for strange dibaryons with the $p+p \rightarrow K^+ + X$ reaction

J.-P. Didelez, R. Frascaria, E. Warde, M. Boivin, B. Saghai, J. Yonnet, J.Y. Grossiord, A. Guichard, J. Ernst, R. Siebert, E. Bovet, J.-P. Egger, C.F. Perdrizat, G.S. Blanpied, G. Pignault and B.M. Preedom
Orsay-Saclay-Lyon-Bonn-Neuchâtel-William and Mary-South Carolina collaboration

A study of the reaction $p+p \rightarrow K^+ + X$ for incident energies covering the ΛN ($\sim$2053 MeV) and Σ N ($\sim$2127 MeV) thresholds was started at the SATURNE II machine at Saclay with the SPES4 spectrometer. The aim of the experiment is to search for narrow dibaryon resonances of strangeness S = -1. The need for an excellent on-line rejection of protons and pions is the main experimental problem. Best results were obtained with a series of plexiglas Cerenkov counters placed behind the SPES4 focal plane. The set-up and first results will be presented and discussed.

PHYSIQUE THEORIQUE

ARTIFICIAL INTELLIGENCE: IMPACT ON PURE AND APPLIED SCIENCE*)

B. Humpert**)

Artificial Intelligence Group
HASLER AG, Research Laboratories
CH-3000 Bern 14, Switzerland

and

Institut de Physique Nucléaire
Université de Lausanne
CH-1000 Lausanne, Switzerland

Abstract

Artificial Intelligence (AI) is at present in a state of rapid scientific and commercial expansion. Concentrating on the fields "Theorem Proving/Automated Reasoning" and "Expert-Systems", we sketch the basic ideas behind them and discuss their present and future impact on pure and applied science.

*) Presented at the Meeting of the Swiss Physical Society, Fribourg, 28-29 March 1985

**) also at CERN

1. The AI-Explosion

Artificial Intelligence [1] is at present in a state of rapid expansion, if not explosion [2]. For a long time AI was considered a "game" for computer specialists and the fundamental impact of sympolic computations remained recognized by only a few.

In the 1950's researchers were developing the foundations of AI including mathematical logic and recursive function theory, which led to the formulation of list processing and the language LISP. LISP [3] is widely in use since it provides a very simple syntax and allows for the evaluation of recursive symbolic expressions. Another, more recent language, is PROLOG [4].

The subsequent developments were aimed at a variety of goals: such as improvement of the computational environments, simulation of the thinking process, development of algebraic compution systems and programs, known as "problem solvers", and others. Focusing on what were labelled "real-world" problems - as opposed to the artificial, small and tough "toy" problems - three primary subfields emerged after a decade of work: expert-systems, natural language, robotics, whereby the last field includes vision, speech and locomotion.

The Stanford group pioneered by creating artificial experts [1,2], meaning computer programs which mainly consist of a knowledge-base (data + rules) and a deductive component (inference engine). The techniques developed for DENDRAL, the truly first expert system (for the identification of chemical structures from mass spectrograms), proved to be of highly practical value. They were immediately improved, expanded and refined, and also applied to a great variety of other knowledge domains; knowledge engineering began to florish!

Around 1970 and the successive years, another, not less important breakthrough, was achieved in "Theorem Proving/ Automated Reasoning" [5] with the Robinson-Principle. Its application allows for formal mathematical proof and intricate deduction procedures within the framework of Propositional and Predicate Logic. In the same way expert-systems play much emphasis on the knowledge-base with many different rules, theorem proving programs are on the other hand endowed with a highly efficient reasoning component for the simultaneous logical intercorrelation of a number of factors. The theoretical development and the practical exploitation of these new techniques took place simultaneously with the development of bigger and more powerful computers thus allowing for the treatment of more and more demanding problems. Mathematics was soon left behind and complex analyses in a large variety of technical and practical domains were carried out; automated reasoning began to florish!

Both fields - expert-systems and automated reasoning - (as well as other AI subfields) are in a state of rapid

intellectual development, prolific growth of application and booming commercialization. The finance-commercial world is convinced of its utility and has started to invest in computer science and AI in particular; the cultural institutions follow [6]. In the following we give a few illustrative examples [7]:

- Schlumberger, a leading oil services firm, determined that its future growth depended on knowledge engineering and formed two groups to build expert data interpretation systems.
- Japan's Ministry of International Trade and Industry determined that the country's future economic viability required leadership in knowledge system technology and launched a $ 500 million, 10-year program in fifth-generation computing.
- Responding to a perceived technological and competitive threat, UK's Alvey Commission retracted that country's longstanding disaproval of AI and urged a major push forward in knowledge system technology, a recommendation that the present government implemented.
- The European Economic Community (EEC) set up the European Strategic Program for Research and Development in Information Technologies, short ESPRIT program [8], with an investment of 1.5 billion ECU for the 1st period of 5 years to fund the development of a strong European infrastructure in this technology.
- The US Department of Defense claimed that knowledge systems would become the front line of US defense in the 1990's and initiated a $ 500 million, 5-year strategic computing program.
- IBM licensed and sold its first two AI programs (LISP, INTELLECT) and publicly endorsed the AI field as relevant and applicable. Similarly CDC will put its knowledge engineering tool KEE on the market, and DEC offers the OPS5-tool and INTERLISP to its customers.
- IBM's principle competitors ($\sim$ 15 firms) teamed to form the Microelectronics and Computer Consortium (MCC, Austin TX) and identified knowledge systems as an area of primary concern.
- General Motors took an equity position in a knowledge-engineering firm to hasten the introduction of knowledge systems into its business.
- Three European computer companies BULL, ICL, SIEMENS started recently the European Computer-Industry Research Center ECRC, similar to MCC, at Munich with pure research goals in AI [9].
- The US government has recently agreed to sponsor four national super-computer centers at: Princeton, San Diego, Illinois, Cornell [10]; two more such centers at Atlanta and Tallahassee already exist.

Focussing now on the Swiss scene, we observe:

- A team of French scientists recently set up an AI software company (NOESIS) at Neuchâtel.
- Cap Gemini, a contractor company for theoretical studies, participates in six ESPRIT-projects.
- Mettler, Cerberus, Ciba-Geigy and others have small research teams working in AI.
- Hasler AG has recently added a small AI research group to its research laboratories.
- At the Swiss Universities Bern, Geneva, Lausanne, EPFL, Neuchâtel research in AI is carried out.

With the following presentation we aim to attract the interest to this rapidly developing field. In section 2 we give an elementary introduction into Symbolic Logic, as a theoretical basis for the discussion of Theorem Proving/Automated Reasoning in section 3. Section 4 explains the basic components of an expert-system, presents a typical example session of MYCIN and shows a list of interesting knowledge-based systems. In section 5 we aim at an assessment of the impacts of AI on pure and applied science.

The following presentation addresses itself to readers not familiar with the above discussed AI-technologies. It is incomplete, sketchy and fragmentary, simply to leave an overall impression of the type of reasoning in this field, as well as of the possible impacts and spinoffs.

2. Symbolic Logics

Symbolic Logics [11] considers languages whose essential purpose is to symbolize reasoning encountered not only in mathematics, but also in practical problems of technical nature, and even in daily life; it was invented by G.Boole (1854) and G.Frege (1879).

By introducing some of its elementary notions, we aim to demonstrate in this and the following section the type of reasoning which is at the base of many AI activities.

Propositions/Predicates:

The most simple declarative objects are propositions (= simple statements) and predicates (= relations between objects). We give a few examples:

It is hot	:	Q	(Proposition)
x likes y	:	L(x,y)	(Predicate)
x = y	:	E(x,y)	(Predicate)
MOTHER(PETER):		Peter's mother	(Predicate)

Propositions/Predicates can either be true ($\equiv T$) or false ($\equiv F$) meaning that their truth value (= TV) is: TV(P) = T or F.

Logical Connectives:

From Propositions/Predicates we can build compound propositions by using the logical connectives: $\sim$ (not), $\vee$ (or), $\wedge$ (and),

$\longrightarrow$ (if...then), $\longleftrightarrow$ (if and only if = iff), which act as operators in the Boolean (T, F)-space. These five logical connectives can be used to build compound propositions from more elementary propositions, and more generally they can be used to build more complicated compound propositions by applying them repeatedly.

$\forall, \exists$-Quantifiers:

Since we have introduced variables, we need two special symbols to characterize the variable type. The symbols $\forall$ and $\exists$ are called the "universal quantifier" and the "existential quantifier" respectively. If x is a variable, $(\forall x)$ reads as "for all, each, every x", while $(\exists x)$ instead reads "there exists an x; for some x; for at least one x".

Formulas:

The above-defined ingredients of Propositional/Predicate Logic allow for the formation of formulas. Defining the propositions

H: It is hot, U: It is humid, R: It will rain

one may form the formulas

$F_o \triangleq [(H \wedge U) \longrightarrow R]$: If it is hot and humid, then it will rain.

$F_o \triangleq [(\forall x)(\exists y)E(x,y)]$: For all x, there exists a y, such that x=y.

Truth Table:

We earlier stated that Propositions/Predicates can either be true ($\equiv T$) or false ($\equiv F$). The action of the logical connectives in the (T,F)-space is defined by the truth Table 2.1. Note that in symbolic logics some of the T, F-assignments are not the same as one would naively expect form daily-life experience; these cases are indicated by the $\checkmark$ sign in the previous Table. We now are in the position to evaluate the truth value of any formula such as, for instance:

$$F_o \triangleq [(H \wedge U) \longrightarrow R] = \{T, F\} \qquad (2.1)$$

We write down all possible combinations of truth assignments for the three propositions H, U and R and evaluate subsequently the the truth value of F_o by going through the the procedure of "truth table checking" shown in Table 2.2.

Interpretation:

The assignment of a particular set of truth values to the Propositions/Predicates of a formula is called an interpretation. Thus, each line in the previous table defines a particular interpretation and the first three colums specify the particular T, F-assignment for the Propositions/

Predicates. A formula which is true for any interpretation is called a "valid formula" or a "tautology". Similarly a formula which is false for any interpretation is called "inconsistent" or a "contradiction":

valid = always true $\Longrightarrow$ Tautology ($\equiv \blacksquare$)
inconsistent = always false $\Longrightarrow$ Contradiction ($\equiv \square$)

Equivalent Formulas (Calculation Laws):

Two (or more) formulas are called equivalent if, for any interpretation, they have the same truth value. We give a few typical examples:

iff	Law	: $G \leftrightarrow H = (G \rightarrow H) \wedge (H \rightarrow G)$
if-then	Law	: $G \rightarrow H = (\sim G) \vee H$
Commutative	Law	: $G \veebar H = H \veebar G$
Associative	Law	: $(G \veebar H) \veebar M = G \veebar (H \veebar M)$
Distributive	Law	: $G \vee (H \wedge M) = (G \vee H) \wedge (G \vee M)$, $G \wedge (H \vee M) = (G \wedge H) \vee (G \wedge M)$
		$G \veebar \blacksquare = \{ \blacksquare, G \quad G \veebar \square = \{ G, \square$
$\square, \blacksquare$	Laws	: $\blacksquare \veebar \blacksquare = \blacksquare, \quad \square \veebar \square = \square, \quad \blacksquare \veebar \square = \{ \blacksquare, \square$
Negation	Law	: $G \veebar (\sim G) = \{ \blacksquare, \square, \quad \sim(\sim G) = G$
Morgan's	Law	: $\sim(G \updownarrow H) = (\sim G) \veebar (\sim H)$

Note in particular the commutative, associative and distributive laws conerning the $\wedge, \vee$ logical connectives.

Logical Consequence:

A formula F_2 is called a "logical conseqence (Lcons)" of a formula F_1, if the formula F_2 is true for all interpretations for which F_1 is also true:

$$\forall I : \quad TV(F_1) = T \quad \underset{\text{Lcons}}{\Longrightarrow} \quad TV(F_2) = T \qquad (2.2)$$

3. Theorem Proving/Automated Reasoning

In this section we demonstrate how Symbolic Logics is used to prove (or disprove) theorems in mathematics. We are here not talking about numerical calculations but rather symbolic, algebraic and formal evalutations of mathematical expressions. The theoretical basis of theorem proving was strongly influenced by Herbrand (1930), Church-Turing (1936) and Robinson (1965)[see Ref.11], and more recently by a number of researchers [5,11,12].

Deduction Theorem:

A mathematical theorem usually consists of a set of axioms $Ax_1, \ldots, Ax_n$ and a conjecture C which all are understood as

formulas in the earlier discussed sense of Symbolic Logics. The correctness of a theorem is proven by establishing that formula C is a logical consequence (Lcons) of the conjoined axioms $Ax \equiv (Ax_1 \wedge \ldots \wedge Ax_n)$; whenever the axiom set is true, the conjecture C follows.

The "Deduction Theorem" of Symbolic Logics provides a formal mean to decide whether this indeed holds. It states: given formulas $Ax_1,\ldots,Ax_n$ and a formula C; C is a logical consequence of $Ax_1,\ldots,Ax_n$ iff the formula $(Ax_1 \wedge \ldots \wedge Ax_n) \rightarrow C$ is valid. Thus

$$C \quad \text{(Lcons)} \quad (Ax_1 \wedge \ldots \wedge Ax_n) \Longleftrightarrow \overbrace{[(Ax_1 \wedge \ldots \wedge Ax_n) \rightarrow C]}^{\text{Mathem. Theorem}} = \blacksquare \ (\equiv \top)$$

$$\Longleftrightarrow \underbrace{[\, Ax_1 \wedge \ldots \wedge Ax_n \wedge (\sim C)]}_{\text{logical formula S}} = \square \ (\equiv \bot) \qquad (3.1)$$

The proof of correctness of a mathematical theorem is thus reduced to a proof of the validity (or tautology) of a logical formula S. Carrying out equivalent formula manipulations the negated, second form is found; it usually is taken as the starting point for all following manipulations where one tries to spot an inconsistency (or contradiction).

Equivalent Manipulations:

The form of the above "logical formula S" is usually complicated. Due to the presence of variables with a continuous range of values, the contradiction proof can usually not be established via truth table checking. Several slightly more complicated formula manipulations have to be carried out which, however, leave the formula's truth value unchanged. We here skip all these details and restrict ourselves to the net result:

$$S \triangleq \underbrace{(\forall y)(\exists x)}_{\text{Quantifiers}} \ldots \underbrace{[\, G_1 \wedge G_2 \wedge \ldots]}_{\text{Clauses}} \qquad (3.2)$$

The logical formula S is factorized into a first part containing all quantifiers, and a second part containing the predicates and the logical connectives $\wedge, \vee$ only; all other logical connectives have been eliminated by the equivalent formula manipulations. The "clauses" $G_i \equiv L_\alpha \vee L_\beta \vee L_\gamma \ldots$ are composed of "literals", which stand for predicates or their negation, whereby only disjunctions occur. In short: a clause is a disjunction of literals.

To describe the subsequent procedure in detail would go beyond the aims of this report, and we therefore limit ourselves to a qualitative description of its main steps. All ($\exists$ -quantified) variables are replaced by "Skolem functions", and afterwards all $\forall$ - and $\exists$ -quantifiers are dropped.

Herbrand Proof Procedure:

Herbrand has given a general procedure as to how the contradiction of S can be established. It essentially boils down to the replacement of all the left ($\forall$ -quantified) variables by constants out of the "Herbrand-Universe". This, in general, consists of an infinite set of possible constants, the so-called "ground-terms". For every possible Herbrand-constant assignment (to the variables in the formula) truth table checking is carried out. If, for any specific constant assignment, and for all the corresponding interpretations, the formula always is false (meaning it is a contradiction), then the inconsistency of S and consequently the correctness of the original mathematical formula is established. The above procedure proved to be of little use for concrete problems since it leads to an explosive number of possibilities to be checked. Its main value, however, lies on the purely theoretical side where it provides an "in principle" working, general proof technique.

Church-Turing Theorem:

Finding a general decision procedure to verify the validity/inconsistency of a formula was considered long ago. It was not until Church and Turing that this was proved impossible. Church and Turing independently showed:

> There is no general decision procedure to decide "a priori" on the truth or falsehood of formulas in first order Predicate Logic. However, there are proof procedures which can verify that a formula is "valid", if indeed it is valid. For invalid formulas, these procedures will never terminate.

In view of the result of Church and Turing this is the best we can expect to get from any proof procedure. Note, by changing a formula into its negative, the above insight with the replacements, "valid" $\rightarrow$ "inconsistent", "invalid" $\rightarrow$ "consistent", remains applicable in the same way. Thus for the proof procedure of Herbrand we have:

there exists no general $\mathbb{T}$ or $\mathbb{F}$ (both) decision procedure
If $\square$, Herbrand technique will find.
If $\blacksquare$, search process will not stop.

Robinson Principle:

A major step forward was achieved by Robinson who was able to conceive a calculation technique that no longer needed truth-table checking in the Herbrand base. Generally speaking, it "resolves" one clause with another clause to generate new clauses which, however, have less literals. Repeating this process successively one is able to generate new clauses with less and less literals until the empty clause is found. Since, by definition, the empty clause is a contradiction ($\equiv \square$) the inconsistency of Eq. 3.2 is established and the correctness of the mathematical theorem Eq. 3.1 is proved. However,

if the logical formula under investigation is not a contradiction this search process for □ can go on forever. The Robinson principle is not the end of the story; it allows for a large number of further improvements [11] which, unfortunately, can not be dealt with in this limited report.

Theorem Proving Programs:

Mechanical Theorem Proving goes back to the 1960's where Gilmore and Prawitz, shortly followed by Davis and Putnam, made the first attempts to implement Herbrand's procedure on digital computers. This AI branch has meanwhile considerably progressed and several useful computer systems, to a large extent based on Robinson's principle, exist. We mention:

TPU	: Chang, Lee [11]	(SLISP)
LMA/ITP	: Wos, Overbeck, Lusk [12]	(PASCAL-Dialect)
BM-TP	: Boyer, Moore [13]	(INTER-LISP)
HS-TP	: Bundy [11]	(PROLOG)

In the first column we list the name of the particular system, in the second column the authors, and in the third one the employed AI language. Instead of focusing on the particularities of their construction let us form an opinion on what these systems are able to achieve.

Examples in Mathematics:

Several of these theorem proving programming systems were used to prove (or disprove) mathematical theorems. We mention a few typical examples [14] such as:

Theorem: In an associative system with left and right solutions, there is an identity element.
Theorem: In an associative system with an identity element, if the square of every element is the identity, the system is commutative.
Theorem: Any number greater than 1 has a prime divisor.
Theorem: There exists an infinity of prime numbers.

An impressive result was achieved in the analysis of ternary Boolean algebra, where the independence of the usual set of five axioms was in debate. The axioms, proposed for the first time in 1947, read:

$$
\begin{aligned}
&1)\ f(f(v,w,x),y,f(v,w,z)) = f(v,w,f(x,y,z)) \\
&2)\ f(y,x,x) = x \\
&3)\ f(x,y,g(y)) = x \qquad (3.3) \\
&4)\ f(x,x,y) = x \\
&5)\ f(g(y),y,x) = x
\end{aligned}
$$

Intuitively, the function f that occurs in each of the five axioms can be thought of as a three-place product, and the function g as the inverse of an individual element. We mention in passing that from a ternary Boolean algebra with appropriate defintions of union, intersection, complement, 0,

and 1, in terms of the functions f and g, one can produce a Boolean algebra, and conversely. The problem now is to determine which, if any, of the five axioms is independent of the remaining four. If an axiom is dependent, then a proof can be found of that fact. If an axiom is independent, then a model exists that satisfies the other four but does not satisfy the independent axiom. Axioms 4) and 5) where known to be dependent even before proofs were obtained with two unrelated theorem-proving programs in 1969.

Axioms 1), 2) and 3) are independent, and the required models were found (in 1977) using the LMA/ITP-system. Note that before this study, the methodology for generating models and counter examples with an automated reasoning program did not exist.

Another impressive success was achieved in the area of formal logic where the adequacy or inadequacy of various formulas, to serve as shortest single axioms for the Equivalent Calculus, was in debate. In short, the Equivalent Calculus is concerned with the abstraction of "equivalent", and it consists of the formulas that can be composed from variables x,y,z,..., and the two-place function E. With assistance from the LMA/ ITP-system several of the previously unclassified formulas were proven too weak to be a shortest single axiom, and two new ones were unexpectedly found.

Automated Reasoning:

With the continuous improvement of theorem-proving systems, more and more demanding problems could be attacked. The application range soon grew out of the narrow domain of mathematics into a great variety of fields. They required the simultaneous intercorrelation of different facts with a particular action - constrained and tailored according to the assembled facts - thus leading to the notion of "Automated Reasoning".

The research and application areas in which a reasoning program can be used include:

- mathematics
- formal logics
- program verification and debugging
- logic circuit design
- logic circuit validation
- chemical synthesis
- real-time systems control (e.g. in nuclear power stations)
- database inquiry
- robotics
- expert systems
- questioning-answering
- .
- .
- .
- .

It would go far beyond the purpose of this report to go into the details of the contributions in these fields using automated reasoning systems. We refer, instead, to the excellent recent book: "Automated Reasoning" by Wos, Overbeek, Lusk and Boyle [12] which gives a scholarly introduction into the field and, in addition, offers a detailed account of the possible applications. Note that the field is in rapid expansion!

4. Expert-Systems

In the previous section we concentrated on computational systems with almost no stored information on a particular knowledge domain, but with a highly developed logical-deductive component instead.

In the AI subfield - expert-system [1,15] - which we consider in this section, the inferential component is less developed, but detailed (and sometimes even unprecise) knowledge on a particular, specialized domain is stored in the knowledgebase. In the following we explain their essential function mode, present a typical sample session and discuss a set of well-known expert-systems.

What is an Expert-system?

A precise answer to this question is today almost impossible; the specialists are at variance as to the precise characteristics of an expert-system and the application range of the essential reasoning and computational techniques is in a state of rapid, almost unlimited expansion. We nevertheless can spot some of the key features in the "traditional" expert-systems which we would like to present in the subsequent discussion:

> An expert-system is a knowledge-intensive symbolic computer program that solves problems of a limited domain normally requiring human expertise.

It performs many of the secondary functions that an expert does, such as asking relevant questions and explaining its reasoning. Some of the common relevant expert-systems characteristics are:

- manipulate and reason about symbolic descriptions,
- solve difficult problems as good as (or even better than) human experts,
- reason heuristically with "rules of thumb",
- function with erroneous data and uncertain judgment rules,
- interact with humans in appropriate ways, including the use of natural language,
- contemplate multiple competing hypotheses simultaneously,
- ask and motivate its questions,
- justify its conclusions.

In addition to their fruitful impact, one should also keep in mind the limits of present (and future?) expert-systems. It is obvious that human qualities such as creativity, intuition, synthesizing, drawing analogies, recognizing and understanding fundamental principles, learning, relying on common sense, etc. will never be fully replaced by mechanical devices. All the laws and deeper interrelations of these qualities, however, will be recognize (partially with the help of expert-systems) and used for the global simulation of human behaviour. Expert-systems ordinarly address small tasks typi-

cally performed by professionals in a few minutes or hours: interpreting, diagnosing, planning, scheduling, and so forth. To accomplish these tasks, an expert-system makes judicious use of data and reasons with it, generally examining a large number of possibilities or constructing a solution dynamically.

How Does an Expert-System Work?

The basic programming components of a typical rule-based expert-system are:

1. Knowledge-Base (Data + Rules)
2. Reasoning Component (Inference Engine)
3. Input, Output, Control facilities.

The knowledge-base generally consists of conceptual taxonomic relationships and rules which have been extracted from one or several experts by the knowledge engineer. These rules and relationships thus constitute the "built-in" knowledge of an expert-system. They provide for interrelations between the actual facts or data which are fed into the expert-system once it is used for a practical application in its target domain. Some generally valid estimates about the number of such relationships/rules in the knowledge base are:

. interesting demonstration	$\gtrsim$	50 rules
. convincing demonstration	$\gtrsim$	250 rules
. commercially practical system	$\gtrsim$	50 rules
. expert level	$\sim$	500-1000 rules
. expertise in profession	$\sim$	10'000 rules
. human limit	$\sim$	100'000 rules

The reasoning component, also called problem solving engine, provides a high-level architecture: executive, inference procedure, and related inference engine. These components structure the knowledge system's problem-solving work and carry it out, generally using a goal-directed or backward-chaining mechanism, to determine a solution. In this approach, the system initially possesses a set of candidate solutions, each of which it considers in turn. For each candidate solution, it seeks knowledge-base rules that can achieve that solution and attempts to find data for each that satisfy the antecendent conditon of the rule. If this doesn't work, it will attempt to find other rules that can infer or achieve the necessary conditions. Failing that, it may query the end user to establish the prerequisites. Each rule in such systems usually possesses a measure of certainty (the certainty factor). As the system draws new inferences, it calculates their certainty factors according to some heuristic method. This architecture has worked well for selection, diagnosis and consultation applications.

Several other architectures have proven useful. In data-driven forward-chaining systems the problem solving engine operates by selecting one satisfiable rule to execute at a time. At any time, the input data and previous conclusions determine which rules can be satisfied, namely those whose conditions appear true or "certain". Usually, the systems opt

for executing the one rule that has most recently become satisfiable or the one satisfiable rule that is most specific. Once executed, the rule produces new intermediate conclusions that may make additional rules satisfiable. The select-execute cycle then repeats. This architecture has proved useful for modelling cognitive processes and for solving diverse problems requiring very broad, but shallow knowledge. The Hearsay-like or "blackboard" systems emphasize the use of multiple cooperating sub-expert-systems, or "specialists". Each of them examines a global problem-solution database, called the "blackboard", for intermediate relevant results. Generally, these systems segment the blackboard into distinct levels of abstraction and impose on it spatial and temporal dimensions as dictated by the problem domain. Each independent specialist then volunteers to make a contribution, and the potential actions of each are prioritized by a scheduling specialist, which maintains an agenda. This architecture has proved attractive for complex problems in speech, vision, design and planning.

Although the input, output, control component is also of considerable importance, in particular for the system-unfamiliar end-user, we limit ourselves to a few observations. To help amass and maintain these rule bases, most research and commercial knowledge-engineering tools provide various automated aids. These generally include a range of supports from token completion and spelling correction to line-of-reasoning traces, knowledge-base browsing, and automated facilities for system testing and validation.

Rules:

The relations/rules in the knowledge-base, also called production rules, usually take the logical form

$$(P_1 \wedge P_2 \wedge \ldots) \longrightarrow (Q_1 \wedge Q_2 \wedge \ldots). \qquad (4.1)$$

Each rule is highly stylized: with an IF...THEN format and the conditions P_i in the premise. A typical example reads:

IF 1) the infection is primary-bacteremia, AND
2) the site of the culture is one of the sterile sites, AND
3) the suspected portal of entry of the organism is the gastrointestinal tract,

THEN there is suggestive evidence that the identity of the organism is bacteroides.

Each premise is in fact a Boolean combination of one or more clauses, each of which is constructed from a predicate function with an associative triplet (attribute, object, value) as its arguments. Thus, each premise clause typically has the following four arguments

⟨predicate function⟩ ⟨object⟩ ⟨attribute⟩ ⟨value⟩ (4.2)

For example the second clause 2) in the above rule takes the form

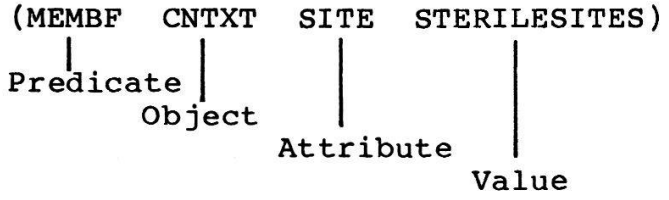

MEMBF is a predicate, and the successive triple says that the site of the current object (an organism, in this case) is a member of the class of sterile sites. A standardize set of 24 domain-independent

. predicate functions (SAME, KNOWN, DEFINITE, MEMBF,...)

and a range of domain-specific

. objects (ORGANISM, CULTURE, INFECT,...),
. attributes (IDENTITY, SITE, CNTXT,...),
. associated values (E.COLI, BLOOD,...),

form the vocabulary of conceptual primitives for constructing the rules. Once encoded in LISP-format the above rule reads:

```
Premise: (AND  (SAME CNTXT INFECT PRIMARY-BACTEREMIA)
               (MEMBF CNTXT SITE STERILESITES)
               (SAME CNTXT PORTAL GI)  )

Action : (CONCLUDE CNTXT IDENT BACTEROIDES TALLY  .7)
```

Schematic Procedure:

The schematic procedure of the essential function mode of a rule-based expert-system such as, for example, MYCIN is illustrated in Table 4.1. On the left-hand side the production rules (R1)-(R6) as part of the knowledge-base are listed. On the right-hand side the derivation chain is shown. The latter follows from the input data, the statements H, K, as indicated under b). Starting at the bottom of the derivation chain, in particular from the conclusion of rule (R6) with a successive search process to satisfy the other rules is called "backward-chaining". Similarly, starting from the available data at the top to arrive finally at the bottom rule and all the preceding ones, is called "forward-chaining".

We present a sample session of MYCIN [16], one of the first and representative expert-systems for medical diagnosis and therapy of infectious diseases.

```
**PATIENT-1**
1) Patients name ?      Fred Smith
   (MYCIN collects data about the patient)
2) Sex ?                Male
3) Age ?                55
```

4) Have you been able to obtain positive cultures
from a site at which Fred Smith has an infection ?
Yes

INFECTION-1

5) What is the infection ?
Primary-bacteremia

6) Please give the data and approximate time when signs
or symptoms of primary-bacteremia (Infection-1) first
appeared: (mo/da/yr) ?
May 5, 1980

The most recent positive culture associated with the
primary-bacteremia (Infection-1) will be referred to as:

CULTURE-1

7) From what site was the specimen for culture-1 taken ?
Blood

8) Please give the data and time when this blood culture
(Culture-1) was obtained: (mo/da/yr) ?
May 9, 1980

The first significant organism from this blood culture
(Culture-1) will be referred to as:

ORGANISM-1

9) Enter the identity of organism-1 ?
Unknown

10) Is organism-1 a rod, or coccus, or ...?
Rod

11) The gram stain of organism-1 ?
Gramneg

. . . . .

. (MYCIN asks more questions)

My therapy recommendations will be based on the following
probable infection(s) and potential causative organism(s):

INFECTION-1: is PRIMARY BACTEREMIA

Item 1: The identity of organism-1 may be PSEODOMONAS-AERUGINOSA
Item 2: The identity of organism-1 may be KLEMSIELLA-PNEUMONIAE

. . . .

46) On a scale 1 to 4, where higher number indicate increasing
severity, how would you rate Fred Smith's degree of sickness?
3

47) Does Fred Smith have a clinically significant allergic
reaction to any antimicrobial agents ?
No

48) Fred Smith's weight in kilograms (or number pounds) ?
70

RECOMMENDATION-1: my preferred therapy recommendation is
In order to cover for Items ‹1 2 3 5 6 › :
Give: GENTAMICIN
Dose: 119 mg (1.7 mg/kg) q8h IV (for IM) for 14 days
Cmts: Modify dose in renal failure
.
.
.
Do you wish to see the next-choice therapy ?
Yes
Which if any of the above drugs do you wish eliminated from consideration ? Clindamycin

RECOMMENDATION-2: next best therapy recommendation ?
In order to cover for Items ‹2 3 4 5 6›:
Give: CHLORAMPHENICOL
Dose: 1 mg (15 mg/kg) q8h IV for 14 days
Cmts: Monitor patient's white count
.
.
.

A Few Knowledge-Based Expert-Systems:

The Table 4.2 [17] gives a list of almost arbitrarily chosen expert-systems. It is representative in the sense that it gives insight into the widely differing application domains, and it also points to the fact that besides of the traditional academic research institutions there are small specialized companies and large industry-based research laboratories deeply involved in this new field of knowledge engineering.

5. AI Impacts

In the preceeding sections we have introduced three important subfields of AI (logic, automated reasoning, expert-systems) and we discuss in this section their present and coming impacts.

Mathematics:

In Chapter 2 of this section we gave an introduction into (classical) Propositional and first-order Predicate Logic since it provides a useful theoretical basis for the computer analysis of "reasoning", "knowledge" and "knowledge processing". In addition of these classical logic calculus there also exists what is called "Non-Standard Logics" [18]. Such logics can be roughly divided into two groups: those that rival classical logics and those which extend it. In the first group we place the multi-valued logics, fuzzy logic an intuitionistic logic, while the socond encompasses modal and temporal logics.

Rival systems of logic do not differ from classical Propositional or Predicate Logic in terms of the language employed. Rather, rival logics differ in that certain of the theorems of classical logic are rendered false in the non-standard systems. A typical example of this concerns the law of the excluded middle, A or not A. This is provable in clas-

sical logic but not in either intuitionistic logic or in any of the standard systems of 3-valued logic.

Logics, which extend classical logic, sanction all the theorems of classical logic but, generally, supplement it in two ways. Firstly, the languages of these non-standard logics are extensions of those of classical logic, and secondly, the theorems of these non-standard systems supplement those of classical logic. Usually, such supplementation is provided by the enriched vocabulary of these non-standard systems. For example, modal logic is enriched by the addition of two new operators L (it is necessary that) and M (it is possible that). Under this new regime the sentence $A \rightarrow MA$ is taken as axiomatic. The addition of such axioms, and appropriate rules of inference involving these operators, facilitates the derivation of theorems which are not even expressible in the language of the predicate calculus. The study of and the interest in non-standard logics is greatly enhanced by the problems in AI, whereby the transition between computer science and mathematics (or philosophy?) becomes more and more fluid. The interaction and interdependence between these two fields is of considerable importance and probably will even increase.

Our discussion in Section 3 aimed to show the interest of theorem proving programs, so called "Theorem Provers", for abstract and formal mathematics. If the performance of these systems improves further, we may expect that they will be of invaluable help in the determination of the consistency of a mathematical theory, quite apart from the fact that they allow for the proving or disproving of theorems.

Theory Applications:

In the list of knowledge-based expert-systems in section 4 we have cited MACSYMA [19] and SMP [20]. MACSYMA (Project MAC's SYmbolic MAnipulation System) is a large programming system written in LISP and used for performing symbolic as well as numerical mathematical manipulations. It was developed by the Mathlab Group of the MIT Laboratory for Computer Science (formerly Project MAC) and is currently distributed by Symbolics, Inc.. With MACSYMA the user can differentiate, integrate, take limits, solve systems of linear or polynomial equations, factor polynomials, expand functions in Laurent or Taylor series, solve differential equations (using direct or transform methods), compute Poisson series, plot curves, and manipulate matrices and tensors. MACSYMA has a language similar to ALGOL-60 to permit the user to write his own program for transforming symbolic expressions. It is written in (MAC)LISP. Another, more recent system, called SMP [20], is written in the C-language of the UNIX operating system. Similar systems and algebraic manipulation frameworks of the kind described above have proved of considerable help in theory calculations of high energy physics as well as other branches of physics; we mention: REDUCE [21], SCHOONSHIP [22], MAPLE [23] ASHMEDAI [24], ORTOCARTAN [25] and others. The REDUCE system distinguishes itself from many others in that it allows for

the switching from algebraic to symbolic formula manipulations (and back) in the successive flow of a data evaluation. Since it is built in the framework of Standard LISP [26], which can be accessed easily during the course of a calculation, REDUCE is doubtless one of the most flexible systems of its kind. The considerable strength of all these systems lies in the numerous applications in the fields of applied mathematics, theoretical physics and engineering. Computer symbolic manipulation has hitherto been utilized primarily in three major areas of theoretical physics: 1) Feynman diagram evaluation, 2) Celestical Mechanics, 3) General Relativity. In the first case, the basic procedure is to evaluate products of Dirac gamma matrices; then either a Feynman-parametric form may be generated, and integrated numerically, or analytical results for integrals of each type of term may be substituted from a table. Numerical procedures were obligatory for the very high order calculations carried out in massive QED; recently massless QCD calculations have usually been amenable to purely analytical (symbolic) techniques. In celestical mechanics, Poisson trigonometric series approximations to orbits are used, and their parameters are determined symbolically by substitution into differential equations of motion. In general relativity, symbolic manipulation has been used to simplify complicated tensor expressions. A notable feature of all these applications is that in realistic cases huge intermediate expressions are usually generated; much of this intermediate complexity often cancels out in the final result, leaving a simple answer. Spectacular examples of this phenomenon are often seen in Feynman diagram calculations.

Knowledge Engineering:

For nearly 500 years, books have been the primary means of storing knowledge and transmitting it between humans. The development of printing made an enormous impact on human culture by distributing knowledge in large quantities. However, because it could not explain or apply its knowledge directly, the (passive) book left much of the work to the individual reader. As technology progressed and economics advanced, knowledge transfer and knowledge processing became a bottleneck in cultural development. The computer now has created the opportunity and also the need to enhance the distribution of knowledge. This fact necessitates a deeper understanding of knowledge, its manipulation and processing, as well as its useful practical application has given rise to the expression: "Knowledge Engineering". Knowledge-based systems address themselves to that need, with new trends in three directions:

- new and speculative products,
- applications in commercial and industrial organizations,
- closer integration of knowledge systems and data processing.

Knowledge engineering entails several other activities such as: expert-system tools (or shells), AI languages, higher performance computers, better inference engines, etc., etc..

Expert-system tools for research and experimentation address the needs of AI researchers, offering a diversity of functions within the structure of a programming environment such as MACLISP or INTERLISP and help the AI programmer to cope more easily and more quickly with a knowledge engineering problem. They grew from specific expert-systems by dropping the stored data and rules in the knowledge-base; examples are: EMYCIN from MYCIN, KAS from PROSPECTOR, EXPERT from CASNET (see Ref. 1) and so on. There is a variety of languages being used in AI programming such as: LISP [3], PROLOG [4], LOGLISP [27], SMALLTALK [28], C [29], PASCAL [39], MODULA-2 [31], PORTAL [32] etc., which all have their fruitful particularities. One may expect and hope, as time goes on, that all this versatility will be integrated into one single, high performance language complex.

Economics:

The economic impacts of knowledge engineering can be surmised from the list of institutions investing at present in AI (see section 1). As another piece of evidence we add Fig. 5.1 which gives the growth prediction of the annual AI market as published by the International Resource Development Inc. [17]. Several industrial and commercial application areas are considered as likely to allow for the exploitation of the knowledge engineering techniques: expert-systems for automotive equipment and repair, heuristic control systems for military functions and industrial automation, knowledge-aided design systems, automated interpretation systems for sensors and instruments. One, however, should keep in mind that the flow of the knowledge technology into all sections of the economy is rather difficult to predict since it concerns something new - namely knowledge!

Very recently, three types of commercial applications have emerged, viz. tools for the construction of knowledge systems (KEE, KES, OPS5,...), specialized hardware and systems software for general AI programming (personal workstations by HP, Tektonix, Xerox,...), and finally the commercial expert-systems for giving problem-specific artificial advice. Applications of this type have appeared in several different fields such as CAD, data interpretation, computer selection, mathematical problem solving and many others. The Fig. 5.2, which was taken from the excellent article in Ref. 7, helps the reader to orient himself in the variety of the current and projected state of the commercialization. The innermost hexagon represents the major ingredients of the knowledge systems technology, and the three rings indicate the increasing commercialization. The first ring shows the type of products now available; in particular the supporting software and hardware, the knowledge-engineering tools and equipments, and the knowledge system applications. The next ring portrays the primary areas of new products, anticipated in the next three years. In the outermost ring the key, mid-term commercial targets are shown, which are expected to be met by 1990.

Social and Economical:

Knowledge systems may also be expected to bring about changes in economic and social institutions. We have illustrated this fact by Fig. 5.3.

Knowledge transfer has given rise to service professions and institutions such as accounting, legal profession, etc. (see top-right). The new technologies: knowledge engineering, personal computing, telecommunications (as indicated on the left-hand side) allow for new ways of knowledge transfer, distribution and exploitation (bottom-left).As new knowledge is being developed and becomes available in an amount which hardly can be handled by individual humans, one may expect a radically new basis for the (specialized) knowledge transfer and access, and one may expect that many individuals and companies will attempt to meet old needs with new products leading in turn to new professions, institutions and also new needs as they are indicated in Fig. 5.3 (see bottom-right).

7. Summary

In this paper we have considered the artificial intelligence (AI) subfields: logic, theorem proving/automated reasoning, expert-systems. We aimed to give an introduction into the essentials of their reasoning techniques, to provide a limited insight into the practical use of all these activities and to show the present interest and most recent strong support, in order to attract the readers attention to the highly interesting developments and questions being currently dealt with in AI. This purpose guided us to an obviously sketchy and incomplete discussion of the possible impacts one may expect. One clearly should abstain from overemphasising a particular scientific domain, but one should equally recognize its achievements and potential impacts - this was the prime goal of this report.

Acknowledgements

The author thanks N. Buss, E. Dubuis and Drs. T. Lindelof, D. Ryter for their reading of the manuscript, and Dr. P.Vogel, Prof. C. Joseph for their kind interest and support.
The author also thanks the CERN Theoretical Physics Division, where part of this work was done, for its kind hospitality.

References

[1] A. Barr and E.A. Feigenbaum, The Handbook of Artificial Intelligence: I+II+III, HeurisTech Press, Stanford CA (USA), 1981.

[2] E. Rich, The Gradual Expansion of Artificial Intelligence, IEEE Computer Society, May 1984, pp.4.
F. Hayes-Roth, Knowledge-Based Expert Systems, IEEE Computer Society, October 1984, pp. 263.
P. Kinnucan, Computers That Think Like Experts, High Technology, January 1984.
K.N.Karna, Artificial Intelligence for Man-Machine Interface, September 1984, pp.8 (and further articles in this issue).
R.L. Lillestrand, Seminar Notes, March 1984.

[3] P.H. Winston and B.K.P. Horn, LISP, Addison-Wesley Publishing Company, Reading MA (USA), 1984 (2nd Edition).
G.L. Steele Jr., Common LISP, Digital Press (USA), 1984.
C. Weissman, LISP 1.5 Primer, Dickenson Publishing Company, Inc., Belmont CA, 1967.
L. Siklossy, Let's Talk Lisp, Prentice-Hall, Inc., Englewood CA, 1976.

[4] W.F. Clocksin and C.S. Mellish, Programming in Prolog, Springer-Verlag, Berlin, 1981.
K.L. Clark and F.G. McCabe, Micro-Prolog: Programming in Logic, Prentice-Hall International Series in Computer Science, 1984.

[5] L. Wos, Achievements in Automated Reasoning, SIAM News, July and September 1984.
L. Wos, Automated Reasoning: Real Uses and Potential Uses, IJCAI Proceedings, 1983.

[6] Note, this report is for the Swiss scene.

[7] partially from: F. Hayes-Roth, Knowledge-Based Systems, IEEE Computer Society, October 1984, pp.263.

[8] M. English, EEC Esprit, EF Paris Conference 1984, pp.19.

[9] H. Gallaire, Europas Weg zu AI, COM Siemens-Magazin für Computer & Communications, January 1985, pp.27.

[10] K.G. Wilson, R.N. Sudan and K.M. King, A Proposal to the National Science Foundation to Establish the: Center for Theory and Simulation in Science and Engineering, Cornell University, CTSSE, 84-2 (and Appendix).
L. Smarr et al., PROPOSAL: A Center for Scientific and Engineering Supercomputing, University of Illinois at Urbana-Champaign, 1984.

[11] J.A. Robinson, Logic: Form and Function, Edinburgh University Press, Edinburgh, 1979 [we recommend this reference for a balanced appreciation of the historical development of this field].
C.L.Chang and R.C.T. Lee, Symbolic Logic and Mechanical Theorem Proving, Academic Press, New York, 1973.
A. Bundy, The Computer Modelling of Mathematical Reasoning, Academic Press, New York, 1973.

D.W. Loveland, Automated Theorem Proving: A Logical Basis, North Holland Publishing Company, Amsterdam, 1978.
for a recent tutorial see: B. Humpert, "Theorem Proving with First-Order Predicate Logic: I", HASLER F+S AI/111, March 1985.

[12] L. Wos, R. Overbeek, E. Lusk, J. Boyle, Automated Reasoning: Introduction and Applications, Prentice Hall, Inc., New Jersey, 1984.
Ed.J. Siekman and G. Wrightson, Automation of Reasoning: 1+2, Springer Verlag, Berlin, 1983.

[13] R.S. Boyer and J.S. Moore, A Computational Logic, Academic Press, N.Y. 1979.
R.S. Boyer and J.S. Moore, The Correctness Problem in Computer Science, Academic Press, London, 1981.

[14] see: L. Wos et al., in Ref. [12].

[15] F. Hayes-Roth, D.A. Waterman and D.B. Lenat, Building Expert-Systems, Addison-Wesley Publishing Company, Reading MA (USA), 1984.

[16] B.G. Buchanan and E.H. Shortliffe, Rule-Based Expert-Systems: The MYCIN Experiments of the Stanford Heuristic Programming Project, Addison-Wesley Publishing Company, Reading MA (USA), 1984.

[17] from: R.L. Lillestrand, Seminar Notes, March 1984.

[18] R. Turner, Logic for Artificial Intelligence, Ellis Horwood Limited, Sussex, 1984.
V.R. Pratt, Six Lectures on Dynamic Logic, MIT/LCS/TM-117, 1979.

[19] The Mathlab Group, MACSYMA Reference Manual: Vol.I+II, Laboratory for Computer Science MIT, December 1983; Computer Algebra, Scientific American 245, No. 6, December 1981, pp. 136.

[20] S. Wolfram, The SMP Reference Manual, Inference Corporation, Los Angeles, 1983; Doing Physics with Computers, Physics Today, Vol.36, No.5, May 1983.

[21] A.C. Hearn, REDUCE User's Manual: Version 3.1, The Rand Corporation, Santa Monica CA, April 1984.

[22] M. Veltman, (unpublished), 1967; H. Strubbe, Comp. Phys. Comm. 8 (1974) 1.

[23] K.O. Geddes, G.H. Gonnet and B.W. Char, MAPLE User's Manual: 3rd Edition, Department of Computer Science, University of Waterloo, Waterloo (Canada) Research Report CS-83-41, 1983.

[24] M. Levine, J. Comp. Phys. 1 (1967) 454; Ashmedai User's Guide, CMU preprint COO-3066-44, January 1975.

[25] A. Krasinski, Z. Otwinowski and M. Perkowski, The System ORTOCARTAN: Detailed Description, Copernicus Astronomical Center, Warsaw University, October 1979.

[26] J. Fitch, Manual for Standard LISP on IBM System 360 and 370, University of Utah Technical Report No. TR-6, August 1976.

J.B. Marti, A.C. Hearn, M.L. Griss and C. Griss, The Standard LISP Report, University of Utah, UCP-60, January 1978.

[27] J.A. Robinson, E.E. Sibert and K.J. Greene, The LOGLISP Programming System, Logic Programming Research Center, Syracus University.
J.P. Muller, LOGLISP: Study and Modification of a Logic Programming Language, EPFL-Report, 1984.

[28] A. Goldberg and D. Robson, Smalltalk-80: The language and its Implementation, Addison-Wesley Series in Computer Science, 1983.

[29] A. Kelly and I. Pohl, A Book on C, The Benjamin/Cummings Publishing Company Inc., 1984.
B.W. Kernighan and D.M. Ritchie, The C Programming Language, Prentice-Hall Inc., Engleswood Cliffs NJ, 1978.

[30] R. Zaks, Introduction to Pascal, Sybex Inc., 1980.

[31] N. Wirth, Programming in Modula-2, Springer-Verlag Berlin, 1983.

[32] A. Businger, PORTAL Sprachbeschreibung, Zentrallabor Landis & Gyr, Zug, 1983.

Table Captions

Table 2.1: Truth table of the logical connectors in the first order Propositional/Predicate Logic.

Table 2.2: Truth table checking of Eq. 2.1.

Table 4.1: Simplified example of the derivation chain in the reasoning component of a rule-based expert-system.

Table 4.2: Sample list of expert-systems in a variety of fields.

Figure Captions

Figure 5.1: Annual growth of the AI market as predicated by International Resource Development Inc.

Figure 5.2: The commercialization phases of the knowledge system technology (from Hayes-Roth, Ref.[2]).

Figure 5.3: The impact of knowledge systems on the economic and social institutions.

G	H	∼G (not)	G ∧ H (conjunction)	G ∨ H (disjunction)	G → H (if..then)	G ⟷ H (if and only if)
T	T	F	T	T ✓	T	T
T	F	F	F	T	F	F
F	T	T	F	T	T ✓	F
F	F	T	F	F	T	T

Table 2.1

H	U	R	(H∧U)	F_O
T	T	T	T	T
T	F	T	F	T
F	T	T	F	T
F	F	T	F	T
T	T	F	T	F
T	F	F	F	T
F	T	F	F	T
F	F	F	F	T

Table 2.2

(R1)	A — E		
(R2)	B — D	H — A	(R3)
(R3)	H — A	A — E	(R1)
(R4)	E ∧ G — C	E ∧ K — B	(R5)
(R5)	E ∧ K — B	B — D	(R2)
(R6)	D ∧ E ∧ K — C	D ∧ E ∧ K — C	(R6)
(R7)	G ∧ K ∧ F — A		
	a) Rules	b) Data: H, K	c) Deriv. Chain

forward chaining
backward chaining

Table 4.1

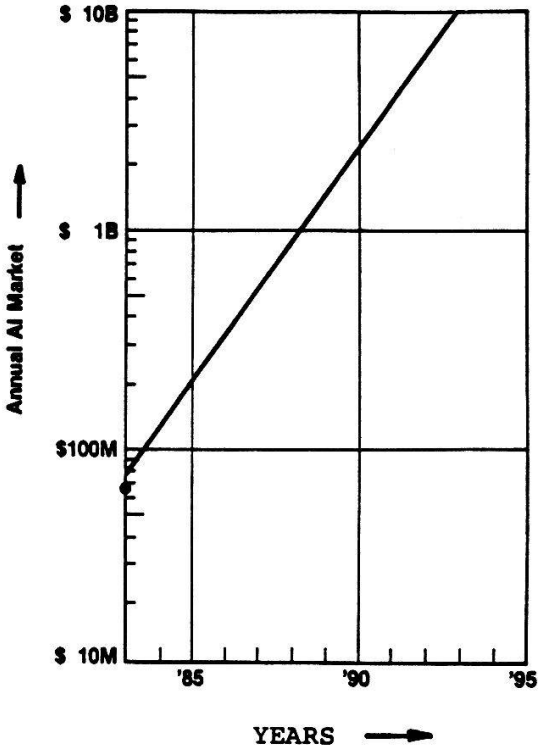

Fig. 5.1

KNOWLEDGE TRANSFER ⟸ SERVICE PROFESS.+INSTITUTIONS

NEW TECHNOLOGIES
K-ENGINEERING +
PERSONAL COMP. +
TELECOMM'S

ACCOUNTING, LAW,
CONSULTING, TEACHING,
BOOK PUBLG. + LIBRARIES,
SCHOOLS+UNIVERSITIES,
ETC.

NEW BASIS FOR
K-DISTRIBUT. & EXPLOIT. ⟹ NEW PRODUCTS,
PROFESSIONS,
INSTITUTIONS, NEEDS

HOME BANKING,
FINANCE PLANING,
CENTRAL ELECTRONIC UNIV'S.
ELECTRONIC LIBRARIES,
ELECTRONIC ACCOUNTANTS +
CONSULTANTS
ELECTRONIC LAWYERS
EXPERT - EXPERT K-TRANSFER
ETC.

Fig. 5.3

Name	Function	Builder
ACE	Manages Telephone-Cable Maintenance	AT&T Bell Labs
ADA, TUTOR	Teaches ADA Programming	Computer Thought
AIRPLAN	Manages Take-off and Recovery of Airplanes	U.S. Navy for USS Carl Vinson
DENDRAL	Is Mass Spectrometry Analyzer	Stanford University
DIP METER ADVISOR	Interprets Oil-Well Drilling-Bit Sticking Problems	Teknowledge for Elf-Acquitane
EXPLORER	Is User Interface to Complex Geological Program	Cognitive Systems
PROSPECTOR	Aids Mineral Exploration	SRI International
INDUCE/ PLANT	Diagnoses Soybean Disease	University of Illinois
MYCIN	Diagnoses Blood Diseases	Stanford University
PUFF	Diagnoses Lung Ailments	Stanford University
MOLGEN	Designs Experiments in Molecular Biology	Stanford University
MACSYMA	Solves Mathematical Formulae	MIT
SMP	Does Symbolic Mathematics	Inference Corporation

Table 4.2

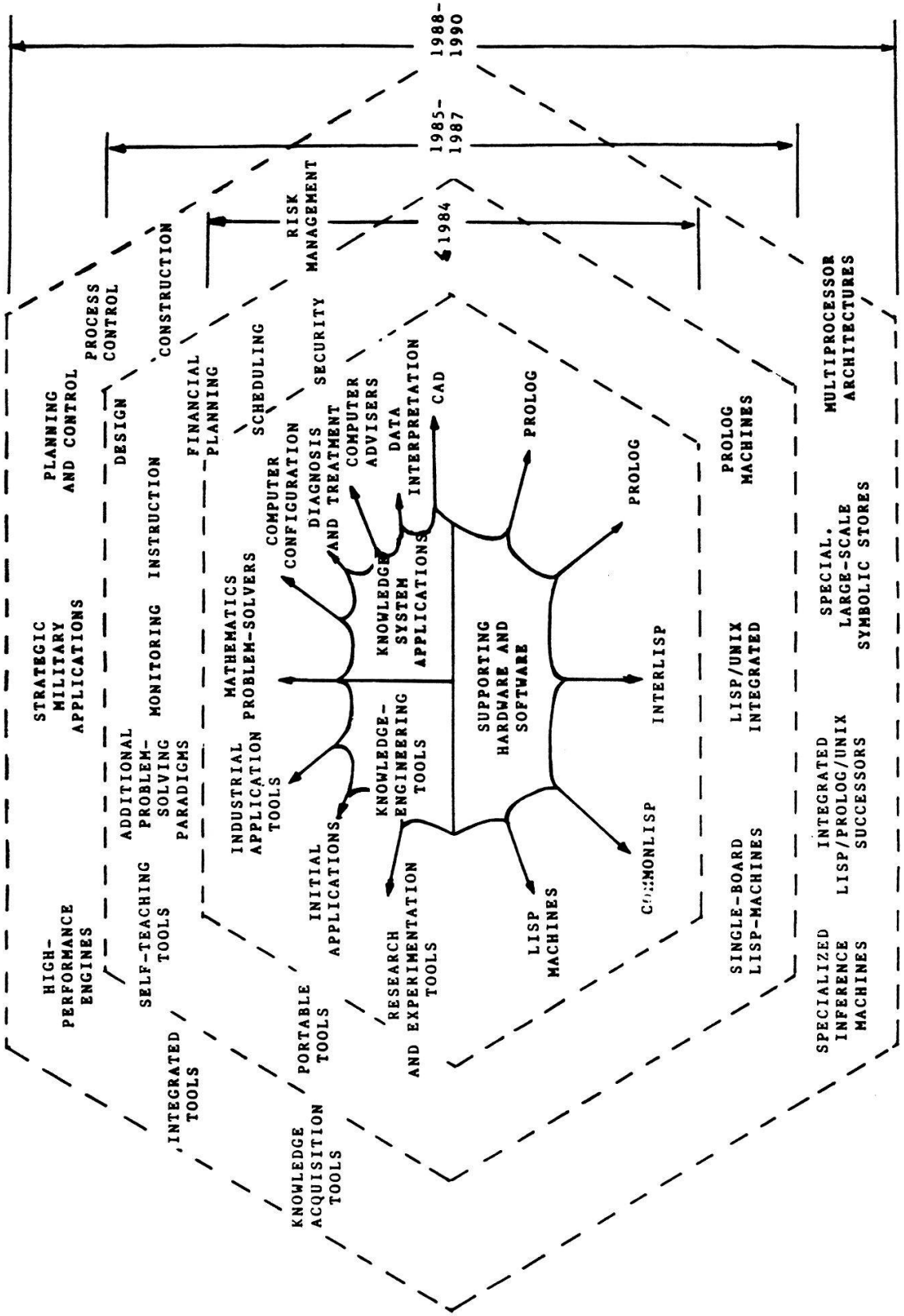

The commercialization of knowledge system technology.

Fig. 5.2

ESPACE DE PHASE ET GRANDS ORDRES DE PERTURBATION

Vincent Rivasseau (CPT, Ecole Polytechnique, F91128 Palaiseau)

Abstract The phase space expansion, a technical device of constructive field theory, is also useful for the rigorous analysis of large orders of perturbation theory. In particular one can study with it the singularities which occur in the Borel transform of the perturbation series and govern their large order behavior, such as "instantons" or "renormalons".

Résumé Le développement dans l'espace de phase, une technique de théorie constructive des champs, peut aussi s'appliquer à l'analyse du comportement aux grands ordres de la théorie perturbative des champs. En particulier il permet une étude rigoureuse des singularités de la transformée de Borel du développement perturbatif ("instantons" ou "renormalons").

Le développement dans l'espace de phase a été introduit par Glimm et Jaffe [1] pour la construction de théories des champs superrenormalisables comme φ^4_3, puis développé récemment et appliqué à la construction de modèles strictement renormalisables par Feldman et al. [2]. C'est une technique de découpage à la fois dans l'espace direct et dans l'espace des moments très proche des idées initiales de Wilson sur le groupe de renormalisation. Comme le groupe de renormalisation, le développement dans l'espace de phase est né d'une réflexion approfondie sur la théorie des perturbations; comme lui, il permet souvent de réduire la résolution d'un problème apparemment difficile, car comportant beaucoup de degrés de libertés, à la résolution de problèmes plus simples portant sur des systèmes qui n'ont que peu de degrés de libertés. Nous illustrerons ce point de vue en prenant pour exemple l'étude des grands ordres de la théorie φ^4 par la méthode de Lipatov, puis nous évoquerons le problème des "renormalons de φ^4_4".

I. Méthode de Lipatov.

Le modèle φ^4 massif (de masse 1) Euclidien en dimension d discrétisé sur un réseau $c\mathbb{Z}^d \cap \Lambda$ de maille c, avec cutoff de volume Λ et des conditions au bord X est défini par la mesure normalisée:

$$Z_X(\Lambda,c)^{-1} \exp\{ -(1/2) <\varphi,(-\Delta_X+1)\varphi> - g \sum_{x\in\mathbb{Z}^d\cap\Lambda} \varphi^4(x) \} D\varphi \qquad (I.1)$$

où $D\varphi$ signifie $\prod_{x\in c\mathbb{Z}^d\cap\Lambda} d^d\varphi(x)$. Des quantités simples ayant un développement perturbatif renormalisé intéressant sont par exemple en dimension 1,2 ou 3 la pression:

$$p(g) = \lim_{c\to 0,\Lambda\to\infty} p_{\Lambda,c} = \sum_n (-g)^n a_n^R \; ; \; p_{\Lambda,c} = 1/|\Lambda| \; \mathrm{Log}\, Z_X(\Lambda) \qquad (I.2)$$

ou, en dimension 4, la fonction de Schwinger à 6 points, à moments externes nuls:

$$S_6(g) = \sum_n (-g)^n a_n^R \qquad (I.3)$$

(si l'on utilise la prescription de renormalisation BPHZ habituelle (soustraction à moments externes nuls), la pression ou les fonctions à 2 et 4 points ont, par définition, un développement renormalisé trivial à moments externes nuls). Dans (I.2) ou (I.3), a_n^R désigne la somme des amplitudes renormalisées des graphes connexes d'ordre n (respectivement à 0 ou 6 pattes externes).

La méthode de Lipatov [3] prédit pour l' ordre n de perturbation le comportement:

$$a_n^R \simeq_{n\to\infty} n!\, a^n n^b c\,(1+O(1/n)) \qquad (I.4)$$

où a, b et c sont des constantes, et a, qui ne dépend que du modèle, vaut:

$$a = \exp\{-\inf S(\varphi) + 2\}\ , \quad S(\varphi) = 1/2\,\{\int(\nabla\varphi)^2 + \varphi^2\} - \mathrm{Log}\int\varphi^4 \qquad (I.5)$$

Remarquons qu'avec cette prédiction, la transformée de Borel $B(t)= \sum_n(-t)^n b_n$, $b_n = a_n^R/n!$, a sa première singularité sur l'axe réél négatif au point $-1/a$. C'est une singularité de type "instanton". Donnons une brève justification de cette prédiction pour a, lorsque le nombre de degrés de libertés du système n'est pas trop grand; plus précisément nous supposerons que le nombre de sites du réseau $c\mathbb{Z}^d \cap \Lambda$ n'est que de l'ordre de n^ε, ε étant petit. En admettant alors que les effets dûs à la renormalisation puissent être négligés, ainsi que la restriction de connexité des graphes, on obtiendrait:

$$\begin{aligned}[a_n^R/n!\,]^{1/n} &\simeq [1/(n!)^2 \int\{\int\varphi^4\}^n \exp\{-(1/2)\int(\nabla\varphi)^2+\varphi^2\}\, D\varphi\,]^{1/n} \\ &= [n^2/(n!)^{2/n}]\,(\sqrt{n})^{n^{\varepsilon-1}}\, \| \exp -S_n(\varphi) \|_n \quad (S_n \text{ est un analogue de S mais avec cutoffs}) \\ &\to_{n\to\infty} e^2 \| \exp -S(\varphi) \|_\infty = \exp\{-\inf S(\varphi) + 2\} \quad (\text{car } \varepsilon<1) \qquad (I.6)\end{aligned}$$

II. Le développement dans l'espace de phase

Le principe du développement est de découper en "tranches" de moments qui suivent une progression géométrique (ici, pour un problème ultraviolet ces tranches correspondent approximativement à des moments d'ordre $1, M, M^2$,..etc..), et de découper l'espace direct selon des réseaux successifs de cubes de cotés correspondants $1, M^{-1}, M^{-2}$,..etc... Dans les cas simples comme ici où la perturbation se fait autour d'une mesure gaussienne évidente on peut obtenir le découpage en moments par simple découpage de la covariance (dans des cas plus compliqués (comme les théories de jauge non abéliennes) on pourrait se servir de transformations de bloc-spin). En représentant l'espace direct horizontalement et l'espace des moments verticalement, on obtient la théorie des perturbations sous la forme de propagateurs horizontaux reliant des vertex qui sont eux mêmes des lignes verticales

reliant quatre demi-propagateurs qui peuvent bien sûr être de moments différents. Dans cette représentation on a à la fois décroissance exponentielle horizontale (dans le réseau de cubes adaptés à l'échelle des moments) parce que dans chaque tranche de moments il y a un cutoff infrarouge d'échelle correspondante, et décroissance exponentielle "verticale" (qui n'est autre que le "power counting" habituel, mais vu selon une échelle logarithmique) pourvu que les graphes considérés soient convergents ou renormalisés [2]. On conçoit donc que des techniques de développement de haute température (cluster expansion, Mayer exapnsion) soient applicables, à condition de les généraliser convenablement, c'est à dire de les appliquer à la fois dans les directions horizontales (espace habituel) et verticale (espace des moments). Donnons une idée du type de raisonnements que l'on peut alors utiliser; dans le cas du problème de Lipatov, pour rendre rigoureux l'argument schématisé par l'équation (I.6), on peut distinguer deux cas, selon que les graphes de la perturbation, avec leurs vertex et leurs propagateurs, s'étalent sur beaucoup de cubes (de toutes tailles) par rapport à n, l'ordre de perturbation considéré, ou selon qu'ils sont concentrés dans un petit nombre de cubes, "densément peuplés". Dans le premier cas la décroissance exponentielle dans chaque direction assure que la contribution correspondante est négligeable; dans le second cas, le nombre de degrés de libertés effectif est faible, et l'argument (I.6) peut alors être rendu rigoureux. Dans le cas superrenormalisable (φ^4_1,φ^4_2 ou φ^4_3) on obtient les résultats (en dimension 1 ou 2 l'espace de phase n'est pas indispensable):

Théorème ([4])

Le rayon de convergence de la transformée de Borel du développement perturbatif est a^{-1} comme prédit par la méthode de Lipatov, et la première singularité dans le plan de Borel se trouve sur l'axe réél négatif au point $-a^{-1}$.

III. Renormalons

Dans le cas de théories strictement renormalisables comme φ^4_4, d'autres singularités, sur l'axe réél positif, dues à la renormalisation et donc appelées renormalons [5], sont plus proches de l'origine du plan de Borel que les instantons et doivent donc dominer le comportement aux grands ordres. Là encore le développement dans l'espace de phase devrait être très utile pour prouver l'existence de ces singularités et analyser rigoureusement leur structure, un programme important pour la compréhension du développement de Wilson, des règles de somme de QCD, etc... [6].

Voici un exemple d'un résultat déja obtenu dans cette direction:

Theorème [7]

Le rayon de convergence de la transformée de Borel du développement renormalisé de ϕ^4_4 est au moins égal à la valeur exacte $(2/\beta_2)$ conjecturée par le calcul de la position du premier renormalon.

Donnons une idée de la démonstration; par une resommation des contretermes "inutiles" [2] les plus divergents, on peut transformer le développement renormalisé en un développement "partiellement renormalisé" (mais toujours sans divergences ultraviolettes) avec des constantes de couplage effectives $\lambda_i \simeq \lambda/(1-\beta_2\lambda i)$, où i désigne le Log de l'énergie, λ la constante de couplage renormalisée et β_2 le premier coeeficient de la fonction β. Ce développement partiellement renormalisé obéit alors à la borne de Lipatov [7], le renormalon appparaissant comme des divergences ultraviolettes dans la transformée de Borel au point $t=2/\beta_2$ [5], qui se trouve être plus près de l'origine que le premier instanton à $-a^{-1}$ par un facteur 2/3. Pour la théorie φ^4_4 ordinaire il est difficile de prouver que ces divergences au point $2/\beta_2$ ne se compensent pas miraculeusement. Par contre dans le modèle à N composantes, N grand (mais fini!), une preuve de l'existence du premier renormalon sur l'axe positif nous semble facile (sans même faire appel à la borne de Lipatov, car à N grand les instantons sont loin de l'origine dans le plan de Borel), et l'on doit aussi dans ce cas pouvoir rendre rigoureux le développement de Wilson et les résultats ordre par ordre en 1/N de [6].

REFERENCES

[1] J. Glimm, A. Jaffe, Fort. der Phys.21, 327 (1973).

[2] J. Feldman, J. Magnen, V. Rivasseau, R. Sénéor, Comm. Math Phys. 98,273(1985); 100,23 (1985); 103,67 (1986); et papiers à paraître.

[3] L. Lipatov, Sov. Phys. JETP 44, 1055(1976) et 45, 216 (1977); E. Brézin, J.C. Le Guillou et J. Zinn Justin, Phys. Rev. D15, 1544 (1977).

[4] T. Spencer, Comm. Math. Phys 74, 273 (1980); S. Breen, Comm. Math. Phys. 92, 179 (1983); J. Magnen, V. Rivasseau, Comm. Math. Phys. 102, 59 (1985); J. Feldman, V. Rivasseau, à paraître dans Annales de l'Institut Henri Poincaré.

[5] G. Parisi, Phys. Rep. 49, 215 (1979)

[6] F. David, Nucl. Phys. B209 433 (1982); M. Bergère, F. David, Phys. Lett. 135B, 412 (1984)

[7] J. Magnen, F. Nicolo, V. Rivasseau, R. Sénéor, preprint Ecole Polytechnique, à paraître dans Comm. Math. Phys.; J. Feldman, V. Rivasseau, non publié.

RECHERCHE DE PARTICULES SUPERSYMETRIQUES

P. Sorba, LAPP, B.P. 909, 74019 Annecy-le-Vieux Cedex, France

Abstract : Si la supersymétrie est une symétrie de la nature, c'est à travers la brisure de cette symétrie qu'elle pourra être observée. Dans le cas où cette brisure a lieu aux énergies maîtrisables aujourd'hui ($\sim$ 100 GeV), des partenaires supersymétriques des particules usuelles devraient être observés dans les expériences $p\bar{p}$ au SPS ou e^+e^- au LEP ou au SLC. Mais si l'échelle de brisure est bien plus élevée, elle permettra d'autres spéculations, à savoir l'identification des quarks et des leptons comme partenaires fermioniques de supermultiplets de Goldstone.

1. Introduction

Il n'est bien sûr pas question de faire ici une revue aussi bien de la phénoménologie que des modèles théoriques envisagés en particules élémentaires autour de la supersymétrie. J'ai sélectionné dans cette contribution un exemple de détection de particules supersymétriques avec des faisceaux e^+e^- polarisés, (une étude très complète des possibilités de détection de particules supersymétriques à LEP peut être trouvée dans le rapport jaune du CERN noté en réf.[1]). Je commenterais ensuite une étude dans laquelle quarks et leptons apparaissent comme partenaires supersymétriques de champs de Goldstone dans une théorie supersymétrique dont le groupe de symétrie interne est spontanément brisé.

2. Polarisation et supersymétrie dans les expériences e^+e^-

Il est assez naturel de se demander si la polarisation des faisceaux $e^\pm$ ne serait pas utile dans la recherche de particules supersymétriques, ces dernières se distinguant des particules ordinaires d'abord par leur spin, et leurs propriétés chirales (ainsi bien sûr que par leur masse).

Dans les expériences du SLC, un des deux faisceaux sera complètement polarisé. Grâce aux récents progrès sur les problèmes de spin dans les anneaux de stockage, il apparaît aussi possible aujourd'hui de produire des faisceaux $e^\pm$ hautement polarisés dans la première phase de LEP, et peut-être même à plus haute énergie. Les effets de depolarisation pourraient être contrôlés pour des énergies de l'ordre de 50 GeV. La polarisation longitudinale serait obtenue grâce à des rotations de spin dont la mise en place constitue

surtout un problème financier.

Une étude détaillée de la production à partir de faisceaux $e^{\pm}$ polarisés (mais de particules sortantes non polarisées) des leptons et de quarks scalaires[2] ainsi que des partenaires fermioniques des bosons de jauge[3] a été effectuée : nous indiquons ici quelques résultats.

a) Production de leptons et de quarks scalaires

Deux quantités pourront être observées : l'asymétrie longitudinale $\tilde{A}_{//}$ et l'asymétrie transverse ou azimuthale $\tilde{A}_{\perp}$. Notons que l'observation de $\tilde{A}_{\perp}$ nécessite la polarisation des deux faisceaux, alors que $\tilde{A}_{//}$ peut être étudiée à partir d'un seul faisceau polarisé.

Considérons par exemple la production de $\tilde{\mu}$: les deux asymétries longitudinales $A_{//}$ relatives à μ_L et μ_R respectivement (i.e. $e^+e^- \to \tilde{\mu}_x^+\tilde{\mu}_x^- \to \mu_x^+\mu_x^- \tilde{\gamma}\tilde{\gamma}$ avec x = L ou R) et obtenues à partir des $\tilde{A}_{//}$ après les désintégrations séquentielles $\tilde{\mu}^{\pm} \to \mu^{\pm}\tilde{\gamma}$ sont grandes, très différentes du cas standard $e^+e^- \to \mu^+\mu^-$ et opposées en signe. Elles doivent par suite constituer un bon signal pour la production de muons scalaires si $\tilde{\mu}_L$ et $\tilde{\mu}_R$ ne sont pas dégénérés en masse. Dans le cas où $\tilde{\mu}_L$ et $\tilde{\mu}_R$ ont même masse, la somme des deux contributions redonnerait le même résultat que $e^+e^- \to \mu^+\mu^-$. L'asymétrie transverse $A_{\perp}$ quant à elle présente un changement de signe par rapport au cas $e^+e^- \to \mu^+\mu^-$, et cet effet est très prononcé autour de $\sqrt{s} = 100$ GeV si le muon scalaire n'est pas trop lourd. Le même type d'analyse peut être obtenu pour les quarks scalaires. Mentionnons une propriété commune à tous ces processus d'annihilation, à savoir que $\tilde{A}_{//}$ est maximum quand $\tilde{A}_{\perp}$ est minimum, et vice-versa.

Pour les processus $e^+e^- \to \tilde{e}^+\tilde{e}^- \to e^+e^-\tilde{\gamma}\tilde{\gamma}$ on doit ajouter les contributions correspondant à l'échange de jauginos, c'est-à-dire considérer aussi les réactions $e_R^+e_R^- \to \tilde{e}_L^+\tilde{e}_R^-$ et $e_L^+e_L^- \to \tilde{e}_R^+\tilde{e}_L^-$. Il y a à nouveau des différences nettes avec la réaction standard $e^+e^- \to e^+e^-$. L'asymétrie longitudinale est sensible pour des valeurs petites de l'angle polaire θ à la masse du photino, et sa courbe reste bien différente de celle du modèle standard. L'asymétrie transverse $A_{\perp}$ apparaît à nouveau de signe opposé à celle du cas standard, et sa sensibilité à la masse du zino apparaît pour $\sqrt{s} \geq 150$ GeV.

b) Production de jauginos

L'étude de la production des partenaires fermioniques des bosons de jauge - ou jauginos - présente par rapport au cas précédent une difficulté supplémentaire; ces états physiques sont en effet des mélanges dont le paramètre est inconnu d'états fermioniques apparaissant dans les supermultiplets vec-

teurs de jauge - jaugino - et dans les supermultiplets chiraux de Higgs - Higgsino. L'étude théorique des asymétries de polarisation $\tilde{A}$ et $\tilde{A}$ qui a donc été faite[3] tient compte des différentes masses possibles pour les jauginos mais aussi de différentes valeurs de paramètres de mélange. Le cas qui apparaît le plus intéressant parmi les productions de paires de jauginos $e^+e^- \to \tilde{W}^+\tilde{W}^-$, $\tilde{\gamma}\tilde{\gamma}$, $\tilde{\gamma}\tilde{Z}$ et $\tilde{Z}\tilde{Z}$ semble être celui de la désintégration en particules chargées. En effet, sa section efficace est plus importante que les autres, de l'ordre du nanobarn au pic du Z. Si $2m_{\tilde{W}} < m_Z$ la production en paires de Winos sera accessible dans la première phase de LEP avant celle de W^+W^-, permettant ainsi un test du couplage $Z\tilde{W}^+\tilde{W}^-$ de Yang Mills avant celui de ZW^+W^-. Une étude de la dépendance en $\theta_{\tilde{W}}$ de $\tilde{A}$ à $\sqrt{s} = M_Z$ donne des résultats bien différents suivant différents modèles de mélange jaugino-Higgsino. Signalons aussi que $\tilde{A}$ apparaît très sensible à la masse du neutrino scalaire échangé pour une telle production.

3. Quarks et leptons partenaires supersymétriques de Goldstone?

Considérant une théorie supersymétrique dans laquelle le groupe d'invariance de dimension n est spontanément brisé en un sous-groupe de dimension m, il apparaîtra (n-m) superchamps chiraux de Goldstone, ou superGoldstone. La partie de spin 0 contiendra le pseudo-scalaire de Goldstone ainsi qu'un scalaire, et la partie fermionique un spineur de Weyl auquel pourra être associé un quark ou un lepton. Un problème à résoudre dans la considération de tels modèles, est celui de la brisure de supersymétrie permettant à la partie fermionique du Goldstone de rester légère, tandis que les scalaires deviennent très lourds et donc peuvent être ignorés à "faible" énergie.

Une explication à ce phénomène est peut-être apportée par un modèle de sac, confinant des particules supersymétriques dans une très petite région de l'espace[4]. Ce modèle est une généralisation du modèle de sac de MIT pour les quarks, dans lequel les contraintes de symétrie chirale sont responsables de bosons de Goldstone pseudoscalaires tels que les pions. Outre la brisure de la symétrie chirale, si les particules confinées sont supersymétriques, cette supersymétrie sera brisée à la frontière du sac, conséquence de la perte d'invariance par translation à la surface du sac. Considérons pour cela des supermultiplets chiraux dont les composantes seront appelées "urons", dans une petite partie de l'espace. A l'intérieur du sac les urons groupés en superchamps chiraux droits et gauches satisferont un Lagrangien supersymétrique et invariant sous un groupe $G_L \times G_R$, lequel sera brisé à la surface du sac en G_{L+R} par une

condition de bord supersymétrique. Afin de générer des supercourants axiaux continus à travers la surface, on introduira des superchamps de (pseudo) Goldstone à l'extérieur du sac (champs de "super-pions"), satisfaisant à présent l'hypothèse de super-PCAC. Un modèle de source statique pour la partie pseudoscalaire π du super-Goldstone permettra de relier sa masse m_π à la masse des urons m_{ur} et fournira pour des valeurs du rayon du sac r_B "petits" la relation $m_\pi \sim 2\sqrt{m_{ur}/r_B}$. Super-PCAC, la (non) conservation des supercourants (axiaux) vecteurs et la condition de bord supersymétrique donneront après de longs calculs, la simple relation de masse suivante entre urons et partenaire fermionique $\tilde{\pi}$ du pion : $m_{\tilde{\pi}} = 2m_{ur}$ (relation linéaire entre $m_{\tilde{\pi}}$ et m_{ur} en accord avec la version supersymétrique de la relation de Dashen). On voit donc que pour des petites valeurs de r_B, $m_{\tilde{\pi}} << m_\pi$. Quel est l'ordre de grandeur de r_B ? Si nous considérons des quarks légers, soit $m_{\tilde{\pi}} \sim 10$ MeV, sachant d'après les études expérimentales que les partenaires supersymétriques des quarks ne sont pas attendus à des masses inférieures à 20 GeV au moins, la relation précédente $r_B \sim 4m_{ur}/m_\pi^2 = 2m_{\tilde{\pi}}/m_\pi^2$ donne $r_B < 2 \times 10^{-6}$ GeV^{-1}.

Ce modèle dans lequel quarks et leptons apparaîtraient comme partenaires supersymétriques de bosons de Goldstone permet donc d'obtenir des fermions légers alors que les bosons de Goldstone restent très lourds. Reste à présent à obtenir un groupe d'invariance $G_L \times G_R$ permettant de produire ces fermions de Goldstone avec les nombres quantiques désirés et un "bon" Lagrangien d'interaction. Plusieurs groupes apparaissent comme des candidats potentiels, et c'est bien sûr à l'aide des modèles σ supersymétriques que nous espérons progresser.

4. Références

[1] "Physics at LEP", Cern Yellow Report 86.02 edited by J. Ellis and R. Peccei.

[2] P. Chiappetta, F.M. Renard, J. Soffer, P. Sorba and P. Taxil, Nucl. Phys. B259, 365 (1985).

[3] P. Chiappetta, F.M. Renard, J. Soffer, P. Sorba and P. Taxil, Nucl. Phys. B262, 495 (1985).

[4] G. Girardi, H. Högaasen and P. Sorba, Phys. Lett. 164B, 80 (1985).

THEO I :

2-D and 3-D hydrodynamics on lattice gases.

D. d'Humières and P. Lallemand, *Laboratoire de Physique de l'Ecole Normale Supérieure, 24 rue Lhomond, 75231 Paris Cedex 05, FRANCE.*

Abstract : The 2-D and 3-D Navier-Stokes equations are obtained from lattice gas models on regular lattices using particles speed zero, one and $\sqrt{2}$. Preliminary investigations of the linear behavior are presented for the two dimensional case.

1. Introduction

Lattice gases consist of particles moving in a fully discrete world. They are made of "Boolean particles", residing at the sites of a regular lattice. Their discrete velocities are chosen so that in a unit time they can propagate to a neighboring site. Several particles may be at a given site, but each velocity direction is subject to an exclusion principle of at most single occupancy. The updating of the lattice is done by alternating propagation and collision steps. The latter take place at each site and are chosen to have the same conservation laws as the true micro-world (i.e. particle number, momentum and energy) and no spurious unphysical conservation laws.

Hardy, de Pazzis and Pomeau (HPP) [1] first introduced lattice gas models on a square lattice. Despite interesting dynamical properties, this lattice gas was too simple to give realistic hydrodynamics. Frisch, Hasslacher and Pomeau (FHP) [2] have shown that similar lattice gases on a triangular lattice simulate the Navier-Stokes equation in two dimensions. This result is supported by several numerical simulations exhibiting good qualitative [3-5] or quantitative [4,6] agreement with usual hydrodynamics. Recently, d'Humières, Lallemand and Frisch [7] have extended the FHP result to the three dimensional case using particle speeds zero, one and $\sqrt{2}$. Contrary to HPP and FHP, this model has independent particle number and energy conservation relations. Thus, the density and temperature can be adjusted independently, and suitable combinations exist which make the non-linear term in the Navier-Stokes equations isotropic for both 2-D square and 3-D cubic lattices.

In the next section, we describe the model, recall the main results of ref. 7 and give the sound speed obtained by the first order Chapman-Enskog expansion. In section 3, we present preliminary investigations of this model on a 2-D square lattice using the relaxation technique described in ref. 4. However, since thermal effect exists in this model and the viscous stress tensor is anisotropic, the simulation results are more difficult to interpret than in the FHP case and we are still waiting theoritical progress to complete the measurement of the viscosities and thermal diffusion.

2. Multi speeds lattice gas models.

Let consider a gas of particles moving on a regular lattice of arbitrary dimensionality D, with possible velocities $\mathbf{c}_l$ taken along the links between nodes, within a given class of neighbourhood. In what follows, greek subscripts will refer to components of the D-dimensional vectors and capital roman indices to discrete velocities of particles. In the multi-speed models considered here, it may be convenient to write l=(i,j), where i refers to speeds (i=0 correspond to resting particles) and j refers to velocity directions.

Collision laws are assumed to conserve the number of particles, momentum ($\sum \mathbf{c}_l$) and energy ($\sum c_l^2$) at each node of the lattice. In terms of the local average population N_l of the l^{th} velocity direction, the local density ρ, momentum $\rho\mathbf{u}$ and energy density ρe are given by:

$$\rho = \sum_l N_l , \qquad \rho\mathbf{u} = \sum_l N_l \mathbf{c}_l , \qquad 2\rho e = \sum_l N_l c_l^2 ; \tag{1}$$

If detailed balance is assumed for the collision laws, it may be shown that the average populations N_l are given by Fermi-Dirac distibutions depending only on the collision invariants ρ, $\rho\mathbf{u}$ and e. For $\mathbf{u}=0$, the equilibrium populations only depend on ρ, e and c_i^2 and will be denoted d_i. For small $\mathbf{u}$, Taylor expansion of the Fermi-Dirac distibution and use of eqn.1 leads after some algebra to:

$$N_l = d_i + \beta_0 d_i(1-d_i)[\mathbf{c}_l.\mathbf{u} + (\alpha_2 + \gamma_2 c_i^2)u^2] + 0.5\,\beta_0^2 d_i(1-d_i)(1-2d_i)(\mathbf{c}_{ij}.\mathbf{u})^2 + O(u^3), \tag{2}$$

where

$$\beta_0 = -\rho D/(\sum_l d_i(1-d_i)c_l^2). \tag{3}$$

and the coefficients α_2 and γ_2, which depend on ρ and e, will not de needed.

Using the Boltzmann equation, which describe the space and time evolution of the populations N_l, and eqn. 2, one get the momentum equation which is given, up to the irrelevant terms, by:

$$\partial_t(\rho u_\alpha) + \sum_{\beta,\gamma,\delta} \partial_\beta(T_{\alpha\beta\gamma\varepsilon} u_\gamma u_\varepsilon) = -\partial_\alpha p + \sum_{\beta,\gamma,\varepsilon} \partial_\beta(S_{\alpha\beta\gamma\varepsilon}\partial_\gamma u_\varepsilon), \tag{4}$$

where the pressure p is given by:

$$p = (\sum_l d_i c_l^2)/D, \tag{5}$$

and the nonlinear term in (4) involves the fourth order completly symmetrical tensor:

$$T_{\alpha\beta\gamma\varepsilon} = 0.5\,\beta_0^2 \sum_l d_i(1-d_i)(1-2d_i) c_{l,\alpha} c_{l,\beta} c_{l,\gamma} c_{l,\varepsilon}. \tag{6}$$

In general, both tensors T and S are anisotropic and the dynamics of lattice gases is not isotropic as in usual fluids. However, the d_i can be adjusted to get

isotropic *inviscid* hydrodynamics. In particular, if one considers particles with speeds zero, one and $\sqrt{2}$, this condition can be writen:

$$d_1(1-d_1)(1-2d_1)=4\,d_2(1-d_2)(1-2d_2). \qquad (7)$$

for a square lattice, and:

$$d_1(1-d_1)(1-2d_1)=2\,d_2(1-d_2)(1-2d_2). \qquad (8)$$

for a cubic lattice.

In both cases, the collision laws are: head-on colliding particles leave head-off at a right angle (same as HPP), speed one particles colliding at right angle produce a rest particle and a speed $\sqrt{2}$ particle and conversely. In this case, d_0, d_1 and d_2 are related by:

$$d_0 d_2(1-d_1)^2 = d_1^2(1-d_0)(1-d_2). \qquad (9)$$

The diffusion term involves the fourth order tensor S which can be evaluated in the Boltzmann approximation using the Chapman-Enskog expansion [8,9] or represented by a Green-Kubo formula [1,10] in terms of equilibrium two-time correlations. The first order Chapman-Enskog expansion gives the sound speed:

$$c=\sqrt{[\textstyle\sum_i d_i(1-d_i)c_i^4] \,/\, [D\sum_i d_i(1-d_i)c_i^2]}, \qquad (10)$$

and shows the existence of two diffusive modes (viscous shear and thermal diffusion). The computation of the diffusion tensor requires the second order terms and will be presented elsewhere.

3. Linear hydrodynamics on a 2-D square lattice.

Using a lattice gas model on a square lattice, we have started numerical simulations to test the quantitative properties of these multi-speed models. For that, we consider particles with three different possible speeds: 0, 1 and $\sqrt{2}$. Zero velocity corresponds to rest particles, unit speed to particles moving along the lattice links to the four nearest neighbours, and speed $\sqrt{2}$ to particles moving diagonally along the lattice links to the four next-nearest neighbours. Thus this model require nine bits to code each site.

The collision rules are those given in the previous section, plus all the multi-particle interactions which conserve particle number, momentum and energy. The rest particles play a key role to mix both kinds of moving particles. Eqn. 9 holds despite the additional collision laws and was used along eqn. 1 to relate the populations d_i to ρ and e.

The linear dynamical properties of the gas were studied using the time relaxation of a periodic perturbation of the density, and velocity field as in ref. 4. As long as the dissipative phenomena can be neglected, the numerical results agree with the theory; in particular, the difference between the measured sound speed and its theoritical value, given by eqn. 10, is less than

10^{-3} for values in the available range $[1/\sqrt{2}, 1]$.

However, since viscous and thermal effect are mixed in both the sound waves and the thermal diffusion, the measurement of the diffusion coefficients is more difficult than in the FHP case. To separate the two effects, one need to define precisely the temperature and the heat flow. Due to the Fermi-Dirac statistics, the derivation of these quantities is not straightforward. Since the theoritical work was not done yet, we were unable to make more quantitative analysis of the simulation results.

4. Conclusion.

In conclusion, we have presented the first numerical results obtained for a multi-speed model. These simulations show that more theoritical works have to be done in order to make further analysis of the results for linear dynamics. This first step is absolutely necessary to start quantitative comparisons between results obtained on a triangular lattice and those obtained for a square lattice with everything adjusted, in theory, to get isotropic hydrodynamics. This kind of comparisons will provide tests of the practical interest of multi-speed model for 3-D hydrodynamics.

References.

[1] J. Hardy, O. de Pazzis and Y. Pomeau, Phys. Rev. **A13**, 1949 (1975).
[2] U. Frish, B. Hasslacher and Y. Pomeau, Phys. Rev. Lett. (1986).
[3] D. d'Humières, Y. Pomeau and P. Lallemand, C. R. Acad. Sci. Paris II, **301**, 1391 (1985).
[4] D. d'Humières, P. Lallemand and T. Shimomura, "An experimental study of lattice gas hydrodynamics", submitted to Phys. Rev. Lett. (1985).
[5] P. Salem and S. Wolfram, submitted to Phys. Rev. Lett. (1985).
[6] D. d'Humières and P. Lallemand, "Flow on a lattice gas between two parallel plates: development of the Poiseuille profile" C. R. Acad. Sci. Paris II (1986)..
[7] D. d'Humières, P. Lallemand and U. Frisch, "Lattice gas models for 3-D hydrodynamics" submitted to Europhysics Lett. (1986).
[8] R. Gatignol, "Théorie Cinétique des Gaz à Répartition Discrète de Vitesses" (Springer-Verlag, Lectures Notes in Physics, Berlin, 1975) and Refs. therein.
[9] J.P. Rivet and U. Frisch, C. R. Acad. Sci. Paris II, **302**, 267 (1986).
[10] H.S. Green, J. Math. Phys., **2**, 344 (1961).

ON THE ASYMPTOTICAL THEORY OF THE AMBIPOLAR DIFFUSION

Yu.S. Sayasov, Institute of Physics, University of Fribourg,
CH-1700 FRIBOURG, Switzerland

Basic equations describing diffusion of electrons and ions in a slightly ionized, slighly magnetized, isothermal plasma are known to be of the form [1]:

$$\frac{\partial n_e}{\partial t} = -\nabla \vec{j}_e + W, \qquad \vec{j}_e = -D_e \left(\nabla n_e + \frac{\vec{F}_e}{T} n_e\right)$$

$$\frac{\partial n_i}{\partial t} = -\nabla \vec{j}_i + W, \qquad \vec{j}_i = -D_i \left(\nabla n_i - \frac{\vec{F}_i}{T} n_i\right) \qquad (1)$$

$$\nabla_{\vec{r}} \vec{F} = 4\pi e^2 (n_i - n_e), \quad \vec{F}_{e,i} = \pm e \left(\vec{E} + \frac{1}{c}[\vec{u}_{e,i} \times \vec{B}_o]\right)$$

Here n_e, n_i, D_e, D_i, u_e, u_i are resp. densities, diffusion coefficients and hydrodynamical velocities of electrons and ions, W is their production rate, $\vec{E}$ is the electric field, $\vec{B}_o$ is an externae magnetic field, T is the plasma temperature. Following usual arguments due to Schottky one assumes that in plasmas characterised by a dimension L which is big compared to the plasma Debye-length $r_d = (T/4\pi n e_c^2)^{1/2}$ the densities of electrons and ions are equal, $n_e = n_i = n$, and their fluxes $\vec{j}_e$, $\vec{j}_i$ are equal as well, $\vec{j}_e = \vec{j}_i$, (here n_c is a characteristic density of electrons). With these assumptions one gets from (1) (for $\vec{B}_o = o$) the equations of the ambipolar diffusion approximation (ADA)

$$\frac{\partial n}{\partial t} = D_a \Delta n + W, \quad \vec{F} = e\vec{E} = -pT\nabla \ln n, \quad D_a = \frac{2D_i D_e}{D_e + D_i}, \quad p = \frac{D_e - D_i}{D_e + D_i} \qquad (2)$$

This procedure does not alow to evaluate the errors in ADA and is basicaly incomplete since for $n \to o$ the field $\vec{E}$, as shows (2), can tend to infinity.

Consequent theory of the ambipolar diffusion free from these ambiguities can be developed with a help of the asymptotical approach based on utilisation of the small parameter $\varepsilon=r_d^2/L^2$ [2]. In this paper this approach is modified and generalised in a few respects, ans is applied for investigation of some new problems. The asymptotical theory can be formulated in a most natural way with a help of the dimensionless variables $n=(n_i+n_e)/2n_c$, $\nu=(n_i-n_e)/2n_c$, $w=W/n_c$, $\vec{r}'=\vec{r}/L$ alowing to reduce (1) to the set of equations

$$\frac{\partial n}{\partial t} + p\frac{\partial \nu}{\partial t} = \frac{1}{L^2} D_a \nabla \left[\nabla n - \vec{f}\,\nu + \vec{f}_h (n-\nu)\right] + w \qquad (3)$$

$$p\frac{\partial n}{\partial t} + \frac{\partial \nu}{\partial t} = \frac{1}{L^2} D_a \nabla \left[\nabla n - \vec{f}\, n + \vec{f}_h (n-\nu)\right] + p\, w$$

$$\varepsilon \nabla \vec{f} = \nu, \quad \vec{f} = e\vec{E}, \quad \vec{f}_h = e\left[\vec{u}_e \times \vec{B}_o\right] / 2cT \qquad \text{(We have taken here } u_i=o)$$

We will consider now, using (3), a few particular cases.

1. Stationary non-magnetized bounded plasmas, e.g. the positive column of a gas discharge ($\vec{B}_o = o$)

In this case the terms $\partial n/\partial t$, $\partial \nu/\partial t$ in (3) must be omitted and the corresponding set of equations must be complemented by the boundary conditions $n(S)=o, \nu(S)=0$ following from the usual boundary conditions $n_e(S)=n_i(S)=0$ (here S is the plasma boundary). The set (3) allows solutions in the form of the expansions in powers of ε :

$$n = n_o+\varepsilon n_1+\ldots, \quad \nu=\varepsilon\nu_1+\ldots, \quad \vec{f} = \vec{f}_o+\varepsilon\vec{f}_1+\ldots$$

which, if inserted in (3), give in approximation ε^o just ADA. Nearby the plasma boundary h_o must have the form $n_o=\lambda z/L, \lambda=\partial n_o/\partial z$ where z is the distance counted from a point on S, along a normale to it. The coefficient λ is, in general, a function of position of this point. The correction n_1 can be shown to have for $z \to o$ the form $1/2p^2\lambda(L/z)^2$. The ADA breaks down if $n_o \approx \varepsilon n_1$ i.e. in the interval $\Delta Z \approx L^{1/3} r_d^{2/3}$ adjoining the boundary S. In the interval $o<z\approx\Delta z$ the asymptotical solutions must be replaced by some boundary layer solutions valid for $z \to o$. The boundary layer solutions for the component f of $\vec{f}$ normal to S can be shown to be defined to the terms of the order of $\varepsilon^{1/3}$ by the Painlevé equation, $f = \varepsilon^{1/3}\lambda^{1/3}\Psi(\xi)$,

$$\frac{d^2\Psi}{d\xi^2} - \frac{1}{2}\Psi^3 - \left[\xi - \frac{1}{2}\Psi^2(0)\right]\xi + p = 0, \quad \xi = \lambda^{1/3} z \cdot \varepsilon^{1/3} \qquad (4)$$

satisfying the boundary conditions $d\Psi/d\xi = 0$ for $\xi=0$, $\Psi=p/[\xi-(1/2)\Psi^2(o)]$ for $\xi \to \infty$. The ADA approximation (2) and (4) coincide in the common interval $\varepsilon^{1/3}L \ll z \ll L$. As follows from this representation the electric field E arising as a result of the ambipolar diffusion in the interval $z \approx \Delta z$ at the plasma boundary is of the order of $T/eL\varepsilon^{1/3}$ while the potential drop across of this boundary layer is of the order of $T\ell n\varepsilon^{-1/3}/e$.

2. Hall - effect in the diffusion - controlled plasmas

We will now consider a diffusion-controlled plasma situated between two parallel plates (where $n_e=n_i=o$) separated by the distance 2L in a magnetic field B_o directed parallel to the plates and perpendicular to electric current $en_e u$ flowing parallel to these plates. The equations (3) for this stationary problem reduce in case $W = k_i n_a n_e$ to

$$n'' - \frac{1}{2}\varepsilon f^{2''} - \alpha (n' - \varepsilon f'') + q^2 (n - \varepsilon f') = o \qquad (5)$$

$$\varepsilon f''' - (fn)' + \alpha (n' - \varepsilon f) + q^2 p (n - \varepsilon f') = o, \quad q^2 = \frac{k_i n_a L^2}{D_a} \qquad (6)$$

where $\alpha = |eU_H|/4T$, $U_H = 2LuB_{o/c}$ is the Hall-voltage, k_i is the ionisation constant, n_a is the neutral particle density; prime means differentiation over x/L,- $L<X<L$. Neglecting the terms containing the small parameter $\varepsilon=r_d^2/L^2$ we get the ADA equation

$$n_o'' - \alpha n_o' + q^2 n_o = o \qquad (7)$$

Its solution $n_o = e^{\alpha x'/2} \cos \frac{\pi}{2} x'$, $x' = x/L$, has a maximum at some point X_m shifted from the middle plane $x = o$ as a result of assymetry provoked by the magnetic field B_o. The distribution of the electric field E(x) directed perpendicular the plates and due both to the Hall effect and to the diffu-

sion can be now represented by the formula $f = eEL/_T = (p+1)\alpha + \tilde{f}$. In the interval $X_m \ll x \ll L$ the function $\tilde{f}$ is defined as
$\tilde{f} = - p\, d\, \ell n\, n_o/d\, x' \leftrightarrow \varepsilon^{1/3}\, \lambda_1^{1/3}\, \Psi_1(\xi), \xi = \lambda_1^{1/3}\, (1-x')/\varepsilon^{1/3}$, Ψ being a solution of (4) with $\lambda_1 = \frac{\pi}{2}\, e^{2\alpha}$. In the interval $-L \ll X \ll x_m$ $\tilde{f}$ is defined as $\tilde{f} = - p d \ell n n_o/dx' \leftrightarrow \varepsilon^{-1/3} \lambda_2^{1/3} \Psi_2(\xi)$, $\xi = \lambda_2^{1/3}(1+X')/\varepsilon^{1/3}$

where Ψ_2 is a solution of (4) with $\lambda_2 = \pi/2$ (The sign $\leftrightarrow$ means that the "left" representation goes over smoothly into the "right" representation for $x \to \pm L$)- The potential U between the plates is now defined as

$$U = \frac{T}{eL} \int_{-1}^{1} f dx' = \frac{1}{2}\,(1+P)U_H - \frac{TP}{e}\,\ell n\,\left(\frac{\lambda_1}{\lambda_2}\right)^{2/3} = \frac{1}{2}\,(1+P)U_H - \frac{1}{6}\,pU_H \qquad (8)$$

The part $\frac{1}{2}(1+P)U_H$ can be attributed to the Hall - effect while the part $U_d = -\frac{1}{6}\,pU_H$ is due to distorsion of the charge distribution provoked by diffusion. As $p \approx 1$ one can also put $U_d = -\frac{1}{6}\,U_H$. The diffusion effect leads, hence, to an additional voltage between the plates which is equal to one third of the Hall-voltage U_H and is directed opposite to it. One can show that this result obtained for isothermal plasmas must be replaced for strongly nonisothermal plasmas (i.e for $T_e \gg T_i$) by $U_d = -pU_H/3$.

It is necessary to note here that the effect of reduction of the Hall-voltage due to diffusion was investigated earlier in [3] with the help of ADA. It was found in [3] that the additional potential U_d is equal to $-U_H/2$ (instead of $-U_H/3$). This discrepancy is due to the fact that ADA for the field $E \sim -d\ell n n_o/dx'$ with n_o given by (7) leads to singularities at the boundaries $x' \to \pm 1$ and, hence, it can not be used for a consequent calculation of the voltage between the plates.

3. References

[1] Allis W.P. in: Handbuch der Physik, V. 21, p. 397, Springer (1956)
[2] Cohen I.M., Phys. Fluids 6, 1492 (1963)
[3] Kunkel W.B., Am. Journ. Physics 49, 733 (1981).

VISCOELASTICITY OF THE PEARSON GAS

F.Bavaud, Institut de Physique théorique, EPFL, CH-1015 Lausanne

Abstract : We discuss the viscoelastic properties of an exactly solvable statistical model, and the possibility of representing them by a rheological circuit.

1. Some background [1]

When a constant deformation u is applied to a mechanical system at t = 0, its stress τ increases with :

$$\Delta\tau_{\alpha\beta}(t) = (B_{\alpha\beta\gamma\delta} + K_{\alpha\beta\gamma\delta}(t))\ u_{\gamma\delta} \qquad (1.1)$$

where B is the static elastic moduli tensor, K(t) with $K(\infty) = 0$ is the relaxation function, related to the relaxation spectrum $R(\tau) \geq 0$ by

$$K_{\alpha\beta\gamma\delta}(t) = \int_0^\infty d\tau\ R_{\alpha\beta\gamma\delta}(\tau)\ \exp(-t/\tau) \qquad (1.2)$$

As a general rule, the Laplace transforms of the stress and the deformation are related by the response function :

$$\overline{\Delta\tau}_{\alpha\beta}(s) = H_{\alpha\beta\gamma\delta}(s)\bar{u}_{\gamma\delta}(s) \qquad (1.3)$$

$$H_{\alpha\beta\gamma\delta}(s) = B_{\alpha\beta\gamma\delta} + s\,\bar{K}_{\alpha\beta\gamma\delta}(s) \qquad (1.4)$$

Simple mechanical models are the spring of constant E and the dashpot of viscosity F, represented respectively by :

$$H(s) = E \qquad \text{—}\sim\sim\text{—}$$

$$H(s) = F\,s \qquad \text{—}[\,|\,\text{—} \qquad (1.5)$$

The circuit constructed by coupling in series or in parallel a finite number of these elements possesses a response function of the form :

$$H(s) = Q(s)/P(s) \quad , \quad \deg Q(s) \geq \deg P(s) \qquad (1.6)$$

where Q and P are polynomials in s.
For noninteracting independent particles, the statistical mechanical expression for the relaxation function is [2]:

$$K_{\alpha\beta\gamma\delta}(t) = \rho(kT)^{-1}m^2\{v_\alpha(t)v_\beta(t);v_\gamma(0)v_\delta(0)\} \qquad (1.7)$$

where {...} denotes statistical average.

2. The model

We consider a particle undergoing successive independent diffusions in $\mathbb{R}^2$. The diffusion length l, the diffusion angle θ and the time τ between diffusions are given respectively by the probability densities $p(l,\theta)$ and $f(\tau)$ (generalised Pearson walk [3]). The particle velocity is defined as the random variable $v_\alpha = l_\alpha/\tau, \alpha = 1,2$. Let $A(v_\alpha(t))$ be a velocity dependent observable. Computing the Laplace transform of its mean value, we get :

$$\{\bar{A}(v_\alpha(s))\} = s^{-1}\langle 1-\exp(-\tau s)\rangle^{-1}\langle (1-\exp(-\tau s))\, A(l_\alpha/\tau)\rangle \tag{2.1}$$

$$\langle \ldots \rangle = \int_0^\infty d\tau\, f(\tau) \int_0^\infty dl\, l \int_0^{2\pi} d\theta\, p(l,\theta) \ldots \tag{2.2}$$

(2.1) allows us to compute the initial and final value of the square of the velocity. We obtain :

$$\{v^2(0)\} = \lim_{s\to\infty} s\{\overline{v^2}(s)\} = \langle l^2\rangle\langle \tau^{-2}\rangle \tag{2.3}$$

$$\{v^2(\infty)\} = \lim_{s\to 0} s\{\overline{v^2}(s)\} = \langle l^2\rangle\langle \tau\rangle^{-1}\langle \tau^{-1}\rangle \tag{2.4}$$

By Jensen's inequality, $\langle \tau\rangle^{-1}\langle \tau^{-1}\rangle \leq \langle \tau^{-2}\rangle$ and the kinetic energy decreases: we are therefore dealing with a dissipative system. Its temperature is defined by :

$$2\,kT/m := \lim_{t\to\infty} \{v^2(t)\} = \langle l^2\rangle\langle \tau\rangle^{-1}\langle \tau^{-1}\rangle \tag{2.5}$$

We get also :

$$\{\bar{A}(v_\alpha(s))\, B(v_\gamma(0))\} = s^{-1}\langle (1-\exp(-\tau s))\, A(l_\alpha/\tau)\, B(l_\gamma/\tau)\rangle$$
$$+ s^{-1}\langle 1-\exp(-\tau s)\rangle^{-1}\langle (1-\exp(-\tau s))\, A(l_\alpha/\tau)\rangle\langle \exp(-\tau s)\, B(l_\gamma/\tau)\rangle \tag{2.6}$$

The diffusion coefficient is then given by :

$$2D := \int_0^\infty d\tau\, \{v_\alpha(\tau)\, v_\alpha(0)\} = \{\bar{v}_\alpha(0)\, v_\alpha(0)\} = \langle \tau^{-1}\rangle\langle l^2\rangle \tag{2.7}$$

where we assumed $\langle l_\alpha\rangle = 0$ in order to keep D finite. The pressure of the system is the one of the ideal gas. It is also the case for the elastic tensor B when $f(\tau)$ is the delta distribution and $p(l,\theta)$ is gaussian. The relaxation function (1.7) is :

$$\bar{K}_{\alpha\beta\gamma\delta}(s) = s^{-1}(kT)^{-1}\rho\, m^2 \big(\langle l_\alpha l_\beta l_\gamma l_\delta\rangle\langle (1-\exp(-\tau s))\, \tau^{-4}\rangle$$
$$- \langle l_\alpha l_\beta\rangle\langle l_\gamma l_\delta\rangle\langle 1-\exp(-\tau s)\rangle^{-1}\langle (1-\exp(-\tau s))\, \tau^{-2}\rangle^2 \big) \tag{2.8}$$

It is easy to see that the viscosity $\eta_{\alpha\beta\gamma\delta} := \bar{K}_{\alpha\beta\gamma\delta}(0)$ is non-negative, and is vanishing if and only if $f(\tau)$ and $p(l,\theta)$ are the

delta distributions, i.e. if the motion is determinist. As in the case of the kinetic energy, we find that the dissipative behavior is associated with the fluctuation of the trajectory. The response function $H_{\alpha\beta\gamma\delta}(s)$ is represented by

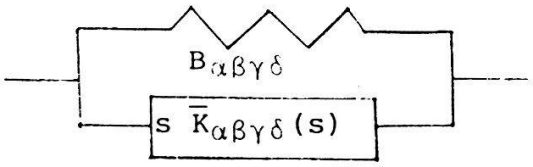

(2.9)

which leads to the infinite-frequency or adiabatic elastic tensor

$$B_{\alpha\beta\gamma\delta}(\infty) = B_{\alpha\beta\gamma\delta} + \lim_{s\to\infty} s\ \bar{K}_{\alpha\beta\gamma\delta}(s) \qquad (2.10)$$

In order to simplify what follows, we consider the shear component $(\alpha\beta\gamma\delta) = (1212)$, and assume $\langle l_1 l_2 \rangle = 0$. We get :

$$K(t) = \hat{\alpha} \int_t^\infty d\tau\ f(\tau)\ \tau^{-4} \qquad (\ \hat{\alpha} = \rho\ (kT)^{-1} m^2 \langle l_1^2 l_2^2 \rangle\ ) \qquad (2.11)$$

The problem which naturally arises is to decompose $s\ \bar{K}(s)$ into "springs and dashpots". But it appears that $s\ \bar{K}(s)$, as given by (2.8), cannot be of the form (1.6). If the circuit in question exists, it is therefore constitued by an infinite number of elements. Some trials get us to study the following infinite ladder network :

$s\ \bar{K}(s) =$

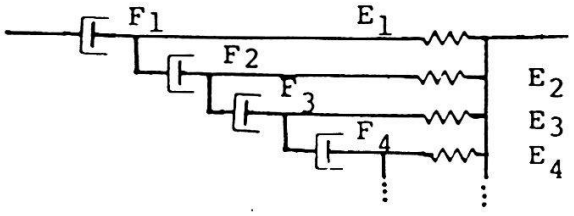

(2.12)

Independently of the particular model considered here, the following theorem holds [4] :

Theorem : the following statements are equivalent :

(a) $K(t)$ is completely monotonic in $(0,\infty)$, i.e. $K(t)$ is C^∞ and $(-1)^k\ K^{(k)}(t) \geq 0$, $k = 0,1,2...$

(b) $K(t)$ possesses a relaxation spectrum (1.2)

(c) $s\ \bar{K}(s)$ possesses the (unique) decomposition (2.12)

On the other hand, let $s\ \bar{K}_n(s)$ be given by the circuit (2.12), truncated by making repectively $E_n = \infty$, $F_n = 0$. Then $s\ \bar{K}_n(s)$ $(n=1,2,3...)$ is monoton decreasing, resp. increasing, with $s\ \bar{K}(s)$ as common limit.

For example, $f(\tau) = \delta(\tau - T)$ implies $K(t) = \hat{\alpha}\theta(T-t)\ T^{-4}$ (given a constant deformation beginning at $t = 0$, the required stress is constant for $t < T$ and vanishing afterwards. We suppose here

that B_{1212}, the shear modulus, is zero). Since K(t) is not C^{∞}, the decomposition (2.12) does not hold. An other example is provided by

$$f(\tau) = (1/6)\ a^4\ \tau^3\ \exp(-a\tau) \tag{2.13}$$

(the factor τ^3 insures the existence of $\bar{K}(s)$). The relaxation function is

$$K(t) = \hat{\gamma} \int_t^{\infty} d\tau\ \tau^{-1}\ \exp(-a\tau) \qquad (\ \hat{\gamma} = (\hat{\alpha}/6)\ a^4) \tag{2.14}$$

whose complete monotonicity is easily checked. We get :

$$s\ \bar{K}(s) = \hat{\gamma}\ \ln(1+s/a) = \cfrac{\hat{\gamma}\ s/a}{1 + \cfrac{s/a}{2 + \cfrac{s/a}{3 + \cfrac{4\ s/a}{4 + \cfrac{4\ s/a}{5 + \cfrac{9\ s/a}{\ddots}}}}}} \tag{2.15}$$

(See reference [5]). The identification of (2.12) and (2.14) leads finally to :

$$F_n = \frac{\hat{\gamma}}{(2n-1)\ a} \qquad E_n = \frac{\hat{\gamma}}{n} \tag{2.16}$$

3. Conclusion

The model presented here can be seen as a rigorous treatment of the elementary kinetic of gases [6]. Restricting the diffusion angles distribution to a sum of delta functions allows us to study lattice models. Finally, the representation of a physical system by a rheological circuit, considered as a purely formal device by some authors, appears here as possessing a firm foundation.

References

[1] B.Gross "Mathematical Structure of the Theories of Viscoelasticity " (Hermann 1953)
R.M.Christensen "Theory of Viscoelasticity" (Academic Press 1971)
[2] R.Balescu "Equilibrium and Nonequilibrium Statistical Mechanics " (Wiley 1975) p.675
[3] E.W.Montroll and J.L.Lebowitz "Studies in Statistical Mechanics, Vol.VII " (North-Holland 1979) p.74
[4] F.Bavaud , to be published
[5] O.Perron "Die Lehre von den Kettenbrüchen " (Chelsea Publishing Company 1929) p.349
[6] D.A.McQuarrie " Statistical Mechanics " (Harper and Row 1973) p.357

Transition rates in multistable systems with moderate noise

D. Ryter, Hasler AG, Research Labs, 3000 Bern 14

On the slow time scale of the transitions the system behaviour is shown to become a Markovian jump process, and a feasible computation of the transition rates is outlined. The technique applies much more widely than the well-known weak noise methods; in particular it also includes multiple transitions (e.g. of massive particles at low friction), and the nature of the attractors and of the transition regions is immaterial.
The validity is easily checked in every application. Particularly simple results hold for systems that are periodic in one of the state variables.

THEO II :

MOUVEMENT CHAOTIQUE ET UNIVERSALITE DES FLUCTUATIONS SPECTRALES

Oriol BOHIGAS, Marie-Joya GIANNONI et Charles SCHMIT
Division de Physique Théorique*, IPN, F-91406 Orsay

1. INTRODUCTION

"Comment se manifestent, dans un système quantique, les propriétés de singularité ou au contraire de stochasticité de la mécanique classique sous-jacente?". En d'autres mots, "peut-on déceler dans certaines propriétés quantiques des manifes-de chaoticité classique ?". Cette question, née des progrès récents dans l'analyse des propriétés de systèmes classiques chaotiques, présente un intérêt fondamental, notamment du point de vue de la compréhension des systèmes quantiques en termes semi-classiques. Les éléments de réponse apportés ici concernent des systèmes indépendants du temps, les "signatures" de chaos classiques étant recherchées dans les propriétés spectrales. Les concepts et techniques présentés ici sont développés dans la Réf.[BG-84].

2. FLUCTUATIONS SPECTRALES

A - L'outil

Considérons une suite de points $E_1,\ldots,E_n,\ldots$ distribués sur la demi-droite $\mathbb{R}^+$; Dans la suite, ces points représenteront des niveaux d'énergie d'un système quantique, ou des fréquences propres de vibration d'une membrane. Soit N(E) la densité cumulative de niveaux, égale au nombre de points E_i tels que $E_i \leqslant E$. N(E) est une fonction en escalier, que l'on peut décomposer en une partie moyenne $N_{av}(E)$ et une partie de fluctuations autour de la moyenne $N_{fl}(E)$:

$$N(E) = N_{av}(E) + N_{fl}(E) \quad . \qquad (1)$$

Pour illustrer la représentation (1) de N(E), considérons le spectre d'énergies propres de vibration d'une membrane ou, de façon équivalente, le spectre d'énergies d'une particule libre dans une boîte à deux dimensions ("billard quantique"). Pour des conditions de Dirichlet sur la frontière du billard, on sait que (Weyl-Kac) :

$$N(E) \underset{E\to\infty}{\sim} N_{av}(E) = \frac{\sigma}{4\pi} E - \frac{\gamma}{4\pi}\sqrt{E} + K + O(E^{-\eta/2} \ln \sqrt{E}) \quad [0<\eta\leqslant 1] \ , \qquad (2)$$

où le facteur σ du terme dominant représente *l'aire* du billard, γ est le *périmètre* de la frontière, et K est une constante contenant de l'information sur certaines propriétés géométriques et topologiques du billard. Toutes les expériences

* Laboratoire Associé au CNRS

numériques montrent que l'expression (2) de $N_{av}(E)$ est une remarquable représentation de la densité moyenne dès le bas du spectre, bien que (2) soit une formule asymptotique. Ainsi la connaissance de la densité de fréquences propres permet "d' entendre" l'aire et le périmètre de la membrane. Ces propriétés géométriques *macroscopiques* ne contiennent évidemment pas d'information sur la chaoticité du billard classique associé ; la densité moyenne $N_{av}(E)$ "n'entend" donc pas la nature —chaotique ou régulière— du billard, i.e. n'est pas sensible aux propriétés dynamiques, résultant de la géométrie du système à l'échelle *microscopique*. Qu'en est-il de la partie de fluctuations $N_{fl}(E)$? Les raisons suggérant de considérer $N_{fl}(E)$ comme un éventuel instrument de détection de chaos classique seront évoquées en 2-B. Nous présentons ici quelques éléments d'étude de $N_{fl}(E)$.

Avant d'étudier les fluctuations, il est nécessaire de s'affranchir des variations de la densité moyenne, en transformant le spectre initial $\{E_i\}$ en un spectre $\{\in_i\}$ de densité moyenne $\rho_{av}(\in) = \frac{dN_{av}(\in)}{d\in} = 1$, ou, de façon équivalente, d'espacement moyen entre premiers voisins normalisé à l'unité

$$<\in_{i+1} - \in_i> = 1. \qquad (3)$$

Le spectre $\{\in_i\}$ est transformé de $\{E_i\}$ par l'application $\in_i = N_{av}(E_i)$.

Les fluctuations sont complètement caractérisées par les fonctions de corrélation à k points. Nous considérons ici seulement

i) la distribution d'espacements $p(x)$ entre premiers voisins [$\int_0^\infty p(x)\,dx = 1$ d'après (3)]

ii) des quantités caractérisant la variable aléatoire $n(L)$ = nombre de niveaux présents dans un intervalle de longueur L [$<n(L)> = L$ d'après (3)] , comme la variance $\Sigma^2(L)$, l'asymétrie $\gamma_1(L)$ et l'excès $\gamma_2(L)$ [contenant de l'information respectivement sur les fonctions de corrélation à 2, 2+3, 2+3+4 points]

A titre d'exemple, citons deux cas extrêmes :

i) distribution en peigne de Dirac : $\in_n = n$. D'où $p(x)=\delta(x-1)$, et $\Sigma^2(L)=0$: dans tout intervalle de longueur L, on trouve exactement L niveaux : le spectre est parfaitement "rigide". Les *corrélations* entre niveaux sont *maximales*.

ii) distribution Poissonienne, définie par $p(x) = e^{-x}$, et par la condition *d'indépendance statistique* de tous les espacements $S_i = \in_{i+1} - \in_i$. Dans ce cas, on trouve en moyenne, dans un intervalle de longueur L, $L \pm \sqrt{L}$ niveaux ($\Sigma^2(L) = L$). Un tel spectre est très peu rigide, et donne une impression de grande irrégularité (petits espacements favorisés, d'où, en contrepartie, présence de "trous" dans le spectre).

B - Matrices aléatoires et spectres nucléaires

Pour décrire les résonances du noyau composé autour du seuil d'émission de neutrons, où la densité de niveaux est très forte, seule une théorie statistique était envisageable. Dans la théorie des matrices aléétoires (RMT), le Hamiltonien H est considéré comme une matrice stochastique NxN ; l'ensemble de matrices aléatoires est spécifié par la densité de probabilité $\mathcal{P}(H)\,dH$. Cette théorie se distingue par i) l'absence de paramètre ajustable ii) l'absence d'ingrédients physiques autres que des propriétés d'invariance.

Les deux ensembles auxquels il sera fait référence dans ce qui suit sont l'ensemble gaussien orthogonal (GOE) et l'ensemble gaussien unitaire (GUE). GOE et GUE sont respectivement adaptés à la description de systèmes invariants et non invariants par renversement du sens du temps. De nombreux résultats analytiques sont à présent connus pour les propriétés de fluctuations. La distribution d'espacement pour GOE est très bien représentée par $p(x) = \frac{\pi}{2} x \exp(-\frac{\pi}{4} x^2)$. Cette distribution est très différente de celle d'un spectre Poissonien (e^{-x}). En particulier, elle présente le phénomène de "*répulsion de niveaux*" (faibles espacements peu probables). La répulsion de niveaux est plus forte encore pour GUE : $p(x) \underset{x\sim o}{\sim} \frac{\pi^2}{3} x^2$ pour GUE, $p(x) \underset{x\sim o}{\sim} \frac{\pi^2}{6} x$ pour GOE. La variance $\Sigma^2(L)$ de la variable aléatoire n(L) est donnée, pour GOE, par $\Sigma^2(L) = \frac{2}{\pi^2} \ln L + 0.44$ $(L \gtrsim 1)$. La croissance logarithmique de $\Sigma^2(L)$ indique une *forte rigidité spectrale* (contrairement au cas Poissonien pour lequel la croissance est linéaire). $\Sigma^2(L)$ a le même type de comportement pour GUE, avec une rigidité plus forte (croissance en $\frac{1}{\pi^2} \ln L$).

Les résultats présentés dans la Fig.1 (reproduite de [HPB-82, BHP-85])

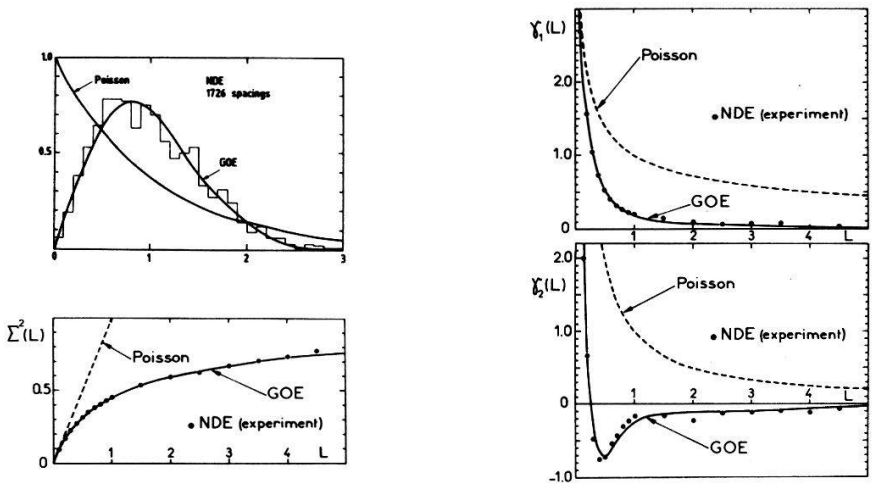

Fig. 1

proviennent de l'analyse d'environ 1700 énergies de résonances d'une trentaine de noyaux (NDE : nuclear data ensemble), et sont comparés aux prédictions de GOE et Poisson. L'accord avec GOE est remarquable, même pour des quantités aussi "fines" que $\gamma_1(L)$ et $\gamma_2(L)$, testant les corrélations à 3 et 4 points. Un tel pouvoir de prédiction d'une théorie sans paramètre ajustable et ne contenant pas d'information sur les propriétés spécifiques du noyau suggère l'existence d'une *universalité des lois de fluctuations*. Quelques analyses de spectres atomiques et moléculaires vont dans le sens de cette conjecture, sans toutefois être aussi convaincantes que dans le cas nucléaire (faibles échantillonnages, résonances mal séparées).

La question se pose donc de cerner le domaine d'universalité: les systèmes concernés possèdent-ils tous un grand nombre de degrés de liberté, ou bien sont-ils *complexes* en un autre sens à définir?

3. UNIVERSALITE DES FLUCTUATIONS SPECTRALES

A - Billards quantiques

L'idée que la complexité peut être entendue au sens "mouvement classique complexe", indépendamment du nombre de degrés de liberté, conduit à considérer des systèmes à deux dimensions, dont les analogues classiques sont *chaotiques*. Certains billards classiques ont la propriété d'être très fortement chaotiques. Le billard en forme de stade, par exemple, a un mouvement ergodique dans l'espace des phases, et les orbites se séparent exponentiellement (grande instabilité). Une première étude de ce système [MK-79] semblait indiquer le phénomène de répulsion de niveaux. Une analyse portant sur un millier d'énergies propres du billard quantique associé est représentée dans la figure 2 (reproduite de [BGS-

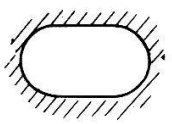

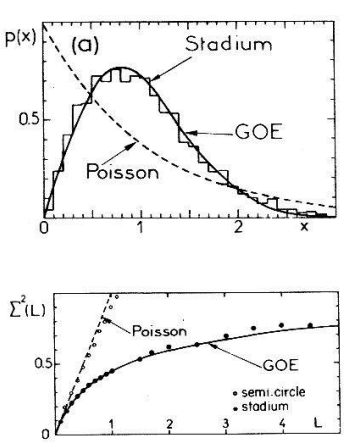

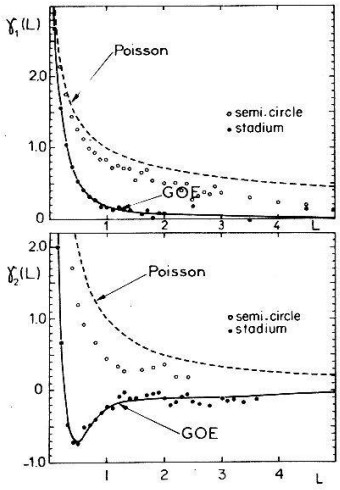

Fig. 2

84b]). A titre de comparaison, sont figurés également les résultats concernant le billard circulaire (système régulier car intégrable). Les fluctuations du billard circulaire sont en bon accord avec Poisson, résultat prédit pour les systèmes séparables [BT-77]. Au contraire, les fluctuations du billard stade suivent les lois GOE ; les mêmes conclusions ont été obtenues pour un autre billard chaotique, le billard de Sinai [BGS-84a]

B - Autres systèmes

Au cours des deux dernières années les expériences numériques sur d'autres systèmes à deux degrés de liberté se sont multipliées, et confirment la conjecture d'universalité pour des systèmes chaotiques invariants par renversement du sens du temps. Seligman et al [SVZ-84] étudient un système avec potentiels polynomiaux, dont la structure de l'espace des phases classique peut varier avec un paramètre ; ils observent une transition de Poisson à GOE lorsque le système passe de l'état intégrable à l'état ergodique. Des études d'autres systèmes conduisent à la même conclusion [HKC-84, IY-85] . Berry [Be-85] propose une dérivation de la rigidité spectrale en termes semi-classiques. Des travaux récents [JC-86, Iz-86] montrent que les fluctuations spectrales de l'opérateur d'évolution de systèmes typiques non conservatifs soumis à une perturbation périodique suivent également les lois GOE.

Pour des systèmes non-invariants par renversement du sens du temps, la théorie des matrices aléatoires prédit les propriétés de fluctuations de l'ensemble GUE. Les premières études [SV-85, BR-85, SGB-85] confirment qu'il y a également universalité des fluctuations spectrales (GUE) pour les systèmes non T-invariants.

L'existence de lois de fluctuations spectrales universelles est à présent bien établie, mais la question essentielle demeure : quelle est l'origine profonde de l'universalité, et quelle est son étendue ? Quels types de propriétés mathématiques d'opérateurs différentiels définissent les classes GOE et GUE ? Y-a-t-il d'autres types de spectres, non définis en termes de valeurs propres de matrices, possédant les propriétés d'universalité ? Il semble, par exemple ([Mo-74, Od-84]), que le spectre de zéros de la fonction ζ de Riemann obéissent aux lois de fluctuations de GUE ; cette conjecture renforce l'idée que l'universalité est encore loin d'être comprise, et que le sujet est encore largement ouvert.

REFERENCES

[Be-85] M.V. BERRY, Proc. Roy. Soc. London A400 (1985) 229.

[BG-84] O. BOHIGAS and M.J. GIANNONI, in Proceedings of the School "Mathematical and Computational Methods in Nuclear Physics", Granada 1983, J.S. Dehesa, J.M.G. Gomez and A. Polls (eds.), Springer-Verlag, 1984, pp. 1-99.

[BGS-84a] O. BOHIGAS, M.J. GIANNONI and C. SCHMIT, Phys. Rev. Lett. 52 (1984) 1.

[BGS-84b] O. BOHIGAS, M.J. GIANNONI and C. SCHMIT, J. Physique Lett. 45 (1984) L-1015.

[BHP-85] O. BOHIGAS, R.U. HAQ and A. PANDEY, Phys. Rev. Lett. 54 (1985) 1645.

[BR-85] M.V. BERRY and M. ROBNIK, to be published.

[BT-77] M.V. BERRY and M. TABOR, Proc. Roy. Soc. London A356 (1977) 375.

[HKC-84] E. HALLER, H. KÖPPEL and L.S. CEDERBAUM, Phys. Rev. Lett. 52 (1984) 1665.

[HPB-82] R.U. HAQ, A. PANDEY and O. BOHIGAS, Phys. Rev. Lett. 48 (1982) 1086.

[IY-85] T. ISHIKAWA and T. YUKAWA, Phys. Rev. Lett. 54 (1985) 1617.

[Iz-86] F.M. IZRAILEV, Phys. Rev. Lett. 56 (1986) 541.

[JC-86] J.V. JOSE and R. CORDERY, Phys. Rev. Lett. 56 (1986) 290.

[MK-79] S.W. McDONALD and A.N. KAUFMAN, Phys. Rev. Lett. 42 (1979) 1189.

[Mo-74] H.L. MONTGOMERY, Proc. of Int. Congr. of Mathematicians, Vancouver, 1974.

[Od-84] A. ODLYZKO, private communication, 1984.

[SGB-85] C. SCHMIT, M.J. GIANNONI and O. BOHIGAS, Proc. of Topical Meeting on Phase Space Approach to Nuclear Dynamics, I.C.T.P., 1985.

[SV-85] T.H. SELIGMAN and J.J.M. VERBAARSCHOT, Phys. Lett. 108A (1985) 183.

[SVZ-84] T.H. SELIGMAN, J.J.M. VERBAARSCHOT and M.R. ZIRNBAUER, Phys. Rev. Lett. 53 (1984) 456.

Symétrie d'échelle en phyllotaxie

F. Rothen et A.-J. Koch
Institut de Physique Expérimentale, 1015 Lausanne

La phyllotaxie est l'étude des arrangements floraux comme ceux des écailles d'ananas ou de pommes de pin, des inflorescences de marguerites ou de tourne-sols. On sait que les éléments de l'arrangement (écailles ou inflorescences) se disposent sur des spirales logarithmiques leur assurant une invariance de forme. Il est également notoire que les nombres de Fibonacci et le nombre d'or $\tau = \frac{5+1}{2}$ jouent un rôle important dans la phyllotaxie dite normale. Nous soulignons que cette phyllotaxie normale possède une symétrie supplémentaire vis-à-vis d'un changement d'échelle radiale, symétrie liée aux propriétés de τ.

Towards an ab initio determination of the mixing parameters in the Anderson model

L. Degiorgi, R. Monnier and D.D. Koelling*
Laboratorium für Festkörperphysik, ETH-Hönggerberg, 8093 Zürich
* Argonne National Laboratory, Argonne, Illinois 60439

We have developed a method for computing the mixing parameters in the Anderson degenerate impurity model for heavy rare earth compounds, based in a LCAO fit to a selfconsistent bandstructure calculation. Exitation Spectra (XPS and BIS) have then been calculated with an appropriate average of these mixing parameters within the many body formalism of Gunnarsson and Schönhammer. Applications to YbP and YbAs are presented.

Degenerate Hopf Bifurcation in the Presence of Symmetry

P.Jordan, H.Thomas
Institut für Physik, Klingelbergstr.82, CH-4056 Basel
K.-H.Höck
Institut für Festkörperphysik, THD, D-6100 Darmstadt, FRG

We study the bifurcation of periodic solutions from a stationary state of a dynamical system at an instability characterized by a degenerate complex-conjugate pair of eigenvalues. This case occurs generically in the presence of certain symmetries for order-parameter spaces of even dimension ≥ 4. At such a "degenerate Hopf bifurcation" there bifurcates a star of symmetry-related limit cycles, in analogy to the star of symmetry-related domains at a symmetry-breaking phase transition. For a specific example, we calculate by means of a bifurcation expansion the structure of the solutions and study their stability properties.

On the critical dynamics of one dimensional models

M. Droz, J. Kamphorst Leal da Silva and A. Malaspinas
Département de Physique Théorique, 1211 Genève 4

The critical slowing down of several one dimensional models is studied using different approaches both for Glauber and Kawasaki dynamics. For the q state Potts model it is found that the dynamic exponent z depends upon the chosen transition rate and the value of q. For a ferromagnetic Ising chain with two coupling constants ($J_1 > J_2$) the z exponent is found to be non universal, depending continuously of the ration J_1/J_2. The more general case is which J_1 and J_2 are randomly distributed is also discussed.

THEO III :

CONDITION DE CONSISTENCE DES THEORIES OBTENUES PAR REDUCTION DIMENSIONELLE ET MODELES G-INVARIANTS DE TYPE KALUZA-KLEIN

R. Coquereaux, Centre de Physique Theorique - CNRS, Luminy, 13288 MARSEILLE, France.

Ce que nous voyons et ce que nous mesurons (l'espace-temps à 4 dimensions M) est seulement, pensons nous, l'ombre d'une réalité qui se décrit à l'aide d'un espace-temps E dont la dimensionalité est (beaucoup) plus grande que quatre. Pour expliquer l'*apparence* quadri - dimensionelle de notre univers, nous devons supposer que certaines métriques de E jouent un rôle plus important que d'autres: la plus grande partie de l'information qui est codée dans ces métriques particulières peut être analysée et décrite en terme de l'espace - temps usuel M. Afin d'implémenter cette idée, nous devons tout d'abord spécifier la topologie ainsi que la structure différentiable de E, puis nous devons faire le choix d'un genre particulier de structure métrique sur E (cet "ansatz" doit être, en un sens, "dimensionellement réductible").

Supposons tout d'abord que E est un espace fibré dont la base est M et la fibre type est un espace homogène G/H (pour un groupe de Lie, G). Cette hypothèse de travail doit être précisée, en effet il existe des espaces qui, localement, peuvent s'écrire $M \times G/H$ et sur lesquels le groupe G agit globalement et d'autres espaces, qui localement s'écrivent de la même façon mais sur lesquels G n'agit pas. Rappelons que si G est un groupe de Lie non-abelien, il opère sur lui-même à gauche et à droite : nous avons une action du groupe $G \times G$ sur l'espace G; cependant, dans le cas d'un espace homogène $G/H = \{ gH, g \in G\}$, nous avons seulement une action du groupe $G \times N(H)|H$ sur l'espace G/H; N(H) étant le normalisateur de H dans G; l' action à gauche de G et celle, à droite de N(H)|H sur l'espace homogène (à gauche) G/H sont evidemment des opérations qui commutent. Si P désigne un espace fibré principal de base M et de groupe structural G, alors, il n'existe aucune action de G sur le fibré associé $E = P \times_G G/H$ qui, localement s'écrit pourtant comme $M \times G/H$, en effet nous avons divisé par l'action de G (par example, prenons $P=S^7$ et $E = S^7 \times_{SU(2)} S^2$, ici $S^2 = SU(2)/U(1)$, bien que E soit localement isomorphe à $S^4 \times S^2$, il n'existe aucune action (verticale) globale du groupe SU(2) sur E). Au contraire, si P désigne un espace fibré principal à gauche de base M et de groupe structural N(H)|H, nous pouvons

construire le fibré associé $E = P \times_{N(H)|H} G/H$; cet espace s'écrit encore localement $M \times G/H$ mais maintenant nous avons, sur cet espace, une action globale de G (par example, considérons $P=S^7=Sp(2)/Sp(1)$ comme un SU(2) fibré principal au dessus de S^4, et construisons $E = S^7 \times_{SU(2)} S^7$ _localement $S^4 \times S^7$_, nous utilisons ici la propriété pour $Sp(1) \times SU(2)$ d'être le normalisateur de Sp(1) dans Sp(2); il existe ici une action globale (verticale) de Sp(2) sur E).

Ce qui précède est assez bien connu mais revêt une certaine importance lorsque nous en venons à discuter les sortes de métriques "interessantes" sur E. Plusieurs catégories de métriques ont été proposées dans la litterature, elles ont le plus souvent définies en terme de coordonnées locales, et nous désirons maintenant effectuer quelques commentaires sur leur signification géométrique. L'extension la plus naturelle de la vieille idée de Kaluza-Klein consiste à choisir un espace E qui s'écrive localement $M \times G/H$, et sur lequel il existe une action globale de G, il ne reste plus alors qu'à considérer sur cet espace, une métrique G-invariante; cet approche a été considérée essentiellement par A. Jadczyk et l'auteur au sein d'une série d'articles [1],[2],[3],[4], et est de nos jours désignée sous le nom ansatz de Kaluza-Klein G-invariant; dans ce contexte, nous obtenons le "Théorème de réduction dimensionelle" : Il existe une correspondance bi-univoque entre les métriques G-invariantes sur E et les triplets $(\gamma_{\mu\nu}, A_\mu{}^{\hat{a}}, h_{\alpha\beta})$, où $\gamma_{\mu\nu}$ est une métrique sur la base M, $A_\mu{}^{\hat{a}}$ est un champ de Yang-Mills à valeurs dans l'algèbre de Lie de N(H)|H, et où l'ensemble des champs scalaires $h_{\alpha\beta}$ décrit une métrique G-invariante dans la copie de G/H au dessus ds $x \in M$. En particulier, la matrice $h_{\alpha\beta}(x)$ est soumise à une contrainte d'invariance par rapport à Ad(H). Le scalaire de courbure R^E, quantité qui apparait dans n'importe quel type raisonable de Lagrangien sur E, puisque la gravitation usuelle doit être décrite dans tout modèle, est alors une quantité constante le long des fibres c'est à dire une fonction de $x \in M$ seulement; son expression est donnée en (Eq.1). Notons qu'avant d'interpréter $R^E\ g^{1/2}$ comme un morceau du lagrangien effectif sur M, il est souhaitable d'effectuer une transformation conforme sur les champs $\gamma_{\mu\nu}(x)$ et $h_{\alpha\beta}(x)$, ce, afin d'éliminer le facteur lié à la variation de l'élément de volune interne $\gamma^{1/2}(x)$, cf .Eq 2. Il existe une autre sorte d'"ansatz" que nous désignerons sous le nom d' "ansatz populaire" et qui a été proposé par example dans [5],[6]; nous résumons ici sa signification géométrique; il existe en fait deux scenarii. Premier scenario: nous distinguons deux sous cas; si G opère globalement sur E nous construisons $\bar{E} = E \times G$, alors que si G n'opère pas, nous construisons $\bar{E} = P \times G/H$, où P -localement M×G- est le fibré principal associé à E; dans l'un comme

dans l'autre cas nous obtenons une action bien définie de GxG sur $\bar{E}$, et nous pouvons alors construire des métriques invariantes par GxG sur $\bar{E}$, ces dernières étant a fortiori G^{diag} -invariantes peuvent être définies au niveau du quotient $\bar{E}/G^{diag} = E$; les métriques que nous obtenons ainsi sur E ne sont pas G-invariantes en général. Le groupe de jauge émergeant d'une réduction dimensionelle directe de $\bar{E}$ to M serait $\bar{N}|\bar{H} \tilde{=} N|H \times G$. Deuxième scenario: nous considérons une métrique G-invariante sur l'espace fibré principal $P \tilde{=} M \times G$, une telle métrique est a fortiori invariante par rapport à un sous groupe H de G, une telle métrique peut alors être définie au niveau du quotient E = P/H; bien entendu, l'invariance par rapport à G est perdue après cette opération.

Pour un modèle donné (c'est à dire après avoir choisi un Lagrangien dans un espace -temps de dimension $d \geq 4$) on peut s'interesser à une certaine famille de métriques , c'est à dire faire le choix d'un "ansatz", et chercher si cette famille contient ou non des solutions; il se pose alors un problème de compatibilité ("consistency"). Un schéma _un ansatz_, est dit "consistent" s'il admet au moins une solution ("compactifying ground state solution") et si toute solution des équations de champ pour la théorie effective en dimension m (égale à 4 en général) peut aussi s'interpreter comme une solution de la théorie originelle à (m+s) dimensions. Nous prétendons que l'ansatz G-invariant est généralement consistent mais que l'ansatz populaire (qui n'est pas G-invariant) doit être en général consideré comme "coupable" d'inconsistence, à mons qu'il puisse prouver son innocence dans le cadre d'un modèle donné. Afin d'illustrer cette afirmation, nous considérons l'action d' Einstein-Hilbert dans E avec constante cosmologique Λ, c'est à dire le Lagrangien $\{(R^E - 2\Lambda)\sqrt{g}\}$; un calcul détaillé [4] montre que toute solution des équations de champ effectives (obtenues en calculant la variation de l'action effective en dimension m par rapport aux quantités $(\delta_{\mu\nu}, A_\mu{}^a, h_{\alpha\beta})$ ainsi qu'en tenant compte des contraintes d'Ad(H)-invariance sur les champs scalaires $h_{\alpha\beta}$ en introduisant des multiplicateurs de Lagrange), est aussi une solution des équations de champ originelle dans E (obtenues en calculant la variation de l' action en dimension d= m+s, par rapport à la métrique g de E). Par contre, l'ansatz populaire conduit généralement à des inconsistences qui sont liées au fait que la courbure scalaire dépend alors des coordonnées "internes", c'est à dire encore qu'elle ne dépend pas seulement des points de l'espace temps usuel M.

Eq. 1

$$R^E = R^M + R^{G/H} - 1/4\, F_{\mu\nu,\hat{a}} F_{\mu\nu,\hat{b}} - 1/4\, D_\mu h_{\alpha\beta} D_\mu h_{\alpha\beta} - 1/4\, h_\mu h_\mu - D_\mu h_\mu$$

$R^M(x)$ désigne la courbure scalaire de M pour la métrique $\delta_{\mu\nu}(x)$.

$R^{G/H}(x)$ désigne la courbure scalaire de G/H pour la métrique $h_{\alpha\beta}(x)$.

$F_{\mu\nu,\hat{a}}$ désigne la courbure de la connexion(le champ de Yang Mills $A_{\mu\hat{a}}$),

avec $h_\mu = h^{\alpha\beta} D_\mu h_{\alpha\beta}$,

et $D_\mu h_{\alpha\beta} = \partial_\mu h_{\alpha\beta} + C^{\delta}{}_{\alpha\hat{a}}\, A_\mu{}^{\hat{a}}\, h_{\delta\beta} + C^{\delta}{}_{\beta\hat{a}}\, A_\mu{}^{\hat{a}}\, h_{\alpha\delta}$.

Les indices μ, ν sont ceux de l'espace-temps usuel, les indices α,β sont ceux de G/H et les indices $\hat{a},\hat{b}$ ceux de l'algèbre de Lie de N(H)|H.

Les sommations à effectuer sur des indices répétés de même niveau doivent toujours être effectuées en utilisant $\delta_{\mu\nu}$, $h_{\alpha\beta}$ ou leurs inverses.

Eq. 2

$$R^E\, g^{1/2} = [\, R^M + R^{G/H} - 1/4\, F_{\mu\nu,\hat{a}} F_{\mu\nu,\hat{b}} - 1/4\, D_\mu \bar{h}_{\alpha\beta} D_\mu \bar{h}_{\alpha\beta} + 1/(4(d-2))\, \bar{h}_\mu \bar{h}_\mu \,]\, \bar{\delta}^{1/2} - \partial_\mu [(\bar{h}^\mu (\bar{h})^{-1/(d-2)}\, \bar{\delta}^{1/2}\,]$$

where

$$\bar{\delta}_{\mu\nu} = h^r\, \delta_{\mu\nu}\,, \quad \bar{h}_{\alpha\beta} = h^r\, h_{\alpha\beta}\,, \quad d = \dim M + \dim G/H$$

$$h = \det h_{\alpha\beta}\,, \qquad \bar{h} = \det \bar{h}_{\alpha\beta}\,, \quad r = 1/(\dim M - 2)$$

REFERENCES

[1] R. Coquereaux and A. Jadczyk, Comm. Math. Phys. 80 (1983) 79-100
[2] R. Coquereaux and A. Jadczyk, Comm. Math. Phys. 98 (1984) 97-104
[3] R. Coquereaux and A. Jadczyk, Class. Quantum Grav. 3 (1986) 29-42
[4] R. Coquereaux and A. Jadczyk, CERN-TH. 4305/85, à paraître dans Nucl. Phys. B.
[5] E. Witten, Nucl. Phys. B186 (1982) 412-428
[6] J. Strathdee, in "Unification of the fundamental particle interactions II", Eds J. Ellis and S. Ferrara, Plenum Press (1983)

Algèbre des anomalies dans les théories de jauge.

C. Viallet. L.P.T.H.E. Université P. et M. Curie. Tour 16, 1° Etage. 75230 PARIS 05.

Abstract: Anomalous terms in quantum gauge theories verify a consistency equation (Wess-Zumino[1]) which can be written as a problem of cohomology of the group of gauge transformations. By using the appropriate algebraic methods we solve [2] these equations for all dimensions of space-time and all structure groups (local "isospin" group) with reductive Lie algebra (ie: all groups which are a product of simple factors and abelian factors).

Quantum anomalies are the breaking, at the quantum level (generated by purely quantum interaction diagrams, especially fermion loops), of the classical gauge symmetry [3]. On the one side, the existence of such anomalies has been extensively used recently to rule out a number of theories [see A. Neveu's talk in this Conference]. On the other side, anomalous terms in the commutation of quantum currents (Schwinger terms) may not be a definitive obstacle to the definition of a coherent quantum theory [4]. It is then quite useful to know all possible anomalous terms for a given theory.

These terms have to verify a consistency equation (Wess-Zumino consistency equation [1]) which can be easily written if one uses the notion of Faddeev-Popov ghost χ [5], and the differential Becchi-Rouet-Stora operator δ to implement infinitesimal gauge transformations [6]: an anomaly $\mathcal{A}$ (e.g. the non vanishing variation of the quantum action under gauge transformations) is an integral over space-time of some polynomial Q in the fields (gauge potential, ghost,...) and their derivatives, such that

$$\delta \mathcal{A} = \delta \int Q = 0. \qquad \text{(eq. 1)}$$

This equation can be rewritten, with the help of the exterior differential $\mathbf{d}$ on space time [7]:

$$\delta Q + \mathbf{d} Q' = 0. \qquad \text{(eq. 2)}$$

where Q' is also some polynomial in the fields.

The differential operators $\mathbf{d}$ and δ verify (see later):

$$\mathbf{d}^2 = \delta^2 = (\mathbf{d} + \delta)^2 = 0. \qquad \text{(eq. 3)}$$

It is thus clear that any Q of the form

$$Q = \delta L + \mathbf{d} M. \qquad \text{(eq. 4)}$$

where L and M are polynomials in the fields, is automatically a solution of (eq. 2). In fact solutions of that form should be considered as spurious. They do not correspond to a true anomaly, for they can be absorbed in a redefinition of the action.

Solving the consistency equation amounts to solve (eq. 2) modulo solutions of (eq. 4) on the set of polynomials in the fields and their derivatives. This a typical problem of cohomology (*local* cohomology, see [8]).

We consider gauge theory over space-time of generic dimension D, with structure group G. The Lie algebra of G is denoted by $\mathbf{g}$. If T_α (α=1...dimG) is a basis of $\mathbf{g}$, we denote by $C^\alpha{}_{\beta\gamma}$ the structure constants, i.e:$[T_\beta,T_\gamma]=C^\alpha{}_{\beta\gamma}T_\alpha$.

We have to specify which polynomials of the fields we consider:

We shall take the algebra generated by the components (in $\mathbf{g}$) A^α, χ^α, F^α, $\mathbf{d}\chi^\alpha$,of the gauge potential A, the ghost χ, the curvature F (field strength $F^\alpha=\mathbf{d}A^\alpha+{}^1/_2\,C^\alpha{}_{\beta\gamma}A^\beta A^\gamma$), and differential of the ghost field $\mathbf{d}\chi$ respectively . This will be a restriction on the number and combinations of derivatives of the fields which appear.

There is a natural bidegree on such objects: (degree as form on space-time, ghost number)= ($\mathbf{d}$-degree, δ-degree). A is of bidegree (1,0), F is of bidegree (2,0), χ is of bidegree (0,1), and $\mathbf{d}\chi$ is of bidegree (1,1). The total degree is the sum of $\mathbf{d}$-degree and δ-degree.

We have the following action of $\mathbf{d}$ and δ:

$A^\alpha \to F^\alpha - {}^1/_2\,C^\alpha{}_{\beta\gamma}A^\beta A^\gamma$ (by $\mathbf{d}$) and $A^\alpha \to -\mathbf{d}\chi^\alpha - C^\alpha{}_{\beta\gamma}A^\beta\chi^\gamma$ (by δ)

$F^\alpha \to C^\alpha{}_{\beta\gamma}F^\beta A^\gamma$ $\qquad$ $F^\alpha \to C^\alpha{}_{\beta\gamma}F^\beta\chi^\gamma$

$\chi^\alpha \to \mathbf{d}\chi^\alpha$ $\qquad$ $\chi^\alpha \to -{}^1/_2\,C^\alpha{}_{\beta\gamma}\chi^\beta\chi^\gamma$

$\mathbf{d}\chi^\alpha \to 0$ $\qquad$ $\mathbf{d}\chi^\alpha \to -C^\alpha{}_{\beta\gamma}(\mathbf{d}\chi^\beta)\chi^\gamma$

We will call $\mathcal{A}(\mathbf{g})$ the space of <u>all</u> polynomials generated by A^α, χ^α, F^α,$\mathbf{d}\chi^\alpha$, with the only restriction that two monomials commute unless they are both of odd total degree, in which case they anticommute.

In other words $\mathcal{A}(\mathbf{g})$ is the free graded commutative algebra generated by A^α, χ^α, F^α, $\mathbf{d}\chi^\alpha$, or better $\mathcal{A}(\mathbf{g}) = \Lambda\mathbf{g}^* \otimes S\mathbf{g}^* \otimes \Lambda\mathbf{g}^* \otimes S\mathbf{g}^*$.

$\mathbf{d}$ and δ are extended to $\mathcal{A}(\mathbf{g})$ as two mutually anticommuting antiderivations of square zero. Clearly $\mathbf{d}$ (resp δ) incræses the $\mathbf{d}$-degree (resp δ-degree) by one unit.

$\mathcal{A}(\mathbf{g})$ can be decomposed according to the bidegree: $\mathcal{A}(\mathbf{g})=\oplus\mathcal{A}(\mathbf{g})^{r,s}$.

What we have to compute is the δ cohomology modulo $\mathbf{d}$, denoted $H(\delta|\mathbf{d})$ ($= \oplus\ H^{r,s}(\delta|\mathbf{d})$) , of $\mathcal{A}(\mathbf{g})$, that is to say find all polynomials Q in $\mathcal{A}(\mathbf{g})$ such that $\delta Q=0$ modulo the $\mathbf{d}$ of some Q', after factoring out all 'trivial' solutions of the form $Q=\delta L+\mathbf{d}M$ with L and M in $\mathcal{A}(\mathbf{g})$.

We will compute the cohomologies of $\mathbf{d}$, $\mathbf{d}+\delta$, and δ on $\mathcal{A}(\mathbf{g})$, (resp. $H(\mathbf{d})$, $H(\mathbf{d}+\delta)$, and $H(\delta)$), and then use them to solve our problem, with the help of some powerful concepts of (co)-homology theory.[9]

$H(\mathbf{d})$ is trivial (it reduces to $H^{0,0}=R$) because we may find a system of generators of $\mathcal{A}$ of the form $\{x_i,\mathbf{d}x_i\}$. This indeed implies the existence of a contracting homotopy k (antiderivation of degree minus 1):

k: $A^\alpha \to 0$, $\chi^\alpha \to 0$, $\mathbf{d}A^\alpha \to A^\alpha$, $\mathbf{d}\chi^\alpha \to \chi^\alpha$.

$N_d=k\mathbf{d}+\mathbf{d}k$ is invertible except on $H^{0,0}$: If $P\in\mathcal{A}$ verifies $\mathbf{d}P=0$, then $P=\mathbf{d}Q$ with $Q=N_d^{-1}kP$.

$H(\mathbf{d}+\delta)$ is trivial for the same reason. The corresponding system of generators is A^α, χ^α, $(\mathbf{d}+\delta)A^\alpha$, $(\mathbf{d}+\delta)\chi^\alpha$.

There is no such a thing as a contracting homotopy for δ. A system of generators of $\mathcal{A}$ is $\{A^\alpha,\ \delta A^\alpha,\ \chi^\alpha,\ F^\alpha\}$. It is only partially of the form $\{x_i,\delta x_i\}$. $H(\delta)$ thus reduces to the cohomology of δ on the algebra generated by $\{\chi^\alpha,F^\alpha\}$. This is a standard object: it is the cohomology $H(\mathbf{g},S\mathbf{g}^*)$ of $\mathbf{g}$ with values in the polynomials on $\mathbf{g}$.

For a reductive Lie algebra [10], we have $H(\mathbf{g},S\mathbf{g}^*)=\mathbf{I}_\Lambda\mathbf{g}\otimes\mathbf{I}_S\mathbf{g}$, where $\mathbf{I}_\Lambda\mathbf{g}$ is the algebra of invariant linear forms on $\mathbf{g}$ (known [11] to be the exterior algebra ΛP_0 of the space P_0 of invariant primitive forms on $\mathbf{g}$), and $\mathbf{I}_S\mathbf{g}$ is the space of invariant polynomials on $\mathbf{g}$. There is a correspondence between $\mathbf{I}_\Lambda g$ and $\mathbf{I}_S g$: one can construct an (in fact many non canonical) application τ (transgression), taking a basis of P_0 into a generating system of $\mathbf{I}_S\mathbf{g}$.

In other words $H(\delta)$ is generated in the reductive case by primitive forms $P(\chi,[\chi,\chi],\ldots,[\chi,\chi])$ and their transgression $P(F,F,\ldots,F)$, with $P\in\mathbf{I}_S\mathbf{g}$, e.g. $\mathrm{Tr}\chi^3$, $\mathrm{Tr}\chi^5$, $\mathrm{Tr}F^2$, $\mathrm{Tr}F^3$ for SU(3).

We see in particular that $H^{2r+1,s}=0$.

We then proceed in calculating $H(\delta|d)$. We first define $H^{ev}(\delta|d)$ as the part of $H(\delta|d)$ with even d-degree, and $H^{ev\ 0,0}=0$ and then relate it to $H(\delta)$ through an exact couple [9].

$$H^{ev}(\delta|d) \xrightarrow{\partial^2} H^{ev}(\delta|d), \qquad H^{ev}(\delta|d) \xrightarrow{p} H(\delta) \xrightarrow{i} H^{ev}(\delta|d)$$

∂: $H(\delta|d)\to H(\delta|d)$ is defined on representatives: if $\delta Q+dQ'=0$, ∂ of the class of Q in $H(\delta|d)$ is the class of Q' in $H(\delta|d)$.

i(class of Q in $H(\delta|d)$)= class of dQ in $H(\delta)$.

If $\delta Q=0$, p(class of Q in $H(\delta)$)=class of Q in $H(\delta|d)$.

It is straightforward to check that these mappings are indeed defined between the various cohomology classes, and that the triangle is exact at each corner (Kernel of a mapping = Image of the preceeding one).

Defining $E_0=H(\delta)$ and the antiderivation $d_0=i\bullet p$, we may construct the sequence of derived couples, leading to a spectral sequence (E_r,d_r), where $E_{r+1}=H(E_r,d_r)$. This is standard in cohomology theory.

We are able to calculate explicitely E_r and d_r:

$E_r=\Lambda P_r \otimes S\tau(P_r)$ where P_r is the vector space of primitive forms of degree $\geq 2r+1$.

On P_r, the antiderivation d_r is determined by: $d_r\omega=\tau(\omega)$ if ω is primitive of degree $2r+1$, and d_r vanishes on all other generators.

Finally, noticing that $H(\delta|\mathbf{d}) \approx \oplus_r E_r/\mathrm{Ker}\, p_r$ we get an explicit determination of all independent (non spurious) solutions of the Wess-Zumino consistency equation.

In particular, for the chiral anomaly (ghost degree 1), in a space-time of even dimension 2n, this shows that all possible anomalies are obtained from invariant polynomials on $\mathbf{g}$ of degree (n+1).

For higher ghost degree (for example Schwinger terms in the commutation of quantum currents), more complicated quantities appear, showing how δ cohomology modulo $\mathbf{d}$ is an enriched version of the cohomology of the Lie algebra $\mathbf{g}$ [see [2] for more details, and examples].

References:

[1] J. Wess,B. Zumino: Phys. Lett. 37B (1971), 95.
[2] M. Dubois-Violette, M. Talon, CM. Viallet: Phys. Lett. 158B (1985), 231.
Comm. Math. Phys. 102 (1985),105.
Ann. Inst. H. Poincaré 44 (1986),103.
[3] S Adler: Brandeis Summer School (1970). (M.I.T. Press).
[4] L. Faddeev: Phys. Lett. 145B (1984), 81.
[5] L. Faddeev, V.N. Popov: Phys. Lett. 25B (1967),29.
[6] C. Becchi, A. Rouet, R. Stora: Ann. Phys. 98 (1976), 287.
[7] J. A. Dixon: Cohomology and renormalisation of gauge theories (1976).
R. Stora: Cargèse Lectures 1976. M. Lévy, P.K. Mitter ed.(Plenum).
B. Zumino:LesHouches Lectures 1983. B.S. de Witt, R. Stora ed. (North-Holland).
R. Stora: Cargèse Lectures 1983. G. t'Hooft et al. ed.(Plenum).
J. Thierry-Mieg: Phys. Lett. 147B (1984), 430.
J. Manes, R. Stora, B. Zumino: Comm. Math. Phys. 102 (1985), 157.
[8] L. Bonora,P. Cotta-Ramusino: Comm. Math. Phys 87 (1983), 589.
[9] S. Mac Lane: Homology (Springer, 1963).
W. Greub, S. Halperin, R. Vanstone: Connections, Curvature and Cohomology, Vol 3 (Academic Press, 1976).
[10] G. Hochschild, J. P. Serre, Ann. Math. 57 (1953) 591.
[11] J. L. Koszul, Bull. Soc. Math. France 78 (1950) 65.

A Dodecagonal Quasiperiodic Lattice in Two Dimensions

P. Stampfli, freie Universität Berlin, FB 20 WE 5,
Arnimalle 14, D-1 Berlin 33, Germany

Abstract : We present a new planar quasiperiodic lattice with 12-fold rotational symmetry consisting of equal sided triangles, squares and rhombs as elementary units.There are isolated triangles which are not connected to other triangles through their sides. Two different methods of construction are discussed,one of them produces a lattice without any rhombs.We obtain good agreement with the quasicrystalline structure of small planar NiCr particles.

1. Introduction

Quasicrystals have only quasiperiodic rather than periodic translational symmetry,this allows rotational symmetries which are not allowed in crystals.Their properties have been discussed extensively (1,2).Small thin NiCr particles can have a 2-dimensional quasiperiodic structure with 12-fold rotational symmetry (3) .This structure is built of unit elements in the shape of equal sided triangles,squares and a few rhombs (30^{o} acute angle).

2. The first method of construction using a grid

Using the grid-method described in (2) it is easy to produce a quasiperiodic lattice of 12-fold rotational symmetry.But it would be impossible to obtain isolated triangles.That model fails to describe the NiCr structure in other respects too.Our method is more general than the one presented in (2).We use a grid composed of two periodic grids of regular hexagons rotated 90^{o} with respect to each other.For each point where 3 lines meet we have to draw an equal sided triangle and for each point where two lines cross a square or a rhomb with its sides perpendicular to the lines (fig. 1) .The resulting lattice is quasiperiodic with 12-fold rotational symmetry.It has a similar inflation property as the Penrose tiling (4).Rotating the lattice 15^{o} around the center of perfect rotational symmetry and increasing the lengths by a factor of $\sqrt{2+\sqrt{3}}$ we obtain a new lattice whose corner points match the ones of the original lattice (fig. 1).

The rhomboidal units represent vacancy defects and are essentially void in the NiCr structure.The space of two rhombs can be filled up by a square unit,requiring only local restructuring of the lattice constructed with the grid method.Very few rhombs remain as defects.The resulting structure is similar to fig. 2D and closely resembles the NiCr structure (3).

3. Second method of construction as a compound tesselation

A dodecagon can be devided into squares and equal sided triangles (fig. 2A).The squares and triangles themselves can be devided into smaller dodecagons,squares and triangles (fig. 2B,C).The length of their sides is smaller by a factor of $2 + \sqrt{3}$ .This process can be repeated to obtain a tiling of the whole plane.The ratio of the number of triangles to the number of squares is $4/\sqrt{3}$.

This becomes more transparent if we consider the corner points of the squares and the triangles.The process then replaces each point by the 19 points of a subdivided dodecagon (fig. 2A),the distance between the points being reduced by $2 + \sqrt{3}$ .Some points at the periphery of different dodecagons coincide.The triangles which have their corners at the point uniquely define the orientation of the dodecagon and the inscribed triangles and squares.

The resulting structure could represent a model of the ideal quasicrystalline NiCr structure without defects (or rhombs).

4. Conclusions

We have presented two different methods of construction of a quasiperiodic lattice which could serve as a crystallographic model for the quasycrystalline NiCr structure.The grid-method together with a reconstruction produces a lattice with few rhomboidal defects such as have been observed (3), whereas a compound tesselation produces an ideal lattice without defects.

Acknowledgements

It is a pleasure for me to thank H.-U. Nissen and T. Ishimasa for many stimulating discussions and helpful cooperation.Without their encouragement this work would not have been done.

References

(1) D. Levine and P.J. Steinhardt, Phys.Rev.Lett 53, 2477, (1984)

(2) J.E.S. Socolar, P.J. Steinhardt and D. Levine, Phys.Rev B 32, 5547, (1985)

(3) T. Ishimasa, H.-U. Nissen and Y. Fukano Phys.Rev.Lett 55, 511, (1985)

(4) M.Gardner, Scientific American 236, 110, (1977)

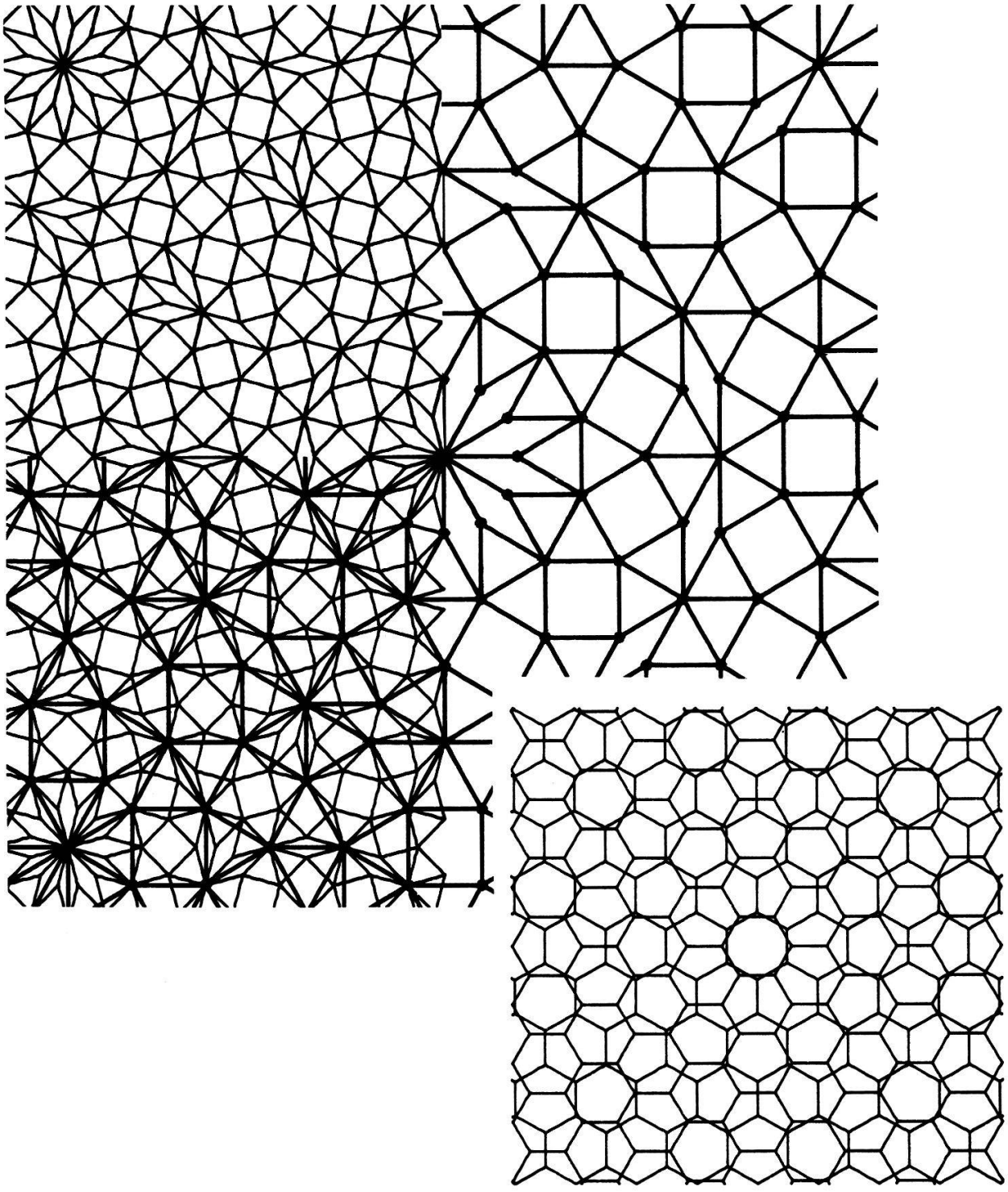

Figure 1

The new quasiperiodic lattice as obtained from the grid method. The left half demonstrates the inflation property discussed in the text. The inset at the right shows the grid used for construction.

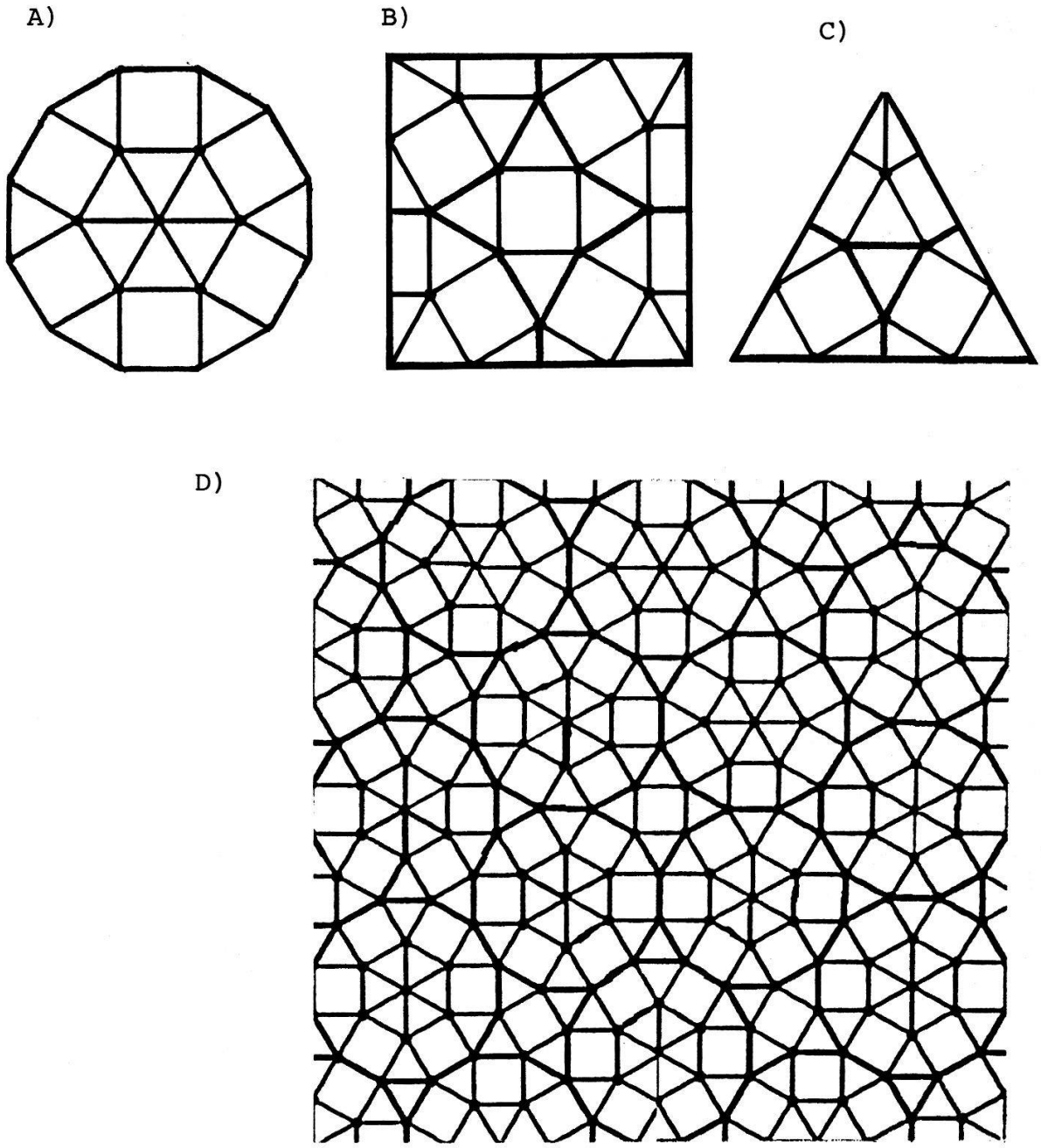

Figure 2

The dodecagonal compound tesselation.

With A) the decomposition of the dodecagon into squares and equal sided triangles, B) the subdivision of a square into dodecagons at its corners and squares and triangles, C) the subdivision of a triangle, D) a further subdivision of B) .Repeating this procedure we obtain a tesselation of the whole plane.

Spatially homogeneous torsion extending the Friedmann metric and the standard cosmological equations.

Peter Minkowski, Institut für theoretische Physik, Universität Bern, Sidlerstrasse 5, 3012 Bern

The Cartan-Einstein equations admit a unique extension including torsion compatible with homogeneity of space. This extension can reconcile spherical space geometry with open time evolution of the curvature radius.

Automated Reasoning: Theory

B.Humpert
HASLER Research Laboratories, CH-3000 BERN

We give an introduction into first-order predicate logic and its resolution techniques which allow for mathematical theorem proving and, more generally, for automated (or computer) reasoning.

Automated Reasoning: Applications

B.Humpert
HASLER Research Laboratories, CH-3000 BERN

Automated (or Computer) Reasoning is used in a number of fields such as: logic circuit design, logic circuit validation, mathematics, formal logic, real-time systems control, program debugging and verification, question answering, expert systems, ... and so on. We give an introduction into the applications of automated reasoning by simple examples.